PLACE IN RETURN BOX to remove this checkout from your record.
TO AVOID FINES return on or before date due.
MAY BE RECALLED with earlier due date if requested.

DATE DUE	DATE DUE	DATE DUE

5/08 K:/Proj/Acc&Pres/CIRC/DateDue.indd

ELECTROMAGNETIC MATERIAL CHARACTERIZATION OF A CONDUCTOR-BACKED MATERIAL USING THE TWO LAYER, TWO THICKNESS, AND TWO IRIS WAVEGUIDE PROBE METHODS: ERROR ANALYSIS, SIMULATION, AND EXPERIMENTAL RESULTS

VOLUME I

By

Gary Dean Dester

A DISSERTATION

Submitted to
Michigan State University
in partial fulfillment of the requirements
for the degree of

DOCTOR OF PHILOSOPHY

Electrical Engineering

2008

Copyright by

Gary Dean Dester

2008

ABSTRACT

ELECTROMAGNETIC MATERIAL CHARACTERIZATION OF A CONDUCTOR-BACKED MATERIAL USING THE TWO LAYER, TWO THICKNESS, AND TWO IRIS WAVEGUIDE PROBE METHODS: ERROR ANALYSIS, SIMULATION, AND EXPERIMENTAL RESULTS

By

Gary Dean Dester

Three material characterization techniques are investigated in this dissertation for their ability to extract the electromagnetic properties of a conductor-backed material *in situ*. All three techniques use a waveguide probe with a rectangular aperture placed against a conductor-backed layered material. To extract the complex material parameters, two independent complex measurements are needed. The first technique uses two thicknesses of the unknown material to obtain the two independent measurements. The second method uses a measurement of one layer of an unknown material, and a second measurement where a top layer of a known material is added. The third technique is a new method developed in this dissertation, which utilizes two irises of different sizes in the waveguide aperture to obtain the two measurements.

It is desirable in any material characterization method to understand the sensitivity of the method to errors. In this dissertation, the sensitivity of these three methods to random measurement errors is investigated. Since the fields in the waveguide aperture are approximated by using a finite number of transverse waveguide mode functions, the effect of the number of modes used in the material parameter extraction are also examined through simulation and experiment. Measurement data is used to extract the material parameters and evaluate the characterization methods.

The error sensitivity analysis, the modal analysis, and experimental results demonstrate that the two thickness method is the least sensitive to errors in the extraction

process. However, this method is not practical for use as an *in situ* technique, since the material parameters must be known *a priori*. It is found that the two layer method, with a low loss dielectric material as the top layer, and the two iris method work equally well in extracting the material parameters. They are, however, more sensitive to random measurement error than the two thickness method.

For Toni, Abigail, Emma, and Jadon

ACKNOWLEDGMENTS

I first want to thank my wife, Toni, for her support, encouragement, and motivation. If it wasn't for you, I would not have even considered going down this path. It has not been easy, but I appreciate all of the times you've been there to help me make it through. Second, I thank my children for being patient with me and understanding as I finished up this dissertation. I look forward to being with you and enjoying more time together.

I want to thank Dr. Ed Rothwell for all of his patient guidance, direction and teaching over the past three years. Thank you for your ideas about pursuing the two iris method, and providing much input for this dissertation. It has been a privilege to learn from you and I am thankful I have had the opportunity to study under you. I am still amazed that you took a chance on a 39-year-old who had not practiced engineering in 15 years! I am truly grateful. To Dr. Leo Kempel, thank you for always showing and expressing confidence in me. Your confidence and encouragement and help with the job search has been extremely valuable. To Dr. Shanker Balasubrimanian, thank you for the open door policy and excellence in teaching you have exhibited. Your insights into the world of electromagnetics have proven helpful to me time and time again. And the times on the basketball court gave me some much needed exercise! Thanks are also in order to Dr. Guowei Wei for agreeing to serve on my Ph.D. committee.

In addition, thank you to Dr. Mike Havrilla for several insightful conversations and help setting up the network analyzer. Most of the measurements in this thesis

were made possible through your insight into the experimental side of the material characterization problem. Thanks also to Captain James Stewart and Captain Milo Hyde, IV, from AFIT, for sharing measurement data and ideas with me. And also a huge thank you to Major Alan Albert, Garrett Stenholm, and Juan Calzada from AFRL for their role in sponsoring this research under UTC Subcontract 05-S508-017-C1. Thanks to all of my fellow students, office mates, and friends. You have made this an enjoyable journey.

Finally, and most importantly, thanks to Jesus Christ. I owe everything to Him.

TABLE OF CONTENTS

LIST OF TABLES xiv

LIST OF FIGURES xvi

KEY TO SYMBOLS AND ABBREVIATIONS xxxiii

CHAPTER 1
Introduction and Background 1
1.1 Introduction and Background 1
1.2 Related work 3
1.2.1 Free Space Methods 3
1.2.2 Coaxial Probe Methods 4
1.2.3 Waveguide Probe Methods 4
1.2.3.1 Conductor-backed material characterization 5
1.2.3.2 Characterization of both ϵ and μ 7
1.2.3.3 Modal Solution Analysis 8
1.2.3.4 Error sensitivity analysis 9
1.3 Overview of the research 10

CHAPTER 2
Electromagnetic Material Parameter Extraction Using the Two Layer Method and the Two Thickness Method 12
2.1 Introduction 12
2.2 Two Layer Method: Problem Overview 13
2.3 Two Layer Method Extraction Algorithm 16
2.4 Problem Formulation 19
2.4.1 Waveguide Fields 19
2.4.2 Parallel Plate Fields 20
2.5 MFIE and the Method of Moments Solution 22
2.6 The Two Thickness Method 26
2.6.1 Implementing the Two Thickness Method Algorithm Using the Two Layer Method 27

CHAPTER 3
Derivation of the Hertzian Potential Two Layer Parallel Plate Green's Function 29
3.1 Introduction 29
3.2 Problem Formulation 29
3.3 Hertzian Potential Expression of Electromagnetic Fields 31
3.4 Electric and Magnetic Field Boundary Conditions in Terms of Hertzian Potentials 32
3.5 Potential Boundary conditions for an x-directed source 33
3.5.1 Boundary Condition 1 33
3.5.2 Boundary Condition 2 34

3.5.3 Boundary Condition 3 34
3.5.4 Boundary Condition 4 35
3.5.5 Boundary Condition 5 36
3.5.6 Boundary Condition 6 36
3.5.7 Boundary Condition 7 36
3.5.8 Boundary Condition 8 37
3.5.9 Summary of Hertzian Potential Boundary Conditions for $\vec{J}_m = \hat{x}J_{1x}$ 37
3.6 Potential Boundary Conditions for y-directed Source 37
3.6.1 Boundary Condition 1 38
3.6.2 Boundary Condition 2 38
3.6.3 Boundary Condition 3 39
3.6.4 Boundary Condition 4 39
3.6.5 Boundary Condition 5 40
3.6.6 Boundary Condition 6 40
3.6.7 Boundary Condition 7 40
3.6.8 Boundary Condition 8 41
3.6.9 Summary of Hertzian Potential Boundary Conditions for $\vec{J}_m = \hat{y}J_{1y}$ 41
3.7 Formulation of Potentials in Parallel Plate Region 41
3.7.1 Source-Free, or Scattered Potential 42
3.7.2 Solution for Potential Due to Sources (Primary Potential) . . 44
3.7.3 Summary of Potential Representation 49
3.8 Calculation of the Hertzian Potential Green's Function in the Parallel Plate Region 50
3.8.1 Potential Due to an x-directed Source in Region 1 51
3.8.1.1 Summary of Potential Amplitude Equations for an x-directed Source in Region 1 59
3.8.1.2 Solution for the Amplitude Coefficients of the Upward and Downward Traveling Waves 60
3.8.1.3 x-directed potential 65
3.8.1.4 y-directed potential 68
3.8.1.5 z-directed potential 68
3.8.2 Potential due to a y-directed source in region 1 69
3.8.2.1 x-directed potential 69
3.8.2.2 y-directed potential 69
3.8.2.3 z-directed potential 70

CHAPTER 4
Numerical Solution of the Two Layer MFIE 72
4.1 Introduction 72
4.2 The Forcing Function 72
4.3 The Coupling Matrix, A 73
4.4 Solution to the Matrix Equation for TE and TM Mode Coupling . . . 83
4.4.1 Case 1: $TE_{un\,vn}$ source with $TE_{um\,vm}$ observer 83

4.4.2 Case 2: $TE_{un\,vn}$ source with $TM_{um\,vm}$ observer 87
4.4.3 Case 3: $TM_{un\,vn}$ source with $TE_{um\,vm}$ observer 89
4.4.4 Case 4: $TM_{un\,vn}$ source with $TM_{um\,vm}$ observer 91
4.5 Numerical computation of the matrix elements A_{mn} 92
4.5.1 Integration in k_y 93
4.5.1.1 Singular points on the k_y axis 94
4.5.2 Integration in k_x 102
4.6 Numerical Integration Implementation Notes 103

CHAPTER 5
Modal Analysis of the Two Layer and Two Thickness Methods of Material Parameter Extraction 105
5.1 Introduction 105
5.2 How many modes are necessary? 105
5.3 Generation of S_{11}^{thy} for a single conductor-backed layer. 107
5.4 Generation of S_{11}^{thy} for a two-layered conductor-backed material stack 111
5.5 Extrapolated values of S_{11}^{thy} at X-band 112
5.6 Modal analysis of extracted parameters 115
5.6.1 Two Thickness Method Modal Analysis 131
5.6.2 Two Layer Method Modal Analysis 136
5.6.2.1 Two Layers of Eccosorb FGM125 136
5.6.2.2 Top Layer of Nylon, Bottom Layer of Eccosorb FGM125 139
5.7 Conclusions 148

CHAPTER 6
Sensitivity Analysis due to Measurement Error in the Two Thickness Method and Two Layer Method 154
6.1 Introduction 154
6.2 Definitions 154
6.3 Assumptions for this Error Sensitivity Analysis 155
6.4 Random noise propagation of errors 157
6.4.1 Calculation of derivatives 162
6.4.2 Confidence Interval 164
6.5 Monte Carlo Method 164
6.5.1 Normally distributed random noise generation 165
6.5.2 Comparison of the Monte Carlo method and the standard propagation of errors 167
6.6 Sensitivity Analysis for the Two Thickness Method and Two Layer Method 169
6.7 Error sensitivity analysis results 175
6.8 Sensitivity analysis for additional materials as a top layer 178
6.9 Variations in thicknesses 181
6.10 Error Sensitivity Conclusions 185

CHAPTER 7
Two Iris Method 187
7.1 Introduction 187
7.2 Two Iris Algorithm 187
7.3 Problem Formulation 188
7.3.1 Waveguide and Aperture Fields 188
7.4 Parallel Plate Fields 192
7.5 Matching Boundary Conditions 192
7.5.1 Matching Tangential Electric Fields at $z = d_2$ 193
7.5.2 Matching Tangential Magnetic Fields at $z = d_2$ 194
7.5.3 Matching Tangential Magnetic Fields at $z = 0$ 196
7.6 Matrix Equation 198
7.6.1 Right hand side 200
7.6.2 Evaluation of $\int_{\Omega_{ap}} \vec{e}_m^{wg}(\vec{\rho}) \cdot \vec{e}_n^{ap}(\vec{\rho})\, ds$ used in D_2 and D_3 . . . 201
7.6.2.1 Case 1, $TE^{wg}_{um\,vm} \cdot TE^{ap}_{un\,vn}$ 201
7.6.2.2 Case 2, $TE^{wg}_{um\,vm} \cdot TM^{ap}_{un\,vn}$ 201
7.6.2.3 Case 3, $TM^{wg}_{um\,vm} \cdot TE^{ap}_{un\,vn}$ 202
7.6.2.4 Case 4, $TM^{wg}_{um\,vm} \cdot TM^{ap}_{un\,vn}$ 202
7.6.3 Evaluation of $\int_{\Omega_{ap}} \vec{h}_m^{ap}(\vec{\rho}) \cdot \vec{h}_n^{wg}(\vec{\rho}) ds$ used in D_4 and b_2 203
7.6.3.1 Case 1, $TE^{ap}_{um\,vm} \cdot TE^{wg}_{un\,vn}$ 203
7.6.3.2 Case 2, $TE^{ap}_{um\,vm} \cdot TM^{wg}_{un\,vn}$ 203
7.6.3.3 Case 3, $TM^{ap}_{um\,vm} \cdot TE^{wg}_{un\,vn}$ 204
7.6.3.4 Case 4, $TM^{ap}_{um\,vm} \cdot TM^{wg}_{un\,vn}$ 204
7.6.4 Evaluation of $\int_{\Omega_{ap}} \vec{h}_m^{ap}(\vec{\rho}) \cdot \vec{h}_n^{pp}(\vec{\rho})\, ds$ used in D_8 and D_9 . . . 205
7.6.4.1 Integral formulation 205
7.6.4.2 Case 1, $TE^{ap}_{um\,vm} \cdot TE^{ap}_{un\,vn}$ 209
7.6.4.3 Case 2, $TE_{um\,vm} \cdot TM_{un\,vn}$ 211
7.6.4.4 Case 3, $TM_{um\,vm} \cdot TE_{un\,vn}$ 212
7.6.4.5 Case 4, $TM_{um\,vm} \cdot TM_{un\,vn}$ 213
7.7 Numerical Computation of the matrix elements D^8_{mn} 214
7.7.1 Reduction to one-sided integrals 215
7.7.2 Examination of poles on the real k_x and k_y axes. 220
7.7.2.1 Evaluation of poles on the real k_y axis 221
7.7.2.2 Evaluation of poles on the real k_x axis 227
7.8 Implementation 229

CHAPTER 8
Two Aperture Modal Analysis and Error Sensitivity Analysis 230
8.1 Introduction 230
8.2 Reflection Coefficient Analysis 230
8.2.1 Aperture Geometries 231
8.3 Extrapolation procedure 237
8.4 Sensitivity Analysis for the Two Aperture Method 257
8.5 Modal Analysis for Aperture H 269

8.6 Simulation Conclusions 274

CHAPTER 9
Experimental Material Parameter Extractions Using the Two Layer Method, Two Thickness Method, and the Two Iris Method. 276
9.1 Introduction 276
9.2 Experimental Setup 276
9.2.1 Calibration 278
9.2.2 VNA settings 280
9.2.3 Measurement Procedure 280
9.2.4 Sample materials 281
9.2.5 Measurement Position 282
9.3 Two Thickness Method Results 282
9.3.1 Introduction 282
9.3.2 Measured reflection coefficients 283
9.3.3 Extraction results 284
9.3.4 Two thickness extraction of Eccosorb FGM40 302
9.4 Two Layer Method 312
9.4.1 Modal Analysis for 2 layers of Eccosorb FGM125 312
9.4.2 Additional Analysis for Two Layers of Eccosorb FGM125 . . . 318
9.4.3 Two Layer Method Extractions with Plastic Top Layer 320
9.5 Two Iris Method 336
9.5.1 Measurement vs. Theory 341
9.5.2 Modal Analysis 341
9.5.2.1 Discussion of Modal Analysis 348
9.5.3 Two Iris Method Extractions 349
9.6 Discussion of Results for Eccosorb FGM125 363

CHAPTER 10
Conclusions 369
10.1 Suggestions for Future work 371

APPENDIX A
Waveguide Transverse Mode Functions and Associated Integrals 374
A.1 Transverse Waveguide Mode Functions 374
A.2 Normalization constants 376
A.3 Calculation of $f_{xn}(k_x, k_y)$, $f_{yn}(k_x, k_y)$, $g_{xm}(k_x, k_y)$, and $g_{ym}(k_x, k_y)$. 377
A.3.1 Function values for TE_z modes 380
A.3.2 Function values for TM_z modes 381

APPENDIX B
Derivative Equality 383

APPENDIX C
The Relationship of the Single Layer and Two Layer Parallel Plate Green's Functions 385
C.1 Case 1: $z' > z$ 388
C.2 Case 2: $z' < z$ 389

APPENDIX D
Waveguide Cutoff Frequencies for WR-90 Waveguide 393

APPENDIX E
Transverse Aperture Mode Functions and Associated Integrals 395
E.1 Transverse Aperture Mode Functions 395
E.2 Calculation of $f_{xn}^{ap}(k_x, k_y)$, $f_{yn}^{ap}(k_x, k_y)$, $g_{xm}^{ap}(k_x, k_y)$, and $g_{ym}^{ap}(k_x, k_y)$. 397
E.2.1 Function values for TE_z modes 398
E.2.2 Function values for TM_z modes 400
E.3 Evaluation of Integrals Used in the Two Iris Method 401
E.3.1 Integral used in D_2 and D_3 401
E.3.2 Calculation of the Integral used in D_4 and b_2 403

APPENDIX F
Nominal Material Parameters used in Simulations and Extractions 406

BIBLIOGRAPHY 412

LIST OF TABLES

Table 4.1 Value of the function $Q(k_y)$ at the singular points 101

Table 5.1 Material parameters for Eccossorb FGM125, $\epsilon = \epsilon_0(\epsilon'_r - j\epsilon''_r)$ and $\mu = \mu_0(\mu'_r - j\mu''_r)$. These data were obtained using the waveguide T/R method. Data provided by Captain Milo Hyde IV from the Air Force Institute of Technology, Wright-Patterson AFB, Dayton, OH. 108

Table 5.2 Key for modes used in the two thickness and two layer extraction methods, for two thicknesses of Eccosorb FGM125 135

Table 5.3 Key for modes used in 2 Layer Extraction Method using Nylon as the top layer. 150

Table 6.1 Potential sources of error in the two layer and two thickness methods 157

Table 6.2 Mean, μ, and standard deviation, σ, for the Monte Carlo method and standard deviation, σ, for the standard error propagation method of the two thickness method. Simulation was for two thicknesses of Eccossorb FGM125, 0.125" and 0.250" thick. 166

Table 8.1 Key for modes used in two aperture extraction method, Aperture H 269

Table 9.1 Actual measured dimensions of Aperture WR and Aperture H. . . 278

Table 9.2 Material samples used in the material parameter extraction methods. 282

Table 9.3 Key for modes used in the two thickness method extraction of experimental data. 287

Table 9.4 Key for modes used in two iris extraction method, Aperture H and Aperture WR 343

Table D.1 Index of waveguide modes and cutoff frequencies for WR-90 Waveguide 394

Table F.1 Nominal material parameters for Plexiglass, $\epsilon = \epsilon_0(\epsilon'_r - j\epsilon''_r)$ and $\mu = \mu_0(\mu'_r - j\mu''_r)$. These data were obtained using the waveguide T/R method. Data provided by Captain Milo Hyde IV from the Air Force Institute of Technology, Wright-Patterson AFB, Dayton, OH. 406

Table F.2 Nominal material parameters for Nylon, $\epsilon = \epsilon_0(\epsilon'_r - j\epsilon''_r)$ and $\mu = \mu_0(\mu'_r - j\mu''_r)$. These values were estimated from data found in [6], Figures 27 and 28, and were used in simulations and two layer method extractions. 407

Table F.3 Nominal material parameters for PVC, $\epsilon = \epsilon_0(\epsilon'_r - j\epsilon''_r)$ and $\mu = \mu_0(\mu'_r - j\mu''_r)$. These values were estimated from data found in [6], Figures 27 and 28, and were used in simulations and two layer method extractions. 408

Table F.4 Nominal material parameters for FGM40, $\epsilon = \epsilon_0(\epsilon_r' - j\epsilon_r'')$ and $\mu = \mu_0(\mu_r' - j\mu_r'')$. These data were obtained using the waveguide T/R method. Data provided by Captain Milo Hyde IV from the Air Force Institute of Technology, Wright-Patterson AFB, Dayton, OH. 409

Table F.5 Material parameters for Material 1.5, $\epsilon = \epsilon_0(\epsilon_r' - j\epsilon_r'')$ and $\mu = \mu_0(\mu_r' - j\mu_r'')$. These values are for a fictitious material and are used in the sensitivity analysis to simulate a low loss, low-dielectric constant material 410

LIST OF FIGURES

Figure 2.1 Side view (a) and top view (b) for two layers of material interrogated by a single waveguide probe 14

Figure 2.2 Measurement of reflection coefficient on (a) one layer of material and (b) two layers of material 17

Figure 3.1 Geometry for a two-layered material bounded by parallel PEC plates, infinite in the x- and y-directions. 30

Figure 3.2 The contour integral in the complex k_z plane for $z > 0$ 47

Figure 4.1 Plot of $|F_1(k_x, k_y)|$ in the complex k_y plane at 10.0 GHz. This plot created with $k_x = 10$, 0.125" thick layer of Plexiglass on top of Eccosorb FGM125, 0.125" thick, using $TE_{1\,0}$ source mode coupling with $TM_{1\,2}$ observer mode. 95

Figure 5.1 Magnitude and phase of the reflection coefficient for 1 layer of Eccosorb FGM125, 0.125" thick, at 8.2 GHz, using different numbers of modes in the solution. 113

Figure 5.2 Magnitude of S_{11}^{thy} for 1 layer of Eccosorb FGM125, 0.125" thick, at 8.2 GHz. 114

Figure 5.3 Magnitude and phase of the reflection coefficient for 1 layer of Eccosorb FGM125, 0.125" thick, at 8.2 GHz, using only modes that contribute significantly to the solution. The reflection coefficient is computed by including the modes up to the $TM_{1\,v}$ mode. These values are plotted vs. $1/v$. 115

Figure 5.4 Magnitude and phase of the reflection coefficient for 1 layer of Eccosorb FGM125, 0.125" thick, at 10.09 GHz, using only the modes that contribute significantly to the solution. The reflection coefficient is computed by including the modes up to the $TM_{1\,v}$ mode. These values are plotted vs. $1/v$. 116

Figure 5.5 Magnitude and phase of the reflection coefficient for 1 layer of Eccosorb FGM125, 0.125" thick, at 12.40 GHz, using only the modes that contribute significantly to the solution. The reflection coefficient is computed by including the modes up to the $TM_{1\,v}$ mode. These values are plotted vs. $1/v$. 117

Figure 5.6 Magnitude and phase of the reflection coefficient for 1 layer of Eccosorb FGM125, 0.250" thick, at 10.09 GHz. 118

Figure 5.7 Magnitude and phase of the reflection coefficient for 1 layer of Eccosorb FGM125, 0.250" thick, at 10.09 GHz, using only the modes that contribute significantly to the solution. The reflection coefficient is computed by including the modes up to the $TM_{1\,v}$ mode. These values are plotted vs. $1/v$. 119

Figure 5.8 Magnitude and phase of the reflection coefficient for 1 layer of Plexiglass 0.125" thick on top of a 0.125" layer of Eccosorb FGM125, at 10.09 GHz. 120

Figure 5.9 Magnitude and phase of the reflection coefficient for 1 layer of Plexiglass 0.125" thick on top of a 0.125" thick layer of Eccosorb FGM125, at 10.09 GHz. Horizontal axis is the reciprocal of the number of modes used in the solution. 121

Figure 5.10 Magnitude and phase of the reflection coefficient for 1 layer of Plexiglass, 0.125" thick, on top of Eccosorb FGM125, 0.125" thick, at 8.2 GHz, using only the modes that contribute significantly to the solution. The reflection coefficient is computed by including the modes up to the $TM_{1\,v}$ mode. These values are plotted vs. $1/v$. 122

Figure 5.11 Magnitude and phase of the reflection coefficient for 1 layer of Plexiglass, 0.125" thick, on top of Eccosorb FGM125, 0.125" thick, at 10.09 GHz, using only the modes that contribute significantly to the solution. The reflection coefficient is computed by including the modes up to the $TM_{1\,v}$ mode. These values are plotted vs. $1/v$. 123

Figure 5.12 Magnitude and phase of the reflection coefficient for 1 layer of Nylon, 0.125" thick, on top of Eccosorb FGM125, 0.125" thick, at 10.09 GHz, using only the modes that contribute significantly to the solution. The reflection coefficient is computed by including the modes up to the $TM_{1\,v}$ mode. These values are plotted vs. $1/v$. 124

Figure 5.13 Magnitude and phase of the reflection coefficient for 1 layer of FGM40, 0.040" thick, on top of Eccosorb FGM125, 0.125" thick, at 10.09 GHz, using only the modes that contribute significantly to the solution. The reflection coefficient is computed by including the modes up to the $TM_{1\,v}$ mode. These values are plotted vs. $1/v$. 125

Figure 5.14 Extrapolated values of the magnitude and phase of S_{11}^{thy} for 1 layer of Eccosorb FGM125, 0.125" thick, and Eccosorb FGM125, 0.250" thick, for 8.2-12.4 GHz. Linear extrapolation was performed using $TM_{1\,62}$ and $TM_{1\,60}$ modes. 126

Figure 5.15 Extrapolated values of the magnitude and phase of S_{11}^{thy} for 1 layer of Eccosorb FGM40, 0.040" thick for 8.2-12.4 GHz. Linear extrapolation was performed using $TM_{1\,40}$ and $TM_{1\,38}$ modes. 127

Figure 5.16 Extrapolated values of the magnitude and phase of S_{11}^{thy} for 1 layer of Eccosorb FGM40, 0.040" thick on top of 1 layer of Eccosorb FGM125, 0.125" thick, for 8.2-12.4 GHz. Linear extrapolation was performed using $TM_{1\,40}$ and $TM_{1\,38}$ modes. 128

Figure 5.17 Extrapolated values of the magnitude and phase of S_{11}^{thy} for 1 layer of Plexiglass, 0.125" thick on top of 1 layer of Eccosorb FGM125, 0.125" thick, for 8.2-12.4 GHz. Linear extrapolation was performed using $TM_{1\,16}$ and $TM_{1\,14}$ modes. 129

Figure 5.18 Extrapolated values of the magnitude and phase of S_{11}^{thy} for 1 layer of Nylon, 0.125" thick on top of 1 layer of Eccosorb FGM125, 0.125" thick, for 8.2-12.4 GHz. Linear extrapolation was performed using $TM_{1\,16}$ and $TM_{1\,14}$ modes. 130

Figure 5.19 Extrapolated values of the magnitude and phase of S_{11}^{thy} for 1 layer of PVC, 0.119" thick on top of 1 layer of Eccosorb FGM125, 0.125" thick, for 8.2-12.4 GHz. Linear extrapolation was performed using $TM_{1\,16}$ and $TM_{1\,14}$ modes. 133

Figure 5.20 Extracted values of ϵ_r' using the two thickness method with different modes in the extraction. Extraction was simulated for two thicknesses of Eccosorb FGM125, 0.125" and 0.250" thick, for 8.2-12.4 GHz. Nominal values were used to generate $S_{11(1T)}^{extr}$ and $S_{11(2T)}^{extr}$. The key for each line is found in Table 5.2. 134

Figure 5.21 Extracted values of ϵ_r'' using the two thickness method with different modes in the extraction. Extraction was simulated for two thicknesses of Eccosorb FGM125, 0.125" and 0.250" thick, for 8.2-12.4 GHz. Nominal values were used to generate $S_{11(1T)}^{extr}$ and $S_{11(2T)}^{extr}$. The key for each line is found in Table 5.2. 135

Figure 5.22 Extracted values of μ_r' for the two thickness method with different modes in the extraction. Extraction was simulated for two thicknesses of Eccosorb FGM125, 0.125" and 0.250" thick, for 8.2-12.4 GHz. Nominal values were used to generate $S_{11(1T)}^{extr}$ and $S_{11(2T)}^{extr}$. The key for each line is found in Table 5.2. 140

Figure 5.23 Extracted values of μ_r'' for the two thickness method with different modes in the extraction. Extraction was simulated for Eccosorb FGM125, 0.125" and 0.250" thick, for 8.2-12.4 GHz. Nominal values were used to generate $S_{11(1T)}^{extr}$ and $S_{11(2T)}^{extr}$. The key for each line is found in Table 5.2. 141

Figure 5.24 Extracted values of ϵ_r' for the two layer method with different modes in the extraction. Extraction was simulated for a bottom layer of Eccosorb FGM125, 0.125" thick. The top layer was also a layer of Eccosorb FGM125, 0.125" thick. Simulations are over 8.2-12.4 GHz. Nominal values were used to generate $S_{11(1)}^{extr}$ and $S_{11(2)}^{extr}$, and nominal values were used for the top layer in the extraction. The key for each line is found in Table 5.2. 142

Figure 5.25 Extracted values of ϵ_r'' for the two layer method with different modes in the extraction. Extraction was simulated for a bottom layer of Eccosorb FGM125, 0.125" thick. The top layer was also a layer of Eccosorb FGM125, 0.125" thick. Simulations are over 8.2-12.4 GHz. Nominal values were used to generate $S_{11(1)}^{extr}$ and $S_{11(2)}^{extr}$, and nominal values were used for the top layer in the extraction. The key for each line is found in Table 5.2. 143

Figure 5.26 Extracted values of μ_r' for the two layer method with different modes in the extraction. Extraction was simulated for a bottom layer of Eccosorb FGM125, 0.125" thick. The top layer was also a layer of Eccosorb FGM125, 0.125" thick. Simulations are over 8.2-12.4 GHz. Nominal values were used to generate $S_{11(1)}^{extr}$ and $S_{11(2)}^{extr}$, and nominal values were used for the top layer in the extraction. The key for each line is found in Table 5.2. 144

Figure 5.27 Extracted values of μ_r'' for the two layer method with different modes in the extraction. Extraction was simulated for a bottom layer of Eccosorb FGM125, 0.125" thick. The top layer was also a layer of Eccosorb FGM125, 0.125" thick. Simulations are over 8.2-12.4 GHz. Nominal values were used to generate $S_{11(1)}^{extr}$ and $S_{11(2)}^{extr}$, and nominal values were used for the top layer in the extraction. The key for each line is found in Table 5.2. 145

Figure 5.28 Extracted values of ϵ_r' for the two layer method with different modes in the extraction. Extraction was simulated for a bottom layer of Eccosorb FGM125, 0.125" thick. The top layer was also a layer of Nylon, 0.125" thick. Simulations are over 8.2-12.4 GHz. Nominal values were used to generate $S_{11(1)}^{extr}$ and $S_{11(2)}^{extr}$, and nominal values were used for the top layer in the extraction. Key for each line in the plot is found in Table 5.3 150

Figure 5.29 Extracted values of ϵ_r'' for the two layer method with different modes in the extraction. Extraction was simulated for a bottom layer of Eccosorb FGM125, 0.125" thick. The top layer was also a layer of Nylon, 0.125" thick. Simulations are over 8.2-12.4 GHz. Nominal values were used to generate $S_{11(1)}^{extr}$ and $S_{11(2)}^{extr}$, and nominal values were used for the top layer in the extraction. Key for each line in the plot is found in Table 5.3 151

Figure 5.30 Extracted values of μ_r' for the two layer method with different modes in the extraction. Extraction was simulated for a bottom layer of Eccosorb FGM125, 0.125" thick. The top layer was also a layer of Nylon, 0.125" thick. Simulations are over 8.2-12.4 GHz. Nominal values were used to generate $S_{11(1)}^{extr}$ and $S_{11(2)}^{extr}$, and nominal values were used for the top layer in the extraction. Key for each line in the plot is found in Table 5.3 152

Figure 5.31 Extracted values of μ_r'' for the two layer method with different modes in the extraction. Extraction was simulated for a bottom layer of Eccosorb FGM125, 0.125" thick. The top layer was also a layer of Nylon, 0.125" thick. Simulations are over 8.2-12.4 GHz. Nominal values were used to generate $S_{11(1)}^{extr}$ and $S_{11(2)}^{extr}$, and nominal values were used for the top layer in the extraction. Key for each line in the plot is found in Table 5.3 153

Figure 6.1 Normal distribution, with mean μ, and standard deviation, σ. . . 159

Figure 6.2 Worst case error for measurements on HP8510, from "HP8510 Specifications & Performance Verification Program". Figure reproduced with permission from [57]. 160

Figure 6.3 A histogram of the extracted parameters using the Monte Carlo Method. M is the number in each bin out of the 60 samples. . . . 168

Figure 6.4 The derivatives calculated from 8.2 - 12.4GHz in the computation of $\sigma_{\epsilon_r'}$. Derivatives were calculated for the two layer and two thickness methods for two layers/thicknesses of Eccosorb FGM125, 0.125" thick and 0.250" thick. 171

Figure 6.5 The derivatives calculated from 8.2 - 12.4GHz in the computation of $\sigma_{\epsilon_r''}$. Derivatives were calculated for the two layer and two thickness methods for two layers/thicknesses of Eccosorb FGM125, 0.125" thick and 0.250" thick. 172

Figure 6.6 The derivatives calculated from 8.2 - 12.4GHz in the computation of $\sigma_{\mu_r'}$. Derivatives were calculated for the two layer and two thickness methods for two layers/thicknesses of Eccosorb FGM125, 0.125" thick and 0.250" thick. 173

Figure 6.7 The derivatives calculated from 8.2 - 12.4GHz in the computation of $\sigma_{\mu_r''}$. Derivatives were calculated for the two layer and two thickness methods for two layers/thicknesses of Eccosorb FGM125, 0.125" thick and 0.250" thick. 174

Figure 6.8 Sensitivity analysis for the two layer and two thickness methods for two layers of Eccosorb FGM125, 0.125" thick and 0.250" thick. Error bars show the 95% confidence level due to network analyzer uncertainty from an HP8510 network analyzer. 176

Figure 6.9 Normalized standard deviation of the two layer method using different layers for the top layer. The following thicknesses are used for the top layer: FGM125 = 0.125",.FGM40 = .040", Plexiglass = 0.125", Nylon = 0.125", PVC = 0.119". Bottom layer is Eccosorb FGM 125, 0.125" thick. Each plot is normalized to the two thickness method for comparison. 180

Figure 6.10 Standard deviation of the two layer method using different thicknesses for a top layer of Plexiglass at 10.09 GHz. The bottom layer was simulated as 0.125" of Eccosorb FGM125. 181

Figure 6.11 Standard deviation of the two layer method using different thicknesses for a top layer of Rexolite at 10.09 GHz. The bottom layer was simulated as 0.125" of Eccosorb FGM125. 182

Figure 6.12 Standard deviation of the two layer method using different thicknesses for a top layer of Material 1.5 at 10.09 GHz. The bottom layer was simulated as 0.125" of Eccosorb FGM125. 183

Figure 7.1 Side view for a single layer of material interrogated by a reduced aperture waveguide probe. 189

Figure 7.2 Top view for a single layer of material interrogated by a reduced aperture waveguide probe. 191

Figure 7.3 The poles of $M_1(k_x, k_y)$ in the complex k_y plane. 222

Figure 8.1 Apertures A-D for the two iris method. 232

Figure 8.2 Apertures E-H for the two iris method 232

Figure 8.3 Plot of $|S_{11}^{thy(2I)}|$ as a function of number of modes for Apertures A, B, C and D at 8.2 GHz. Aperture thickness, d_2 =0.125". Material under test: Eccosorb FGM125, $h = 0.125''$. All possible modes are considered. 238

Figure 8.4 Plot of the phase of $S_{11}^{thy(2I)}$ as a function of number of modes for Apertures A, B, C and D at 8.2 GHz. Aperture thickness, d_2 =0.125". Material under test: Eccosorb FGM125, $h = 0.125''$. All possible modes are considered. 239

Figure 8.5 Plot of $|S_{11}^{thy(2I)}|$ as a function of number of modes for Apertures E, F, G, and H at 8.2 GHz. Aperture thickness, d_2 =0.125". Material under test: Eccosorb FGM125, $h = 0.125''$. All possible modes are considered. 240

Figure 8.6 Plot of the phase of $S_{11}^{thy(2I)}$ as a function of number of modes for Apertures E, F, G, and H at 8.2 GHz. Aperture thickness, d_2 =0.125". Material under test: Eccosorb FGM125, $h = 0.125''$. All possible modes are considered. 241

Figure 8.7 Plot of $|S_{11}^{thy(2I)}|$ as a function of number of modes for Apertures A and B at 10.09 GHz. Aperture thickness, d_2 =0.125". Material under test: Eccosorb FGM125, $h = 0.125''$. All possible modes are considered. 242

Figure 8.8 Plot of the phase of $S_{11}^{thy(2I)}$ as a function of number of modes for Apertures A and B at 10.09 GHz. Aperture thickness, d_2 =0.125". Material under test: Eccosorb FGM125, $h = 0.125''$. All possible modes are considered. 243

Figure 8.9 Plot of $|S_{11}^{thy(2I)}|$ as a function of number of modes for Apertures C and D at 10.09 GHz. Aperture thickness, d_2 =0.125". Material under test: Eccosorb FGM125, $h = 0.125''$. All possible modes are considered. 244

Figure 8.10 Plot of the phase of $S_{11}^{thy(2I)}$ as a function of number of modes for Apertures C and D at 10.09 GHz. Aperture thickness, d_2 =0.125". Material under test: Eccosorb FGM125, $h = 0.125''$. All possible modes are considered. 245

Figure 8.11 Plot of $|S_{11}^{thy(2I)}|$ as a function of number of modes for Apertures E and H at 10.09 GHz. Aperture thickness, d_2 =0.125". Material under test: Eccosorb FGM125, $h = 0.125''$. All possible modes are considered. 246

Figure 8.12 Plot of the phase of $S_{11}^{thy(2I)}$ as a function of number of modes for Apertures E and H at 10.09 GHz. Aperture thickness, d_2 =0.125". Material under test: Eccosorb FGM125, $h = 0.125''$. All possible modes are considered. 247

Figure 8.13 Plot of $|S_{11}^{thy(2I)}|$ as a function of number of modes for Apertures F and G at 10.09 GHz. Aperture thickness, d_2 =0.125". Material under test: Eccosorb FGM125, $h = 0.125''$. All possible modes are considered. 248

Figure 8.14 Plot of the phase of $S_{11}^{thy(2I)}$ as a function of number of modes for Apertures F and G at 10.09 GHz. Aperture thickness, d_2 =0.125". Material under test: Eccosorb FGM125, $h = 0.125''$. All possible modes are considered. 249

Figure 8.15 Magnitude and phase of the reflection coefficient for 1 layer of Eccosorb FGM125, 0.125" thick, at 10.09 GHz, using only the modes that contribute significantly to the solution for Aperture F. The reflection coefficient is computed by including the modes up to the $TM_{1\,v}$ mode. Aperture thickness, d_2 =0.125". These values are plotted vs. $1/v$. 251

Figure 8.16 Magnitude and phase of the reflection coefficient for 1 layer of Eccosorb FGM125, 0.125" thick, at 10.09 GHz, using only the modes that contribute significantly to the solution for Aperture G. The reflection coefficient is computed by including the modes up to the $TM_{1\,v}$ mode. Aperture thickness, d_2 =0.125". These values are plotted vs. $1/v$. 252

Figure 8.17 Magnitude and phase of the reflection coefficient for 1 layer of Eccosorb FGM125, 0.125" thick, at 10.09 GHz, using only the modes that contribute significantly to the solution for Aperture H. The reflection coefficient is computed by including the modes up to the $TM_{1\,v}$ mode. Aperture thickness, d_2 =0.125". These values are plotted vs. $1/v$. 253

Figure 8.18 Magnitude of the reflection coefficient for 1 layer of Eccosorb FGM125, 0.125" thick for Apertures F, G, H. The reflection coefficient, $S_{11}^{(2I)extr}$, is computed by extrapolating from the $TM_{1\,40}$ mode. Aperture thickness, d_2 =0.125". 254

Figure 8.19 Phase of the reflection coefficient for 1 layer of Eccosorb FGM125, 0.125" thick for Apertures F, G, H. The reflection coefficient, $S_{11}^{(2I)extr}$, is computed by extrapolating from the $TM_{1\,40}$ mode. Aperture thickness, d_2 =0.125". 255

Figure 8.20 Magnitude of the reflection coefficient for 1 layer of Eccosorb FGM125, 0.125" thick, at 8.2-12.4 GHz for Apertures F, G, and H. The reflection coefficient, $S_{11}^{(2I)extr}$, is computed by extrapolating from the $TM_{1\,40}$ mode. Aperture thickness, d_2 =0.600". 258

Figure 8.21 Phase of the reflection coefficient for 1 layer of Eccosorb FGM125, 0.125" thick, at 8.2-12.4 GHz for Apertures F, G, and H. The reflection coefficient, $S_{11}^{(2I)extr}$, is computed by extrapolating from the $TM_{1\,40}$ mode. Aperture thickness, d_2 =0.600". 259

Figure 8.22 Magnitude of the reflection coefficient for 1 layer of Eccosorb FGM125, 0.125" thick, at 8.2-12.4 GHz for Apertures F, G, and H. The reflection coefficient, $S_{11}^{(2I)extr}$, is computed by extrapolating from the $TM_{1\,40}$ mode. Aperture thickness, d_2 =1.000". 260

Figure 8.23 Phase of the reflection coefficient for 1 layer of Eccosorb FGM125, 0.125" thick, at 8.2-12.4 GHz for Apertures F, G, and H. The reflection coefficient, $S_{11}^{(2I)extr}$, is computed by extrapolating from the $TM_{1\,40}$ mode. Aperture thickness, d_2 =1.000". 261

Figure 8.24 Geometry for Aperture I 264

Figure 8.25 Standard deviations relative to the two thickness method of the material parameters due to random measurement error for the two aperture method at 8.20 GHz. Extractions were performed with the extrapolation method using the $TM_{1\,20}$ mode. Simulations are for 1 layer of Eccosorb FGM125, 0.125" thick. Aperture thicknesses for all apertures is 0.125". 265

Figure 8.26 Standard deviations relative to the two thickness method of the material parameters due to random measurement error for the two aperture method at 10.09 GHz. Extractions were performed with the extrapolation method using the $TM_{1\,20}$ mode. Simulations are for 1 layer of Eccosorb FGM125, 0.125" thick. Aperture thicknesses for all apertures is 0.125". 266

Figure 8.27 Sensitivity analysis for the two iris method due to random measurement error using Aperture H from 8.20 GHz to 12.40 GHz. Extractions were performed with the extrapolation method using the $TM_{1\,20}$ mode. Error bars show the 95% confidence level. Simulations are for 1 layer of Eccosorb FGM125, 0.125" thick. Aperture thickness, $d_2 = 0.125$". 268

Figure 8.28 Extracted values of ϵ_r' for the two iris method with different numbers of modes used in the extraction. Simulations used Aperture H as the iris, from 8.20 GHz to 12.40 GHz. Simulations were for 1 layer of Eccosorb FGM125, 0.125" thick. The key for each line is found in Table 8.1 Aperture thickness = 0.125". 270

Figure 8.29 Extracted values of ϵ_r'' for the two iris method with different numbers of modes used in the extraction. Simulations used Aperture H as the iris, from 8.20 GHz to 12.40 GHz. Simulations were for 1 layer of Eccosorb FGM125, 0.125" thick. The key for each line is found in Table 8.1 Aperture thickness = 0.125". 271

Figure 8.30 Extracted values of μ_r' for the two iris method with different numbers of modes used in the extraction. Simulations used Aperture H as the iris, from 8.20 GHz to 12.40 GHz. Simulations were for 1 layer of Eccosorb FGM125, 0.125" thick. The key for each line is found in Table 8.1 Aperture thickness = 0.125". 272

Figure 8.31 Extracted values of μ_r'' for the two iris method with different numbers of modes used in the extraction. Simulations used Aperture H as the iris, from 8.20 GHz to 12.40 GHz. Simulations were for 1 layer of Eccosorb FGM125, 0.125" thick. The key for each line is found in Table 8.1 Aperture thickness = 0.125". 273

Figure 9.1 Top view of aluminum flange plate with aperture opening and side view of the aluminum plate with the waveguide attached. Dimensions a, b, and d_2 correspond to the aperture dimensions shown in Figure 7.1. 277

Figure 9.2 Photo of the measurement apparatus. The waveguide is attached to the top aluminum flange plate. The material sample is placed between the top plate and bottom aluminum conducting plate. . . 279

Figure 9.3 Measurement Positions for the material samples 283

Figure 9.4 Comparison of $|S_{11}^{meas}|$ and $|S_{11}^{extr}|$ for two thicknesses of Eccosorb FGM125. Measurements were made for all 5 positions. 285

Figure 9.5 Comparison of $\phi_{(1T)}^{meas}$ and $\phi_{(2T)}^{meas}$ for Eccosorb FGM125. Measurements were made for all 5 positions. 286

Figure 9.6 Extracted ϵ_r' values for Eccosorb FGM125 using the two thickness method. Bottom layer: sample 2. Top layer: sample 1. Different numbers of significantly contributing modes were included in the solution. The key for lines A-E is found in Table 9.3. Measurements taken at position 1. 288

Figure 9.7 Extracted ϵ_r'' values for Eccosorb FGM125 using the two thickness method. Bottom layer: sample 2. Top layer: sample 1. Different numbers of significantly contributing modes were included in the solution. The key for lines A-E is found in Table 9.3. Measurements taken at position 1. 289

Figure 9.8 Extracted μ_r' values for Eccosorb FGM125 using the two thickness method. Bottom layer: sample 2. Top layer: sample 1. Different numbers of significantly contributing modes were included in the solution. The key for lines A-E is found in Table 9.3. Measurements taken at position 1. 290

Figure 9.9 Extracted μ_r'' values for Eccosorb FGM125 using the two thickness method. Bottom layer: sample 2. Top layer: sample 1. Different numbers of significantly contributing modes were included in the solution. The key for lines A-E is found in Table 9.3. Measurements taken at position 1. 291

Figure 9.10 Extracted values for ϵ_r' for sample 2 of Eccosorb FGM125 using the two thickness method. Bottom layer: sample 2. Top layer: sample 1. These measurements were taken on 5 separate days. Measurement taken at position 1. 292

Figure 9.11 Extracted values for ϵ_r'', μ_r', and μ_r'', for sample 2 of Eccosorb FGM125 using the two thickness method. Bottom layer: sample 2. Top layer: sample 1. These measurements were taken on 5 separate days. Extractions were performed using the first 10 modes. Measurement taken at position 1. 293

Figure 9.12 Mean extracted values for ϵ_r' for sample 2 of Eccosorb FGM125 using the first 10 modes in the two thickness method. Bottom layer: sample 2. Top layer: sample 1. The error bars represent the $\pm 2\sigma$, or 95% confindence intervals, for the extracted data shown in Figure 9.10. Measurement taken at position 1. 294

Figure 9.13 Mean extracted values for ϵ_r'', μ_r', and μ_r'', of Eccosorb FGM125 using the first 10 modes in the two thickness method. Bottom layer: sample 2. Top layer: sample 1. The error bars represent the $\pm 2\sigma$, or 95% confindence intervals, for the extracted data shown in Figure 9.11. Measurement taken at position 1. 295

Figure 9.14 Extracted values for ϵ_r' for sample 1 of Eccosorb FGM125 using the two thickness method. Bottom layer: sample 1. Top layer: sample 2. These measurements were taken on 5 separate days. Measurement taken at position 1. 296

Figure 9.15 Extracted values for ϵ_r'', μ_r', and μ_r'', for sample 1 of Eccosorb FGM125 using the two thickness method. Bottom layer: sample 1. Top layer: sample 2. These measurements were taken on 5 separate days. Extractions were performed using the first 10 modes. Measurement taken at position 1. 297

Figure 9.16 Mean extracted values for ϵ_r' of Eccosorb FGM125, using the first 10 modes in the two thickness method. Bottom layer: sample 1. Top layer: sample 2. The error bars represent the $\pm 2\sigma$, or 95% confindence intervals, for the extracted data shown in Figure 9.14. Measurement taken at position 1. 298

Figure 9.17 Mean extracted values for ϵ_r'', μ_r', and μ_r'', of Eccosorb FGM125, using the first 10 modes in the two thickness method. Bottom layer: sample 1. Top layer: sample 2. The error bars represent the $\pm 2\sigma$, or 95% confindence intervals, for the extracted data shown in Figure 9.15. Measurement taken at position 1. 299

Figure 9.18 Comparison of the mean extracted values for ϵ_r' of Eccosorb FGM125 from Figure 9.12 and Figure 9.16. Legend describes the bottom layer. The error bars represent the $\pm 2\sigma$, or 95% confindence intervals. Measurement taken at position 1. 300

Figure 9.19 Comparison of the mean extracted values for ϵ_r'', μ_r', and μ_r'' of Eccosorb FGM125 from Figure 9.13 and Figure 9.17. Dotted line is for Sample 2 as the bottom layer, solid line is for Sample 1 as the bottom layer. The error bars represent the $\pm 2\sigma$, or 95% confindence intervals. Measurement taken at position 1. 301

Figure 9.20 The extracted values for ϵ_r' from Eccosorb FGM125. Measurements taken at all 5 positions with Sample 2 as bottom layer 303

Figure 9.21 The extracted values for ϵ_r'', μ_r', and μ_r'' of Eccosorb FGM125. Measurements taken at all 5 positions with Sample 2 as bottom layer. 304

Figure 9.22 The extracted values for ϵ_r' from Eccosorb FGM40, with Sample 1 as the bottom layer. Measurement taken at all 5 positions. Nominal values are shown by $-\square-$. 305

Figure 9.23 The extracted values for ϵ_r'', μ_r', and μ_r'' of Eccosorb FGM40, with Sample 1 as the bottom layer. Measurement taken at all 5 positions. Nominal values are shown by $-\square-$ markers. 306

Figure 9.24 The mean extracted values for ϵ_r' from Eccosorb FGM40, with Sample 1 as the bottom layer. Solid line : position 1. Dotted line: position 2. Error bars are 95% confidence levels. 307

Figure 9.25 The mean extracted values for ϵ_r'', μ_r', and μ_r'' from Eccosorb FGM40, with Sample 1 as the bottom layer. Solid line : position 1. Dotted line: position 2. Error bars are 95% confidence levels. 308

Figure 9.26 The mean extracted values for ϵ_r' from Eccosorb FGM40, with Sample 2 as the bottom layer. Solid line : position 1. Dotted line: position 2. Error bars are 95% confidence levels. 310

Figure 9.27 The mean extracted values for ϵ_r'', μ_r', and μ_r'' from Eccosorb FGM40, with Sample 2 as the bottom layer. Solid line : position 1. Dotted line: position 2. Error bars are 95% confidence levels. 311

Figure 9.28 The extracted values for μ_r' from Eccosorb FGM125 using the two layer method, with Sample 1 as the top layer and Sample 2 as the bottom layer. Different numbers of modes used in the extraction. Measurements made at Position 1. Key for different numbers of modes found in Table 9.3. 314

Figure 9.29 The extracted values for μ_r'' from Eccosorb FGM125 using the two layer method, with Sample 1 as the top layer and Sample 2 as the bottom layer. Different numbers of modes used in the extraction. Measurements made at Position 1. Key for different numbers of modes found in Table 9.3. 315

Figure 9.30 The extracted values for ϵ_r' from Eccosorb FGM125 using the two layer method, with Sample 1 as the top layer and Sample 2 as the bottom layer. Different numbers of modes used in the extraction. Measurements made at Position 1. Key for different numbers of modes found in Table 9.3. 316

Figure 9.31 The extracted values for ϵ_r'' from Eccosorb FGM125 using the two layer method, with Sample 1 as the top layer and Sample 2 as the bottom layer. Different numbers of modes used in the extraction. Measurements made at Position 1. Key for different numbers of modes found in Table 9.3. 317

Figure 9.32 The extracted values for ϵ_r' from Eccosorb FGM125 using the two layer method, with Sample 2 as the top layer and Sample 1 as the bottom layer. Measurement taken at all 5 positions. 320

Figure 9.33 The extracted values for ϵ_r'' of Eccosorb FGM125 using the two layer method, with Sample 2 as the top layer, and Sample 1 as the bottom layer. Measurement taken at all 5 positions. 321

Figure 9.34 The extracted values for μ_r' of Eccosorb FGM125 using the two layer method, with Sample 2 as the top layer, and Sample 1 as the bottom layer. Measurements taken at all 5 positions. 322

Figure 9.35 The extracted values for μ_r'' of Eccosorb FGM125 using the two layer method, with Sample 2 as the top layer, and Sample 1 as the bottom layer. Measurements taken at all 5 positions. 323

Figure 9.36 The extracted values for ϵ_r' of Eccosorb FGM125 using the two layer method, with Sample 1 as the top layer, and Sample 2 as the bottom layer. Measurements taken at position 1. 324

Figure 9.37 The extracted values for ϵ_r'' of Eccosorb FGM125 using the two layer method, with Sample 1 as the top layer, and Sample 2 as the bottom layer. Measurements taken at position 1. 325

Figure 9.38 The extracted values for μ_r' of Eccosorb FGM125 using the two layer method, with Sample 1 as the top layer, and Sample 2 as the bottom layer. Measurements taken at position 1. 326

Figure 9.39 The extracted values for μ_r'' of Eccosorb FGM125 using the two layer method, with Sample 1 as the top layer, and Sample 2 as the bottom layer. Measurements taken at position 1. 327

Figure 9.40 Comparison of $|S_{11(2L)}^{meas}|$ and $|S_{11(2L)}^{extr}|$ for one layer of Nylon on top of Eccosorb FGM125, and one layer of PVC on top of Eccosorb FGM125. Measurements made for position 1. PVC is Sample 1, Nylon is Sample 2. 329

Figure 9.41 Comparison of $\phi_{(2L)}^{meas}$ and $\phi_{(2L)}^{thy}$ for one layer of Nylon on top of Eccosorb FGM125, and one layer of PVC on top of Eccosorb FGM125. Measurements made for position 1. PVC is Sample 1. Nylon is Sample 2. 330

Figure 9.42 The extracted values for ϵ_r' of Eccosorb FGM125 using the two layer method, with Plexiglass, Nylon, and PVC as the top layer, and Sample 2 as the bottom layer. These results are compared with the extracted values obtained using the two thickness method. Measurements taken at position 1. PVC is Sample 1, Nylon is Sample 2, Plexiglass is Sample 2. 332

Figure 9.43 The extracted values for ϵ_r'' of Eccosorb FGM125 using the two layer method, with Plexiglass, Nylon, and PVC as the top layer, and Sample 2 as the bottom layer. Measurements taken at position 1. PVC is Sample 1, Nylon is Sample 2, Plexiglass is Sample 2. . 333

Figure 9.44 The extracted values for μ_r' of Eccosorb FGM125 using the two layer method, with Plexiglass, Nylon, and PVC as the top layer, and Sample 2 as the bottom layer. Measurements taken at position 1. PVC is Sample 1, Nylon is Sample 2, Plexiglass is Sample 2. . 334

Figure 9.45 The extracted values for μ_r'' of Eccosorb FGM125 using the two layer method, with Plexiglass, Nylon, and PVC as the top layer, and Sample 2 as the bottom layer. Measurements taken at position 1. PVC is Sample 1, Nylon is Sample 2, Plexiglass is Sample 2. . 335

Figure 9.46 The extracted values for ϵ_r' of Eccosorb FGM125 using the two layer method, with PVC, Sample 1, as the top layer, and Sample 2 as the bottom layer. These results are compared with the extracted values obtained using the two thickness method. Measurements taken at position 1. Error bars denote the 95% confidence interval for the two layer method. 337

Figure 9.47 The extracted values for ϵ_r'' of Eccosorb FGM125 using the two layer method, with PVC, Sample 1, as the top layer, and Sample 2 as the bottom layer. These results are compared with the extracted values obtained using the two thickness method. Measurements taken at position 1. Error bars denote the 95% confidence interval for the two layer method. 338

Figure 9.48 The extracted values for μ_r' of Eccosorb FGM125 using the two layer method, with PVC, Sample 1, as the top layer, and Sample 2 as the bottom layer. These results are compared with the extracted values obtained using the two thickness method. Measurements taken at position 1. Error bars denote the 95% confidence interval for the two layer method. 339

Figure 9.49 The extracted values for μ_r'' of Eccosorb FGM125 using the two layer method, with PVC, Sample 1, as the top layer, and Sample 2 as the bottom layer. These results are compared with the extracted values obtained using the two thickness method. Measurements taken at position 1. Error bars denote the 95% confidence interval for the two layer method. 340

Figure 9.50 Comparison of the magnitude and phase of $S_{11(2I)}^{meas}$ and $S_{11(2I)}^{extr}$ for the two iris method. Simulated reflection coefficient is for Eccosorb FGM125, 0.125" thick. Measurements are at all 5 positions for Sample 2 of Eccosorb FGM125, 0.122" thick. 342

Figure 9.51 Extracted values of ϵ_r' using the two iris method. Different numbers of significant modes were used in the extraction. The key for each line is shown in Table Table 9.4. Measurements taken at position 1. 344

Figure 9.52 Extracted values of ϵ_r'' using the two iris method. Different numbers of significant modes were used in the extraction. The key for each line is shown in Table Table 9.4. Measurements taken at position 1. 345

Figure 9.53 Extracted values of μ_r' using the two iris method. Different numbers of significant modes were used in the extraction. The key for each line is shown in Table Table 9.4. Measurements taken at position 1. 346

Figure 9.54 Extracted values of μ_r'' using the two iris method. Different numbers of significant modes were used in the extraction. The key for each line is shown in Table Table 9.4. Measurements taken at position 1. 347

Figure 9.55 Extracted values of ϵ_r' using the two iris method at five different measurement positions. The significant modes up to the TM_{18} mode were used in the extraction. 350

Figure 9.56 Extracted values of ϵ_r'' using the two iris method at five different measurement positions. The significant modes up to the TM_{18} mode were used in the extraction. 351

Figure 9.57 Extracted values of μ_r' using the two iris method at five different measurement positions. The significant modes up to the TM_{18} mode were used in the extraction. 352

Figure 9.58 Extracted values of μ_r'' using the two iris method at five different measurement positions. The significant modes up to the TM_{18} mode were used in the extraction. 353

Figure 9.59 Extracted values of ϵ_r' using the two iris method at four different measurement positions. The significant modes up to the TM_{18} mode were used in the extraction. 354

Figure 9.60 Extracted values of ϵ_r'' using the two iris method at four different measurement positions. The significant modes up to the TM_{18} mode were used in the extraction. 355

Figure 9.61 Extracted values of μ_r' using the two iris method at four different measurement positions. The significant modes up to the TM_{18} mode were used in the extraction. 356

Figure 9.62 Extracted values of $\mu_r"'$ using the two iris method at four different measurement positions. The significant modes up to the TM_{18} mode were used in the extraction. 357

Figure 9.63 Mean extracted values of ϵ_r' using the two iris method at three different measurement positions. Four independent observations were averaged at each measurement position on each sample. The significant modes up to the TM_{18} mode were used in the extraction. 359

Figure 9.64 Mean extracted values of ϵ_r'' using the two iris method at three different measurement positions. Four independent observations were averaged at each measurement position on each sample. The significant modes up to the TM_{18} mode were used in the extraction. 360

Figure 9.65 Mean extracted values of μ_r' using the two iris method at three different measurement positions. Four independent observations were averaged at each measurement position on each sample. The significant modes up to the TM_{18} mode were used in the extraction. 361

Figure 9.66 Mean extracted values of μ_r'' using the two iris method at three different measurement positions. Four independent observations were averaged at each measurement position on each sample. The significant modes up to the TM_{18} mode were used in the extraction. 362

Figure 9.67 Mean extracted values of ϵ_r' using the two iris method, two thickness method, and the two layer method, where PVC was the top layer. Three extractions were averaged at each measurement position for the two iris method, 5 independent extractions were averaged for the two layer method, and two extractions were averaged for the two thickness method. All extractions performed using the extrapolation technique for that method. 363

Figure 9.68 Mean extracted values of ϵ_r'' using the two iris method, two thickness method, and the two layer method, where PVC was the top layer. Three extractions were averaged at each measurement position for the two iris method, 5 independent extractions were averaged for the two layer method, and two extractions were averaged for the two thickness method. All extractions performed using the extrapolation technique for that method. 364

Figure 9.69 Mean extracted values of μ_r' using the two iris method, two thickness method, and the two layer method, where PVC was the top layer. Three extractions were averaged at each measurement position for the two iris method, 5 independent extractions were averaged for the two layer method, and two extractions were averaged for the two thickness method. All extractions performed using the extrapolation technique for that method. 365

Figure 9.70 Mean extracted values of μ_r'' using the two iris method, two thickness method, and the two layer method, where PVC was the top layer. Three extractions were averaged at each measurement position for the two iris method, 5 independent extractions were averaged for the two layer method, and two extractions were averaged for the two thickness method. All extractions performed using the extrapolation technique for that method. 366

Figure C.1 Equivalent problem coordinate systems for a) this dissertation and b) Hanson's derivation. For case 1, where $z' > z$. 391

Figure C.2 Equivalent problem coordinate systems for a) this dissertation and b) Hanson's derivation. For case 2, where $z' < z$. 392

KEY TO SYMBOLS AND ABBREVIATIONS

CS: Cross Section

EM: Electromagnetic

MAGRAM: Magnetic Radar Absorbing Material

MFIE: Magnetic Field Integral Equation

MoM: Method of Moments

NDE: Non-Destructive Evaluation

NRW: Nicholson-Ross-Wier

PEC: Perfect Electric Conductor

TE: Transverse Electric

TM: Transverse Magnetic

T/R: Transmission/Reflection

TRL: Thru-Reflect Line

VNA: Vector Network Analyzer

VSWR: Voltage Standing Wave Ratio

CHAPTER 1

INTRODUCTION AND BACKGROUND

1.1 Introduction and Background

The research community has long been interested in determining the electromagnetic (EM) properties of materials [1]. Various methods have been designed and implemented to increase understanding of these properties, and this knowledge has been employed in industrial, military, and civilian applications.

In recent years, the use of microwave frequencies has had an increasing role in everyday life. Understanding the behavior of EM materials in the presence of microwave energy has led to an increased utilization of these materials in new antenna design, radar cross section reduction, microwave shielding, and many other applications. As the clock speeds of computers and electronic devices continue to increase in the microwave frequency range, there has been increasing interest in the properties of the materials used in the construction, packaging, and operation of these devices.

Regardless of the actual use of the materials, the goal of material characterization is to determine the permeability and permittivity of the material, also known as the constitutive parameters, as accurately as possible. Several methods have been developed for the characterization of EM materials. These methods include resonator methods [2], waveguide methods [4]-[6], microstrip sensors [7], coaxial probes [8], free space methods [9], and waveguide probe methods [9]-[14]. Each of the material characterization methods has advantages and limitations in accurately determining the material properties. Factors differentiating the methods include operational bandwidth, precision of the method, robustness of the method, expense, and mobility of the testing apparatus. For example, cavity resonator methods can be highly accurate, but the analysis is restricted to a laboratory environment [9]. Test samples are

usually machined to a specific size and/or shape for accurate parameter extraction, and these methods cannot be easily deployed in field applications.

These different methods use a variety of algorithms to extract the material parameters. One of the most widely used extraction algorithms is the Nicolson-Ross-Weir (NRW) algorithm [15]-[16], which is usually associated with the waveguide transmission/reflection (T/R) method or the coaxial transmission line T/R method [12], although some free space T/R methods also utilize the NRW algorithm [17]. Most material extraction methods require two complex measurements in order to perform a full characterization of the permittivity, ϵ, and permeability, μ, of the material. This is accomplished in the waveguide T/R method by measuring the reflection and transmission coefficients for a material that has been machined to the proper size and placed inside the waveguide. The advantage of the waveguide T/R method is that the material parameters can be derived using a closed form solution. However, this method does have limitations. The sample must be of a certain shape and size, properly aligned in the waveguide, and it does not work well when the sample length is a mutiple of the half wavelength of the operating frequency. A transmission coefficient is also difficult to obtain for some materials. The coaxial transmission line T/R method and the free space T/R method face similar limitations.

For some industrial applications it is desirable to be able to determine the EM properties of a material that has been applied to a conductor without removing it from the conductor. It is possible that the constitutive parameters of the material have changed over time, have degraded due to exposure to environmental causes, or the material may have developed a defect which no longer allows it to perform its original intended function. However, if the material properties have not changed, it is desirable that the test allows the material to continue in its application without experiencing damage or significant cost from removal.

Thus, the ability to perform a non-destructive evaluation (NDE) of the material

in situ is a desirable goal of a material characterization method. Free space methods, coaxial probes, and waveguide probes are the most common methods that have been examined for viability in performing this task. Each of these methods has the ability to do a full characterization of the permeability and permittivity of the material. This chapter provides a brief overview and survey of these methods while focusing on recent research involving non-destructive EM characterization of a material using flanged rectangular waveguide probes.

1.2 Related work

1.2.1 Free Space Methods

Free space techniques [18], [19], [20] involve the interrogation of the material under question using antenna probes, with free space as the transmission medium from the transmitter to the receiver. Most methods use two antennas with a planar sample placed between them, and a thru-reflect line (TRL) calibration is performed. Free space techniques do not require physical contact with the material, which does make them advantageous over other methods in the laboratory. These techniques do not require machining of the sample in the way that traditional waveguide techniques require. Some methods have employed a spot-focused beam to reduce the effects of diffraction and other spurious reflections from the surrounding environment. This spot-focused beam method has successfully determined the dielectric properties of a curved dielectric material [21].

Another advantage of this technique is the ability to study the response of a material to parallel or perpendicular polarizations [22] or as a function of incidence angle [23]. In a bistatic application, simultaneous measurement of both ϵ and μ have been extracted from a conductor-backed planar material [24]. The temperature dependence of the material properties can be analyzed by heating or cooling the sample because the material sample is independently located from the transmitter and

receiver [17]-[18]. This type of analysis can be particularly well suited for evaluation of materials that will be subjected to a wide variety of operating temperatures.

However, these systems are usually set up in a fixed position on a table or an arch range, and are not very portable. They require a considerable amount of calibration to reduce multiple reflections between the sample and the antenna, and are sensitive to environmental conditions. An additional concern is the effects of edge diffraction as the incident wave illuminates the material under test. The spot-focused beam free-space methods require that the conductor-backed material be removed from the conductor, thus eliminating the desired *in situ* application.

1.2.2 Coaxial Probe Methods

Open-ended flanged coaxial probes have received significant research as a method of material characterization [8], [25]. The coaxial probe is placed against a material sample and the reflection coefficient is used to determine the permittivity of the material in most applications. These probes use a relatively small material test area and they possess wideband characteristics, but this method is extremely sensitive to any airgap between the center conductor and the material. Great care must be taken to avoid any probe lift-off [26]-[28]. Thus, it is most useful for biomedical, powder, or liquid measurements, in which the probe may be immersed in the material with very little possibility of lift-off. When an airgap is known to be present, it must be accounted for theoretically.

In general, coaxial probes are rather inexpensive and portable, but they are less robust than the waveguide probes and are not as well-suited for measurement of magnetic materials.

1.2.3 Waveguide Probe Methods

Waveguide probes have the advantage of being robust, portable, and relatively inexpensive. The radiation characteristics of waveguide probes provide deeper penetration

into a lossy material than that provided by coaxial probes [29]. At lower frequencies, waveguide probes can become rather large and difficult to handle, but in the X-band range, the standard WR-90 waveguide is quite portable.

Different types of waveguide probe methods have been developed in recent years to determine the EM properties of materials, and these include methods using both open-ended circular and open-ended rectangular waveguides. Tantot [30] used a circular waveguide technique to extract both permittivity and permeability from a multilayered medium. The inclusion and modeling of an airgap also allowed for the determination of the thickness of the material. One drawback of the circular waveguide is the difficulty in characterizing anisotropic material, which one study involving a rectangular waveguide has overcome [31]. In addition, the solution method employed by Tantot sometimes requires additional measurements to insure achievement of a unique solution.

In research involving open-ended rectangular waveguide probes, several methods and configurations have been examined. The motivation for this dissertation is to investigate possible methods for constitutive parameter extraction of a conductor-backed material using a flanged rectangular waveguide probe. It is desirable to find a technique that allows for the simultaneous extraction of permeability and permittivity from the material, and to be able to characterize the sensitivity to measurement errors in the extraction method. It is also desirable to extract the material parameters while using a reasonable amount of computational resources. Thus, the related rectangular waveguide characterization work is surveyed with respect to these desires.

1.2.3.1 Conductor-backed material characterization

Several authors have conducted material characterization research using a conductor-backed material. Teodoridis [32] considers a conductor-backed dielectric material by using an integral equation formulation solved using a multimode solution. In the X-band frequency range, he demonstrated that the inclusion of a higher number of modes

in the matrix solution increased the agreement of the theoretical results to measured results for the voltage standing wave ratio (VSWR) for a waveguide radiating into half space. Unfortunately these results were not shown for the conductor-backed material. Teodoris also employs a two-dimensional polynomial interpretation as the inversion algorithm and a dyadic Green's function for use in a multi-layered medium.

Bakhtiari [33] also examines a conductor-backed material, but the purpose is to determine the thickness of a lossy dielectric material. He uses a dominant mode assumption to describe the aperture field distribution and concludes that the addition of higher order modes is not significant, affecting the end result less than 3%.

Maode [34] also studies a conductor-backed magnetic and dielectric material, and obtains simultaneous extraction of permeability and permittivity. She employs an approximate variational method to determine the waveguide admittance and hence the reflection coefficient of the conductor-backed material. Both single and multiple layers of material are considered in the formulation. The extraction algorithm uses either two thicknesses of the same material to provide two independent reflection coefficients, or one measurement with one material and a second measurement with a known material as a top layer. She also concludes that the waveguide flange dimension should be greater than one wavelength for adequate decay of the field when measuring high loss materials with a conductor backing.

Stewart [35], [36] has also conducted studies of conductor-backed materials using a rigorous full-wave integral equation method that employs single and dual aperture probes. When utilizing the single aperture probe, Stewart uses measurements made from two thicknesses of the same material to extract the material parameters. This method is referred to here as the two thickness method. He also examined the size of the waveguide flange and concluded that for magnetic radar absorbing material (MAGRAM), a 6" flange was sufficient for adequate decay of the edge-diffracted field. This study is an important step related to this dissertation, as this two thickness method is

examined in greater detail in chapters 2-6 of this work. The dual aperture probe utilizes a similar formulation, but obtains two independent scattering parameters from a single measurement.

1.2.3.2 Characterization of both ϵ and μ

The initial research using flanged rectangular waveguide probes focused primarily on the extraction of permittivity from the material under test [32],[37], although Chang [31] also examined anisotropic dielectric materials. Bois [37] studied a dielectric half space regarding the effect of higher order modes on the material parameter extraction.

Interest has increased in characterizing both permittivity and permeability using waveguide probes with the use of more magnetically loaded materials and polymers. Maode and Stewart have carried out extraction of both parameters, and Chang [38] also characterizes both properties using an integral equation formulation and modal analysis, but does so using a free space backing. Stewart compares his extracted results with the traditional waveguide T/R method, and found that the extracted permeability values from the two thickness method agreed with those extracted using the T/R method. The permittivity value extractions, however, did not agree as well with the waveguide T/R method.

Hyde recently published an additional technique involving two offset probes [39]. In this method two flanged rectangular probes are separated by a magnetic material sheet, and the reflection and transmission coefficients are simultaneously observed. Thus, both magnetic and electric properties are extracted from the measurement. This formulation is similar to that of Stewart [36], but shows the ability to extract permittivity more effectively while the permeability shows a greater deviation when compared to the waveguide T/R method.

In a related method, Bogle [40] attempted the extraction of both parameters using a slotted waveguide approach. Using a single slot, this method was partially successful at material characterization. Bogle, Hyde, and Stewart all used a single

layer parallel plate Green's function approach in their integral equation formulations. In the research surveyed, there was not a clear formulation of a two layer parallel plate Green's function, thus the need for the derivation presented in Chapter 3.

1.2.3.3 Modal Solution Analysis

One parameter that affects computational time and accuracy is the number of modes used in the integral equation solution. Depending on the technique and purpose, authors have concluded that different numbers of higher order modes are needed to achieve convergence of the desired properties. Bakhtiari [33] only uses the dominant TE_{10} mode when determining the thickness. Chang [31] states that good convergence is achieved when the first four modes are used in the characterization of isotropic dielectric materials backed by free space. He also shows that for anisotropic material backed by free space, using the first 9 modes allows the theoretical solution to agree more closely with the measured values than using 1 or 4 modes.

Teodoridis [32] examines the case of a flanged waveguide radiating into a half space composed of air. He notes that using 10 modes in the solution achieves a VSWR that agrees much more closely with measured values than simply using the dominant mode. Stewart [35] demonstrates that using the first 4 modes achieves good convergence, but adding the next 6 modes does not make a noticeable change in the extracted parameters for the conductor-backed magnetic material extraction problem. Hyde [39] sees similar results to those of Stewart by incorporating the first 4 and 10 modes.

Bois [37] does an interesting study of modal inclusion for an open-ended rectangular waveguide radiating into a dielectric half-space. He examines the effect of the number of modes included in the solution on the reflection coefficient, S_{11}. Bois shows that if one assumes that final convergence is achieved with 20 modes, a solution involving the dominant mode only contains at least a 3% error on $|S_{11}|$. If the solution uses the first 15 modes, that error is reduced to less than .25%. In addition, he shows

that the modes which have the highest magnitude for the amplitude coefficient after the dominant TE_{10} mode are the TM_{12}, TE_{30}, and the TE_{12} modes, which are the first four modes when ordered from lowest to highest cutoff frequency. It should be noted that no author has explored the effect of more than 20 modes on the extracted parameter values or the reflection coefficient. In this dissertation, the effect of higher order modes is considered on the reflection coefficient and the extracted parameters in chapters 5, 8, and 10.

1.2.3.4 Error sensitivity analysis

Certainly there is great interest by researchers in the material characterization field to understand the effect of various types of measurement errors on the final extracted result. In the rectangular waveguide probe measurements, possible sources of error include uncertainty in the thickness of the materials under test, random noise error in test equipment, inhomogeneities in the material, and variation in material composition. Some of the authors surveyed consider possible sources of error. Maode considers flange quality, measurement accuracy, sample thickness, and operating frequency stability using the standard propagation of error formulation. She used these error estimates to determine the effect on the accuracy of the extracted parameters. Maode also demonstrates that the sample thickness must be in an acceptable range for this method. If it is too thin or too thick, the variation in the reflection coefficient may not be enough to obtain two independent measurements. Stewart [36] and Hyde [39] also conduct a sensitivity analysis using the potential errors in flange and sample thickness measurements, but do not consider the possibility of random S-parameter measurement error. In this dissertation, a sensitivity analysis to this random measurement error is presented in Chapters 6 and 9 for the two layer, two thickness and two iris methods.

1.3 Overview of the research

The motivation for this dissertation is to investigate possible methods for constitutive parameter extraction of a conductor-backed material *in situ* using a flanged rectangular waveguide, and to do so while minimizing the effects of S-parameter measurement error. The most promising method surveyed is the two thickness method developed by Stewart. However, in a practical application where an unidentified material has been applied to a conductor, providing two thicknesses of that material is not possible. It does hold promise as an effective laboratory method for extraction using materials for which two samples can be provided. The two thickness method is investigated for its sensitivity to S-parameter measurement errors and as a comparison to the other methods that are explored.

Two additional methods have been proposed to accomplish the goal of parameter extraction. In the first method, one measurement is obtained from one layer of conductor-backed material. Then a second measurement is taken by placing a known material layer on top of the unknown layer. This method is termed the two layer method. The second method uses two different irises in the waveguide aperture to obtain two independent measurements, and is thus termed the two iris method. These two additional methods are investigated for their ability to perform material extraction, and all three methods are analyzed with respect to their sensitivity to measurement error and the number of modes needed to obtain accurate extraction of the material parameters.

The organization of this dissertation is as follows. The general extraction algorithm for the two layer method and the two thickness method is described in Chapter 2. In addition, an integral equation is formulated and transformed into a matrix equation using the Method Moments (MoM). The solution to this matrix equation is then used to obtain the theoretical scattering parameters.

Chapter 3 contains the derivation of the two layer Green's function for use in the two layer method. This Green's function can also be used in the two thickness method with proper specialization. The matrix solution steps and numerical analysis techniques are detailed in Chapter 4 using the Green's function derived in Chapter 3.

The modal analysis of the theoretical S_{11} parameters is discussed in Chapter 5 using the formulation for the two layer method. In addition, a method for estimating the reflection coefficient for an infinite number of modes is presented. This analysis examines both a single layer of material and two layers of material. Simulated extraction results using higher order modes are also presented.

Chapter 6 is a description of the error sensitivity analysis and the theory and practice used to estimate the effect of S-parameter measurement errors on the two thickness and two layer methods.

The third method under investigation, the two iris method, is developed in Chapter 7 using a coupled integral equation and mode matching formulation. The numerical analysis techniques used in the solution of the two iris method are also discussed in Chapter 7. A sensitivity analysis and a modal analysis for the two iris method is presented in Chapter 8.

Chapter 9 compares the experimental complex material parameter extraction results using the two thickness, two layer, and two iris methods. Conclusions and suggestions for future work are presented in Chapter 10.

CHAPTER 2

ELECTROMAGNETIC MATERIAL PARAMETER EXTRACTION USING THE TWO LAYER METHOD AND THE TWO THICKNESS METHOD

2.1 Introduction

This chapter presents the theory needed to solve a material extraction problem using the two layer and two thickness methods. The desired result of any extraction problem is the determination of the complex permittivity, $\epsilon = \epsilon_0(\epsilon_r' - j\epsilon_r'')$, and the complex permeability, $\mu = \mu_0(\mu_r' - j\mu_r'')$, of the material. Here ϵ_0 is the permittivity of free space and μ_0 is the permeability of free space. The methods under investigation require two independent measurements of the complex reflection coefficient for the unknown material. The two thickness method developed by Stewart [35] obtains the two independent measurements from two different thicknesses of the same conductor-backed material using a flanged rectangular waveguide probe. The two layer method, formulated here, obtains one measurement of the unknown conductor-backed material using a similar probe. A second measurement is made by placing a known material on top of the unknown material and measuring that reflection coefficient.

The integral equation formulation for these two problems is quite similar. The primary difference in the formulation is the Green's function used for determining the fields in the parallel plate region. As is shown in Appendix C, the Green's function for the two layer problem reduces to the single layer Green's function when both layers are the same material. This chapter formulates the integral equation for two layers of material, which is the more general case. The adaptation of this formulation to a single layer of material is also discussed.

The other difference between the two thickness and two layer methods is found in

the extraction algorithm. The algorithm for the two layer method is presented first, then the two thickness method algorithm is presented. The differences between the two methods are discussed at the end of the chapter.

In the two layer method, a representation of the fields in the waveguide and parallel plate regions is developed. Then a magnetic field integral equation (MFIE) is derived and solved using the Method of Moments. The solution to the MFIE provides the theoretical reflection coefficient, S_{11}^{thy}, for a two-layered, conductor-backed material stack interrogated by a rectangular waveguide probe. This reflection coefficient is calculated and compared to the measured reflection coefficient, and an iterative process is used to extract the material parameters.

2.2 Two Layer Method: Problem Overview

Consider the geometry shown in Figure 2.1. A single, open-ended rectangular waveguide probe is connected to an infinite plate, or flange, with an opening of equal size to that of the waveguide aperture. This open-ended waveguide fixture is placed on the top surface of the two layers of material, where the top layer is a known material of permittivity ϵ_1 and permeability μ_1, and the bottom layer is the unknown material with material parameters ϵ_2 and μ_2. Both regions are assumed to be linear, isotropic, and homogeneous. It is also assumed that the thicknesses of both layers of material are known and that the extent of the flange and material samples are infinite in the transverse directions. The flange, at $z = 0$, and conductor, at $z = -h$, are each modeled as a Perfect Electric Conductor (PEC).

The X-band WR90 waveguide is designed such that only the dominant TE_{10} mode propagates within the band of interest, therefore allowing the transverse parts of the

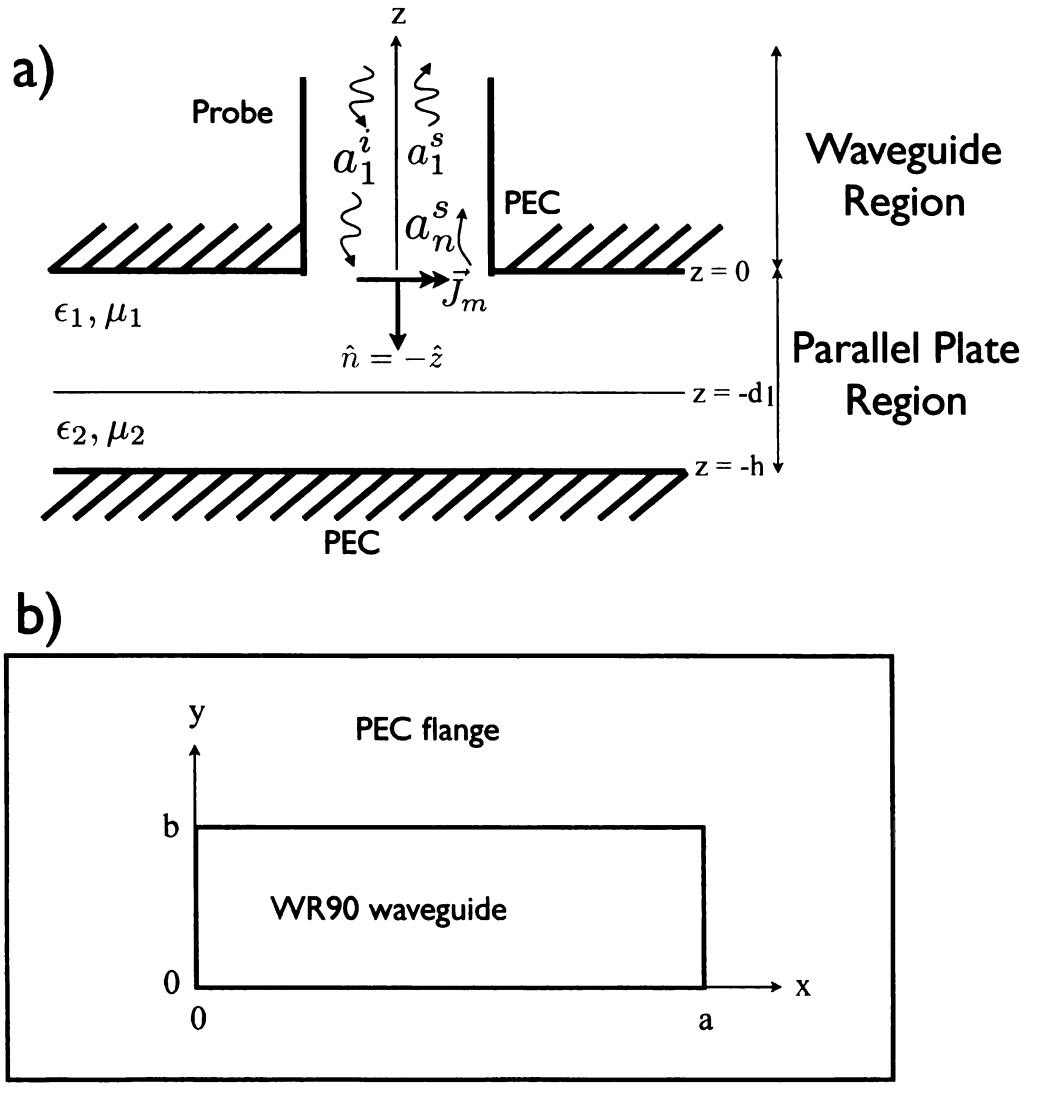


Figure 2.1. Side view (a) and top view (b) for two layers of material interrogated by a single waveguide probe

incident fields (with $e^{j\omega t}$ time dependence suppressed) to be characterized as

$$\vec{E}_t^i(\vec{r}) = a_1^i \vec{e}_1^{wg}(\vec{\rho}) e^{jk_{z1}^{wg} z} \tag{2.1}$$

$$\vec{H}_t^i(\vec{r}) = -a_1^i \vec{h}_1^{wg}(\vec{\rho}) e^{jk_{z1}^{wg} z}, \tag{2.2}$$

where a_1^i is the amplitude of the incident mode, and the electric and magnetic field transverse waveguide functions for the nth waveguide mode are denoted by $\vec{e}_n^{wg}$ and $\vec{h}_n^{wg}$ [41]. The axial wavenumber for mode n is given by

$$k_{zn}^{wg} = \sqrt{k_0^2 - \left(\frac{u_n \pi}{a}\right)^2 - \left(\frac{v_n \pi}{b}\right)^2}, \tag{2.3}$$

where a and b are the waveguide dimensions shown in Figure 2.1, and $k_0^2 = \omega^2 \mu_0 \epsilon_0$ is the square of the free space wavenumber. The variables u_n and v_n correspond to the indices (u, v) for a TE_{uv} wave (if the nth mode is TE_z) or a TM_{uv} wave (if the nth mode is TM_z).

As the incident field interrogates the material in the parallel plate region, an infinite number of modes of amplitude a_n^s are scattered by the conductor-backed material layers back toward the source. For practical and computational implementation, it is assumed that the reflected field can be truncated to N modes. Thus the total transverse fields in the waveguide are described by

$$\vec{E}_t^{wg}(\vec{r}) = a_1^i \vec{e}_1^{wg}(\vec{\rho}) e^{jk_{z1}^{wg} z} + \sum_{q=1}^{N} a_q^s \vec{e}_q^{wg}(\vec{\rho}) e^{-jk_{zq}^{wg} z} \tag{2.4}$$

$$\vec{H}_t^{wg}(\vec{r}) = -a_1^i \vec{h}_1^{wg}(\vec{\rho}) e^{jk_{z1}^{wg} z} + \sum_{q=1}^{N} a_q^s \vec{h}_q^{wg}(\vec{\rho}) e^{-jk_{zq}^{wg} z}. \tag{2.5}$$

The reflection coefficient, or S_{11} parameter, is the desired result of this theoretical problem formulation. Only the dominant TE_{10} mode ($n = 1$) propagates through the

waveguide and arrives back at the network analyzer, while all other modes evanesce. The reflection coefficient is defined as the ratio of the scattered dominant mode wave amplitude to the incident wave amplitude, which is the complex quantity

$$S_{11} = \frac{a_1^s}{a_1^i}. \tag{2.6}$$

2.3 Two Layer Method Extraction Algorithm

The extraction algorithm used in the the two layer method minimizes the difference between the theoretical and measured reflection coefficients of the material under test. To simultaneously solve for the complex permittivity, ϵ_2, and permeability, μ_2, of the unknown material, two complex independent measurements of the reflection coefficient are needed. The first, $S_{11(1)}^{meas}$, is taken with the probe placed on the layer of unknown, conductor-backed material, as shown in Figure 2.2a. The second material, of known constitutive parameters ϵ_1 and μ_1, is then placed on the first layer and a second measurement, $S_{11(2)}^{meas}$, is taken, as shown in Figure 2.2b. The thicknesses of the top layer, d_1, and bottom layer, h_1, are known.

The extraction algorithm used in the two layer method also requires the computation of the theoretical reflection coefficient for one and two layers of material. These theoretical S_{11} parameters are calculated using the full-wave MFIE formulation described in sections 2.4 and 2.5. The theoretical reflection coefficient for the single layer of material, $S_{11(1)}^{thy}$, is calculated using the known thickness of the material and a guess for the material parameters ϵ_2 and μ_2. A second reflection coefficient, $S_{11(2)}^{thy}$, is calculated for the two layers of material by using the same values for ϵ_2 and μ_2, the known thicknesses, and the known material parameters for the top layer, ϵ_1 and

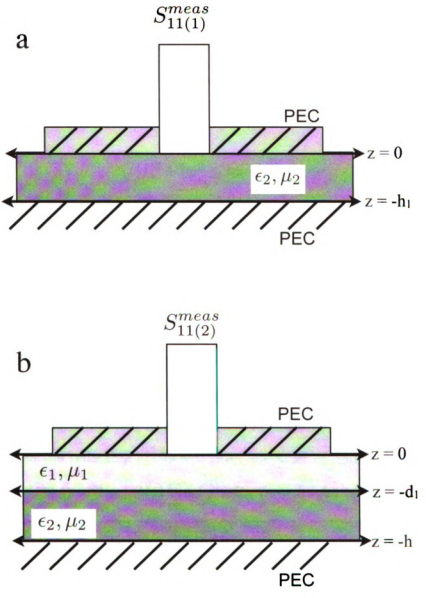


Figure 2.2. Measurement of reflection coefficient on (a) one layer of material and (b) two layers of material

μ_1. Two functions are then constructed, one for each layer configuration,

$$\begin{aligned} f(\epsilon_2, \mu_2,) &= S_{11(1)}^{meas} - S_{11(1)}^{thy} \\ g(\epsilon_2, \mu_2) &= S_{11(2)}^{meas} - S_{11(2)}^{thy}. \end{aligned} \tag{2.7}$$

These functions are simultaneously minimized using a two-dimensional Newton's root finding method to determine the permittivity and permeability of the material. In this application, the stopping criterion of

$$\sqrt{|f|^2 + |g|^2} \leq tolerance \tag{2.8}$$

is employed. When the stopping criterion has been reached, the resulting material parameters produce the same theoretical S_{11} as the reflection coefficients that have been measured, within the specified tolerance.

It should be noted that the reflection coefficient of one layer of material, $S_{11(1)}^{thy}$, is straightforward to calculate using the two layer method formulation. Consider the special case of the two layer problem in Figure 2.2b, when $\epsilon_1 = \epsilon_2$ and $\mu_1 = \mu_2$. The reflection coefficient for two layers of identical material of total thickness h has the same value as the reflection coefficient from one layer of material, which has the material parameters ϵ_2 and μ_2, and has a thickness of h. As noted in Appendix C, the two layer Green's function reduces to the single layer Green's functions when $\epsilon_1 = \epsilon_2$ and $\mu_1 = \mu_2$. Thus, both $S_{11(1)}^{thy}$ and $S_{11(2)}^{thy}$ for the two layer method can be calculated using the two layer formulation described in this chapter.

2.4 Problem Formulation

2.4.1 Waveguide Fields

To develop the MFIE and solve for the amplitude a_1^s, it is necessary to develop a theoretical description of the transverse magnetic fields in the waveguide region and the parallel plate region so that continuity of tangential magnetic field at the boundary, $z = 0$, can be enforced. Continuity of the fields is expressed as

$$\vec{H}_t^{pp}(\vec{\rho}, z = 0^-) = \vec{H}_t^{wg}(\vec{\rho}, z = 0^+) \qquad \vec{\rho} \in CS, \tag{2.9}$$

where $\vec{H}_t^{wg}(\vec{\rho}, z = 0^+)$ and $\vec{H}_t^{pp}(\vec{\rho}, z = 0^-)$ are the transverse magnetic fields in the waveguide and parallel plate region at the aperture plane, respectively. The cross sectional region of the waveguide, CS, is defined as $0 \leq x \leq a$, and $0 \leq y \leq b$.

A useful identity that is employed in this derivation is the orthogonality of the transverse electric field waveguide mode functions [42] over the cross section of the waveguide at $z = 0$,

$$\int_{CS} \vec{e}_n^{wg}(\vec{\rho}) \cdot \vec{e}_q^{wg}(\vec{\rho}) ds = \begin{cases} 1 & n = q \\ 0 & n \neq q \end{cases} = \delta_{qn} \tag{2.10}$$

Applying the operator $\int_{CS} \vec{e}_n^{wg}(\vec{\rho}) \cdot \{\} ds$ to both sides of (2.4) yields

$$\begin{aligned} \int_{CS} \vec{e}_n^{wg}(\vec{\rho}) \cdot \vec{E}_t^{wg}(\vec{\rho}, z = 0^+) ds &= \int_{CS} a_1^i \vec{e}_n^{wg}(\vec{\rho}) \cdot \vec{e}_1^{wg}(\vec{\rho}) ds \\ &\quad + \int_{CS} \sum_{q=1}^{N} a_q^s \vec{e}_n^{wg}(\vec{\rho}) \cdot \vec{e}_q^{wg}(\vec{\rho}) ds \\ &= a_1^i \delta_{n1} + a_n^s, \qquad n = 1, 2, ..., N, \end{aligned} \tag{2.11}$$

or

$$a_n^s = \int_{CS} \vec{e}_n^{wg}(\vec{\rho}) \cdot \vec{E}_t^{wg}(\vec{\rho}, z = 0^+) ds - a_1^i \delta_{n1}, \qquad n = 1, 2, ..., N. \tag{2.12}$$

Using (2.12) in (2.5), the total tangential field in the waveguide region is

$$\vec{H}_t^{wg}(\vec{\rho}, z = 0^+) = -2a_1^i \vec{h}_1^{wg}(\vec{\rho}) + \sum_{n=1}^{N} \vec{h}_n^{wg}(\vec{\rho}) \left[\int_{CS} \vec{e}_n^{wg}(\vec{\rho}) \cdot \vec{E}_t^{wg}(\vec{\rho}, z = 0^+) ds \right], \tag{2.13}$$

where $\vec{\rho} \in CS$.

2.4.2 Parallel Plate Fields

The next step is to determine the fields in the parallel plate region. Using Love's equivalence principle, an equivalent problem may be established by replacing the waveguide aperture with a PEC surface and a magnetic current source that is in the parallel plate region, at $z = 0^-$. This current source covers the same transverse area covered by the waveguide aperture. The magnetic current source (as seen in Figure 2.1) is given by

$$\vec{J}_m(\vec{r}) = -\hat{n} \times \vec{E}_t^{wg}(\vec{\rho}, z = 0^+) = \hat{z} \times \vec{E}_t^{wg}(\vec{\rho}, z = 0^+). \tag{2.14}$$

Due to the continuity of tangential electric field at the boundary $z = 0$, the electric field is equal on either side of the boundary. Thus the following equality

$$\vec{E}_t^{wg}(\vec{\rho}, z = 0^+) = \vec{E}_t^{pp}(\vec{\rho}, z = 0^-) = \vec{E}_t^{wg}(\vec{\rho}, z = 0) \tag{2.15}$$

will be used in the MFIE formulation. Since the volume current $\vec{J}_m$ is only defined in the aperture region at $z = 0$, it can be alternatively written in terms of the surface current, $\vec{K}_m$,

$$\vec{J}_m(\vec{r}) = \vec{K}_m(\vec{\rho}) \delta(z) \tag{2.16}$$

where

$$\vec{K}_m(\vec{\rho}) = \hat{z} \times \vec{E}_t^{wg}(\vec{\rho}). \tag{2.17}$$

Since the current source in region 1 is a magnetic current source, the fields in the parallel plate region can be determined using Maxwell's equations with a magnetic current source [43]. Using magnetic Hertzian potentials, the field relationships are given by

$$\vec{E}(\vec{r}) = -j\omega\mu\nabla \times \vec{\Pi}_m(\vec{r}) \tag{2.18}$$

$$\vec{H}(\vec{r}) = k^2\vec{\Pi}_m(\vec{r}) + \nabla\left[\nabla \cdot \vec{\Pi}_m(\vec{r})\right], \tag{2.19}$$

and the magnetic Hertzian potential inhomogeneous wave equation is

$$\left(\nabla^2 + k^2\right)\vec{\Pi}_m(\vec{r}) = -\frac{\vec{J}_m(\vec{r})}{j\omega\mu}. \tag{2.20}$$

A Green's function approach is taken to solve (2.20), the derivation of which is found in Chapter 3. Using this approach, the solution of the magnetic Hertzian potential wave equation is written as

$$\vec{\Pi}_m(\vec{r}) = \int_V \bar{\bar{G}}^{pp}\left(\vec{r}|\vec{r}'\right) \cdot \vec{J}_m(\vec{r}')dV', \tag{2.21}$$

where $\bar{\bar{G}}^{pp}\left(\vec{r}|\vec{r}'\right)$ is the Hertzian potential dyadic Green's function for a two-layered material in a parallel plate waveguide. This Green's function represents the potential maintained at the observation point $\vec{r}$ by a point source at $\vec{r}'$. Using (2.16) and (2.17) in (2.21) allows the expression for the potential to be rewritten as

$$\vec{\Pi}_m(\vec{r}) = \int_{CS} \bar{\bar{G}}^{pp}\left(\vec{\rho}|\vec{\rho}'; z|z' = 0\right) \cdot \vec{K}_m(\vec{\rho}')ds'. \tag{2.22}$$

Once the dyadic Green's function is known, the expression for the magnetic field

at the aperture in the parallel plate region can be written as

$$\vec{H}_t^{pp}(\vec{\rho}, z=0) = (k_1^2 + \nabla_t \nabla\cdot) \int_{CS} \bar{\bar{G}}^{pp}(\vec{\rho}|\vec{\rho}'; z|z'=0) \cdot \left(\hat{z} \times \vec{E}_t^{wg}(\vec{\rho}', z'=0)\right) ds'\Big|_{z=0}, \quad \vec{\rho} \in CS \qquad (2.23)$$

where $k_1^2 = \omega^2 \mu_1 \epsilon_1$ is the square of the wavenumber in region 1, and ∇_t is the tangential gradient operator.

2.5 MFIE and the Method of Moments Solution

Matching the tangential magnetic fields at the boundary by applying $\vec{H}_t^{wg}(\vec{\rho}, z = 0^+) = \vec{H}_t^{pp}(\vec{\rho}, z = 0^-)$ produces

$$-2a_1^i \vec{h}_1^{wg}(\vec{\rho}) + \sum_{n=1}^{N} \vec{h}_n^{wg}(\vec{\rho}) \left[\int_{CS} \vec{E}_t^{wg}(\vec{\rho}'') \cdot \vec{e}_n^{wg}(\vec{\rho}'')\, ds''\right] = (k_1^2 + \nabla_t \nabla\cdot) \int_{CS} \bar{\bar{G}}^{pp}(\vec{\rho}|\vec{\rho}') \cdot \left(\hat{z} \times \vec{E}_t^{wg}(\vec{\rho}')\right) ds'\Big|_{z=0}, \quad \vec{\rho} \in CS. \qquad (2.24)$$

The notation $\bar{\bar{G}}^{pp}(\vec{\rho}|\vec{\rho}')$ is chosen to replace $\bar{\bar{G}}^{pp}(\vec{\rho}|\vec{\rho}'; z|z'=0)$, and $\vec{E}_t^{wg}(\vec{\rho}')$ is chosen to replace $\vec{E}_t^{wg}(\vec{\rho}', z'=0)$ for convenience.

The Method of Moments (MoM) approach [44] is employed to solve this integral equation. The electric field in the waveguide aperture is expanded using a set of basis functions. A testing function is then used to create a matrix equation that is solved for the amplitude coefficients of the reflected waves. As shown in (2.10), one of the useful properties of the transverse waveguide mode functions $\vec{e}_n^{wg}(\vec{\rho})$ is the orthogonality relationship. This relationship makes these functions useful as entire domain basis functions.

The transverse electric field in the aperture is expanded as a sum of the transverse

electric field waveguide mode functions, yielding

$$\vec{E}_t(\vec{\rho}, z=0) = a_1^i \sum_{q=1}^{N} c_q \vec{e}_q^{\,wg}(\vec{\rho}), \tag{2.25}$$

where $a_1^i c_q$ is the complex amplitude of the qth waveguide mode expansion in the aperture. The constant a_1^i is the amplitude of the incident TE_{10} wave and is useful for normalization.

The expression for the transverse electric field in the waveguide aperture in (2.24) can now be replaced by (2.25) , which produces

$$-2a_1^i \vec{h}_1^{\,wg}(\vec{\rho}) + \sum_{n=1}^{N} \vec{h}_n^{\,wg}(\vec{\rho}) \left[\int_{CS} a_1^i \sum_{q=1}^{N} c_q \vec{e}_q^{\,wg}(\vec{\rho}'') \cdot \vec{e}_n^{\,wg}(\vec{\rho}'')\, ds'' \right] =$$
$$(k_1^2 + \nabla_t \nabla \cdot) \int_{CS} \bar{\bar{G}}^{pp}(\vec{\rho}|\vec{\rho}') \cdot \left(\hat{z} \times a_1^i \sum_{n=1}^{N} c_n \vec{e}_n^{\,wg}(\vec{\rho}') \right) ds' \Bigg|_{z=0} . \tag{2.26}$$

The orthogonality of $\vec{e}_n^{\,wg}(\vec{\rho})$ is useful in evaluating the integral in the square brackets on the left hand side of the equation. In addition, one of the properties of the transverse waveguide mode functions is the relationship between the electric and magnetic field functions, $\vec{e}_n^{\,wg}(\vec{\rho})$ and $\vec{h}_n^{\,wg}(\vec{\rho})$ [41],

$$Z_n^{wg} \vec{h}_n^{\,wg}(\vec{\rho}) = \hat{z} \times \vec{e}_n^{\,wg}(\vec{\rho}), \tag{2.27}$$

where Z_n^{wg} is the directional impedance in the waveguide for mode number n. This waveguide impedance is defined differently depending on whether the waveguide mode is TE_z or TM_z. Formulas are given in Chapter 4. Using (2.27), (2.26) can be rewritten

as

$$-2a_1^i \vec{h}_1^{wg}(\vec{\rho}) + \sum_{n=1}^{N} \vec{h}_n^{wg}(\vec{\rho}) \left[a_1^i c_n\right] = (k_1^2 + \nabla_t \nabla\cdot) Z_n \int_{CS} \bar{\bar{G}}^{pp}(\vec{\rho}|\vec{\rho}') \cdot \left(a_1^i \sum_{n=1}^{N} c_n \vec{h}_n^{wg}(\vec{\rho}') \right) ds' \Bigg|_{z=0}. \quad (2.28)$$

After factoring out the constant a_1^i, some brief algebraic manipulation produces

$$2\vec{h}_1^{wg}(\vec{\rho}) = \sum_{n=1}^{N} c_n \left[\vec{h}_n^{wg}(\vec{\rho}) - Z_n \left(k_1^2 + \nabla_t \nabla\cdot\right) \int_{CS} \bar{\bar{G}}^{pp}(\vec{\rho}|\vec{\rho}') \cdot \vec{h}_n^{wg}(\vec{\rho}') ds' \Big|_{z=0} \right], \quad (2.29)$$

or

$$2\vec{h}_1^{wg}(\vec{\rho}) = \sum_{n=1}^{N} c_n \left[\vec{h}_n^{wg}(\vec{\rho}) - \vec{h}_n^{pp}(\vec{\rho}) \right]. \quad (2.30)$$

Here, by reintroducing the dependence on z and z' in the dyadic Green's function, the term $\vec{h}_n^{pp}(\vec{\rho})$ is defined as

$$\vec{h}_n^{pp}(\vec{\rho}) = Z_n \left(k_1^2 + \nabla_t \nabla\cdot\right) \int_{CS} \bar{\bar{G}}^{pp}(\vec{\rho}|\vec{\rho}'; z|z'=0) \cdot \vec{h}_n^{wg}(\vec{\rho}') ds' \Big|_{z=0}. \quad (2.31)$$

Note that both $\vec{h}_n^{wg}(\vec{\rho})$ and $\vec{h}_n^{pp}(\vec{\rho})$ in (2.30) contain the transverse magnetic waveguide mode functions, $\vec{h}_n^{wg}(\vec{\rho})$. The choice of the testing function to be $\vec{h}_m^{wg}(\vec{\rho})$ allows for the use of the orthogonality properties of the transverse magnetic waveguide mode function.

By applying the operator $\int_{CS} \vec{h}_m^{wg}(\vec{\rho}) \cdot \{\ \} ds$ to (2.30), the resulting equation is

$$2\int_{CS} \vec{h}_m^{wg}(\vec{\rho}) \cdot \vec{h}_1^{wg}(\vec{\rho}) ds = \sum_{n=1}^{N} c_n \int_{CS} \vec{h}_m^{wg}(\vec{\rho}) \cdot \left[\vec{h}_n^{wg}(\vec{\rho}) - \vec{h}_n^{pp}(\vec{\rho})\right] ds$$

$$m = 1, 2, 3, ..., N. \tag{2.32}$$

This can be written in matrix form as

$$[A][c] = [b], \tag{2.33}$$

where each of the elements of matrix A and the vector b are given by

$$A_{mn} = \int_{CS} \vec{h}_m^{wg}(\vec{\rho}) \cdot \left[\vec{h}_n^{wg}(\vec{\rho}) - \vec{h}_n^{pp}(\vec{\rho})\right] ds, \tag{2.34}$$

$$b_m = 2\int_{CS} \vec{h}_m^{wg}(\vec{\rho}) \cdot \vec{h}_1^{wg}(\vec{\rho}) ds. \tag{2.35}$$

Thus, (2.32) produces a system of N equations with N unknowns, where the unknowns are the amplitude coefficients c_n. The elements of the matrix A show how the fields in the waveguide and parallel plate region from the nth mode maintained by the source couple into the mth observation mode fields in the waveguide. The elements of the vector b are the forcing functions, or amplitudes of the excitation.

Recall that the goal of this formulation is the theoretical reflection coefficient, S_{11}^{thy}, as defined in (2.6). Note that the equations (2.4) and (2.25) each describe the tangential field in the waveguide aperture at $z = 0$. Applying the operator

$\int_{CS} \vec{e}_n^{wg}(\vec{\rho}) \cdot \{\ \} ds$ to both equations and setting them equal yields

$$a_1^i \int_{CS} \vec{e}_n^{wg}(\vec{\rho}) \cdot \vec{e}_1^{wg}(\vec{\rho}) ds + \sum_{q=1}^{N} a_q^s \int_{CS} \vec{e}_n^{wg}(\vec{\rho}) \cdot \vec{e}_q^{wg}(\vec{\rho}) ds$$
$$= a_1^i \sum_{q=1}^{N} c_q \int_{CS} \vec{e}_n^{wg}(\vec{\rho}) \cdot \vec{e}_q^{wg}(\vec{\rho}) ds, \tag{2.36}$$

or

$$a_1^i \delta_{n1} + a_n^s = a_1^i c_n. \tag{2.37}$$

Using these relationships, the reflection coefficient is found by

$$S_{11}^{thy} = \frac{a_1^s}{a_1^i} = \frac{a_1^i (c_1 - 1)}{a_1^i} = c_1 - 1. \tag{2.38}$$

Solving the matrix equation (2.33) and obtaining the expansion function amplitude coefficient, c_1, provides a straightforward way of obtaining the theoretical reflection coefficient for the two layer method.

2.6 The Two Thickness Method

As mentioned in section 2.1, the formulation for the two thickness method is quite similar to that of the two layer method. The two thickness method uses a rectangular, flanged, open-ended waveguide probe to interrogate two different thicknesses of a conductor-backed material [35], [36]. The first reflection coefficient, $S_{11(1T)}^{meas}$, is obtained from the first sample of the material, which has a thickness h_1. The second reflection coefficient measurement, $S_{11(2T)}^{meas}$, is taken from a second sample of the same material, which has thickness h.

Using an initial guess for the parameters of the unknown material, the theoretical reflection coefficients are calculated for the first thickness, $S_{11(1T)}^{thy}$, and the second

thickness, $S^{thy}_{11(2T)}$, of the unknown material. These reflection coefficients are calculated in a similar manner to the process shown in sections 2.4 - 2.5. However, instead of the two layer Green's function, $\bar{\bar{G}}^{pp}(\vec{\rho}|\vec{\rho}')$, shown in (2.29), the two thickness method uses a single layer parallel plate Green's function, $\bar{\bar{G}}^{pp}_{1L}(\vec{\rho}|\vec{\rho}')$, [45], [40] to calculate the elements of the matrix A. The diagonal elements of this Green's function are shown in (C.10). Two functions, f_{2T} and g_{2T}, are then constructed:

$$\begin{aligned} f_{2T}(\epsilon,\mu) &= S^{meas}_{11(1T)} - S^{thy}_{11(1T)} \\ g_{2T}(\epsilon,\mu) &= S^{meas}_{11(2T)} - S^{thy}_{11(2T)}. \end{aligned} \tag{2.39}$$

These functions are simultaneously minimized in a manner similar to the two layer method by varying the parameters ϵ and μ until the tolerance criterion is met.

There are some subtle differences which exist between the two methods. The next section briefly outlines the algorithm differences, and they are discussed in greater detail in the error sensitivity analysis in section 6.7 of Chapter 6.

2.6.1 Implementing the Two Thickness Method Algorithm Using the Two Layer Method

Because the formulation for these two methods is quite similar, the two thickness method developed by Stewart [35] can be implemented using the two layer method. In section 2.3 it was noted that the theoretical reflection coefficient for one layer of material can be calculated using the two layer formulation by setting $\epsilon_1 = \epsilon_2$ and $\mu_1 = \mu_2$. Thus, both the theoretical reflection coefficient for one layer of material, $S^{thy}_{11(1T)}$, and the reflection coefficient for a layer which has a different thickness, $S^{thy}_{11(2T)}$, can be calculated using the two layer method formulation by letting $\epsilon_2 = \epsilon_1 = \epsilon$, and $\mu_2 = \mu_1 = \mu$. As shown in Appendix C, when the material parameter values of the top and bottom layer are equal, the two layer parallel plate Green's function derived in Chapter 3 reduces to the single layer parallel plate Green's function used in the

two thickness method. Thus, the formulation presented in sections 2.4 - 2.5 for the two layer method can be used to compute the theoretical S_{11} parameters for use in the two thickness method by letting $\epsilon_2 = \epsilon_1 = \epsilon$, and $\mu_2 = \mu_1 = \mu$.

Although the two layer method may be used to implement the two thickness method, the extraction algorithms used in the respective methods utilize different iterative processes to extract the material parameters. In the two thickness method, the iterative process varies the parameters ϵ and μ in the calculation of $S^{thy}_{11(1T)}$, where $\epsilon_2 = \epsilon_1 = \epsilon$, and $\mu_2 = \mu_1 = \mu$. These same values for ϵ and μ are used to calculate $S^{thy}_{11(2T)}$ in each step of the iterative process. As shown in Chapter 3 and Appendix C, only the first two diagonal elements of the dyadic Green's function are needed in the computation of the reflection coefficient for either thickness.

The two layer method extraction algorithm varies the unknown values ϵ_2 and μ_2, while the material parameters of the top layer, ϵ_1 and μ_1, remain fixed. The calculation of the theoretical reflection coefficient for two layers of material, $S^{thy}_{11(2)}$, requires four elements of the dyadic Green's function, as shown in Chapter 3. These elements are much more complicated to evaluate numerically and the calculation process is more computationally expensive when compared to the single layer Green's function. The two layer method is more sensitive to any random noise in the system and is also more sensitive to the number of modes included in the solution than the two thickness method. These sensitivity issues are examined in greater detail in Chapters 6 and 7.

The development of the solution to the MFIE in (2.32) requires the two layer parallel plate Hertzian potential Green's function and the subsequent numerical analysis in order to determine each matrix element A_{mn}. The derivation of the Green's function is shown in Chapter 3 and the calculation of the matrix entries and solution steps are presented in Chapter 4.

CHAPTER 3

DERIVATION OF THE HERTZIAN POTENTIAL TWO LAYER PARALLEL PLATE GREEN'S FUNCTION

3.1 Introduction

An open-ended waveguide attached to a metal flange and placed against a conductor-backed material surface, as shown in Figure 2.1a, can be replaced by an equivalent problem using Love's equivalence principle. In the equivalent problem, the waveguide aperture is replaced by a PEC surface, and an equivalent magnetic current is placed in the material layer tangential to that PEC surface. The equivalent current covers the same transverse area that was covered by the waveguide aperture in the original problem. As mentioned in chapter 2, it is necessary to match the tangential magnetic field in the waveguide region with the magnetic field in the parallel plate region in the integral equation formulation. This is addressed by using a Green's function approach to determine the magnetic field in region 1 due to a source in region 1, where region 1 is the top layer in Figure 2.1a. The goal of this chapter is to derive the Hertzian potential two layer parallel plate dyadic Green's function for a magnetic current source. Since the equivalent magnetic current induced in region 1 is limited to the transverse direction, only those terms of the dyadic Green's function that contribute to the tangential magnetic field are considered.

3.2 Problem Formulation

Consider a two-layered material bounded on the upper and lower surfaces with two parallel PEC plates, infinite in horizontal extent, as shown in Figure 3.1. The region below the top plate (region 1, $0 > z > -d_1$) is assumed to have the complex material parameters ϵ_1 and μ_1, while the region above the lower plate (region 2, $-d_1 > z > -h$)

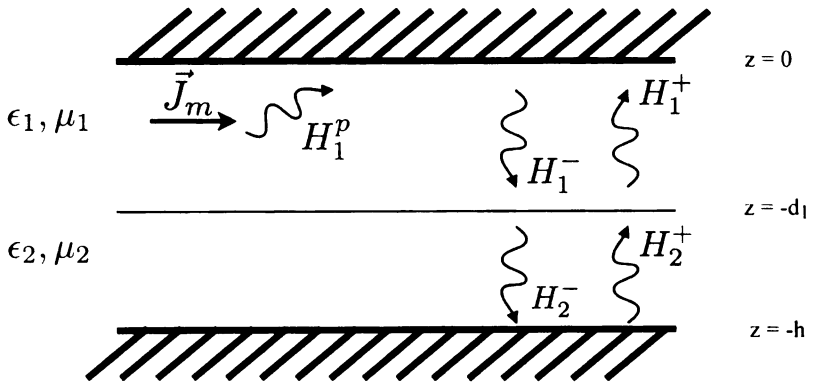


Figure 3.1. Geometry for a two-layered material bounded by parallel PEC plates, infinite in the x- and y-directions.

has complex material parameters ϵ_2 and μ_2. Both regions are assumed to be linear, isotropic, and homogeneous.

A magnetic current source in region 1 produces a magnetic field in both regions 1 and 2. The magnetic field in region 1 is composed of a primary wave H_1^p emanating from the source, and two reflected waves, H_1^+, which travels in the $+z$ direction, and H_1^-, which travels in the $-z$ direction. The primary field is the same as that produced by an identical source in an unbounded space with material parameters ϵ_1 and μ_1. The reflected wave H_1^+ is the reflection from the material boundary at $z = -d_1$, and H_1^- is the reflected wave from the interface at $z = 0$.

Similarly, the fields in region 2 can be decomposed into two traveling waves, H_2^- and H_2^+. The wave H_2^- represents the wave transmitted from region 1 to region 2, while H_2^+ is the wave that reflects off the interface at $z = -h$.

3.3 Hertzian Potential Expression of Electromagnetic Fields

The electric and magnetic fields in regions 1 and 2 can be expressed in terms of Hertzian potentials as [43]

$$\vec{E} = -j\omega\mu\nabla \times \vec{\Pi}_m, \tag{3.1}$$

$$\vec{H} = k^2\vec{\Pi}_m + \nabla\left(\nabla \cdot \vec{\Pi}_m\right). \tag{3.2}$$

The inhomogeneous wave equation for magnetic Hertzian potentials is

$$\left(\nabla^2 + k^2\right)\vec{\Pi}_m = -\frac{\vec{J}_m}{j\omega\mu}. \tag{3.3}$$

Since only magnetic Hertzian potentials are used in this derivation, the m subscript is dropped and $\vec{\Pi}_m$ shall henceforth be denoted as $\vec{\Pi}$. Carrying out the derivatives from (3.2), the scalar components of the magnetic field are

$$H_x = k^2\Pi_x + \frac{\partial}{\partial x}\left(\nabla \cdot \vec{\Pi}\right), \tag{3.4}$$

$$H_y = k^2\Pi_y + \frac{\partial}{\partial y}\left(\nabla \cdot \vec{\Pi}\right), \tag{3.5}$$

$$H_z = k^2\Pi_z + \frac{\partial}{\partial z}\left(\nabla \cdot \vec{\Pi}\right). \tag{3.6}$$

Carrying out the derivatives for (3.1) yields

$$E_x = -j\omega\mu\left(\frac{\partial}{\partial y}\Pi_z - \frac{\partial}{\partial z}\Pi_y\right), \tag{3.7}$$

$$E_y = -j\omega\mu\left(\frac{\partial}{\partial z}\Pi_x - \frac{\partial}{\partial x}\Pi_z\right), \tag{3.8}$$

$$E_z = -j\omega\mu\left(\frac{\partial}{\partial x}\Pi_y - \frac{\partial}{\partial y}\Pi_x\right). \tag{3.9}$$

3.4 Electric and Magnetic Field Boundary Conditions in Terms of Hertzian Potentials

Since the Hertzian potentials describe the fields produced by the current source in the parallel plate region, the boundary conditions on those potentials are deduced by enforcing the boundary conditions on the tangential fields at the upper and lower PEC plates, and at the material interface at $z = -d_1$. At $z = -d_1$, $E_{1x} = E_{2x}$ produces

$$-j\omega\mu_1\left(\frac{\partial}{\partial y}\Pi_{1z} - \frac{\partial}{\partial z}\Pi_{1y}\right) = -j\omega\mu_2\left(\frac{\partial}{\partial y}\Pi_{2z} - \frac{\partial}{\partial z}\Pi_{2y}\right). \tag{3.10}$$

At $z = -d_1$, $E_{1y} = E_{2y}$ produces

$$-j\omega\mu_1\left(\frac{\partial}{\partial z}\Pi_{1x} - \frac{\partial}{\partial x}\Pi_{1z}\right) = -j\omega\mu_2\left(\frac{\partial}{\partial z}\Pi_{2x} - \frac{\partial}{\partial x}\Pi_{2z}\right). \tag{3.11}$$

At $z = -d_1$, $H_{1x} = H_{2x}$ produces

$$k_1^2\Pi_{1x} + \frac{\partial}{\partial x}\left(\nabla\cdot\vec{\Pi}_1\right) = k_2^2\Pi_{2x} + \frac{\partial}{\partial x}\left(\nabla\cdot\vec{\Pi}_2\right). \tag{3.12}$$

At $z = -d_1$, $H_{1y} = H_{2y}$ produces

$$k_1^2\Pi_{1y} + \frac{\partial}{\partial y}\left(\nabla\cdot\vec{\Pi}_1\right) = k_2^2\Pi_{2y} + \frac{\partial}{\partial y}\left(\nabla\cdot\vec{\Pi}_2\right). \tag{3.13}$$

At $z = 0$, $E_{1x} = 0$ requires

$$-j\omega\mu_1\left(\frac{\partial}{\partial y}\Pi_{1z} - \frac{\partial}{\partial z}\Pi_{1y}\right) = 0. \tag{3.14}$$

At $z = 0$, $E_{1y} = 0$ requires

$$-j\omega\mu_1 \left(\frac{\partial}{\partial z}\Pi_{1x} - \frac{\partial}{\partial x}\Pi_{1z} \right) = 0. \tag{3.15}$$

At $z = -h$, $E_{2x} = 0$ requires

$$-j\omega\mu_2 \left(\frac{\partial}{\partial y}\Pi_{2z} - \frac{\partial}{\partial z}\Pi_{2y} \right) = 0. \tag{3.16}$$

At $z = -h$, $E_{2y} = 0$ requires

$$-j\omega\mu_2 \left(\frac{\partial}{\partial z}\Pi_{2x} - \frac{\partial}{\partial x}\Pi_{2z} \right) = 0. \tag{3.17}$$

3.5 Potential Boundary conditions for an x-directed source

Consider an x-directed source in region 1: $\vec{J}_m = \hat{x}J_{1x}$. The horizontal magnetic current source can be described completely by a Hertzian potential with x and z components, (see Appendix B)

$$\vec{\Pi}_1 = \hat{x}\Pi_{1x} + \hat{z}\Pi_{1z}. \tag{3.18}$$

3.5.1 Boundary Condition 1

The boundary conditions on the potential for an x-directed source are specializations of the boundary conditions found in (3.10) - (3.17), with $\Pi_y = 0$. Applying this criteria to boundary condition (3.10) gives

$$\mu_1 \frac{\partial}{\partial y}\Pi_{1z} = \mu_2 \frac{\partial}{\partial y}\Pi_{2z} \qquad at\ z = -d_1. \tag{3.19}$$

As shown in Appendix B, using a Fourier transform approach allows (3.19) to be rewritten as

$$\Pi_{1z} = \frac{\mu_2}{\mu_1}\Pi_{2z} \qquad at\ z = -d_1. \tag{3.20}$$

3.5.2 Boundary Condition 2

Since $\Pi_{1y} = \Pi_{2y} = 0$ it is possible to rewrite (3.13) as

$$\frac{\partial}{\partial y}\left(\nabla \cdot \vec{\Pi}_1\right) = \frac{\partial}{\partial y}\left(\nabla \cdot \vec{\Pi}_2\right) \qquad at\ z = -d_1. \tag{3.21}$$

This reduces to

$$\nabla \cdot \vec{\Pi}_1 = \nabla \cdot \vec{\Pi}_2 \qquad at\ z = -d_1, \tag{3.22}$$

by using the Fourier transform and Fourier integral theorem approach used for (3.20). Rewriting boundary condition (3.12) results in

$$k_1^2\Pi_{1x} + \frac{\partial}{\partial x}\left(\nabla \cdot \vec{\Pi}_1\right) = k_2^2\Pi_{2x} + \frac{\partial}{\partial x}\left(\nabla \cdot \vec{\Pi}_2\right) \qquad at\ z = -d_1. \tag{3.23}$$

Using the relationship between the divergence of the potentials found in (3.22) allows for the reduction of (3.23) to

$$k_1^2\Pi_{1x} = k_2^2\Pi_{2x} \qquad at\ z = -d_1, \tag{3.24}$$

or

$$\Pi_{1x} = \frac{\mu_2\epsilon_2}{\mu_1\epsilon_1}\Pi_{2x} \qquad at\ z = -d_1. \tag{3.25}$$

3.5.3 Boundary Condition 3

If the divergence in (3.22) is written in expanded form, that equation can be rewritten as

$$\frac{\partial}{\partial x}\Pi_{1x} + \frac{\partial}{\partial z}\Pi_{1z} = \frac{\partial}{\partial x}\Pi_{2x} + \frac{\partial}{\partial z}\Pi_{2z} \qquad at\ z = -d_1, \tag{3.26}$$

or

$$\frac{\partial}{\partial x}\left(\Pi_{1x}-\Pi_{2x}\right)=\frac{\partial}{\partial z}\left(\Pi_{2z}-\Pi_{1z}\right) \qquad at\ z=-d_1. \tag{3.27}$$

Substituting (3.25) in (3.27) yields

$$\frac{\partial}{\partial x}\left(\frac{\mu_2\epsilon_2}{\mu_1\epsilon_1}\Pi_{2x}-\Pi_{2x}\right)=\frac{\partial}{\partial z}\left(\Pi_{2z}-\Pi_{1z}\right) \qquad at\ z=-d_1, \tag{3.28}$$

or

$$-\left(\frac{\mu_2\epsilon_2}{\mu_1\epsilon_1}-1\right)\frac{\partial}{\partial x}\Pi_{2x}=\frac{\partial}{\partial z}\left(\Pi_{1z}-\Pi_{2z}\right) \qquad at\ z=-d_1. \tag{3.29}$$

3.5.4 Boundary Condition 4

Applying boundary condition (3.11) yields

$$\mu_1\left(\frac{\partial}{\partial z}\Pi_{1x}-\frac{\partial}{\partial x}\Pi_{1z}\right)=\mu_2\left(\frac{\partial}{\partial z}\Pi_{2x}-\frac{\partial}{\partial x}\Pi_{2z}\right) \qquad at\ z=-d_1. \tag{3.30}$$

Using (3.20) in (3.30) yields

$$\mu_1\left[\frac{\partial}{\partial z}\Pi_{1x}-\frac{\partial}{\partial x}\left(\frac{\mu_2}{\mu_1}\Pi_{2z}\right)\right]=\mu_2\left(\frac{\partial}{\partial z}\Pi_{2x}-\frac{\partial}{\partial x}\Pi_{2z}\right), \tag{3.31}$$

which, after rearranging terms, produces

$$\frac{\partial}{\partial z}\left(\mu_1\Pi_{1x}-\mu_2\Pi_{2x}\right)=\frac{\partial}{\partial x}\left(\mu_2\Pi_{2z}-\mu_2\Pi_{2z}\right)=0, \tag{3.32}$$

or

$$\mu_1\frac{\partial}{\partial z}\Pi_{1x}=\mu_2\frac{\partial}{\partial z}\Pi_{2x} \qquad at\ z=-d_1. \tag{3.33}$$

3.5.5 Boundary Condition 5

Applying (3.14) at the top perfect conductor interface gives

$$-j\omega\mu_1\left(\frac{\partial}{\partial y}\Pi_{1z}-\frac{\partial}{\partial z}\Pi_{1y}\right)=0 \qquad at\ z=0. \tag{3.34}$$

Thus, (3.34) simplifies to

$$\frac{\partial}{\partial y}\Pi_{1z}=0 \qquad at\ z=0. \tag{3.35}$$

3.5.6 Boundary Condition 6

Applying boundary condition (3.15) gives

$$-j\omega\mu_1\left(\frac{\partial}{\partial z}\Pi_{1x}-\frac{\partial}{\partial x}\Pi_{1z}\right)=0 \qquad at\ z=0, \tag{3.36}$$

which simplifies to

$$\frac{\partial}{\partial z}\Pi_{1x}=\frac{\partial}{\partial x}\Pi_{1z} \qquad at\ z=0. \tag{3.37}$$

3.5.7 Boundary Condition 7

Applying boundary condition (3.16) at the lower PEC interface yields

$$\left(\frac{\partial}{\partial y}\Pi_{2z}-\frac{\partial}{\partial z}\Pi_{2y}\right)=0 \qquad at\ z=-h. \tag{3.38}$$

Since $\Pi_{1y}=0$, the resulting condition is

$$\frac{\partial}{\partial y}\Pi_{2z}=0 \qquad at\ z=-h. \tag{3.39}$$

3.5.8 Boundary Condition 8

Applying boundary condition (3.17) at $z = -h$ gives

$$\frac{\partial}{\partial z}\Pi_{2x} - \frac{\partial}{\partial x}\Pi_{2z} = 0, \tag{3.40}$$

or

$$\frac{\partial}{\partial z}\Pi_{2x} = \frac{\partial}{\partial x}\Pi_{2z} \qquad at\ z = -h. \tag{3.41}$$

3.5.9 Summary of Hertzian Potential Boundary Conditions for $\vec{J}_m = \hat{x}J_{1x}$

$$\Pi_{1z} = \frac{\mu_2}{\mu_1}\Pi_{2z} \qquad at\ z = -d_1. \tag{3.42}$$

$$\Pi_{1x} = \frac{\mu_2\epsilon_2}{\mu_1\epsilon_1}\Pi_{2x} \qquad at\ z = -d_1. \tag{3.43}$$

$$-\left(\frac{\mu_2\epsilon_2}{\mu_1\epsilon_1} - 1\right)\frac{\partial}{\partial x}\Pi_{2x} = \frac{\partial}{\partial z}\left(\Pi_{1z} - \Pi_{2z}\right) \qquad at\ z = -d_1. \tag{3.44}$$

$$\mu_1\frac{\partial}{\partial z}\Pi_{1x} = \mu_2\frac{\partial}{\partial z}\Pi_{2x} \qquad at\ z = -d_1. \tag{3.45}$$

$$\frac{\partial}{\partial y}\Pi_{1z} = 0 \qquad at\ z = 0. \tag{3.46}$$

$$\frac{\partial}{\partial z}\Pi_{1x} = \frac{\partial}{\partial x}\Pi_{1z} \qquad at\ z = 0. \tag{3.47}$$

$$\frac{\partial}{\partial y}\Pi_{2z} = 0 \qquad at\ z = -h. \tag{3.48}$$

$$\frac{\partial}{\partial z}\Pi_{2x} = \frac{\partial}{\partial x}\Pi_{2z} \qquad at\ z = -h. \tag{3.49}$$

3.6 Potential Boundary Conditions for y-directed Source

Consider a y-directed source in region 1: $\vec{J}_m = \hat{y}J_{1y}$. Similar to the x-directed source, the fields from a horizontal magnetic current source can be described completely by a magnetic Hertzian potential oriented in the same direction ($\hat{y}$) and the normal

direction ($\hat{z}$) (see Appendix B). Thus, the potential in region 1 is given by

$$\vec{\Pi}_1 = \hat{y}\Pi_{1y} + \hat{z}\Pi_{1z}. \tag{3.50}$$

3.6.1 Boundary Condition 1

Using the boundary conditions on the potential for a y-directed source are specializations of the boundary conditions found in (3.10) - (3.17), with $\Pi_x = 0$. Applying this criteria to boundary condition (3.11) yields

$$\mu_1 \frac{\partial}{\partial x}\Pi_{1z} = \mu_2 \frac{\partial}{\partial x}\Pi_{2z} \qquad at\ z = -d_1. \tag{3.51}$$

This can be rewritten as

$$\Pi_{1z} = \frac{\mu_2}{\mu_1}\Pi_{2z} \qquad at\ z = -d_1. \tag{3.52}$$

3.6.2 Boundary Condition 2

Applying boundary condition (3.10) yields

$$\mu_1 \left(\frac{\partial}{\partial y}\Pi_{1z} - \frac{\partial}{\partial z}\Pi_{1y} \right) = \mu_2 \left(\frac{\partial}{\partial y}\Pi_{2z} - \frac{\partial}{\partial z}\Pi_{2y} \right). \tag{3.53}$$

Using (3.52) in (3.53) produces

$$\mu_1 \left(\frac{\partial}{\partial y}\frac{\mu_2}{\mu_1}\Pi_{2z} - \frac{\partial}{\partial z}\Pi_{1y} \right) = \mu_2 \left(\frac{\partial}{\partial y}\Pi_{2z} - \frac{\partial}{\partial z}\Pi_{2y} \right), \tag{3.54}$$

which reduces to

$$\mu_1 \frac{\partial}{\partial z}\Pi_{1y} = \mu_2 \frac{\partial}{\partial z}\Pi_{2y} \qquad at\ z = -d_1. \tag{3.55}$$

3.6.3 Boundary Condition 3

Since $\Pi_{1x} = \Pi_{2x} = 0$, boundary condition (3.12) reduces to

$$\frac{\partial}{\partial x}\left(\nabla \cdot \vec{\Pi}_1\right) = \frac{\partial}{\partial x}\left(\nabla \cdot \vec{\Pi}_2\right) \qquad at\ z = -d_1, \tag{3.56}$$

or

$$\nabla \cdot \vec{\Pi}_1 = \nabla \cdot \vec{\Pi}_2 \qquad at\ z = -d_1. \tag{3.57}$$

Using (3.57) in boundary condition (3.13) yields

$$k_1^2 \Pi_{1y} + \frac{\partial}{\partial y}\left(\nabla \cdot \vec{\Pi}_1\right) = k_2^2 \Pi_{2y} + \frac{\partial}{\partial y}\left(\nabla \cdot \vec{\Pi}_1\right), \tag{3.58}$$

or

$$k_1^2 \Pi_{1y} = k_2^2 \Pi_{2y}, \tag{3.59}$$

which can be alternatively written as

$$\Pi_{1y} = \frac{\mu_2 \epsilon_2}{\mu_1 \epsilon_1} \Pi_{2y} \qquad at\ z = -d_1. \tag{3.60}$$

3.6.4 Boundary Condition 4

The relationship found in (3.57) can be rewritten as

$$\frac{\partial}{\partial y}\Pi_{1y} + \frac{\partial}{\partial z}\Pi_{1z} = \frac{\partial}{\partial y}\Pi_{2y} + \frac{\partial}{\partial z}\Pi_{2z} \qquad at\ z = -d_1. \tag{3.61}$$

Using (3.60) and rearranging terms produces

$$\frac{\partial}{\partial y}\left(\frac{\mu_2 \epsilon_2}{\mu_1 \epsilon_1}\Pi_{2y}\right) - \frac{\partial}{\partial y}\Pi_{2y} = \frac{\partial}{\partial z}\Pi_{2z} - \frac{\partial}{\partial z}\Pi_{1z} \qquad at\ z = -d_1, \tag{3.62}$$

or

$$-\left(\frac{\mu_2\epsilon_2}{\mu_1\epsilon_1}-1\right)\frac{\partial}{\partial y}\Pi_{2y}=\frac{\partial}{\partial z}\left(\Pi_{1z}-\Pi_{2z}\right) \qquad at\ z=-d_1. \tag{3.63}$$

3.6.5 Boundary Condition 5

Applying boundary condition (3.14) at the upper PEC interface yields

$$-j\omega\mu_1\left(\frac{\partial}{\partial y}\Pi_{1z}-\frac{\partial}{\partial z}\Pi_{1y}\right)=0 \qquad at\ z=0, \tag{3.64}$$

which simplifies to

$$\frac{\partial}{\partial y}\Pi_{1z}=\frac{\partial}{\partial z}\Pi_{1y} \qquad at\ z=0. \tag{3.65}$$

3.6.6 Boundary Condition 6

Applying boundary condition (3.15) at the upper PEC interface yields

$$-j\omega\mu_1\left(\frac{\partial}{\partial z}\Pi_{1x}-\frac{\partial}{\partial x}\Pi_{1z}\right)=0 \qquad at\ z=0. \tag{3.66}$$

However, due to the y-directed source, $\Pi_{1x}=0$, which produces

$$\frac{\partial}{\partial x}\Pi_{1z}=0 \qquad at\ z=0. \tag{3.67}$$

3.6.7 Boundary Condition 7

Applying boundary condition (3.16) at the lower PEC interface produces

$$\left(\frac{\partial}{\partial y}\Pi_{2z}-\frac{\partial}{\partial z}\Pi_{2y}\right)=0 \qquad at\ z=-h, \tag{3.68}$$

or

$$\frac{\partial}{\partial y}\Pi_{2z}=\frac{\partial}{\partial z}\Pi_{2y} \qquad at\ z=-h. \tag{3.69}$$

3.6.8 Boundary Condition 8

Finally, applying boundary condition (3.17) at $z = -h$ gives

$$\frac{\partial}{\partial z}\Pi_{2x} - \frac{\partial}{\partial x}\Pi_{2z} = 0 \qquad at\ z = -h. \tag{3.70}$$

Since $\Pi_{2x} = 0$ the result is

$$\frac{\partial}{\partial x}\Pi_{2z} = 0 \qquad at\ z = -h. \tag{3.71}$$

3.6.9 Summary of Hertzian Potential Boundary Conditions for $\vec{J}_m = \hat{y}J_{1y}$

$$\Pi_{1z} = \frac{\mu_2}{\mu_1}\Pi_{2z} \qquad at\ z = -d_1. \tag{3.72}$$

$$\mu_1\frac{\partial}{\partial z}\Pi_{1y} = \mu_2\frac{\partial}{\partial z}\Pi_{2y} \qquad at\ z = -d_1. \tag{3.73}$$

$$\Pi_{1y} = \frac{\mu_2\epsilon_2}{\mu_1\epsilon_1}\Pi_{2y} \qquad at\ z = -d_1. \tag{3.74}$$

$$-\left(\frac{\mu_2\epsilon_2}{\mu_1\epsilon_1} - 1\right)\frac{\partial}{\partial y}\Pi_{2y} = \frac{\partial}{\partial z}\left(\Pi_{1z} - \Pi_{2z}\right) \qquad at\ z = -d_1. \tag{3.75}$$

$$\frac{\partial}{\partial y}\Pi_{1z} = \frac{\partial}{\partial z}\Pi_{1y} \qquad at\ z = 0. \tag{3.76}$$

$$\frac{\partial}{\partial x}\Pi_{1z} = 0 \qquad at\ z = 0. \tag{3.77}$$

$$\frac{\partial}{\partial y}\Pi_{2z} = \frac{\partial}{\partial z}\Pi_{2y} \qquad at\ z = -h. \tag{3.78}$$

$$\frac{\partial}{\partial x}\Pi_{2z} = 0 \qquad at\ z = -h. \tag{3.79}$$

3.7 Formulation of Potentials in Parallel Plate Region

Note that the potential boundary conditions are all enforced at specific locations of z ($z = 0$, $z = -d_1$, and $z = -h$) for all points parallel to the x-y plane. In addition, the geometry along the boundaries in the x and y-directions is invariant. Thus, it

is useful to consider the Hertzian potentials as a linear superposition of plane waves propagating along the z-axis [46] using a Fourier transform approach. Because the boundary conditions are enforced at locations along the z-axis, the transform variable for the potential is in the coordinates tangential to the direction of propagation. The two dimensional Fourier transform in the spatial frequency domain is defined as

$$\widetilde{\Pi}_{\alpha\beta}\left(k_x, k_y, z\right) = \iint_{-\infty}^{+\infty} \Pi_{\alpha\beta}\left(x, y, z\right) e^{-j\vec{k}\cdot\vec{\rho}} dxdy, \tag{3.80}$$

where $\alpha = 1, 2$, corresponding to either region 1 or 2, $\beta = x, y, z$, $\vec{k} = k_x\hat{x} + k_y\hat{y}$ and $\vec{\rho} = x\hat{x} + y\hat{y}$. The inverse transform is likewise defined as

$$\Pi_{\alpha\beta}\left(x, y, z\right) = \frac{1}{(2\pi)^2} \iint_{-\infty}^{+\infty} \widetilde{\Pi}_{\alpha\beta}\left(k_x, k_y, z\right) e^{j\vec{k}\cdot\vec{\rho}} dk_x dk_y. \tag{3.81}$$

The advantage of this representation is that it allows the wave equation to be reduced from a partial differential equation to an ordinary differential equation, thus simplifying the solution process.

3.7.1 Source-Free, or Scattered Potential

From (3.3) the scalar Helmholz equation for each component of the scattered potential in a source-free region is given by

$$\left(\nabla^2 + k^2\right) \Pi^s_{\alpha\beta}\left(\vec{r}\right) = 0. \tag{3.82}$$

Using the Fourier Transform relationship (3.81) allows (3.82) to be rewritten as

$$\left(\nabla^2 + k^2\right) \frac{1}{(2\pi)^2} \iint_{-\infty}^{+\infty} \widetilde{\Pi}^s_{\alpha\beta}\left(k_x, k_y, z\right) e^{j\vec{k}\cdot\vec{\rho}} dk_x dk_y = 0, \tag{3.83}$$

and bringing the derivatives inside the integral produces

$$\frac{1}{(2\pi)^2}\iint_{-\infty}^{+\infty}\left(\frac{\partial^2}{\partial x^2}+\frac{\partial^2}{\partial y^2}+\frac{\partial^2}{\partial z^2}+k^2\right)\widetilde{\Pi}^s_{\alpha\beta}\left(k_x,k_y,z\right)e^{j\vec{k}\cdot\vec{\rho}}dk_xdk_y=0. \tag{3.84}$$

By carrying out the derivatives, (3.84) progresses to

$$\frac{1}{(2\pi)^2}\iint_{-\infty}^{+\infty}\left[\left(\left(k^2-k_x^2-k_y^2\right)+\frac{\partial^2}{\partial z^2}\right)\widetilde{\Pi}^s_{\alpha\beta}\left(k_x,k_y,z\right)\right]e^{j\vec{k}\cdot\vec{\rho}}dk_xdk_y=0, \tag{3.85}$$

which is the inverse transform of the term in the square brackets. According to the Fourier integral theorem [47], if the inverse tranform of a function is zero, then the function itself must be zero. Thus (3.85) leads to the equation

$$\left(k^2-k_x^2-k_y^2\right)\widetilde{\Pi}^s_{\alpha\beta}\left(k_x,k_y,z\right)+\frac{\partial^2}{\partial z^2}\widetilde{\Pi}^s_{\alpha\beta}\left(k_x,k_y,z\right)=0. \tag{3.86}$$

For simplification purposes, let

$$p^2=k_x^2+k_y^2-k^2. \tag{3.87}$$

Then (3.86) becomes the ordinary differential equation

$$\left[\frac{\partial^2}{\partial z^2}-p^2\right]\widetilde{\Pi}^s_{\alpha\beta}\left(k_x,k_y,z\right)=0. \tag{3.88}$$

This equation has the solution

$$\widetilde{\Pi}^s_{\alpha\beta}\left(k_x,k_y,z\right)=W^s_{\alpha\beta}\left(k_x,k_y\right)e^{\mp pz}, \tag{3.89}$$

where $W^s_{\alpha\beta}$ is an amplitude independent of z. Since the complex quantity p is determined by the square root function, the proper choice of signs is necessary for the real

and imaginary parts of p. For a conventional material that possesses positive real parts of permeability and permittivity and negative imaginary parts of permittivity and permeability, the quantity p^2 is in the upper half space of the complex p plane. Thus, the value for p lies in either the first or third quadrant. If p is defined such that $p = p_r + jp_i$, then $p_r > 0$ and $p_i > 0$ for proper propagation and decay. Waves that are traveling in the $+z$ direction have the negative sign in (3.89), while those traveling in the $-z$ direction maintain the positive sign in (3.89). Thus the scattered potential in a source-free region can be expressed as

$$\Pi^s_{\alpha\beta}(x,y,z) = \frac{1}{(2\pi)^2}\iint_{-\infty}^{+\infty} W^s_{\alpha\beta}(k_x,k_y)\, e^{\mp pz} e^{j\vec{k}\cdot\vec{\rho}} dk_x dk_y. \tag{3.90}$$

3.7.2 Solution for Potential Due to Sources (Primary Potential)

From (3.3) the Helmholz equation for the potential due to a magnetic source current $\vec{J}_m$ is

$$\left(\nabla^2 + k^2\right)\vec{\Pi}^p(\vec{r}) = -\frac{\vec{J}_m(\vec{r})}{j\omega\mu}. \tag{3.91}$$

It is desirable to solve this equation using the Green's function representation for a Hertzian potential due to a point source. The final solution for the magnetic potential is obtained as a linear superposition integral of the Green's function and the magnetic current distribution, and the magnetic field is obtained from (3.2). In an unbounded space, the Green's function for a primary Hertzian potential represents the potential due to a point source and satisfies

$$\left(\nabla^2 + k^2\right) G^p(\vec{r},\vec{r}') = -\delta(\vec{r}-\vec{r}'). \tag{3.92}$$

This Green's function depends only on the difference between the source and observation vectors,

$$G^p\left(\vec{r},\vec{r}'\right) = G^p\left(\vec{r}-\vec{r}'\right). \tag{3.93}$$

By choosing $\vec{r}' = 0$ for convenience, equation (3.92) becomes

$$\left(\nabla^2 + k^2\right) G^p\left(\vec{r}\right) = -\delta\left(\vec{r}\right). \tag{3.94}$$

The final result may then be shifted to any source point, $\vec{r}' \neq 0$.

Using a similar convention to (3.80) and (3.81), the Fourier Transform pairs for the spectral domain are defined as

$$\widetilde{G}^p\left(k_x,k_y,z\right) = \iint_{-\infty}^{+\infty} G^p\left(x,y,z\right) e^{-j\vec{k}\cdot\vec{\rho}} dxdy \tag{3.95}$$

$$G^p\left(x,y,z\right) = \frac{1}{(2\pi)^2} \iint_{-\infty}^{+\infty} \widetilde{G}^p\left(k_x,k_y,z\right) e^{j\vec{k}\cdot\vec{\rho}} dk_x dk_y. \tag{3.96}$$

Using (3.96) in (3.94) yields

$$\left(\nabla^2 + k^2\right)\left[\frac{1}{(2\pi)^2} \iint_{-\infty}^{+\infty} \widetilde{G}^p\left(k_x,k_y,z\right) e^{j\vec{k}\cdot\vec{\rho}} dk_x dk_y\right] = -\delta\left(\vec{r}\right). \tag{3.97}$$

The Fourier transform identity for a two-dimensional delta function is [43]

$$\begin{aligned}\delta\left(\vec{r}-\vec{r}'\right) &= \delta\left(x-x'\right)\delta\left(y-y'\right)\delta\left(z-z'\right) \\ &= \frac{1}{(2\pi)^2} \iint_{-\infty}^{+\infty} \delta\left(z-z'\right) e^{j\vec{k}\cdot\left(\vec{\rho}-\vec{\rho}'\right)} dk_x dk_y.\end{aligned} \tag{3.98}$$

Employing this to the right hand side of (3.97) yields

$$\frac{1}{(2\pi)^2}\iint_{-\infty}^{+\infty}\left[\left(k^2-k_x^2-k_y^2\right)+\frac{\partial^2}{\partial z^2}\right]\widetilde{G}^p\left(k_x,k_y,z\right)e^{j\vec{k}\cdot\vec{\rho}}dk_xdk_y$$

$$=-\frac{1}{(2\pi)^2}\iint_{-\infty}^{+\infty}\delta\left(z\right)e^{j\vec{k}\cdot\vec{\rho}}dk_xdk_y, \tag{3.99}$$

or

$$\frac{1}{(2\pi)^2}\iint_{-\infty}^{+\infty}\left[\left(\frac{\partial^2}{\partial z^2}-p^2\right)\widetilde{G}^p\left(k_x,k_y,z\right)+\delta\left(z\right)\right]e^{j\vec{k}\cdot\vec{\rho}}dk_xdk_y=0. \tag{3.100}$$

Employing the Fourier integral theorem, the term inside the brackets must be zero, so

$$\left(\frac{\partial^2}{\partial z^2}-p^2\right)\widetilde{G}^p\left(k_x,k_y,z\right)+\delta\left(z\right)=0. \tag{3.101}$$

Defining the spatial Fourier Transform pair for the z-direction as

$$\tilde{\widetilde{G}}^p\left(k_x,k_y,k_z\right)=\int_{-\infty}^{+\infty}\widetilde{G}^p\left(k_x,k_y,z\right)e^{-jk_zz}dz \tag{3.102}$$

$$\widetilde{G}^p\left(k_x,k_y,z\right)=\frac{1}{2\pi}\int_{-\infty}^{+\infty}\tilde{\widetilde{G}}^p\left(k_x,k_y,k_z\right)e^{jk_zz}dk_z, \tag{3.103}$$

and noting the Fourier integral identity [43]

$$\delta(z)=\frac{1}{2\pi}\int_{-\infty}^{+\infty}e^{jk_zz}dk_z, \tag{3.104}$$

then (3.101) can be rewritten using (3.103) and (3.104) as

$$\left(\frac{\partial^2}{\partial z^2}-p^2\right)\frac{1}{2\pi}\int_{-\infty}^{+\infty}\tilde{\widetilde{G}}^p\left(k_x,k_y,k_z\right)e^{jk_zz}dk_z+\frac{1}{2\pi}\int_{-\infty}^{+\infty}e^{jk_zz}dk_z=0. \tag{3.105}$$

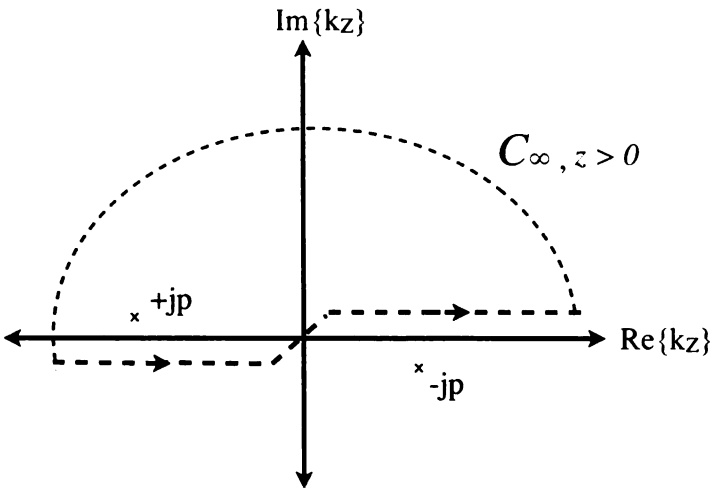


Figure 3.2. The contour integral in the complex k_z plane for $z > 0$

Rearranging and carrying through derivatives results in

$$\frac{1}{2\pi}\int_{-\infty}^{+\infty}\left[\left(-k_z^2-p^2\right)\tilde{\tilde{G}}^p\left(k_x,k_y,k_z\right)+1\right]e^{jk_zz}dk_z=0, \tag{3.106}$$

which produces

$$\tilde{\tilde{G}}^p\left(k_x,k_y,k_z\right)=\frac{1}{\left(k_z^2+p^2\right)}. \tag{3.107}$$

Making use of the Fourier transform relationship (3.103) gives

$$\begin{aligned}\widetilde{G}^p\left(k_x,k_y,z\right)&=\frac{1}{2\pi}\int_{-\infty}^{+\infty}\frac{e^{jk_zz}}{\left(k_z^2+p^2\right)}dk_z\\&=\frac{1}{2\pi}\int_{-\infty}^{+\infty}\frac{e^{jk_zz}}{\left(k_z+jp\right)\left(k_z-jp\right)}dk_z.\end{aligned} \tag{3.108}$$

The poles of the integrand in (3.108) are found in the lower right quadrant and upper left quadrant of the complex k_z plane, since $p_r > 0$ and $p_i > 0$, as shown in

Figure 3.2. By closing a contour integral in the upper half plane (corresponding to $z > 0$), and using Cauchy's residue theorum [48], the countour integral can be written as

$$\int_{-\infty}^{+\infty} \frac{e^{jk_z z}}{(k_z + jp)(k_z - jp)} dk_z + \int_{C_\infty} \frac{e^{jk_z z}}{(k_z + jp)(k_z - jp)} dk_z = 2\pi j Res. \tag{3.109}$$

It can be shown [43] that the integral over the contour C_∞ vanishes as the radius of the contour goes to infinity. The residue is found as

$$Res = \left. \frac{e^{jk_z z}}{(k_z + jp)} \right|_{k_z = jp} = \frac{e^{-pz}}{2jp}. \tag{3.110}$$

Thus, for the upper half space, by using (3.108) -(3.110) the Green's function for the primary source in the spatial frequency domain is

$$\widetilde{G}^p(k_x, k_y, z) = \frac{e^{-pz}}{2p}, \qquad z > 0. \tag{3.111}$$

By using a similar process, the Green's function for the lower half space is

$$\widetilde{G}^p(k_x, k_y, z) = \frac{e^{pz}}{2p}, \qquad z < 0. \tag{3.112}$$

Combining the two expressions results in

$$\widetilde{G}^p(k_x, k_y, z) = \frac{e^{-p|z|}}{2p}, \qquad -\infty < z < \infty, \tag{3.113}$$

with $p_r > 0$ and $p_i > 0$.

To find the Green's function for the primary source in the spatial domain one can

use the Fourier transform relationship (3.96), which produces

$$G^p(\vec{r}) = \frac{1}{(2\pi)^2} \iint_{-\infty}^{+\infty} \frac{e^{-p|z|}}{2p} e^{j\vec{k}\cdot\vec{\rho}} dk_x dk_y. \tag{3.114}$$

Replacing $\vec{r}$ with $(\vec{r} - \vec{r}')$ for a current source centered at some location $\vec{r}'$, the Green's function for the particular solution is

$$G^p(\vec{r}|\vec{r}') = \frac{1}{(2\pi)^2} \iint_{-\infty}^{+\infty} \frac{e^{-p|z-z'|}}{2p} e^{j\vec{k}\cdot(\vec{\rho}-\vec{\rho}')} dk_x dk_y. \tag{3.115}$$

The primary potential is then found by forming the superposition integral

$$\vec{\Pi}^p(\vec{r}) = \int_V G^p(\vec{r}|\vec{r}') \frac{\vec{J}_m(\vec{r}')}{j\omega\mu} dV'. \tag{3.116}$$

3.7.3 Summary of Potential Representation

In summary, from (3.116) the primary potential is given by

$$\vec{\Pi}^p(\vec{r}) = \int_V \frac{\vec{J}_m(\vec{r}')}{j\omega\mu} \left\{ \frac{1}{(2\pi)^2} \iint_{-\infty}^{+\infty} \frac{e^{-p|z-z'|}}{2p} e^{j\vec{k}\cdot(\vec{\rho}-\vec{\rho}')} dk_x dk_y \right\} dV', \tag{3.117}$$

and from (3.90) the scattered potentials are

$$\vec{\Pi}^s_\alpha(\vec{r}) = \hat{x}\Pi^s_{\alpha x}(\vec{r}) + \hat{y}\Pi^s_{\alpha y}(\vec{r}) + \hat{z}\Pi^s_{\alpha z}(\vec{r}) \tag{3.118}$$

$$\Pi^s_{\alpha\beta}(\vec{r}) = \frac{1}{(2\pi)^2} \iint_{-\infty}^{+\infty} W^s_{\alpha\beta}(k_x, k_y) e^{\mp pz} e^{j\vec{k}\cdot\vec{\rho}} dk_x dk_y. \tag{3.119}$$

where $\alpha = 1, 2$ and $\beta = x, y, z$.

3.8 Calculation of the Hertzian Potential Green's Function in the Parallel Plate Region

Recall that the goal of this chapter is to derive a Hertzian potential Green's function that allows for the calculation of the magnetic Hertzian potential in region 1 due to a magnetic current source in region 1. Once this potential is obtained, the transverse magnetic field in the parallel plate region at the waveguide aperture can be matched to the transverse magnetic field in the waveguide region to form the MFIE that is described in Chapter 2.

In the previous section, expressions for the primary and scattered potentials in the parallel plate region are given. In this section, the potential boundary conditions (3.42) - (3.49) and (3.72) - (3.79) are employed to solve for the amplitude coefficients of the upward and downward traveling potentials in each region. These amplitude coefficients are then used to obtain the elements of the Hertzian potential dyadic Green's function for the two layer parallel plate region.

Suppose that a magnetic current source, $\vec{J}_m$, exists in region 1. Note that in region 1, the potential is a combination of primary and scattered potentials,

$$\vec{\Pi}_1 = \vec{\Pi}_1^p + \vec{\Pi}_1^+ + \vec{\Pi}_1^-, \tag{3.120}$$

where $\vec{\Pi}_1^+$ and $\vec{\Pi}_1^-$ are the upward and downward propagating versions of the scattered potential from (3.119). The potential in region 2 is given as a combination of only the scattered potentials

$$\vec{\Pi}_2 = \vec{\Pi}_2^+ + \vec{\Pi}_2^-, \tag{3.121}$$

since region 2 is source free.

3.8.1 Potential Due to an x-directed Source in Region 1

Suppose that the current source $\vec{J}_m$ in region 1 is aligned in the x-direction in, i.e. $\vec{J}_m = \hat{x}J_{1x}$. Using boundary condition (3.43), (3.120) and (3.121) produce

$$\Pi_{1x}^{p} + \Pi_{1x}^{+} + \Pi_{1x}^{-} = \frac{\mu_2\epsilon_2}{\mu_1\epsilon_1}\left(\Pi_{2x}^{+} + \Pi_{2x}^{-}\right) \qquad at\ z = -d_1. \tag{3.122}$$

At $z = -d_1$, note that $|z - z'| = (z' - z) = (z' + d_1)$. Thus, using (3.117) and (3.119), equation (3.122) becomes

$$\begin{aligned}
&\int_V \frac{J_{1x}\left(\vec{r}\,'\right)}{j\omega\mu_1}\left\{\frac{1}{(2\pi)^2}\iint_{-\infty}^{+\infty}\frac{e^{-p_1\left(z'+d_1\right)}}{2p_1}e^{j\vec{k}\cdot\left(\vec{\rho}-\vec{\rho}\,'\right)}dk_x dk_y\right\}dV' \\
&\qquad + \frac{1}{(2\pi)^2}\iint_{-\infty}^{+\infty}\left[W_{1x}^{+}e^{p_1 d_1} + W_{1x}^{-}e^{-p_1 d_1}\right]e^{j\vec{k}\cdot\vec{\rho}}dk_x dk_y \\
&\qquad = \frac{1}{(2\pi)^2}\iint_{-\infty}^{+\infty}\frac{\epsilon_2\mu_2}{\epsilon_1\mu_1}\left[W_{2x}^{+}e^{p_2 d_1} + W_{2x}^{-}e^{-p_2 d_1}\right]e^{j\vec{k}\cdot\vec{\rho}}dk_x dk_y.
\end{aligned} \tag{3.123}$$

Rearranging (3.123) results in

$$\begin{aligned}
\frac{1}{(2\pi)^2}\iint_{-\infty}^{+\infty}\Bigg[&\int_V \frac{J_{1x}\left(\vec{r}\,'\right)}{j\omega\mu_1}\frac{e^{-p_1\left(z'+d_1\right)}e^{-j\vec{k}\cdot\vec{\rho}\,'}}{2p_1}dV' + W_{1x}^{+}e^{p_1 d_1} \\
&+W_{1x}^{-}e^{-p_1 d_1} - \frac{\epsilon_2\mu_2}{\epsilon_1\mu_1}\left(W_{2x}^{+}e^{p_2 d_1} + W_{2x}^{-}e^{-p_2 d_1}\right)\Bigg]e^{j\vec{k}\cdot\vec{\rho}}dk_x dk_y = 0.
\end{aligned} \tag{3.124}$$

By the Fourier integral theorem, the terms inside the bracket are set to zero and rearranged such that

$$\begin{aligned}
\int_V \frac{J_{1x}\left(\vec{r}\,'\right)}{j\omega\mu_1}\frac{e^{-p_1\left(z'+d_1\right)}e^{-j\vec{k}\cdot\vec{\rho}\,'}}{2p_1}dV' &= \frac{\epsilon_2\mu_2}{\epsilon_1\mu_1}\left(W_{2x}^{+}e^{p_2 d_1} + W_{2x}^{-}e^{-p_2 d_1}\right) \\
&\quad -W_{1x}^{+}e^{p_1 d_1} - W_{1x}^{-}e^{-p_1 d_1}.
\end{aligned} \tag{3.125}$$

By defining

$$V_{1x} = \int_V \frac{J_{1x}\left(\vec{r}\,'\right)}{j\omega\mu_1} \frac{e^{-p_1\left(z'+d_1\right)} e^{-j\vec{k}\cdot\vec{\rho}\,'}}{2p_1} dV', \tag{3.126}$$

(3.125) can be rewritten as

$$V_{1x} = \frac{\epsilon_2\mu_2}{\epsilon_1\mu_1}\left(W_{2x}^{+}e^{p_2d_1} + W_{2x}^{-}e^{-p_2d_1}\right) - \left(W_{1x}^{+}e^{p_1d_1} + W_{1x}^{-}e^{-p_1d_1}\right). \tag{3.127}$$

Employing boundary condition (3.42) and making use of (3.120) and (3.121) produces

$$\Pi_{1z}^{p} + \Pi_{1z}^{+} + \Pi_{1z}^{-} = \frac{\mu_2}{\mu_1}\left(\Pi_{2z}^{+} + \Pi_{2z}^{-}\right) \qquad at\ z = -d_1. \tag{3.128}$$

However, in this case note that the primary potential, $\Pi_{1z}^{p} = 0$ due to the x-directed source ($J_{1z} = 0$). Using (3.119) yields

$$\frac{1}{(2\pi)^2}\iint_{-\infty}^{+\infty}\left[W_{1z}^{+}e^{-p_1z} + W_{1z}^{-}e^{p_1z}\right]e^{j\vec{k}\cdot\vec{\rho}}dk_xdk_y = \frac{1}{(2\pi)^2}\frac{\mu_2}{\mu_1}\iint_{-\infty}^{+\infty}\left[W_{2z}^{+}e^{-p_2z} + W_{2z}^{-}e^{p_2z}\right]e^{j\vec{k}\cdot\vec{\rho}}dk_xdk_y \quad at\ z = -d_1. \tag{3.129}$$

Letting $z = -d_1$, (3.129) becomes

$$\frac{1}{(2\pi)^2}\iint_{-\infty}^{+\infty}\left[W_{1z}^{+}e^{p_1d_1} + W_{1z}^{-}e^{-p_1d_1} - \frac{\mu_2}{\mu_1}\left(W_{2z}^{+}e^{p_2d_1} + W_{2z}^{-}e^{-p_2d_1}\right)\right]e^{j\vec{k}\cdot\vec{\rho}}dk_xdk_y = 0. \tag{3.130}$$

Using the Fourier integral theorem on this equation yields

$$W_{1z}^{+}e^{p_1d_1} + W_{1z}^{-}e^{-p_1d_1} - \frac{\mu_2}{\mu_1}\left(W_{2z}^{+}e^{p_2d_1} + W_{2z}^{-}e^{-p_2d_1}\right) = 0. \tag{3.131}$$

Next, employing boundary condition (3.45) produces

$$\mu_1 \frac{\partial}{\partial z}\left[\Pi_{1x}^{p} + \Pi_{1x}^{+} + \Pi_{1x}^{-}\right] = \mu_2 \frac{\partial}{\partial z}\left[\Pi_{2x}^{-} + \Pi_{2x}^{+}\right] \quad at\ z = -d_1. \tag{3.132}$$

Using (3.117) and (3.119) in (3.132) yields

$$\begin{aligned}
&\frac{\partial}{\partial z}\left\{\int_V \frac{J_{1x}\left(\vec{r}\,'\right)}{j\omega\mu_1}\left[\frac{1}{(2\pi)^2}\iint_{-\infty}^{+\infty}\frac{e^{-p_1\left|z-z'\right|}}{2p_1}e^{j\vec{k}\cdot\left(\vec{\rho}-\vec{\rho}\,'\right)}dk_x dk_y\right]dV'\right. \\
&\qquad\left. + \frac{1}{(2\pi)^2}\iint_{-\infty}^{+\infty}\left[W_{1x}^{+}e^{-p_1 z} + W_{1x}^{-}e^{p_1 z}\right]e^{j\vec{k}\cdot\vec{\rho}}dk_x dk_y\right\} \\
&\qquad = \frac{\mu_2}{\mu_1}\frac{\partial}{\partial z}\left\{\frac{1}{(2\pi)^2}\iint_{-\infty}^{+\infty}\left[W_{2x}^{+}e^{-p_2 z} + W_{2x}^{-}e^{p_2 z}\right]e^{j\vec{k}\cdot\vec{\rho}}dk_x dk_y\right\} \quad at\ z = -d_1.
\end{aligned} \tag{3.133}$$

Note that for $z < z'$, $|z - z'| = z' - z$. Therefore, the first differentiation in (3.133) yields

$$\frac{\partial}{\partial z}e^{-p_1\left(z'-z\right)} = p_1 e^{-p_1\left(z'-z\right)}. \tag{3.134}$$

Interchanging the order of integration and carrying out the differentiation produces

$$\begin{aligned}
&\frac{1}{(2\pi)^2}\iint_{-\infty}^{+\infty}\left[\int_V \frac{J_{1x}\left(\vec{r}\,'\right)}{j\omega\mu_1}\frac{p_1 e^{-p_1\left(z'-z\right)}}{2p_1}e^{-j\vec{k}\cdot\vec{\rho}\,'}dV' - p_1 W_{1x}^{+}e^{-p_1 z}\right. \\
&\qquad\left. + W_{1x}^{-}e^{p_1 z} - \frac{\mu_2}{\mu_1}\left(p_2 W_{2x}^{-}e^{p_2 z} - p_2 W_{2x}^{+}e^{-p_2 z}\right)\right]e^{j\vec{k}\cdot\vec{\rho}}dk_x dk_y = 0 \quad at\ z = -d_1.
\end{aligned} \tag{3.135}$$

Letting $z = -d_1$ produces

$$\frac{1}{(2\pi)^2}\int\!\!\!\int_{-\infty}^{+\infty}\left[\int_V \frac{J_{1x}\left(\vec{r}'\right)}{j\omega\mu_1}\frac{p_1 e^{-p_1\left(z'+d_1\right)}}{2p_1}e^{-j\vec{k}\cdot\vec{\rho}'}dV' - p_1 W_{1x}^{+}e^{p_1 d_1}\right.$$
$$\left. + W_{1x}^{-}e^{-p_1 d_1} - \frac{\mu_2}{\mu_1}\left(p_2 W_{2x}^{-}e^{-p_2 d_1} - p_2 W_{2x}^{+}e^{p_2 d_1}\right)\right] e^{j\vec{k}\cdot\vec{\rho}}dk_x dk_y = 0. \quad (3.136)$$

Note that the volume integral term inside the brackets is $p_1 V_{1x}$. Setting the terms inside the brackets equal to zero yields

$$p_1 V_{1x} + p_1\left(W_{1x}^{-}e^{-p_1 d_1} - W_{1x}^{+}e^{p_1 d_1}\right) - \frac{\mu_2}{\mu_1}p_2\left(W_{2x}^{-}e^{-p_2 d_1} - W_{2x}^{+}e^{p_2 d_1}\right) = 0. \quad (3.137)$$

Employing boundary condition (3.44), and noting again that for an x-directed source $\Pi_{1z}^{p} = 0$, yields

$$\frac{\partial}{\partial z}\left[\Pi_{1z}^{+} + \Pi_{1z}^{-} - \Pi_{2z}^{+} - \Pi_{2z}^{-}\right] = -\left(\frac{\mu_2\epsilon_2}{\mu_1\epsilon_1} - 1\right)\frac{\partial}{\partial x}\left[\Pi_{2x}^{+} + \Pi_{2x}^{-}\right] \quad at\ z = -d_1. \quad (3.138)$$

Using (3.119) in (3.138) gives

$$\frac{\partial}{\partial z}\left\{\frac{1}{(2\pi)^2}\int\!\!\!\int_{-\infty}^{+\infty}\left[W_{1z}^{+}e^{-p_1 z} + W_{1z}^{-}e^{p_1 z} - W_{2z}^{+}e^{-p_2 z} - W_{2z}^{-}e^{p_2 z}\right]e^{j\vec{k}\cdot\vec{\rho}}dk_x dk_y\right\} =$$
$$-\left(\frac{\mu_2\epsilon_2}{\mu_1\epsilon_1} - 1\right)\frac{\partial}{\partial x}\left\{\frac{1}{(2\pi)^2}\int\!\!\!\int_{-\infty}^{+\infty}\left[W_{2x}^{+}e^{-p_2 z} + W_{2x}^{-}e^{p_2 z}\right]e^{j\vec{k}\cdot\vec{\rho}}dk_x dk_y\right\}$$
$$at\ z = -d_1. \quad (3.139)$$

Carrying out the derivatives and letting $z = -d_1$ gives

$$\frac{1}{(2\pi)^2}\iint_{-\infty}^{+\infty}\Big[-p_1 W_{1z}^{+}e^{p_1 d_1} + p_1 W_{1z}^{-}e^{-p_1 d_1} + p_2 W_{2z}^{+}e^{p_2 d_1} - p_2 W_{2z}^{-}e^{-p_2 d_1}\Big]\, e^{j\vec{k}\cdot\vec{\rho}}dk_x dk_y = -\left(\frac{\mu_2\epsilon_2}{\mu_1\epsilon_1} - 1\right)\frac{1}{(2\pi)^2}\iint_{-\infty}^{+\infty} jk_x\left[W_{2x}^{+}e^{p_2 d_1} + W_{2x}^{-}e^{-p_2 d_1}\right] e^{j\vec{k}\cdot\vec{\rho}}dk_x dk_y. \tag{3.140}$$

Noting that both sides of the equation are integrations over the same domain, (3.140) can be rearranged into one double integral. The terms in the integrand can then be set to zero resulting in

$$p_1\left(W_{1z}^{-}e^{-p_1 d_1} - W_{1z}^{+}e^{p_1 d_1}\right) + p_2\left(W_{2z}^{+}e^{p_2 d_1} - W_{2z}^{-}e^{-p_2 d_1}\right) + jk_x\left(\frac{\mu_2\epsilon_2}{\mu_1\epsilon_1} - 1\right)\left[W_{2x}^{+}e^{p_2 d_1} + W_{2x}^{-}e^{-p_2 d_1}\right] = 0. \tag{3.141}$$

Employing boundary condition (3.46) and using (3.119) produces

$$\frac{\partial}{\partial y}\left\{\frac{1}{(2\pi)^2}\iint_{-\infty}^{+\infty}\left[W_{1z}^{+}e^{-p_1 z} + W_{1z}^{-}e^{p_1 z}\right] e^{j\vec{k}\cdot\vec{\rho}}dk_x dk_y\right\} = 0 \quad at\ z = 0. \tag{3.142}$$

Moving the derivative inside the integral, carrying out the derivatives, and letting $z = 0$, results in

$$\frac{1}{(2\pi)^2}\iint_{-\infty}^{+\infty} jk_y\left[W_{1z}^{+} + W_{1z}^{-}\right] e^{j\vec{k}\cdot\vec{\rho}}dk_x dk_y = 0. \tag{3.143}$$

Using the Fourier integral theorem yields

$$W_{1z}^{+} + W_{1z}^{-} = 0. \tag{3.144}$$

Employing boundary condition (3.47) and using (3.117) and (3.119) produces

$$\begin{aligned}
&\frac{\partial}{\partial z}\left\{\int_V \frac{J_{1x}\left(\vec{r}'\right)}{j\omega\mu_1}\left[\frac{1}{(2\pi)^2}\iint_{-\infty}^{+\infty}\frac{e^{-p_1\left|z-z'\right|}}{2p_1}e^{j\vec{k}\cdot\left(\vec{\rho}-\vec{\rho}'\right)}dk_x dk_y\right]dV'\right. \\
&\qquad\left. + \frac{1}{(2\pi)^2}\iint_{-\infty}^{+\infty}\left[W_{1x}^{+}e^{-p_1 z} + W_{1x}^{-}e^{p_1 z}\right]e^{j\vec{k}\cdot\vec{\rho}}dk_x dk_y\right\} \\
&= \frac{\partial}{\partial x}\left\{\frac{1}{(2\pi)^2}\iint_{-\infty}^{+\infty}\left[W_{1z}^{+}e^{-p_1 z} + W_{1z}^{-}e^{p_1 z}\right]e^{j\vec{k}\cdot\vec{\rho}}dk_x dk_y\right\} \quad at\ z = 0.
\end{aligned} \tag{3.145}$$

Note that for $z' \leq z = 0$, $|z - z'| = z - z'$. Using this substitution, the first derivative on the left hand side of (3.145) is

$$\frac{\partial}{\partial z}\left[e^{-p_1\left(z-z'\right)}\right] = -p_1 e^{-p_1\left(z-z'\right)}. \tag{3.146}$$

Performing the other derivatives and letting $z = 0$ yields

$$\begin{aligned}
&\frac{1}{(2\pi)^2}\iint_{-\infty}^{+\infty}\left[\int_V \frac{J_{1x}\left(\vec{r}'\right)}{j\omega\mu_1}\frac{\left(-p_1\right)e^{p_1 z'}}{2p_1}e^{-j\vec{k}\cdot\vec{\rho}'}dV' - p_1 W_{1x}^{+} + p_1 W_{1x}^{-}\right]e^{j\vec{k}\cdot\vec{\rho}}dk_x dk_y \\
&\qquad = \frac{1}{(2\pi)^2}\iint_{-\infty}^{+\infty} jk_x\left[W_{1z}^{+} + W_{1z}^{-}\right]e^{j\vec{k}\cdot\vec{\rho}}dk_x dk_y.
\end{aligned} \tag{3.147}$$

Rearranging this equation yields

$$\frac{1}{(2\pi)^2}\iint_{-\infty}^{+\infty}\left[-p_1\int_V \frac{J_{1x}\left(\vec{r}'\right)}{j\omega\mu_1}\frac{e^{p_1 z'}}{2p_1}e^{-j\vec{k}\cdot\vec{\rho}'}dV' + p_1\left(W_{1x}^- - W_{1x}^+\right)\right.$$
$$\left. -jk_x\left(W_{1z}^+ + W_{1z}^-\right)\right]e^{j\vec{k}\cdot\vec{\rho}}dk_x dk_y = 0. \qquad (3.148)$$

By defining the term

$$V_{2x} = \int_V \frac{J_{1x}\left(\vec{r}'\right)}{j\omega\mu_1}\frac{e^{p_1 z'}}{2p_1}e^{-j\vec{k}\cdot\vec{\rho}'}dV', \qquad (3.149)$$

and employing (3.144), (3.148) can be rearranged as

$$\frac{1}{(2\pi)^2}\iint_{-\infty}^{+\infty}\left[-p_1 V_{2x} + p_1\left(W_{1x}^- - W_{1x}^+\right)\right]e^{j\vec{k}\cdot\vec{\rho}}dk_x dk_y = 0. \qquad (3.150)$$

Employing the Fourier integral theorem allows the terms in the square brackets to be set to zero, yielding

$$-p_1 V_{2x} + p_1\left(W_{1x}^- - W_{1x}^+\right) = 0, \qquad (3.151)$$

or

$$V_{2x} = W_{1x}^- - W_{1x}^+. \qquad (3.152)$$

Employing boundary condition (3.48) and using (3.119) produces

$$\frac{\partial}{\partial y}\left\{\frac{1}{(2\pi)^2}\iint_{-\infty}^{+\infty}\left[W_{2z}^+ e^{-p_2 z} + W_{2z}^- e^{p_2 z}\right]e^{j\vec{k}\cdot\vec{\rho}}dk_x dk_y\right\} = 0 \quad at\ z = -h. \qquad (3.153)$$

Carrying the derivative inside the integral, performing the derivative, letting $z = -h$, and setting the integrand equal to zero yields

$$W_{2z}^+ e^{p_2 h} + W_{2z}^- e^{-p_2 h} = 0. \qquad (3.154)$$

Employing boundary condition (3.49) and using (3.119) produces

$$\frac{\partial}{\partial z}\left\{\frac{1}{(2\pi)^2}\iint_{-\infty}^{+\infty}\left[W_{2x}^{+}e^{-p_2 z}+W_{2x}^{-}e^{p_2 z}\right]e^{j\vec{k}\cdot\vec{\rho}}dk_x dk_y\right\}$$
$$=\frac{\partial}{\partial x}\left\{\frac{1}{(2\pi)^2}\iint_{-\infty}^{+\infty}\left[W_{2z}^{+}e^{-p_2 z}+W_{2z}^{-}e^{p_2 z}\right]e^{j\vec{k}\cdot\vec{\rho}}dk_x dk_y\right\}\quad at\ z=-h. \quad (3.155)$$

Bringing the differential operators inside the integrals and carrying out the derivatives yields

$$\frac{1}{(2\pi)^2}\iint_{-\infty}^{+\infty}\left[-p_2 W_{2x}^{+}e^{-p_2 z}+p_2 W_{2x}^{-}e^{p_2 z}\right]e^{j\vec{k}\cdot\vec{\rho}}dk_x dk_y$$
$$=\frac{1}{(2\pi)^2}\iint_{-\infty}^{+\infty}jk_x\left[W_{2z}^{+}e^{-p_2 z}+W_{2z}^{-}e^{p_2 z}\right]e^{j\vec{k}\cdot\vec{\rho}}dk_x dk_y=0\quad at\ z=-h. \quad (3.156)$$

Setting $z=-h$, and rearranging the equation gives

$$\frac{1}{(2\pi)^2}\iint_{-\infty}^{+\infty}\Big[p_2 W_{2x}^{-}e^{-p_2 h}-p_2 W_{2x}^{+}e^{p_2 h}$$
$$-jk_x\left(W_{2z}^{+}e^{p_2 h}+W_{2z}^{-}e^{-p_2 h}\right)\Big]e^{j\vec{k}\cdot\vec{\rho}}dk_x dk_y=0. \quad (3.157)$$

By using the Fourier integral theorem, the term inside the brackets may be set to zero, which results in

$$p_2\left[W_{2x}^{-}e^{-p_2 h}-W_{2x}^{+}e^{p_2 h}\right]-jk_x\left[W_{2z}^{+}e^{p_2 h}+W_{2z}^{-}e^{-p_2 h}\right]=0. \quad (3.158)$$

Note that the term in the second set of brackets equals 0 from (3.154). The relationship between the upward and downward traveling wave amplitudes W_{2x}^{+} and W_{2x}^{-} is

thus given by

$$W_{2x}^{-}e^{-p_2 h} - W_{2x}^{+}e^{p_2 h} = 0 \tag{3.159}$$

3.8.1.1 Summary of Potential Amplitude Equations for an x-directed Source in Region 1

For a magnetic source, $\vec{J}_m = \hat{x}J_{1x}$, the equations relating the potential amplitudes are summarized as follows:

$$V_1 x = \frac{\epsilon_2 \mu_2}{\epsilon_1 \mu_1}\left(W_{2x}^{+}e^{p_2 d_1} + W_{2x}^{-}e^{-p_2 d_1}\right) - \left(W_{1x}^{+}e^{p_1 d_1} + W_{1x}^{-}e^{-p_1 d_1}\right), \tag{3.160}$$

$$W_{1z}^{+}e^{p_1 d_1} + W_{1z}^{-}e^{-p_1 d_1} - \frac{\mu_2}{\mu_1}\left(W_{2z}^{+}e^{p_2 d_1} + W_{2z}^{-}e^{-p_2 d_1}\right) = 0, \tag{3.161}$$

$$p_1 V_{1x} + p_1\left(W_{1x}^{-}e^{-p_1 d_1} - W_{1x}^{+}e^{p_1 d_1}\right) - \frac{\mu_2}{\mu_1}p_2\left(W_{2x}^{-}e^{-p_2 d_1} - W_{2x}^{+}e^{p_2 d_1}\right) = 0, \tag{3.162}$$

$$\begin{aligned} p_1\left(W_{1z}^{-}e^{-p_1 d_1} - W_{1z}^{+}e^{p_1 d_1}\right) + p_2\left(W_{2z}^{+}e^{p_2 d_1} - W_{2z}^{-}e^{-p_2 d_1}\right) \\ + jk_x\left(\frac{\mu_2 \epsilon_2}{\mu_1 \epsilon_1} - 1\right)\left[W_{2x}^{+}e^{p_2 d_1} + W_{2x}^{-}e^{-p_2 d_1}\right] = 0, \end{aligned} \tag{3.163}$$

$$W_{1z}^{+} + W_{1z}^{-} = 0, \tag{3.164}$$

$$V_{2x} = W_{1x}^{-} - W_{1x}^{+}, \tag{3.165}$$

$$W_{2z}^{+}e^{p_2 h} + W_{2z}^{-}e^{-p_2 h} = 0, \tag{3.166}$$

$$W_{2x}^{-}e^{-p_2 h} - W_{2x}^{+}e^{p_2 h} = 0. \tag{3.167}$$

The quantities V_{1x} and V_{2x} are defined as

$$V_{1x} = \int_V \frac{J_{1x}\left(\vec{r}\,'\right)}{j\omega\mu_1}\frac{e^{-p_1\left(z'+d_1\right)}e^{-j\vec{k}\cdot\vec{\rho}\,'}}{2p_1}dV', \tag{3.168}$$

$$V_{2x} = \int_V \frac{J_{1x}\left(\vec{r}'\right)}{j\omega\mu_1} \frac{e^{p_1 z'} e^{-j\vec{k}\cdot\vec{\rho}'}}{2p_1} dV'. \tag{3.169}$$

3.8.1.2 Solution for the Amplitude Coefficients of the Upward and Downward Traveling Waves

To solve for the amplitude coefficients in the equations (3.160)–(3.167) requires solving the 8 equations for the 8 unknowns, W_{1x}^+, W_{1x}^-, W_{2x}^+, W_{2x}^-, W_{1z}^+, W_{1z}^-, W_{2z}^+, and W_{2z}^-.

Note that (3.164)–(3.167) can be rewritten as

$$W_{1z}^+ = -W_{1z}^-, \tag{3.170}$$

$$W_{1x}^- = V_{2x} + W_{1x}^+, \tag{3.171}$$

$$W_{2z}^- = -W_{2z}^+ e^{2p_2 h}, \tag{3.172}$$

$$W_{2x}^- = W_{2x}^+ e^{2p_2 h}. \tag{3.173}$$

Using (3.170) and (3.172) in (3.161) yields

$$\left(W_{1z}^- e^{-p_1 d_1} - W_{1z}^- e^{p_1 d_1}\right) - \frac{\mu_2}{\mu_1}\left(W_{2z}^+ e^{p_2 d_1} - W_{2z}^+ e^{2p_2 h} e^{-p_2 d_1}\right) = 0. \tag{3.174}$$

The terms for W_{1z}^- and W_{2z}^+ can be grouped, and the equation is rewritten as

$$W_{1z}^- \sinh p_1 d_1 + \frac{\mu_2}{\mu_1} W_{2z}^+ e^{p_2 h} \sinh\left(p_2\left(d_1 - h\right)\right) = 0. \tag{3.175}$$

Inserting (3.171) and (3.173) in (3.160) yields

$$V_{1x} - \frac{\epsilon_2\mu_2}{\epsilon_1\mu_1}\left(W_{2x}^+ e^{2p_2 h} e^{-p_2 d_1} + W_{2x}^+ e^{p_2 d_1}\right) + W_{1x}^+ e^{p_1 d_1} + \left(V_{2x} + W_{1x}^+\right) e^{-p_1 d_1} = 0. \tag{3.176}$$

After grouping amplitude coefficient terms, this can be rewritten as

$$V_{1x} + V_{2x}e^{-p_1 d_1} + 2W_{1x}^{+}\cosh p_1 d_1 - 2\frac{\epsilon_2\mu_2}{\epsilon_1\mu_1}W_{2x}^{+}e^{p_2 h}\cosh\left(p_2\left(d_1 - h\right)\right) = 0. \quad (3.177)$$

Inserting (3.171) and (3.173) in (3.162) yields

$$p_1 V_{1x} - p_1 W_{1x}^{+}e^{p_1 d_1} + p_1 e^{-p_1 d_1}\left(V_{2x} + W_{1x}^{+}\right) - \frac{\mu_2}{\mu_1}p_2\left(W_{2x}^{+}e^{2p_2 h}e^{-p_2 d_1} - W_{2x}^{+}e^{p_2 d_1}\right) = 0. \quad (3.178)$$

Equation (3.178) can be rearranged to yield

$$p_1 V_{1x} + p_1 V_{2x}e^{-p_1 d_1} - 2p_1 W_{1x}^{+}\sinh p_1 d_1 + 2\frac{\mu_2}{\mu_1}p_2 W_{2x}^{+}e^{p_2 h}\sinh\left(p_2\left(d_1 - h\right)\right) = 0. \quad (3.179)$$

Multiplying (3.177) by p_1 and subtracting from (3.179) yields

$$2\frac{\mu_2}{\mu_1}W_{2x}^{+}e^{p_2 h}\left[p_2\sinh\left(p_2\left(d_1 - h\right)\right) + \frac{\epsilon_2}{\epsilon_1}p_1\cosh\left(p_2\left(d_1 - h\right)\right)\right] - 2p_1 W_{1x}^{+}\left(\sinh p_1 d_1 + \cosh p_1 d_1\right) = 0. \quad (3.180)$$

This equation can be rearranged so that W_{1x}^{+} can be defined in terms of W_{2x}^{+},

$$W_{1x}^{+} = \frac{\mu_2}{\mu_1}W_{2x}^{+}e^{p_2 h}e^{-p_1 d}\left[\frac{p_2}{p_1}\sinh\left(p_2\left(d_1 - h\right)\right) + \frac{\epsilon_2}{\epsilon_1}\cosh\left(p_2\left(d_1 - h\right)\right)\right]. \quad (3.181)$$

Using (3.181) in (3.177), an equation involving V_{1x}, V_{2x}, and W_{2x}^{+} is given by

$$V_{1x} + V_{2x}e^{-p_1 d_1} + 2\frac{\mu_2 p_2}{\mu_1 p_1}W_{2x}^{+}\cosh p_1 d_1 e^{p_2 h}e^{-p_1 d_1}\sinh\left(p_2\left(d_1 - h\right)\right) + 2\frac{\mu_2\epsilon_2}{\mu_1\epsilon_1}W_{2x}^{+}e^{p_2 h}\cosh\left(p_2\left(d_1 - h\right)\right)\left[e^{-p_1 d_1}\cosh p_1 d_1 - 1\right] = 0. \quad (3.182)$$

This equation can be rearranged as

$$2\frac{\mu_2}{\mu_1}W_{2x}^{+}e^{p_2 h}e^{-p_1 d_1}\left[\frac{p_2}{p_1}\cosh p_1 d_1 \sinh\left(p_2\left(d_1-h\right)\right)-\right.$$
$$\left.\frac{\epsilon_2}{\epsilon_1}\sinh p_1 d_1 \cosh\left(p_2\left(d_1-h\right)\right)\right]+V_{1x}+V_{2x}e^{-p_1 d_1}=0. \tag{3.183}$$

For ease of notation, the term in the square brackets in (3.183) is defined as

$$T_m=\frac{p_2}{p_1}\cosh p_1 d_1 \sinh\left(p_2\left(d_1-h\right)\right)-\frac{\epsilon_2}{\epsilon_1}\sinh p_1 d_1 \cosh\left(p_2\left(d_1-h\right)\right). \tag{3.184}$$

Note that the zeroes of this equation are the eigen modes for TM to z waves in a parallel-plate waveguide filled with two layers of material [42]. An expression for W_{2x}^{+} can be obtained by rearranging (3.183), yielding

$$W_{2x}^{+}=-\left[V_{1x}+V_{2x}e^{-p_1 d_1}\right]\frac{\mu_1 e^{-p_2 h}e^{p_1 d_1}}{2\mu_2 T_m}. \tag{3.185}$$

By using (3.185) in (3.181), a resulting expression for W_{1x}^{+} is given as

$$W_{1x}^{+}=-\left[V_{1x}+V_{2x}e^{-p_1 d_1}\right]\frac{\left[\frac{p_2}{p_1}\sinh\left(p_2\left(d_1-h\right)\right)+\frac{\epsilon_2}{\epsilon_1}\cosh\left(p_2\left(d_1-h\right)\right)\right]}{2T_m}. \tag{3.186}$$

In addition, using (3.185) in (3.173) results in

$$W_{2x}^{-}=-\left[V_{1x}+V_{2x}e^{-p_1 d_1}\right]\frac{\mu_1 e^{p_2 h}e^{p_1 d_1}}{2\mu_2 T_m}. \tag{3.187}$$

An additional substitution of (3.186) in (3.171) yields

$$W_{1x}^{-}=V_{2x}-U_{1x}\frac{\left[\frac{p_2}{p_1}\sinh\left(p_2\left(d_1-h\right)\right)+\frac{\epsilon_2}{\epsilon_1}\cosh\left(p_2\left(d_1-h\right)\right)\right]}{2T_m}. \tag{3.188}$$

where an additional term, U_{1x}, that combines V_{1x} and V_{2x}, is defined as

$$U_{1x} = V_{1x} + V_{2x}e^{-p_1 d_1}. \tag{3.189}$$

Inserting the definitions of V_{1x} and V_{2x} in (3.189) leads to

$$U_{1x} = \int_V \frac{J_{1x}(\vec{r}')}{j\omega\mu_1 p_1} e^{-p_1 d_1} \cosh(p_1 z') e^{-j\vec{k}\cdot\vec{\rho}'} dV'. \tag{3.190}$$

Thus far, all four expressions for the wave amplitudes in the x direction have been derived as a function of V_{1x} and V_{2x}. Next, the z-component amplitudes are found.

Inserting (3.170) and (3.172) in (3.163) yields

$$\begin{aligned} p_1 W_{1z}^- \left(e^{-p_1 d_1} + e^{p_1 d_1}\right) + p_2 W_{2z}^+ e^{p_2 h} \left(e^{p_2 d_1} e^{-p_2 h} + e^{p_2 h} e^{-p_2 d_1}\right) \\ + jk_x \left(\frac{\mu_2\epsilon_2}{\mu_1\epsilon_1} - 1\right) W_{2x}^+ e^{p_2 h} \left[e^{-p_2 h} e^{p_2 d_1} + e^{p_2 h} e^{-p_2 d_1}\right] = 0, \end{aligned} \tag{3.191}$$

or

$$\begin{aligned} p_1 W_{1z}^- \cosh p_1 d_1 + p_2 W_{2z}^+ e^{p_2 h} \cosh(p_2(d_1 - h)) \\ + jk_x \left(\frac{\mu_2\epsilon_2}{\mu_1\epsilon_1} - 1\right) W_{2x}^+ e^{p_2 h} \cosh(p_2(d_1 - h)) = 0. \end{aligned} \tag{3.192}$$

Rewriting (3.175) as

$$W_{1z}^- = -\frac{\mu_2}{\mu_1} W_{2z}^+ e^{p_2 h} \frac{\sinh(p_2(d_1 - h))}{\sinh p_1 d_1} \tag{3.193}$$

allows the expression for W_{1z}^{-} to be inserted in (3.192), which produces

$$-p_1\frac{\mu_2}{\mu_1}W_{2z}^{+}e^{p_2h}\frac{\cosh p_1d_1\sinh\left(p_2\left(d_1-h\right)\right)}{\sinh p_1d_1}+p_2W_{2z}^{+}e^{p_2h}\cosh\left(p_2\left(d_1-h\right)\right)$$
$$+jk_x\left(\frac{\mu_2\epsilon_2}{\mu_1\epsilon_1}-1\right)W_{2x}^{+}e^{p_2h}\cosh\left(p_2\left(d_1-h\right)\right)=0. \qquad (3.194)$$

The expression for W_{2x}^{+} is found in (3.185), and it can be used in (3.194), yielding

$$W_{2z}^{+}e^{p_2h}\left[p_2\cosh\left(p_2\left(d_1-h\right)\right)-p_1\frac{\mu_2}{\mu_1}\frac{\cosh p_1d_1\sinh\left(p_2\left(d_1-h\right)\right)}{\sinh p_1d_1}\right]$$
$$-jk_x\left[V_{1x}+V_{2x}e^{-p_1d_1}\right]\frac{\mu_1e^{p_1d_1}}{2\mu_2T_m}\left(\frac{\mu_2\epsilon_2}{\mu_1\epsilon_1}-1\right)\cosh\left(p_2\left(d_1-h\right)\right)=0. \qquad (3.195)$$

This may be rewritten as

$$W_{2z}^{+}e^{p_2h}T_e$$
$$-jk_x\frac{\sinh(p_1d_1)}{p_1}U_{1x}\frac{\mu_1e^{p_1d_1}}{2\mu_2T_m}\left(\frac{\mu_2\epsilon_2}{\mu_1\epsilon_1}-1\right)\cosh\left(p_2\left(d_1-h\right)\right)=0, \qquad (3.196)$$

where

$$T_e=\frac{p_2}{p_1}\cosh\left(p_2\left(d_1-h\right)\right)\sinh p_1d_1-\frac{\mu_2}{\mu_1}\cosh p_1d_1\sinh\left(p_2\left(d_1-h\right)\right). \qquad (3.197)$$

The equation $T_e=0$ is the characteristic equation for the eigen modes for a TE to z field in a two-layered medium between two parallel plates [42]. Equation (3.196) can be rearranged as

$$W_{2z}^{+}=jk_xU_{1x}\cdot$$
$$\frac{\mu_1}{\mu_2}\frac{e^{-p_2h}e^{p_1d_1}}{2p_1T_mT_e}\left(\frac{\mu_2\epsilon_2}{\mu_1\epsilon_1}-1\right)\sinh p_1d_1\cosh\left(p_2\left(d_1-h\right)\right). \qquad (3.198)$$

Using (3.198) in (3.172), (3.193), and (3.170) allows for the determination of the remaining z-directed amplitudes,

$$W_{2z}^{-} = -jk_x U_{1x} \cdot \frac{\mu_1}{\mu_2} \frac{e^{p_2 h} e^{p_1 d_1}}{2p_1 T_m T_e} \left(\frac{\mu_2 \epsilon_2}{\mu_1 \epsilon_1} - 1 \right) \sinh p_1 d_1 \cosh\left(p_2 \left(d_1 - h\right)\right), \tag{3.199}$$

$$W_{1z}^{-} = -jk_x \frac{e^{p_1 d_1}}{2p_1 T_m T_e} \left(\frac{\mu_2 \epsilon_2}{\mu_1 \epsilon_1} - 1 \right) U_{1x} \frac{\sinh\left(2p_2 \left(d_1 - h\right)\right)}{2}, \tag{3.200}$$

$$W_{1z}^{+} = jk_x \frac{e^{p_1 d_1}}{2p_1 T_m T_e} \left(\frac{\mu_2 \epsilon_2}{\mu_1 \epsilon_1} - 1 \right) U_{1x} \frac{\sinh\left(2p_2 \left(d_1 - h\right)\right)}{2}. \tag{3.201}$$

3.8.1.3 x-directed potential

To obtain the x-directed potential from an x-directed source, an application of (3.120) yields

$$\Pi_{1x}(\vec{r}) = \Pi_{1x}^{p}(\vec{r}) + \Pi_{1x}^{+}(\vec{r}) + \Pi_{1x}^{-}(\vec{r}). \tag{3.202}$$

Using (3.117) and (3.119), equation (3.202) becomes

$$\Pi_{1x}(\vec{r}) = \int_V \frac{J_{1x}\left(\vec{r}'\right)}{j\omega\mu} \left\{ \frac{1}{(2\pi)^2} \int_{-\infty}^{+\infty} \frac{e^{-p\left|z-z'\right|}}{2p_1} e^{j\vec{k}\cdot\left(\vec{\rho}-\vec{\rho}'\right)} dk_x dk_y \right\} dV' + \frac{1}{(2\pi)^2} \int_{-\infty}^{+\infty} \left[W_{1x}^{+} e^{-p_1 z} + W_{1x}^{-} e^{p_1 z} \right] e^{j\vec{k}\cdot\vec{\rho}} dk_x dk_y. \tag{3.203}$$

Note that the quantity inside the square brackets in (3.203) can be rewritten as

$$W_{1x}^{+} e^{-p_1 z} + W_{1x}^{-} e^{p_1 z} = 2W_{1x}^{+} \cosh p_1 z + V_{2x} e^{p_1 z} \tag{3.204}$$

with the use of (3.171). Replacing W_{1x}^{+} by employing (3.186) yields

$$W_{1x}^{+}e^{-p_1 z} + W_{1x}^{-}e^{p_1 z} = V_{2x}e^{p_1 z} - \cosh p_1 z \left[V_{1x} + V_{2x}e^{-p_1 d_1}\right] \cdot \frac{\left[\frac{p_2}{p_1}\sinh\left(p_2\left(d_1 - h\right)\right) + \frac{\epsilon_2}{\epsilon_1}\cosh\left(p_2\left(d_1 - h\right)\right)\right]}{T_m}. \quad (3.205)$$

It should be noted that the zeroes of the expression in the square brackets in (3.205) are the eigen frequencies for TM to z modes of surface waves in a grounded dielectric slab [42], [49]. This expression is defined here as

$$T_{ms} = \left[\frac{p_2}{p_1}\sinh\left(p_2\left(d_1 - h\right)\right) + \frac{\epsilon_2}{\epsilon_1}\cosh\left(p_2\left(d_1 - h\right)\right)\right]. \quad (3.206)$$

Using this notation, (3.205) can be rewritten as

$$W_{1x}^{+}e^{-p_1 z} + W_{1x}^{-}e^{p_1 z} = V_{2x}\left(e^{p_1 z} - \frac{T_{ms}}{T_m}e^{-p_1 d_1}\cosh p_1 z\right) - V_{1x}\frac{T_{ms}}{T_m}\cosh p_1 x. \quad (3.207)$$

Using (3.207), and interchanging the integrals in (3.203), an expression for $\Pi_{1x}(\vec{r})$ is given by

$$\Pi_{1x}(\vec{r}) = \frac{1}{(2\pi)^2}\int_{-\infty}^{+\infty}\iint_V \frac{J_{1x}\left(\vec{r}'\right)}{j\omega\mu}\frac{e^{-p\left|z-z'\right|}}{2p_1}e^{j\vec{k}\cdot\left(\vec{\rho}-\vec{\rho}'\right)}dV'dk_x dk_y \quad (3.208)$$

$$+ \frac{1}{(2\pi)^2}\int_{-\infty}^{+\infty}\iint \left[V_{2x}\left(e^{p_1 z} - \frac{e^{-p_1 d_1}T_{ms}}{T_m}\cosh p_1 z\right) - V_{1x}\frac{T_{ms}}{T_m}\cosh p_1 z\right] e^{j\vec{k}\cdot\vec{\rho}}dk_x dk_y. \quad (3.209)$$

Using (3.168) and (3.169), the equation for the x-directed potential can be rewritten

as

$$\Pi_{1x}(\vec{r}) = \frac{1}{(2\pi)^2} \iint_{-\infty}^{+\infty} \int_V J_{1x}(\vec{r}\,') \frac{e^{j\vec{k}\cdot(\vec{\rho}-\vec{\rho}\,')}}{j2\omega\mu_1 p_1} \cdot \tag{3.210}$$
$$\left[e^{-p_1|z-z'|} + e^{p_1(z+z')} - \left(e^{p_1(z'-d_1)} + e^{-p_1(z'+d_1)} \right) \frac{T_{ms}}{T_m} \cosh p_1 z \right] dV' dk_x dk_y$$

Recall that the goal of this section is to obtain the magnetic Hertzian potential by the superposition integral of the magnetic current source and the two layer parallel plate dyadic Green's function for the Hertzian potential. Note that if the integrals are interchanged (3.210) takes the form

$$\vec{\Pi}_\alpha(\vec{r}) = \int_V \bar{\bar{G}}^{\alpha,\beta}(\vec{r}|\vec{r}\,') \cdot \vec{J}_\beta(\vec{r}\,') dV', \tag{3.211}$$

where α is the observer region, and β is the source region. In this case of the x-directed potential due to an x-directed source, the scalar equation is

$$\Pi_{1x}(\vec{r}) = \int_V G_{xx}^{1,1}(\vec{r}|\vec{r}\,') \cdot J_{1x}(\vec{r}\,') dV'. \tag{3.212}$$

Thus, the Green's function for an x-directed potential in region 1 from an x-directed source in region 1 is

$$G_{xx}^{1,1}(\vec{r}|\vec{r}\,') = \frac{1}{(2\pi)^2} \iint_{-\infty}^{+\infty} \frac{e^{j\vec{k}\cdot(\vec{\rho}-\vec{\rho}\,')}}{j2\omega\mu_1 p_1} \cdot \tag{3.213}$$
$$\left[e^{-p_1|z-z'|} + e^{p_1(z+z')} - 2\cosh p_1 z \cosh p_1 z' \frac{T_{ms}}{T_m} e^{-p_1 d_1} \right] dk_x dk_y.$$

3.8.1.4 y-directed potential

As evident in (3.18), the y-directed potential Π_{1y} from an x-directed magnetic current source is zero. Thus the dyadic Green's function element in (3.211) is

$$G_{yx}^{1.1}(\vec{r}|\vec{r}') = 0. \tag{3.214}$$

3.8.1.5 z-directed potential

The z-directed potential from an x-directed source is obtained from (3.121),

$$\Pi_{1z}(\vec{r}) = \Pi_{1z}^{+}(\vec{r}) + \Pi_{1x}^{-}(\vec{r}). \tag{3.215}$$

Employing (3.119) in (3.215) yields

$$\Pi_{1z}(\vec{r}) = \frac{1}{(2\pi)^2} \iint_{-\infty}^{+\infty} \left[W_{1z}^{+} e^{-p_1 z} + W_{1z}^{-} e^{p_1 z}\right] e^{j\vec{k}\cdot\vec{\rho}} dk_x dk_y. \tag{3.216}$$

By employing (3.170) and (3.200), the bracketed term of (3.216) can be shown to be

$$\begin{aligned}\left[W_{1z}^{+} e^{-p_1 z} + W_{1z}^{-} e^{p_1 z}\right] &= 2W_{1z}^{-} \sinh p_1 z \\ &= -jk_x \frac{e^{p_1 d_1}}{2p_1 T_m T_e} \left(\frac{\mu_2 \epsilon_2}{\mu_1 \epsilon_1} - 1\right) \cdot \\ &\quad U_{1x} \sinh(p_1 z) \sinh(2p_2 (d_1 - h)).\end{aligned} \tag{3.217}$$

Using (3.190) and (3.217) in (3.216), the z-directed potential can be expressed as

$$\begin{aligned}\Pi_{1z}(\vec{r}) = -\frac{1}{(2\pi)^2} \iint_{-\infty}^{+\infty} \int_V J_{1x}(\vec{r}') \frac{e^{j\vec{k}\cdot(\vec{\rho}-\vec{\rho}')}}{j2\omega\mu_1 p_1} \cdot \\ \left[jk_x \left(\frac{\mu_2 \epsilon_2}{\mu_1 \epsilon_1} - 1\right) \frac{\sinh(2p_2 (d_1 - h))}{p_1 T_m T_e} \cosh p_1 z' \sinh p_1 z\right] dV' dk_x dk_y.\end{aligned} \tag{3.218}$$

By examining (3.218) in the form found in (3.211), the Green's function for a z-directed potential from an x-directed source is

$$G_{zx}^{1,1}(\vec{r}|\vec{r}') = -\frac{1}{(2\pi)^2}\iint_{-\infty}^{+\infty} \frac{e^{j\vec{k}\cdot(\vec{\rho}-\vec{\rho}')}}{j2\omega\mu_1 p_1} \cdot \left[jk_x\left(\frac{\mu_2\epsilon_2}{\mu_1\epsilon_1}-1\right)\frac{\sinh\left(2p_2\left(d_1-h\right)\right)}{p_1 T_m T_e}\cosh p_1 z' \sinh p_1 z\right] dk_x dk_y. \tag{3.219}$$

3.8.2 Potential due to a y-directed source in region 1

Similar to the derivation found in section 3.8.1, suppose that the current source $\vec{J}_m$ is aligned in the y-direction in region 1, i.e. $\vec{J}_m = \hat{y}J_{1y}$. Note that for an infinite planar interface, the problem is identical to that for the x-directed source with a change of coordinates. Without repeating the entire derivation, the potential due to a y-directed source is identical to that for the x-directed source with the subscripts appropriately changed.

3.8.2.1 x-directed potential

By a similar argument given in section 3.8.1.4, the x-directed potential, Π_{1x}, from a y-directed magnetic current source is zero. Thus the dyadic Green's function element from (3.211) is

$$G_{xy}^{1,1}(\vec{r}|\vec{r}') = 0. \tag{3.220}$$

3.8.2.2 y-directed potential

The y-directed potential for a y-directed source is

$$\Pi_{1y}(\vec{r}) = \frac{1}{(2\pi)^2}\iint_{-\infty}^{+\infty}\int_V J_{1y}\left(\vec{r}'\right)\frac{e^{j\vec{k}\cdot(\vec{\rho}-\vec{\rho}')}}{j2\omega\mu_1 p_1} \cdot \left[e^{-p_1|z-z'|}+e^{p_1(z+z')}-\left(e^{p_1(z'-d_1)}+e^{-p_1(z'+d_1)}\right)\frac{T_{ms}}{T_m}\cosh p_1 z\right] dV' dk_x dk_y. \tag{3.221}$$

Thus, the Green's function for a y-directed potential from a y-directed source is

$$G_{yy}^{1,1}(\vec{r}|\vec{r}') = \frac{1}{(2\pi)^2}\iint_{-\infty}^{+\infty} \frac{e^{j\vec{k}\cdot(\vec{\rho}-\vec{\rho}')}}{j2\omega\mu_1 p_1} \cdot \left[e^{-p_1|z-z'|} + e^{p_1(z+z')} - 2\cosh p_1 z \cosh p_1 z' \frac{T_{ms}}{T_m} e^{-p_1 d_1}\right] dk_x dk_y. \tag{3.222}$$

Note that this expression is identical to the Green's function $G_{xx}^{1,1}(\vec{r}|\vec{r}')$ found in (3.213).

3.8.2.3 z-directed potential

The z-directed potential in region 1 due to a y-directed source in region 1 is given by

$$\Pi_{1z}(\vec{r}) = -\frac{1}{(2\pi)^2}\iint_{-\infty}^{+\infty}\int_V J_{1y}(\vec{r}') \frac{e^{j\vec{k}\cdot(\vec{\rho}-\vec{\rho}')}}{j2\omega\mu_1 p_1} \cdot \left[jk_y\left(\frac{\mu_2\epsilon_2}{\mu_1\epsilon_1} - 1\right)\frac{\sinh\left(2p_2\left(d_1 - h\right)\right)}{p_1 T_m T_e}\cosh p_1 z' \sinh p_1 z\right] dV' dk_x dk_y. \tag{3.223}$$

The z-directed Green's function for a y-directed source is thus

$$G_{zy}^{1,1}(\vec{r}|\vec{r}') = -\frac{1}{(2\pi)^2}\iint_{-\infty}^{+\infty} \frac{e^{j\vec{k}\cdot(\vec{\rho}-\vec{\rho}')}}{j2\omega\mu_1 p_1} \left[jk_y\left(\frac{\mu_2\epsilon_2}{\mu_1\epsilon_1} - 1\right)\frac{\sinh\left(2p_2\left(d_1 - h\right)\right)}{p_1 T_m T_e}\cosh p_1 z' \sinh p_1 z\right] dk_x dk_y. \tag{3.224}$$

Note that for the y-directed source, the z-directed potential and Green's functions are almost identical to those for an x-directed source, with the replacement of k_x by k_y in the bracketed term. Also note that when the two layers are made of the same material, i.e. $\epsilon_1 = \epsilon_2$ and $\mu_2 = \mu_1$, the z-directed elements are equal to zero and only the diagonal elements remain. As is shown in Appendix C, these elements reduce to the single layer Green's function.

Because the induced equivalent magnetic current is only in the transverse direction

($\vec{J}_{1m} = \hat{x}J_{1x} + \hat{y}J_{1y}$), and no vertical component exists, only these portions of the dyadic Green's function are necessary for the computation of the magnetic field. In matrix form, the Green's function can be represented as

$$\bar{\bar{G}}^{pp} = \begin{bmatrix} G_{xx} & 0 & \triangle \\ 0 & G_{yy} & \square \\ G_{zx} & G_{zy} & \Diamond \end{bmatrix}, \tag{3.225}$$

where the terms indicated as $\triangle$, $\square$, and $\Diamond$ were not derived in this chapter. The additional elements of the dyadic Green's function could be derived by following similar methods to those used here, but is not done in this dissertaion.

The Green's function (3.225) is used in the calculation of the magnetic Hertzian potential, and subsequently in the calculation of the magnetic field in the parallel plate region used in the magnetic field integral equation. Chapter 4 uses this Green's function in the numerical solution of the MFIE and subsequent numerical analysis.

CHAPTER 4

NUMERICAL SOLUTION OF THE TWO LAYER MFIE

4.1 Introduction

Recall from Chapter 2 that matching the tangential magnetic fields in the waveguide and parallel plate regions leads to the establishment of a magnetic field integral equation. A Method of Moments technique for solving the MFIE is also presented in Chapter 2, and the Green's function needed to compute the matrix elements in the MoM solution is derived in Chapter 3. In this chapter the details of the numerical solution steps to the MFIE are presented. These details include the numerical computation of the right hand side vector elements, b_m, and the computation of the left hand side matrix elements, A_{mn}, using the two layer parallel plate Green's function from Chapter 3. In addition, details regarding numerical techniques used in the solution are discussed.

4.2 The Forcing Function

The elements b_m of the right hand side of (2.33) are considered first. These elements correspond to the forcing function in this problem, which is the incident TE_{10} wave excitation. Note the relationship found in (2.27) between the transverse electric and magnetic field mode functions. Employing this relationship in (2.35) yields

$$b_m = 2\int_{CS} \frac{\hat{z} \times \vec{e}_m^{wg}(\vec{\rho})}{Z_m^{wg}} \cdot \frac{\hat{z} \times \vec{e}_1^{wg}(\vec{\rho})}{Z_1^{wg}} ds, \qquad m = 1, 2, ...N. \tag{4.1}$$

Using the well-known vector identity to evaluate the vector products in (4.1) produces

$$(\hat{z} \times \vec{e}_m) \cdot (\hat{z} \times \vec{e}_1) = (\vec{e}_m \cdot \vec{e}_1)(\hat{z} \cdot \hat{z}) - (\vec{e}_m \cdot \hat{z})(\hat{z} \cdot \vec{e}_1)$$
$$= \vec{e}_m \cdot \vec{e}_1, \tag{4.2}$$

with the $\vec{\rho}$ dependence suppressed for notational convenience. Rewriting (4.1) yields

$$b_m = 2 \int_{CS} \frac{\vec{e}_m^{wg}(\vec{\rho}) \cdot \vec{e}_1^{wg}(\vec{\rho})}{Z_m^{wg(TE)} Z_1^{wg(TE)}} ds$$
$$= \frac{2}{Z_m^{wg(TE)} Z_1^{wg(TE)}} \delta_{m1}. \tag{4.3}$$

Thus, only the first entry, b_1, will be nonzero. Note from Table D.1 that the first waveguide mode is the dominant TE_{10} mode. The waveguide impedance for a TE to z mode is

$$Z_m^{wg(TE)} = \frac{\omega \mu_o}{k_{zm}}. \tag{4.4}$$

Thus, the right hand side of the MFIE matrix equation is established.

4.3 The Coupling Matrix, A

The determination of each matrix element, A_{mn}, requires the derivation of the two layer Hertzian potential Green's function found in Chapter 3, and the subsequent numerical analysis, which is detailed in this chapter. The matrix element equation (2.34) can be rewritten

$$A_{mn} = A_{mn}^{wg} - A_{mn}^{pp}, \tag{4.5}$$

where

$$A_{mn}^{wg} = \int_{CS} \vec{h}_m^{wg}(\vec{\rho}) \cdot \vec{h}_n^{wg}(\vec{\rho}) ds, \tag{4.6}$$

$$A_{mn}^{pp} = \int_{CS} \vec{h}_m^{wg}(\vec{\rho}) \cdot \vec{h}_n^{pp}(\vec{\rho}) ds. \tag{4.7}$$

and $m = 1, 2, ...N$, $n = 1, 2, ...N$. Equation (4.6) describes the coupling between a source mode n in the waveguide and an observer mode m in the waveguide, and it is evaluated in a manner similar to the steps used to evaluate b_m, which yields

$$\begin{aligned} A_{mn}^{wg} &= \int_{CS} \frac{\hat{z} \times \vec{e}_m^{wg}(\vec{\rho})}{Z_m^{wg}} \cdot \frac{\hat{z} \times \vec{e}_n^{wg}(\vec{\rho})}{Z_n^{wg}} ds \\ &= \frac{\delta_{mn}}{Z_n^{wg} Z_m^{wg}}. \end{aligned} \tag{4.8}$$

These terms will be nonzero when $m = n$, along the diagonal elements of the matrix A. The waveguide impedances Z_n^{wg} and Z_m^{wg} will be either TM_z or TE_z, depending on the orientation of the nth mode.

The next step is to determine A_{mn}^{pp}, which describes the coupling that occurs between the nth waveguide source mode and the mth observer mode in the parallel plate region. Substituting the definition of $\vec{h}_n^{pp}(\vec{\rho})$ found in (2.31) into (4.7) yields

$$\begin{aligned} A_{mn}^{pp}(\vec{\rho}) = \int_{CS} & \vec{h}_m^{wg}(\vec{\rho}) \cdot \\ & \left[Z_n(k_1^2 + \nabla_t \nabla \cdot) \int_{CS} \bar{\bar{G}}^{pp}(\vec{\rho}|\vec{\rho}'; z|z' = 0) \cdot \vec{h}_n^{wg}(\vec{\rho}') ds' \right]_{z=0} ds. \end{aligned} \tag{4.9}$$

To evaluate this integral, the different vector-matrix operations will be carefully examined to arrive at an expression which can be evaluated numerically.

The transverse waveguide mode functions are decomposed into their scalar com-

ponents,

$$\vec{h}_n^{wg}(\vec{\rho}) = \hat{x}h_{xn}^{wg}(\vec{\rho}) + \hat{y}h_{yn}^{wg}(\vec{\rho}) \tag{4.10}$$

$$\vec{h}_m^{wg}(\vec{\rho}) = \hat{x}h_{xm}^{wg}(\vec{\rho}) + \hat{y}h_{ym}^{wg}(\vec{\rho}). \tag{4.11}$$

The decomposition of $h_n^{pp}(\vec{\rho})$ into its scalar components requires the evaluation of the $\nabla_t\nabla\cdot$ operator in (4.9). When the operator is expanded and operates on a vector $\vec{A}$, the result is

$$\nabla_t\nabla\cdot\vec{A} = \hat{x}\frac{\partial}{\partial x}\left(\frac{\partial A_x}{\partial x} + \frac{\partial A_y}{\partial y} + \frac{\partial A_z}{\partial z}\right) + \hat{y}\frac{\partial}{\partial y}\left(\frac{\partial A_x}{\partial x} + \frac{\partial A_y}{\partial y} + \frac{\partial A_z}{\partial z}\right). \tag{4.12}$$

Recall that the dyadic Green's function elements which are needed in this derivation are given in sections 3.8.1.3 - 3.8.2.3. Using those elements and (4.10), the components of the matrix-vector product $\bar{\bar{G}}^{pp}\left(\vec{\rho}, z|\vec{\rho}', z'\right)\cdot\vec{h}_n^{wg}(\vec{\rho}')$ are given by

$$\bar{\bar{G}}^{pp}\cdot\vec{h}_n^{wg} = \hat{x}G_{xx}h_{xn}^{wg} + \hat{y}G_{yy}h_{yn}^{wg} + \hat{z}\left[G_{zx}h_{xn}^{wg} + G_{zy}h_{yn}^{wg}\right], \tag{4.13}$$

where the dependence on $\vec{\rho}$ and $\vec{\rho}'$ has been temporarily suppressed in this equation for notational convenience.

Using (4.12) and (4.13) $\vec{h}_n^{pp}(\vec{\rho})$ is decomposed into its transverse scalar components, producing

$$\begin{aligned} h_{xn}^{pp}(\vec{\rho}) = \Bigg[&\left(k_1^2 + \frac{\partial^2}{\partial x^2}\right) Z_n \int_{CS} G_{xx}(\vec{\rho}, z|\vec{\rho}', z')h_{xn}^{wg}(\vec{\rho}')ds' \\ &+ \frac{\partial^2}{\partial x\partial y} Z_n \int_{CS} G_{yy}(\vec{\rho}, z|\vec{\rho}', z')h_{yn}^{wg}(\vec{\rho}')ds' \\ &+ \frac{\partial^2}{\partial x\partial z} Z_n \int_{CS} \left[G_{zx}(\vec{\rho}, z|\vec{\rho}', z')h_{xn}^{wg}(\vec{\rho}')\right. \\ &\left.+G_{zy}(\vec{\rho}, z|\vec{\rho}' z')h_{yn}^{wg}(\vec{\rho}')\right] ds'\Bigg]_{z=0,z'=0} \end{aligned} \tag{4.14}$$

and

$$h_{yn}^{pp}(\vec{\rho}) = \left[\frac{\partial^2}{\partial x \partial y} Z_n \int_{CS} G_{xx}(\vec{\rho}, z|\vec{\rho}', z') h_{xn}^{wg}(\vec{\rho}') ds' \right.$$
$$+ \left(k_1^2 + \frac{\partial^2}{\partial y^2}\right) Z_n \int_{CS} G_{yy}(\vec{\rho}, z|\vec{\rho}', z') h_{yn}^{wg}(\vec{\rho}') ds'$$
$$+ \frac{\partial^2}{\partial y \partial z} Z_n \int_{CS} \left[G_{zx}(\vec{\rho}, z|\vec{\rho}', z') h_{xn}^{wg}(\vec{\rho}')\right.$$
$$\left.\left. + G_{zy}(\vec{\rho}, z|\vec{\rho}', z') h_{yn}^{wg}(\vec{\rho}')\right] ds' \right]_{z=0, z'=0,} \tag{4.15}$$

where the transverse part of $\vec{h}_n^{pp}(\vec{\rho})$ is $\hat{x} h_{xn}^{pp}(\vec{\rho}) + \hat{y} h_{yn}^{pp}(\vec{\rho})$.

The dyadic Green's function elements in the spatial domain are related to the Green's function elements in the spectral domain by the the inverse transform relationship

$$G_{cd}(\vec{\rho}, z|\vec{\rho}', z') = \frac{1}{(2\pi)^2} \iint_{-\infty}^{+\infty} \widetilde{G}_{cd}(k_x, k_y, z, z') e^{j\vec{k}\cdot(\vec{\rho}-\vec{\rho}')} dk_x dk_y, \tag{4.16}$$

where $c = x, y, z$ and $d = x, y, z$. Using this notation, the spectral representation of

the dyadic Green's function elements from (3.213), (3.219), (3.222), and (3.224) are

$$\widetilde{G}_{xx}(k_x, k_y, z, z') = \frac{1}{j2\omega\mu_1 p_1} \cdot \left[e^{-p_1|z-z'|} + e^{p_1(z+z')} - 2\cosh p_1 z \cosh p_1 z' \frac{T_{ms}}{T_m} e^{-p_1 d_1} \right], \tag{4.17}$$

$$\widetilde{G}_{zx}(k_x, k_y, z, z') = \frac{-1}{j2\omega\mu_1 p_1} \cdot \left[jk_x \left(\frac{\mu_2\epsilon_2}{\mu_1\epsilon_1} - 1 \right) \frac{\sinh\left(2p_2\left(d_1 - h\right)\right)}{p_1 T_m T_e} \cosh p_1 z' \sinh p_1 z \right], \tag{4.18}$$

$$\widetilde{G}_{yy}(k_x, k_y, z, z') = \frac{1}{j2\omega\mu_1 p_1} \cdot \left[e^{-p_1|z-z'|} + e^{p_1(z+z')} - 2\cosh p_1 z \cosh p_1 z' \frac{T_{ms}}{T_m} e^{-p_1 d_1} \right], \tag{4.19}$$

$$\widetilde{G}_{zy}(k_x, k_y, z, z') = \frac{-1}{j2\omega\mu_1 p_1} \cdot \left[jk_y \left(\frac{\mu_2\epsilon_2}{\mu_1\epsilon_1} - 1 \right) \frac{\sinh\left(2p_2\left(d_1 - h\right)\right)}{p_1 T_m T_e} \cosh p_1 z' \sinh p_1 z \right]. \tag{4.20}$$

Inserting the inverse transform definition from (4.16) in (4.14) yields

$$
\begin{aligned}
&h_{xn}^{pp}(\vec{\rho}) = \\
&\left[\left(k_1^2+\frac{\partial^2}{\partial x^2}\right) Z_n \int_{CS} \left(\frac{1}{(2\pi)^2}\iint_{-\infty}^{+\infty} \widetilde{G}_{xx}(k_x,k_y,z,z')e^{j\vec{k}\cdot(\vec{\rho}-\vec{\rho}')}dk_x dk_y\right) h_{xn}^{wg}(\vec{\rho}')ds' \right. \\
&+\frac{\partial^2}{\partial x\partial y} Z_n \int_{CS} \left(\frac{1}{(2\pi)^2}\iint_{-\infty}^{+\infty} \widetilde{G}_{yy}(k_x,k_y,z,z')e^{j\vec{k}\cdot(\vec{\rho}-\vec{\rho}')}dk_x dk_y\right) h_{yn}^{wg}(\vec{\rho}')ds' \\
&+\frac{\partial^2}{\partial x\partial z} Z_n \int_{CS} \left[\left(\frac{1}{(2\pi)^2}\iint_{-\infty}^{+\infty} \widetilde{G}_{zx}(k_x,k_y,z,z')e^{j\vec{k}\cdot(\vec{\rho}-\vec{\rho}')}dk_x dk_y\right) h_{xn}^{wg}(\vec{\rho}')\right. \\
&\qquad \left.\left. +\left(\frac{1}{(2\pi)^2}\iint_{-\infty}^{+\infty} \widetilde{G}_{zy}(k_x,k_y,z,z')e^{j\vec{k}\cdot(\vec{\rho}-\vec{\rho}')}dk_x dk_y\right) h_{yn}^{wg}(\vec{\rho}')\right] ds'\right]_{z=0,z'=0}.
\end{aligned}
\tag{4.21}
$$

The next step in the derivation is to interchange the integral and differential operators such that terms which are integrated over $\vec{\rho}'$ are collected in one integrand. Performing this step yields

$$
\begin{aligned}
&h_{xn}^{pp}(\vec{\rho}) = \\
&\left[\left(k_1^2+\frac{\partial^2}{\partial x^2}\right)\frac{Z_n}{4\pi^2}\iint_{-\infty}^{+\infty} \widetilde{G}_{xx}(k_x,k_y,z,z')e^{j\vec{k}\cdot\vec{\rho}}\int_{CS} h_{xn}^{wg}(\vec{\rho}')e^{-j\vec{k}\cdot\vec{\rho}'}ds'dk_x dk_y\right. \\
&\qquad +\frac{\partial^2}{\partial x\partial y}\frac{Z_n}{4\pi^2}\iint_{-\infty}^{+\infty} \widetilde{G}_{yy}(k_x,k_y,z,z')e^{j\vec{k}\cdot\vec{\rho}}\int_{CS} h_{yn}^{wg}(\vec{\rho}')e^{-j\vec{k}\cdot\vec{\rho}'}ds'dk_x dk_y \\
&\qquad +\frac{\partial^2}{\partial x\partial z}\frac{Z_n}{4\pi^2}\left[\iint_{-\infty}^{+\infty} \widetilde{G}_{zx}(k_x,k_y,z,z')e^{j\vec{k}\cdot\vec{\rho}}\int_{CS} h_{xn}^{wg}(\vec{\rho}')e^{-j\vec{k}\cdot\vec{\rho}'}ds'\,dk_x dk_y\right. \\
&\qquad \left.\left. +\iint_{-\infty}^{+\infty} \widetilde{G}_{zy}(k_x,k_y,z,z')e^{j\vec{k}\cdot\vec{\rho}}\int_{CS} h_{yn}^{wg}(\vec{\rho}')e^{-j\vec{k}\cdot\vec{\rho}'}ds'dk_x dk_y\right]\right]_{z=0,z'=0}.
\end{aligned}
\tag{4.22}
$$

A further helpful step for obtaining the solution is to define two functions

$$f_{xn}(k_x, k_y) = \int_{CS} h_{xn}^{wg}(\vec{\rho}\,')e^{-j\vec{k}\cdot\vec{\rho}\,'}ds', \tag{4.23}$$

$$f_{yn}(k_x, k_y) = \int_{CS} h_{yn}^{wg}(\vec{\rho}\,')e^{-j\vec{k}\cdot\vec{\rho}\,'}ds'. \tag{4.24}$$

Carrying out the derivatives with respect to x and y in (4.22) and using (4.23) and (4.24) produces

$$\begin{aligned} h_{xn}^{pp}(\vec{\rho}) = \Bigg[& \left(k_1^2 - k_x^2\right)\frac{Z_n}{4\pi^2}\iint_{-\infty}^{+\infty}\widetilde{G}_{xx}(k_x, k_y, z, z')e^{j\vec{k}\cdot\vec{\rho}}f_{xn}(k_x, k_y)dk_x dk_y \\ & -k_x k_y \frac{Z_n}{4\pi^2}\iint_{-\infty}^{+\infty}\widetilde{G}_{yy}(k_x, k_y, z, z')e^{j\vec{k}\cdot\vec{\rho}}f_{yn}(k_x, k_y)dk_x dk_y \\ & +jk_x\frac{Z_n}{4\pi^2}\frac{\partial}{\partial z}\Bigg[\iint_{-\infty}^{+\infty}\widetilde{G}_{zx}(k_x, k_y, z, z')e^{j\vec{k}\cdot\vec{\rho}}f_{xn}(k_x, k_y)dk_x dk_y \\ & +\iint_{-\infty}^{+\infty}\widetilde{G}_{zy}(k_x, k_y, z, z')e^{j\vec{k}\cdot\vec{\rho}}f_{yn}(k_x, k_y)dk_x dk_y\Bigg]\Bigg]_{z=0,z'=0}. \end{aligned} \tag{4.25}$$

If the off-diagonal elements of the dyadic Green's function are defined such that

$$\widetilde{G}_{zx}(k_x, k_y, z, z') = \widetilde{X}(k_x, k_y, z')\sinh(p_1 z) \tag{4.26}$$

$$\widetilde{G}_{zy}(k_x, k_y, z, z') = \widetilde{Y}(k_x, k_y, z')\sinh(p_1 z), \tag{4.27}$$

the derivatives in (4.25) produce

$$\frac{\partial}{\partial z}\widetilde{G}_{zx}(k_x, k_y, z, z') = \widetilde{X}(k_x, k_y, z')p_1\cosh(p_1 z) \tag{4.28}$$

$$\frac{\partial}{\partial z}\widetilde{G}_{zy}(k_x, k_y, z, z') = \widetilde{Y}(k_x, k_y, z')p_1\cosh(p_1 z), \tag{4.29}$$

where

$$\widetilde{X}(k_x,k_y,z') = -\frac{1}{j2\omega\mu_1 p_1}\left[jk_x\left(\frac{\mu_2\epsilon_2}{\mu_1\epsilon_1}-1\right)\frac{\sinh\left(2p_2\left(d_1-h\right)\right)}{p_1T_mT_e}\cosh p_1z'\right] \quad (4.30)$$

$$\widetilde{Y}(k_x,k_y,z') = -\frac{1}{j2\omega\mu_1 p_1}\left[jk_y\left(\frac{\mu_2\epsilon_2}{\mu_1\epsilon_1}-1\right)\frac{\sinh\left(2p_2\left(d_1-h\right)\right)}{p_1T_mT_e}\cosh p_1z'\right]. \quad (4.31)$$

Also note that $\widetilde{G}_{xx}(k_x,k_y,z,z') = \widetilde{G}_{yy}(k_x,k_y,z,z')$. Using these expressions, (4.25) can be rewritten as

$$\begin{aligned} h_{xn}^{pp}(\vec{\rho}) = \Bigg[\frac{Z_n}{4\pi^2}\iint_{-\infty}^{+\infty}\Big[&\left(k_1^2-k_x^2\right)\widetilde{G}_{xx}(k_x,k_y,z,z')f_{xn}(k_x,k_y) \\ &- k_xk_y\widetilde{G}_{xx}(k_x,k_y,z,z')f_{yn}(k_x,k_y) \\ &+ jk_xp_1\Big(\widetilde{X}(k_x,k_y,z')\cosh(p_1z)f_{xn}(k_x,k_y) \\ &+ \widetilde{Y}(k_x,k_y,z')\cosh\left(p_1z\right)f_{yn}(k_x,k_y)\Big)\Big]e^{j\vec{k}\cdot\vec{\rho}}dk_xdk_y\Bigg]_{z=0,z'=0}. \end{aligned} \quad (4.32)$$

Now that the partial derivatives with respect to z have been carried out, (4.32) may be evaluated at $z=0$ and $z'=0$. By inserting these values, (4.32) yields

$$\begin{aligned} h_{xn}^{pp}(\vec{\rho}) =& \frac{Z_n}{4\pi^2}\iint_{-\infty}^{+\infty} \\ &\Big\{\widetilde{G}_{xx}(k_x,k_y,z=0,z'=0)\left[\left(k_1^2-k_x^2\right)f_{xn}(k_x,k_y)-k_xk_yf_{yn}(k_x,k_y)\right] \\ &+ jk_xp_1\left(\widetilde{X}(k_x,k_y,z'=0)f_{xn}(k_x,k_y)+\widetilde{Y}(k_x,k_y,z'=0)f_{yn}(k_x,k_y)\right)\Big\} \\ &e^{j\vec{k}\cdot\vec{\rho}}dk_xdk_y. \end{aligned} \quad (4.33)$$

A similar series of steps also allows for the derivation of the y-component,

$$h_{yn}^{pp}(\vec{\rho}) = \frac{Z_n}{4\pi^2} \iint_{-\infty}^{+\infty} \left\{ \widetilde{G}_{xx}(k_x, k_y, z=0, z'=0) \left[\left(k_1^2 - k_y^2 \right) f_{yn}(k_x, k_y) - k_x k_y f_{xn}(k_x, k_y) \right] + jk_y p_1 \left(\widetilde{X}(k_x, k_y, z'=0) f_{xn}(k_x, k_y) + \widetilde{Y}(k_x, k_y, z'=0) f_{yn}(k_x, k_y) \right) \right\} e^{j\vec{k}\cdot\vec{\rho}} dk_x dk_y. \tag{4.34}$$

The expression for the parallel plate portions of the matrix, A_{mn}^{pp}, may be obtained by inserting (4.33) and (4.34) in (4.7). For simplicity of formulation, $z = 0$ and $z' = 0$ will be assumed for the remainder of the derivation in the functions $\widetilde{G}_{xx}$, $\widetilde{X}$ and $\widetilde{Y}$, and they are represented as functions of k_x and k_y only. Thus A_{mn}^{pp} is given by

$$\begin{aligned} A_{mn}^{pp} &= \int_{CS} h_{xm}^{wg}(\vec{\rho}) h_{xn}^{pp}(\vec{\rho}) ds + \int_{CS} h_{ym}^{wg}(\vec{\rho}) h_{yn}^{pp}(\vec{\rho}) ds \\ &= \frac{Z_n}{4\pi^2} \int_{CS} h_{xm}^{wg}(\vec{\rho}) \iint_{-\infty}^{+\infty} \left\{ \widetilde{G}_{xx}(k_x, k_y) \left[\left(k_1^2 - k_x^2 \right) f_{xn}(k_x, k_y) \right. \right. \\ &\quad \left. \left. - k_x k_y f_{yn}(k_x, k_y) \right] + jk_x p_1 \left(\widetilde{X}(k_x, k_y) f_{xn}(k_x, k_y) + \widetilde{Y}(k_x, k_y) f_{yn}(k_x, k_y) \right) \right\} \\ &\quad e^{j\vec{k}\cdot\vec{\rho}} dk_x dk_y ds \\ &\quad + \frac{Z_n}{4\pi^2} \int_{CS} h_{ym}^{wg}(\vec{\rho}) \iint_{-\infty}^{+\infty} \left\{ \widetilde{G}_{xx}(k_x, k_y) \left[\left(k_1^2 - k_y^2 \right) f_{yn}(k_x, k_y) \right. \right. \\ &\quad \left. \left. - k_x k_y f_{xn}(k_x, k_y) \right] + jk_y p_1 \left(\widetilde{X}(k_x, k_y) f_{xn}(k_x, k_y) + \widetilde{Y}(k_x, k_y) f_{yn}(k_x, k_y) \right) \right\} \\ &\quad e^{j\vec{k}\cdot\vec{\rho}} dk_x dk_y ds \end{aligned} \tag{4.35}$$

In order to further simplify the solution, two additional functions are defined that

integrate over the spatial variables x and y,

$$g_{xm}(k_x, k_y) = \int_{CS} h_{xm}^{wg}(\vec{\rho}) e^{j\vec{k}\cdot\vec{\rho}} ds \tag{4.36}$$

$$g_{ym}(k_x, k_y) = \int_{CS} h_{ym}^{wg}(\vec{\rho}) e^{j\vec{k}\cdot\vec{\rho}} ds. \tag{4.37}$$

Then the expression for the parallel plate matrix coupling terms becomes

$$\begin{aligned} A_{mn}^{pp} = \frac{Z_n}{4\pi^2} \iint_{-\infty}^{+\infty} & \left\{ \widetilde{G}_{xx}(k_x, k_y) \left[\left(k_1^2 - k_x^2 \right) f_{xn}(k_x, k_y) - k_x k_y f_{yn}(k_x, k_y) \right] \right. \\ & \left. + jk_x p_1 \left(\widetilde{X}(k_x, k_y) f_{xn}(k_x, k_y) + \widetilde{Y}(k_x, k_y) f_{yn}(k_x, k_y) \right) \right\} g_{xm}(k_x, k_y) dk_x dk_y \\ + \frac{Z_n}{4\pi^2} \iint_{-\infty}^{+\infty} & \left\{ \widetilde{G}_{xx}(k_x, k_y) \left[\left(k_1^2 - k_y^2 \right) f_{yn}(k_x, k_y) - k_x k_y f_{xn}(k_x, k_y) \right] \right. \\ & \left. + jk_y p_1 \left(\widetilde{X}(k_x, k_y) f_{xn}(k_x, k_y) + \widetilde{Y}(k_x, k_y) f_{yn}(k_x, k_y) \right) \right\} g_{ym}(k_x, k_y) dk_x dk_y. \end{aligned} \tag{4.38}$$

At this point, an expression for all the elements of the matrix A and the forcing function b have been described by (4.3), (4.8), and (4.38), and the matrix is positioned to obtain the solution to the MFIE. Note, however, that the functions $f_{xn}(k_x, k_y)$ and $f_{yn}(k_x, k_y)$ will be different if the nth mode is TE_z than they will be if the nth mode is TM_z. Similarly, $g_{xm}(k_x, k_y)$ and $g_{ym}(k_x, k_y)$ will be different for the two types of modes. With these functions, there are four possible combinations, and the next sections examine the possible combinations of coupling between TE and TM modes in calculating the matrix elements A_{mn}.

In this solution process, the notation for the modes is chosen as follows. If the nth mode is a TE mode, it will be represented as a $TE_{u_n v_n}$ mode. The subscripts are chosen such that the first subscript, u_n, denotes the nth mode index in the x-dimension. The second subscript is chosen to denote the nth y-direction mode index.

For example, if the modes are arranged from the lowest cutoff frequency to the highest for an empty WR-90 waveguide, as shown in Table D.1, the 4th mode is the $TM_{1\,2}$ mode. In this case, $n = 4$, $u_n = 1$ and $v_n = 2$.

4.4 Solution to the Matrix Equation for TE and TM Mode Coupling

Each matrix element A_{mn} is calculated as a combination of the waveguide coupling term A_{mn}^{wg} and the parallel plate coupling term A_{mn}^{pp},

$$A_{mn} = A_{mn}^{wg} - A_{mn}^{pp}. \tag{4.39}$$

In both terms, there are 4 possible combinations between the source and the observer waveguide mode functions. Each case must be considered for its contribution to the coupling matrix, A_{mn}.

4.4.1 Case 1: $TE_{un\,vn}$ source with $TE_{um\,vm}$ observer

In this case, the source term, denoted by the n subscript, is a TE_z mode, and the observer is also a TE_z mode, and is noted by the m subscript. The waveguide coupling is given by

$$A_{mn}^{wg} = \frac{\delta_{mn}}{Z_m^{wg(TE)} Z_n^{wg(TE)}}, \tag{4.40}$$

where for the TE_z case, the waveguide impedance is given by

$$Z_\alpha^{wg(TE)} = \frac{\omega\mu_0}{k_{z\alpha}^{wg}}, \qquad \alpha = m, n. \tag{4.41}$$

The portions of (4.38) that need to be determined for each case are the expressions for $f_{xn}(k_x, k_y)$, $f_{yn}(k_x, k_y)$, $g_{xm}(k_x, k_y)$, and $g_{ym}(k_x, k_y)$. From Appendix A, the following expressions are valid for Case 1:

$$g_{xm}(k_x, ky) = -\frac{K_{um\,vm}}{Z_m^{wg(TE)}} \frac{k_y k_{xm}^2 (e^{jk_y b} - 1)(e^{jk_x a} + 1)}{j(k_y^2 - k_{ym}^2)(k_x^2 - k_{xm}^2)} = k_y k_{xm}^2 g_m(k_x, ky) \tag{4.42}$$

$$g_{ym}(k_x,ky) = -\frac{K_{um\,vm}}{Z_m^{wg(TE)}}\frac{k_x k_{ym}^2(e^{jkyb}-1)(e^{jkxa}+1)}{j(k_y^2-k_{ym}^2)(k_x^2-k_{xm}^2)} = k_x k_{ym}^2 g_m(k_x,ky) \quad (4.43)$$

$$f_{xn}(k_x,ky) = \frac{K_{un\,vn}}{Z_n^{wg(TE)}}\frac{k_y k_{xn}^2(e^{-jkyb}-1)(e^{-jkxa}+1)}{j(k_y^2-k_{yn}^2)(k_x^2-k_{xn}^2)} = k_y k_{xn}^2 f_n(k_x,ky) \quad (4.44)$$

$$f_{yn}(k_x,ky) = \frac{K_{un\,vn}}{Z_n^{wg(TE)}}\frac{k_x k_{yn}^2(e^{-jkyb}-1)(e^{-jkxa}+1)}{j(k_y^2-k_{yn}^2)(k_x^2-k_{xn}^2)} = k_x k_{yn}^2 f_n(k_x,ky). \quad (4.45)$$

The common terms are defined as

$$g_m(k_x,ky) = -\frac{K_{um\,vm}}{Z_m^{wg(TE)}}\frac{(e^{jkyb}-1)(e^{jkxa}+1)}{j(k_y^2-k_{ym}^2)(k_x^2-k_{xm}^2)} \quad (4.46)$$

$$f_n(k_x,ky) = \frac{K_{un\,vn}}{Z_n^{wg(TE)}}\frac{(e^{-jkyb}-1)(e^{-jkxa}+1)}{j(k_y^2-k_{yn}^2)(k_x^2-k_{xn}^2)}. \quad (4.47)$$

Since the dyadic Green's function is evaluated at $z=0$ and $z'=0$, the diagonal elements found in (4.38) and defined in (4.17) become

$$\widetilde{G}_{xx}(k_x,k_y)|_{z=0,z'=0} = \frac{1}{j2\omega\mu_1 p_1}\left[2-2\frac{T_{ms}}{T_m}e^{-p_1 d_1}\right] = \frac{\widetilde{G}_T(k_x,k_y)}{j2\omega\mu_1 p_1 T_m}, \quad (4.48)$$

where

$$\widetilde{G}_T(k_x,k_y) = \frac{p_2}{p_1}\sinh\left(p_2\left(d_1-h\right)\right)\sinh p_1 d_1 - \frac{\epsilon_1}{\epsilon_2}\cosh\left(p_2\left(d_1-h\right)\right)\cosh p_1 d_1. \quad (4.49)$$

Similarly, the terms $\widetilde{X}(k_x,k_y)$ and $\widetilde{Y}(k_x,k_y)$ evaluated at $z'=0$, and are defined as

$$\widetilde{X}(k_x,k_y,z')|_{z'=0} = k_x\widetilde{C}(k_x,k_y) \quad (4.50)$$

$$\widetilde{Y}(k_x,k_y,z')|_{z'=0} = k_y\widetilde{C}(k_x,k_y), \quad (4.51)$$

where

$$\widetilde{C}(k_x,k_y)=-\frac{1}{2\omega\mu_1 p_1}\left[\left(\frac{\mu_2\epsilon_2}{\mu_1\epsilon_1}-1\right)\frac{\sinh\left(2p_2\left(d_1-h\right)\right)}{p_1T_mT_e}\right]. \tag{4.52}$$

Applying these simplifications to (4.38), the parallel plate coupling term becomes

$$\begin{aligned}A_{mn}^{pp}=&\frac{Z_n^{wg(TE)}}{4\pi^2}\int\!\!\int_{-\infty}^{+\infty}\Big\{\widetilde{G}_{xx}(k_x,k_y)f_n(k_x,k_y)\left[\left(k_1^2-k_x^2\right)k_yk_{xn}^2-k_yk_x^2k_{yn}^2\right]\\&+jk_xp_1\widetilde{C}(k_x,k_y)f_n(k_x,k_y)\left(k_xk_yk_{xn}^2+k_yk_xk_{yn}^2\right)\Big\}k_yk_{xm}^2g_m(k_x,k_y)dk_xdk_y\\&+\frac{Z_n^{wg(TE)}}{4\pi^2}\int\!\!\int_{-\infty}^{+\infty}\Big\{\widetilde{G}_{xx}(k_x,k_y)f_n(k_x,k_y)\left[\left(k_1^2-k_y^2\right)k_xk_{yn}^2-k_xk_y^2k_{xn}^2\right]\\&+jk_yp_1\widetilde{C}(k_x,k_y)f_n(k_x,k_y)\left(k_xk_yk_{xn}^2+k_yk_xk_{yn}^2\right)\Big\}k_xk_{ym}^2g_m(k_x,k_y)dk_xdk_y.\end{aligned} \tag{4.53}$$

To evaluate this expression numerically, a two-dimensional spectral integral must be evaluated, which is computationally expensive. It is desirable to simplify this expression as much as possible in order to reduce the computational time. Note that the terms $\widetilde{G}_{xx}(k_x,k_y)f_n(k_x,k_y)g_m(k_x,k_y)$ and $jp_1\widetilde{C}(k_x,k_y)g_m(k_x,k_y)f_n(k_x,k_y)$ can be grouped together. After some algebraic manipulation, (4.53) can be rearranged as

$$\begin{aligned}A_{mn}^{pp}=&\frac{Z_n^{wg(TE)}}{4\pi^2}\int\!\!\int_{-\infty}^{+\infty}\Big\{\widetilde{G}_{xx}(k_x,k_y)f_n(k_x,k_y)g_m(k_x,k_y)\left[k_1^2\left(k_y^2(k_{xn}^2k_{xm}^2)\right)\right.\\&\left.+k_x^2(k_{yn}^2k_{ym}^2)-k_x^2k_y^2k_{cn}^2k_{cm}^2\right]\\&+jp_1\widetilde{C}(k_x,k_y)f_n(k_x,k_y)g_m(k_x,k_y)k_x^2k_y^2k_{cn}^2k_{cm}^2\Big\}dk_xdk_y.\end{aligned} \tag{4.54}$$

Additional grouping of terms is possible to further reduce the number of two-

dimensional integrals necessary to solve for the matrix element, which yields

$$A_{mn}^{pp} = \frac{1}{4\pi^2} \frac{K_{un\,vn}^{wg}}{j\omega\mu_1} \frac{K_{um\,vm}^{wg}}{Z_m^{wg(TE)}} \left[\int_{-\infty}^{+\infty} \widetilde{G}_1(k_x) \left\{ \int_{-\infty}^{+\infty} \widetilde{F}_1(k_x, k_y) dk_y \right\} dk_x \right.$$
$$\left. + k_1^2 k_{xn}^2 k_{xm}^2 \int_{-\infty}^{+\infty} \widetilde{G}_2(k_x) \left\{ \int_{-\infty}^{+\infty} \widetilde{F}_4(k_x, k_y) dk_y \right\} dk_x \right]. \quad (4.55)$$

Note that only two double integrals need to be computed for this solution. The following terms are used in (4.55):

$$\widetilde{F}_1(k_x, k_y) = k_1^2 k_{ym}^2 k_{yn}^2 \widetilde{F}_2(k_x, k_y) + k_{cn}^2 k_{cm}^2 \left(\widetilde{F}_3(k_x, k_y) - \widetilde{F}_4(k_x, k_y) \right) \quad (4.56)$$

$$\widetilde{F}_2(k_x, k_y) = \frac{\widetilde{G}_T(k_x, k_y)}{p_1 T_m} \frac{\left(e^{-jk_y b} - 1\right)\left(e^{jk_y b} - 1\right)}{\left(k_y^2 - k_{yn}^2\right)\left(k_y^2 - k_{ym}^2\right)} \quad (4.57)$$

$$\widetilde{F}_4(k_x, k_y) = k_y^2 \widetilde{F}_2(k_x, k_y) \quad (4.58)$$

$$\widetilde{F}_3(k_x, k_y) = \left(\frac{\epsilon_2 \mu_2}{\epsilon_1 \mu_1} - 1 \right) \frac{\sinh(2p_2 (d_1 - h))}{2p_1 T_m T_e} \frac{k_y^2 \left(e^{-jk_y b} - 1\right)\left(e^{jk_y b} - 1\right)}{\left(k_y^2 - k_{yn}^2\right)\left(k_y^2 - k_{ym}^2\right)} \quad (4.59)$$

$$\widetilde{G}_2(k_x) = \frac{\left(e^{-jk_x a} + 1\right)\left(e^{jk_x a} + 1\right)}{\left(k_x^2 - k_{xn}^2\right)\left(k_x^2 - k_{xm}^2\right)} \quad (4.60)$$

$$\widetilde{G}_1(k_x) = k_x^2 \widetilde{G}_2(k_x) \quad (4.61)$$

The following equations are a summary of the additional terms from (4.56) - (4.61):

$$T_m = \frac{p_2}{p_1} \sinh\left(p_2(d_1 - h)\right) \cosh p_1 d_1 - \frac{\epsilon_2}{\epsilon_1} \cosh\left(p_2(d_1 - h)\right) \sinh p_1 d_1 \quad (4.62)$$

$$T_e = \frac{p_2}{p_1}\cosh\left(p_2(d_1-h)\right)\sinh p_1 d_1 - \frac{\mu_2}{\mu_1}\sinh\left(p_2(d_1-h)\right)\cosh p_1 d_1 \tag{4.63}$$

$$p_1 = \sqrt{k_x^2 + k_y^2 - k_1^2}, \qquad p_2 = \sqrt{k_x^2 + k_y^2 - k_2^2} \tag{4.64}$$

$$Z_\alpha^{wg} = \frac{\omega\mu_0}{k_{z\alpha}} \qquad k_{z\alpha} = \sqrt{k_0^2 - k_{c\alpha}^2} \quad , \quad \alpha = m, n \tag{4.65}$$

$$k_{c\alpha}^2 = k_{x\alpha}^2 + k_{y\alpha}^2 \quad , \quad \alpha = m, n \tag{4.66}$$

$$k_{x\alpha} = \frac{u_\alpha \pi}{a} \ , \qquad k_{y\alpha} = \frac{v_\alpha \pi}{b} \quad \alpha = m, n \tag{4.67}$$

The normalization constants $K_{un\,vn}^{wg}$ and $K_{um\,vm}^{wg}$ are defined in (A.17), and $\widetilde{G}_T(k_x, k_y)$ is given in (4.49).

The matrix element A_{mn} is found using (4.39),

$$\begin{aligned} A_{mn} &= A_{mn}^{wg} - A_{mn}^{pp} \\ &= \frac{\delta_{mn}}{Z_m^{wg(TE)} Z_n^{wg(TE)}} - \frac{1}{4\pi^2}\frac{K_{un\,vn}^{wg}}{j\omega\mu_1}\frac{K_{um\,vm}^{wg}}{Z_m^{wg(TE)}}\left[\int_{-\infty}^{+\infty}\widetilde{G}_1(k_x)\left\{\int_{-\infty}^{+\infty}\widetilde{F}_1(k_x,k_y)dk_y\right\}dk_x\right. \\ &\qquad \left. + k_1^2 k_{xn}^2 k_{xm}^2 \int_{-\infty}^{+\infty}\widetilde{G}_2(k_x)\left\{\int_{-\infty}^{+\infty}\widetilde{F}_4(k_x,k_y)dk_y\right\}dk_x\right]. \end{aligned} \tag{4.68}$$

4.4.2 Case 2: $TE_{un\,vn}$ source with $TM_{um\,vm}$ observer

The second possible coupling combination occurs when the source mode is TE_z and the observer mode is a TM_z mode. In this case, the functions $f_{xn}(k_x, k_y)$ and $f_{yn}(k_x, k_y)$ are identical to case 1, since the nth mode is TE_z. The functions $g_{xm}(k_x, k_y)$, and $g_{ym}(k_x, k_y)$ must be used for the TM_z case.

From Appendix A, the functions $g_{xm}(k_x, k_y)$, and $g_{ym}(k_x, k_y)$ are found to be

$$g_{xm}(k_x, ky) = -\frac{N_{um\,vm}}{Z_m^{wg(TM)}} \frac{k_y k_{xm} k_{ym} (e^{jk_y b} - 1)(e^{jk_x a} + 1)}{j(k_y^2 - k_{ym}^2)(k_x^2 - k_{xm}^2)}$$
$$= k_y k_{xm} k_{ym} g_{m2}(k_x, k_y) \tag{4.69}$$

$$g_{ym}(k_x, ky) = \frac{N_{um\,vm}}{Z_m^{wg(TM)}} \frac{k_x k_{ym} k_{xm} (e^{jk_y b} - 1)(e^{jk_x a} + 1)}{j(k_y^2 - k_{ym}^2)(k_x^2 - k_{xm}^2)}$$
$$= -k_x k_{ym} k_{xm} g_{m2}(k_x, k_y), \tag{4.70}$$

where

$$g_{m2}(k_x, k_y) = -\frac{N_{um\,vm}}{Z_m^{wg(TM)}} \frac{(e^{jk_y b} - 1)(e^{jk_x a} + 1)}{j(k_y^2 - k_{ym}^2)(k_x^2 - k_{xm}^2)}. \tag{4.71}$$

Applying these terms to (4.38), grouping common terms and simplifying the expression produces

$$A_{mn}^{pp} = \frac{Z_n^{wg(TE)}}{4\pi^2} \iint_{-\infty}^{+\infty} \Big\{ \widetilde{G}_{xx}(k_x, k_y) f_n(k_x, ky) g_{m2}(k_x, ky) \cdot$$
$$\left[k_1^2 k_{xm} k_{ym} \left(k_y^2 k_{xn}^2 - k_x^2 k_{yn}^2 \right) \right] \Big\} dk_x dk_y. \tag{4.72}$$

Rearranging terms so that the minimal amount of two-dimensional integration is performed, the parallel plate coupling term is given by

$$A_{mn}^{pp} = \frac{1}{4\pi^2} \frac{N_{um\,vm}^{wg}}{j\omega\mu_1} \frac{K_{un\,vn}^{wg}}{Z_m^{wg(TM)}} k_1^2 k_{xm} k_{ym} \cdot$$
$$\left[k_{xn}^2 \int_{-\infty}^{+\infty} \widetilde{G}_2(k_x) \left\{ \int_{-\infty}^{+\infty} \widetilde{F}_4(k_x, k_y) dk_y \right\} dk_x \right.$$
$$\left. -k_{yn}^2 \int_{-\infty}^{+\infty} \widetilde{G}_1(k_x) \left\{ \int_{-\infty}^{+\infty} \widetilde{F}_2(k_x, k_y) dk_y \right\} dk_x \right]. \tag{4.73}$$

All of the terms in this case are defined in case 1, with the exception of the normalization constant for the TM_z mode, $N^{wg}_{um\,vm}$, which is found in (A.18) in Appendix A. The waveguide impedance for the TM_z wave is

$$Z_m^{wg(TM)} = \frac{k_{zm}}{\omega\epsilon_o}. \tag{4.74}$$

The matrix element A_{mn} is found using (4.39),

$$\begin{aligned} A_{mn} &= A^{wg}_{mn} - A^{pp}_{mn} \\ &= \frac{\delta_{mn}}{Z_m^{wg(TM)} Z_n^{wg(TE)}} - \frac{1}{4\pi^2} \frac{N^{wg}_{um\,vm}}{j\omega\mu_1} \frac{K^{wg}_{un\,vn}}{Z_m^{wg(TM)}} k_1^2 k_{xm} k_{ym} \cdot \\ &\left[k_{xn}^2 \int_{-\infty}^{+\infty} \widetilde{G}_2(k_x) \left\{ \int_{-\infty}^{+\infty} \widetilde{F}_4(k_x, k_y) dk_y \right\} dk_x \right. \\ &\left. -k_{yn}^2 \int_{-\infty}^{+\infty} \widetilde{G}_1(k_x) \left\{ \int_{-\infty}^{+\infty} \widetilde{F}_2(k_x, k_y) dk_y \right\} dk_x \right]. \end{aligned} \tag{4.75}$$

4.4.3 Case 3: $TM_{un\,vn}$ source with $TE_{um\,vm}$ observer

The third possible coupling combination occurs when the source mode is TM_z and the observer mode is a TE_z mode. In this case, the functions $g_{xm}(k_x, k_y)$ and $g_{ym}(k_x, k_y)$ are identical to case 1, since the mth mode is TE_z. The functions $f_{xn}(k_x, k_y)$, and $f_{yn}(k_x, k_y)$ must be determined for the TM_z case.

From Appendix A, $f_{xn}(k_x, k_y)$, and $f_{yn}(k_x, k_y)$ are determined to be

$$\begin{aligned} f_{xn}(k_x, ky) &= \frac{N_{un\,vn}}{Z_n^{wg(TM)}} \frac{k_y k_{xn} k_{yn} (e^{-jkyb} - 1)(e^{-jkxa} + 1)}{j(k_y^2 - k_{yn}^2)(k_x^2 - k_{xn}^2)} \\ &= k_y k_{xn} k_{yn} f_{n3}(k_x, ky) \end{aligned} \tag{4.76}$$

$$f_{yn}(k_x, ky) = -\frac{N_{un\,vn}}{Z_n^{wg(TM)}} \frac{k_x k_{yn} k_{xn}(e^{-jkyb} - 1)(e^{-jkxa} + 1)}{j(k_y^2 - k_{yn}^2)(k_x^2 - k_{xn}^2)}$$
$$= -k_x k_{yn} k_{xn} f_{n3}(k_x, ky), \tag{4.77}$$

where

$$f_{n3}(k_x, ky) = \frac{N_{un\,vn}}{Z_n^{wg(TM)}} \frac{(e^{-jkyb} - 1)(e^{-jkxa} + 1)}{j(k_y^2 - k_{yn}^2)(k_x^2 - k_{xn}^2)}. \tag{4.78}$$

Applying these terms to (4.38), grouping common terms, and simplifying the expression produces

$$A_{mn}^{pp} = \frac{Z_n^{wg(TM)}}{4\pi^2} \iint_{-\infty}^{+\infty} \left\{ \widetilde{G}_{xx}(k_x, k_y) f_{n3}(k_x, ky) g_m(k_x, ky) \cdot \right.$$
$$\left. \left[k_1^2 k_{xn} k_{yn} \left(k_y^2 k_{xm}^2 - k_x^2 k_{ym}^2 \right) \right] \right\} dk_x dk_y. \tag{4.79}$$

Since the n subscript is a TM_z mode, the impedance for the nth mode in Case 3 is

$$Z_n^{wg(TM)} = \frac{k_{zn}}{\omega \epsilon_0}. \tag{4.80}$$

The matrix element A_{mn} is found using (4.39) to be

$$A_{mn} = A_{mn}^{wg} - A_{mn}^{pp}$$
$$= \frac{\delta_{mn}}{Z_m^{wg(TE)} Z_n^{wg(TM)}} - \frac{1}{4\pi^2} \frac{N_{un\,vn}^{wg}}{j\omega\mu_1} \frac{K_{um\,vm}^{wg}}{Z_m^{wg(TE)}} k_1^2 k_{xn} k_{yn} \cdot$$
$$\left[k_{xm}^2 \int_{-\infty}^{+\infty} \widetilde{G}_2(k_x) \left\{ \int_{-\infty}^{+\infty} \widetilde{F}_4(k_x, k_y) dk_y \right\} dk_x \right.$$
$$\left. - k_{ym}^2 \int_{-\infty}^{+\infty} \widetilde{G}_1(k_x) \left\{ \int_{-\infty}^{+\infty} \widetilde{F}_2(k_x, k_y) dk_y \right\} dk_x \right]. \tag{4.81}$$

4.4.4 Case 4: $TM_{un\,vn}$ source with $TM_{um\,vm}$ observer

The fourth possible coupling combination occurs when the source mode is TM_z and the observer mode is a TM_z mode. In this case, the functions $g_{xm}(k_x, k_y)$ and $g_{ym}(k_x, k_y)$ are identical to case 2, since the mth mode is TM_z, and the functions $f_{xn}(k_x, k_y)$, and $f_{yn}(k_x, k_y)$ are the same as for case 3, where the source mode is TM_z.

Using (4.76), (4.77), (4.69), and (4.70) in (4.38) yields

$$A_{mn}^{pp} = \frac{Z_n^{wg(TM)}}{4\pi^2} \iint_{-\infty}^{+\infty} \left\{ \widetilde{G}_{xx}(k_x, k_y) f_{n3}(k_x, k_y) g_{m2}(k_x, k_y) \cdot \right.$$
$$\left. k_1^2 k_{xn} k_{yn} k_{xm} k_{ym} \left[k_x^2 + k_y^2 \right] \right\} dk_x dk_y. \quad (4.82)$$

After substituting terms, simplifying others, and using (4.39), the matrix element A_{mn} is

$$\begin{aligned} A_{mn} &= A_{mn}^{wg} - A_{mn}^{pp} \\ &= \frac{\delta_{mn}}{Z_m^{wg(TM)} Z_n^{wg(TM)}} - \frac{1}{4\pi^2} \frac{N_{un\,vn}^{wg}}{j\omega\mu_1} \frac{N_{um\,vm}^{wg}}{Z_m^{wg(TM)}} k_1^2 k_{xn} k_{yn} k_{xm} k_{ym} \cdot \\ &\quad \left[\int_{-\infty}^{+\infty} \widetilde{G}_2(k_x) \left\{ \int_{-\infty}^{+\infty} \widetilde{F}_4(k_x, k_y) dk_y \right\} dk_x \right. \\ &\quad \left. + \int_{-\infty}^{+\infty} \widetilde{G}_1(k_x) \left\{ \int_{-\infty}^{+\infty} \widetilde{F}_2(k_x, k_y) dk_y \right\} dk_x \right]. \end{aligned} \quad (4.83)$$

Thus, all possible combinations for the mode coupling in the matrix A have been formulated. The next section addresses the method of numerical computation of those matrix elements

4.5 Numerical computation of the matrix elements A_{mn}

The discussion of the computation of the matrix elements by numerical integration is focused on the evaluation of the integrals in Case 1. Note from (4.56) that the function $\widetilde{F}_1(k_x, k_y)$ is a combination of the functions $\widetilde{F}_2(k_x, k_y)$, $\widetilde{F}_3(k_x, k_y)$, and $\widetilde{F}_4(k_x, k_y)$. Also note that the expressions for A_{mn}^{pp} in the additional 3 cases, (4.75), (4.81), and (4.83), involve integrals of $\widetilde{F}_4(k_x, k_y)$, $\widetilde{F}_2(k_x, k_y)$, $\widetilde{G}_1(k_x)$, and $\widetilde{G}_2(k_x)$. Since the functions which are to be integrated in Case 1 are found in the remaining cases, the techniques applied in the numerical evaluation of the associated functions in Case 1 are applied in the other cases as well.

The expression for the parallel plate coupling portion of the matrix element in Case 1 is given by (4.55), which is rewritten as

$$A_{mn}^{pp} = \frac{1}{4\pi^2} \frac{K_{un\,vn}^{wg}}{j\omega\mu_1} \frac{K_{um\,vm}^{wg}}{Z_m^{wg(TE)}} \left[\int_{-\infty}^{+\infty} \widetilde{G}_1(k_x) \left\{ \int_{-\infty}^{+\infty} \widetilde{F}_1(k_x, k_y) dk_y \right\} dk_x \right.$$
$$\left. + k_1^2 k_{xn}^2 k_{xm}^2 \int_{-\infty}^{+\infty} \widetilde{G}_2(k_x) \left\{ \int_{-\infty}^{+\infty} \widetilde{F}_4(k_x, k_y) dk_y \right\} dk_x \right]. \quad (4.84)$$

At least two possible approaches can be taken in the evaluation of these integrals. In similar problems which involve the use of a single layer parallel plate Green's function, three authors have chosen to evaluate two dimensional integrals by undertaking a complex plane analysis in one of the two dimensions [35], [39], [40]. The integral in one dimension is converted to a pole series by the use of Cauchy's residue theorem. The contribution from the pole series is summed, resulting in a more rapid evaluation of the intgral in that dimension. Care must be taken to include the contribution from enough poles in the series such that the integral converges.

The advantages of this complex analysis are an improvement of up to ten times in computational speed and an increased physical insight into the problem [35]. Al-

though the improvements in solution time from complex analysis are desirable, the two layer parallel plate dyadic Green's function is a much more complicated function to evaluate when compared to the single layer Green's function. In order to reduce the integral in one dimension to a pole series, the poles must be determined and the pole contribution obtained at those poles. The determination of the poles in the two layer Green's function is a cumbersome task.

The other approach is to evaluate the two-dimensional integral numerically in both domains. This is more straightforward to implement, but does require additional computational resources and an understanding of the behavior of the integrands. In this dissertation, the second method of two-dimensional numerical integration is employed.

Two observations are in order at the start for simplification. First, the integrals are real-axis integrals in both the k_x and k_y variables, and the integrands must be inspected for any possible singularities along the real axis. Second, upon investigation of the integrands, it is evident that they are even in both k_x and k_y. Thus, for numerical evaluation along the real axis, the integrals may be evaluated as

$$\widetilde{I}_1(k_x) = \int_{-\infty}^{\infty} \widetilde{F}_1(k_x, k_y) dk_y = 2\int_0^{\infty} \widetilde{F}_1(k_x, k_y) dk_y \tag{4.85}$$

$$\widetilde{I}_4(k_x) = \int_{-\infty}^{\infty} \widetilde{F}_4(k_x, k_y) dk_y = 2\int_0^{\infty} \widetilde{F}_4(k_x, k_y) dk_y \tag{4.86}$$

$$\int_{-\infty}^{\infty} \widetilde{G}_1(k_x)\widetilde{I}_1(k_x) dk_x = 2\int_0^{\infty} \widetilde{G}_1(k_x)\widetilde{I}_1(k_x) dk_x \tag{4.87}$$

$$\int_{-\infty}^{\infty} \widetilde{G}_2(k_x)\widetilde{I}_4(k_x) dk_x = 2\int_0^{\infty} \widetilde{G}_2(k_x)\widetilde{I}_4(k_x) dk_x. \tag{4.88}$$

4.5.1 Integration in k_y

The function $\widetilde{F}_1(k_x, k_y)$ can be written as

$$\widetilde{F}_1(k_x, k_y) = k_1^2 k_{ym}^2 k_{yn}^2 \widetilde{F}_2(k_x, k_y) + k_{cn}^2 k_{cm}^2 \left(\widetilde{F}_3(k_x, k_y) - \widetilde{F}_4(k_x, k_y)\right). \tag{4.89}$$

To simplfy the evaluation of (4.89), two additional functions are defined as

$$P(k_y) = \frac{\left(e^{-jk_y b} - 1\right)\left(e^{jk_y b} - 1\right)}{\left(k_y^2 - k_{yn}^2\right)\left(k_y^2 - k_{ym}^2\right)}, \tag{4.90}$$

$$Q(k_y) = \frac{k_y^2\left(e^{-jk_y b} - 1\right)\left(e^{jk_y b} - 1\right)}{\left(k_y^2 - k_{yn}^2\right)\left(k_y^2 - k_{ym}^2\right)} \tag{4.91}$$

These functions allow $\widetilde{F}_2(k_x, k_y)$, $\widetilde{F}_3(k_x, k_y)$, and $\widetilde{F}_4(k_x, k_y)$ to be rewritten as

$$\widetilde{F}_2(k_x, k_y) = \frac{\widetilde{G}_T(k_x, k_y)}{p_1 T_m} P(k_y) \tag{4.92}$$

$$\widetilde{F}_3(k_x, k_y) = \left[\left(\frac{\epsilon_2\mu_2}{\epsilon_1\mu_1} - 1\right)\frac{\sinh(2p_2\,(d_1 - h))}{2p_1 T_m T_e}\right] Q(k_y) \tag{4.93}$$

$$\widetilde{F}_4(k_x, k_y) = \frac{\widetilde{G}_T(k_x, k_y)}{p_1 T_m} Q(k_y). \tag{4.94}$$

4.5.1.1 Singular points on the k_y axis

From an examination of (4.89) - (4.94), poles of the function $\widetilde{F}_1(k_x, k_y)$ are found on the real k_y axis at the points $k_y = k_{ym}$ and $k_y = k_{yn}$. However, it is not clear by inspection if other poles exist. To gain a better insight into the nature of $\widetilde{F}_1(k_x, k_y)$, an investigation was undertaken to determine the poles in the complex k_y plane. Due to the complex nature of the combinations of T_m, T_e, and p_1 in the denominator, and the terms $\widetilde{G}_T$ and $\sinh(2p_2\,(d_1 - h))$ in the numerator, locating these singularities was difficult to determine analytically. As an alternative investigation, the function was evaluated numerically and plotted in the complex k_y plane for various values of k_x to examine possible singularities on the real k_y axis. An example of such a plot is shown in Figure 4.1. When the real axis poles found in the functions $P(k_y)$ and $Q(k_y)$ were excluded, no additional poles were evident on the real k_y axis. Note that for any conventional lossy material, the terms p_1 and p_2 are in the lower right and upper left hand quadrant in the complex k_y plane, respectively, and the associated

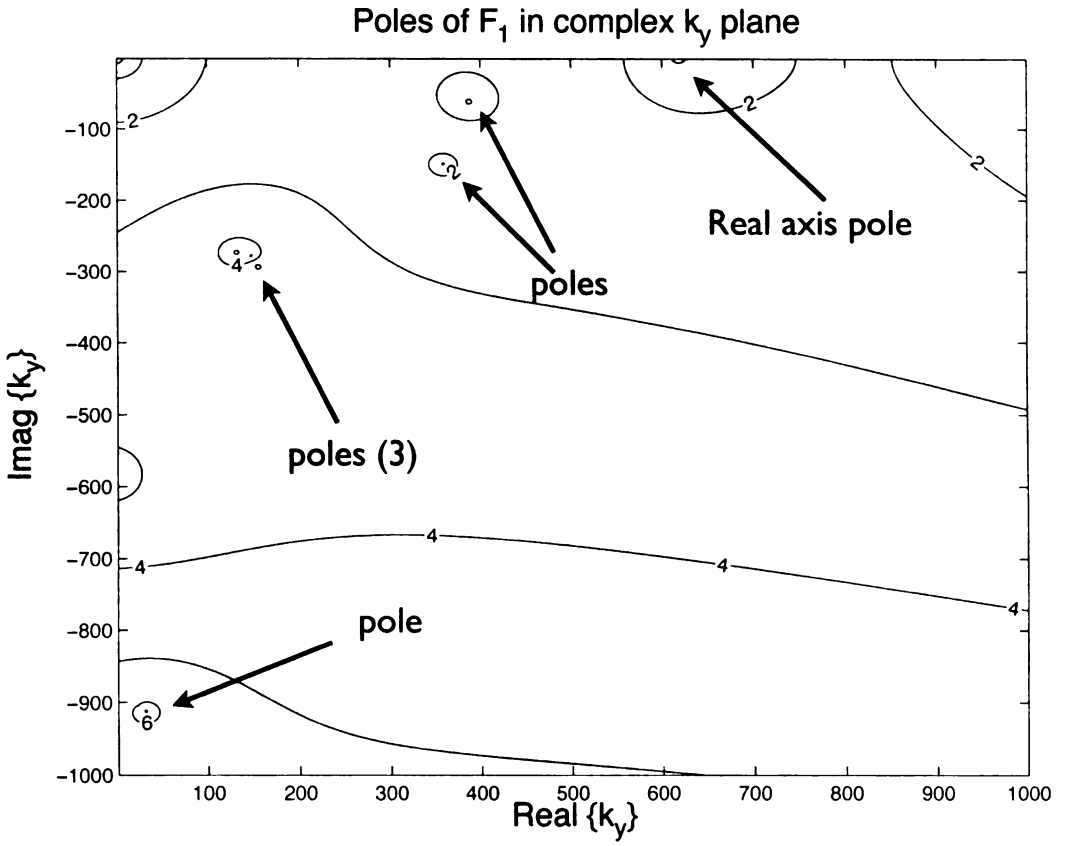


Figure 4.1. Plot of $|F_1(k_x, k_y)|$ in the complex k_y plane at 10.0 GHz. This plot created with $k_x = 10$, 0.125" thick layer of Plexiglass on top of Eccosorb FGM125, 0.125" thick, using $TE_{1\,0}$ source mode coupling with $TM_{1\,2}$ observer mode.

branch cuts do not cross the real axis.

Thus, the poles found in (4.90) and (4.91) at the points $k_y = k_{ym}$ and $k_y = k_{yn}$ must be examined to determine if these points are removable singular points. If they are not, integration in the complex plane around those points must be undertaken.

A removable singularity is analyzed in this case by using a Laurent expansion [48]. If a given function ψ is analytic about an isolated singular point z_0, it can be

expanded about that point as a Laurent series

$$\psi(z) = \sum_{p=0}^{\infty} a_p (z - z_0)^n + \sum_{p=1}^{\infty} \frac{b_p}{(z - z_0)^n} \qquad 0 < |z - z_0| < R_1, \tag{4.95}$$

where R_1 is some region outside the singular point. The principal part of ψ is that part which contains the negative powers of $(z - z_0)$, and its coefficients are

$$b_p = \frac{1}{2\pi j} \int_C \frac{\psi(z)}{(z - z_0)^{-p+1}} dz \qquad p = 1, 2, 3, \ldots \tag{4.96}$$

This integral is on a closed contour around the point z_0. If z_0 is a singular point, and all of the coefficients $b_p = 0$, then z_0 is a removable singular point. [48].

In the examination of the function $\widetilde{F}_1(k_x, k_y)$, first consider the function

$$P(k_y) = \frac{\left(e^{-jk_y b} - 1\right)\left(e^{jk_y b} - 1\right)}{\left(k_y^2 - k_{yn}^2\right)\left(k_y^2 - k_{ym}^2\right)} = \frac{2 - 2\cos k_y b}{\left(k_y^2 - k_{yn}^2\right)\left(k_y^2 - k_{ym}^2\right)}, \tag{4.97}$$

which is analytic about the singular points $k_y = k_{ym}$ and $k_y = k_{yn}$, which are simple poles. Rewriting (4.97) as

$$\begin{aligned} P(k_y) &= \frac{2 - 2\cos k_y b}{\left(k_y^2 - k_{yn}^2\right)\left(k_y - k_{ym}\right)\left(k_y + k_{ym}\right)} \\ &= \frac{P_1(k_y)}{\left(k_y - k_{ym}\right)}, \end{aligned} \tag{4.98}$$

the function is examined to determine if the pole at $k_y = k_{ym}$, $k_{ym} \neq k_{yn}$, is removable. Using Cauchy's residue theorem [48] with (4.96) produces,

$$\begin{aligned} b_1 &= \frac{1}{2\pi j} \int_C \frac{P_1(k_y)}{\left(k_y - k_{ym}\right)} dk_y = P_1(k_{ym}) \\ &= \frac{2 - 2\cos v_m \pi}{2k_{ym}\left(k_{ym}^2 - k_{yn}^2\right)}. \end{aligned} \tag{4.99}$$

From Appendix A, note that v_m is even for the WR90 X-band waveguide, and thus $\cos v_m\pi = 1$. When $k_{ym} \neq k_{yn}$, $b_1 = 0$ for all values of m.

The other b_p coefficients are determined by examining (4.96) for the other values of p. Inserting $P(k_y)$ as the function ψ in (4.96) yields

$$\begin{aligned} b_p &= \frac{1}{2\pi j}\int_C \frac{P_1(k_y)}{(k_y - k_{ym})(k_y - k_{ym})^{-p+1}}dk_y \\ &= \frac{1}{2\pi j}\int_C P_1(k_y)(k_y - k_{ym})^{p-2}dk_y \\ &= 0, \qquad\qquad p > 1. \end{aligned} \tag{4.100}$$

Thus, all the coefficients $b_p = 0$, and the pole at $k_y = k_{ym}$ is removable. A similar result is found for $k_y = k_{yn}$, $k_{ym} \neq k_{yn}$.

If $k_{ym} = k_{yn}$, then the singularity is no longer a simple pole and the Laurent series expansion is employed. Letting $k_{ym} = k_{yn}$, (4.97) is rewritten as

$$\begin{aligned} P(k_y) &= \frac{2 - 2\cos k_y b}{(k_y + k_{ym})^2 (k_y - k_{ym})^2} \\ &= \frac{P_2(k_y)}{(k_y - k_{ym})^2}, \end{aligned} \tag{4.101}$$

where

$$P_2(k_y) = \frac{2 - 2\cos k_y b}{(k_y + k_{ym})^2}. \tag{4.102}$$

Then the Laurent series coefficients are found as

$$\begin{aligned} b_2 &= \frac{1}{2\pi j}\int_C \frac{P_2(k_y)}{(k_y - k_{ym})}dk_y \\ &= P_2(k_y)\big|_{k_y = k_{ym}} \\ &= 0, \end{aligned} \tag{4.103}$$

$$
\begin{aligned}
b_1 &= \frac{1}{2\pi j}\int_C P(k_y)dk_y \\
&= \frac{\partial}{\partial k_y}\left[P_2(k_y)\right]\Big|_{k_y=k_{ym}} \\
&= 0,
\end{aligned} \tag{4.104}
$$

and

$$
\begin{aligned}
b_p &= \frac{1}{2\pi j}\int_C \frac{P_2(k_y)}{(k_y-k_{ym})^2(k_y-k_{ym})^{-p+1}}dk_y \\
&= \frac{1}{2\pi j}\int_C P_2(k_y)(k_y-k_{ym})^{p-3}dk_y \\
&= 0, \qquad\qquad p>2.
\end{aligned} \tag{4.105}
$$

Thus, when $v_n = v_m$, and consequentially, $k_{ym} = k_{yn}$, there is a removable singular point at $k_y = k_{ym}$. What remains is to evaluate the function $P(k_y)$ at that singular point, and then also examine the function $\widetilde{F}_2(k_x, k_y)$ that contains $P(k_y)$.

Note from (4.56), when $k_{ym} = 0$ or $k_{yn} = 0$, the function $\widetilde{F}_2(k_x, k_y)$ is not evaluated and thus neither is $P(k_y)$. When $k_y = k_{ym} \neq 0$ and $k_{ym} \neq k_{yn}$, the evaluation of $P(k_y)$ is

$$
P(k_y)\big|_{k_y=k_{ym}} = \frac{2-2\cos v_m\pi}{\left(k_{ym}^2-k_{yn}^2\right)\left(k_{ym}^2-k_{ym}^2\right)} = \frac{0}{0}. \tag{4.106}
$$

which is indeterminate. Using L'Hopitale's rule,

$$
\begin{aligned}
P(k_y)\big|_{k_y=k_{ym}} &= \left.\frac{\frac{\partial}{\partial k_y}\left(2-2\cos k_y b\right)}{\frac{\partial}{\partial k_y}\left(\left(k_y^2-k_{yn}^2\right)\left(k_y-k_{ym}\right)\left(k_y+k_{ym}\right)\right)}\right|_{k_y=k_{ym}} \\
&= 0.
\end{aligned} \tag{4.107}
$$

It follows from (4.92) that if $k_y = k_{ym}$ and $k_{ym} \neq k_{yn}$, then $\widetilde{F}_2(k_x, k_y) = 0$.

When $k_{ym} = k_{yn}$, evaluating $P(k_y)$ at $k_y = k_{ym} = k_{yn}$ results in an undefined quantity, 0/0. Using L'Hopitale's Rule, the first derivative is also undefined, so evaluation progresses to the second derivative, which produces

$$\begin{aligned} P(k_y)\big|_{k_y=k_{ym}} &= \left.\frac{\frac{\partial^2}{\partial k_y^2}\left(2-2\cos k_y b\right)}{\frac{\partial^2}{\partial k_y^2}\left(\left(k_y^2-k_{yn}^2\right)\left(k_y^2-k_{ym}^2\right)\right)}\right|_{k_y=k_{ym}} \\ &= \left.\frac{2b^2\cos k_y b}{12k_y^2-2\left(k_{yn}^2+k_{ym}^2\right)}\right|_{k_y=k_{ym}} \\ &= \frac{b^2}{4k_{ym}^2}. \end{aligned} \tag{4.108}$$

Thus, at the removable singular points of the function $\widetilde{F}_2(k_x, k_y)$, the value of the function is

$$\widetilde{F}_2(k_x, k_{yn}) = \widetilde{F}_2(k_x, k_{ym}) = \begin{cases} \left.\frac{b^2}{4k_{ym}^2}\frac{\widetilde{G}_T(k_x,k_y)}{p_1 T_m}\right|_{k_y=k_{ym}} & k_{ym} = k_{yn} \\ \\ 0 & k_{ym} \neq k_{yn} \end{cases} \tag{4.109}$$

When assessing the values of $\widetilde{F}_3(k_x, k_y)$ and $\widetilde{F}_4(k_x, k_y)$ at the particular singular points of each function, note that $Q(k_y) = k_y^2 P(k_y)$, or

$$Q(k_y) = \frac{k_y^2\left(e^{-jk_y b}-1\right)\left(e^{jk_y b}-1\right)}{\left(k_y^2-k_{yn}^2\right)\left(k_y^2-k_{ym}^2\right)} = \frac{k_y^2\left(2-2\cos k_y b\right)}{\left(k_y^2-k_{yn}^2\right)\left(k_y^2-k_{ym}^2\right)} \tag{4.110}$$

By proceeding through a similar analysis to that for $P(k_y)$, the singular points of $Q(k_y)$ at $k_y = k_{ym}$ and $k_y = k_{yn}$ are also removable. An examination of the possible values of $Q(k_y)$, and subsequently $\widetilde{F}_3(k_x, k_y)$ and $\widetilde{F}_4(k_x, k_y)$ are presented.

Again, the reader is reminded that

$$k_{ym} = \frac{v_m \pi}{b}, \qquad k_{yn} = \frac{v_n \pi}{b},$$

where v_m and v_n are even integers. In the function $Q(k_y)$, it is possible that $k_{ym} = 0$ and/or $k_{yn} = 0$, so these conditions must be considered as producing singular points.

Consider the case where $k_{ym} = 0$ and $k_{yn} = 0$. The expression in (4.110) may then be rewritten as

$$Q(k_y) = \frac{k_y^2 \left(2 - 2\cos k_y b\right)}{k_y^4} = \frac{\left(2 - 2\cos k_y b\right)}{k_y^2} \tag{4.111}$$

If $Q(k_y)$ is evaluated at $k_y = k_{ym} = 0$, (4.111) produces

$$Q(k_y)\big|_{k_y=0} = \frac{0}{0} \tag{4.112}$$

which is an indeterminate form. Using L'Hopitale's Rule, the first derivative is also indeterminate, so evaluation progresses to the second derivative, which produces

$$\begin{aligned} Q(k_y)\big|_{k_y=k_{ym}=k_{yn}=0} &= \left.\frac{\frac{\partial^2}{\partial k_y^2}\left(2 - 2\cos k_y b\right)}{\frac{\partial^2}{\partial k_y^2}\left(k_y^2\right)}\right|_{k_y=0} \\ &= b^2. \end{aligned} \tag{4.113}$$

Consider the case where $k_{ym} \neq 0$ and $k_{yn} = 0$. Evaluating (4.110) when $k_y = k_{yn}$ produces

$$Q(k_y)\big|_{k_y=k_{yn}=0} = \left.\frac{\left(2 - 2\cos k_y b\right)}{\left(k_y^2 - k_{ym}^2\right)}\right|_{k_y=0} = 0. \tag{4.114}$$

Evaluating (4.110) when $k_{yn} \neq 0$ and $k_y = k_{ym} = 0$ produces a similar result,

$$Q(k_y)\big|_{k_y=k_{ym}=0} = 0. \tag{4.115}$$

Each other possible case may also be examined in a similar manner. The summary of the possible values of $Q(k_y)$ at the singular points is shown in Table 4.1.

k_{ym}	k_{yn}		$Q(k_{ym})$	$Q(k_{yn})$
$=0$	$=0$	$k_{ym} = k_{yn}$	b^2	b^2
$\neq 0$	$=0$	$k_{ym} \neq k_{yn}$	0	0
$=0$	$\neq 0$	$k_{ym} \neq k_{yn}$	0	0
$\neq 0$	$\neq 0$	$k_{ym} = k_{yn}$	$b^2/4$	$b^2/4$
$\neq 0$	$\neq 0$	$k_{ym} \neq k_{yn}$	0	0

Table 4.1. Value of the function $Q(k_y)$ at the singular points

Thus, in the evaluation of the functions $\widetilde{F}_3(k_x, k_y)$ and $\widetilde{F}_4(k_x, k_y)$ at the singular points, the following expressions describe the result:

$$\widetilde{F}_4(k_x, k_{ym}) = \begin{cases} b^2 \left.\dfrac{\widetilde{G}_T(k_x,k_y)}{p_1 T_m}\right|_{k_y=k_{ym}} & k_{ym} = k_{yn} = 0 \\ \dfrac{b^2}{4} \left.\dfrac{\widetilde{G}_T(k_x,k_y)}{p_1 T_m}\right|_{k_y=k_{ym}} & k_{ym} = k_{yn} \neq 0 \\ 0 & k_{ym} \neq k_{yn} \end{cases} \tag{4.116}$$

$$\widetilde{F}_3(k_x, k_{yn}) = \begin{cases} b^2 \left(\dfrac{\epsilon_2\mu_2}{\epsilon_1\mu_1} - 1\right) \left.\dfrac{\sinh(2p_2(d_1-h))}{2p_1 T_m T_e}\right|_{k_y=k_{yn}} & k_{ym} = k_{yn} = 0 \\ \dfrac{b^2}{4} \left(\dfrac{\epsilon_2\mu_2}{\epsilon_1\mu_1} - 1\right) \left.\dfrac{\sinh(2p_2(d_1-h))}{2p_1 T_m T_e}\right|_{k_y=k_{yn}} & k_{ym} = k_{yn} \neq 0 \\ 0 & k_{ym} \neq k_{yn} \end{cases} \tag{4.117}$$

Taking the results from (4.117), (4.116), and (4.109), the function $\widetilde{F}_1(k_x, k_y)$ may be evaluated at the removable singular points, $k_y = k_{ym}$ and $k_y = k_{yn}$. Thus, the integration in the variable k_y may be carried out without the danger of the integrand being undefined at the removable singular points.

4.5.2 Integration in k_x

The next issue to consider is numerical integration in the variable k_x. Notice that all four coupling cases involve the same functions, $\widetilde{G}_2(k_x)$ and $\widetilde{G}_1(k_x)$, when calculating the matrix elements. To remind the reader, these functions are

$$\widetilde{G}_2(k_x) = \frac{\left(e^{-jk_x a} + 1\right)\left(e^{jk_x a} + 1\right)}{\left(k_x^2 - k_{xn}^2\right)\left(k_x^2 - k_{xm}^2\right)} = \frac{2 + 2\cos k_x a}{\left(k_x^2 - k_{xn}^2\right)\left(k_x^2 - k_{xm}^2\right)} \tag{4.118}$$

$$\widetilde{G}_1(k_x) = k_x^2 \widetilde{G}_2(k_x) = \frac{k_x^2\left(2 + 2\cos k_x a\right)}{\left(k_x^2 - k_{xn}^2\right)\left(k_x^2 - k_{xm}^2\right)}. \tag{4.119}$$

In these cases

$$k_{xm} = \frac{u_m \pi}{a}, \qquad k_{xn} = \frac{u_n \pi}{a},$$

where u_m and u_n are odd integers. The investigation of the singularities along the k_x axis is similar to those for the k_y axis, and the conclusion is that the singularities at $k_x = k_{xm}$ and $k_x = k_{xn}$ are removable. Note that the evaluation of (4.118) and (4.119) at $k_x = 0$ will not take place, since u_m and u_n are odd.

The evaluation of (4.118) and (4.119) at the removable singular points is analyzed in a similar manner to the examination of the functions $P(k_y)$ and $Q(k_y)$. The summary of the evaluation of the functions at the singular points is

$$\widetilde{G}_1(k_x) = \begin{cases} \frac{a^2}{4} & k_x = k_{xm} = k_{xn} \\ 0 & k_x = k_{xm} \qquad k_{xm} \neq k_{xn} \\ 0 & k_x = k_{xn} \qquad k_{xm} \neq k_{xn} \end{cases} \tag{4.120}$$

$$\widetilde{G}_2(k_x) = \begin{cases} \frac{a^2}{4k_{xm}^2} & k_x = k_{xm} = k_{xn} \\ 0 & k_x = k_{xm} \qquad k_{xm} \neq k_{xn} \\ 0 & k_x = k_{xn} \qquad k_{xm} \neq k_{xn} \end{cases} \tag{4.121}$$

4.6 Numerical Integration Implementation Notes

This section is a brief discussion of the numerical integration implementation used to calculate the matrix elements and solve the matrix equation. Several different numerical integration techniques are available in prepared and available routines to carry out this integration [50]. The error analysis described in Chapter 6 requires an accurate calculation of the theoretical reflection coefficients, and thus it is important to calculate each of the matrix elements as accurately as possible while managing computer resources.

The evaluation of each integral in the four coupling cases can be reduced to an integration from zero to ∞ because each function that is integrated is even along the real axis. Also note that the integrands along the real k_x and k_y axes are complex-valued functions. To accurately characterize the integration of the complex functions, the real and imaginary parts of each function are integrated separately using a real-valued integration routine.

In this study, the integration routines from the Quadpack set of FORTRAN subroutines were implemented [51]. A finite integration routine was employed where the upper limit of integration was chosen sufficiently beyond the point where the integrand begins to decay. The integration routine, dqag.f, is a general adaptive Gaussian quadrature routine which employs Gauss-Kronrad integration. The stopping criteria for the integration routine was chosed to be when a relative error of 10^{-10} is achieved.

For the calculation of the matrix elements, the integrals required to calculate A_{mn} were integrated in the k_y domain from 0 to 30,000 m^{-1}, and the k_x domain was integrated over the range from 0 to 10,000 m^{-1}. Increasing the range of integration

further only made a change in the sixth significant digit while greatly increasing the computational time. These values are used throughout the simulations and during extraction of the material parameters using the two layer and two thickness methods.

The computation of each element of the matrix A is calculated using the numerical integration considerations detailed in this chapter. Accurate computation of these elements is necessary to achieve an accurate solution in the calculation of the theoretical reflection coefficient. An additional factor that affects the accuracy of the reflection coefficient calculation is the number of modes used in the solution, which also determines the size of the matrix A. This topic is considered in the next chapter.

CHAPTER 5

MODAL ANALYSIS OF THE TWO LAYER AND TWO THICKNESS METHODS OF MATERIAL PARAMETER EXTRACTION

5.1 Introduction

A correct estimation of the theoretical reflection coefficient, S_{11}^{thy}, is critical to the accurate characterization of an unknown material. If the reflection coefficient is not estimated correctly, the extracted parameters will be biased. Accurate numerical integration, as discussed in Chapter 4, is one key element in the calculation of the matrix elements in the MFIE matrix equation. Another important part of the extraction process is determining the number of waveguide modes that should be used in the matrix solution to the MFIE. This chapter examines the effect of the number of the waveguide modes, N, on the calculation of S_{11}^{thy}. The number of modes, in turn affects the resultant extracted material parameters. The extracted material parameters are examined when different values of N are used in the solution for both the two layer method and the two thickness method.

5.2 How many modes are necessary?

Recall from the initial problem formulation in (2.4) that it is assumed that the reflected field in the waveguide can be approximated by truncating the field description to N modes, where the total transverse fields in the waveguide are given by

$$\vec{E}_t^{wg}(\vec{r}) = a_1^i \vec{e}_1^{wg}(\vec{\rho}) e^{jk_{z1}^{wg} z} + \sum_{q=1}^{N} a_q^s \vec{e}_q^{wg}(\vec{\rho}) e^{-jk_{zq}^{wg} z} \tag{5.1}$$

$$\vec{H}_t^{wg}(\vec{r}) = -a_1^i \vec{h}_1^{wg}(\vec{\rho}) e^{jk_{z1}^{wg} z} + \sum_{q=1}^{N} a_q^s \vec{h}_q^{wg}(\vec{\rho}) e^{-jk_{zq}^{wg} z}. \tag{5.2}$$

An important quantity in the material parameter extraction is the theoretical reflection coefficient, $S_{11}^{thy} = a_1^s/a_1^i$. In the MoM solution to the MFIE, the value of the coefficient a_1^s is affected by the number of modes used in the solution. It is therefore desirable to examine the effect of different values of N on the calculation of S_{11}^{thy}. An ideal comparison for these computed values of S_{11}^{thy} would be the true theoretical value, which is the value of S_{11}^{thy} computed using an infinite number of modes. However, calculating the contribution of an infinite number of modes to the reflection coefficient is computationally impossible. It would be desirable to have some scheme or algorithm which could estimate the contribution of an infinite number of modes to S_{11}^{thy}. Fewer modes could be used with a reasonable computational cost to achieve a high accuracy. Yet even a finite number of modes can be computationally expensive if N is large.

Recall that in the formulation of the MoM solution to the MFIE in (2.32), the testing function that is used to develop the matrix equation uses N modes. The matrix A is an $N \times N$ matrix, with N^2 matrix elements which must be calculated. Also recall from Chapter 4 that two-dimensional integration is required to fill each matrix element. In simulations which implement the MoM solution, the time required to invert the matrix A using an iterative solver is minimal in comparison to the cost of filling the matrix. The computational cost for obtaining S_{11}^{thy} is on the order of $N^2 \times integration\,time$, so it is desirable to use a minimal number of modes which would still allow for an accurate estimation of S_{11}^{thy}.

The first step in obtaining values for S_{11}^{thy} is to generate theoretical reflection coefficients from a given set of material parameters using different values of N. Once this has been examined, the effect of the number of modes used in the extraction is considered.

5.3 Generation of S_{11}^{thy} for a single conductor-backed layer.

As noted in section 1.2.3.3, previous research has usually focused on the first few modes when performing material parameter extraction. Bois [37] did examine the effect of including the first 20 modes with a flanged waveguide probe radiating into a dielectric half-space. He also observed that the modes with the highest amplitude coefficient for the scattered fields in the waveguide after the dominant mode were the TE_{30}, TE_{12}, and TM_{12} modes. Note that the Bois study was not conducted on a conductor-backed material. In this dissertation, the effect of even higher order modes with a conductor-backed material is considered.

A set of typical constitutive parameter values for Eccosorb FGM125 is shown in Table 5.1. These values were obtained using the waveguide T/R method at the Air Force Institute of Technology on a sample of Eccosorb FGM125. These material parameters were used to generate the matrix elements of A using the first 150 modes. Using these matrix elements, estimates of S_{11}^{thy} were calculated for varying values of N in the frequency range from 8.2 - 12.4 GHz. An example of the magnitude and phase plotted against the number of modes, N, at 8.2 GHz is shown in Figure 5.1.

Several interesting features are found in Figure 5.1. First, note there are significant changes in both magnitude and phase that occur when modes 4, 15, 31, 57, 87, and 126 are included in the solution matrix. The first 31 modes of the WR90 X-band waveguide, listed in order of ascending cutoff frequency, are found in Table D.1. From this table, note that these modes where significant changes occur correspond to the TM_{1v} modes, where v is even. With each inclusion of the $TM_{1\,even}$ modes, the magnitude decreases, while the phase increases. Also note that the inclusion of most of the other modes has little effect on the magnitude or phase of the reflection coefficient. Upon examination of the possible effect of other modes, only the coupling effect from first two modes, TE_{10} and TE_{30}, and the TE_{1v} and TM_{1v}modes, where

Frequency (GHz)	ϵ_r'	ϵ_r''	μ_r'	μ_r''
8.20	7.258212	0.056008	0.60005	0.76102
8.41	7.277899	0.033793	0.592839	0.721439
8.62	7.298132	0.043095	0.59103	0.686365
8.83	7.311252	0.047493	0.585885	0.654479
9.04	7.304077	0.062643	0.588087	0.625757
9.25	7.308915	0.064257	0.585048	0.596142
9.46	7.317255	0.062025	0.583126	0.568452
9.67	7.304012	0.064737	0.579807	0.541229
9.88	7.309266	0.052926	0.577589	0.512701
10.09	7.319669	0.046408	0.575582	0.484231
10.30	7.330578	0.026938	0.573309	0.454279
10.51	7.334547	0.03407	0.577179	0.430992
10.72	7.351786	0.046136	0.580009	0.405106
10.93	7.354822	0.063693	0.582448	0.37916
11.14	7.348328	0.055837	0.584002	0.356647
11.35	7.337716	0.054682	0.585821	0.332551
11.56	7.319363	0.071406	0.591993	0.306094
11.77	7.336418	0.040073	0.592959	0.283032
11.98	7.328378	0.028185	0.600527	0.259355
12.19	7.279717	0.024518	0.611457	0.23548
12.40	7.374114	0.024937	0.615432	0.212225

Table 5.1. Material parameters for Eccossorb FGM125, $\epsilon = \epsilon_0(\epsilon_r' - j\epsilon_r'')$ and $\mu = \mu_0(\mu_r' - j\mu_r'')$. These data were obtained using the waveguide T/R method. Data provided by Captain Milo Hyde IV from the Air Force Institute of Technology, Wright-Patterson AFB, Dayton, OH.

v =even, has any significant effect on the magnitude and phase of the reflection coefficient.

Another observation from Figure 5.1 is that when the first 150 modes are included in the solution, the value for $|S_{11}^{thy}|$ still has not converged. Consider Figure 5.2, which shows a plot of $|S_{11}^{thy}|$ vs $1/N$ to provide another perspective. It is desirable to estimate the effect of including an infinite number of modes in the solution without actually using a large number of modes. By plotting the magnitude of the reflection coefficient vs. $1/N$, the graph is inspected for a possible trend as $1/N \rightarrow 0$. If such a trend exists, the values for the magnitude, and subsequently the phase, could be extrapolated to estimate their values when $1/N = 0$, corresponding to $N = \infty$. The result would be a much better estimate of S_{11}^{thy} due to an infinite number of modes than only using the first 4, 10 or even 31 modes.

However, extrapolation of this set of data to $1/N = 0$ is not a straightforward task. Several different extrapolation methods are available, including linear extrapolation, polynomial extrapolation, cubic spline extrapolation, least squares extrapolation, etc. To accurately extrapolate the data, it is more helpful to know the general behavior of the function being extrapolated [50]. However, from Figure 5.2 it is not clear whether the behavior of the data is quadratic, linear, etc. The discrete nature of the change in magnitude at the $TM_{1\,even}$ modes makes accurate extrapolation difficult.

As noted earlier, the primary contribution after the first four modes comes from the $TE_{1\,even}$ and $TM_{1\,even}$ modes. The remaining modes do not contribute a significant amount to either the phase or magnitude of the reflection coefficient. To reduce computational time, only the modes which contribute significantly to the reflection coefficient are included in the matrix solution, while the remaining modes are discarded. For example, to calculate S_{11}^{thy} using $N = 126$ would require $N^2 = 15,876$ elements in the matrix if all the modes were included. However, picking just the 14 modes which contribute to the solution up to the 126th mode, which is the $TM_{1\,12}$

mode, requires a 14×14 matrix with 196 elements. By omitting the non-contributing higher order modes, the number of elements needed to fill the matrix A has been reduced by a factor of 81.

By using this method of picking the contributing modes, the calculation of the reflection coefficient including higher modes can be undertaken with less computational time. In a manner similar to Figure 5.2, the magnitude and phase of the reflection coefficient were plotted vs $1/N$. Unfortunately, this also provided no clear trend for extrapolating the data.

As an alternative data plotting method, consider Figure 5.3. The major contributing higher order modes are the $TM_{1\,v}$ modes, where v is even. When the values of $|S_{11}^{thy}|$ at each of these $TM_{1\,v}$ modes are displayed vs $1/v$, where v is the second index of the mode, it is seen that there is a linear trend in the data when v is large enough. A similar linear trend is observed in the plot of the phase. As a result of this observation, a linear extrapolation scheme was used to extrapolate from the last two points calculated to the point $1/v = 0$. This extrapolation scheme is analogous to the inclusion of an infinite number of modes in the solution. Thus, an estimate of the theoretical reflection coefficient due to the contribution of an infinite number of modes is obtained. This linear trend was observed across the frequency band of interest, 8.2 - 12.4 GHz, for this case of one 0.125" thick layer of Eccosorb FGM125. Examples of the linear trend at 10.09 GHz, the middle of the frequency band, and at the upper end, 12.4 GHz, are shown in Figure 5.4 - Figure 5.5.

Another feature is found when considering the linear interpolation scheme. Consider Figure 5.3 again. If the linear interpolation is applied to points for lesser values of v, or points further to the right, note that the result is also quite close to the extrapolation that resulted from the two points furthest to the left. Thus, a smaller number for v can be used with the extrapolation scheme to arrive at an estimate for the reflection coefficient that is close to that obtained using a larger value for v.

Simulations were also undertaken to determine if this extrapolation scheme could be employed for other thicknesses of this material. As an example, the reflection coefficient for a sample of Eccosorb FGM125, 0.250" thick, was calculated for various values of N. As shown in Figure 5.6, the same modes contribute to the reflection coefficient for this thickness as those which contributed to the reflection coefficient for the 0.125" thick sample. Using just the $TE_{1\,0}$, $TE_{3\,0}$, $TE_{1\,even}$, and $TM_{1\,even}$ modes, a plot of the reflection coefficient vs $1/v$ is displayed in Figure 5.7 at midband, 10.09 GHz. Notice that the trend is similar to the linear trend found for the layer that was 0.125" thick in Figure 5.3. This trend was consistent across the frequency band for this thickness. As a result of these observations for different thicknesses of the same material, this extrapolation scheme may be used in the two thickness method.

5.4 Generation of S_{11}^{thy} for a two-layered conductor-backed material stack

Since this extrapolation method works for different thicknesses of FGM125, it is possible that it may also be employed successfully when calculating the theoretical reflection coefficient for one material placed on top of a second conductor-backed material. Such an extrapolation scheme could be useful in the two layer method.

Consider Figure 5.8, which plots the magnitude and phase of the theoretical reflection coefficient for a layer of Plexiglass on top of one layer of Eccosorb FGM125 as a function of the number of modes used in the solution. Note that there are some similar features to the plot shown in Figure 5.2 for one layer of Eccosorb FGM125. The $TE_{1\,even}$ and $TM_{1\,even}$ modes again make a major contribution to both the magnitude and phase of the reflection coefficient. In addition, the $TE_{odd\,0}$ modes also make a contribution to the solution. This is shown more clearly in Figure 5.9, where $|S_{11}^{thy}|$ is plotted vs $1/N$. The contribution of the $TE_{odd\,0}$ modes are smaller than the large discontinuities due to the $TM_{1\,even}$ modes, but they still make a noticable contribution. As a result, these modes are also included as modes which contribute

significantly to the solution when generating the matrix elements.

For the two layer material configuration, it is desirable to employ an extrapolation scheme to estimate the theoretical reflection coefficient due to an infinite number of modes. A similar approach is taken as that employed for a single layer of material. The reflection coefficient is computed by including the modes up to the $TM_{1\,v}$ mode that contribute to the solution. These values are then plotted vs. $1/v$, and this plot is shown in Figure 5.10.

Although the plot is shown only including the contributions up to the $TM_{1\,16}$ mode, note that there is a linear trend in the data. Figure 5.11 also shows a similar plot for the same material stack at 10.09 GHz. At this frequency, and across the X-band frequency range, the same linear trend in the magnitude and phase is observed when plotted vs. $1/v$.

Figure 5.12 - Figure 5.13 show similar relationships for plots of the magnitude and phase with respect to $1/v$ using Nylon and Eccosorb FGM40 as the top layers, respectively. Note the linear trend as the data are plotted vs the reciprocal of the mode index, v. These observations suggest the potential to use this extrapolation scheme for two layers of material.

5.5 Extrapolated values of S_{11}^{thy} at X-band

Using the extrapolation scheme described in the last section, an estimate of the reflection coefficient due to an infinite number of modes in the solution is calculated and displayed in Figure 5.14 - Figure 5.19 for various configurations of materials. These materials were chosen for simulation because they correspond to available materials in the Michigan State University Electromagnetics Research group. Simulations were performed with the potential for later comparison with actual measurements of these materials. These plots show the magnitude and phase calculated at 21 frequencies across the X-band frequency range.

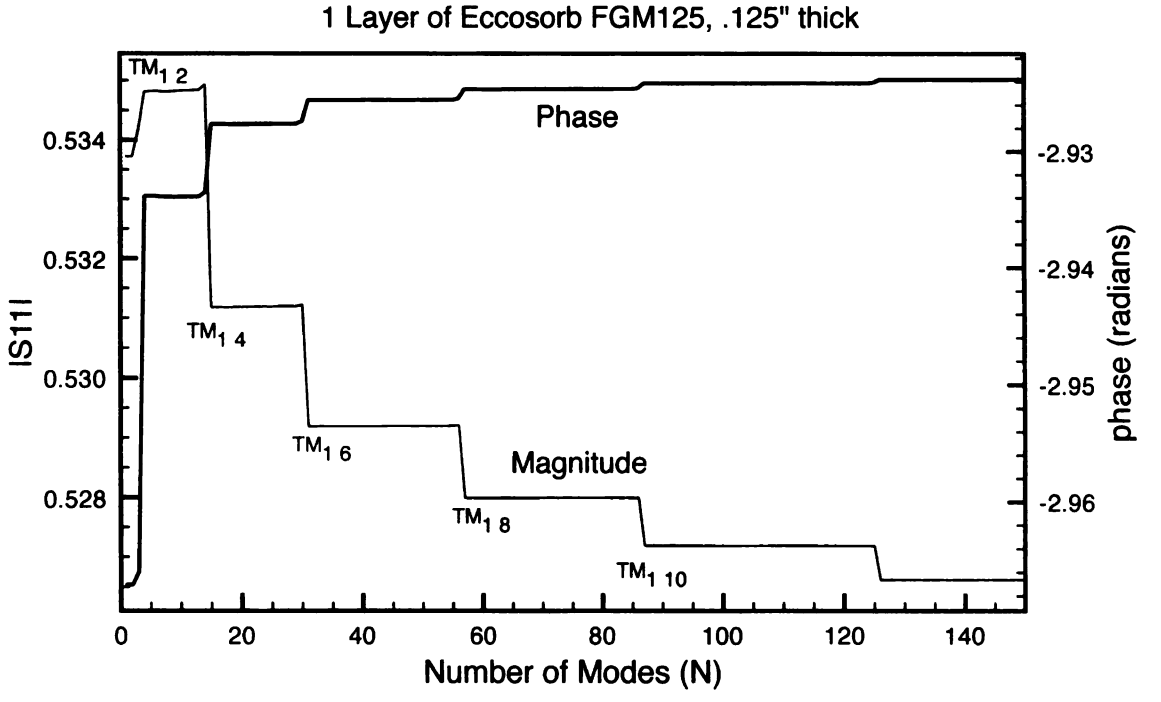


Figure 5.1. Magnitude and phase of the reflection coefficient for 1 layer of Eccosorb FGM125, 0.125" thick, at 8.2 GHz, using different numbers of modes in the solution.

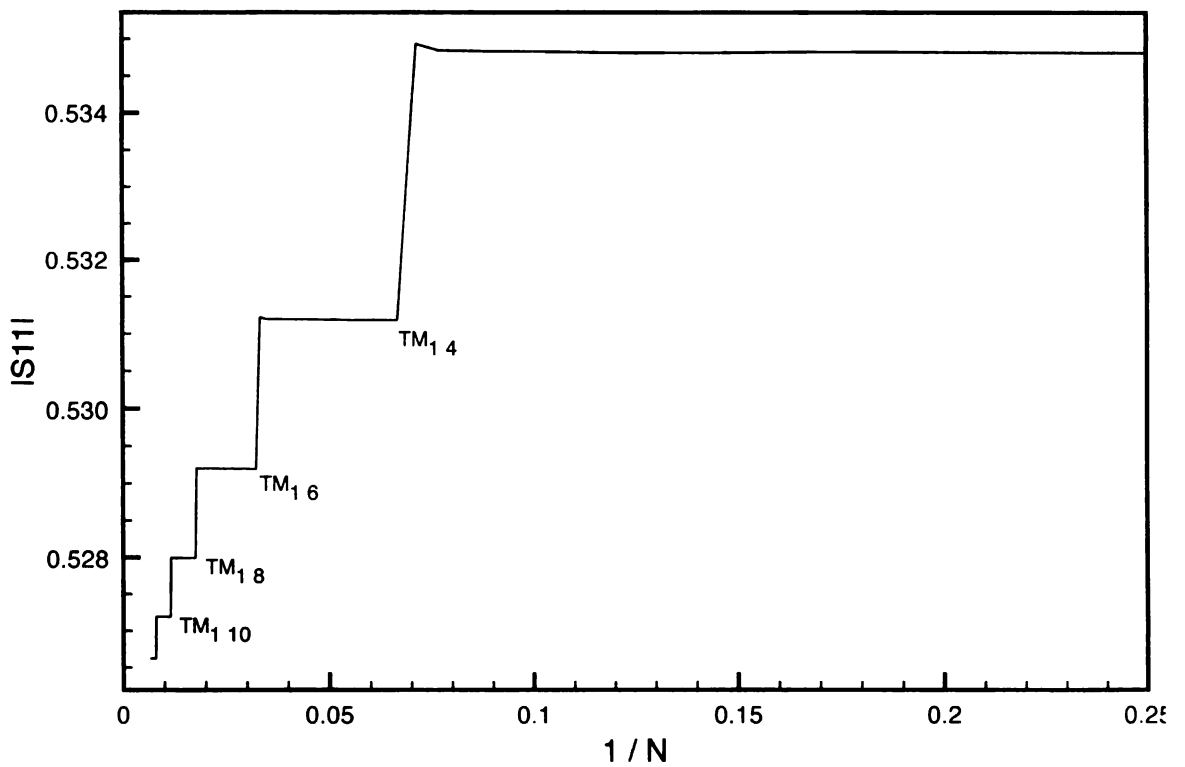


Figure 5.2. Magnitude of S_{11}^{thy} for 1 layer of Eccosorb FGM125, 0.125" thick, at 8.2 GHz.

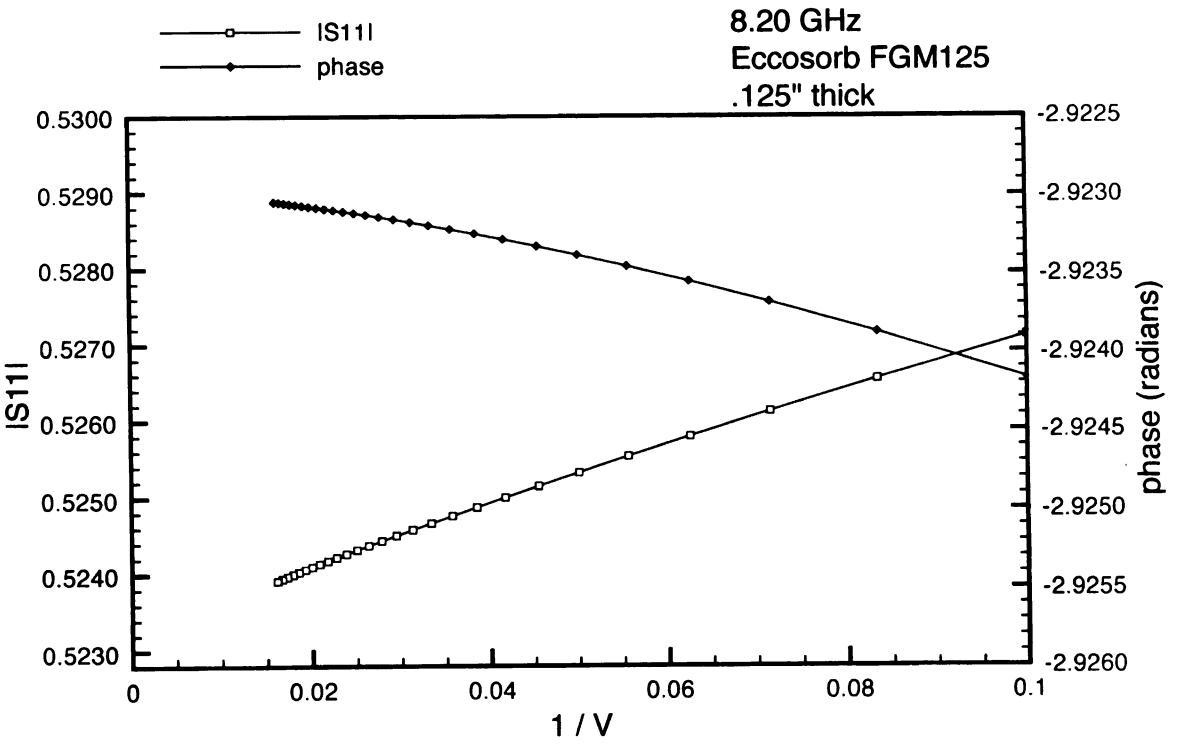


Figure 5.3. Magnitude and phase of the reflection coefficient for 1 layer of Eccosorb FGM125, 0.125" thick, at 8.2 GHz, using only modes that contribute significantly to the solution. The reflection coefficient is computed by including the modes up to the $TM_{1\,v}$ mode. These values are plotted vs. $1/v$.

5.6 Modal analysis of extracted parameters

It is apparent from sections 5.3 and 5.4 that the number of modes included in the solution affects the calculation of S_{11}^{thy}. When this calculation of S_{11}^{thy} is employed in the extraction algorithm, it is desirable to examine how the error in the estimation of S_{11}^{thy} affects the extracted parameters. This section is an investigation of the effect of the number of modes used to calculate S_{11}^{thy} on the material parameters that result from the extraction algorithm. The performance of the two layer method extraction and two thickness method extraction are compared and contrasted on a common set

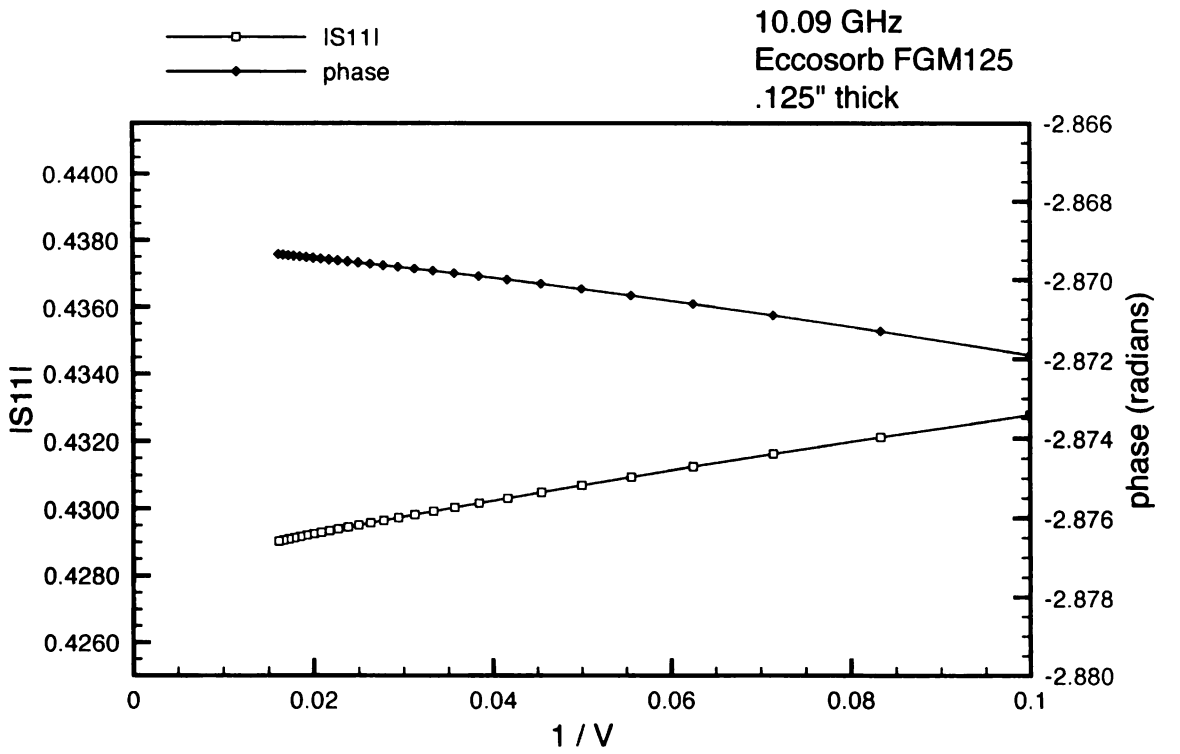


Figure 5.4. Magnitude and phase of the reflection coefficient for 1 layer of Eccosorb FGM125, 0.125" thick, at 10.09 GHz, using only the modes that contribute significantly to the solution. The reflection coefficient is computed by including the modes up to the $TM_{1\,v}$ mode. These values are plotted vs. $1/v$.

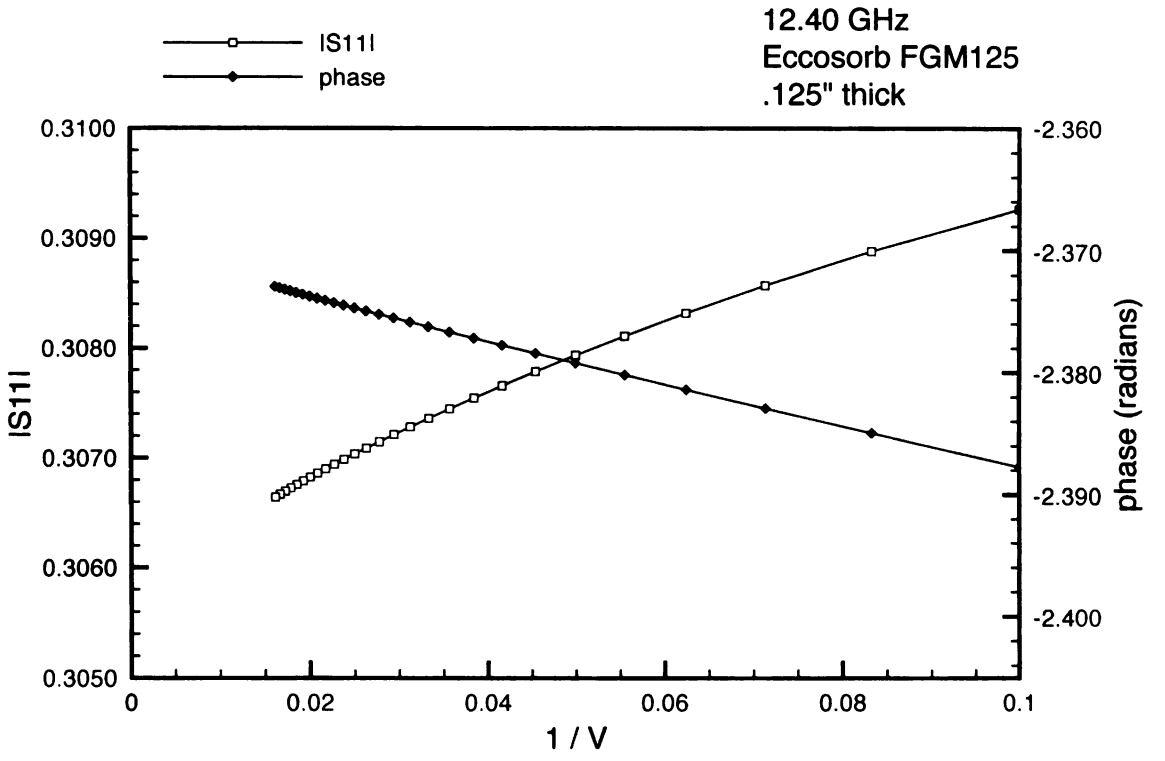


Figure 5.5. Magnitude and phase of the reflection coefficient for 1 layer of Eccosorb FGM125, 0.125" thick, at 12.40 GHz, using only the modes that contribute significantly to the solution. The reflection coefficient is computed by including the modes up to the $TM_{1\,v}$ mode. These values are plotted vs. $1/v$.

IS111

FG
FG

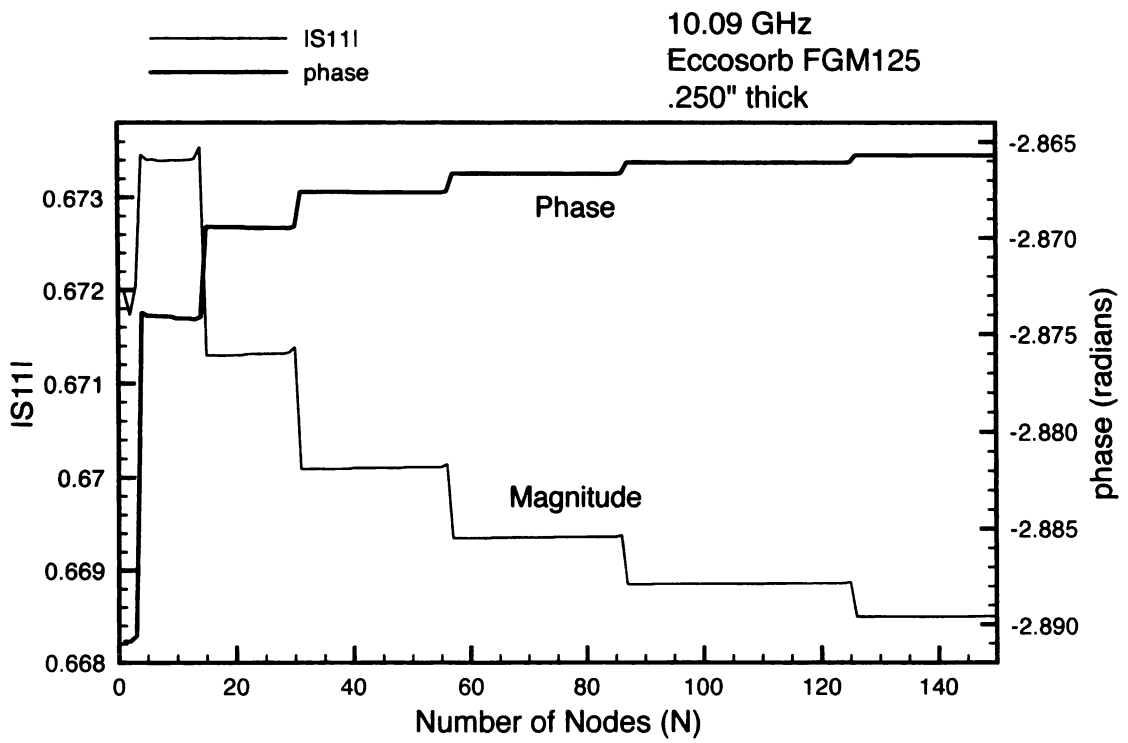


Figure 5.6. Magnitude and phase of the reflection coefficient for 1 layer of Eccosorb FGM125, 0.250" thick, at 10.09 GHz.

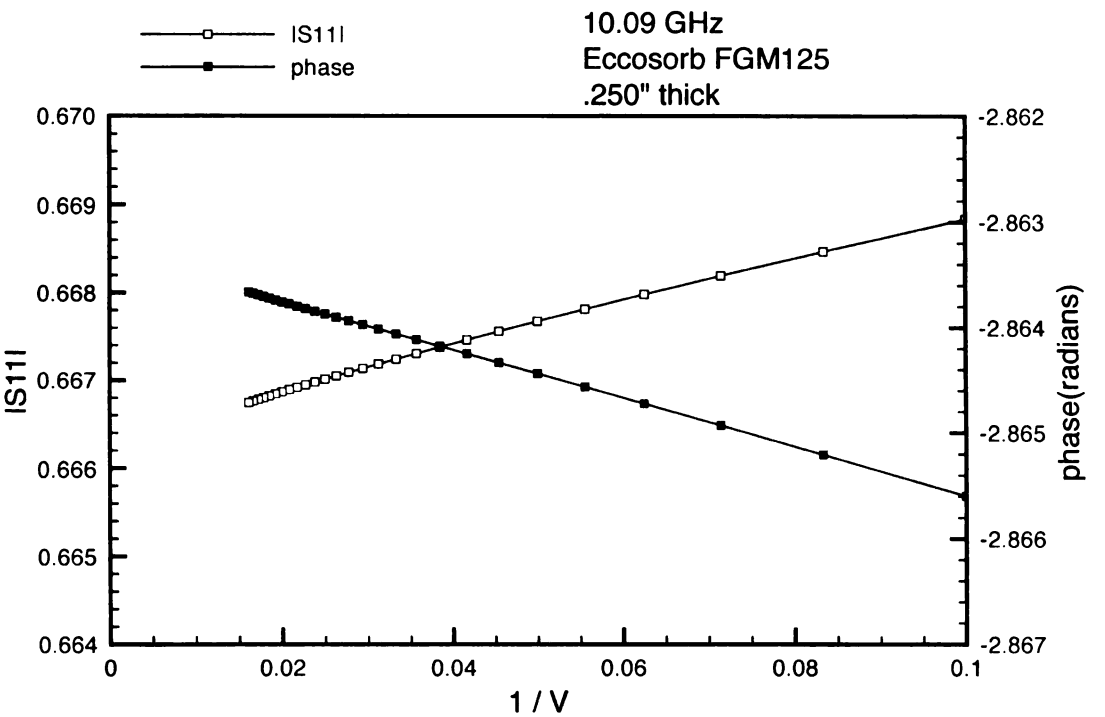


Figure 5.7. Magnitude and phase of the reflection coefficient for 1 layer of Eccosorb FGM125, 0.250" thick, at 10.09 GHz, using only the modes that contribute significantly to the solution. The reflection coefficient is computed by including the modes up to the $TM_{1\,v}$ mode. These values are plotted vs. $1/v$.

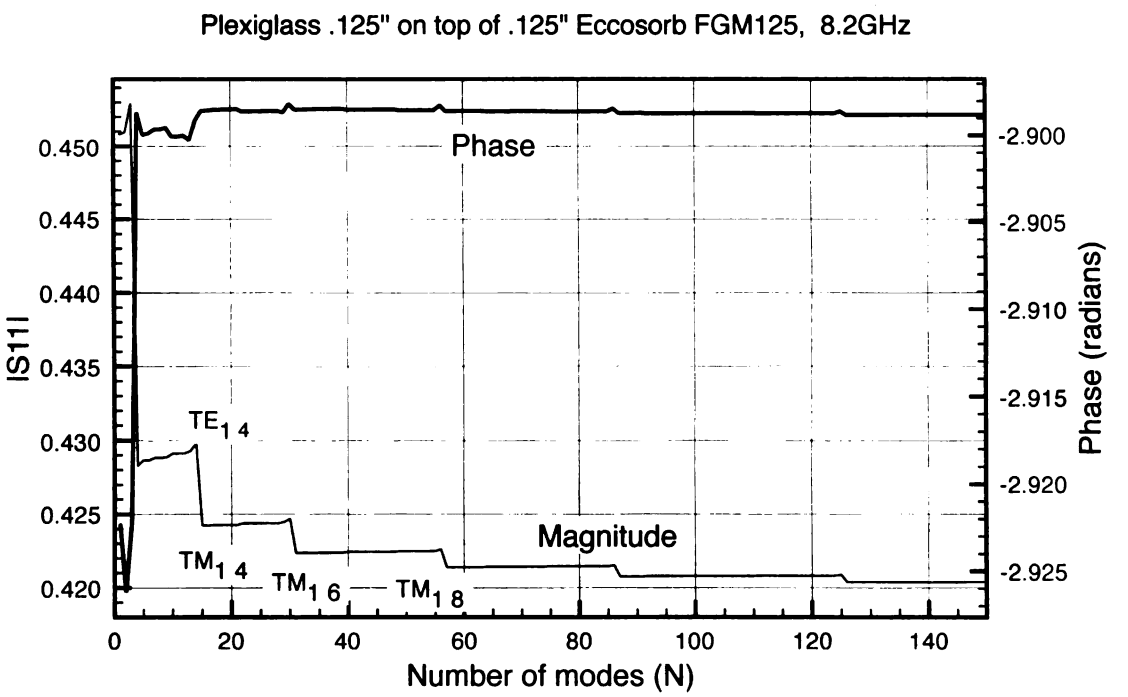


Figure 5.8. Magnitude and phase of the reflection coefficient for 1 layer of Plexiglass 0.125" thick on top of a 0.125" layer of Eccosorb FGM125, at 10.09 GHz.

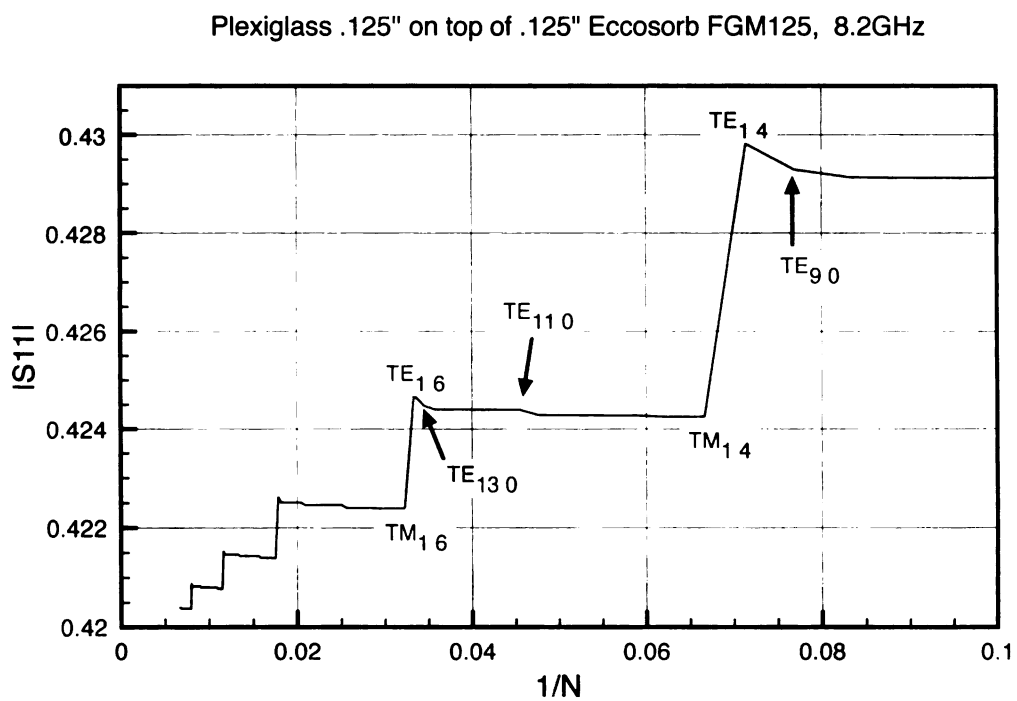


Figure 5.9. Magnitude and phase of the reflection coefficient for 1 layer of Plexiglass 0.125" thick on top of a 0.125" thick layer of Eccosorb FGM125, at 10.09 GHz. Horizontal axis is the reciprocal of the number of modes used in the solution.

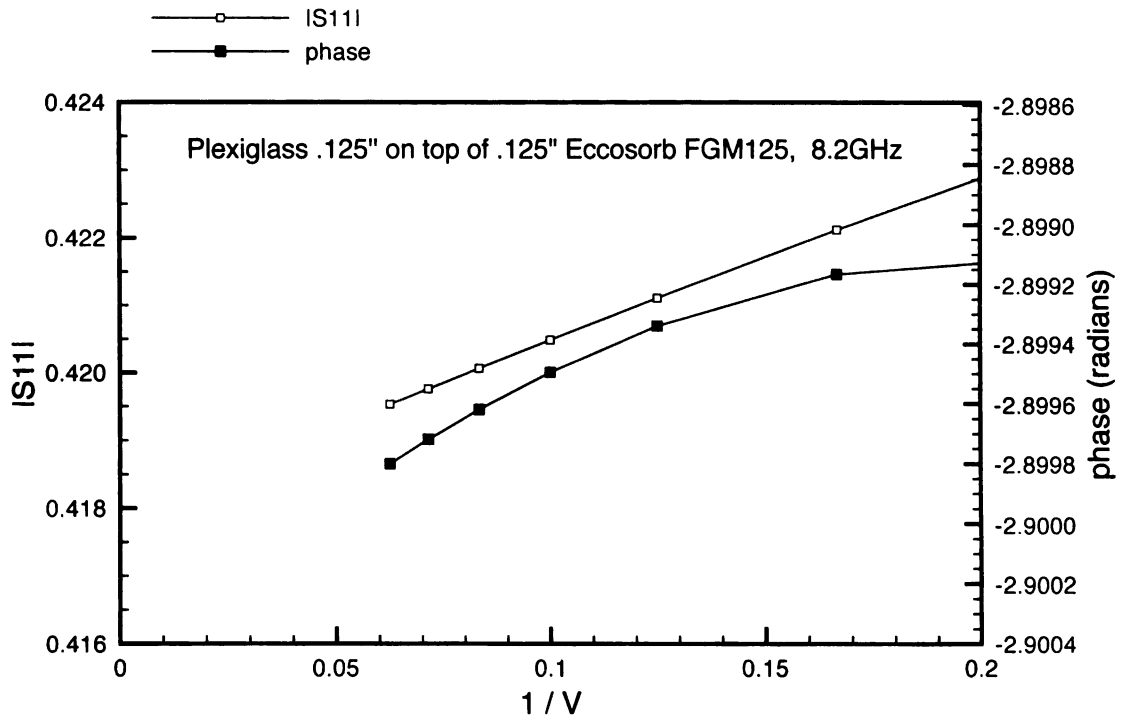


Figure 5.10. Magnitude and phase of the reflection coefficient for 1 layer of Plexiglass, 0.125" thick, on top of Eccosorb FGM125, 0.125" thick, at 8.2 GHz, using only the modes that contribute significantly to the solution. The reflection coefficient is computed by including the modes up to the TM_{1v} mode. These values are plotted vs. $1/v$.

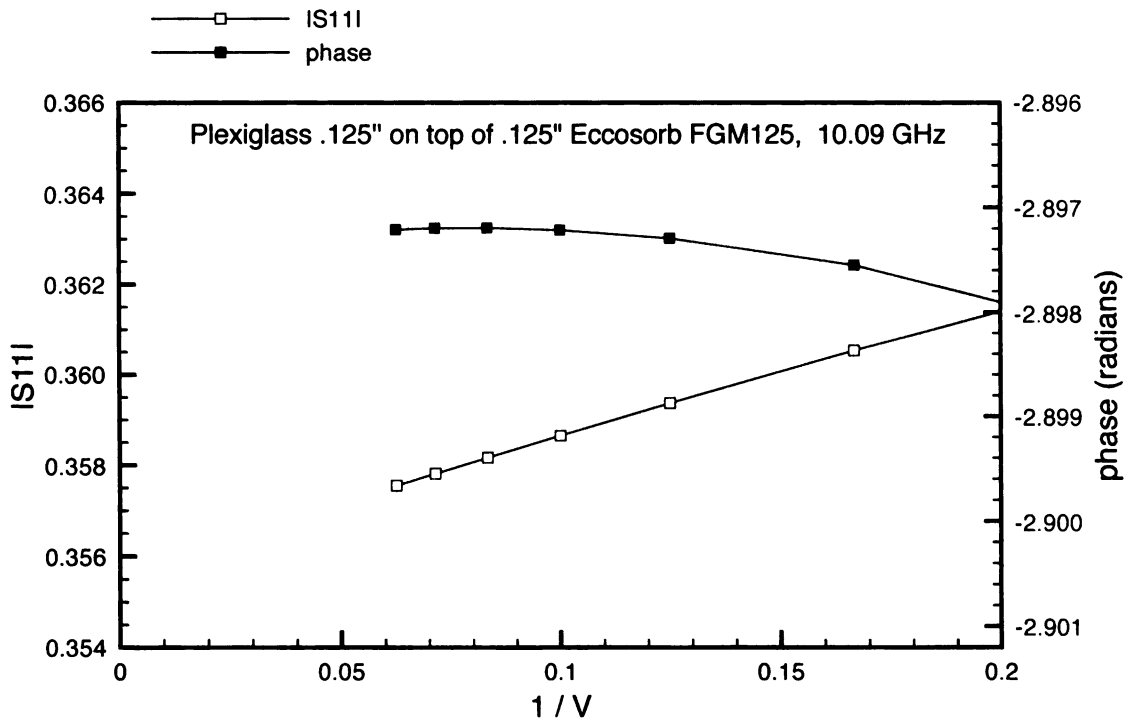


Figure 5.11. Magnitude and phase of the reflection coefficient for 1 layer of Plexiglass, 0.125" thick, on top of Eccosorb FGM125, 0.125" thick, at 10.09 GHz, using only the modes that contribute significantly to the solution. The reflection coefficient is computed by including the modes up to the $TM_{1\,v}$ mode. These values are plotted vs. $1/v$.

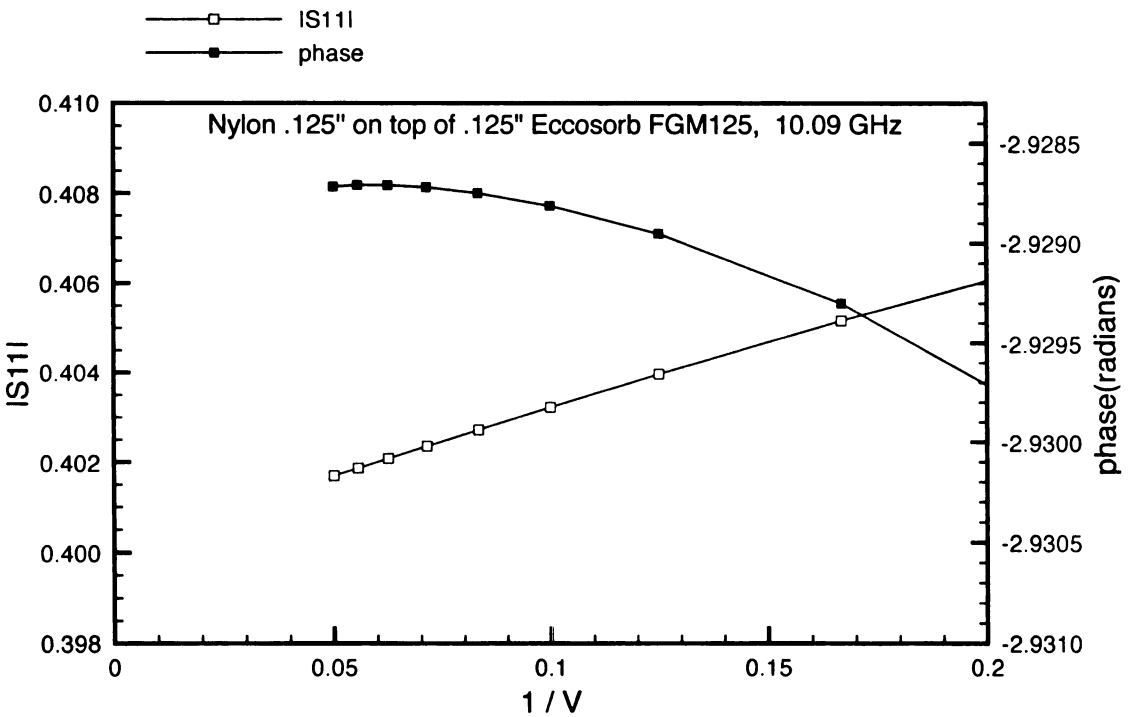


Figure 5.12. Magnitude and phase of the reflection coefficient for 1 layer of Nylon, 0.125" thick, on top of Eccosorb FGM125, 0.125" thick, at 10.09 GHz, using only the modes that contribute significantly to the solution. The reflection coefficient is computed by including the modes up to the $TM_{1\,v}$ mode. These values are plotted vs. $1/v$.

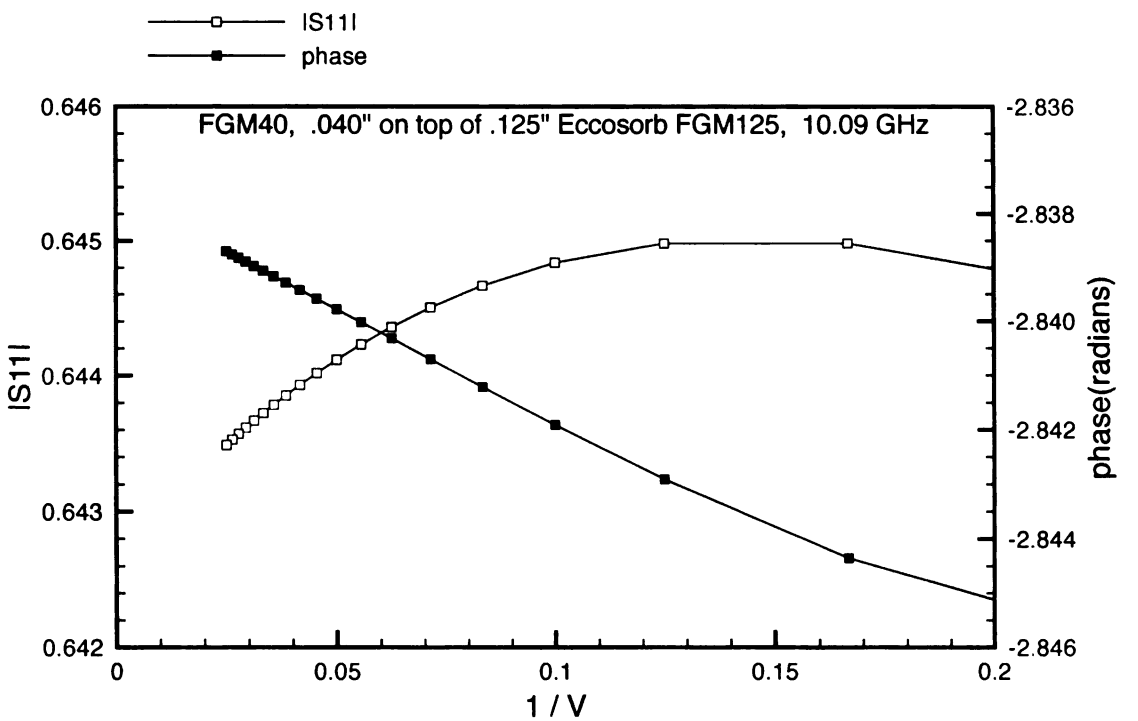


Figure 5.13. Magnitude and phase of the reflection coefficient for 1 layer of FGM40, 0.040" thick, on top of Eccosorb FGM125, 0.125" thick, at 10.09 GHz, using only the modes that contribute significantly to the solution. The reflection coefficient is computed by including the modes up to the $TM_{1\,v}$ mode. These values are plotted vs. $1/v$.

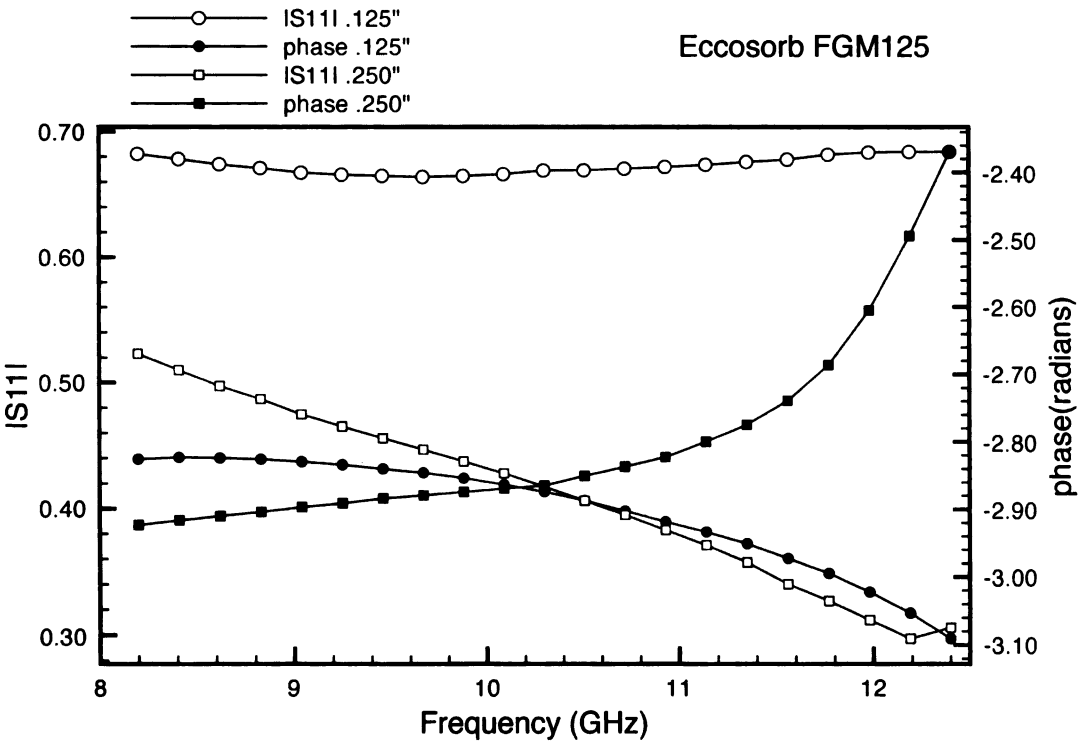


Figure 5.14. Extrapolated values of the magnitude and phase of S_{11}^{thy} for 1 layer of Eccosorb FGM125, 0.125" thick, and Eccosorb FGM125, 0.250" thick, for 8.2-12.4 GHz. Linear extrapolation was performed using $TM_{1\,62}$ and $TM_{1\,60}$ modes.

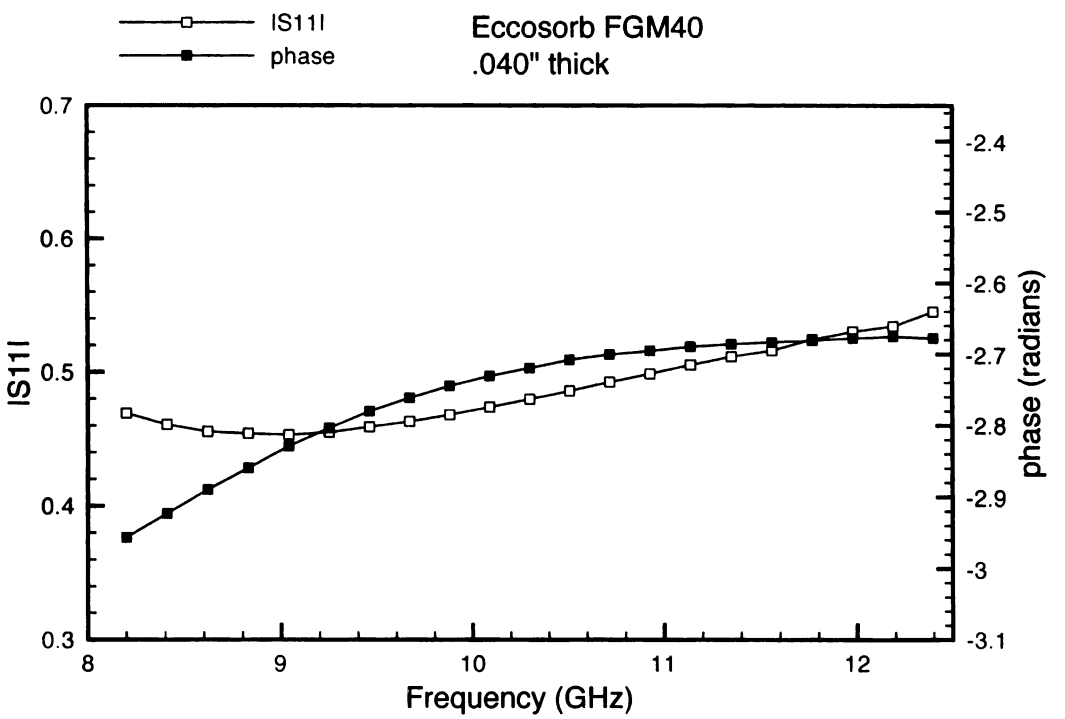


Figure 5.15. Extrapolated values of the magnitude and phase of S_{11}^{thy} for 1 layer of Eccosorb FGM40, 0.040" thick for 8.2-12.4 GHz. Linear extrapolation was performed using $TM_{1\,40}$ and $TM_{1\,38}$ modes.

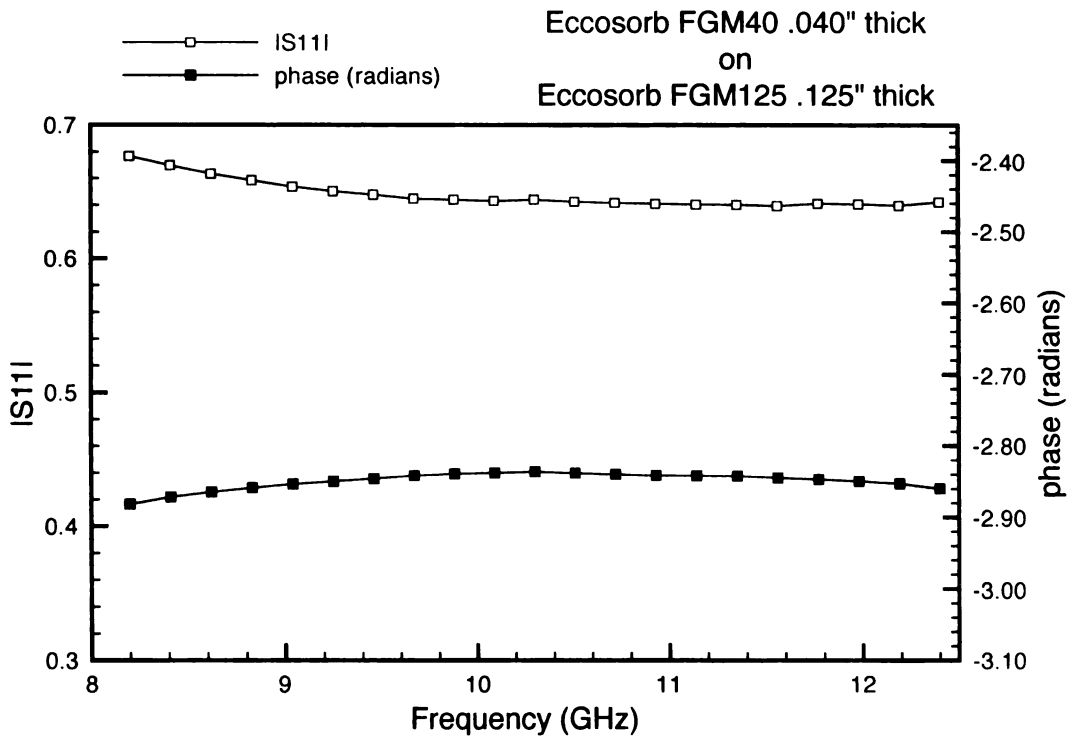


Figure 5.16. Extrapolated values of the magnitude and phase of S_{11}^{thy} for 1 layer of Eccosorb FGM40, 0.040" thick on top of 1 layer of Eccosorb FGM125, 0.125" thick, for 8.2-12.4 GHz. Linear extrapolation was performed using $TM_{1\,40}$ and $TM_{1\,38}$ modes.

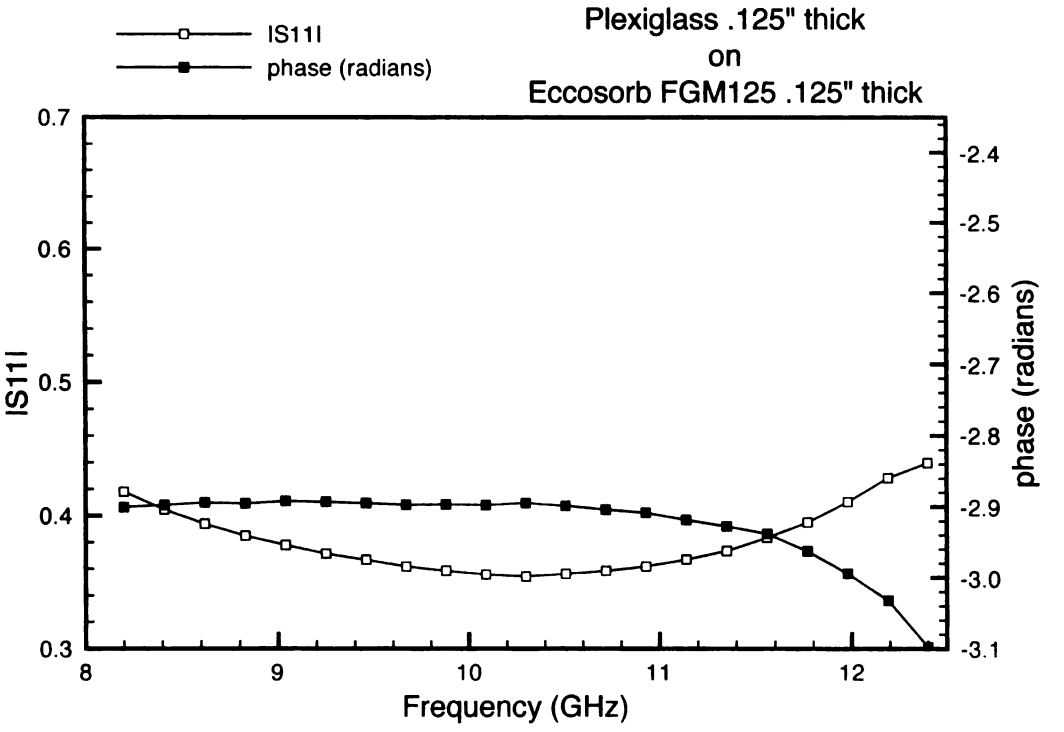


Figure 5.17. Extrapolated values of the magnitude and phase of S_{11}^{thy} for 1 layer of Plexiglass, 0.125" thick on top of 1 layer of Eccosorb FGM125, 0.125" thick, for 8.2-12.4 GHz. Linear extrapolation was performed using $TM_{1\,16}$ and $TM_{1\,14}$ modes.

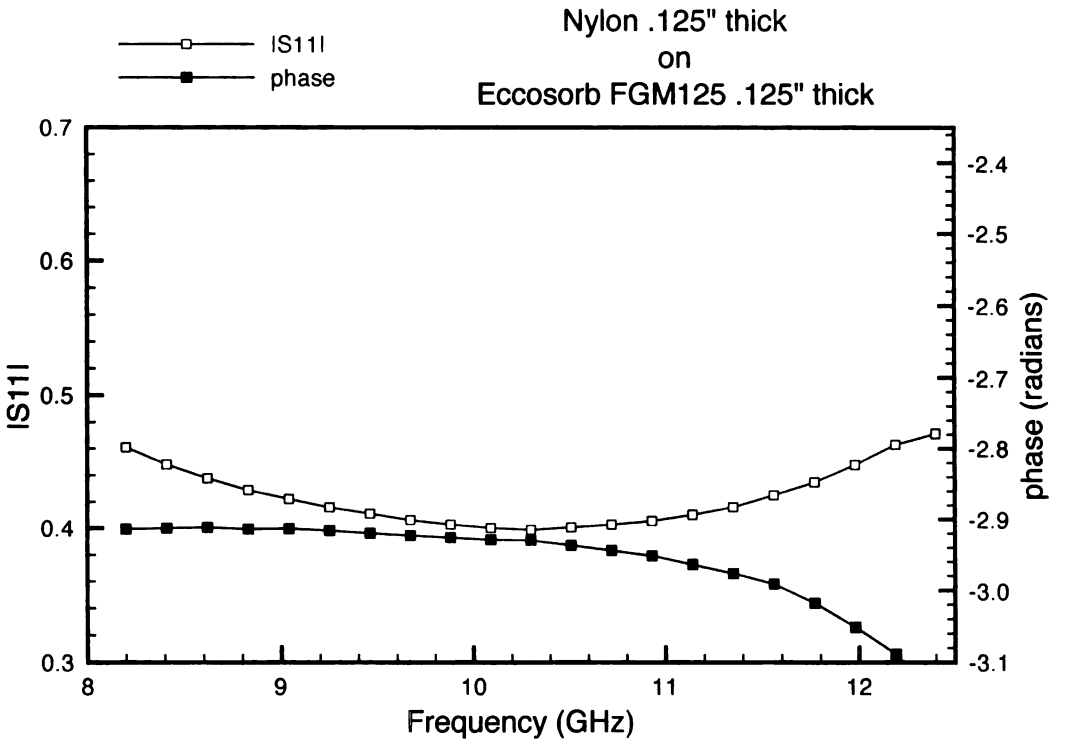


Figure 5.18. Extrapolated values of the magnitude and phase of S_{11}^{thy} for 1 layer of Nylon, 0.125" thick on top of 1 layer of Eccosorb FGM125, 0.125" thick, for 8.2-12.4 GHz. Linear extrapolation was performed using $TM_{1\,16}$ and $TM_{1\,14}$ modes.

of synthetically generated data.

5.6.1 Two Thickness Method Modal Analysis

An estimation of S_{11}^{thy} due to an infinite number of modes was calculated for Eccosorb FGM125 using the nominal values for Eccosorb FGM125 found in Table 5.1. These reflection coefficient values were obtained by extrapolating using the $TM_{1\,62}$ and $TM_{1\,60}$ modes for two different thicknesses of FGM125, where the thicknesses were 0.125" and 0.250". The plots of S_{11}^{thy} in the X-band frequency range for both thicknesses are shown in Figure 5.14. If no errors are present in the extrapolation method, numerical integration, and other numerical processes, the reflection coefficient values represent an accurate estimate of the reflection coefficient due to an infinite number of modes, represented here as S_{11}^{extr}. As mentioned in section 5.1, using fewer modes or some other sources of error results in a reflection coefficient which differs from S_{11}^{extr}. A more rigorous examination of the effect of measurement error or random noise on the measurement system is examined in Chapter 6. To examine the effect of using fewer modes in the two thickness method extraction algorithm, S_{11}^{extr} was used in the extraction process as the 'measured' value. Thus, the two thickness method extraction is undertaken by rewriting (2.39) as

$$\begin{aligned} f_{2T}(\epsilon,\mu) &= S_{11(1T)}^{extr} - S_{11(1T)}^{thy} \\ g_{2T}(\epsilon,\mu) &= S_{11(2T)}^{extr} - S_{11(2T)}^{thy}. \end{aligned} \tag{5.3}$$

The values for $S_{11(1T)}^{thy}$ and $S_{11(2T)}^{thy}$ are calculated by using N modes, and the extraction algorithm simultaneously minimizes $f_{2T}(\epsilon,\mu)$ and $g_{2T}(\epsilon,\mu)$. The results for different values of N are displayed in Figure 5.20 - Figure 5.23. The different lines on the graphs represent the extracted material parameters obtained when using different numbers of modes in the solution.

Consider Figure 5.20, which displays extracted values for ϵ_r' using different num-

bers of modes at 21 frequencies across X-band. Note that a definite shift in the shape of the pattern is found when the number of modes is increased from the first 3 to include the 4th mode, which is the $TM_{1\,2}$ mode. However, also note that when the next 10 modes are included, the value for ϵ_r' changes very little. When the 15th mode is included, which is the $TM_{1\,4}$ mode, note that the value increases by approximately 1% in the direction of the nominal values for ϵ_r'.

In addition, another extraction was performed by excluding modes 5-13, and only including the first 6 modes which make a major contribution to the value of the reflection coefficient, modes 1-4, 14, and 15 from Table D.1. Note that in this extraction, denoted by the label P6, the values are almost identical to those extracted using the first 15 modes. This result is consistent with the observation in section 5.3 that modes 5-13 had very little effect on the magnitude and phase results of the theoretical reflection coefficient. As more of the modes that contribute to the reflection coefficient are added, note that the extracted values move in the direction of the nominal values. When the extrapolation method was employed in the extraction algorithm,the extracted values, denoted by the label $\times$, agree very well with the nominal values. The linear extrapolation was performed using the $TM_{1\,20}$ and $TM_{1\,18}$ modes. This also agrees with the observation made in section 5.3 regarding the linear extrapolation method. By using fewer modes, and in this case extrapolating from the $TM_{1\,20}$ mode, the extracted values were extremely close, with less than 0.1% deviation from the nominal values.

Figure 5.21 shows a similar plot of ϵ_r''. Recall that the permittivity in this dissertation is described as the complex quantity $\epsilon = \epsilon_0(\epsilon_r' - j\epsilon_r'')$. Thus for any conventional material, ϵ_r'' is positive. Note that in Figure 5.21, the majority of the values extracted from the two thickness method are negative, even when the first 14 modes are included in the solution. This is not physically realistic for this type of material. When the $TM_{1\,4}$ mode is included in the solution, most of the extracted values are

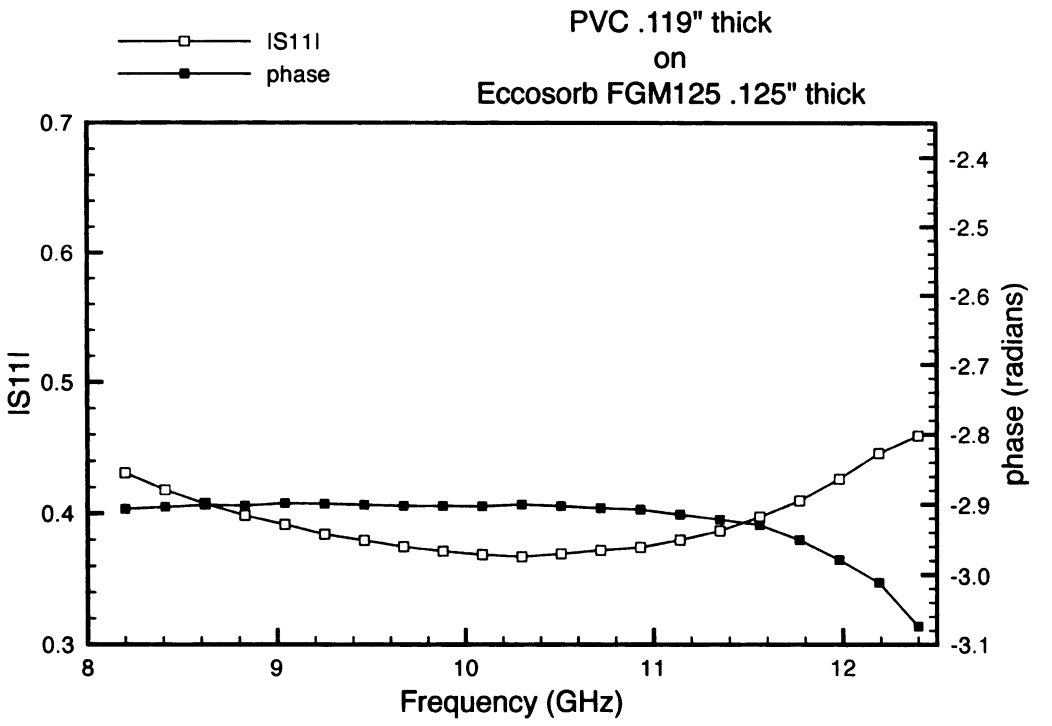


Figure 5.19. Extrapolated values of the magnitude and phase of S_{11}^{thy} for 1 layer of PVC, 0.119" thick on top of 1 layer of Eccosorb FGM125, 0.125" thick, for 8.2-12.4 GHz. Linear extrapolation was performed using $TM_{1\,16}$ and $TM_{1\,14}$ modes.

positive. The extracted values of ϵ_r'' migrate in the direction toward the nominal values as more modes are included in the solution, similar to Figure 5.20. In addition, when the extrapolation method is employed using the $TM_{1\,20}$ and $TM_{1\,18}$ modes in the extraction, again shown by the marker $\times$, the values are almost identical to the nominal values.

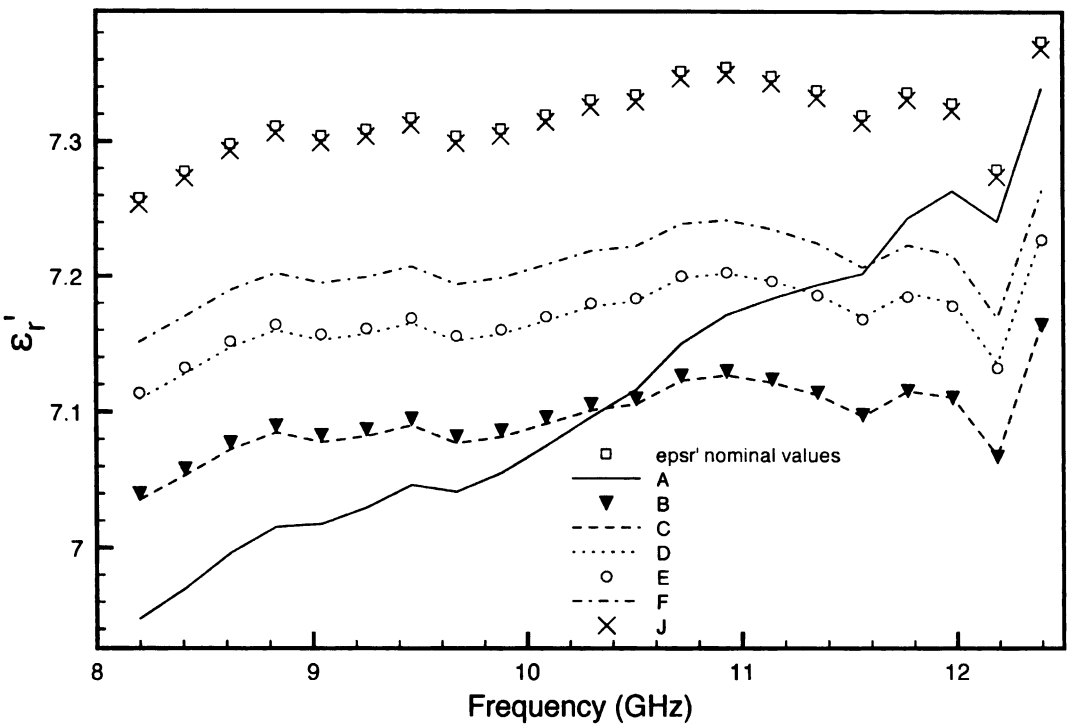


Figure 5.20. Extracted values of ϵ_r' using the two thickness method with different modes in the extraction. Extraction was simulated for two thicknesses of Eccosorb FGM125, 0.125" and 0.250" thick, for 8.2-12.4 GHz. Nominal values were used to generate $S_{11(1T)}^{extr}$ and $S_{11(2T)}^{extr}$. The key for each line is found in Table 5.2.

Consider the plots of the extracted values of μ_r' shown in Figure 5.22. Note that in this figure, when the first three modes are used in the solution, the extracted values are actually quite close to the nominal values of μ_r'. When the fourth mode, the TM_{12} mode is added, the values actually show their greatest error from the nominal values, approximately 3%. As more modes are added to the solution, the extracted values for μ_r' migrate in the direction of the nominal values.

Figure 5.23, in contrast, exhibits the greatest extraction error when only the first 3 modes are used in the extraction of μ_r''. As the number of modes is increased in the solution, the error in the extracted imaginary part of the permeability decreases.

Label	modes used	p	q
A	TE_{10}, TE_{30}, TE_{12}		
B	TE_{10}, TE_{30}, TE_{12}, TM_{12}		
C	1st 14 modes in Table D.1		
D	1st 15 modes in Table D.1		
E	TE_{10}, TE_{30}, TE_{12}, TM_{12}, TE_{14}, TM_{14}		
F	TE_{10}, TE_{30}, TE_{1p}, TM_{1p}	2,4.6	
G	TE_{10}, TE_{30}, TE_{1p}, TM_{1p}	2,4,6,8	
H	TE_{10}, TE_{30}, TE_{1p}, TM_{1p}	2,4,6,8,10	
I	TE_{10}, TE_{30}, TE_{1p}, TM_{1p}	2,4,6,8,10,12	
J	TE_{q0}, TE_{1p}, TM_{1p} + extrapolation	2-20, even	1, 3

Table 5.2. Key for modes used in the two thickness and two layer extraction methods, for two thicknesses of Eccosorb FGM125

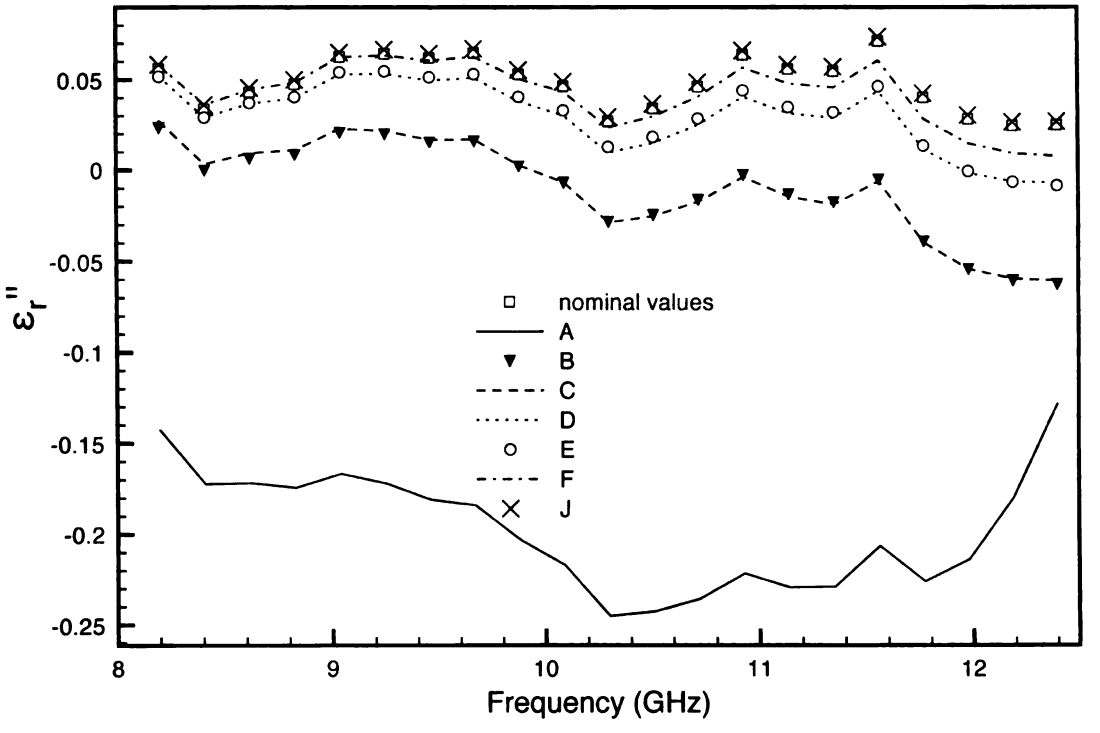


Figure 5.21. Extracted values of ϵ_r'' using the two thickness method with different modes in the extraction. Extraction was simulated for two thicknesses of Eccosorb FGM125, 0.125" and 0.250" thick, for 8.2-12.4 GHz. Nominal values were used to generate $S_{11(1T)}^{extr}$ and $S_{11(2T)}^{extr}$. The key for each line is found in Table 5.2.

In summary, when using just the first four modes in the solution, all extracted parameters are within 3% of the nominal values. Using fewer modes than this further increases the errors for three of the four parts of the permeability and permittivity. Increasing the number of modes in the solution decreases the errors, and it is noted that omitting the modes which do not contribute significantly to the reflection coefficient does not significantly change the extracted parameters.

5.6.2 Two Layer Method Modal Analysis

This section is a study of the effect of using N modes in the two layer method for material parameter extraction. Recall from section 2.6.1 that the two thickness and two layer methods are quite similar in the methods of extracting the material parameters. Both construct two functions that compute the differences between the measured and theoretical reflection coefficients, and those functions are simultaneously minimized to arrive at the extracted material parameters, ϵ and μ. The primary differences exist in the manner in which the theoretical reflection coefficients are calculated.

It is desirable to examine the performance of the two layer method when N modes are used to extract the material parameters in a manner similar to the investigation performed on the two thickness method in section 5.6.1. For the two layer method, the functions which are minimized, from (2.7), are

$$\begin{aligned} f(\epsilon_2, \mu_2,) &= S_{11(1)}^{extr} - S_{11(1)}^{thy} \\ g(\epsilon_2, \mu_2) &= S_{11(2)}^{extr} - S_{11(2)}^{thy}, \end{aligned} \tag{5.4}$$

where $S_{11(1)}^{extr}$ and $S_{11(2)}^{extr}$ are used as the 'measured values'. $S_{11(1)}^{thy}$ and $S_{11(2)}^{thy}$ are calculated using a finite number of modes.

5.6.2.1 Two Layers of Eccosorb FGM125

To give as direct a comparison as possible to the two thickness method, the extraction simulation was undertaken by using the identical 'measured' values that were used

in the two thickness method, so $S_{11(1)}^{extr} = S_{11(1T)}^{extr}$ and $S_{11(2)}^{extr} = S_{11(2T)}^{extr}$. Recall that $S_{11(1T)}^{extr}$ was simulated for one 0.125" thick layer of Eccosorb FGM125, and $S_{11(2T)}^{extr}$ was simulated when another 0.125" layer of Eccosorb FGM125 was placed on top of the first layer, making a total thickness of Eccosorb FGM125 that was 0.250" thick.

In the two layer method extraction, it is assumed that the material parameters of the top layer are known. In this simulated extraction, the nominal values shown in Table 5.1 were used as the material parameters for the top layer. Since the nominal values were used in the extrapolation method to generate $S_{11(1T)}^{extr}$ and $S_{11(2T)}^{extr}$, the primary source of error in this method is the difference in the number of modes used to calculate $S_{11(1)}^{thy}$ and $S_{11(2)}^{thy}$.

Consider Figure 5.24, which displays ϵ_r' extracted using different numbers of modes at 21 frequencies across X-band. The different plots displayed in this figure correspond to different numbers of modes used to extract the material parameters. Only the modes which made a significant contribution to the calculation of the theoretical reflection coefficient were used in this extraction. The justification for this step is twofold. First, the omission of those modes, as was shown in section 5.3, does not significantly affect the values computed for the reflection coefficient. This was shown to not significantly affect the extraction of the material parameters in the two thickness method in Figure 5.20 - Figure 5.23. This observation was also confirmed for the two layer method. The extraction results from the two layer method when the first 15 modes were used in the extraction yield almost identical results for the case when only modes 1, 2, 3, 4, 14, and 15 were used in the extraction. The second justification is related to the computational resources available. Due to the more complicated Green's function used in the two layer method, the numerical integration time needed to compute each matrix element in the MoM solution increased by approximately 50% over the two thickness method. Thus, the computational time saved by only using the modes which contribute to S_{11}^{thy} allowed for comparable results with

less computational expense.

Note that the extracted values of ϵ_r' in Figure 5.24 for the two layer method have a maximum error that is 50% below the nominal values values in the lower half of the frequency band, even when the first 10 significant modes are used in the solution. The use of 10 modes includes the $TM_{1\,8}$ mode. These errors are much larger than the errors observed using the two thickness method for the same material layer configuration in Figure 5.20. The values do migrate in the direction of the nominal values as the number of modes included in the solution is increased. However note that when comparing the same number of modes with the two thickness method extraction, there are greater errors which result. When the extrapolation method was employed in the extraction, as shown by the solid line, the values were much closer to the nominal values. Also note that when 6 modes are used, the extracted values at the upper end of the frequency band are greatly varying.

A similar plot for the extracted values of ϵ_r'' using the two layer method is shown in Figure 5.25. Here again, note that the errors are much larger for the two layer method than they were for the two thickness method, when using the same number of modes. As the number of modes used in the solution increases, the values for ϵ_r'' generally move in the direction of the nominal values. It is also noted that the results are again varying when 6 modes are used in the extraction method.

Consider Figure 5.26, which shows the extracted values for μ_r' using the two layer method. Here the extracted values have errors of approximately 30% for the two layer method even when the first 10 significant modes are included in the solution. Similar to what was observed with the permittivity, when the first 6 significant modes are used in the solution, the values for μ_r' extracted in the upper end of the frequency band are erratic. However, as more significant modes are included in the solution, the results migrate in the direction of the nominal values. When the extrapolation method is employed, the values are quite close to the nominal values. However, just

using the first 10 significant modes does not produce results that are as close as the values extracted using the two thickness method when the same modes are used in the solution.

The imaginary part of the permeability that was extracted using the two layer method is shown in Figure 5.27. Note that the trend observed for this extraction is similar to those found in Figure 5.24 - Figure 5.26. However, at the lower end of the frequency range, the extracted values are much closer to the nominal values, with a maximum deviation of less than 10%. At midband, there is a greater deviation from the nominal values, with a maximum deviation 100% larger than the nominal values. At the higher end the extracted values are again closer to the nominal values, especially when the first 8 and 10 significant modes are used. The exception is when just 6 significant modes are used. These results show a much greater error due to using fewer modes than that observed using the two thickness method.

5.6.2.2 Top Layer of Nylon, Bottom Layer of Eccosorb FGM125

Although the two layer method appears to have greater errors in the extracted parameters by using a finite number of modes in the solution, it is possible that a different top layer material may produce less error in the extracted parameters. As was noted in section 5.4, when dielectric materials are used as the top layer, additional $TE_{odd\,0}$ modes make a significant contribution to the solution. It is possible that the contribution of these additional modes or the different material parameters of the dielectric layer may reduce the errors for this modal analysis of the two layer method. To examine this possibility, a modal analysis of the two layer method was performed using Nylon for the top layer and Eccosorb FGM125 for the bottom layer.

In this simulation, the 'measured' values used in the extraction are the theoretical reflection coefficients for one layer of Eccosorb FGM125, $S^{extr}_{11(1)}$, shown in Figure 5.14, and $S^{extr}_{11(2)}$ calculated for one 0.125" layer of Nylon on top of a 0.125" layer of Eccosorb FGM125, shown in Figure 5.18. It is assumed that the material parameters

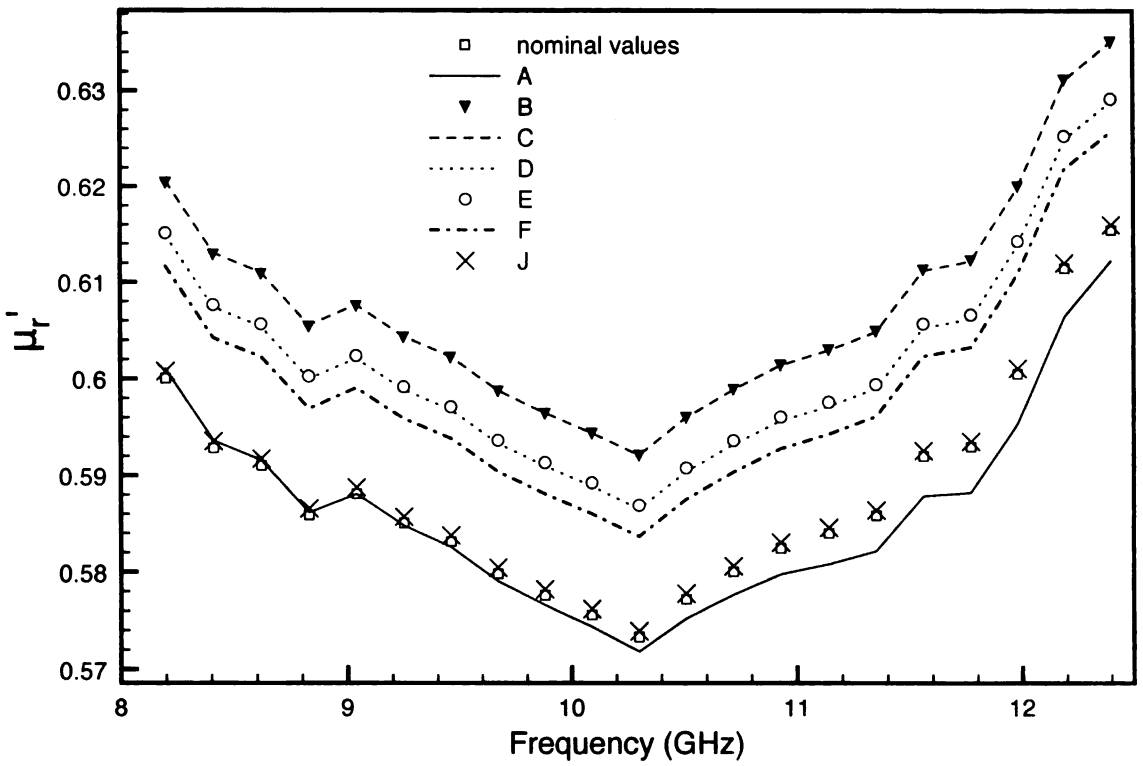


Figure 5.22. Extracted values of μ_r' for the two thickness method with different modes in the extraction. Extraction was simulated for two thicknesses of Eccosorb FGM125, 0.125" and 0.250" thick, for 8.2-12.4 GHz. Nominal values were used to generate $S^{extr}_{11(1T)}$ and $S^{extr}_{11(2T)}$. The key for each line is found in Table 5.2.

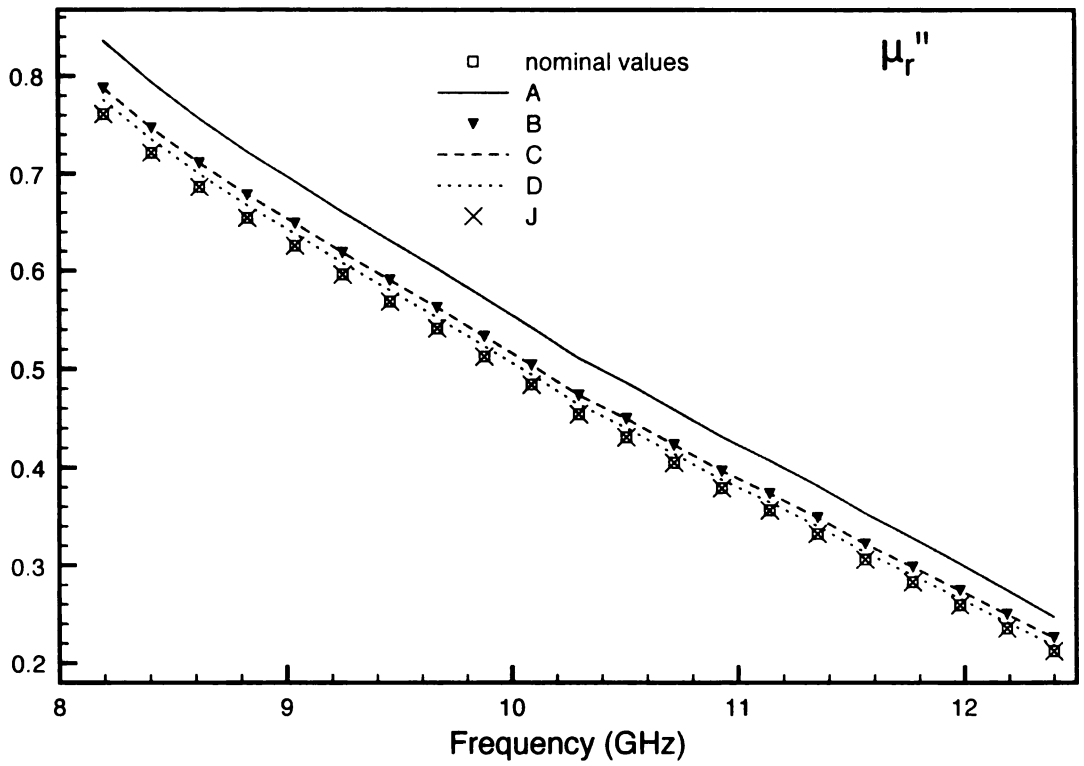


Figure 5.23. Extracted values of μ_r'' for the two thickness method with different modes in the extraction. Extraction was simulated for Eccosorb FGM125, 0.125" and 0.250" thick, for 8.2-12.4 GHz. Nominal values were used to generate $S^{extr}_{11(1T)}$ and $S^{extr}_{11(2T)}$. The key for each line is found in Table 5.2.

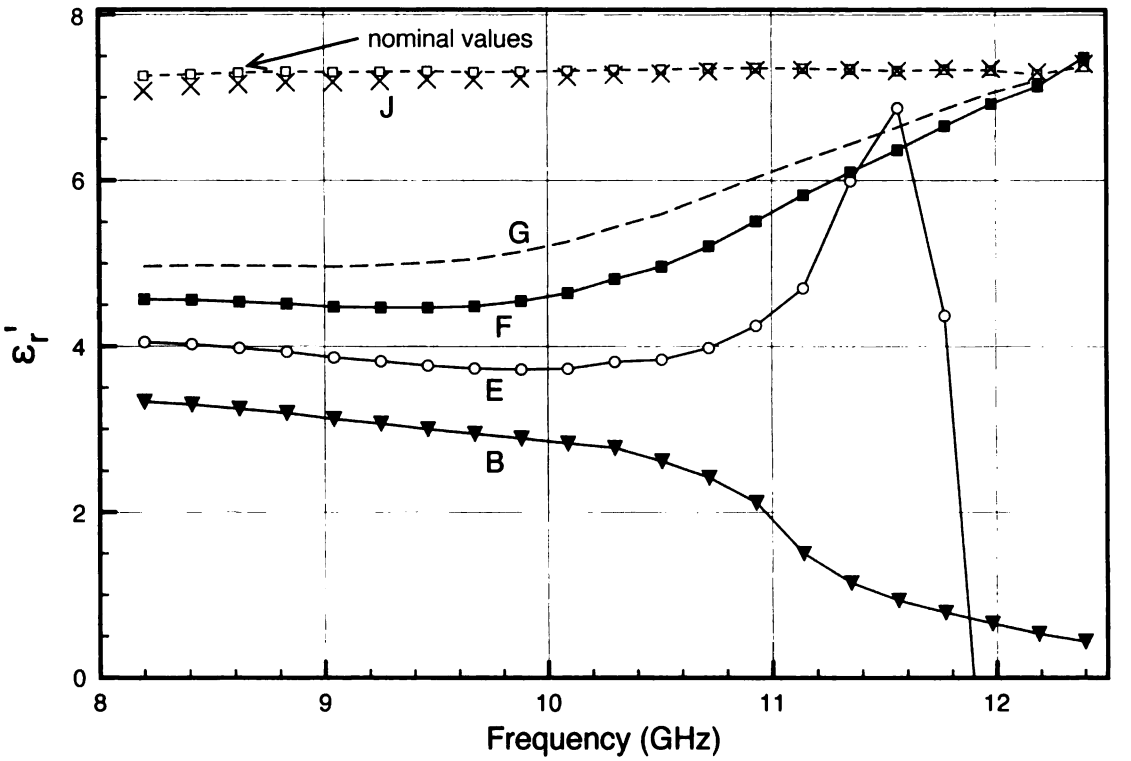


Figure 5.24. Extracted values of ϵ_r' for the two layer method with different modes in the extraction. Extraction was simulated for a bottom layer of Eccosorb FGM125, 0.125" thick. The top layer was also a layer of Eccosorb FGM125, 0.125" thick. Simulations are over 8.2-12.4 GHz. Nominal values were used to generate $S_{11(1)}^{extr}$ and $S_{11(2)}^{extr}$, and nominal values were used for the top layer in the extraction. The key for each line is found in Table 5.2.

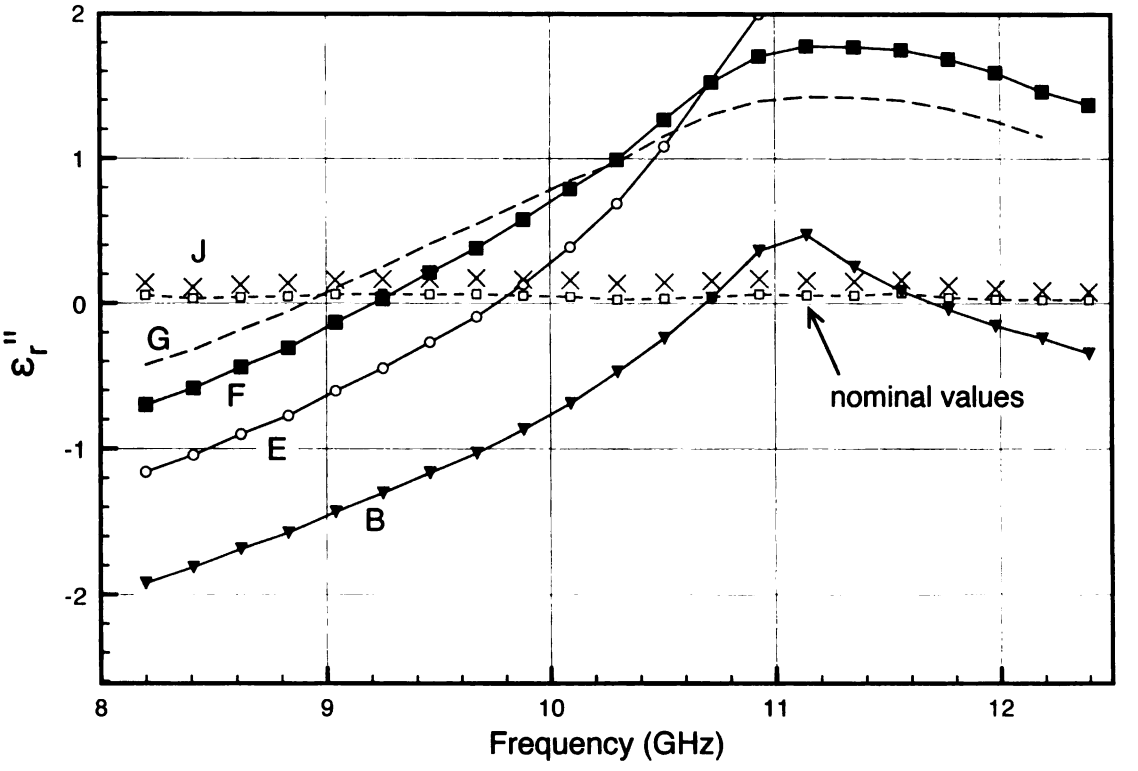


Figure 5.25. Extracted values of ϵ_r'' for the two layer method with different modes in the extraction. Extraction was simulated for a bottom layer of Eccosorb FGM125, 0.125" thick. The top layer was also a layer of Eccosorb FGM125, 0.125" thick. Simulations are over 8.2-12.4 GHz. Nominal values were used to generate $S_{11(1)}^{extr}$ and $S_{11(2)}^{extr}$, and nominal values were used for the top layer in the extraction. The key for each line is found in Table 5.2.

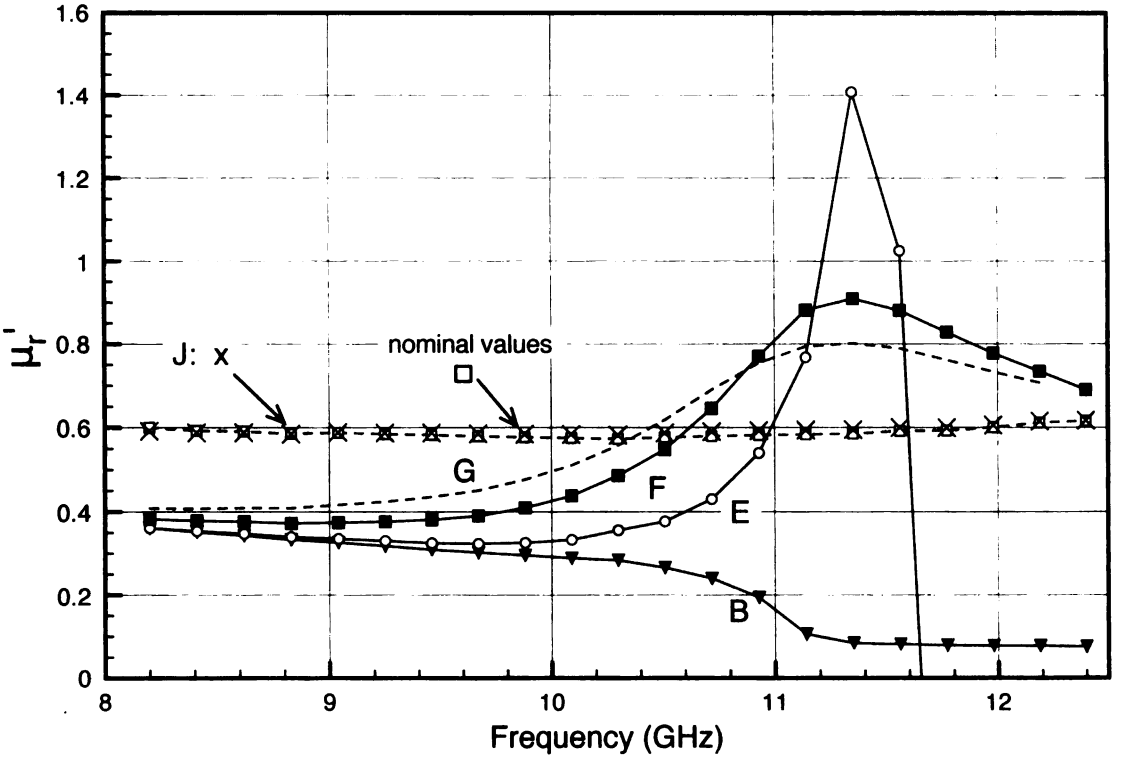


Figure 5.26. Extracted values of μ_r' for the two layer method with different modes in the extraction. Extraction was simulated for a bottom layer of Eccosorb FGM125, 0.125" thick. The top layer was also a layer of Eccosorb FGM125, 0.125" thick. Simulations are over 8.2-12.4 GHz. Nominal values were used to generate $S_{11(1)}^{extr}$ and $S_{11(2)}^{extr}$, and nominal values were used for the top layer in the extraction. The key for each line is found in Table 5.2.

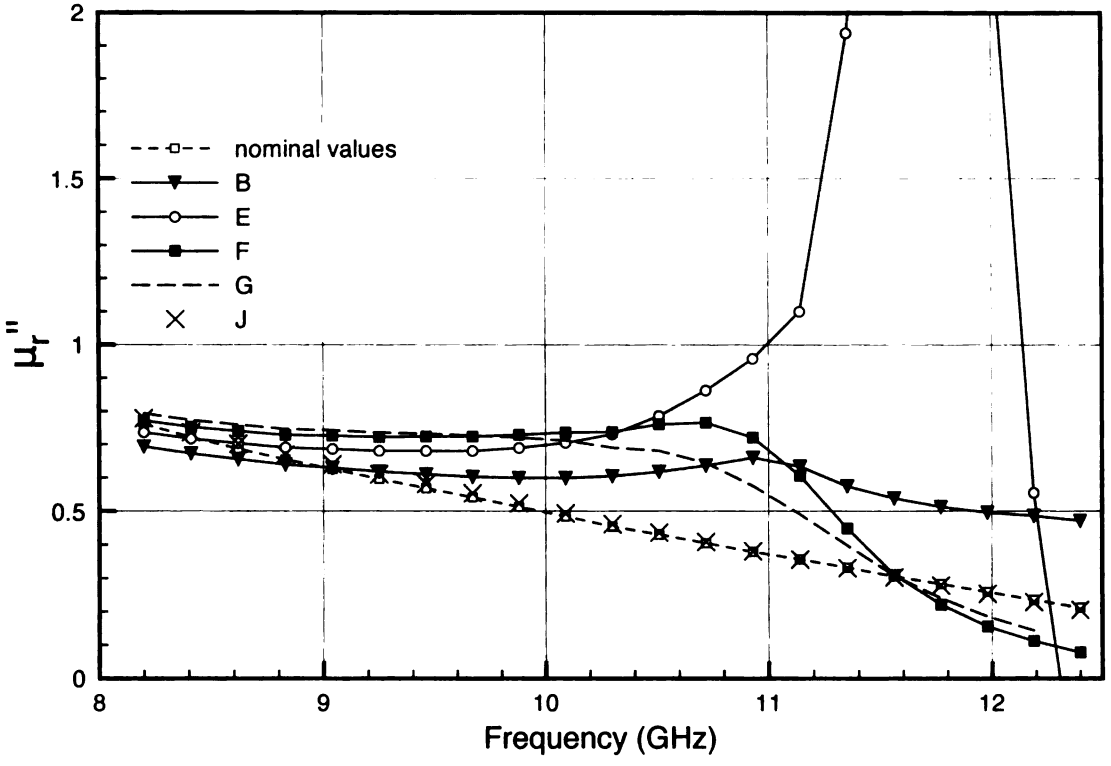


Figure 5.27. Extracted values of μ_r'' for the two layer method with different modes in the extraction. Extraction was simulated for a bottom layer of Eccosorb FGM125, 0.125" thick. The top layer was also a layer of Eccosorb FGM125, 0.125" thick. Simulations are over 8.2-12.4 GHz. Nominal values were used to generate $S_{11(1)}^{extr}$ and $S_{11(2)}^{extr}$, and nominal values were used for the top layer in the extraction. The key for each line is found in Table 5.2.

of the top layer of Nylon are known, and they are found in Table F.2. Extractions were performed using different numbers of modes in the solution, and the results are shown in Figure 5.28 - Figure 5.31.

Consider the extracted values of ϵ_r', found in Figure 5.28. Note that the largest errors are seen at the lower end of the frequency band when just a few modes have been included in the solution. In face, curve a, which shows the results from just the first four modes, shows errors of approximately 33% of the nominal values on the lower end of the frequency band. These errors decrease in the upper end of the frequency band. The other lines, which show the results as additional modes are added to the solution, show a similar shape. The general trend of the extracted values migrate toward the nominal values as more modes are included in the solution. In this simulation, the linear extrapolation method was employed using the contributing modes up to the $TM_{1\,14}$ mode, shown by line g. Note that these values are within 1% of the nominal values.

Compare Figure 5.28 to the results shown for the two layer method with Eccosorb FGM125 as the top layer, in Figure 5.24. When Eccosorb FGM125 was the top layer, the errors were much larger when a smaller number of modes were used in the solution. It is not until the $TM_{1\,6}$ mode is included in Figure 5.24 that the extracted values have approximately the same shape as that shown in Figure 5.28 using the first four modes for Nylon as the top layer. When the extrapolation method is employed, the values are within 1% of the nominal values with either top layer. However, it should be noted that the extrapolation was performed in the Nylon top layer simulation only using the $TM_{1\,14}$ mode, but the total number of modes used was larger. This was due to the fact that the $TE_{odd\,0}$ modes also made a significant contribution to the reflection coefficient and were included in the simulation for the Nylon top layer. Thus, more total modes, 29 in all, were used in the Nylon extrapolation result. The simulation with Eccosorb FGM125 as the top layer used up to the $TM_{1\,20}$ mode in

the extraction, with a total of 22 modes.

The extracted results for ϵ_r'' are shown in Figure 5.29. The general trend of the figure is consistent with the expectation that as more modes are included in the solution, the values for ϵ_r'' move in the direction of the nominal values. The extracted values show errors well in excess of 500% for all of the modal solution, with the exception of the extrapolated results, shown by line g. Those errors are within approximately 100% of the nominal values. However, it should be noted that the values for ϵ_r'' are rather small, mostly below 0.5.

The results shown in Figure 5.29, however, do present a significant improvement over the results shown in Figure 5.25, using Eccosorb FGM125 as the top layer. All of the extracted values using Nylon as the top layer are physically possible material parameters for ϵ_r'', even when using only 4 modes. However, when the top layer was Eccosorb FGM125, the only simulation shown in Figure 5.25 where this is true was obtained using the extrapolation method. Note that when the extrapolation method is employed, the values obtained for ϵ_r'' are within 5% of the nominal values, regardless of the top layer used.

Figure 5.30 displays the extracted results for μ_r' when Nylon is used as the top layer. When only the first 4 modes are used in the solution, both the high and low frequencies in the X-band show errors in the extracted values that are approximately 30% of the nominal values. Near the middle of the frequency band these errors are smaller, with the extracted values within 5% of the nominal values near 10.4 GHz. As the number of modes used in the solution is increased, the extracted values for μ_r' migrate toward the nominal values. When the extrapolation method is employed, the extracted values are within 0.5% of the nominal values for the entire frequency band.

Compare these results with those of Figure 5.26. It is again clear that when all of the modes up to the same TM modes are used in the solution, the use of Nylon as a

top layer produces extracted values that are closer to the nominal values than when Eccosorb FGM125 is used as the top layer.

The imaginary part of the permeability shows a similar trend to the other three extracted parameters, and the results are shown in Figure 5.31. For most of the frequency band, the extracted values of μ_r'' are greater than the nominal values when different numbers of modes are used in the solution. However, these values move closer to the nominal values as more modes are used in the extraction. When compared to similar TM modes shown in Figure 5.27, the extracted results are closer to the nominal values than when Eccosorb FGM125 was used as the top layer.

5.7 Conclusions

In order to practically describe the electric and magnetic fields in a waveguide, it is customary to represent those fields using a finite number of waveguide modes. However, when this representation is used in the two layer and two thickness methods, many higher order modes contribute to calculation of the reflection coefficient. An extrapolation technique is developed in this chapter to obtain a more accurate estimate of the contribution of a large number of modes to the theoretical reflection coefficient calculation. This technique can be utilized to calculate the reflection coefficient for one or two layers of material. This extrapolation technique may then be used in the two thickness and two layer methods.

The effect of a smaller number of modes used in calculating the reflection coefficient has been studied for the two layer and two thickness methods. The conclusion for this group of simulations is that the two thickness method needs fewer modes to obtain satisfactory results than the two layer method when both layers are composed of Eccosorb FGM125. The two layer method is much more sensitive to the error induced by using fewer modes in the solution than is the two thickness method. A similar phenomenon for the two layer method is observed when a Nylon is used as the

top layer. Although it appears to be slightly less sensitive to the error caused by fewer modes in the solution, it is also much larger than the two thickness method. When the extrapolation scheme is used in both methods, the extracted values approach the nominal values. However, errors of less than 5% are obtained using just four modes with the two thickness method. Even using the first 10 significant modes in the two layer method, with both layers comprised of Eccosorb FGM125, yields results that deviate 30% or more from the nominal values for much of the frequency band in all four parameters. A top layer of Nylon showed similar results when one considers the number of modes used in the solution. When the results from the same $TM_{1\,even}$ modes are compared, the extracted results from a top layer of Nylon are closer to the nominal values that using a top layer of Eccosorb FGM125. They do, however, have much greater errors than the two thickness method.

To mitigate the errors caused by truncating the approximation of fields in the waveguide to N modes, the conclusion of this modal analysis is that the extractions performed by the two layer method should employ the extrapolation method

It is noted here that these simulations have dealt only with the error induced in the calculation of the theoretical reflection coefficient by using a finite number of modes. In practice there are additional errors due to physical variations in materials, tolerances in material quantities, defects in the material or measuring devices, random measurement noise, and several other potential sources of error. Random measurement error is examined for its effect on the extracted parameters in the next chapter.

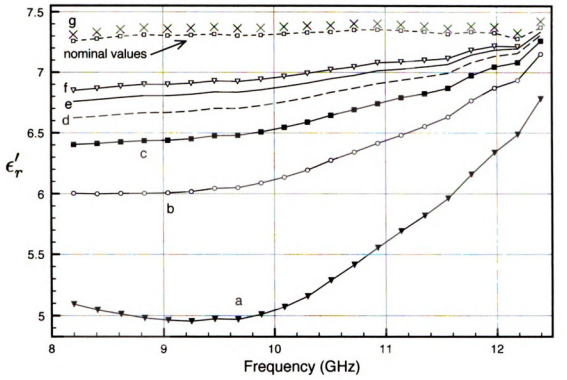


Figure 5.28. Extracted values of ϵ'_r for the two layer method with different modes in the extraction. Extraction was simulated for a bottom layer of Eccosorb FGM125, 0.125" thick. The top layer was also a layer of Nylon, 0.125" thick. Simulations are over 8.2-12.4 GHz. Nominal values were used to generate $S^{extr}_{11(1)}$ and $S^{extr}_{11(2)}$, and nominal values were used for the top layer in the extraction. Key for each line in the plot is found in Table 5.3

Label	modes used	p	q
a	$TE_{10}, TE_{30}, TE_{12}, TM_{12}$		
b	$TE_{q0}, TE_{1p}, TM_{1p}$	2, 4	1, 3, 5, 7, 9
c	$TE_{q0}, TE_{1p}, TM_{1p}$	2, 4, 6	1-13, odd
d	$TE_{q0}, TE_{1p}, TM_{1p}$	2, 4, 6, 8	1-17, odd
e	$TE_{q0}, TE_{1p}, TM_{1p}$	2, 4, 6, 8, 10	1-21, odd
f	$TE_{q0}, TE_{1p}, TM_{1p}$	2-12, even	1-25, odd
g	$TE_{q0}, TE_{1p}, TM_{1p}$ + extrapolation	2-14, even	1-29, odd

Table 5.3. Key for modes used in 2 Layer Extraction Method using Nylon as the top layer.

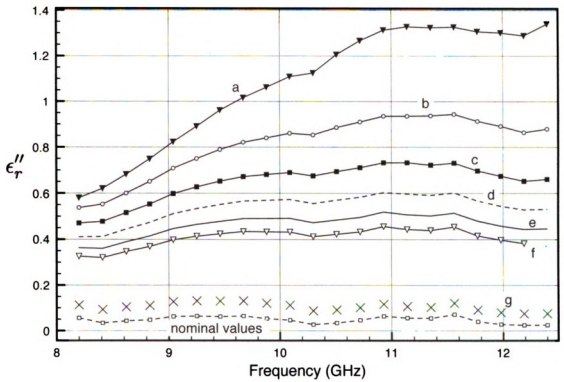


Figure 5.29. Extracted values of ϵ''_r for the two layer method with different modes in the extraction. Extraction was simulated for a bottom layer of Eccosorb FGM125, 0.125" thick. The top layer was also a layer of Nylon, 0.125" thick. Simulations are over 8.2-12.4 GHz. Nominal values were used to generate $S^{extr}_{11(1)}$ and $S^{extr}_{11(2)}$, and nominal values were used for the top layer in the extraction. Key for each line in the plot is found in Table 5.3

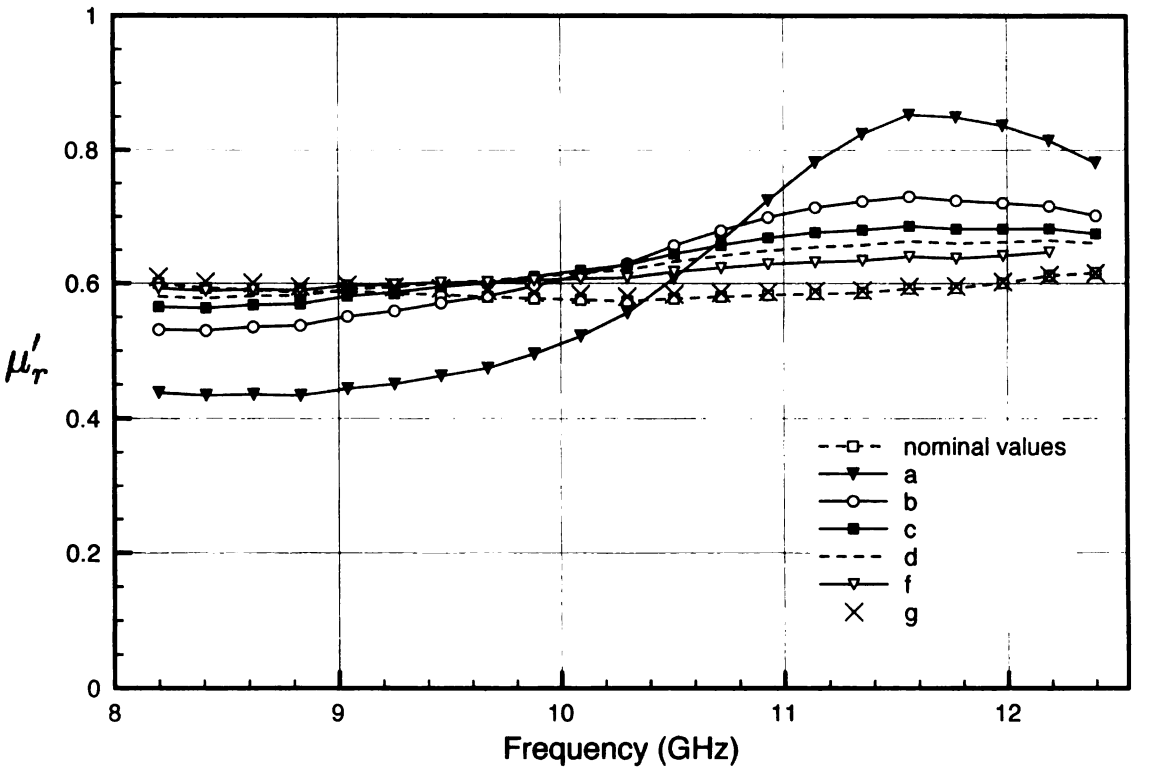


Figure 5.30. Extracted values of μ_r' for the two layer method with different modes in the extraction. Extraction was simulated for a bottom layer of Eccosorb FGM125, 0.125" thick. The top layer was also a layer of Nylon, 0.125" thick. Simulations are over 8.2-12.4 GHz. Nominal values were used to generate $S_{11(1)}^{extr}$ and $S_{11(2)}^{extr}$, and nominal values were used for the top layer in the extraction. Key for each line in the plot is found in Table 5.3

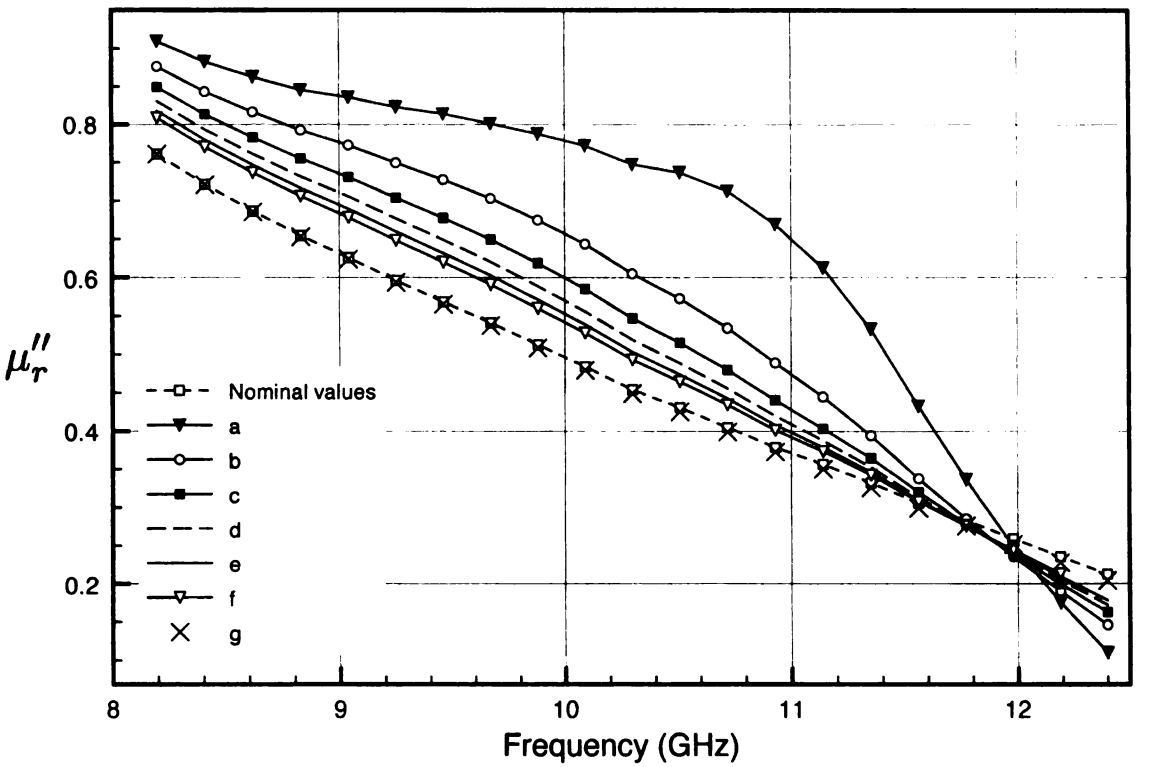


Figure 5.31. Extracted values of μ_r'' for the two layer method with different modes in the extraction. Extraction was simulated for a bottom layer of Eccosorb FGM125, 0.125" thick. The top layer was also a layer of Nylon, 0.125" thick. Simulations are over 8.2-12.4 GHz. Nominal values were used to generate $S_{11(1)}^{extr}$ and $S_{11(2)}^{extr}$, and nominal values were used for the top layer in the extraction. Key for each line in the plot is found in Table 5.3

CHAPTER 6

SENSITIVITY ANALYSIS DUE TO MEASUREMENT ERROR IN THE TWO THICKNESS METHOD AND TWO LAYER METHOD

6.1 Introduction

The goal of studying the two thickness method, the two layer method, and the two iris method is to develop a practical technique for determining the EM properties of a conductor-backed material. The two thickness method has shown promise as a laboratory method, but the two layer method and two iris method can be used for an *in situ* application. It is desirable to measure the true value of the properties of a substance, but there are always errors that are associated with any actual measurement. In this chapter, the uncertainties associated with material parameter extractions obtained using the two thickness method and two layer method are quantified and described as a function of the network analyzer uncertainty. The implications of this uncertainty analysis to the practical use of these methods are discussed.

6.2 Definitions

In any measurement, it is desirable to arrive at the true value of the quantity measured, and a clear definition of the terms associated with measurements and uncertainties is necessary in understanding the process. The *true value* of the measurement is the value that ideally reflects the property that is being measured, with no errors in that measurement. The *measurement error* is the deviation of the measured quantity from the underlying true value [52]. In any real world measurement, there are always some measurement errors. Errors may be present due to several different factors in the measurement process. These can include human error, instrumentation error, errors due to random processes, errors due to environmental conditions, and many

others.

Two primary categories of measurement errors are systematic and random errors. *Systematic errors* are those errors that remain constant in repeated measurements or vary in a regular or systematic manner over a series of identical measurements. It is possible to categorize these errors for later removal in the analysis process. *Random errors* are those errors that are observable when a measurement has been repeated a certain number of times. According to Rabin [52], "If there are differences between the results of separate measurements and these differences cannot be predicted individually and any regularities inherent to them are manifested only in a significant number of results, then the error owing to this scatter of the results is called the *random error*."

Another concept that is discussed in this dissertation is the repeatability of measurements. The *repeatability of measurements* reflects the closeness of measurements that are conducted in essentially the same conditions. These measurements are ideally performed with the same equipment in identical conditions by the same person in a relatively short amount of time [53]. If the random errors are small, the measurements should have a high degree of repeatability.

6.3 Assumptions for this Error Sensitivity Analysis

Several possible errors exist that can take place in any measurement technique, although some of those errors may have a much greater effect on the desired output of the technique than other errors. Some possible sources of error in the two thickness and two layer method are cataloged in Table 6.1. These errors include computational errors, random measurement errors, and errors due to structural or compositional variations in the material under test. It should be noted that each technique has different measurement errors associated with that method. For example, the two thickness method uses two samples of material A, each with a different thickness.

The manufacturing process may lead to variations in the thickness of material A. Thus, the measurement of the thickness may contain errors. The two layer method may use one of the same samples of material A as the bottom layer, but the top layer, composed of material B may come from a different manufacturer. That manufacturing process may have have different error tolerances associated with the sample of material B. These errors in the thickness of the two types of materials may or may not be correlated to each other.

To make a reasonable comparison of the two thickness method and the two layer method, the only errors that are considered in the error sensitivity analysis of this chapter are those random errors that are due to the vector network analyzer measurement. This assumes, therefore, that the thicknesses of the materials under test are known absolutely, and that there are no airgaps present between the metallic flange and the material under test. In addition, the materials are assumed to be homogeneous, linear, isotropic, and perfectly flat. This also assumes that the other potential errors cataloged in Table 6.1 are negligible. Using these assumptions, the error analysis represents a best case scenario for comparing the two methods.

The final concept to be discussed before the technical discussion of the error sensitivity analysis is the propagation of errors. In these methods, the measurements that are obtained are the magnitude and phase of the reflection coefficient of the measured material. These are not, however, the desired output of the method itself. For example, in the two thickness method, $S_{11(1T)}^{meas}$ and $S_{11(2T)}^{meas}$ are the measurements obtained from the first thickness and the second thickness of the material, respectively. The output of the two thickness method is the extracted material parameters, ϵ and μ. The random measurement errors present in $S_{11(1T)}^{meas}$ and $S_{11(2T)}^{meas}$ lead to an uncertainty in the extracted parameters for the two thickness method.

Two methods were chosen to investigate the uncertainty in the extracted parameters due to random measurement error, and the results are included in this chapter.

The first method is the standard propagation of errors method, while the second is a Monte Carlo simulation.

Error	Two Thickness Method	Two Layer Method
Computational Errors		
Numerical Integration	×	×
modes used in S_{11}^{thy} calculation	×	×
Physical Imperfections		
Lower layer thickness	×	×
Upper layer thickness		×
Material defects	×	×
Imperfections in flange plate	×	×
Material properties of top layer		×
Measurement Errors		
Clamp pressure/airgaps	×	×
Interrogation location	×	×
Network analyzer error	×	×

Table 6.1. Potential sources of error in the two layer and two thickness methods

6.4 Random noise propagation of errors

The underlying assumption in this error sensitivity analysis is that the measurement error is due to random noise present in the system. It is common to characterize random noise present in a system as having a normal, or Gaussian probability distribution function [54], which is shown in Figure 6.1. A normal distribution is characterized by the probability density function

$$f(x) = \frac{1}{\sqrt{\sigma 2\pi}} e^{-(x-\mu)^2/2\sigma^2}, \tag{6.1}$$

where the mean is μ and the standard deviation is represented by σ.

It is helpful to know how the changes or uncertainty in the input parameters to an equation affect the uncertainty in the output parameters. Consider a function

$$\mathbf{y} = \mathbf{f}(\mathbf{x}), \tag{6.2}$$

where $\mathbf{y}$, the output, and $\mathbf{x}$, the input, are vector quantities. The uncertainty in the output measurement can be expressed as a matrix equation where the uncertainty in $\mathbf{y}$, given by U_y, is due to the uncertainties in $\mathbf{x}$ through the equation

$$U_y = [J_x][C_y][J_x]^T. \tag{6.3}$$

Here, the matrix J_x is the Jacobian, defined as

$$J_x = \sum_{i=1}^{N} \frac{\partial f}{\partial x_i}, \tag{6.4}$$

where N is the number of elements in the vector $\mathbf{x}$ [54]. The matrix C_y is the covariance matrix describing the uncertainties in the input variables, $u(x_i)$, and the correlations of the uncertainties between variables, $u(x_i, x_j)$. If N = 2, the resulting covariance matrix is

$$C_y = \begin{bmatrix} u(x_1)^2 & u(x_1, x_2) \\ u(x_1, x_2) & u(x_2)^2 \end{bmatrix}. \tag{6.5}$$

If there is no correlation between the uncertainties in the input parameters $\mathbf{x}$, such that $u(x_i, x_j) = 0$, the resulting uncertainty in the output quantity is therefore [54]

$$U_y = \sum_{i=1}^{N} u(x_i)^2 \left(\frac{\partial f}{\partial x_i}\right)^2 \tag{6.6}$$

In the following analysis, it is assumed that the error in a measurement taken with

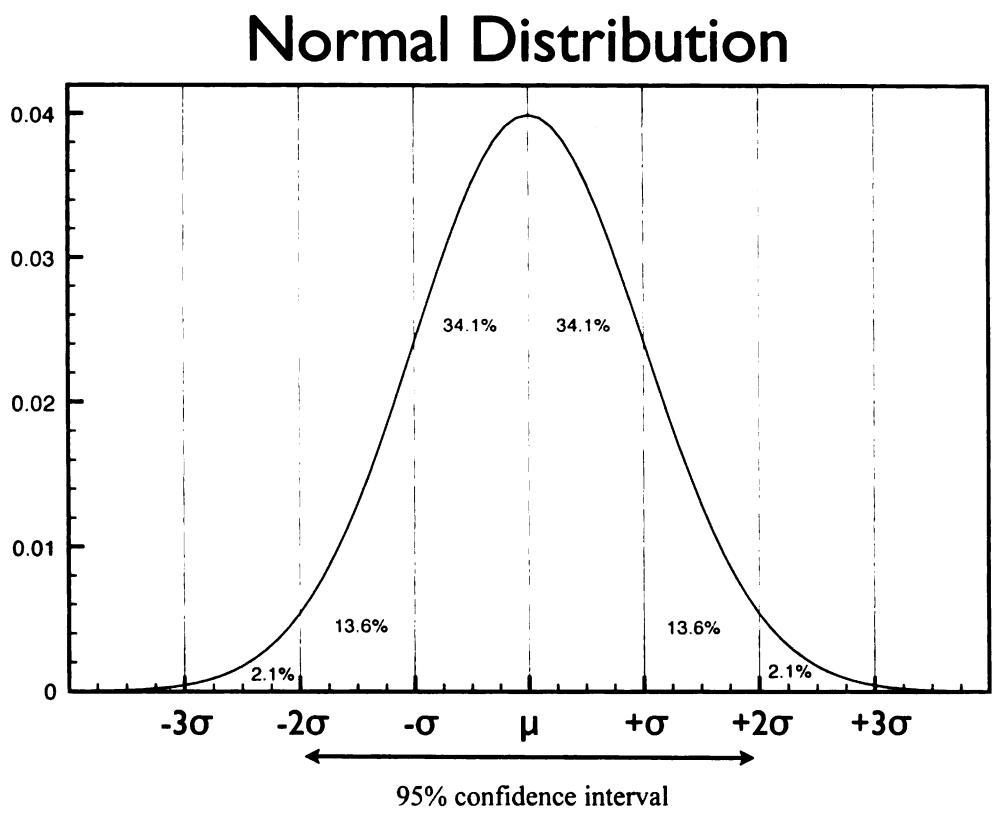


Figure 6.1. Normal distribution, with mean μ, and standard deviation, σ.

the HP8510 network analyzer is normally distributed about a mean value of zero, with a standard deviation of σ. Then, the uncertainty on the measurement is the standard deviation, σ_i. The variance is the standard deviation squared, or σ_i^2. It is also assumed that the error in each of the measured quantities is independent of the errors in the other measured quantities. These assumptions allow the use of the theorem of standard error propagation as defined by Dahlquist [56]:

Assume that the errors $\Delta x_i, i = 1, 2, ...N$ *are independent random variables with mean zero and standard deviations* σ_i. *Then the standard error* σ_y *for* $y =$

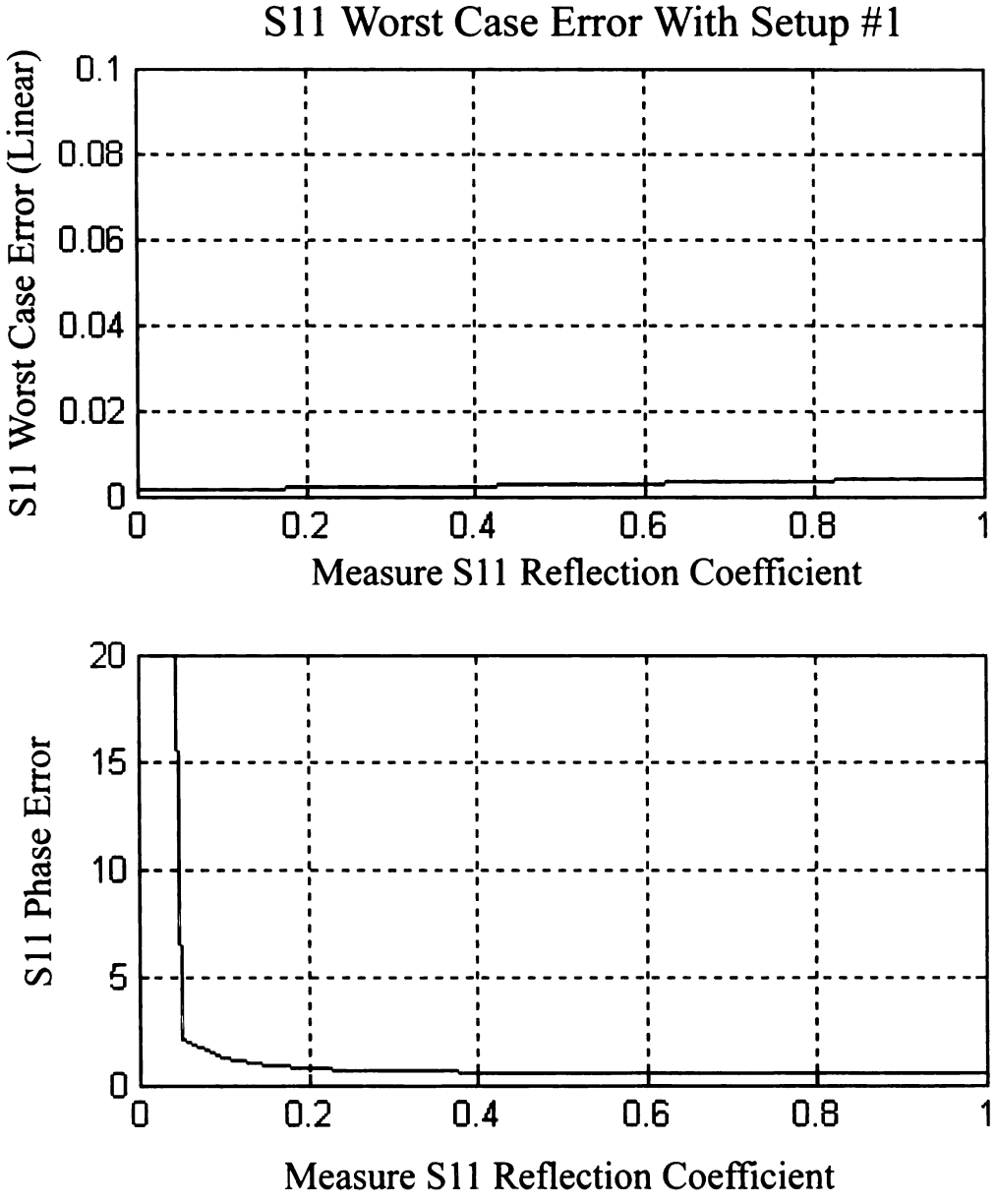


Figure 6.2. Worst case error for measurements on HP8510, from "HP8510 Specifications & Performance Verification Program". Figure reproduced with permission from [57].

$f(x_1, x_2, ...x_N)$ *is given by*

$$\sigma_y \approx \sqrt{\sum_{i=1}^{N} \sigma_i^2 \left(\frac{\partial y}{\partial x_i}\right)^2}. \tag{6.7}$$

As can be seen from (6.7), to obtain a correct estimate of the output uncertainty, σ_y, it is necessary to know the uncertainty, σ_i, of the input quantities, and the derivatives, $\partial y/\partial x_i$.

Using (6.7), the uncertainties in the final output parameters of the extraction algorithm, $\epsilon'_{r1}, \epsilon''_{r1}, \mu'_{r1}, \mu''_{r1}$, may be estimated. The HP8510 Network Analyzer returns magnitude, $|S_{11}|$, and phase, ϕ, measurements. These are the input parameters, denoted by x_i in (6.7). The maximum error of those measurements for a standard measurement setup, as given by the "HP8510 Specifications & Performance Verification Program" [57], is shown in Figure 6.2. For reflection coefficients above magnitude of 0.2, which consistently occurred in these simulations, the estimate of the standard deviation of the phase error is $\sigma_\phi = 0.8°$. The standard deviation of the magnitude error is $\sigma_{|S_{11}|} = 0.004$. The derivatives in (6.7), which are calculated numerically, are described in greater detail in section 6.4.1.

An estimate of the standard deviation of each of the extracted quantities in the two thickness method is given by the following expressions:

$$\sigma_{\epsilon'_r} = \left[\sigma^2_{|S_{11(1T)}|}\left(\frac{\partial \epsilon'_r}{\partial |S_{11(1T)}|}\right)^2 + \sigma^2_{\phi 1T}\left(\frac{\partial \epsilon'_r}{\partial \phi_{1T}}\right)^2 \right. \tag{6.8}$$

$$\left. + \sigma^2_{|S_{11(2T)}|}\left(\frac{\partial \epsilon'_r}{\partial |S_{11(2T)}|}\right)^2 + \sigma^2_{\phi 2T}\left(\frac{\partial \epsilon'_r}{\partial \phi_{2T}}\right)^2\right]^{\frac{1}{2}}$$

$$\sigma_{\epsilon_r''} = \left[\sigma^2_{|S_{11(1T)}|}\left(\frac{\partial\epsilon_r''}{\partial|S_{11(1T)}|}\right)^2 + \sigma^2_{\phi_{1T}}\left(\frac{\partial\epsilon_r''}{\partial\phi_{1T}}\right)^2 + \sigma^2_{|S_{11(2T)}|}\left(\frac{\partial\epsilon_r''}{\partial|S_{11(2T)}|}\right)^2 + \sigma^2_{\phi_{2T}}\left(\frac{\partial\epsilon_r''}{\partial\phi_{2T}}\right)^2\right]^{\frac{1}{2}} \tag{6.9}$$

$$\sigma_{\mu_r'} = \left[\sigma^2_{|S_{11(1T)}|}\left(\frac{\partial\mu_r'}{\partial|S_{11(1T)}|}\right)^2 + \sigma^2_{\phi_{1T}}\left(\frac{\partial\mu_r'}{\partial\phi_{1T}}\right)^2 + \sigma^2_{|S_{11(2T)}|}\left(\frac{\partial\mu_r'}{\partial|S_{11(2T)}|}\right)^2 + \sigma^2_{\phi_{2T}}\left(\frac{\partial\mu_r'}{\partial\phi_{2T}}\right)^2\right]^{\frac{1}{2}} \tag{6.10}$$

$$\sigma_{\mu_r''} = \left[\sigma^2_{|S_{11(1T)}|}\left(\frac{\partial\mu_r''}{\partial|S_{11(1T)}|}\right)^2 + \sigma^2_{\phi_{1T}}\left(\frac{\partial\mu_r''}{\partial\phi_{1T}}\right)^2 + \sigma^2_{|S_{11(2T)}|}\left(\frac{\partial\mu_r''}{\partial|S_{11(2T)}|}\right)^2 + \sigma^2_{\phi_{2T}}\left(\frac{\partial\mu_r''}{\partial\phi_{2T}}\right)^2\right]^{\frac{1}{2}}. \tag{6.11}$$

6.4.1 Calculation of derivatives

The values used for $\sigma_{|S_{11(1T)}|}$, $\sigma_{|S_{11(2T)}|}$, $\sigma_{\phi_{1T}}$ and $\sigma_{\phi_{2T}}$ are the random measurement errors for an HP8510 Network analyzer shown in Figure 6.2. The other parameters needed to evaluate the uncertainty in the extracted parameters are the derivatives in (6.8) - (6.11). Note that there are four derivatives in each equation that must be evaluated. The derivatives in (6.8) - (6.11) act as amplifying terms on the variance of the network analyzer measurement. It is thus important to accurately compute the derivatives. In a standard two-term central difference method, the derivative is

calculated by the formula,

$$\frac{\partial f}{\partial x} \approx \frac{f(x+\delta) - f(x-\delta)}{2\delta}. \tag{6.12}$$

The error in the computation of the derivative is on the order of δ^2, the square of the step size. To obtain an estimate of the derivative with less error, these derivatives were calculated using a four term central difference method [58], where the derivative is estimated by

$$\frac{\partial f}{\partial x} \approx \frac{-f(x+2\delta) + 8f(x+\delta) - 8f(x-\delta) + f(x-2\delta)}{12\delta}. \tag{6.13}$$

The errors associated with this method are on the order of δ^4.

A second method for computing the derivatives was also employed. This method implemented a FORTRAN routine from the Numerical Recipes collection, dfidr.f, which computes the derivative using Ridder's method and gives an estimate of the error in the computation of the derivative [50]. This method routinely computed derivatives with a relative error on the order of 10^{-4}. The four-term central difference method computed derivatives that had a 0.1% relative error with respect to the values calculated by the dfidr.f routine in approximately 30% less time. Both methods were used in these simulations, and the results are appropriately noted.

The algorithm for the computation of the derivatives for the two thickness method requires a two thickness method extraction for each function evaluation in (6.13). These extractions are similar to the method used in the modal analysis in Chapter 5. The theoretical reflection coefficients $S^{extr}_{11(1T)}$ and $S^{extr}_{11(2T)}$ are the same values used in Chapter 5 and are shown in Figure 5.14. These are used as the 'measured' values in the extraction algorithm. In an effort to obtain an accurate extraction, the extrapolation method was used to calculate $S^{thy}_{11(1T)}$ and $S^{thy}_{11(2T)}$ using the $TM_{1\,20}$

mode. The perturbation, or step size δ, was chosen to be 0.0005 for the magnitude, and 0.001 radians for the phase. These derivatives were then used in (6.8) - (6.11) to compute the standard deviation on each extracted parameter.

6.4.2 Confidence Interval

It is customary in the literature to use the calculated standard deviations to establish an uncertainty, or confidence interval, associated with the extracted parameters. These are commonly represented as error bars on the plots. Consider the plot of the Gaussian normal distribution shown in Figure 6.1. The area under the curve represented by $\pm\sigma$ of the mean value is 68% of the area, and the region $\pm 2\sigma$ within the mean contains 95% of the area. The 95% confidence interval is often used as a measure of the confidence one has in the measurement quantities obtained. In the following figures and analysis, error bars are plotted as the bounds $\pm 2\sigma$ of the extracted value, indicating that 95% of the extracted values should statistically lie within this interval.

6.5 Monte Carlo Method

A second method was also explored for this uncertainty analysis, known as the Monte Carlo method [56]. In order to compare the sensitivity analysis results from the two approaches, the Monte Carlo method was implemented using the two thickness method. The theoretical reflection coefficients for two thicknesses of Eccosorb FGM125, $S^{extr}_{11(1T)}$ and $S^{extr}_{11(2T)}$, are also the same values used in Chapter 5 and are shown in Figure 5.14. These values were used as the 'measured' values in the extraction algorithm.

Two sets of normally distributed random variables with the same statistical properties as those used in the standard error propagation method were generated by a process described in section 6.5.1. One set simulates the random measurement error present in the magnitude of the reflection coefficient measurement, while the other

simulates the random measurement error present in the phase measurement. These random variables were then added to the theoretical reflection coefficients. This simulates measurement error that may be present in an actual measurement. The material parameter extraction was then performed, and the extracted values were saved. This process was repeated multiple times, and a statistical analysis was performed on the data collection of extracted material parameter values. The result of this process is an estimate of the standard deviation, σ, for the real and imaginary parts of the permittivity and permeability.

The advantageous property of this method is its straightforward implementation. Random noise is generated and added to the theoretical reflection coefficients to simulate an actual measurement. However, in order to obtain an accurate statistical estimate of the standard deviation, a large number of extractions are required.

6.5.1 Normally distributed random noise generation

In order to obtain results that could be compared to those derived from the standard propagation of errors, it was necessary to generate zero mean normally distributed random numbers that had the same standard deviation as those derived from Figure 6.2. The estimate of the standard deviation of the phase error is $\sigma_\phi = 0.8°$. The standard deviation of the magnitude error is $\sigma_{|S_{11}|} = 0.004$.

A collection of normally distributed random variables with mean μ and standard deviation σ can be obtained by using the Box-Muller transformation [56]. If one has two independent, rectangularly distributed random numbers, A_1 and A_2, on an interval from 0 to 1, these can be used to obtain two zero mean normally distributed random numbers, B_1 and B_2. The numbers B_1 and B_2 have a standard deviation of

1, and are obtained by

$$B_1 = (-2\ln A_1)^{\frac{1}{2}} \cos(2\pi A_2) \tag{6.14}$$

$$B_2 = (-2\ln A_1)^{\frac{1}{2}} \sin(2\pi A_2). \tag{6.15}$$

When this process is repeated M times, a collection of $2M$ normally distributed variables with mean μ and standard deviation σ are then obtained as

$$R_{2m-1} = \mu + \sigma B_{1m} \tag{6.16}$$

$$R_{2m} = \mu + \sigma B_{2m}, \qquad m = 1, 2, ...M, \tag{6.17}$$

where B_{1m} and B_{2m} are B_1 and B_2 generated for the mth implementation of (6.14).

To generate these random numbers, a set of 10,000 uniformly distributed random numbers were obtained from a random number table generated from atmospheric noise [59]. These random numbers were then used in (6.14) - (6.17) to generate a random number set with a standard deviation of $\sigma = 0.004$ and a random number set with a standard deviation of $\sigma = 0.8 * \pi/180$. These correspond to the random error estimations used for the magnitude and phase, respectively, for S_{11} parameters.

Nominal Values	μ Monte Carlo	σ Monte Carlo	σ Standard Error Propagation
$\mu_r' = 0.575582$	0.577004	0.014722	0.012925
$\mu_r'' = 0.484231$	0.484055	0.010596	0.012636
$\epsilon_r' = 7.319669$	7.339548	0.126203	0.140503
$\epsilon_r'' = 0.046408$	0.045848	0.131749	0.107750

Table 6.2. Mean, μ, and standard deviation, σ, for the Monte Carlo method and standard deviation, σ, for the standard error propagation method of the two thickness method. Simulation was for two thicknesses of Eccossorb FGM125, 0.125" and 0.250" thick.

6.5.2 Comparison of the Monte Carlo method and the standard propagation of errors

The Monte Carlo Method was simulated at the middle of the X-band frequency range for the two thickness method, at 10.09 GHz. A total of 60 trials were performed using the two thickness method by adding the normally distributed random variables to $S^{extr}_{11(1T)}$ and $S^{extr}_{11(2T)}$. A histogram of the extracted parameters is shown in Figure 6.3. Note that the general shape of the histograms is a normal distribution. However, due to the limited sample size of 60, the shape of the curves is not the familiar bell curve shape for all of the parameters.

Equations (6.8) - (6.11) were then implemented to evaluate the standard deviation of the extracted material parameters due to random measurement errors using the two thickness method. Both methods carried out the extraction procedure using up to the $TM_{1\,20}$ mode and extrapolating. The comparison between the values obtained using the Monte Carlo method and the standard error propagation method is shown in Table 6.2.

Note that the values for the standard deviations are on the same order for each extracted parameter. However, the standard deviation values obtained with the Monte Carlo method do deviate from the derivative-based method by 10-20% with respect to the derivative-based method. One possible explanation for the differences is related to the number of simulations used in the Monte Carlo method. Only 60 extractions were run for the Monte Carlo method due to the extremely long simulation run times. Although the shape of the histogram in Figure 6.3 resembles a normal distribution, more trials would most likely cause the histogram to have a shape that more closely resembles the normal distribution. It was also observed that as the number of extractions was increased, the mean and standard deviation of the Monte Carlo method results moved closer to the nominal values for the material parameters and the standard deviation of the derivative method, respectively. An increased number

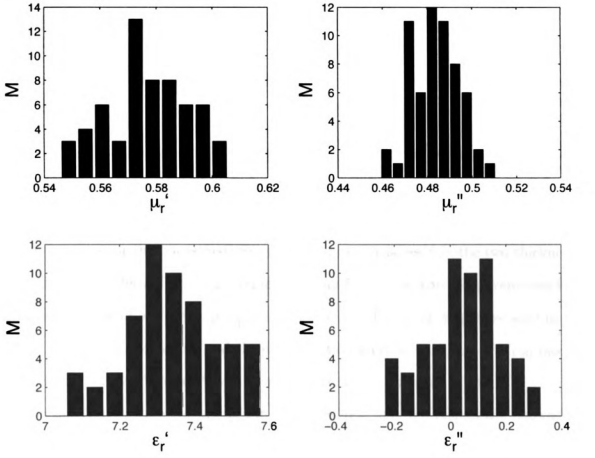


Figure 6.3. A histogram of the extracted parameters using the Monte Carlo Method. M is the number in each bin out of the 60 samples.

of simulations would consume a large amount of computational resources to obtain results that were comparable to those obtained via the derivative based results.

It is desirable to understand how the error in each measured quantity may affect the extracted parameter. In addition, it is also desirable to obtain the error sensitivity information in the least amount of computational time. Due to these two factors, the standard error propagation method is the preferred method of sensitivity analysis. It was used to further analyze the two layer method and the two thickness method.

6.6 Sensitivity Analysis for the Two Thickness Method and Two Layer Method

An error sensitivity analysis was implemented to compare the sensitivity of the two layer method and the two thickness method to random measurement error using (6.8) - (6.11). The derivatives for the two layer method extraction were calculated using the same values for the 'measured' S_{11} parameters as those used in the two thickness method. These values of S_{11}^{extr} are found in Figure 5.14. The material parameters for the known top layer are the values given in Table 5.1. The same step sizes were used for the magnitude and phase, and the extrapolation method using the $TM_{1\,20}$ mode was used for the two layer method in each function evaluation in (6.13).

The derivatives were calculated for both methods and the results are shown in Figure 6.4 - Figure 6.7. Consider Figure 6.4, which contains the derivatives found in (6.8) used to compute $\sigma_{\epsilon_r'}$. Note that the values of the derivatives for the two layer method are much larger for all four parameters at the lower end of the frequency band when compared to the two thickness method. Near 11.5 GHz the derivatives with respect to the magnitude are near in value to one another before diverging further at the higher frequencies. The derivatives with respect to phase are at least 10 times larger for most of the frequency band for the two layer method. Thus, it is expected that the standard deviation, $\sigma_{\epsilon_r'}$ is much larger for the two layer method than the

two thickness method.

The results of the error sensitivity analysis are shown in Figure 6.8 for two thicknesses of Eccosorb FGM125 using the two thickness and two layer methods at 21 frequency points across the range from 8.2 – 12.4 GHz. The error bars in the plots represent the 95% confidence interval, or the region that is $\pm 2\sigma$, for each of the respective methods. Consider the plot of the standard deviation, $\sigma_{\epsilon_r'}$. As expected from the derivatives, the uncertainties associated with the two thickness method are smaller than those for the two layer method. Note that near 11.5 GHz, the 95% confidence levels do not make a significant drop in value, even though $\partial\epsilon_r'/\partial|S_{11(1)}^{extr}|$ and $\partial\epsilon_r'/\partial|S_{11(2)}^{extr}|$ are near zero for the two layer method. It is thus clear that the largest amplifiers in (6.8) are the derivatives with respect to the phase.

A similar conclusion for $\sigma_{\epsilon_r''}$ is reached by examining Figure 6.5. Note that in these plots, the derivatives with respect to the phase are near zero for the two layer method near 11.5 GHz, and are the smallest at the upper end of the frequency band. When examining Figure 6.8, note that the error bars on the plot for $\sigma_{\epsilon_r''}$ are smallest for the two layer method at the upper end of the frequency band. This also agrees with the observation that the largest amplifiers are the derivatives with respect to the phase.

An examination of Figure 6.6 and Figure 6.7 shows some similar results. However, note that even though the derivatives for the two layer method are larger than the two thickness method, they have values that are much lower than the corresponding derivatives in Figure 6.4 - Figure 6.5. Most of the derivatives with respect to the single layer magnitude and phase have a value that is less than 10, and the other two derivatives have a value less than 50 for most of the frequency band. As can be seen in Figure 6.8, the standard deviations for the permeability are larger than the two thickness method, but smaller than the standard deviations computed for ϵ_r' and ϵ_r'' in the two layer method.

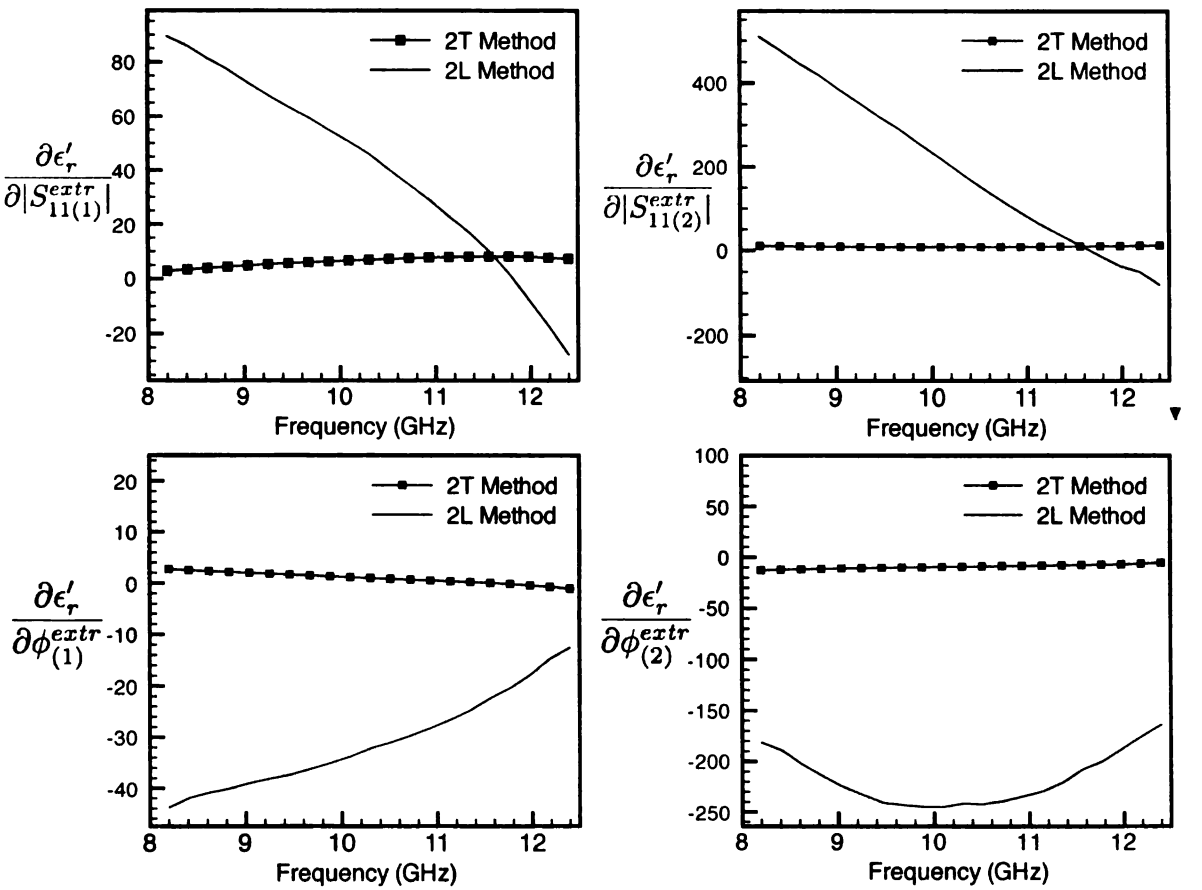


Figure 6.4. The derivatives calculated from 8.2 – 12.4GHz in the computation of $\sigma_{\epsilon_r'}$. Derivatives were calculated for the two layer and two thickness methods for two layers/thicknesses of Eccosorb FGM125, 0.125" thick and 0.250" thick.

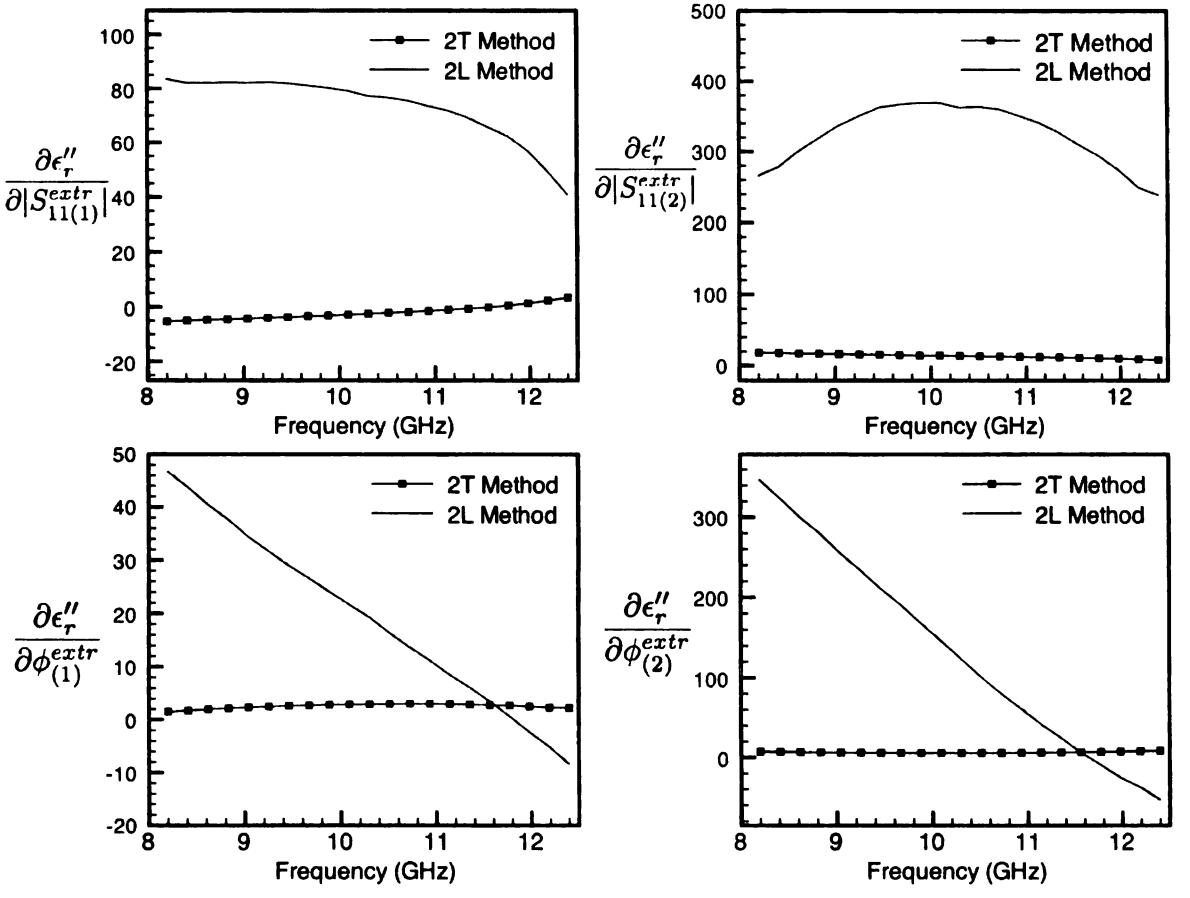


Figure 6.5. The derivatives calculated from 8.2 – 12.4GHz in the computation of $\sigma_{\epsilon_r''}$. Derivatives were calculated for the two layer and two thickness methods for two layers/thicknesses of Eccosorb FGM125, 0.125" thick and 0.250" thick.

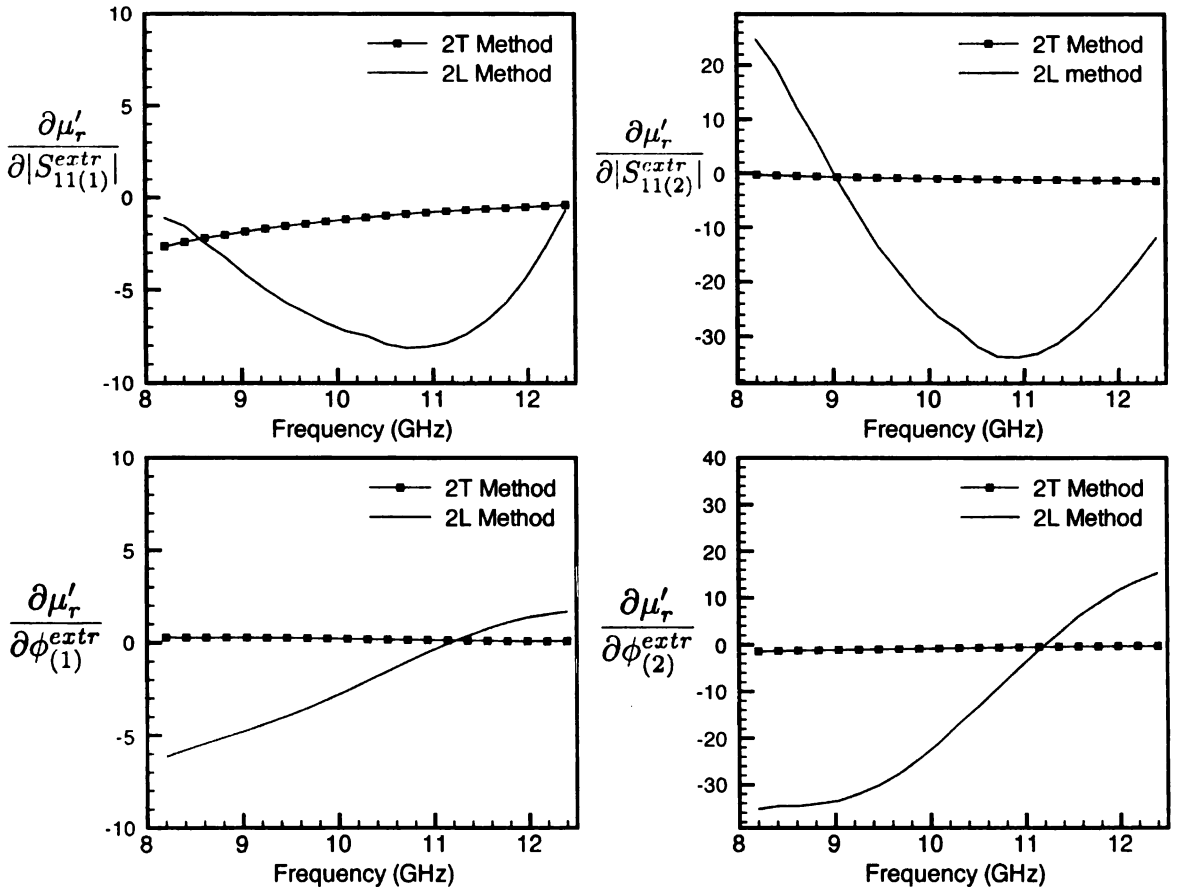


Figure 6.6. The derivatives calculated from 8.2 - 12.4GHz in the computation of $\sigma_{\mu_r'}$. Derivatives were calculated for the two layer and two thickness methods for two layers/thicknesses of Eccosorb FGM125, 0.125" thick and 0.250" thick.

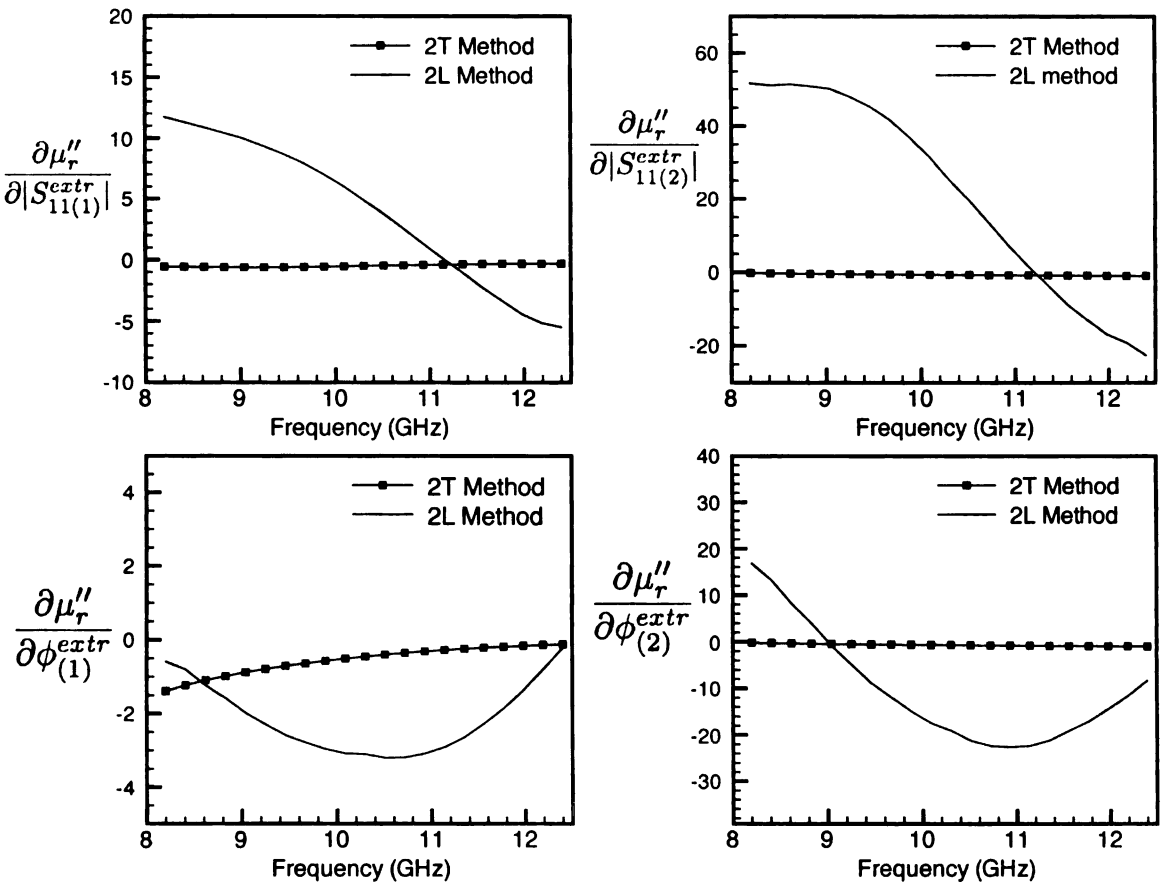


Figure 6.7. The derivatives calculated from 8.2 – 12.4GHz in the computation of $\sigma_{\mu_r''}$. Derivatives were calculated for the two layer and two thickness methods for two layers/thicknesses of Eccosorb FGM125, 0.125" thick and 0.250" thick.

6.7 Error sensitivity analysis results

Again consider the results of the error sensitivity analysis shown in Figure 6.8 for two thicknesses of Eccosorb FGM125 using the two thickness and two layer methods. These values were computed at 21 frequency points across the range from 8.2 – 12.4 GHz. Note that the error bars for the two layer method are much larger than those for the two thickness method for all four extracted parameters, ϵ_r', ϵ_r'', μ_r', and μ_r''. In fact, for ϵ_r'' and μ_r' in particular, some of the values within the bounds of the error bars are negative values, which represent non-physical material parameters. Extracted values consistently in the negative region will render the technique unusable in practical implementation.

This observation is in line with the calculated derivatives displayed in Figure 6.4 - Figure 6.7. This trend is consistent across the entire frequency band, although the ratio between the two methods does vary with respect to frequency. The 95% uncertainty levels at the high end of the frequency band for the two layer method show an improvement of more than 50% for ϵ_r'' and μ_r' over the lower end of the frequency band. However, even at these higher frequencies, the error bars are more than 10 times as large as the error bars for the two thickness method.

Recall that this analysis is only examining the sensitivity to random network analyzer measurement error. The identical values for S_{11}^{extr} were used in both methods as the 'measured' values. From the observations shown here, the two thickness method demonstrates a much more robust response to this measurement error than the two layer method when the measured material is Eccosorb FGM125, a magnetic radar absorbing material. Since the values for the standard deviation of the measurement error was identical for both methods, this analysis suggests that the extracted results from the two layer method would display a larger standard deviation. This amount of uncertainty in the extracted parameters may not be acceptable in many applications.

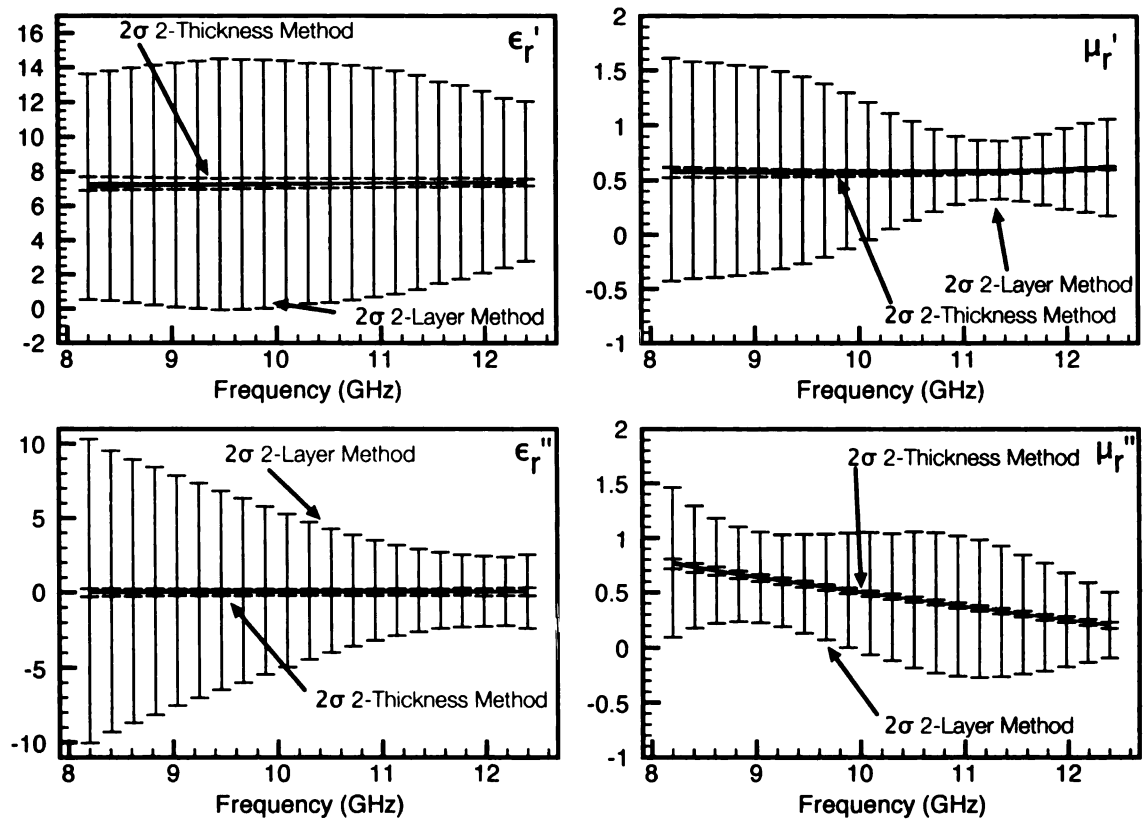


Figure 6.8. Sensitivity analysis for the two layer and two thickness methods for two layers of Eccosorb FGM125, 0.125" thick and 0.250" thick. Error bars show the 95% confidence level due to network analyzer uncertainty from an HP8510 network analyzer.

When this uncertainty analysis problem was first posed, the two thickness method appeared at first glance to be a special case of the two layer method. However, as was noted in section 2.6, some subtle differences exist between the two layer method and the two thickness method that are related to the algorithm and the Green's functions used in the calculation of S_{11}^{thy}.

Is is shown in Appendix C that the two layer parallel plate Green's function used in the two layer method reduces to the single layer parallel plate Green's function when both materials have the same material parameters. When both materials are not identical, two additional off-diagonal elements must be evaluated, and the diagonal elements are much more complicated to evaluate. From (4.17) - (4.20) all of the relevant elements are

$$\widetilde{G}_{xx}(k_x,k_y,z,z') = \frac{1}{j2\omega\mu_1 p_1}\cdot \left[e^{-p_1|z-z'|} + e^{p_1(z+z')} - 2\cosh p_1 z \cosh p_1 z' \frac{T_{ms}}{T_m} e^{-p_1 d_1}\right], \tag{6.18}$$

$$\widetilde{G}_{zx}(k_x,k_y,z,z') = \frac{-1}{j2\omega\mu_1 p_1}\cdot \left[jk_x\left(\frac{\mu_2\epsilon_2}{\mu_1\epsilon_1}-1\right)\frac{\sinh\left(2p_2\left(d_1-h\right)\right)}{p_1 T_m T_e}\cosh p_1 z' \sinh p_1 z\right], \tag{6.19}$$

$$\widetilde{G}_{yy}(k_x,k_y,z,z') = \frac{1}{j2\omega\mu_1 p_1}\cdot \left[e^{-p_1|z-z'|} + e^{p_1(z+z')} - 2\cosh p_1 z \cosh p_1 z' \frac{T_{ms}}{T_m} e^{-p_1 d_1}\right], \tag{6.20}$$

$$\widetilde{G}_{zy}(k_x,k_y,z,z') = \frac{-1}{j2\omega\mu_1 p_1}\cdot \left[jk_y\left(\frac{\mu_2\epsilon_2}{\mu_1\epsilon_1}-1\right)\frac{\sinh\left(2p_2\left(d_1-h\right)\right)}{p_1 T_m T_e}\cosh p_1 z' \sinh p_1 z\right]. \tag{6.21}$$

A possible explanation for the large differences in the sensitivity analysis results is related to the algorithms and the off-diagonal elements. Recall that the two thickness

method treats both layer 1 and layer 2 as if they are made of the same material. In the calculation of $S^{thy}_{11(1T)}$ and $S^{thy}_{11(2T)}$, only (6.18) and (6.20) are used, since (6.19) and (6.21) are zero when $\epsilon_1 = \epsilon_2$, and $\mu_1 = \mu_2$. In addition, the same guesses for ϵ and μ are used in the calculation of the theoretical reflection coefficients for both thicknesses of the material.

In the two layer method used in this simulation, as shown in Figure 2.2, the unknown values of the bottom layer, ϵ_2 and μ_2 , are first given an initial guess. These values are then used to calculate $S^{thy}_{11(1L)}$ in a manner identical to calculating $S^{thy}_{11(1T)}$ in the two thickness method, where only (6.18) and (6.20) are needed. When the second layer is added, the values of the top layer, ϵ_1, μ_1, are assumed to be identical to the nominal values used to generate $S^{extr}_{11(2L)}$. Therefore, these values contained no error to inject into the simulation. The same unknown values ϵ_2 and μ_2 used to calculate $S^{thy}_{11(1L)}$ are then used to calculate $S^{thy}_{11(2L)}$. As long as the initial guess is not the nominal values, the two layer method requires the computation of the off-diagonal elements shown in (6.19) and (6.21), even if the guess is quite close to the original. It should also be noted that the terms T_m, T_e, and T_{ms} also involve the ratios of the material parameters. The two layer method does continue to vary the material parameters ϵ_2 and μ_2. This requires the evaluation of (6.19) and (6.21) until the extracted values match the nominal values that were originally used to generate the reflection coefficient. The two layer method takes approximately 50% longer to evaluate than the two thickness method.

6.8 Sensitivity analysis for additional materials as a top layer

From the analysis in the previous section, it appears that when the bottom layer is Eccosorb FGM125, Eccosorb FGM125 is a poor choice for a top-layer material when using the two layer method. However, other materials may prove to reduce the network analyzer sensitivity to acceptable levels for use in practical *in situ* mea-

surements. To investigate this possibility, additional simulations were undertaken to examine other materials for use as the top layer in the two layer method.

Recall that the theoretical reflection coefficients for two layers of material were calculated in section 5.5 for plexiglass, PVC, nylon, and Eccosorb FGM40 as the top layer, respectively, with Eccosorb FGM125 as the bottom layer. Plots of these reflection coefficients are shown in Figure 5.16 - Figure 5.19. Using these values of $S^{extr}_{11(2L)}$ in the two layer method as the 'measured' values, the standard error propagation method was performed to obtain the standard deviation of the extracted material parameters. The derivatives for each of these layer configurations were calculated using the four-term central difference method, and the standard deviation for each was computed using (6.8) - (6.11) in the middle of the frequency band, at 10.09 GHz. A comparison of the standard deviations for different top layers using the two layer method is shown in Figure 6.9. Each plot is normalized to the standard deviation of the two thickness method for that parameter.

In Figure 6.9, note that a top layer of FGM40 has a larger standard deviation in all four plots than FGM125, indicating that the parameters extracted using this as a known layer are even more sensitive to network analyzer measurement errors. Also notice that the plastic materials, plexiglass, nylon, PVC, and a fictional high loss dielectric with ϵ'_r values the same as plexiglass, referred to here as a lossy form of plexiglass, produce standard deviations that are much lower than when the top layer is composed of FGM125. The standard deviations on the extracted parameters for these materials are roughly 3 to 5 times as large as the two thickness method. Note that the high loss version of plexiglass has standard deviations that are greater than plexiglass. Thus although these materials with a low dielectric constant appear to be not as robust as the two thickness method, they demonstrate an uncertainty in the extracted parameters that may be acceptable for some applications. These materials are investigated in Chapter 9 as the top layer in the two layer method experimental

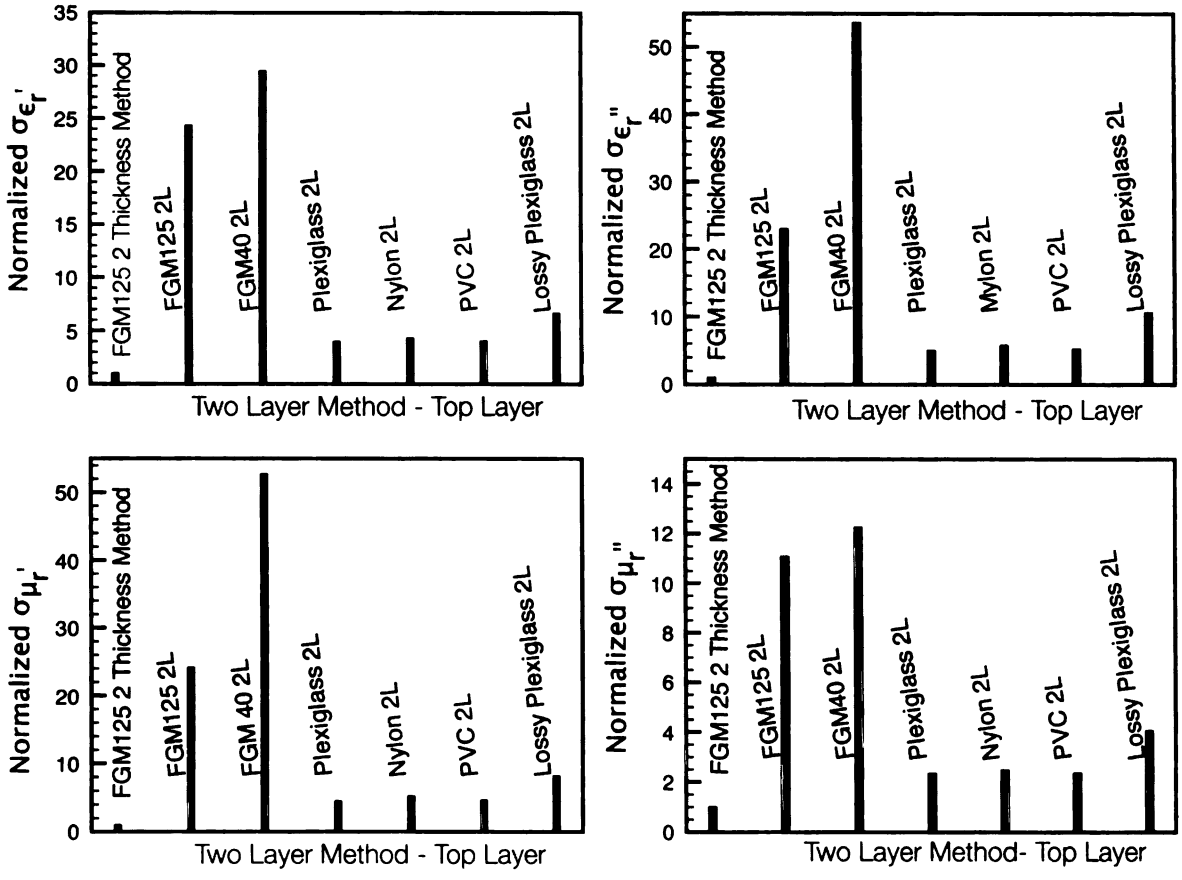


Figure 6.9. Normalized standard deviation of the two layer method using different layers for the top layer. The following thicknesses are used for the top layer: FGM125 = 0.125", FGM40 = .040", Plexiglass = 0.125", Nylon = 0.125", PVC = 0.119". Bottom layer is Eccosorb FGM 125, 0.125" thick. Each plot is normalized to the two thickness method for comparison.

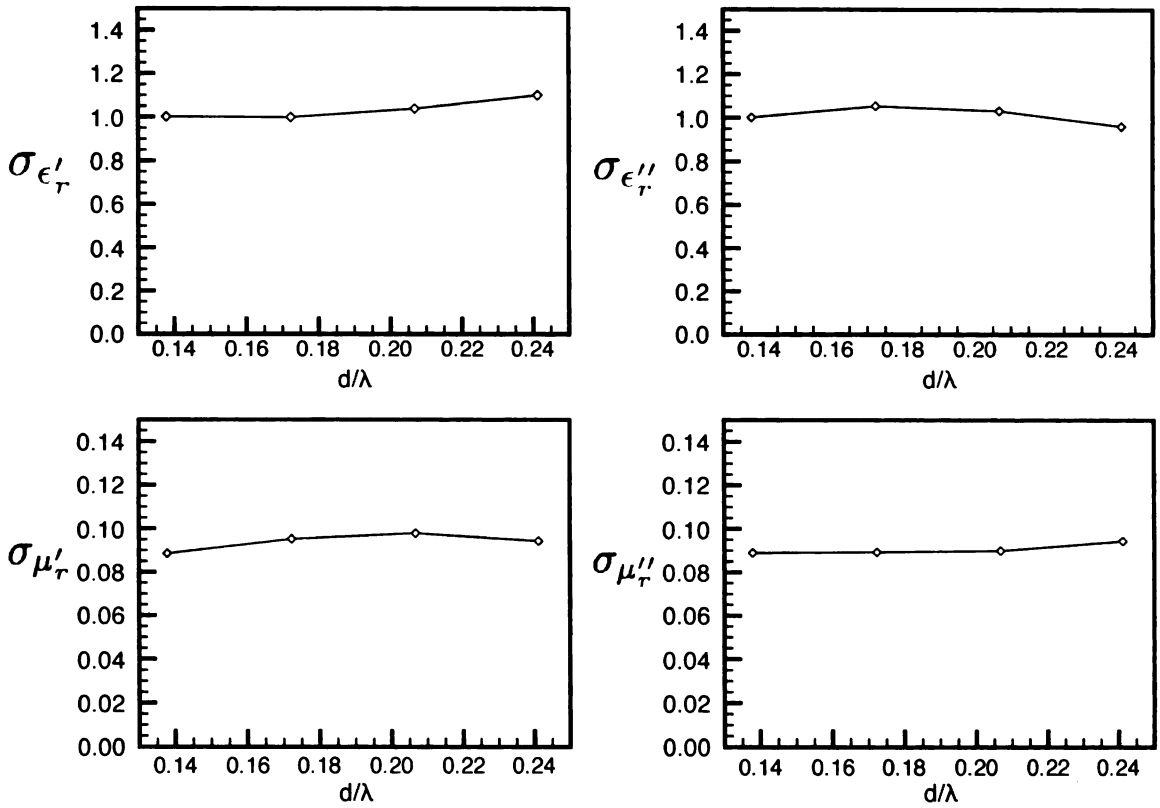


Figure 6.10. Standard deviation of the two layer method using different thicknesses for a top layer of Plexiglass at 10.09 GHz. The bottom layer was simulated as 0.125" of Eccosorb FGM125.

results.

6.9 Variations in thicknesses

The simulations in section 6.8 reveal that the choice of low dielectric constant materials for the top layer resulted in the lowest sensitivity to random measurement error for the two layer method. The thickness chosen for those simulations was 0.125", primarily because it is a standard thickness available from plastic manufacturers. However, it is possible that different thicknesses of the same material may provide less sensitivity to noise.

An additional investigation was undertaken to examine the error sensitivity of

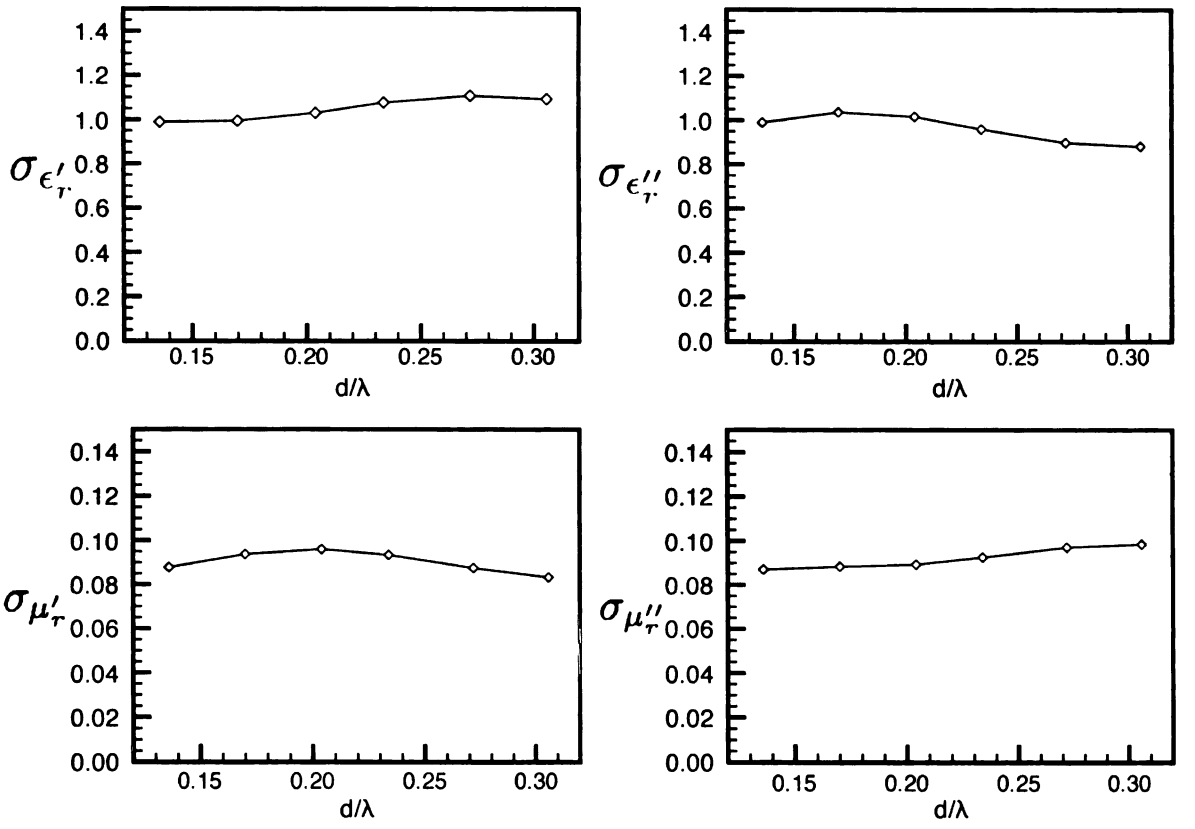


Figure 6.11. Standard deviation of the two layer method using different thicknesses for a top layer of Rexolite at 10.09 GHz. The bottom layer was simulated as 0.125" of Eccosorb FGM125.

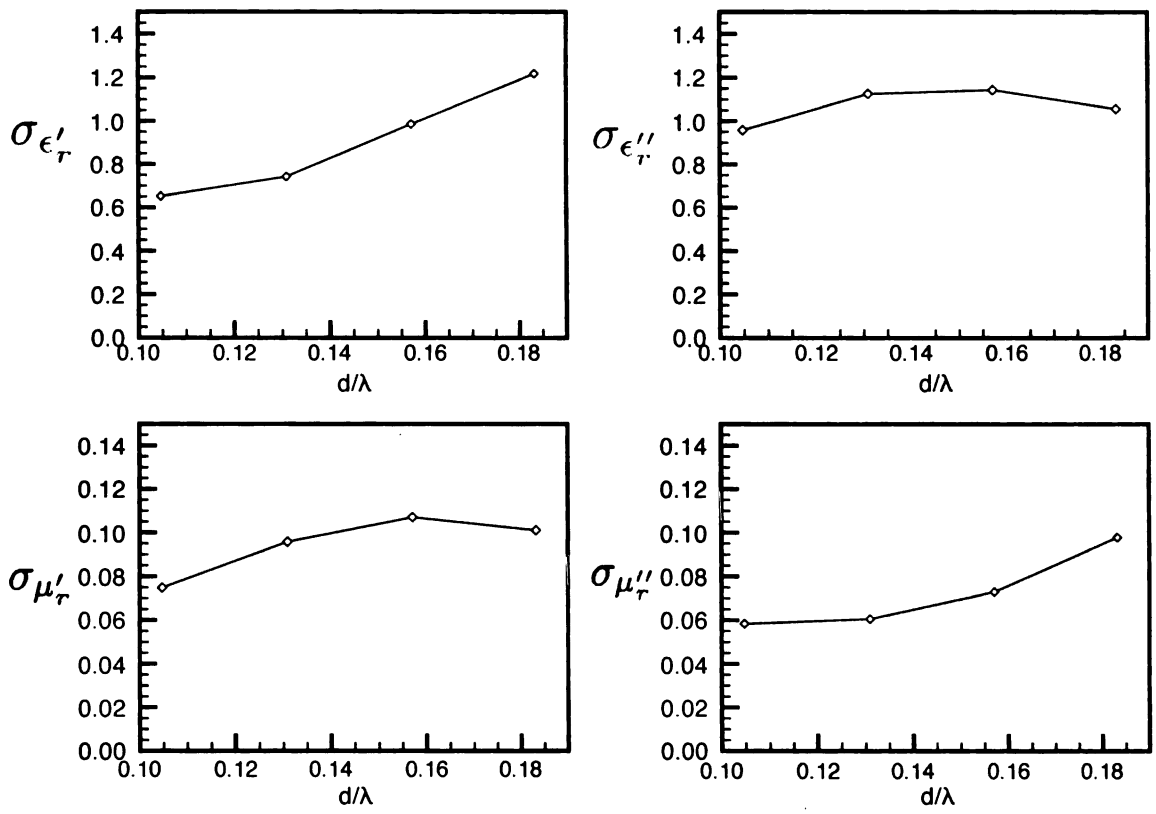


Figure 6.12. Standard deviation of the two layer method using different thicknesses for a top layer of Material 1.5 at 10.09 GHz. The bottom layer was simulated as 0.125" of Eccosorb FGM125.

the two layer method using varying thicknesses of different materials for the top layer. To save computational time, the theoretical reflection coefficient, $S^{thy}_{11(1L)}$, for one layer of Eccosorb FGM125, 0.125" thick, was generated using only the first four modes, instead of the extrapolation method. The reflection coefficient for two layers of material, $S^{thy}_{11(2L)}$, was also generated using the first four modes for three different materials. Simulations showed that the calculation of the derivatives used in (6.8) - (6.11) using only the first four modes were within 1% of the derivative values calculated using the extrapolation method. These derivatives were calculated using the FORTRAN routine dfirdr.f for this analysis.

Since the error sensitivity shown in Figure 6.9 indicates that materials with the lower dielectric constant show the least sensitivity to error, three different low dielectric materials were examined for their sensitivity to random measurement error. This analysis was performed for different thicknesses of the material at 10.09 GHz, and these results are shown in Figure 6.10 - Figure 6.12. The material parameters used to generate these results are shown in Appendix F.

Note that in each figure, the standard deviation for each of the extracted parameters is displayed as a function of the electrical thickness of the material. The error sensitivity of plexiglass, displayed in Figure 6.10, does not change appreciably with respect to the electrical thickness. This is true for all four subplots shown in the figure. The error sensitivity of Rexolite, shown in Figure 6.11, shows some slight variations in the results. The values for $\sigma_{\mu_r'}$ and $\sigma_{\epsilon_r''}$ show a slight improvement when the top layer is thicker, while the values for $\sigma_{\mu_r''}$ and $\sigma_{\epsilon_r'}$ show slightly better results when the layer is thinner. However, there is not a very large difference between the different thickness of Rexolite for this analysis.

The third material examined in this set of simulations is for a fictional low loss material, named Material 1.5 for these simulations. As seen in Appendix F, the material was simulated as having a dielectric constant of $\epsilon_r' = 1.5$ across the frequency

band, with a small varying amount of loss. The general trend of all four subplots found in Figure 6.12 is that the smaller thicknesses of the material appeared to have less sensitivity to random measurement error. The values for $\sigma_{\epsilon_r'}$ show an increase of about 100% when the thickness is increased from approximately 0.10 λ to 0.18 λ. In practice, however, small thicknesses of such a material might be impractical for use, and the material must be thick enough for the single layer and two layer measurements to be independent.

6.10 Error Sensitivity Conclusions

This error analysis has examined the two thickness method and two layer method for their sensitivity to random measurement error. The two thickness method appears to be a rather robust material parameter extraction method, with low sensitivity to random measurement errors when the material under test is Eccosorb FGM125. When the extraction is performed using the two layer method on the same two thicknesses of Eccosorb FGM125, a much higher sensitivity to random noise is observed in the simulations. However, when a low loss dielectric plastic material was used as the top layer in the two layer method, the standard deviation of the extracted parameters is closer to the values observed for the two thickness method. An examination of different thicknesses of low loss, low dielectric constant materials provided no clear insight regarding an optimal thickness of the top layer material.

These simulations suggest that an experiment that employs the two thickness method for two thicknesses of Eccosorb FGM125 should provide an estimate of the material parameters that is least sensitive to random measurement errors. The two layer method is more sensitive to random measurement error. If a low dielectric constant material is used as the top layer in the two layer method, such as PVC or plexiglass, experimental data should be 3-6 times more sensitive to random measurement error than for the two thickness method. This may be an acceptable error

criterion for some applications. These observations are taken into consideration for the design and execution of the proof of concept experiment examined in Chapter 9.

CHAPTER 7

TWO IRIS METHOD

7.1 Introduction

Recall from the discussion of the two layer method and the two thickness method in Chapter 2 that two complex measurements are required to solve for the complex permittivity ϵ, and permeability, μ, of the material. Both of those methods utilize two different reflection coefficient measurements with an open-ended flanged waveguide probe. In this chapter, the theoretical background is laid for a technique which uses two independent measurements obtained with two different apertures, or irises, at the end of a flanged X-band waveguide. This technique is described here as the two iris method.

7.2 Two Iris Algorithm

The algorithm used in the two iris method is similar to that used in the general approach taken in formulating the two thickness method and two layer method in Chapter 2. In the two iris method, one complex measurement, $S_{11(1)}^{meas(2I)}$, of a single layer of material is obtained using a flanged waveguide probe with an aperture of set dimensions, Aperture 1. A second measurement, $S_{11(2)}^{meas(2I)}$, is obtained using a second probe with a different aperture, Aperture 2.

The theoretical reflection coefficients for Aperture 1, $S_{11(1)}^{thy(2I)}$, and Aperture 2, $S_{11(2)}^{thy(2I)}$, are calculated using the formulation described in section 7.3. Two functions are then constructed, one for each aperture,

$$\begin{aligned} f_{Ap1}(\epsilon_1, \mu_1,) &= S_{11(1)}^{meas(2I)} - S_{11(1)}^{thy(2I)} \\ g_{Ap2}(\epsilon_1, \mu_1) &= S_{11(2)}^{meas(2I)} - S_{11(2)}^{thy(2I)}. \end{aligned} \tag{7.1}$$

These functions are then minimized simultaneously using a root search method similar to that employed in (2.7).

In this chapter, the formulation for the theoretical reflection coefficient is presented, as well as computational considerations associated with the computation of the reflection coefficient.

7.3 Problem Formulation

Consider the geometry shown in Figure 7.1. A single layer of conductor-backed material, with permittivity ϵ_1 and permability μ_1, is interrogated by a single open-ended flanged waveguide probe. The material is assumed to be of a known thickness, linear, isotropic, homogeneous, and infinite in the transverse directions. The probe has a reduced aperture at the end of the waveguide, which is of width A_x in the x-direction and heightA_y in the y-direction. The aperture has a thickness of d_2 in the axial direction of the waveguide. The top view of the waveguide with the reduced aperture opening, Ω_{ap}, is shown in Figure 7.2. The flange and conductor are assumed to be PEC surfaces, infinite in the transverse directions.

7.3.1 Waveguide and Aperture Fields

It is assumed that the dominant TE_{10} mode is the only propagating mode which interrogates the waveguide discontinuity caused by the reduced aperture. The incident electric and magnetic fields in the waveguide are given by

$$\vec{E}_i^{wg}(\vec{r}) = a_1^i \vec{e}_1^{wg}(\vec{\rho}) e^{jk_{z1}^{wg}(z-d_2)} \tag{7.2}$$

$$\vec{H}_i^{wg}(\vec{r}) = -a_1^i \vec{h}_1^{wg}(\vec{\rho}) e^{jk_{z1}^{wg}(z-d_2)}, \tag{7.3}$$

where a_1^i is the complex amplitude of the incident wave, d_2 is the thickness of the aperture in the axial direction. The term k_{zn}^{wg} is the axial wavenumber for propagation in the waveguide, and is given by (2.3) . The transverse waveguide functions for the

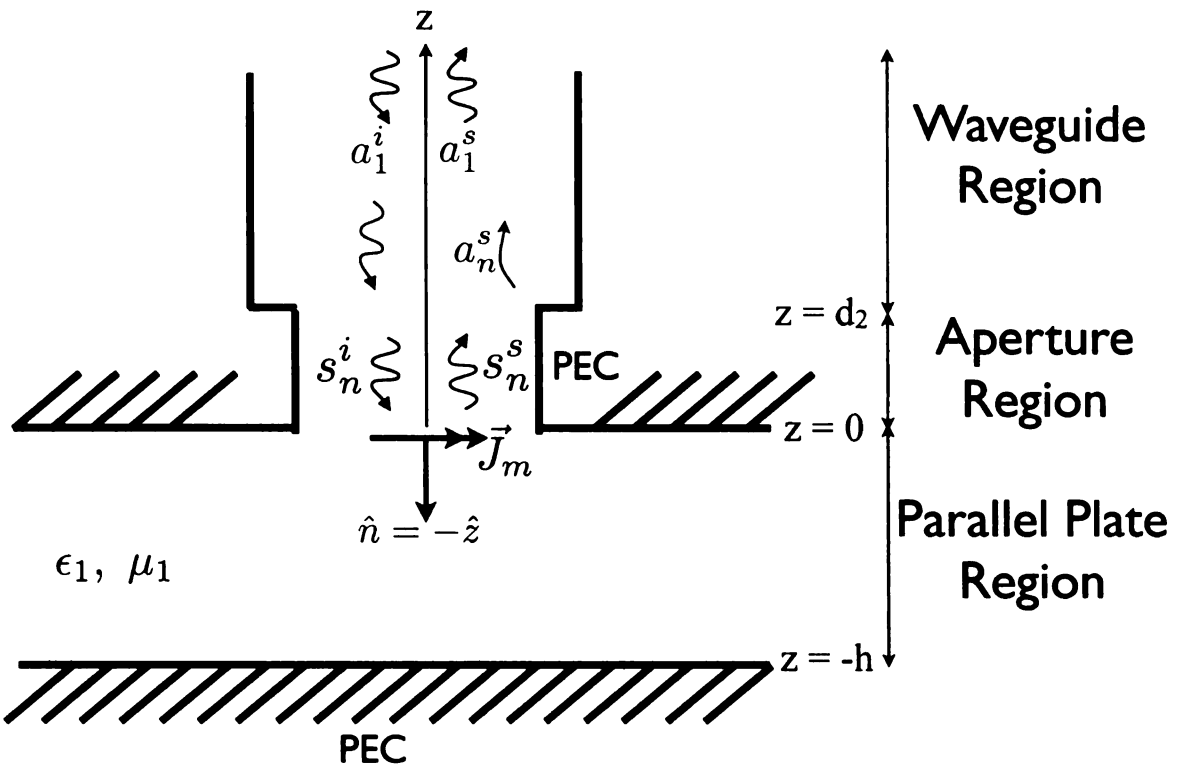


Figure 7.1. Side view for a single layer of material interrogated by a reduced aperture waveguide probe.

n^{th} mode are denoted by $\vec{e}_n^{wg}(\vec{\rho})$ and $\vec{h}_n^{wg}(\vec{\rho})$, and are found in (A.1)-(A.2) and (A.7)-(A.8). In (7.2), $n = 1$, which corresponds to the incident TE_{10} mode.

As the incident wave enters the aperture region, an infinite number of modes are excited at the waveguide discontinuity at $z = d_2$, and propagate toward the parallel plate region. As these modes interrogate the material, and reflect back into the waveguide region, multiple waveguide modes are excited in the aperture region and the waveguide. The scattered waveguide modes are denoted by the amplitudes a_n^s in Figure 7.1. The transverse scattered electric and magnetic fields in the waveguide region are approximated using N modes. Using the transverse waveguide function

representation, the expression for the electric and magnetic fields in the waveguide is

$$\vec{E}_s^{wg}(\vec{r}) = \sum_{n=1}^{N} a_n^s \vec{e}_n^{wg}(\vec{\rho}) e^{-jk_{zn}^{wg}(z-d_2)}, \quad 0 \le z \le d_2, \quad \vec{\rho} \in CS \tag{7.4}$$

$$\vec{H}_s^{wg}(\vec{r}) = \sum_{n=1}^{N} a_n^s \vec{h}_n^{wg}(\vec{\rho}) e^{-jk_{zn}^{wg}(z-d_2)}, \quad 0 \le z \le d_2, \quad \vec{\rho} \in CS. \tag{7.5}$$

Thus, in the waveguide region, $z > d_2$, the total transverse fields are described as

$$\vec{E}_t^{wg}(\vec{r}) = a_1^i \vec{e}_1^{wg}(\vec{\rho}) e^{jk_{z1}^{wg}(z-d_2)} + \sum_{n=1}^{N} a_n^s \vec{e}_n^{wg}(\vec{\rho}) e^{-jk_{zn}^{wg}(z-d_2)},$$
$$0 \le z \le d_2, \quad \vec{\rho} \in CS \tag{7.6}$$

$$\vec{H}_t^{wg}(\vec{r}) = -a_1^i \vec{h}_1^{wg}(\vec{\rho}) e^{jk_{z1}^{wg}(z-d_2)} + \sum_{n=1}^{N} a_n^s \vec{h}_n^{wg}(\vec{\rho}) e^{-jk_{zn}^{wg}(z-d_2)},$$
$$0 \le z \le d_2, \quad \vec{\rho} \in CS. \tag{7.7}$$

These are valid for the cross sectional surface of the waveguide, CS, in the region $0 \le x \le a$, $0 \le y \le b$.

The electric and magnetic fields in the aperture region may also be approximated by using a finite number of modes, denoted here as M. The number M does not have to be the same as the number of modes in the waveguide region, N. Using a representation similar to the waveguide region representation for the total electric and magnetic fields in the aperture region yields

$$\vec{E}_t^{ap}(\vec{r}) = \sum_{p=1}^{M} s_p^i \vec{e}_p^{ap}(\vec{\rho}) e^{jk_{zp}^{ap} z} + \sum_{p=1}^{M} s_p^s \vec{e}_p^{ap}(\vec{\rho}) e^{-jk_{zp}^{ap} z}, \quad 0 \le z \le d_2, \quad \vec{\rho} \in \Omega_{ap} \tag{7.8}$$

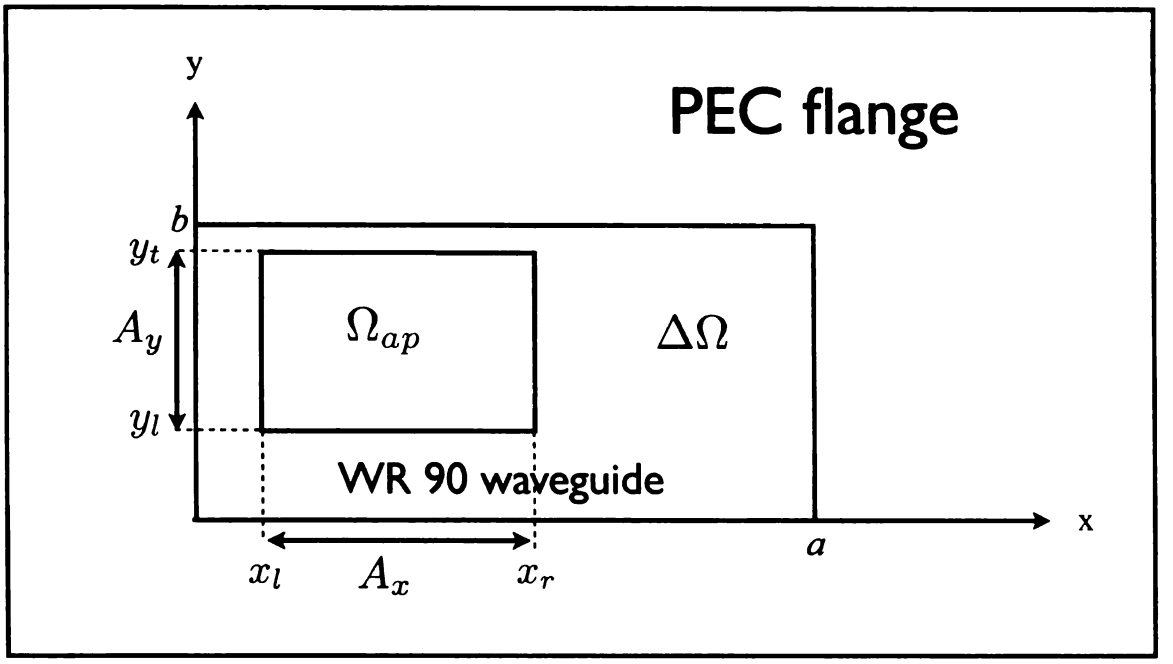


Figure 7.2. Top view for a single layer of material interrogated by a reduced aperture waveguide probe.

$$\vec{H}_t^{ap}(\vec{r}) = -\sum_{p=1}^{M} s_p^i \vec{h}_p^{ap}(\vec{\rho}) e^{jk_{zp}^{ap} z} + \sum_{p=1}^{M} s_p^s \vec{h}_p^{ap}(\vec{\rho}) e^{-jk_{zp}^{ap} z}, \quad 0 \le z \le d_2, \quad \vec{\rho} \in \Omega_{ap} \tag{7.9}$$

Here, s_p^i and s_p^s, are the complex amplitudes for the downward and upward traveling waves, respectively, in the aperture region. The cross sectional surface of the aperture is defined in the region

$$\Omega_{ap} \in \{x_l \le x \le x_r, \quad y_l \le y \le y_t\}. \tag{7.10}$$

Note that $\vec{e}_p^{ap}(\vec{\rho}), \vec{h}_p^{ap}(\vec{\rho})$, and k_{zp}^{ap} are the transverse field distribution functions and axial wavenumber for the pth mode, respectively, in the aperture region. The axial

wavenumber in the aperture region for the pth mode is denoted by

$$k_{zp}^{ap} = \sqrt{k_0^2 - k_{Axp}^2 - k_{Ayp}^2}. \tag{7.11}$$

where $k_{Axp} = \frac{u_p \pi}{A_x}$ and $k_{Ayp} = \frac{v_p \pi}{A_y}$. The transverse waveguide mode functions are given in (E.1), (E.2), (E.6), and (E.7). The variables u_p and v_p correspond to the indices (u, v) for a TE_{uv} wave in the aperture region if the pth mode is TE_z, or a TM_{uv} wave in the aperture region if the pth mode is TM_z.

7.4 Parallel Plate Fields

In the parallel plate region, Love's equivalence principle is used to create an equivalent problem where the field in the aperture opening is replaced by an equivalent magnetic current against a PEC parallel plate. By a procedure similar to that shown in chapter 2, the magnetic field is expressed in terms of magnetic Hertzian potentials. The magnetic field in the parallel plate region is given by

$$\vec{H}_t^{pp(2I)}(\vec{\rho}, z=0) = (k_1^2 + \nabla_t \nabla \cdot) \int_{\Omega_{ap}} \bar{\bar{G}}_{1L}^{pp}(\vec{\rho}|\vec{\rho}'; z|, z'=0) \cdot \left(\hat{z} \times \vec{E}_t^{ap}(\vec{\rho}', z'=0)\right) ds' \Big|_{z=0}. \tag{7.12}$$

This is similar to the expression for the magnetic field in the parallel plate region found in (2.31). However, note that the Green's function employed in (7.12) is the single-layer parallel plate Green's function, whose elements are given by (C.11).

7.5 Matching Boundary Conditions

The desired result of this formulation is the theoretical reflection coefficient for a given aperture,

$$S_{11}^{thy(2I)} = \frac{a_1^s}{a_1^i}. \tag{7.13}$$

Note that three sets of unknown amplitude coefficients, a_n^s, s_n^i, and s_n^s, are found in (7.6)-(7.9). To solve for these constants, three sets of coupled equations are employed. At the boundary $z = d_2$, a mode matching approach is taken for the electric and magnetic fields. At $z = 0$, a MFIE is established by matching tangential magnetic fields from the aperture region and the parallel plate region. The MFIE is similar to the MFIE formulated for the two layer method.

7.5.1 Matching Tangential Electric Fields at $z = d_2$

The first equation to be established is derived from the continuity of tangential electric field at the boundary $z = d_2$. Using the expressions for the tangential electric fields found in (7.6) and (7.8) and setting them equal to each other at the boundary $z = d_2$, yields

$$a_1^i \vec{e}_1^{wg}(\vec{\rho}) + \sum_{n=1}^{N} a_n^s \vec{e}_n^{wg}(\vec{\rho}) = \begin{cases} \sum_{n=1}^{N} s_n^i \vec{e}_n^{ap}(\vec{\rho}) e^{jk_{zn}^{ap} d_2} + \sum_{n=1}^{N} s_n^s \vec{e}_n^{ap}(\vec{\rho}) e^{-jk_{zn}^{ap} d_2}, & \vec{\rho} \in \Omega_{ap}. \\ 0, & \vec{\rho} \in \Delta\Omega \end{cases} \tag{7.14}$$

For simplicity of formulation, it has been chosen to set $M = N$ so that an equal number of modes are used in the both the aperture and waveguide regions to describe the transverse fields. Note that the region $\Delta\Omega$ is the region in the waveguide aperture that is not covered by the cross sectional area of the aperture region, as shown in Figure 7.2. Since it is a PEC surface, the tangential electric field on $\Delta\Omega$ is known to be zero [60], [61].

It is desirable to use this boundary condition equation with the other boundary conditions to establish a matrix equation which may be solved for the unknown

amplitudes. Applying the testing operator $\int_{CS} \vec{e}_m^{wg}(\vec{\rho}) \cdot \{\}ds$ to (7.14) yields

$$a_1^i \int_{CS} \vec{e}_m^{wg}(\vec{\rho}) \cdot \vec{e}_1^{wg}(\vec{\rho})ds + \sum_{n=1}^{N} \int_{CS} a_n^s \vec{e}_m^{wg}(\vec{\rho}) \cdot \vec{e}_n^{wg}(\vec{\rho})ds = \sum_{n=1}^{N} \int_{\Omega_{ap}} s_n^i \vec{e}_m^{wg}(\vec{\rho}) \cdot \vec{e}_n^{ap}(\vec{\rho}) e^{jk_{zn}^{ap} d_2} ds + \sum_{n=1}^{N} \int_{\Omega_{ap}} s_n^s \vec{e}_m^{wg}(\vec{\rho}) \cdot \vec{e}_n^{ap}(\vec{\rho}) e^{-jk_{zn}^{ap} d_2} ds. \quad (7.15)$$

The orthogonality properties of the waveguide mode functions are shown in (2.10). When these orthogonality properties are utilized, (7.15) becomes

$$a_1^i \delta_{m1} + \sum_{n=1}^{N} a_n^s \delta_{mn} = \sum_{n=1}^{N} \left[s_n^i e^{jk_{zn}^{ap} d_2} + s_n^s e^{-jk_{zn}^{ap} d_2} \right] \int_{\Omega_{ap}} \vec{e}_m^{wg}(\vec{\rho}) \cdot \vec{e}_n^{ap}(\vec{\rho})ds, \quad (7.16)$$

where,

$$\delta_{mn} = \begin{cases} 1, & m = n \\ 0, & m \neq n \end{cases}. \quad (7.17)$$

This equation is used with the two other equations to establish a matrix solution for the coupled mode matching and MFIE equations.

7.5.2 Matching Tangential Magnetic Fields at $z = d_2$

The continuity of tangential magnetic field is also enforced at the boundary $z = d_2$:

$$\vec{H}_t^{ap}(\vec{\rho}, z = d_2) = \vec{H}_t^{wg}(\vec{\rho}, z = d_2). \quad (7.18)$$

Using the expression for the tangential magnetic fields found in (7.7) and (7.9), and setting $z = d_2$, yields

$$-a_1^i \vec{h}_1^{wg}(\vec{\rho}) + \sum_{n=1}^{N} a_n^s \vec{h}_n^{wg}(\vec{\rho}) = \\ -\sum_{n=1}^{N} s_n^i \vec{h}_n^{ap}(\vec{\rho}) e^{jk_{zn}^{ap} d_2} + \sum_{n=1}^{N} s_n^s \vec{h}_n^{ap}(\vec{\rho}) e^{-jk_{zn}^{ap} d_2}, \qquad \vec{\rho} \in \Omega_{ap}. \quad (7.19)$$

For simplicity of formulation, it has been chosen to set $M = N$ so that an equal number of modes are used in the both the aperture and waveguide regions to describe the transverse fields. Applying the testing operator $\int_{\Omega_{ap}} \vec{h}_m^{ap}(\vec{\rho}) \cdot \{\}ds$ to (7.19) yields

$$-a_1^i \int_{\Omega_{ap}} \vec{h}_m^{ap}(\vec{\rho}) \cdot \vec{h}_1^{wg}(\vec{\rho}) ds + \sum_{n=1}^{N} a_n^s \int_{\Omega_{ap}} \vec{h}_m^{ap}(\vec{\rho}) \cdot \vec{h}_n^{wg}(\vec{\rho}) ds = \\ -\sum_{n=1}^{N} s_n^i e^{jk_{zn}^{ap} d_2} \int_{\Omega_{ap}} \vec{h}_m^{ap}(\vec{\rho}) \cdot \vec{h}_n^{ap}(\vec{\rho}) ds + \quad (7.20) \\ \sum_{n=1}^{N} s_n^s e^{-jk_{zn}^{ap} d_2} \int_{\Omega_{ap}} \vec{h}_m^{ap}(\vec{\rho}) \cdot \vec{h}_n^{ap}(\vec{\rho}) ds.$$

The transverse waveguide mode functions for the aperture region have the same orthogonality properties as the mode functions for the waveguide region. Thus, the integrals on the right hand side may be rewritten as

$$\int_{\Omega_{ap}} \vec{h}_m^{ap}(\vec{\rho}) \cdot \vec{h}_n^{ap}(\vec{\rho}) ds = \frac{1}{Z_m^{ap} Z_n^{ap}} \delta_{mn}, \quad (7.21)$$

where Z_p^{ap} is the directional impedance in the aperture region for mode number p. If the pth mode in the aperture is TE_z, then Z_p^{ap} is given by (E.3). If the pth mode in

the aperture is TM_z, then Z_p^{ap} is given by (E.8). Using (7.21), (7.20) is written as

$$-a_1^i \int_{\Omega_{ap}} \vec{h}_m^{ap}(\vec{\rho}) \cdot \vec{h}_1^{wg}(\vec{\rho}) ds + \sum_{n=1}^{N} a_n^s \int_{\Omega_{ap}} \vec{h}_m^{ap}(\vec{\rho}) \cdot \vec{h}_n^{wg}(\vec{\rho}) ds =$$
$$\sum_{n=1}^{N} \left[s_n^s e^{-jk_{zn}^{ap} d_2} - s_n^i e^{jk_{zn}^{ap} d_2} \right] \frac{1}{Z_m^{ap} Z_n^{ap}} \delta_{mn}, \qquad \vec{\rho} \in \Omega_{ap}. \quad (7.22)$$

Note that the integrals on the left hand side must be evaluated over the cross section of the aperture. The details of this evaluation are addressed in section 7.6.

7.5.3 Matching Tangential Magnetic Fields at $z = 0$

The third equation is obtained by forming an MFIE at the boundary between the aperture region and the parallel plate region. The details of this equation are quite similar to the establishment of the MFIE given in section 2.5, and this section follows a similar procedure. In the two iris method, the tangential magnetic fields are set equal to each other. Applying $\vec{H}_t^{ap}(\vec{\rho}, z = 0) = \vec{H}_t^{pp(2I)}(\vec{\rho}, z = 0)$ from (7.9) and (7.12) yields

$$-\sum_{n=1}^{N} s_p^i \vec{h}_p^{ap}(\vec{\rho}) + \sum_{n=1}^{N} s_p^s \vec{h}_p^{ap}(\vec{\rho})$$
$$= (k_1^2 + \nabla_t \nabla \cdot) \int_{\Omega_{ap}} \bar{\bar{G}}_{1L}^{pp}(\vec{\rho}|\vec{\rho}'; z|z' = 0) \cdot \left(\hat{z} \times \vec{E}_t^{ap}(\vec{\rho}', z' = 0) \right) ds' \Big|_{z=0}$$
$$\vec{\rho} \in \Omega_{ap} \quad (7.23)$$

The expression for the tangential electric field in the aperture given in (7.8) can be evaluated at $z = 0$, which yields

$$\vec{E}_t^{ap}(\vec{\rho}, z = 0) = \sum_{n=1}^{N} \left[s_n^i + s_n^s \right] \vec{e}_n^{ap}(\vec{\rho}). \quad (7.24)$$

Substituting (7.24) into (7.23),

$$-\sum_{n=1}^{N}\left[s_n^i - s_n^s\right]\vec{h}_n^{ap}(\vec{\rho}) =$$

$$(k_1^2 + \nabla_t\nabla\cdot)\int_{\Omega_{ap}} \bar{\bar{G}}_{1L}^{pp}(\vec{\rho}|\vec{\rho}';z|z'=0)\cdot\left(\hat{z}\times\sum_{n=1}^{N}\left[s_n^i + s_n^s\right]\vec{e}_n^{ap}(\vec{\rho}')\right)ds'\Bigg|_{z=0} \quad (7.25)$$

Recall that the the transverse electric and magnetic mode functions in the aperture region have the same relationship as the mode functions in the waveguide region, namely

$$Z_n^{ap}\vec{h}_n^{ap}(\vec{\rho}) = \hat{z}\times\vec{e}_n^{ap}(\vec{\rho}). \quad (7.26)$$

Thus, the cross product on the right hand side of (7.25) may be replaced by $Z_n^{ap}\vec{h}_n^{ap}(\vec{\rho})$. Note that (7.25) now has the aperture magnetic field transverse mode function, $\vec{h}_n^{ap}(\vec{\rho})$, on both sides of the equation. This allows the waveguide mode function orthogonality properties to again be utilized. Applying the testing operator $\int_{\Omega_{ap}}\vec{h}_m^{ap}(\vec{\rho})\cdot\{\}ds$ to (7.25) yields

$$-\sum_{n=1}^{N}\left[s_n^i - s_n^s\right]\int_{\Omega_{ap}}\vec{h}_m^{ap}(\vec{\rho})\cdot\vec{h}_n^{ap}(\vec{\rho})ds = \int_{\Omega_{ap}}\vec{h}_m^{ap}(\vec{\rho})\cdot\Bigg[Z_n^{ap}\sum_{n=1}^{N}(k_1^2+\nabla_t\nabla\cdot)$$

$$\int_{\Omega'_{ap}}\bar{\bar{G}}_{1L}^{pp}(\vec{\rho}|\vec{\rho}';z|z'=0)\cdot\left(\left[s_n^i + s_n^s\right]\vec{h}_n^{ap}(\vec{\rho}')\right)ds'\Bigg]_{z=0}ds. \quad (7.27)$$

The first integral on the left hand side is known from (7.21). Some additional algebraic manipulation allows (7.27) be rewritten as

$$\sum_{n=1}^{N}s_n^i\left[\frac{1}{Z_m^{ap}Z_n^{ap}}\delta_{mn} + \int_{\Omega_{ap}}\vec{h}_m^{ap}(\vec{\rho})\cdot\vec{h}_n^{pp(2I)}(\vec{\rho})ds\right] -$$

$$\sum_{n=1}^{N}s_n^s\left[\frac{1}{Z_m^{ap}Z_n^{ap}}\delta_{mn} - \int_{\Omega_{ap}}\vec{h}_m^{ap}(\vec{\rho})\cdot\vec{h}_n^{pp(2I)}(\vec{\rho})ds\right] = 0, \quad (7.28)$$

where

$$\vec{h}_n^{pp(2I)}(\vec{\rho}) = Z_n^{ap}\,(k_1^2 + \nabla_t\nabla\cdot)\int_{\Omega_{ap}} \bar{\bar{G}}_{1L}^{pp}(\vec{\rho}|\vec{\rho}';z|z'=0)\cdot\vec{h}_n^{ap}(\vec{\rho}')ds'\Big|_{z=0}. \quad (7.29)$$

7.6 Matrix Equation

The two mode matching equations, (7.16) and (7.22), and the MFIE equation found in (7.28), contain combinations of the coefficients a_n^s, s_n^i, and s_n^s. These coupled equations can be written in matrix form, $D\cdot a = b$, or

$$\left[\begin{array}{c|c|c} D_1 & D_2 & D_3 \\ \hline D_4 & D_5 & D_6 \\ \hline D_7 & D_8 & D_9 \end{array}\right]\cdot\left[\begin{array}{c} a^s \\ \hline s^i \\ \hline s^s \end{array}\right] = \left[\begin{array}{c} b_1 \\ \hline b_2 \\ \hline b_3 \end{array}\right], \quad (7.30)$$

where each of the sub-matrices, D_q, is an $N\times N$ matrix. In this formulation, the size of each sub-matrix is governed by the choice to set $M = N$ in (7.14) and (7.19). If $M \neq N$, then each sub-matrix would be of a different size. Equation (7.16) is contained in the first row, and includes the sub-matrices D_1 through D_3. Equations (7.22) and (7.28) occupy the second and third rows. Thus, the full size of the matrix D is $3N\times 3N$. The composition of the matrices is as follows: D_1 is -1 times an $N\times N$ identitiy matrix, or

$$D_{1_{mn}} = -\delta_{mn}. \quad (7.31)$$

D_2 is a full matrix, where the elements are given by

$$D_{2_{mn}} = e^{jk_{zn}^{ap}d_2}\int_{\Omega_{ap}} \vec{e}_m^{wg}(\vec{\rho})\cdot\vec{e}_n^{ap}(\vec{\rho})ds. \quad (7.32)$$

The structure of D_3 is similarly a full matrix. The elements are given by

$$D_{3_{mn}} = e^{-jk_{zn}^{ap}d_2} \int_{\Omega_{ap}} \vec{e}_m^{wg}(\vec{\rho}) \cdot \vec{e}_n^{ap}(\vec{\rho}) ds. \tag{7.33}$$

D_4 is also a full matrix, with each element representing the coupling between the mth transverse magnetic field function in the aperture with the nth transverse magnetic field function in the waveguide. The elements are given by

$$D_{4_{mn}} = \int_{\Omega_{ap}} \vec{h}_m^{ap}(\vec{\rho}) \cdot \vec{h}_n^{wg}(\vec{\rho}) ds. \tag{7.34}$$

The sub-matrices, D_5 and D_6 are diagonal matrices, where each element calculates the phase change or decay each mode undergoes in the aperture region. The elements are described by

$$D_{5_{mn}} = \frac{e^{jk_{zm}^{ap}d_2}}{Z_m^{ap} Z_n^{ap}} \delta_{mn} \tag{7.35}$$

and

$$D_{6_{mn}} = -\frac{e^{-jk_{zm}^{ap}d_2}}{Z_m^{ap} Z_n^{ap}} \delta_{mn}. \tag{7.36}$$

Matrix D_7 is a zero matrix, and matrices D_8 and D_9 are full matrices. The elements of D_8 are given by

$$D_{8_{mn}} = \frac{\delta_{mn}}{Z_m^{ap} Z_n^{ap}} + \int_{\Omega_{ap}} \vec{h}_m^{ap}(\vec{\rho}) \cdot \vec{h}_n^{pp}(\vec{\rho}) ds. \tag{7.37}$$

Similarly, the elements of D_9 are given by

$$D_{9_{mn}} = -\frac{\delta_{mn}}{Z_m^{ap} Z_n^{ap}} + \int_{\Omega_{ap}} \vec{h}_m^{ap}(\vec{\rho}) \cdot \vec{h}_n^{pp}(\vec{\rho}) ds. \tag{7.38}$$

The formulation of each of the matrix elements described in (7.31) - (7.38) requires

that three integrals be computed,

$$\int_{\Omega_{ap}} \vec{e}_m^{wg}(\vec{\rho}) \cdot \vec{e}_n^{ap}(\vec{\rho}) ds \tag{7.39}$$

$$\int_{\Omega_{ap}} \vec{h}_m^{ap}(\vec{\rho}) \cdot \vec{h}_n^{wg}(\vec{\rho}) ds \tag{7.40}$$

$$\int_{\Omega_{ap}} \vec{h}_m^{ap}(\vec{\rho}) \cdot \vec{h}_n^{pp}(\vec{\rho}) ds. \tag{7.41}$$

Each of these integrals can have four different possible mode combinations, since the mth and n^{th} modes may be either TE_z or TM_z. In order to simplify the derivation in this chapter, the first case of each integral is evaluated in Appendix E. Each of the other cases is straightforward to evaluate, and the solution is presented in this chapter. Once the matrix elements have been calculated, the matrix can be filled and solved for the amplitude coefficients, a_n^s, s_n^i, and s_n^s.

7.6.1 Right hand side

The right hand side of (7.30) is composed of the three column vectors, b_1, b_2, and b_3, each of length N. The first vector is given by

$$b_{1m} = a_1^i \delta_{m1}, \qquad m = 1, 2, ...N. \tag{7.42}$$

The elements of the second vector are obtained by evaluating the integral

$$b_{2m} = a_1^i \int_{\Omega_{ap}} \vec{h}_m^{ap}(\vec{\rho}) \cdot \vec{h}_1^{wg}(\vec{\rho}) ds, \qquad m = 1, 2, ...N. \tag{7.43}$$

The elements of the third vector are zero:

$$b_{3m} = 0, \qquad m = 1, 2, ...N. \tag{7.44}$$

The evaluation of the integral used in (7.43) is identical to the first column of the matrix D_4. Thus, when the elements of D_4 are calculated once for the matrix, the elements of that first column may then be duplicated in the vector b_2.

7.6.2 Evaluation of $\int_{\Omega_{ap}} \vec{e}_m^{wg}(\vec{\rho}) \cdot \vec{e}_n^{ap}(\vec{\rho})\, ds$ used in D_2 and D_3

The integral in (7.39) is computed in four possible ways, depending on the combinations of TE and TM modes.

7.6.2.1 Case 1, $TE^{wg}_{um\,vm} \cdot TE^{ap}_{un\,vn}$

The first possible combination is the coupling of the TE_z mode in the waveguide with the TE_z mode in the aperture. The evaluation of the integral for the first case is obtained in section E.3.1 of Appendix E, and it is given as

$$\int_{\Omega_{ap}} \vec{e}_m^{wg(TE)}(\vec{\rho}) \cdot \vec{e}_n^{ap(TE)}(\vec{\rho}) ds = K^{wg}_{um\,vm} K^{ap}_{un\,vn} \cdot$$
$$\Big\{ k_{ym} k_{Ayn} \Phi_1(k_{xm}, 0, k_{Axn}, -k_{Axn} x_l, x_l, x_r) \Phi_2(k_{ym}, 0, k_{Ayn}, -k_{Ayn} y_l, y_l, y_t)$$
$$- k_{xm} k_{Axn} \Phi_1(k_{ym}, 0, k_{Ayn}, -k_{Ayn} y_l, y_l, y_t) \Phi_2(k_{xm}, 0, k_{Axn}, -k_{Axn} x_l, x_l, x_r) \Big\}. \tag{7.45}$$

The functions Φ_1 and Φ_2 are found in (E.35) and (E.36).

7.6.2.2 Case 2, $TE^{wg}_{um\,vm} \cdot TM^{ap}_{un\,vn}$

The second possible combination is the coupling of the TE_z mode in the waveguide with the TM_z mode in the aperture. By using the waveguide mode function in (A.1) and the aperture mode function in (E.6), the evaluation of the integral for the second

case is

$$\int_{\Omega_{ap}} \vec{e}_m^{\,wg(TE)}(\vec{\rho}) \cdot \vec{e}_n^{\,ap(TM)}(\vec{\rho}) ds = -K^{wg}_{um\,vm} N^{ap}_{un\,vn} \cdot$$
$$\Big\{ k_{ym} k_{Axn} \Phi_1(k_{xm}, 0, k_{Axn}, -k_{Axn} x_l, x_l, x_r) \Phi_2(k_{ym}, 0, k_{Ayn}, -k_{Ayn} y_l, y_l, y_t)$$
$$- k_{xm} k_{Ayn} \Phi_1(k_{ym}, 0, k_{Ayn}, -k_{Ayn} y_l, y_l, y_t) \Phi_2(k_{xm}, 0, k_{Axn}, -k_{Axn} x_l, x_l, x_r) \Big\}. \tag{7.46}$$

7.6.2.3 Case 3, $TM^{wg}_{um\,vm} \cdot TE^{ap}_{un\,vn}$

The third possible combination is the coupling of the TM_z mode in the waveguide with the TE_z aperture mode. Employing the waveguide mode function in (A.7) and the aperture mode function in (E.1) produces the third case integral evaluation, which is given by

$$\int_{\Omega_{ap}} \vec{e}_m^{\,wg(TM)}(\vec{\rho}) \cdot \vec{e}_n^{\,ap(TE)}(\vec{\rho}) ds = -N^{wg}_{um\,vm} K^{ap}_{un\,vn} \cdot$$
$$\Big\{ k_{xm} k_{Ayn} \Phi_1(k_{xm}, 0, k_{Axn}, -k_{Axn} x_l, x_l, x_r) \Phi_2(k_{ym}, 0, k_{Ayn}, -k_{Ayn} y_l, y_l, y_t)$$
$$- k_{ym} k_{Axn} \Phi_1(k_{ym}, 0, k_{Ayn}, -k_{Ayn} y_l, y_l, y_t) \Phi_2(k_{xm}, 0, k_{Axn}, -k_{Axn} x_l, x_l, x_r) \Big\}. \tag{7.47}$$

7.6.2.4 Case 4, $TM^{wg}_{um\,vm} \cdot TM^{ap}_{un\,vn}$

The fourth possible combination is the coupling of the TM_z mode in the waveguide with the TM_z aperture mode. Using the waveguide mode function in (A.7) and the

aperture mode function in (E.1), the integral in the fourth case is given by

$$\int_{\Omega_{ap}} \vec{e}_m^{wg(TM)}(\vec{\rho}) \cdot \vec{e}_n^{ap(TE)}(\vec{\rho}) ds = N^{wg}_{um\,vm} N^{ap}_{un\,vn} \cdot$$
$$\Big\{ k_{xm} k_{Axn} \Phi_1(k_{xm}, 0, k_{Axn}, -k_{Axn} x_l, x_l, x_r) \Phi_2(k_{ym}, 0, k_{Ayn}, -k_{Ayn} y_l, y_l, y_t)$$
$$+ k_{ym} k_{Ayn} \Phi_1(k_{ym}, 0, k_{Ayn}, -k_{Ayn} y_l, y_l, y_t) \Phi_2(k_{xm}, 0, k_{Axn}, -k_{Axn} x_l, x_l, x_r) \Big\}. \tag{7.48}$$

7.6.3 Evaluation of $\int_{\Omega_{ap}} \vec{h}_m^{ap}(\vec{\rho}) \cdot \vec{h}_n^{wg}(\vec{\rho}) ds$ used in D_4 and b_2

The integral found in (7.40) is necessary to fill the matrix D_4 and the right hand side vector b_2. This integral also is evaluated in four possible ways due to the combinations of TM_z modes and TE_z modes.

7.6.3.1 Case 1, $TE^{ap}_{um\,vm} \cdot TE^{wg}_{un\,vn}$

The second possible combination of transverse magnetic mode functions is the coupling of the TE_z aperture mode with the TM_Z waveguide mode. The evaluation of the integral for Case 1 is obtained in section E.3.2 of Appendix E, and it is given by

$$\int_{\Omega_{ap}} \vec{h}_m^{ap}(\vec{\rho}) \cdot \vec{h}_n^{wg}(\vec{\rho}) ds = \frac{K^{ap}_{um\,vm}}{Z_m^{ap(TE)}} \frac{K^{wg}_{un\,vn}}{Z_n^{wg(TE)}} \cdot$$
$$\Big\{ k_{xn} k_{Axm} \Phi_1(k_{Aym}, -k_{Aym} y_l, k_{yn}, 0, y_l, y_t) \Phi_2(k_{Axm}, -k_{Axm} x_l, k_{xn}, 0, x_l, x_r)$$
$$+ k_{yn} k_{Aym} \Phi_1(k_{Axm}, -k_{Axm} x_l, k_{xn}, 0, x_l, x_r) \Phi_2(k_{Aym}, -k_{Aym} y_l, k_{yn}, 0, y_l, y_t) \Big\}. \tag{7.49}$$

7.6.3.2 Case 2, $TE^{ap}_{um\,vm} \cdot TM^{wg}_{un\,vn}$

The second possible combination of transverse magnetic mode functions is the coupling of the TE_z aperture mode with the TM_Z waveguide mode. Making use of the waveguide mode functions in (E.2) and (A.8), the integral for the second case is given

by

$$\int_{\Omega_{ap}} \vec{h}_m^{ap}(\vec{\rho}) \cdot \vec{h}_n^{wg}(\vec{\rho}) ds = \frac{K_{um\,vm}^{ap}}{Z_m^{ap(TE)}} \frac{N_{un\,vn}^{wg}}{Z_n^{wg(TM)}} \cdot$$
$$\Big\{ k_{yn} k_{Axm} \Phi_1(k_{Aym}, -k_{Aym} y_l, k_{yn}, 0, y_l, y_t) \Phi_2(k_{Axm}, -k_{Axm} x_l, k_{xn}, 0, x_l, x_r)$$
$$- k_{xn} k_{Aym} \Phi_1(k_{Axm}, -k_{Axm} x_l, k_{xn}, 0, x_l, x_r) \Phi_2(k_{Aym}, -k_{Aym} y_l, k_{yn}, 0, y_l, y_t) \Big\}. \tag{7.50}$$

7.6.3.3 Case 3, $TM_{um\,vm}^{ap} \cdot TE_{un\,vn}^{wg}$

The third combination of transverse magnetic mode functions includes the TM_z aperture mode and the TE_z waveguide mode. The waveguide mode functions in (E.7) and (A.2) may then be used in the expression for the integral for the third case, which is

$$\int_{\Omega_{ap}} \vec{h}_m^{ap}(\vec{\rho}) \cdot \vec{h}_n^{wg}(\vec{\rho}) ds = \frac{N_{um\,vm}^{ap}}{Z_m^{ap(TM)}} \frac{K_{un\,vn}^{wg}}{Z_n^{wg(TE)}} \cdot$$
$$\Big\{ k_{xn} k_{Aym} \Phi_1(k_{Aym}, -k_{Aym} y_l, k_{yn}, 0, y_l, y_t) \Phi_2(k_{Axm}, -k_{Axm} x_l, k_{xn}, 0, x_l, x_r)$$
$$- k_{yn} k_{Axm} \Phi_1(k_{Axm}, -k_{Axm} x_l, k_{xn}, 0, x_l, x_r) \Phi_2(k_{Aym}, -k_{Aym} y_l, k_{yn}, 0, y_l, y_t) \Big\}. \tag{7.51}$$

7.6.3.4 Case 4, $TM_{um\,vm}^{ap} \cdot TM_{un\,vn}^{wg}$

The fourth possible combination is the coupling of the TM_z mode in the aperture with the TM_z waveguide mode. Using the waveguide mode function in (E.7) and the

aperture mode function in (A.8), the fourth case integral expression is given by

$$\int_{\Omega_{ap}} \vec{h}_m^{ap}(\vec{\rho}) \cdot \vec{h}_n^{wg}(\vec{\rho}) ds = \frac{N_{un\,vm}^{ap}}{Z_m^{ap(TM)}} \frac{N_{un\,vn}^{wg}}{Z_n^{wg(TM)}} \cdot$$
$$\Big\{ k_{xn} k_{Aym} \Phi_1(k_{Aym}, -k_{Aym} y_l, k_{yn}, 0, y_l, y_t) \Phi_2(k_{Axm}, -k_{Axm} x_l, k_{xn}, 0, x_l, x_r)$$
$$+ k_{yn} k_{Axm} \Phi_1(k_{Axm}, -k_{Axm} x_l, k_{xn}, 0, x_l, x_r) \Phi_2(k_{Aym}, -k_{Aym} y_l, k_{yn}, 0, y_l, y_t) \Big\}. \tag{7.52}$$

7.6.4 Evaluation of $\int_{\Omega_{ap}} \vec{h}_m^{ap}(\vec{\rho}) \cdot \vec{h}_n^{pp}(\vec{\rho})\, ds$ used in D_8 and D_9

The third integral to be evaluated is found in (7.41), and it is needed to fill the matrices D_8 and D_9. Recall that these matrices are the result of the formulation of the MFIE as the third boundary condition equation. The calculation of each of the matrix elements is similar to the matrix element calculation in the two layer method which is detailed in Chapter 4. Thus this formulation follows a similar process to the one in that chapter.

7.6.4.1 Integral formulation

Rewriting (7.41) results in

$$D_{8mn}^{pp} = \int_{\Omega_{ap}} \vec{h}_m^{ap}(\vec{\rho}) \cdot \vec{h}_n^{pp}(\vec{\rho}) ds$$
$$= Z_n^{ap} \int_{\Omega_{ap}} \vec{h}_m^{ap}(\vec{\rho}) \cdot (k_1^2 + \nabla_t \nabla \cdot) \int_{\Omega_{ap}} \bar{\bar{G}}_{1L}^{pp}(\vec{\rho}|\vec{\rho}'; z|z'=0) \cdot \vec{h}_n^{ap}(\vec{\rho}') ds' ds \Big|_{z=0.} \tag{7.53}$$

The single layer Green's function is a diagonal dyadic $\bar{\bar{G}}_{1L}^{pp}(\vec{r}|\vec{r}') = \hat{x}\hat{x} G_{xx(1L)}(\vec{r}|\vec{r}') + \hat{y}\hat{y} G_{yy(1L)}(\vec{r}|\vec{r}') + \hat{z}\hat{z} G_{zz(1L)}(\vec{r}|\vec{r}')$. Since the mode function is in the transverse direction, the only elements that are used are the $\hat{x}\hat{x} G_{xx(1L)}(\vec{r}|\vec{r}')$ and the $\hat{y}\hat{y} G_{yy(1L)}(\vec{r}|\vec{r}')$ elements.

The aperture and waveguide mode functions may be decomposed into their scalar

components, producing

$$\vec{h}_m^{wg}(\vec{\rho}) = \hat{x}h_{xm}^{wg}(\vec{\rho}) + \hat{y}h_{ym}^{wg}(\vec{\rho}) \tag{7.54}$$

$$\vec{h}_m^{ap}(\vec{\rho}) = \hat{x}h_{xm}^{ap}(\vec{\rho}) + \hat{y}h_{ym}^{ap}(\vec{\rho}). \tag{7.55}$$

The function $\vec{h}_n^{pp}(\vec{\rho})$ found in (7.29) can also be decomposed into its scalar components, yielding

$$\vec{h}_n^{pp}(\vec{\rho}) = \hat{x}h_{xn}^{pp}(\vec{\rho}) + \hat{y}h_{yn}^{pp}(\vec{\rho}). \tag{7.56}$$

By using the expression found in (4.12) and using it in (7.29), the scalar components of the parallel plate transverse function are

$$\begin{aligned} h_{xn}^{pp}(\vec{\rho}) =& Z_n^{ap}\left[\left(k_1^2 + \frac{\partial^2}{\partial x^2}\right)\int_{\Omega_{ap}} G_{xx(1L)}(\vec{\rho}, z|\vec{\rho}', z')h_{xn}^{ap}(\vec{\rho}')ds'\right. \\ &\left. + \frac{\partial^2}{\partial x \partial y}\int_{\Omega_{ap}} G_{yy(1L)}(\vec{\rho}, z|\vec{\rho}', z')h_{yn}^{ap}(\vec{\rho}')ds'\right]_{z=0,z'=0} \end{aligned} \tag{7.57}$$

$$\begin{aligned} h_{yn}^{pp}(\vec{\rho}) =& Z_n^{ap}\left[\frac{\partial^2}{\partial x \partial y}\int_{\Omega_{ap}} G_{xx(1L)}(\vec{\rho}, z|\vec{\rho}', z')h_{xn}^{ap}(\vec{\rho}')ds'\right. \\ &\left. + \left(k_1^2 + \frac{\partial^2}{\partial y^2}\right)\int_{\Omega_{ap}} G_{yy(1L)}(\vec{\rho}, z|\vec{\rho}', z')h_{yn}^{ap}(\vec{\rho}')ds'\right]_{z=0,z'=0} \end{aligned} \tag{7.58}$$

Using the Fourier Transform relationship that is given by (4.16), (7.57) can be rewrit-

ten as

$$h_{xn}^{pp}(\vec{\rho}) = Z_n^{ap}\Bigg[\left(k_1^2 + \frac{\partial^2}{\partial x^2}\right)\cdot \int\limits_{\Omega_{ap}} \frac{1}{(2\pi)^2}\int\limits_{-\infty}^{+\infty}\!\!\!\!\int \widetilde{G}_{xx(1L)}(k_x,k_y,z,z')e^{j\vec{k}\cdot(\vec{\rho}-\vec{\rho}')}dk_xdk_y \;\; h_{xn}^{ap}(\vec{\rho}')ds' + \frac{\partial^2}{\partial x\partial y}\int\limits_{\Omega_{ap}} \frac{1}{(2\pi)^2}\int\limits_{-\infty}^{+\infty}\!\!\!\!\int \widetilde{G}_{yy(1L)}(k_x,k_y,z,z')e^{j\vec{k}\cdot(\vec{\rho}-\vec{\rho}')}dk_xdk_y \;\; h_{yn}^{ap}(\vec{\rho}')ds'\Bigg]_{z=0,z'=0}. \tag{7.59}$$

By interchanging the integral operators, this equation can be rearranged as

$$h_{xn}^{pp}(\vec{\rho}) = \frac{Z_n^{ap}}{4\pi^2}\Bigg[\left(k_1^2 + \frac{\partial^2}{\partial x^2}\right)\cdot \int\limits_{-\infty}^{+\infty}\!\!\!\!\int \widetilde{G}_{xx(1L)}(k_x,k_y,z,z')e^{j\vec{k}\cdot\vec{\rho}}dk_xdk_y \int_{\Omega_{ap}} h_{xn}^{ap}(\vec{\rho}')e^{-j\vec{k}\cdot\vec{\rho}'}ds' + \frac{\partial^2}{\partial x\partial y}\int\limits_{-\infty}^{+\infty}\!\!\!\!\int \widetilde{G}_{yy(1L)}(k_x,k_y,z,z')e^{j\vec{k}\cdot\vec{\rho}}dk_xdk_y \int_{\Omega_{ap}} h_{yn}^{ap}(\vec{\rho}')e^{-j\vec{k}\cdot\vec{\rho}'}ds'\Bigg]_{z=0,z'=0}. \tag{7.60}$$

To simplify this expression, two functions are defined as

$$f_{xn}^{ap}(k_x,k_y) = \int_{\Omega_{ap}} h_{xn}^{ap}(\vec{\rho}')e^{-j\vec{k}\cdot\vec{\rho}'}ds' \tag{7.61}$$

$$f_{yn}^{ap}(k_x,k_y) = \int_{\Omega_{ap}} h_{yn}^{ap}(\vec{\rho}')e^{-j\vec{k}\cdot\vec{\rho}'}ds'. \tag{7.62}$$

To further simplify the expression, recall from C.11 in Appendix C that $\widetilde{G}_{xx(1L)}(k_x,k_y,z,z') = \widetilde{G}_{yy(1L)}(k_x,k_y,z,z')$. Using this fact, carrying out the deriva-

tives in (7.60), and using (7.61) and (7.62) allows (7.60) to be rewritten as

$$h_{xn}^{pp}(\vec{\rho}) = \frac{Z_n^{ap}}{4\pi^2}\Bigg[\iint_{-\infty}^{+\infty} \widetilde{G}_{xx(1L)}(k_x,k_y,z,z')\cdot \Big[(k_1^2-k_x^2)f_{xn}^{ap}(k_x,k_y) - k_xk_yf_{yn}^{ap}(k_x,k_y)\Big]\, e^{j\vec{k}\cdot\vec{\rho}}dk_xdk_y\Bigg]_{z=0,z'=0}. \quad (7.63)$$

Following a similar set of steps yields

$$h_{yn}^{pp}(\vec{\rho}) = \frac{Z_n^{ap}}{4\pi^2}\Bigg[\iint_{-\infty}^{+\infty} \widetilde{G}_{xx(1L)}(k_x,k_y,z,z')\cdot \Big[(k_1^2-k_y^2)f_{yn}^{ap}(k_x,k_y) - k_xk_yf_{xn}^{ap}(k_x,k_y)\Big]\, e^{j\vec{k}\cdot\vec{\rho}}dk_xdk_y\Bigg]_{z=0,z'=0}. \quad (7.64)$$

Now that an expression for $\vec{h}_n^{pp}(\vec{\rho})$ has been obtained, the elements D_{8mn}^{pp} may be formulated in terms of the Green's function and the mode functions, yielding

$$\begin{aligned} D_{8mn}^{pp} &= \int_{\Omega_{ap}} h_{xm}^{ap}(\vec{\rho})h_{xn}^{pp}(\vec{\rho})ds + \int_{\Omega_{ap}} h_{ym}^{ap}(\vec{\rho})h_{yn}^{pp}(\vec{\rho})ds \\ &= \int_{\Omega_{ap}} h_{xm}^{ap}(\vec{\rho})\Bigg[\frac{Z_n^{ap}}{4\pi^2}\iint_{-\infty}^{+\infty} \widetilde{G}_{xx(1L)}(k_x,k_y,z=0,z'=0) \\ &\Big((k_1^2-k_x^2)f_{xn}^{ap}(k_x,k_y) - k_xk_yf_{yn}^{ap}(k_x,k_y)\Big)\, e^{j\vec{k}\cdot\vec{\rho}}dk_xdk_y\Bigg]ds \\ &+ \int_{\Omega_{ap}} h_{ym}^{ap}(\vec{\rho})\Bigg[\frac{Z_n^{ap}}{4\pi^2}\iint_{-\infty}^{+\infty} \widetilde{G}_{xx(1L)}(k_x,k_y,z=0,z'=0) \\ &\Big((k_1^2-k_y^2)f_{yn}^{ap}(k_x,k_y) - k_xk_yf_{xn}^{ap}(k_x,k_y)\Big)\, e^{j\vec{k}\cdot\vec{\rho}}dk_xdk_y\Bigg]ds. \end{aligned} \quad (7.65)$$

If additional functions are defined as

$$g_{xm}^{ap}(k_x,k_y) = \int_{\Omega_{ap}} h_{xm}^{ap}(\vec{\rho}) e^{j\vec{k}\cdot\vec{\rho}} ds \tag{7.66}$$

$$g_{ym}^{ap}(k_x,k_y) = \int_{\Omega_{ap}} h_{ym}^{ap}(\vec{\rho}) e^{j\vec{k}\cdot\vec{\rho}} ds, \tag{7.67}$$

then (7.65) may be rewritten as

$$\begin{aligned} D_{8mn}^{pp} = \frac{Z_n^{ap}}{4\pi^2} \int_{-\infty}^{+\infty}\!\!\!\!\!\!\iint \widetilde{G}_{xx(1L)}(k_x,k_y,z=0,z'=0) \Big\{ \Big[(k_1^2 - k_x^2) f_{xn}^{ap}(k_x,k_y) \\ - k_x k_y f_{yn}^{ap}(k_x,k_y) \Big] g_{xm}^{ap}(k_x,k_y) \\ + \Big[(k_1^2 - k_y^2) f_{yn}^{ap}(k_x,k_y) - k_x k_y f_{xn}^{ap}(k_x,k_y) \Big] g_{ym}^{ap}(k_x,k_y) \Big\} dk_x dk_y. \end{aligned} \tag{7.68}$$

Similar to the other integrals evaluated in sections 7.6.2 and 7.6.3, there are four possible combinations of modes, depending on whether the mth or n^{th} modes are TM_z or TE_z.

7.6.4.2 Case 1, $TE_{um\,vm}^{ap} \cdot TE_{un\,vn}^{ap}$

The functions $f_{xn}^{ap}(k_x,k_y)$, $f_{yn}^{ap}(k_x,k_y)$, $g_{xm}^{ap}(k_x,k_y)$, and $g_{ym}^{ap}(k_x,k_y)$ are different depending on whether the mth or n^{th} modes are TM_z or TE_z. As shown in Appendix E, the functions take on the following values for the TE modes that are found in Case

1:

$$f_{xn}^{ap}(k_x,k_y) = -\frac{K_{un\,vn}^{ap}}{Z_n^{ap(TE)}}k_{Axn}^2 k_y \cdot \frac{\left[e^{-jk_x x_r}cos(u_n\pi) - e^{-jk_x x_l}\right]\left[e^{-jk_y y_t}cos(v_n\pi) - e^{-jk_y y_l}\right]}{j(k_y^2 - k_{Ayn}^2)(k_x^2 - k_{Axn}^2)} \tag{7.69}$$

$$f_{yn}^{ap}(k_x,k_y) = -\frac{K_{un\,vn}^{ap}}{Z_n^{ap(TE)}}k_{Ayn}^2 k_x \cdot \frac{\left[e^{-jk_x x_r}cos(u_n\pi) - e^{-jk_x x_l}\right]\left[e^{-jk_y y_t}cos(v_n\pi) - e^{-jk_y y_l}\right]}{j(k_y^2 - k_{Ayn}^2)(k_x^2 - k_{Axn}^2)} \tag{7.70}$$

$$g_{xm}^{ap}(k_x,k_y) = \frac{K_{um\,vm}^{ap}}{Z_m^{ap(TE)}}k_{Axm}^2 k_y \cdot \frac{\left[e^{jk_x x_r}cos(u_m\pi) - e^{jk_x x_l}\right]\left[e^{jk_y y_t}cos(v_m\pi) - e^{jk_y y_l}\right]}{j(k_y^2 - k_{Aym}^2)(k_x^2 - k_{Axm}^2)} \tag{7.71}$$

$$g_{ym}^{ap}(k_x,k_y) = \frac{K_{um\,vm}^{ap}}{Z_m^{ap(TE)}}k_{Aym}^2 k_x \cdot \frac{\left[e^{jk_x x_r}cos(u_m\pi) - e^{jk_x x_l}\right]\left[e^{jk_y y_t}cos(v_m\pi) - e^{jk_y y_l}\right]}{j(k_y^2 - k_{Aym}^2)(k_x^2 - k_{Axm}^2)} \tag{7.72}$$

Inserting these four functions in (7.68) yields

$$\begin{aligned} D_{8mn}^{pp} = & \frac{Z_n^{ap(TE)}}{4\pi^2}\frac{K_{um\,vm}^{ap}}{Z_m^{ap(TE)}}\frac{K_{un\,vn}^{ap}}{Z_n^{ap}}\iint_{-\infty}^{+\infty}\widetilde{G}_{xx(1L)}(k_x,k_y,z=0,z'=0)\cdot \\ & \Big\{k_y^2(k_1^2-k_x^2)k_{Axn}^2k_{Axm}^2 - k_x^2k_y^2k_{Ayn}^2k_{Axm}^2 + \\ & k_x^2(k_1^2-k_y^2)k_{Ayn}^2k_{Aym}^2 - k_x^2k_y^2k_{Aym}^2k_{Axn}^2\Big\}\cdot \\ & \frac{\left[e^{-jk_x x_r}cos(u_n\pi) - e^{-jk_x x_l}\right]\left[e^{-jk_y y_t}cos(v_n\pi) - e^{-jk_y y_l}\right]}{j(k_y^2 - k_{Ayn}^2)(k_x^2 - k_{Axn}^2)}\cdot \\ & \frac{\left[e^{jk_x x_r}cos(u_m\pi) - e^{jk_x x_l}\right]\left[e^{jk_y y_t}cos(v_m\pi) - e^{jk_y y_l}\right]}{j(k_y^2 - k_{Aym}^2)(k_x^2 - k_{Axm}^2)}dk_x dk_y. \end{aligned} \tag{7.73}$$

Note that there are several common terms in this equation which can be grouped

together and rearranged. It is desirable to collect the terms in such a way that a minimal number of two dimensional integrations need to be computed. The result of these groupings yields

$$D^{pp}_{8mn} = \frac{Z_n^{ap(TE)}}{j\omega\mu_1 4\pi^2} \frac{K^{ap}_{un\,vn} K^{ap}_{um\,vm}}{Z_n^{ap(TE)} Z_m^{ap(TE)}}$$
$$\left[k_1^2 k_{Axn}^2 k_{Axm}^2 \int_{-\infty}^{+\infty} L_1(k_x) \left\{ \int_{-\infty}^{+\infty} M_2(k_x, k_y) dk_y \right\} dk_x \right.$$
$$- \left(k_{Axn}^2 k_{Axm}^2 + k_{Ayn}^2 k_{Axm}^2 + k_{Ayn}^2 k_{Aym}^2 + k_{Axn}^2 k_{Aym}^2 \right) \cdot$$
$$\int_{-\infty}^{+\infty} L_2(k_x) \left\{ \int_{-\infty}^{+\infty} M_2(k_x, k_y) dk_y \right\} dk_x$$
$$\left. + k_1^2 k_{Ayn}^2 k_{Aym}^2 \int_{-\infty}^{\infty} L_2(k_x) \left\{ \int_{-\infty}^{\infty} M_1(k_x, k_y) dk_y \right\} dk_x \right], \tag{7.74}$$

where

$$L_1(k_x) = \frac{\left(e^{-jk_x x_r} \cos u_n \pi - e^{-jk_x x_l} \right) \left(e^{jk_x x_r} \cos u_m \pi - e^{jk_x x_l} \right)}{\left(k_x^2 - k_{Axn}^2 \right) \left(k_x^2 - k_{Axm}^2 \right)} \tag{7.75}$$

$$L_2(k_x) = k_x^2 L_1(k_x) \tag{7.76}$$

$$M_1(k_x, k_y) = \frac{\cosh p_1 h \left(e^{-jk_y y_t} \cos v_n \pi - e^{-jk_y y_l} \right) \left(e^{jk_y y_t} \cos v_m \pi - e^{jk_y y_l} \right)}{p_1 \sinh p_1 h \left(k_y^2 - k_{Ayn}^2 \right) \left(k_y^2 - k_{Aym}^2 \right)} \tag{7.77}$$

$$M_2(k_x, k_y) = k_y^2 M_1(k_x, k_y). \tag{7.78}$$

7.6.4.3 Case 2, $TE_{um\,vm} \cdot TM_{un\,vn}$

In the second possible set of combinations, the functions $f^{ap}_{xn}(k_x, k_y)$ and $f^{ap}_{yn}(k_x, k_y)$ take on different values than Case 1, since they depend on the mode functions which in this case are for TM_z modes. These functions are shown in Appendix E, and are

given by

$$f_{xn}^{ap}(k_x,k_y) = -\frac{N_{un\,vn}^{ap}}{Z_n^{ap(TM)}} k_{Axn} k_{Ayn} k_y \cdot \frac{\left[e^{-jk_x x_r}cos(u_n\pi) - e^{-jk_x x_l}\right]\left[e^{-jk_y y_t}cos(v_n\pi) - e^{-jk_y y_l}\right]}{j(k_y^2 - k_{Ayn}^2)(k_x^2 - k_{Axn}^2)} \tag{7.79}$$

$$f_{yn}^{ap}(k_x,k_y) = \frac{N_{un\,vn}^{ap}}{Z_n^{ap(TM)}} k_{Ayn} k_{Ayn} k_x \cdot \frac{\left[e^{-jk_x x_r}cos(u_n\pi) - e^{-jk_x x_l}\right]\left[e^{-jk_y y_t}cos(v_n\pi) - e^{-jk_y y_l}\right]}{j(k_y^2 - k_{Ayn}^2)(k_x^2 - k_{Axn}^2)}. \tag{7.80}$$

The functions $g_{xm}^{ap}(k_x,k_y)$, and $g_{ym}^{ap}(k_x,k_y)$ are the same as shown in (7.71) and (7.72) since they are for TE_z modes. Inserting the expressions found in (7.79), (7.80), (7.71), and (7.72) into (7.68) produces

$$D_{8mn}^{pp} = \frac{1}{j\omega\mu_1 4\pi^2} \frac{N_{un\,vn}^{ap} K_{um\,vm}^{ap}}{Z_m^{ap(TE)}} k_1^2 k_{Axn} k_{Ayn} \cdot \left[k_{Axm}^2 \int_{-\infty}^{\infty} L_1(k_x) \left\{ \int_{-\infty}^{\infty} M_2(k_x,k_y) dk_y \right\} dk_x - k_{Aym}^2 \int_{-\infty}^{\infty} L_2(k_x) \left\{ \int_{-\infty}^{\infty} M_1(k_x,k_y) dk_y \right\} dk_x \right]. \tag{7.81}$$

Note that because these involve the TM_z modes, $u_n + v_n > 1$.

7.6.4.4 Case 3, $TM_{um\,vm} \cdot TE_{un\,vn}$

In the third possible set of combinations, the functions $g_{xm}^{ap}(k_x,k_y)$ and $g_{ym}^{ap}(k_x,k_y)$ take on different values than Case 1 or 2, since they depend on the mode functions

for TM_z modes. These functions are shown in Appendix E, and are given by

$$g^{ap}_{xm}(k_x,k_y) = \frac{N^{ap}_{um\,vm}}{Z^{ap(TM)}_m} k_{Axm}k_{Aym}k_y \cdot \frac{\left[e^{jk_xx_r}cos(u_m\pi) - e^{jk_xx_l}\right]\left[e^{jk_yy_t}cos(v_m\pi) - e^{jk_yy_l}\right]}{j(k_y^2 - k^2_{Aym})(k_x^2 - k^2_{Axm})} \tag{7.82}$$

$$g^{ap}_{ym}(k_x,k_y) = -\frac{N^{ap}_{um\,vm}}{Z^{ap(TE)}_m} k_{Aym}k_{Axm}k_x \cdot \frac{\left[e^{jk_xx_r}cos(u_m\pi) - e^{jk_xx_l}\right]\left[e^{jk_yy_t}cos(v_m\pi) - e^{jk_yy_l}\right]}{j(k_y^2 - k^2_{Aym})(k_x^2 - k^2_{Axm})}. \tag{7.83}$$

The functions $f^{ap}_{xn}(k_x,k_y)$ and $f^{ap}_{yn}(k_x,k_y)$ have the same values as in Case 1, and are given in (7.69) and (7.70). Thus, using (7.82), (7.83), (7.69), and (7.70) in (7.68) produces

$$D^{pp}_{8mn} = \frac{1}{j\omega\mu_1 4\pi^2}\frac{K^{ap}_{un\,vn}N^{ap}_{um\,vm}}{Z^{ap(TM)}_m}k_1^2 k_{Axm}k_{Aym} \left[k^2_{Axn}\int_{-\infty}^{\infty} L_1(k_x)\left\{\int_{-\infty}^{\infty} M_2(k_x,k_y)dk_y\right\}dk_x - k^2_{Ayn}\int_{-\infty}^{\infty} L_2(k_x)\left\{\int_{-\infty}^{\infty} M_1(k_x,k_y)dk_y\right\}dk_x\right]. \tag{7.84}$$

Note that because these involve the TM_z modes, $u_m + v_m > 1$.

7.6.4.5 Case 4, $TM_{um\,vm} \cdot TM_{un\,vn}$

The fourth case is a combination of two TM_z modes. The functions $f^{ap}_{xn}(k_x,k_y)$, $f^{ap}_{yn}(k_x,k_y)$, $g^{ap}_{xm}(k_x,k_y)$, and $g^{ap}_{ym}(k_x,k_y)$ have already been shown for the TM_z

modes. Using (7.79), (7.80),(7.82), and (7.83) in (7.68) produces

$$D^{pp}_{8mn} = \frac{1}{j\omega\mu_1 4\pi^2} \frac{N^{ap}_{un\,vn} N^{ap}_{um\,vm}}{Z^{ap(TM)}_m} k_1^2 k_{Axm} k_{Aym} k_{Axn} k_{Ayn} \cdot \left[\int_{-\infty}^{+\infty} L_2(k_x) \left\{ \int_{-\infty}^{+\infty} M_1(k_x, k_y) dk_y \right\} dk_x + \int_{-\infty}^{+\infty} L_1(k_x) \left\{ \int_{-\infty}^{+\infty} M_2(k_x, k_y) dk_y \right\} dk_x \right]. \quad (7.85)$$

Note that since both modes are TM_z modes, $u_m + v_m > 1$ and $u_n + v_n > 1$.

With these equations, the expressions for the calculation of the individual matrix elements for all nine matrices have been derived. The following section is a discussion of the computational considerations used in the numerical computation of the matrix elements.

7.7 Numerical Computation of the matrix elements D^8_{mn}

The numerical computation of the matrix elements of matrices D_1 through D_7 are rather straightforward. However, due to the nature of the MFIE formulation at the aperture/material boundary, it is necessary to calculate the matrix elements of D_8 and D_9 by evaluating the integrals in (7.74), (7.81), (7.84), and (7.85). As mentioned in section 4.5, these integrals could be evaluated by complex plane analysis or by numerical integration. Since the author had already undertaken this type of analysis with the two layer method and the two thickness method, it was rather straightforward to implement the numerical integration procedure for use with the two iris method. The disadvantage of this technique is that two dimensional integration is a computationally intensive process. A definite increase in speed could be achieved by converting one of the integrals to a pole series using Cauchy's residue theorem [36]. However one purpose of this dissertation is to first investigate the viability of the two

iris method as a material parameter extraction method.

In the evaluation of the integrals in (7.74), (7.81), (7.84), and (7.85), note that the four functions $M_1(k_x, k_y)$, $M_2(k_x, k_y)$, $L_1(k_x)$, and $L_2(k_x)$ are present in all four cases. Thus, the details of the numerical integration are examined for these four functions rather than for the specific cases.

One way in which the numerical integration is different in the two iris method than for the two layer method is the types of modes which are incident onto the aperture region/parallel plate region. In the two layer method, only the dominant $TE_{1\,0}$ mode is incident on the parallel plate region. Because of the symmetry of the waveguide, the $TE_{1\,0}$ mode only couples with those modes which are $TE_{odd\,even}$ and $TM_{odd\,even}$ in the two layer method. This does simplify the number of possible modes which can be used in the two layer solution.

In the two iris method, an infinite number of modes are excited at the waveguide discontinuity at $z = d_2$. Although most of the modes evanesce as they traverse the aperture region, some may still have a significant amplitude if the aperture region is thin enough. These modes are then incident on the aperture/material boundary at $z = 0$. It is possible that some of these modes couple with other modes at the material boundary which are not present in the two layer method formulation. Thus, if the aperture is of a general rectangular shape, all the TE and TM modes must be considered in the integral equation. As a result, the integration of $M_1(k_x, k_y)$, $M_2(k_x, k_y)$, $L_1(k_x)$, and $L_2(k_x)$ must consider all of the possible mode indices, u_m, u_n, v_m, and v_n.

7.7.1 Reduction to one-sided integrals

When considering the integrals for each of the four cases, it is clear that all of the integrals in Case 1 are present in the other three cases. These integrals are analyzed

as

$$\widetilde{I}_{12} = \int_{-\infty}^{+\infty} L_1(k_x) \left\{ \int_{-\infty}^{+\infty} M_2(k_x, k_y) dk_y \right\} dk_x \tag{7.86}$$

$$\widetilde{I}_{22} = \int_{-\infty}^{+\infty} L_2(k_x) \left\{ \int_{-\infty}^{+\infty} M_2(k_x, k_y) dk_y \right\} dk_x \tag{7.87}$$

$$\widetilde{I}_{21} = \int_{-\infty}^{+\infty} L_2(k_x) \left\{ \int_{-\infty}^{+\infty} M_1(k_x, k_y) dk_y \right\} dk_x. \tag{7.88}$$

To reduce computational time and to simplify analysis, it is desirable to reduce the limits of integration along the real axis to one side of the real axis, i.e. from 0 to $+\infty$. This may be accomplished if the integrand is an even function with respect to the integration variable.

Consider the expression for $M_1(k_x, k_y)$, which is given by

$$M_1(k_x, k_y) = \frac{\cosh p_1 h \left(e^{-jk_y y_t} \cos v_n \pi - e^{-jk_y y_l} \right) \left(e^{jk_y y_t} \cos v_m \pi - e^{jk_y y_l} \right)}{p_1 \sinh p_1 h \left(k_y^2 - k_{Ayn}^2 \right) \left(k_y^2 - k_{Aym}^2 \right)}. \tag{7.89}$$

Note that $M_1(k_x, k_y)$ is even with respect to the variable k_x, since only p_1 includes the variable k_x, where $p_1 = \sqrt{k_y^2 + k_x^2 - k_1^2}$. The function $M_2(k_x, k_y)$ is also even with respect to the variable k_x.

To determine the even or odd properties of $M_1(k_x, k_y)$ with respect to k_y, the possible combinations of the indices v_n and v_m must be considered. The expression found in (7.89) can be rewritten as

$$M_1(k_x, k_y) = M_{1e}(k_x, k_y) M_{1v}(k_y), \tag{7.90}$$

where the even portion is

$$M_{1e}(k_x, k_y) = \frac{\cosh p_1 h}{p_1 \sinh p_1 h \left(k_y^2 - k_{Ay_n}^2\right)\left(k_y^2 - k_{Ay_m}^2\right)}, \tag{7.91}$$

and the expression which must be evaluated further is

$$M_{1o}(k_y) = \left(e^{-jk_y y_t}\cos v_n\pi - e^{-jk_y y_l}\right)\left(e^{jk_y y_t}\cos v_m\pi - e^{jk_y y_l}\right). \tag{7.92}$$

Upon evaluation of the possible combinations of the indices v_n and v_m, it is found that, with respect to k_y,

$$M_{1o}(k_y) = \begin{cases} 2 + 2\cos k_y A_y, \text{ (EVEN in } k_y) & v_n = odd,\ v_m = odd \\ -2j\sinh k_y A_y, \text{ (ODD in } k_y) & v_n = odd,\ v_m = even \\ 2j\sinh k_y A_y, \text{ (ODD in } k_y) & v_n = even,\ v_m = odd \\ 2 - 2\cos k_y A_y, \text{ (EVEN in } k_y) & v_n = even,\ v_m = even \end{cases} \tag{7.93}$$

This understanding of the behavior of $M_{1o}(k_y)$ allows for the evaluation of $M_1(k_x, k_y)$. Since the product of an even function and an even function is an even function, and the product of an odd function and an even function is an odd function [62], the resulting function behavior of $M_1(k_x, k_y)$ with respect to k_y is

$$M_1(k_x, k_y) \Longrightarrow \begin{cases} \text{EVEN in } k_y & v_n = odd,\ v_m = odd \\ \text{ODD in } k_y & v_n = odd,\ v_m = even \\ \text{ODD in } k_y & v_n = even,\ v_m = odd \\ \text{EVEN in } k_y & v_n = even,\ v_m = even \end{cases} \tag{7.94}$$

As a result of the even and odd behavior of this function, the real axis integral of

the function over the variable k_y can be rewritten as

$$\int_{-\infty}^{+\infty} M_1(k_x,k_y)dk_y = \begin{cases} 2\int_0^{+\infty} M_1(k_x,k_y)dk_y & v_n = odd,\ v_m = odd \\ 0 & v_n = odd,\ v_m = even \\ 0 & v_n = even,\ v_m = odd \\ 2\int_0^{+\infty} M_1(k_x,k_y)dk_y & v_n = even,\ v_m = even \end{cases} \tag{7.95}$$

Since the function $M_2(k_x,k_y) = k_y^2 M_1(k_x,k_y)$ is a product of an even function multiplied by $M_1(k_x,k_y)$, it exhibits a similar behavior,

$$\int_{-\infty}^{+\infty} M_2(k_x,k_y)dk_y = \begin{cases} 2\int_0^{+\infty} M_2(k_x,k_y)dk_y & v_n = odd,\ v_m = odd \\ 0 & v_n = odd,\ v_m = even \\ 0 & v_n = even,\ v_m = odd \\ 2\int_0^{+\infty} M_2(k_x,k_y)dk_y & v_n = even,\ v_m = even \end{cases} \tag{7.96}$$

Now consider the even and odd behavior of the function $L_1(k_x)$ with respect to the variable k_x. Note that the function is written as

$$L_1(k_x) = \frac{\left(e^{-jk_x x_r}\cos u_n\pi - e^{-jk_x x_l}\right)\left(e^{jk_x x_r}\cos u_m\pi - e^{jk_x x_l}\right)}{\left(k_x^2 - k_{Axn}^2\right)\left(k_x^2 - k_{Axm}^2\right)}. \tag{7.97}$$

Similar to the behavior of $M_1(k_x,k_y)$, there are four possible cases for the combination of the indices u_n and u_m. When the four possible cases of the indices u_n and u_m are

examined, it is found that

$$L_1(k_x) = \begin{cases} \dfrac{2 + 2\cos k_x A_x}{\left(k_x^2 - k_{Axn}^2\right)\left(k_x^2 - k_{Axm}^2\right)}, \text{ (EVEN)} & u_n = odd,\ u_m = odd \\ \dfrac{-2j \sinh k_x A_x}{\left(k_x^2 - k_{Axn}^2\right)\left(k_x^2 - k_{Axm}^2\right)}, \text{ (ODD)} & u_n = odd,\ u_m = even \\ \dfrac{2j \sinh k_x A_x}{\left(k_x^2 - k_{Axn}^2\right)\left(k_x^2 - k_{Axm}^2\right)}, \text{ (ODD)} & u_n = even,\ u_m = odd \\ \dfrac{2 - 2\cos k_x A_x}{\left(k_x^2 - k_{Axn}^2\right)\left(k_x^2 - k_{Axm}^2\right)}, \text{ (EVEN)} & u_n = even,\ u_m = even \end{cases} \tag{7.98}$$

The function $L_2(k_x)$ exhibits a similar behavior.

Recall that $M_1(k_x, k_y)$ and $M_2(k_x, k_y)$ are even functions with respect to the variable k_x. Thus, making use of the information in (7.98), the integral $\widetilde{I}_{12}$ becomes

$$\widetilde{I}_{12} = \begin{cases} 2\displaystyle\int_0^{+\infty} L_1(k_x) \left\{ 2\int_0^{+\infty} M_2(k_x, k_y) dk_y \right\} dk_x, & u_n = odd,\ u_m = odd \\ 0, & u_n = odd,\ u_m = even \\ 0, & u_n = even,\ u_m = odd \\ 2\displaystyle\int_0^{+\infty} L_1(k_x) \left\{ 2\int_0^{+\infty} M_2(k_x, k_y) dk_y \right\} dk_x, & u_n = even,\ u_m = even \end{cases} \tag{7.99}$$

Notice that the values for u_n and u_m must be both either odd or even for the value of $\widetilde{I}_{12}$ to be non-zero. Also recall from (7.96) that the non-zero answer is also dependent on the odd or even values of v_n and v_m. Thus, if two additional functions are defined

as

$$\alpha_u = \begin{cases} 1, & u_n = odd,\ u_m = odd \\ 0, & u_n = odd,\ u_m = even \\ 0, & u_n = even,\ u_m = odd \\ 1, & u_n = even,\ u_m = even \end{cases} \tag{7.100}$$

$$\alpha_v = \begin{cases} 1, & v_n = odd,\ v_m = odd \\ 0, & v_n = odd,\ v_m = even \\ 0, & v_n = even,\ v_m = odd \\ 1, & v_n = even,\ v_m = even \end{cases} \tag{7.101}$$

then the integrals from (7.86)-(7.88) may be rewritten as

$$\widetilde{I}_{12} = 4\alpha_u\alpha_v \int_0^{+\infty} L_1(k_x) \left\{ \int_0^{+\infty} M_2(k_x, k_y)dk_y \right\} dk_x \tag{7.102}$$

$$\widetilde{I}_{22} = 4\alpha_u\alpha_v \int_0^{+\infty} L_2(k_x) \left\{ \int_0^{+\infty} M_2(k_x, k_y)dk_y \right\} dk_x \tag{7.103}$$

$$\widetilde{I}_{21} = 4\alpha_u\alpha_v \int_0^{+\infty} L_2(k_x) \left\{ \int_0^{+\infty} M_1(k_x, k_y)dk_y \right\} dk_x \tag{7.104}$$

7.7.2 Examination of poles on the real k_x and k_y axes.

The integrals in (7.102)-(7.104) may be computed numerically for the cases shown. However, the integrands must also be examined to determine if poles exist along the real axes. These poles would cause the integrand to be undefined at their locations.

7.7.2.1 Evaluation of poles on the real k_y axis

First, consider the function $M_1(k_x, k_y)$ from (7.89). Recall that this function is only evaluated when v_n and v_m are both odd numbers or both even numbers. In either case, the poles of the function are shown in Figure 7.3 for the case of a lossy material. Note that the poles due to the parallel plate terms are in the fourth quadrant, and the branch point and branch cut are also in the same quadrant. The branch cut does not cross the real axis. The poles which are on the real axis must be examined to determine if they are removable. If not, integration in the complex plane around those poles must be undertaken.

If the material is lossless, the pole due to the term p and the parallel plate poles will be on the positive real axis and the negative imaginary axis, depending on the order of the poles and the value of k_x. If the poles are on the real axis, they must be evaluated to determine if they are removable, or integration in the complex plane around those poles can be used. In this analysis, it is assumed that the physical properties of the material contain loss. Thus, this analysis will focus on the poles on the real axis at $ky = k_{Aym}$ and $ky = k_{Ayn}$ to determine if they are removable.

In the two layer method, a similar analysis was undertaken on the functions $P(k_y)$ and $Q(k_y)$ in section 4.5. In that analysis, it was determined that the poles of both $P(k_y)$ and $Q(k_y)$ are removable poles. Write $M_1(k_x, k_y)$ as

$$M_1(k_x, k_y) = \frac{\cosh p_1 h}{p_1 \sinh p_1 h} \frac{\left(e^{-jk_y y_t} \cos v_n \pi - e^{-jk_y y_l}\right)\left(e^{jk_y y_t} \cos v_m \pi - e^{jk_y y_l}\right)}{\left(k_y^2 - k_{Ayn}^2\right)\left(k_y^2 - k_{Aym}^2\right)}, \tag{7.105}$$

and let the fraction on the right hand side of (7.105) be defined as

$$P_{2I}(k_y) = \frac{\left(e^{-jk_y y_t} \cos v_n \pi - e^{-jk_y y_l}\right)\left(e^{jk_y y_t} \cos v_m \pi - e^{jk_y y_l}\right)}{\left(k_y^2 - k_{Ayn}^2\right)\left(k_y^2 - k_{Aym}^2\right)}. \tag{7.106}$$

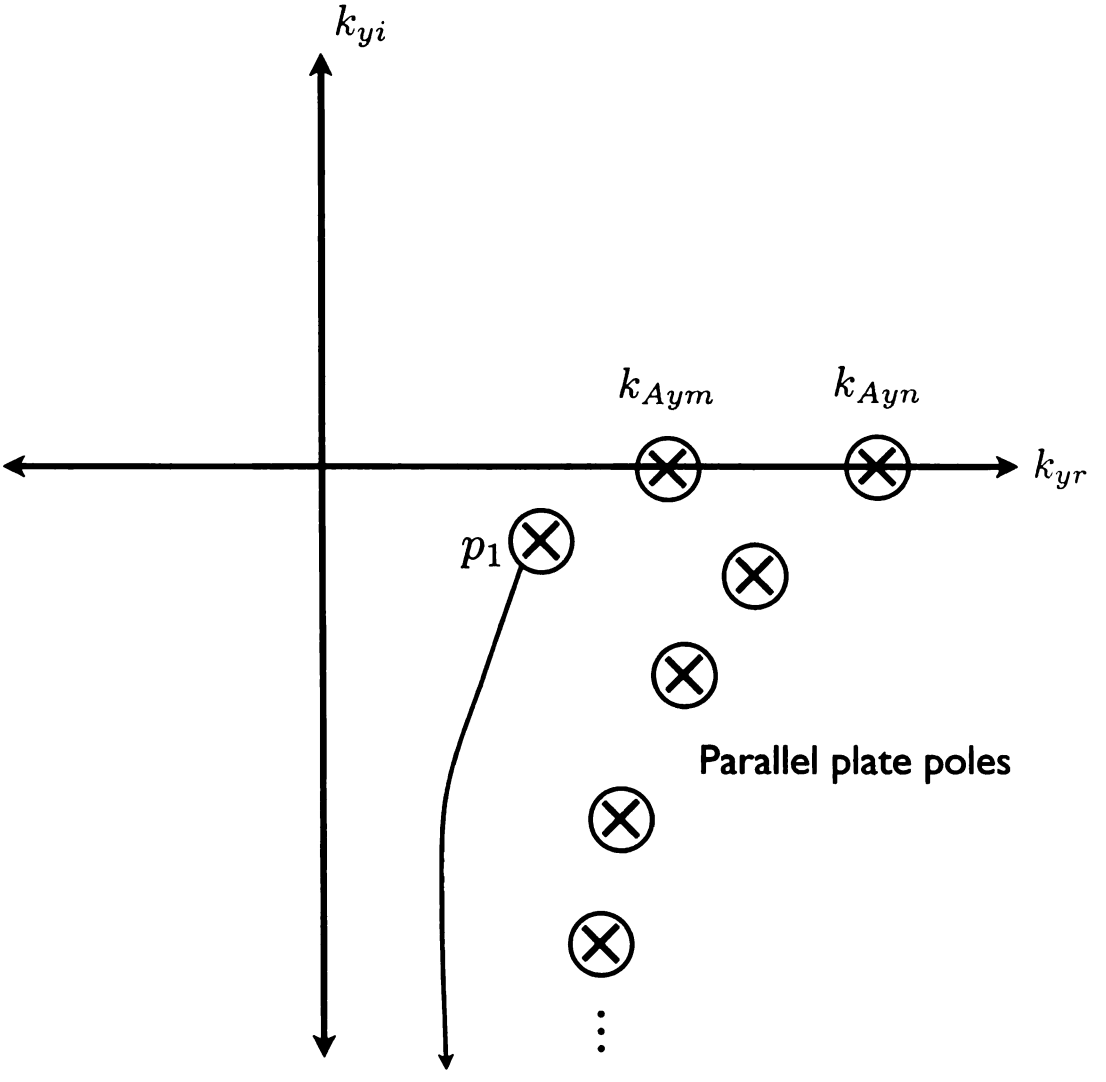


Figure 7.3. The poles of $M_1(k_x, k_y)$ in the complex k_y plane.

When v_n and v_m are even, $P_{2I}(ky)$ becomes

$$P_{2I}(k_y) = \frac{(2 - 2\cos k_y A_y)}{\left(k_y^2 - k_{Ayn}^2\right)\left(k_y^2 - k_{Aym}^2\right)}, \tag{7.107}$$

which is almost identical to the expression for $P(k_y)$ given in (4.97). The only difference is the values given for the locations of the poles in (7.107), which are at $k_y = k_{Aym}$ and $k_y = k_{Ayn}$ in (7.107) instead of $k_y = k_{ym}$ and $k_y = k_{yn}$ in (4.97). By the arguments presented in section 4.5, when v_n and v_m are even the poles of $P_{2I}(k_y)$ are found to be removable.

Using the results from section 4.5, when v_n and v_m are even,

$$M_1(k_x, k_y)\big|_{k_y = k_{Aym}} = \begin{cases} \dfrac{\cosh p_1 h}{p_1 \sinh p_1 h} \cdot \dfrac{A_y^2}{4k_{Aym}^2}, & k_{Aym} = k_{Ayn} \\ 0, & k_{Aym} \neq k_{Ayn} \end{cases} \tag{7.108}$$

When $v_n = 0$ or $v_m = 0$, $k_{Aym} = 0$ and $k_{Ayn} = 0$. This special case does not need to be considered, because when $k_{Aym} = 0$ or $k_{Ayn} = 0$, the integral $\widetilde{I}_{21}$ is not evaluated.

In a similar manner, the function $M_2(k_x, k_y)$ may be rewritten as

$$M_2(k_x, k_y) = \frac{\cosh p_1 h}{p_1 \sinh p_1 h} \frac{k_y^2 \left(e^{-jk_y y_t} \cos v_n \pi - e^{-jk_y y_l}\right)\left(e^{jk_y y_t} \cos v_m \pi - e^{jk_y y_l}\right)}{\left(k_y^2 - k_{Ayn}^2\right)\left(k_y^2 - k_{Aym}^2\right)}. \tag{7.109}$$

If the fraction on the right hand side is written as

$$Q_{2I}(k_y) = \frac{k_y^2 \left(e^{-jk_y y_t} \cos v_n \pi - e^{-jk_y y_l}\right)\left(e^{jk_y y_t} \cos v_m \pi - e^{jk_y y_l}\right)}{\left(k_y^2 - k_{Ayn}^2\right)\left(k_y^2 - k_{Aym}^2\right)}, \tag{7.110}$$

then when v_n and v_m are even $Q_{2I}(ky)$ becomes

$$Q_{2I}(k_y) = \frac{k_y^2\left(2 - 2\cos k_y A_y\right)}{\left(k_y^2 - k_{Ayn}^2\right)\left(k_y^2 - k_{Aym}^2\right)}. \tag{7.111}$$

Note that this function is the same as the function $Q(k_y)$ found in (4.110) with a change of variables. By the arguments presented in section 4.5, when v_n and v_m are even the poles of $Q_{2I}(k_y)$ are removable.

Thus, when v_n and v_m are even, using the results from section 4.5 produces

$$M_2(k_x, k_y)\big|_{k_y = k_{Aym}} = \begin{cases} \dfrac{\cosh p_1 h}{p_1 \sinh p_1 h} A_y^2, & k_{Aym} = k_{Ayn} = 0 \\ \dfrac{\cosh p_1 h}{p_1 \sinh p_1 h} \cdot \dfrac{A_y^2}{4}, & k_{Aym} = k_{Ayn} \neq 0 \\ 0, & k_{Aym} \neq k_{Ayn} \end{cases} \tag{7.112}$$

What remains is to determine if the poles of $M_1(k_x, k_y)$ and $M_2(k_x, k_y)$ are removable when v_n and v_m are odd. When v_n and v_m are odd, the function $P_{2I}(ky)$ becomes

$$P_{2I}(k_y) = \frac{\left(2 + 2\cos k_y A_y\right)}{\left(k_y^2 - k_{Ayn}^2\right)\left(k_y^2 - k_{Aym}^2\right)}. \tag{7.113}$$

Following the procedure outlined in (4.95) - (4.100), all of coefficients of the principal part of $P_{2I}(k_y)$ are zero, showing that $k = k_{Aym}$ and $k = k_{Ayn}$ are removable poles. What remains is to evaluate $P_{2I}(k_y)$ at the poles. When $k_y = k_{Aym} \neq k_{Ayn}$ the evaluation of $P_{2I}(k_y)$ is

$$P_{2I}(k_y)\big|_{k_y = k_{Aym}} = \frac{\left(2 + 2\cos v_m \pi\right)}{\left(k_{Aym}^2 - k_{Ayn}^2\right)\left(k_{Aym}^2 - k_{Aym}^2\right)} = \frac{0}{0}, \tag{7.114}$$

which is indeterminate. Using L'Hopital's rule,

$$P_{2I}(k_y)\big|_{k_y=k_{Aym}} = \left.\frac{\frac{\partial}{\partial k_y}\left(2+2\cos k_y A_y\right)}{\frac{\partial}{\partial k_y}\left(\left(k_y^2-k_{Ayn}^2\right)\left(k_y^2-k_{Aym}^2\right)\right)}\right|_{k_y=k_{Aym}}$$
$$= 0. \tag{7.115}$$

It thus follows that if $k = k_{Aym} \neq k_{Ayn}$ then $M_1(k_x, k_y) = 0$.

When v_n and v_m are odd and $k_{Aym} = k_{Ayn}$, evaluating $P_{2I}(k_y)$ at $k_y = k_{Aym} = k_{Ayn}$ results in the indeterminate quantity 0/0. Using L'Hopital's rule, the first derivative is also undefined. Evaluation then progresses to the second derivative, which yields

$$P_{2I}(k_y)\big|_{k_y=k_{Aym}} = \left.\frac{\frac{\partial^2}{\partial k_y^2}\left(2+2\cos v_m\pi\right)}{\frac{\partial^2}{\partial k_y^2}\left(\left(k_y^2-k_{Ayn}^2\right)\left(k_y^2-k_{Aym}^2\right)\right)}\right|_{k_y=k_{Aym}}$$
$$= \left.\frac{-2A_y^2\cos k_y A_y}{12k_y^2-2(k_{Ayn}^2+k_{Aym}^2)}\right|_{k_y=k_{Aym}}$$
$$= \frac{A_y^2}{4k_{Aym}^2}. \tag{7.116}$$

Thus, using the results from (7.115) and (7.116), the value of the function $M_1(k_x, k_y)$ at the poles when v_n and v_m are odd is

$$M_1(k_x,k_y)\big|_{k_y=k_{Aym}} = \begin{cases} \left.\frac{A_y^2}{4k_{Aym}^2}\frac{\cosh p_1 h}{p_1\sinh p_1 h}\right|_{k_y=k_{Aym}}, & k_{Aym}=k_{Ayn} \\ 0, & k_{Aym}\neq k_{Ayn} \end{cases} \tag{7.117}$$

When v_n and v_m are odd, the function $Q_{2I}(ky)$ becomes

$$Q_{2I}(k_y) = \frac{k_y^2\left(2 + 2\cos k_y A_y\right)}{\left(k_y^2 - k_{Ayn}^2\right)\left(k_y^2 - k_{Aym}^2\right)}. \tag{7.118}$$

An analysis of $Q_{2I}(k_y)$ also shows that the poles at $k_y = k_{Aym}$ and $k_y = k_{Ayn}$ are removable poles. When $k_y = k_{Aym} \neq k_{Ayn}$, the function $Q_{2I}(k_y)$ becomes

$$Q_{2I}(k_y)\big|_{k_y = k_{Aym}} = \frac{k_y^2\left(2 + 2\cos v_m \pi\right)}{\left(k_{Aym}^2 - k_{Ayn}^2\right)\left(k_{Aym}^2 - k_{Aym}^2\right)} = \frac{0}{0}, \tag{7.119}$$

which is undefined. Using L'Hopital's rule produces

$$\begin{aligned} Q_{2I}(k_y)\big|_{k_y = k_{Aym}} &= \left.\frac{\frac{\partial}{\partial k_y}\left(k_y^2\left(2 + 2\cos k_y A_y\right)\right)}{\frac{\partial}{\partial k_y}\left(\left(k_y^2 - k_{Ayn}^2\right)\left(k_y^2 - k_{Aym}^2\right)\right)}\right|_{k_y = k_{Aym}} \\ &= 0. \end{aligned} \tag{7.120}$$

Therefore, if $k_y = k_{Aym} \neq k_{Ayn}$, $M_2(k_x, k_y) = 0$.

If $k_y = k_{Aym} = k_{Ayn}$, evaluating $Q_{2I}(k_y)$ at $k_y = k_{Ayn} = k_{Aym}$ results in the indeterminate quantity 0/0. Using L'Hopital's rule, the first derivatives are also undefined. Evaluation then progresses to the second derivative, which yields

$$\begin{aligned} Q_{2I}(k_y)\big|_{k_y = k_{Aym}} &= \left.\frac{\frac{\partial^2}{\partial k_y^2}\left(k_y^2\left(2 + 2\cos k_y A_y\right)\right)}{\frac{\partial^2}{\partial k_y^2}\left(\left(k_y^2 - k_{Ayn}^2\right)\left(k_y^2 - k_{Aym}^2\right)\right)}\right|_{k_y = k_{Aym}} \\ &= \frac{A_y^2}{4}. \end{aligned} \tag{7.121}$$

Therefore, using the results from (7.120) and (7.121), the value of the function

$M_2(k_x, k_y)$ at the removable poles when v_n and v_m are odd is

$$M_2(k_x,k_y)\big|_{k_y=k_{Aym}} = \begin{cases} \dfrac{A_y^2}{4}\dfrac{\cosh p_1 h}{p_1 \sinh p_1 h}\Big|_{k_y=k_{Aym}}, & k_{Aym} = k_{Ayn} \\ 0, & k_{Aym} \neq k_{Ayn} \end{cases} \tag{7.122}$$

The result of this examination is that the poles of the functions $M_1(k_x, k_y)$ and $M_2(k_x, k_y)$ are removable when v_n and v_m are both odd or both even. The values of $M_1(k_x, k_y)$ and $M_2(k_x, k_y)$ at those poles are given by (7.108), (7.112) (7.117) and (7.122), respectively. As a result, the integrals in (7.102) and (7.104) may be computed by numerical integration routines without the need to detour around the poles.

7.7.2.2 Evaluation of poles on the real k_x axis

The functions $L_1(k_x)$ and $L_2(k_x)$ must also be examined at the poles to determine if they are also removable. Recall that these are only evaluated when u_m and u_n are either both even or both odd.

When u_m and u_n are both even, the function $L_1(k_x)$ becomes

$$L_1(k_x) = \frac{2 - 2\cos k_x A_x}{\left(k_x^2 - k_{Axn}^2\right)\left(k_x^2 - k_{Axm}^2\right)}. \tag{7.123}$$

Note that this takes the same form as $P_{2I}(k_y)$ in (7.106). Employing the same results in this case yields

$$L_1(k_x) = \begin{cases} \dfrac{A_x^2}{4k_{Axm}^2}, & k_{Axm} = k_{Axn} \\ 0, & k_{Axm} \neq k_{Axn} \end{cases} \tag{7.124}$$

When $u_n = 0$ or $u_m = 0$, the integral $\widetilde{I}_{21}$ is not evaluated.

In a similar manner, when u_n and u_m are both even, the function $L_2(k_x)$ takes

the form

$$L_2(k_x)|_{k_x=k_{Axm}} = \frac{k_x^2\,(2-2\cos k_x A_x)}{\left(k_x^2-k_{Axn}^2\right)\left(k_x^2-k_{Axm}^2\right)}. \tag{7.125}$$

This takes the same form as $Q_{2I}(k_y)$ in (7.111). Using those results, when u_n and u_m are both even, the function $L_2(k_x)$ is

$$L_2(k_x)|_{k_x=k_{Axm}} = \begin{cases} A_x^2, & k_{Axm}=k_{Axn}=0 \\ \dfrac{A_x^2}{4}, & k_{Axm}=k_{Axn}\neq 0 \\ 0, & k_{Axm}\neq k_{Axn} \end{cases} \tag{7.126}$$

When u_m and u_n are both odd, the functions $L_1(k_x)$ and $L_2(k_x)$ again take the form of the functions $P_{2I}(k_y)$, as found in (7.113), and $Q_{2I}(k_y)$, as found in (7.118), respectively. Following the same arguments, when these functions are evaluated at the removable poles when u_m and u_n are both odd, the result is

$$L_1(k_x)|_{k_x=k_{Axm}} = \begin{cases} \dfrac{A_x^2}{4k_{Axm}^2}\dfrac{\cosh p_1 h}{p_1\sinh p_1 h}\Big|_{k_x=k_{Axm}}, & k_{Axm}=k_{Axn} \\ 0, & k_{Axm}\neq k_{Axn} \end{cases} \tag{7.127}$$

$$L_2(k_x)|_{k_x=k_{Axm}} = \begin{cases} \dfrac{A_x^2}{4}\dfrac{\cosh p_1 h}{p_1\sinh p_1 h}\Big|_{k_x=k_{Axm}}, & k_{Axm}=k_{Axn} \\ 0, & k_{Axm}\neq k_{Axn} \end{cases} \tag{7.128}$$

Using these expressions, the removable poles on the real k_x and k_y axes may be evaluated. These allow the integrals $\widetilde{I}_{12}$, $\widetilde{I}_{22}$, and $\widetilde{I}_{21}$ to be computed numerically so that the matrix elements for the matrices D_8 and D_9 may be calculated. The numerical solution to the coupled mode matching and MFIE equations ma then be computed.

7.8 Implementation

To solve for the amplitude constant of the scattered dominant mode in the waveguide, a_1^s, it is necessary to solve the matrix equation given in (7.30). Real axis integration is used to obtain a value for the three equations given in (7.39)-(7.41).

The identical Gauss-Kronrod integration routine used in the two layer method is employed in the two iris method to calculate the elements of the matrix D. The stopping criteria for the integration routine was chosen to be when a relative error of 10^{-10} is achieved. The integration performed in the k_x domain was from 0 to 30,000 m^{-1}, while the k_y domain was integrated over the range from 0 to 50,000 m^{-1}. Increasing the range of integration further only made a change in the sixth significant digit while greatly increasing the computational time. These values of k_x and k_y are used throughout the simulations, sensitivity analysis, and the material parameter extraction carried out using the two iris method.

The accurate computation of each matrix element is necessary to obtain an accurate estimate of the theoretical reflection coefficient in the two iris method. It is also necessary to examine the effect of the number of modes used to estimate the reflection coefficient and the effect of random measurement noise present in the reflection coefficient measurement. These issues are addressed in the next chapter.

MICHIGAN STATE UNIVERSITY LIBRARIES
3 1293 03063 2933

THESIS
5
2009
V. 2

LIBRARY
Michigan State
University

PLACE IN RETURN BOX to remove this checkout from your record.
TO AVOID FINES return on or before date due.
MAY BE RECALLED with earlier due date if requested.

DATE DUE	DATE DUE	DATE DUE

5/08 K:/Proj/Acc&Pres/CIRC/DateDue.indd

ELECTROMAGNETIC MATERIAL CHARACTERIZATION OF A CONDUCTOR-BACKED MATERIAL USING THE TWO LAYER, TWO THICKNESS, AND TWO IRIS WAVEGUIDE PROBE METHODS: ERROR ANALYSIS, SIMULATION, AND EXPERIMENTAL RESULTS

VOLUME II

By

Gary Dean Dester

A DISSERTATION

Submitted to
Michigan State University
in partial fulfillment of the requirements
for the degree of

DOCTOR OF PHILOSOPHY

Electrical Engineering

2008

CHAPTER 8

TWO APERTURE MODAL ANALYSIS AND ERROR SENSITIVITY ANALYSIS

8.1 Introduction

Chapters 5 and 6 of this dissertation examine the effect of two potential sources of error on the extracted parameters. Chapter 5 examines the effect that the number of significantly contributing modes has on the final solution. An extrapolation technique is utilized to obtain an estimate of the reflection coefficient due to a large number of modes in the two layer and two thickness methods. Chapter 6 examines the effect of random measurement error on the extracted parameters for both extraction methods.

In this chapter, both the modal analysis and the error sensitivity analysis are presented for the two iris method. Potential geometries for the reduced aperture are considered, and an extrapolation method for the reflection coefficient from those apertures is examined. The error sensitivity analysis is used to identify the aperture geometry that is the least sensitive to measurement error so that the best candidate for the aperture, or iris, may be chosen.

8.2 Reflection Coefficient Analysis

Recall from the two iris problem formulation in Chapter 7 that the matrix equation which is established to obtain the scattered dominant mode amplitude involves a $3N \times 3N$ matrix. In this method, N is the number of modes used to approximate the fields in both the aperture and waveguide regions. It should be noted that the field structure in the waveguide is different from the field structure in the aperture, and the dimensions of the aperture may cause different modes to make a more significant contribution to the matrix solution.

The goal of the simulations in this chapter is to determine an aperture geometry that will be built for the experimental evaluation of the two iris method. The first step is to analyze how different modes contribute to the calculation of the reflection coefficient. Similar to the two layer method, it is desirable to accurately estimate the reflection coefficient by using the least number of modes.

8.2.1 Aperture Geometries

An infinite number of possible aperture geometries are available as candidates for use in the two iris method. For simplicity of formulation and analysis, a rectangular iris, or aperture, is the design used in this investigation, as shown in Figure 7.1. The dimensions of the iris in the transverse direction, A_x, and A_y, as well as the thickness of the aperture, d_2, may be varied in the analysis. In addition, the placement of the aperture within the waveguide cross section, governed by the coordinates of the corner of the iris, x_l and y_l, may also be shifted.

An initial group of 8 possible candidates for the apertures is shown in Figure 8.1 and Figure 8.2. These rectangular apertures were chosen because the transverse waveguide mode functions and aperture mode functions that were utilized in the formulation of the problem in Chapter 7 are well known. Notice that several possible orientations are considered. All of the irises, with the exception of Apertures B and E, share at least one aperture wall with a waveguide wall. Apertures B, F, G, and H are centered in the x-direction of the waveguide cross section. Apertures A, B, C, F, G, and H are centered in the y-direction of the waveguide cross section. An additional iris, Aperture E, is neither flush with a waveguide wall nor centered in the waveguide cross section.

The first 150 modes were used to generate the matrix elements of D, when the material under test is a sample of Eccosorb FGM125, 0.125" thick. The nominal values for Eccosorb FGM125, shown in Table 5.1, were used to generate these matrix elements. All possible combinations of TE and TM modes were considered, and no

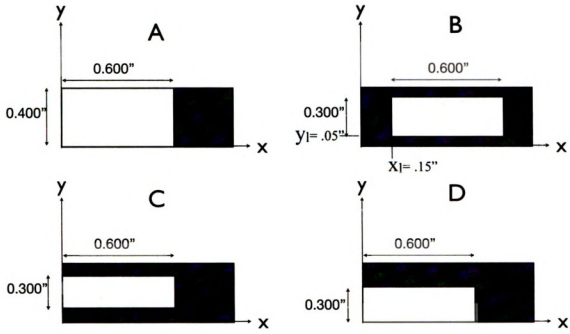


Figure 8.1. Apertures A-D for the two iris method.

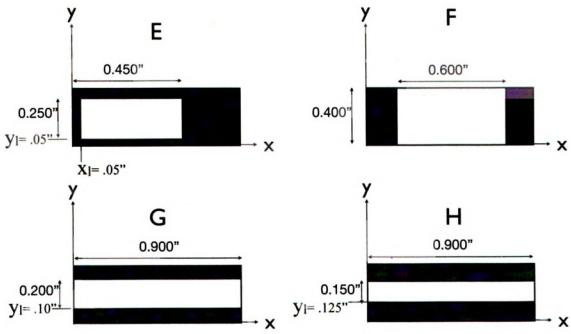


Figure 8.2. Apertures E-H for the two iris method

modes were eliminated from consideration due to symmetry arguments. Thus, all $TE_{u\,v}$ modes, where $u = 0, 1, 2, ...$, $v = 0, 1, 2, ...$, and $u + v > 0$, and all $TM_{u\,v}$ modes, where $u = 1, 2, 3, ...$, $v = 1, 2, 3, ...$, were used in the solution. Estimates of the theoretical reflection coefficient, $S_{11}^{thy(2I)}$ were computed for different values of N in the X-band frequency range. Note that the total size of the matrix is 450×450.

Consider the plot of the magnitudes of $S_{11}^{thy(2I)}$ for Apertures A-D in Figure 8.3 for 8.20 GHz. Each of the lines display the magnitude of the reflection coefficient as a function of the number of modes for each aperture. Note that a large number of modes make a significant contribution to the magnitude of Apertures A and B. Aperture B does not have any aperture walls in common with the waveguide walls, but is centered in the waveguide opening. Aperture A, on the other hand, does share an entire wall with the waveguide, and covers part of the top and lower walls.

In contrast, Apertures C and D have a common aperture wall with the waveguide at $x = 0$, but the entire wall is not shared with the waveguide. Aperture C is centered in the y-direction of the waveguide cross section, but Aperture D is not centered in either direction. The plots of the reflection coefficient magnitude for Apertures C and D show a more erratic pattern than apertures A and B, and a large number of modes make a significant contribution to the magnitude. The plots for Aperture C and D are very similar and display a similar behavior as more modes are used in the solution. This is not surprising, since the dimensions of both apertures are identical. The discrete drops in the magnitude occur at many of the same modes, indicating that many of the same modes have a significant contribution for both apertures. Also note that Aperture B, which has the same dimensions A_x and A_y as Apertures C and D, does share some similarities to the pattern observed for those two apertures. However, Aperture B is positioned in the center of the waveguide and has a less jagged profile. It is conjectured that the symmetrical positioning, especially in the x-direction, reduces the number of modes which are excited at the waveguide/aperture

discontinuity. This conjecture is considered with the other apertures. Aperture B also has the lowest overall magnitude of the four apertures in this figure. Due to the symmetry, more energy from the incident TE_{10} mode is able to interrogate the material. Apertures C and D, on the other hand, are not centered in the waveguide. Thus, more less coupling and more reflection occurs, resulting in a higher magnitude for the reflection coefficient.

The plot of the phase, displayed in Figure 8.4 as a function of the number of modes, shows similar behavior. Note that the plot of the phase for Apertures C and D are almost identical. The phase plot of Aperture A and B also shows similar behavior.

The magnitudes of $S_{11}^{thy(2I)}$ for Apertures E-H are shown in Figure 8.5. The magnitude of the reflection coefficient for Aperture E is the highest, near a value near 0.92 for most of the graph. Note that the dimensions of Aperture E are smaller than any of the other apertures, with $A_x = 0.25''$, and $A_y = 0.45''$. The lowest cutoff frequency for this aperture is $f_c = 13.114$ GHz for the TE_{10} mode, and thus all modes in X-band are evanescent in this aperture. Since the thickness of the aperture in the axial direction, d_2, is only $0.125''$, some of the energy from the lower order modes still interacts with the material. Most of the energy, however, is reflected. Aperture E is also not centered in either direction in the waveguide cross section, similar to Aperture D. Note also that a large number of modes makes a contribution to the magnitude of the reflection coefficient, similar to Aperture C and D.

Consider the plot for Aperture F, in Figure 8.5, which shares aperture walls with the waveguide at $y = 0$ and $y = 0.400''$. This aperture is also centered in the waveguide cross section in both dimensions. The magnitude of of $S_{11}^{thy(2I)}$ for Aperture F is the lowest for the 8 apertures examined in this stage of analysis. Although several modes make a significant contribution to the reflection coefficient, fewer significant modes are observed in the plot for Aperture F than Apertures A - E.

Note that the plots for Apertures G and H shown in Figure 8.5 have a similar structure. The aperture walls at $x = 0$ and $x = a$ are flush with the waveguide walls for these two apertures, and they are centered in the y-direction of the waveguide cross section. In addition, these two apertures have the least discrete changes occurring over the 150 modes observed. It is observed that the overall pattern for these two apertures shares some similarities to the plot shown in Figure 5.1, which is the full WR-90 waveguide opening placed against a layer of Eccosorb FGM125. Recall that the changes at the higher order modes in Figure 5.1 occurred at the $TM_{1\,even}$ modes. The corresponding modes at which the significant changes in magnitude occur for both Apertures G and H are also the $TM_{1\,even}$ modes for the aperture region.

It is noted that the incident wave which interacts with the aperture at $z = d_2$ is the $TE_{1\,0}$ waveguide mode. Since the waveguide walls are flush with the Apertures G and H, the structure of the transverse electric and magnetic fields in the aperture couples well with the $TE_{1\,0}$ mode and the $TM_{1\,even}$ modes. In addition, note that $|S_{11}^{thy(2I)}|$ is larger for Aperture H than for Aperture G. This is also consistent with the geometry of the two apertures, where the opening of Aperture H is smaller than that of Aperture G.

The phase of $S_{11}^{thy(2I)}$ for Apertures E-H is plotted in Figure 8.6 as a function of the number of modes. Apertures G and H also display the primary contributions to the phase at the $TM_{1\,even}$ modes. The phase plots for Apertures E and F show that a large number of modes contribute to the phase, as with the magnitude plots.

It is also desirable to examine the behavior of these different apertures at other frequencies in the band of interest. Similar plots of the magnitude and phase at 10.09 GHz, near the middle of the X-band, are shown in Figure 8.7 for apertures A and B. The plots at this frequency are plotted on an expanded magnitude scale to reveal more of the details of the magnitude plot, and the observations are similar to those shown at 8.2 GHz. As is marked in the figure, the $TM_{1\,even}$ modes make a significant

contribution to the magnitude. It is more clear in this figure that a large number of modes make a significant contribution to the magnitude for Apertures A and B. When N = 150 modes, the magnitude for either aperture has not converged to a clear solution. Upon examination of the figure, it is not clear if any specific pattern of TM or TE modes cause the discrete changes in the magnitude. The phase for these two apertures is shown in Figure 8.8.

The plots of the magnitude and phase of $S_{11}^{thy(2I)}$ for Apertures C and D are shown in Figure 8.9 and Figure 8.10, respectively. Several of the first 15 modes make a contribution to the magnitudes of both apertures. Also, similar to the results for these apertures at 8.2 GHz, significant decreases in magnitude occur at the modes which correspond to the $TM_{1\,even}$ modes in the aperture region. Similar observations are made for the phase plot in Figure 8.10.

The magnitude plots for Apertures E and H are shown in Figure 8.11 at 10.09 GHz. With the expanded scale, it is clear that Aperture H has only a few modes which contribute to the solution. The increase and decrease in the plot at modes 15 and 16 correspond to the TE_{12} and TM_{12} waveguide modes, respectively. In addition, the discontinuities at modes 56, 57, 126, and 127 correspond to the TE_{14}, TM_{14} TE_{16} and TM_{16} waveguide modes. As is labeled in the graph, the other drops in the magnitude occur at the $TM_{1\,even}$ aperture modes. Additional investigation confirmed that the significant contributions to the magnitude for Aperture H occur at the waveguide $TE_{1\,even}$ and $TM_{1\,even}$ waveguide modes and at the $TM_{1\,even}$ aperture modes. Compare the plot for Aperture H to the plot shown for Aperture E. For Aperture E, a large number of the first 150 modes make a contribution to the magnitude. This indicates that a large number of modes are excited at $z = d_2$, and these modes contribute a significant amount to the magnitude of the reflection coefficient. The phase plot in Figure 8.12 also displays a similar structure.

In Figure 8.13 and Figure 8.14, the plots for Aperture F and Aperture G are

shown. Aperture G shows a similar behavior to Aperture H, where the modes that have the most significant effect are the $TM_{1\,even}$ modes in the aperture region. In addition, contributions are also observed from the waveguide $TE_{1\,even}$ and $TM_{1\,even}$ modes. The only difference in the geometry for Apertures G and H is the width of the aperture. Aperture F, in contrast, shows more modes which contribute to the solution, but not as many as are found for Apertures A-E. Note that Aperture F has symmetry in the y-direction, which affects the number of possible mode combinations at the discontinuity at $z = d_2$.

Consider the discontinuities in $S_{11}^{thy(2I)}$ for Aperture F over the first 51 modes. Contributions to the magnitude of the reflection coefficient are occur at the $TE_{odd\,0}$ aperture modes, modes 1,9, 28, and 51; the $TE_{1\,even}$ aperture modes, modes 10 and 40; and the $TM_{1\,even}$ aperture modes, modes 11 and 41. Additional contributions correspond to the $TE_{odd\,0}$ waveguide modes, modes 6 and 19.

When considering the best candidates for use in the two aperture method, one key criterion is an aperture which will take the least amount of time to fill the matrix. As was noted in the observations of Apertures A-H, several apertures require a large number of modes to capture the significant contributions of the modes under consideration. Using this criteria, Apertures B and E are eliminated from consideration. The use of these apertures requires a large number of modes to accurately estimate the reflection coefficient, and would thus require more computational time. In addition, a large number of modes contribute to the magnitude of Apertures A, C and D. Thus, the next step of the analysis focuses on Apertures F, G, and H.

8.3 Extrapolation procedure

An examination of the magnitude and phase of the reflection coefficient in Figure 8.3-Figure 8.14 reveals that the $S_{11}^{thy(2I)}$ values for those apertures have not converged, even after using the first 150 modes. A reasonable conjecture for the two iris method is

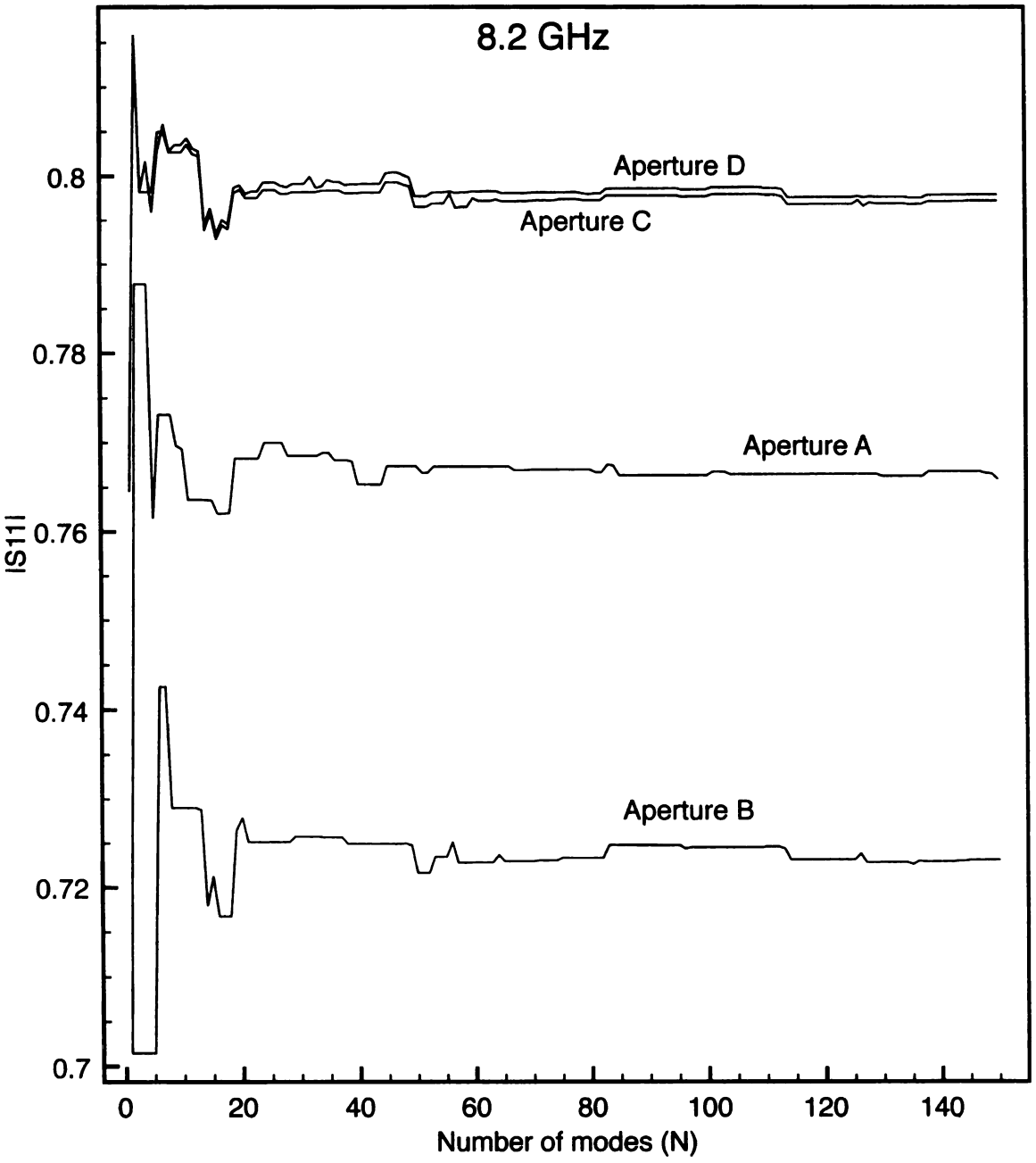


Figure 8.3. Plot of $|S_{11}^{thy(2I)}|$ as a function of number of modes for Apertures A, B, C and D at 8.2 GHz. Aperture thickness, d_2 =0.125". Material under test: Eccosorb FGM125, $h = 0.125''$. All possible modes are considered.

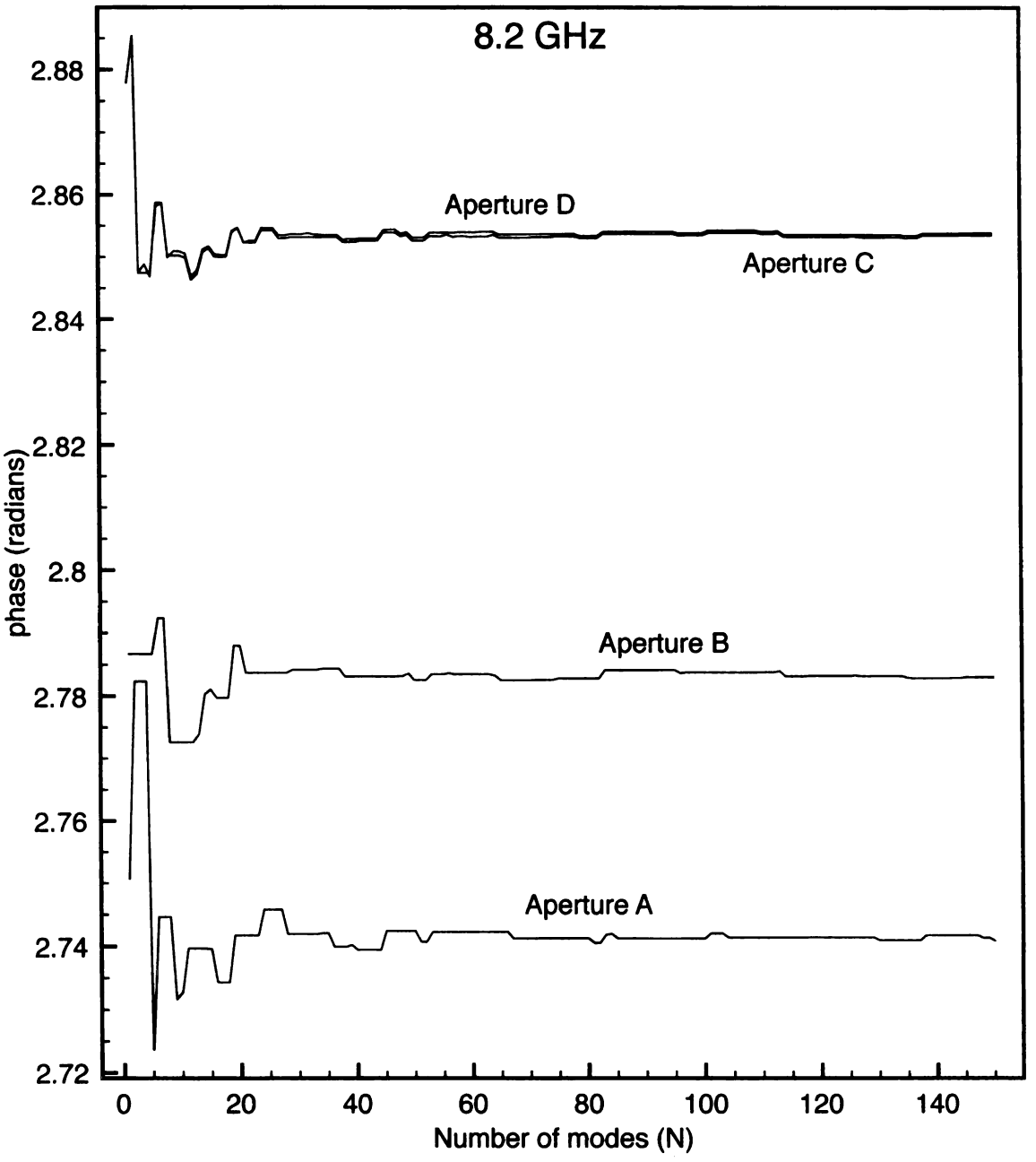


Figure 8.4. Plot of the phase of $S_{11}^{thy(2I)}$ as a function of number of modes for Apertures A, B, C and D at 8.2 GHz. Aperture thickness, d_2 =0.125". Material under test: Eccosorb FGM125, $h = 0.125''$. All possible modes are considered.

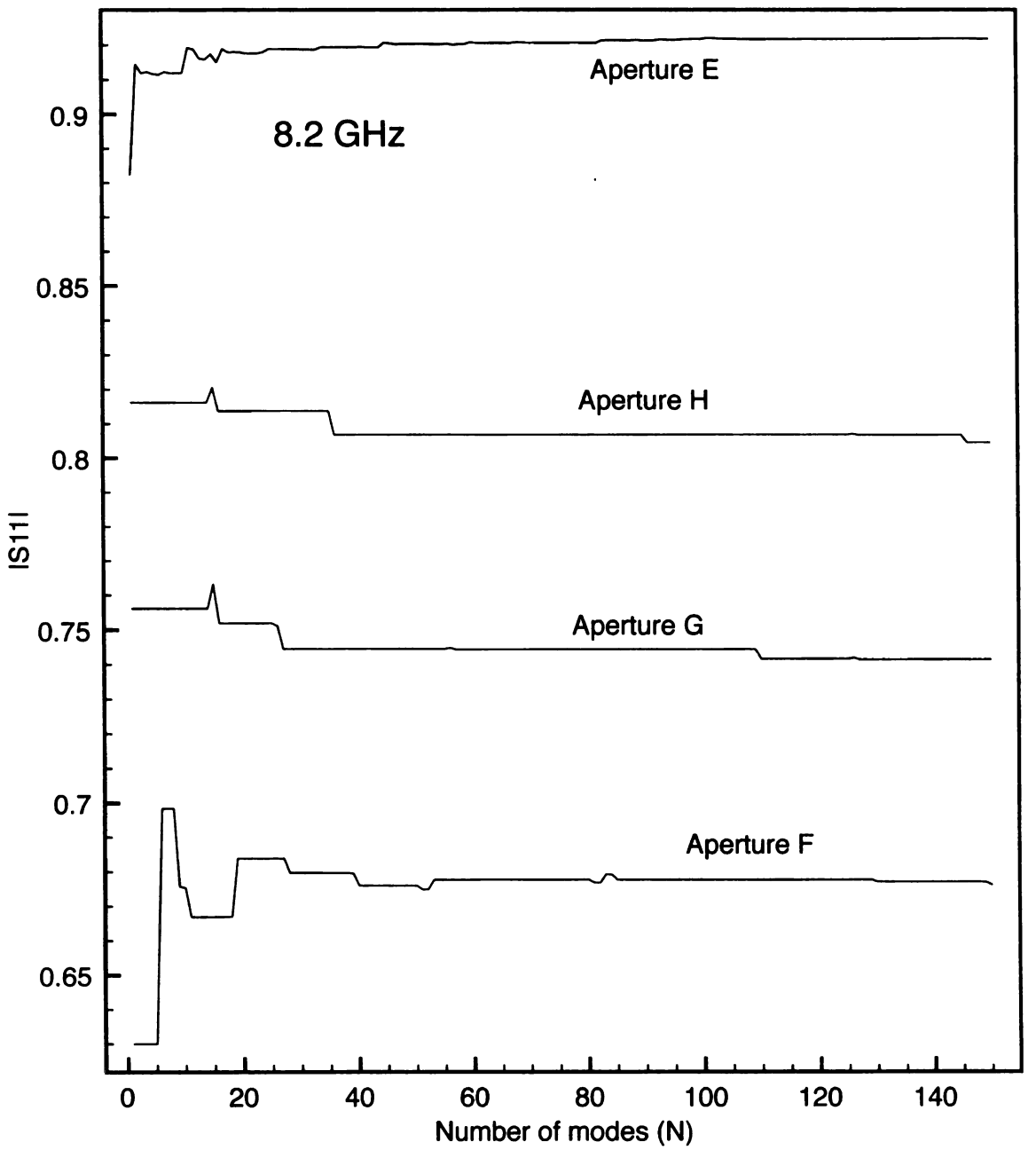


Figure 8.5. Plot of $|S_{11}^{thy(2I)}|$ as a function of number of modes for Apertures E, F, G, and H at 8.2 GHz. Aperture thickness, d_2 =0.125". Material under test: Eccosorb FGM125, $h = 0.125''$. All possible modes are considered.

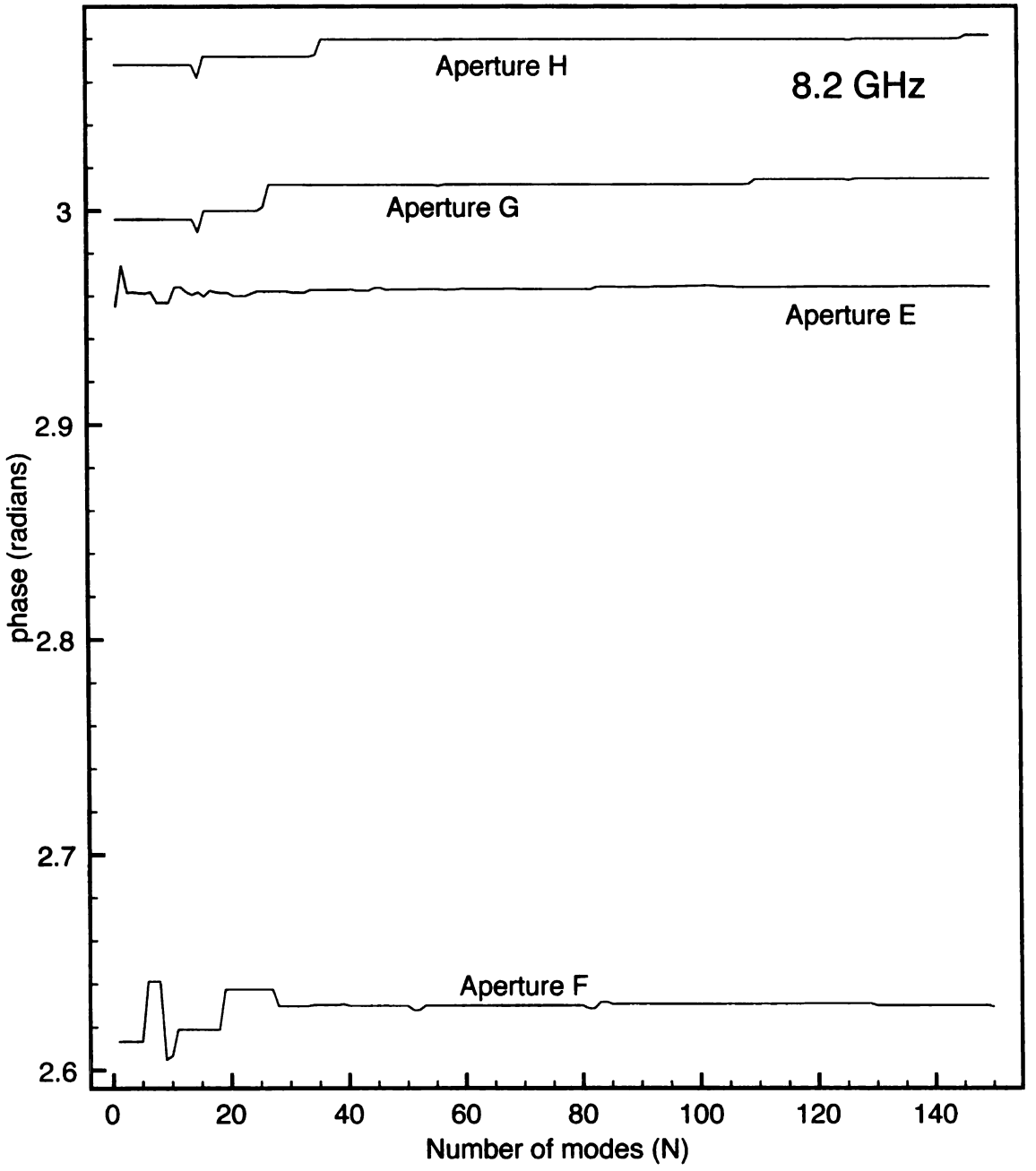


Figure 8.6. Plot of the phase of $S_{11}^{thy(2I)}$ as a function of number of modes for Apertures E, F, G, and H at 8.2 GHz. Aperture thickness, d_2 =0.125". Material under test: Eccosorb FGM125, $h = 0.125''$. All possible modes are considered.

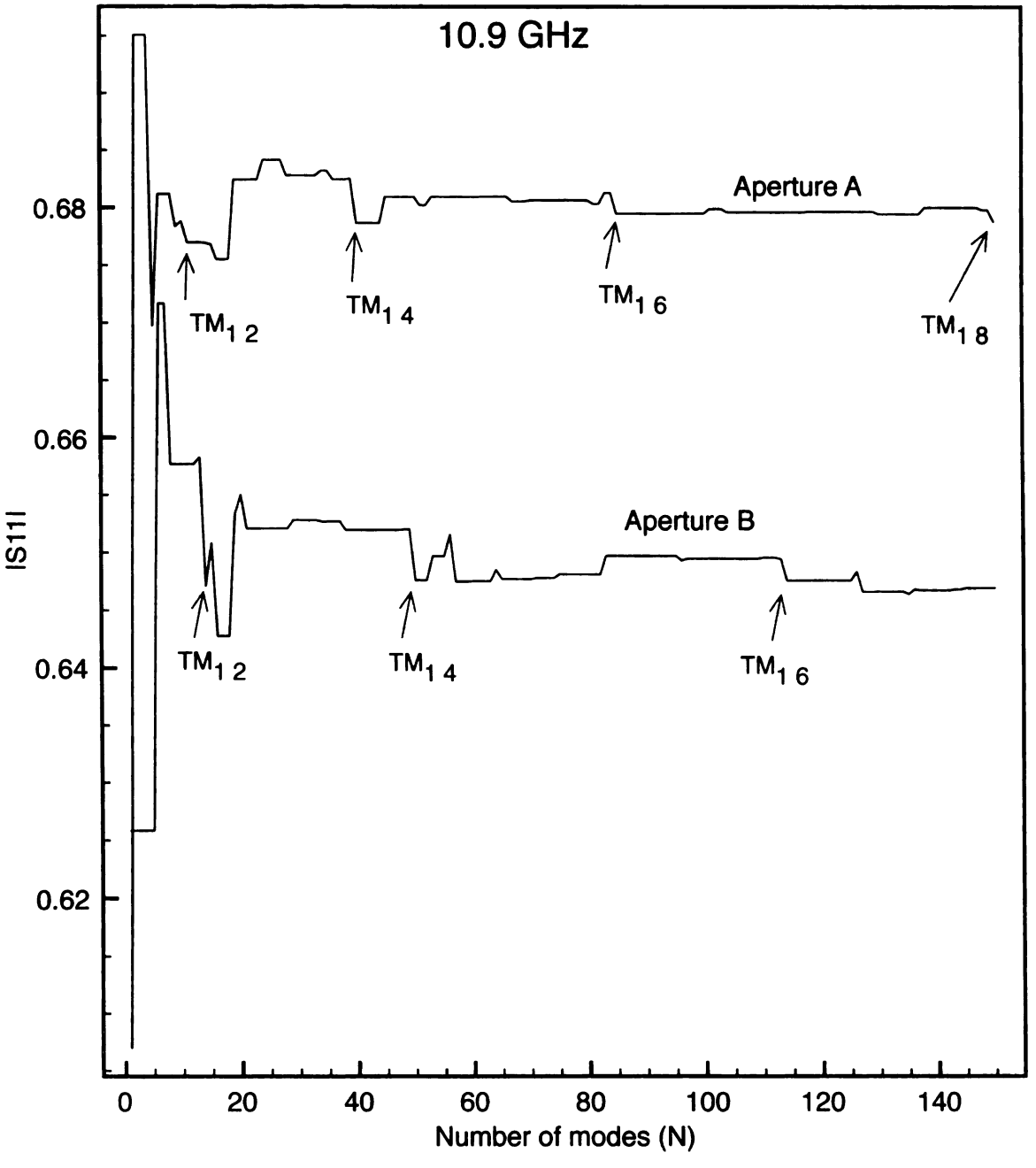


Figure 8.7. Plot of $|S_{11}^{thy(2I)}|$ as a function of number of modes for Apertures A and B at 10.09 GHz. Aperture thickness, d_2 =0.125". Material under test: Eccosorb FGM125, $h = 0.125''$. All possible modes are considered.

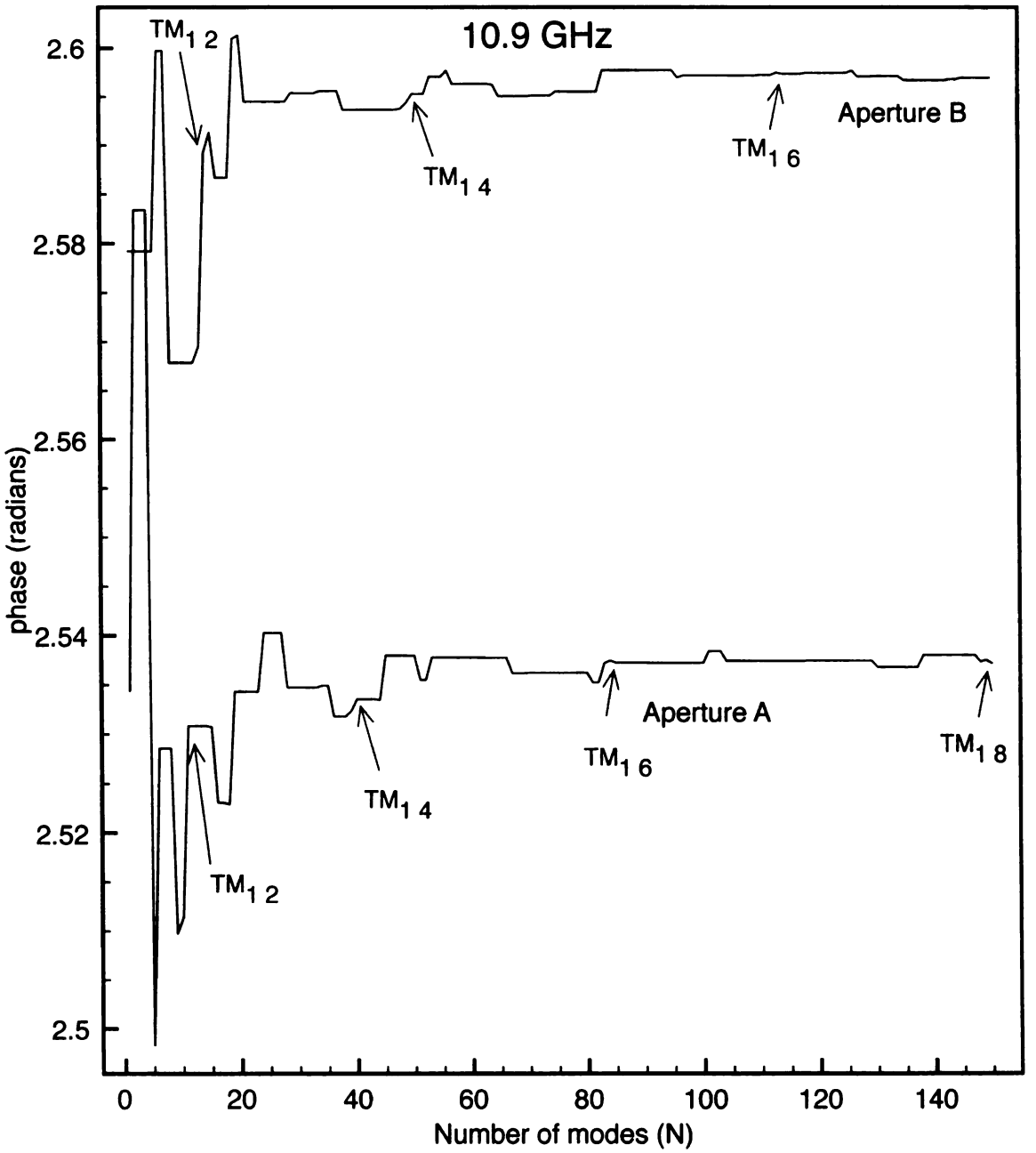


Figure 8.8. Plot of the phase of $S_{11}^{thy(2I)}$ as a function of number of modes for Apertures A and B at 10.09 GHz. Aperture thickness, d_2 =0.125". Material under test: Eccosorb FGM125, $h = 0.125''$. All possible modes are considered.

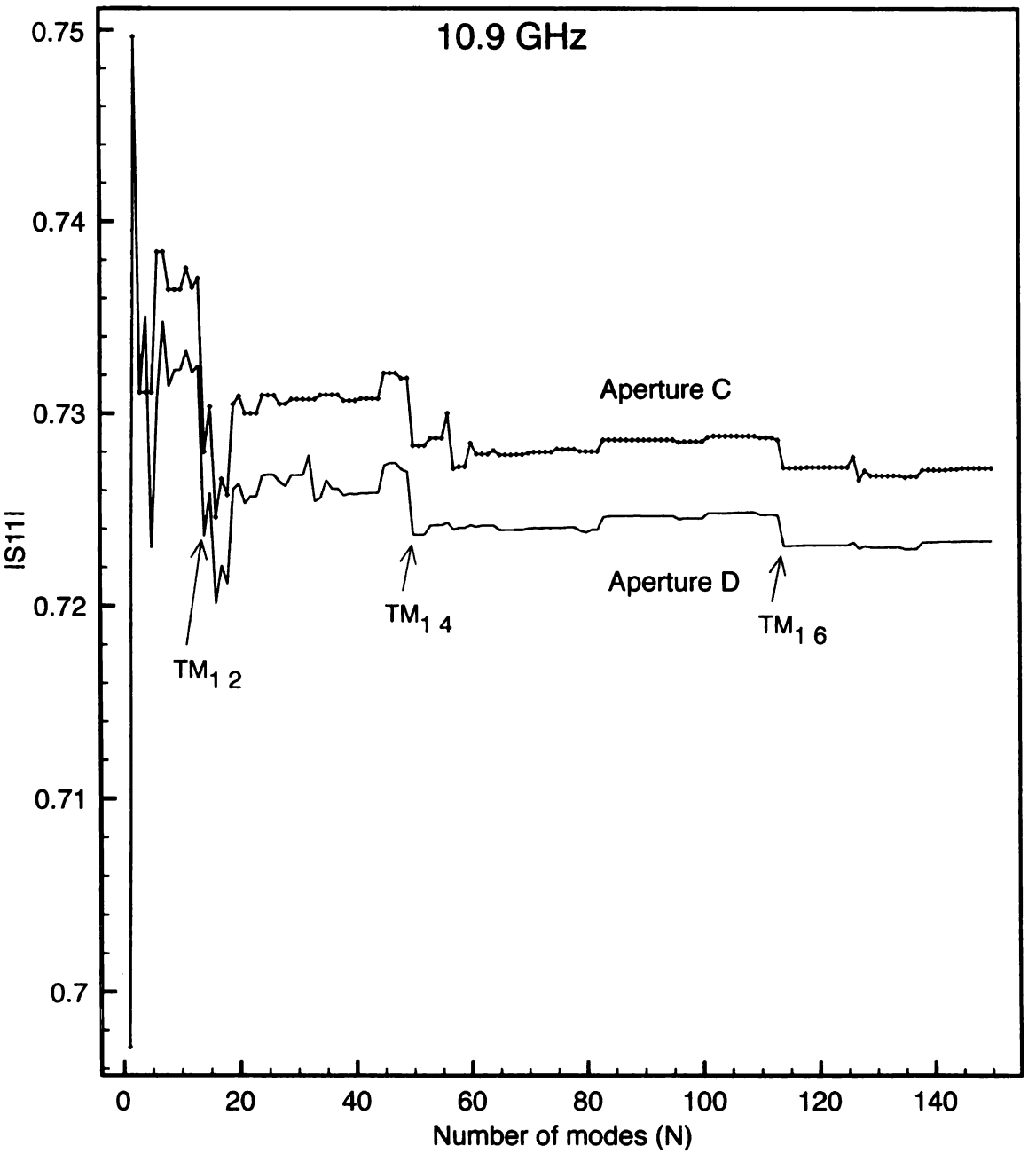


Figure 8.9. Plot of $|S_{11}^{thy(2I)}|$ as a function of number of modes for Apertures C and D at 10.09 GHz. Aperture thickness, d_2 =0.125". Material under test: Eccosorb FGM125, $h = 0.125''$. All possible modes are considered.

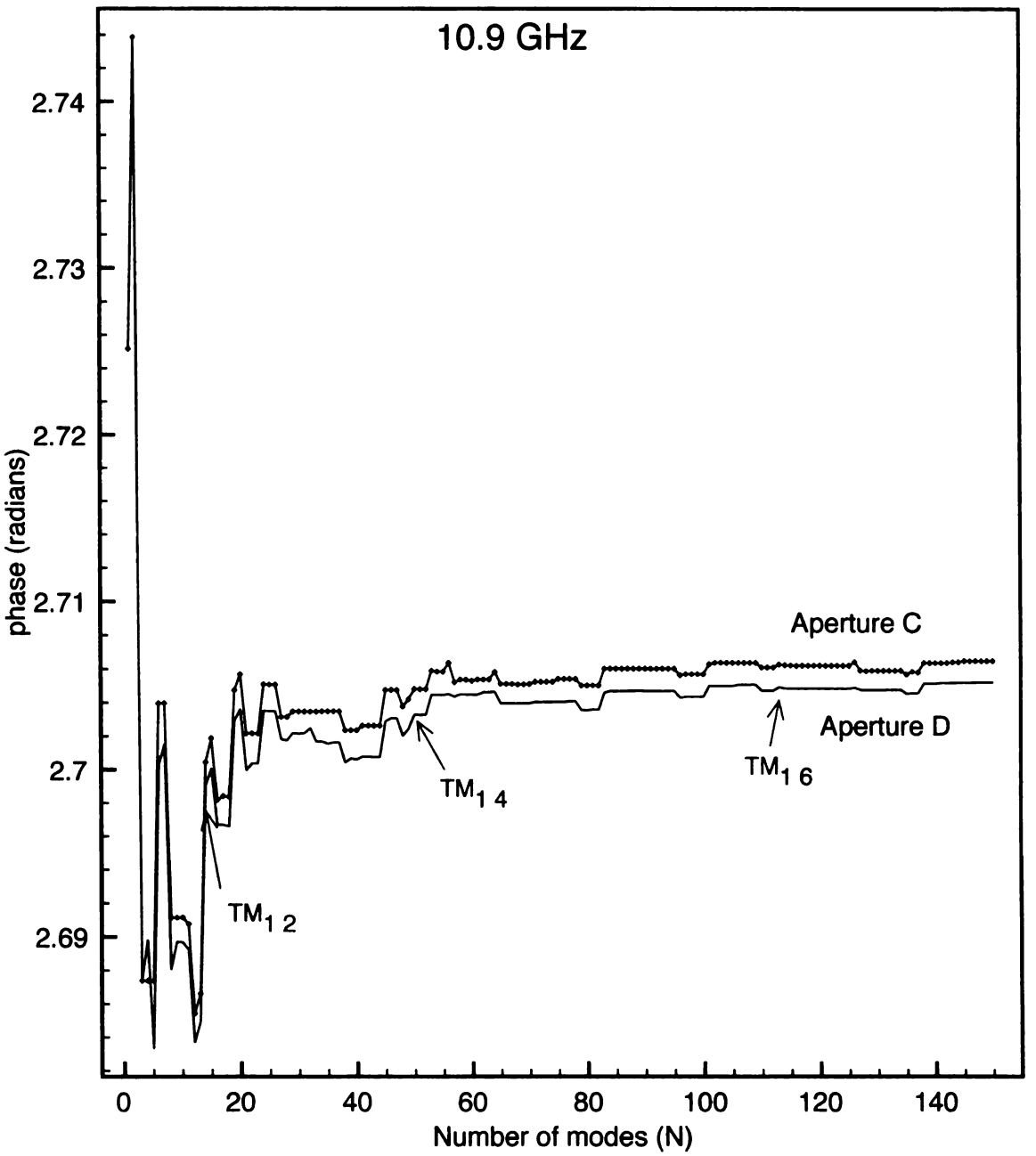


Figure 8.10. Plot of the phase of $S_{11}^{thy(2I)}$ as a function of number of modes for Apertures C and D at 10.09 GHz. Aperture thickness, d_2 =0.125". Material under test: Eccosorb FGM125, $h = 0.125''$. All possible modes are considered.

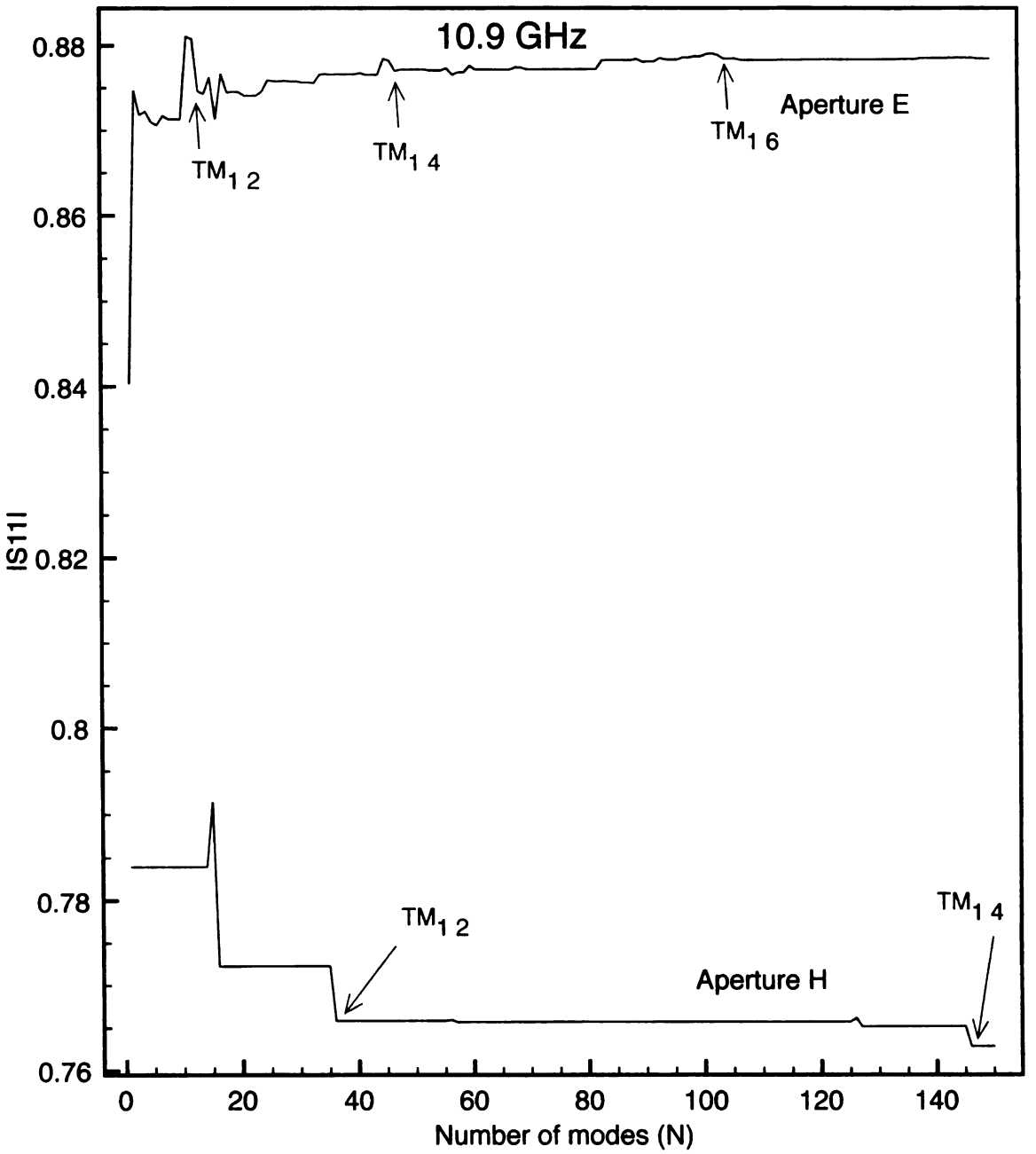


Figure 8.11. Plot of $|S_{11}^{thy(2I)}|$ as a function of number of modes for Apertures E and H at 10.09 GHz. Aperture thickness, d_2 =0.125". Material under test: Eccosorb FGM125, $h = 0.125''$. All possible modes are considered.

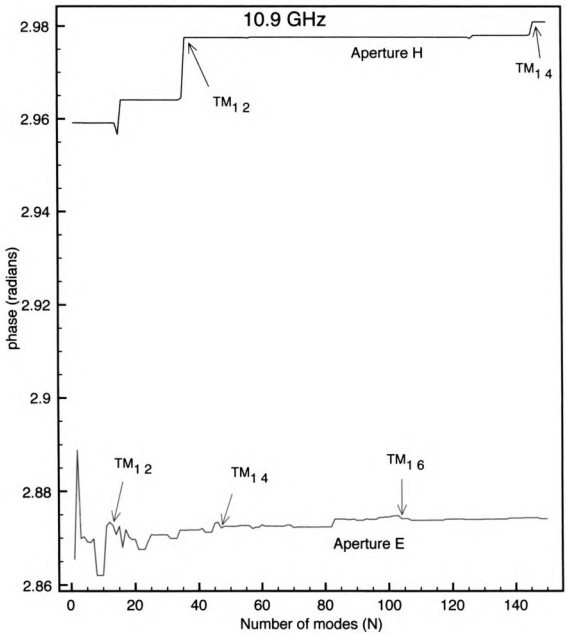


Figure 8.12. Plot of the phase of $S_{11}^{thy(2I)}$ as a function of number of modes for Apertures E and H at 10.09 GHz. Aperture thickness, d_2 =0.125". Material under test: Eccosorb FGM125, $h = 0.125''$. All possible modes are considered.

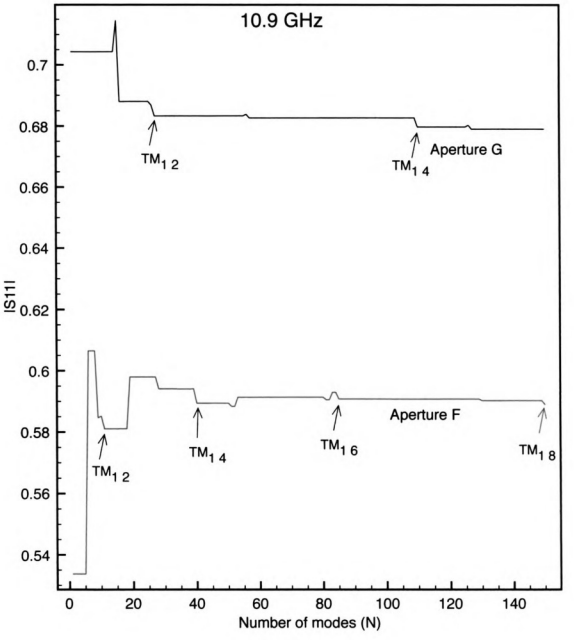


Figure 8.13. Plot of $|S_{11}^{thy(2I)}|$ as a function of number of modes for Apertures F and G at 10.09 GHz. Aperture thickness, d_2 =0.125". Material under test: Eccosorb FGM125, $h = 0.125''$. All possible modes are considered.

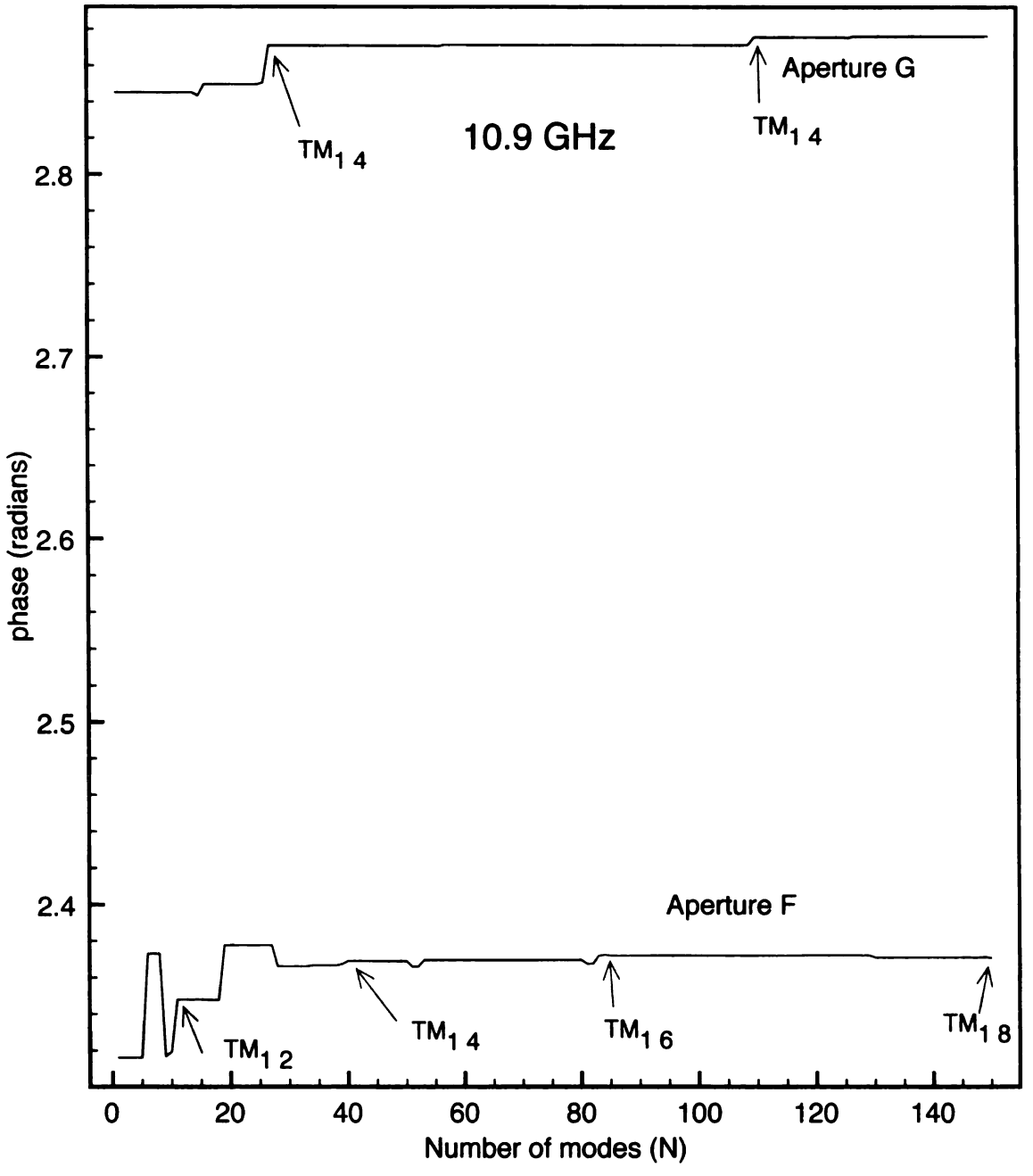


Figure 8.14. Plot of the phase of $S_{11}^{thy(2I)}$ as a function of number of modes for Apertures F and G at 10.09 GHz. Aperture thickness, d_2 =0.125". Material under test: Eccosorb FGM125, $h = 0.125''$. All possible modes are considered.

that an extrapolation procedure similar to what is employed in the two layer method might be used to obtain a better estimate of the contribution of a large number of modes.

The major contributions to the reflection coefficient occur at the aperture region $TM_{1\,even}$ modes for Apertures F, G, and H. This is similar to the observations made for the two layer method. However, for Aperture F, the $TE_{1\,even}$ and $TE_{odd\,0}$ aperture modes also contribute. In addition, the $TE_{1\,even}$ and $TM_{1\,even}$ waveguide modes also make a significant contribution. The magnitude and phase of the theoretical reflection coefficient, $S_{11}^{thy(2I)}$, were calculated by picking the higher order aperture modes and waveguide modes that make a significant contribution to the reflection coefficient.

To investigate the possibility of using the extrapolation method from Chapter 5, the magnitude and phase of $S_{11}^{thy(2I)}$ at each $TM_{1\,v}$ mode were plotted vs $1/v$, where v is the second index of the mode. The magnitude and phase for Apertures F, G, and H are plotted in Figure 8.15 - Figure 8.17.

Note that for Apertures G and H, these plots exhibit a linear nature when plotted in this manner for both the magnitude and phase. The values for Aperture F appear to be nearing a converging linear nature on the left hand side of the figure, as $1/v$ decreases. Thus it is reasonable to conclude that the linear extrapolation scheme that was employed for the two layer method may also be employed for the two iris method. The extrapolated values are a better approximation of the reflection coefficient than using 10 of the lower order modes, as has been attempted by others [35], [39]. The result of using the extrapolation method is a reduction of the error in the calculation of the reflection coefficient. The extrapolated reflection coefficient is labeled in subsequent references and graphs as $S_{11}^{(2I)extr}$. Plots of the magnitude and phase of the extrapolated reflection coefficient, $S_{11}^{(2I)extr}$, for Apertures F, G, and H are shown in Figure 8.18 and Figure 8.19, respectively. The thickness of the aperture for these simulations is $d_2 = 0.125''$.

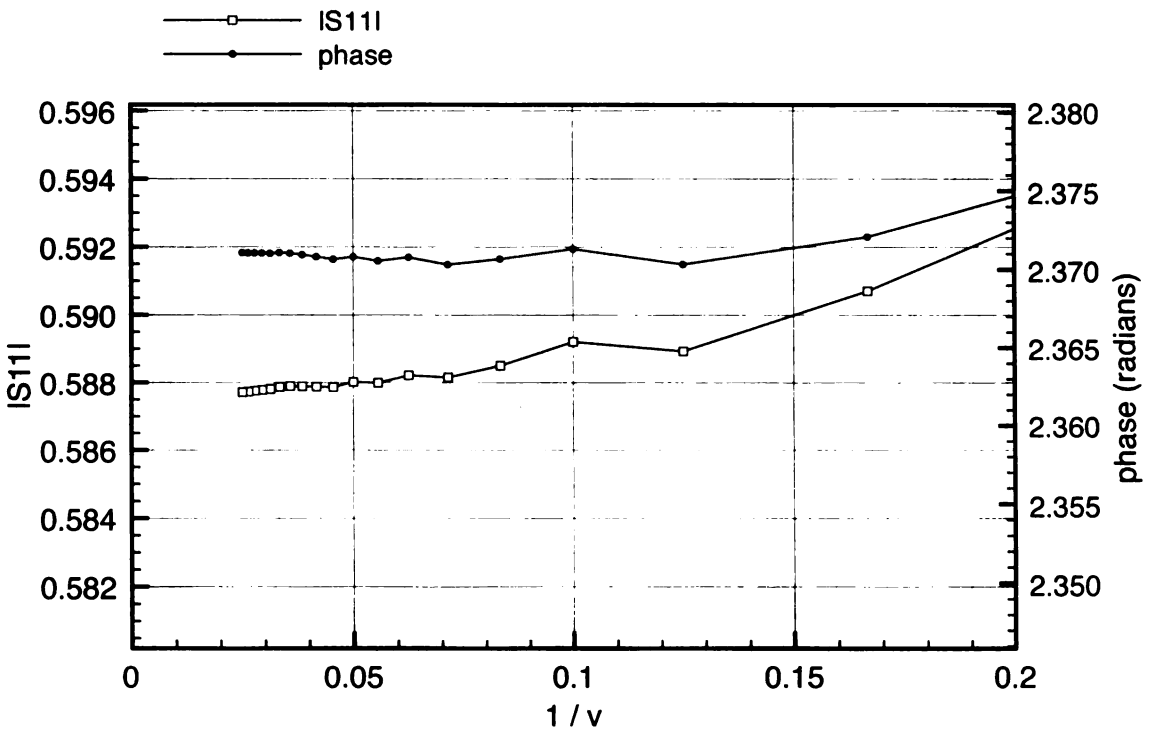


Figure 8.15. Magnitude and phase of the reflection coefficient for 1 layer of Eccosorb FGM125, 0.125" thick, at 10.09 GHz, using only the modes that contribute significantly to the solution for Aperture F. The reflection coefficient is computed by including the modes up to the $TM_{1\,v}$ mode. Aperture thickness, d_2 =0.125". These values are plotted vs. $1/v$.

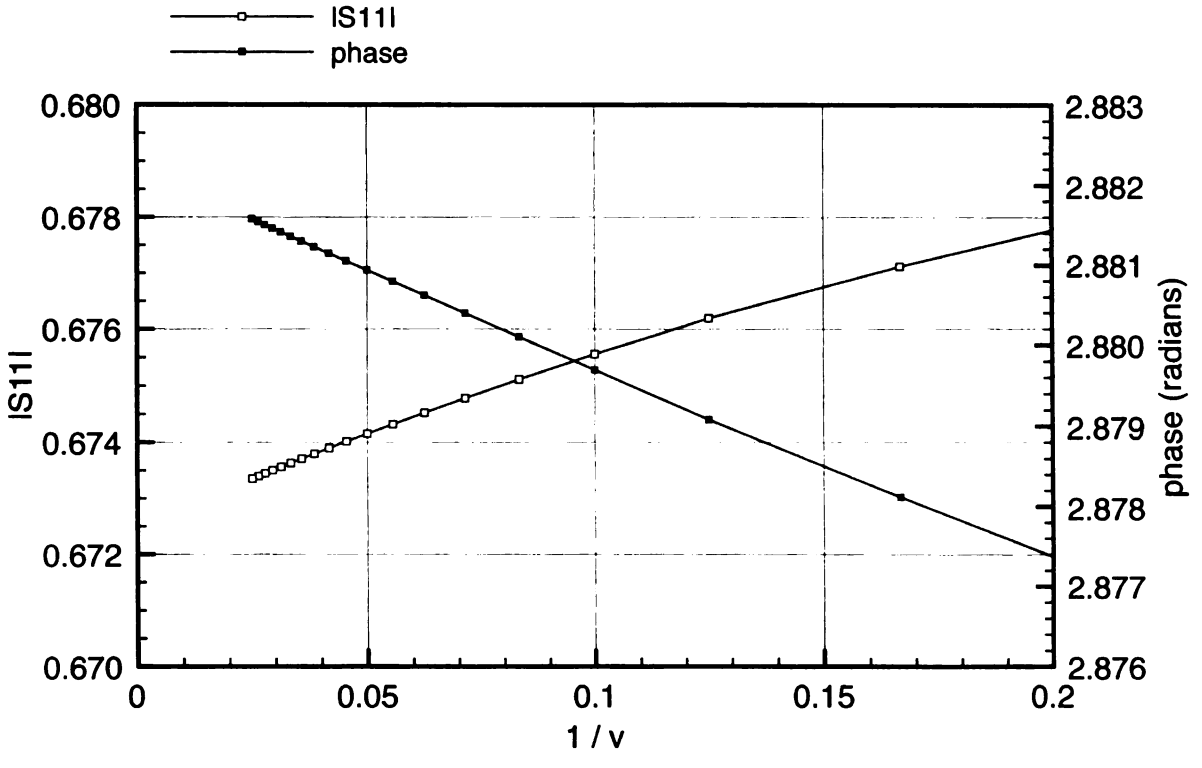


Figure 8.16. Magnitude and phase of the reflection coefficient for 1 layer of Eccosorb FGM125, 0.125" thick, at 10.09 GHz, using only the modes that contribute significantly to the solution for Aperture G. The reflection coefficient is computed by including the modes up to the $TM_{1\,v}$ mode. Aperture thickness, d_2 =0.125". These values are plotted vs. $1/v$.

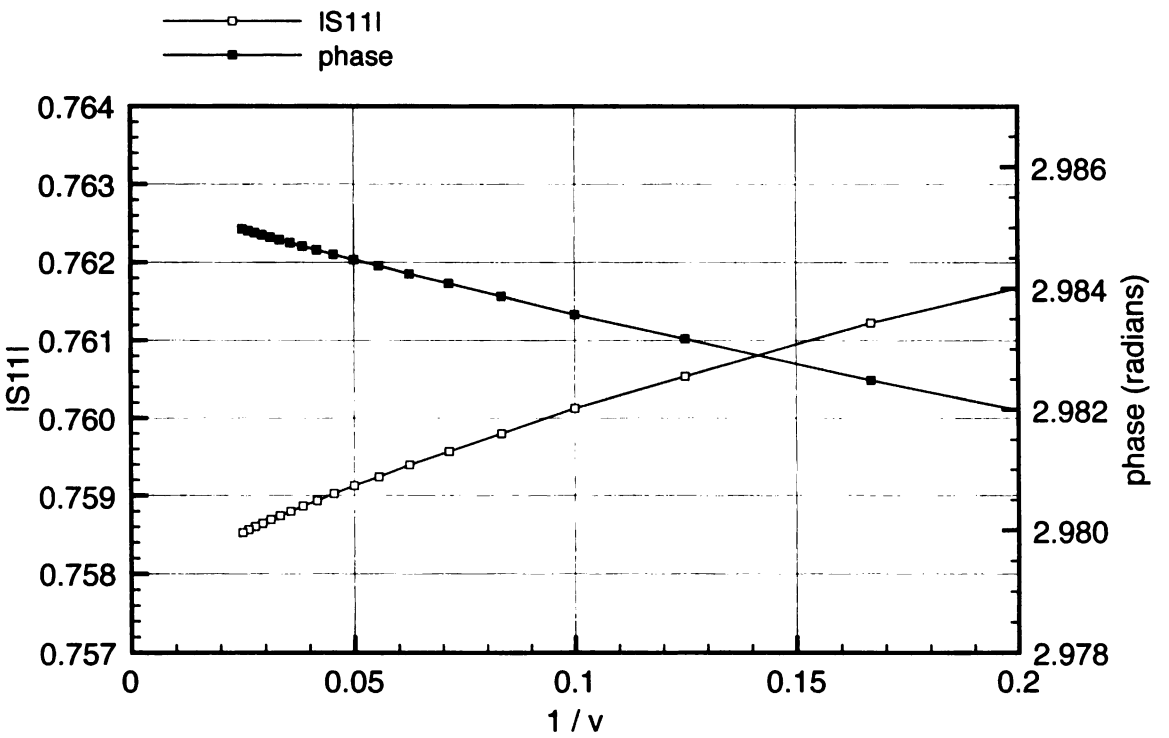


Figure 8.17. Magnitude and phase of the reflection coefficient for 1 layer of Eccosorb FGM125, 0.125" thick, at 10.09 GHz, using only the modes that contribute significantly to the solution for Aperture H. The reflection coefficient is computed by including the modes up to the $TM_{1\,v}$ mode. Aperture thickness, d_2 =0.125". These values are plotted vs. $1/v$.

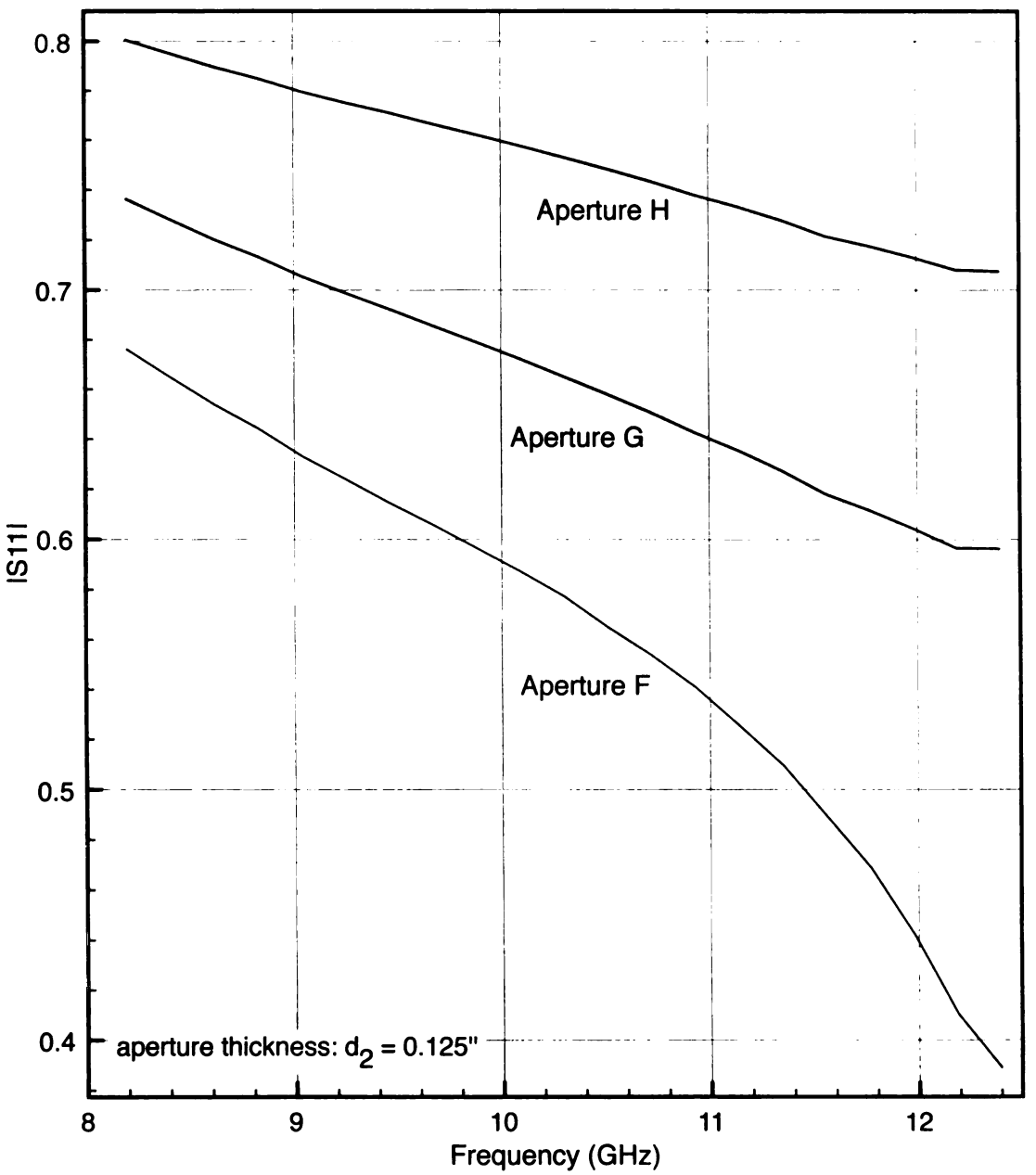


Figure 8.18. Magnitude of the reflection coefficient for 1 layer of Eccosorb FGM125, 0.125" thick for Apertures F, G, H. The reflection coefficient, $S_{11}^{(2I)extr}$, is computed by extrapolating from the $TM_{1\,40}$ mode. Aperture thickness, d_2 =0.125".

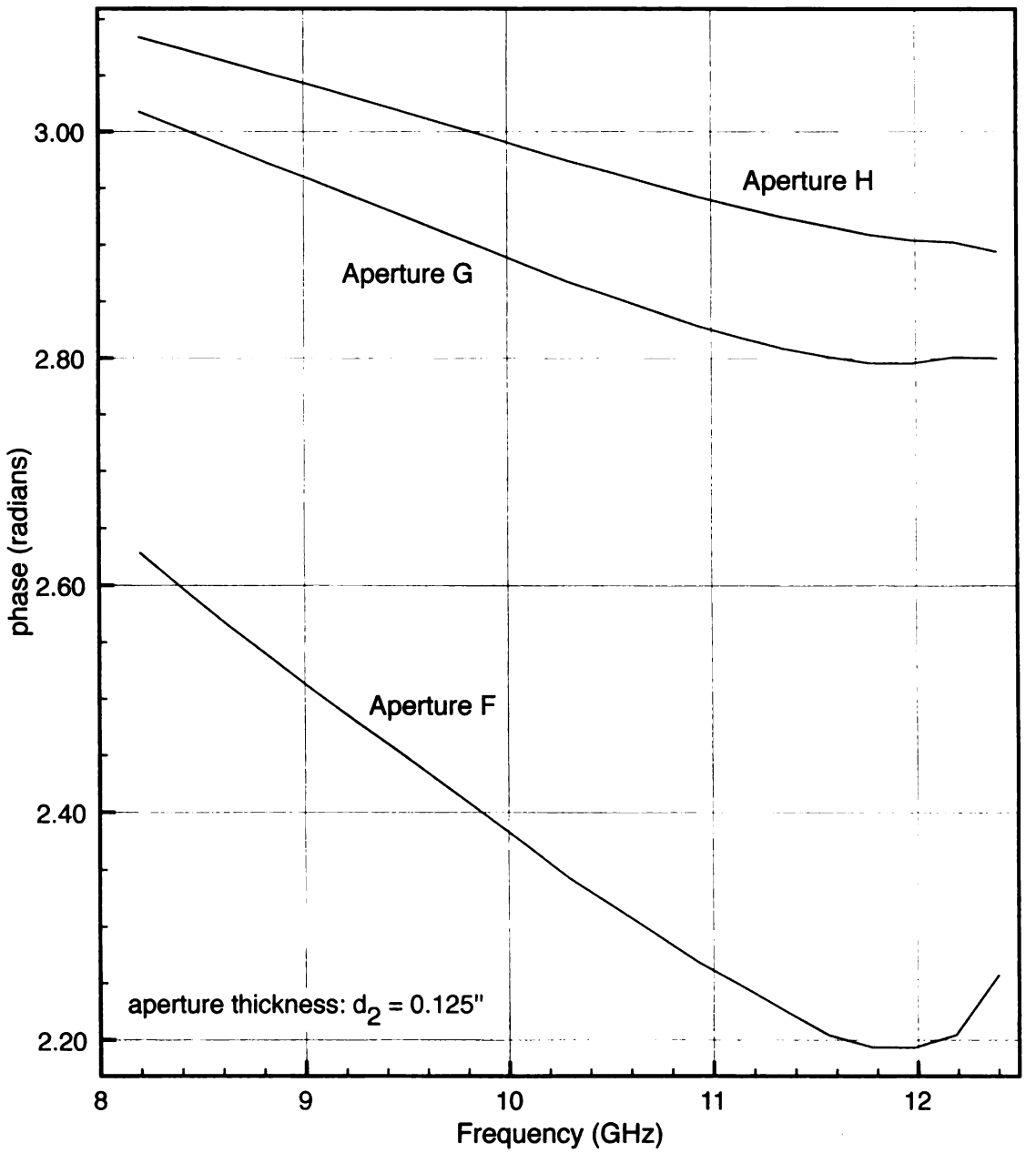


Figure 8.19. Phase of the reflection coefficient for 1 layer of Eccosorb FGM125, 0.125" thick for Apertures F, G, H. The reflection coefficient, $S_{11}^{(2I)extr}$, is computed by extrapolating from the $TM_{1\,40}$ mode. Aperture thickness, d_2 =0.125".

The opening of Aperture H is smaller than the opening for Aperture G. Thus, it would be expected that more energy would be reflected back towards the source for Aperture H, which is what is observed in Figure 8.18. Also note that the plot of $|S_{11}^{extr}|$ is similar for Apertures G and H across the frequency band, with the magnitude of Aperture H larger than Aperture G. The geometrical structure of Aperture F is larger than G and H in the y-direction, yet it has been reduced in the x-direction. Note that the plot of the magnitude for Aperture F is higher across the frequency band, indicating that more of the incident energy from the incident $TE_{1\,0}$ mode is reflected than is reflected for Apertures G and H. Similar results are seen for the plot of the phase in Figure 8.19.

For all three apertures, the $TE_{1\,0}$ mode is the only propagating mode in the aperture. The cutoff frequency for the $TE_{1\,0}$ mode is 6.557 GHz for Apertures G and H, and 9.836 GHz for Aperture F. All other modes are evanescent. The cutoff frequency of the next higher order aperture mode that contributes to the reflection coefficient, the $TM_{1\,2}$ mode, is $f_c = 59.377$ GHz, for Apertures G and H. The next higher order aperture mode that contributes to the reflection coefficient for Aperture F, the $TE_{3\,0}$ mode, has a cutoff frequency of $f_c = 29.507$ GHz. If the aperture thickness is larger, these and the other higher mode amplitudes will evanesce. To examine the effect of a longer aperture on the reflection coefficient, additional simulations were performed for different thicknesses of the aperture. The results of these simulations are shown in Figure 8.20 - Figure 8.23.

Note that when the aperture thickness d_2 is larger, the reflection coefficient magnitude for Aperture F is near unity until the frequency surpasses the cutoff frequency of the $TE_{1\,0}$ mode, $f_c = 9.836$ GHz. For the lower part of the frequency band, all of the modes excited at the waveguide/aperture discontinuity evanesce. At those frequencies, most of the energy of the incident $TE_{1\,0}$ mode is reflected back towards the source. Above the cutoff frequency, the $TE_{1\,0}$ mode propagates through the aperture

to interrogate the materials. Also note that the shape of the plots for Apertures G and H in all four figures are similar to one another across the frequency band, which is also expected.

It is desirable to achieve as strong of an interrogation field in the material as possible. With a thicker aperture, the evanescent modes decay and do not provide much interrogation of the material under test. It is also noted that procuring and machining a thicker piece of metal is of greater expense than a thinner one. Thus, a thinner aperture is considered more desirable than a thicker one.

8.4 Sensitivity Analysis for the Two Aperture Method

As was noted in the previous section, Apertures G and H are desirable apertures for further investigation. The extrapolation method may be used to estimate the reflection coefficient due to a large number of modes for these apertures. This method is employed to reduce the error in the calculation of the theoretical reflection coefficient, and to do so efficiently. Aperture F, in contrast, requires the inclusion of additional modes to the solution.

A sensitivity analysis was undertaken for the two iris method to determine which of the apertures under consideration would be the least sensitive to random measurement error. This analysis follows the same steps and assumptions as the error sensitivity analysis that is described in Chapter 6 for the two layer and two thickness methods. The theorem of standard error propagation was employed in this analysis due to the straightforward application of the simulation code that was used for the two layer method. In addition, considerably less computer simulation time was required than for the Monte Carlo method.

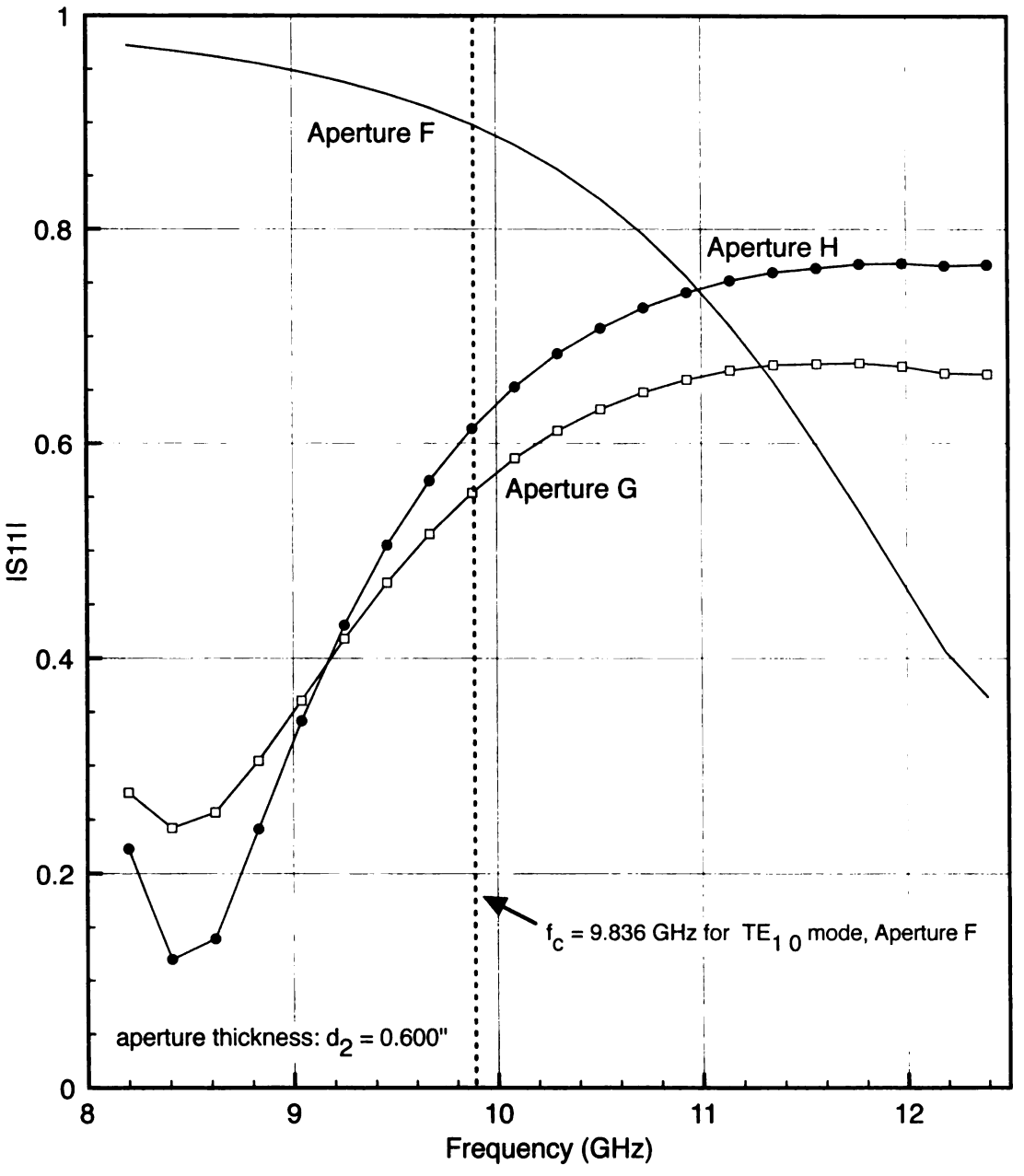


Figure 8.20. Magnitude of the reflection coefficient for 1 layer of Eccosorb FGM125, 0.125" thick, at 8.2-12.4 GHz for Apertures F, G, and H. The reflection coefficient, $S_{11}^{(2I)extr}$, is computed by extrapolating from the $TM_{1\,40}$ mode. Aperture thickness, d_2 =0.600".

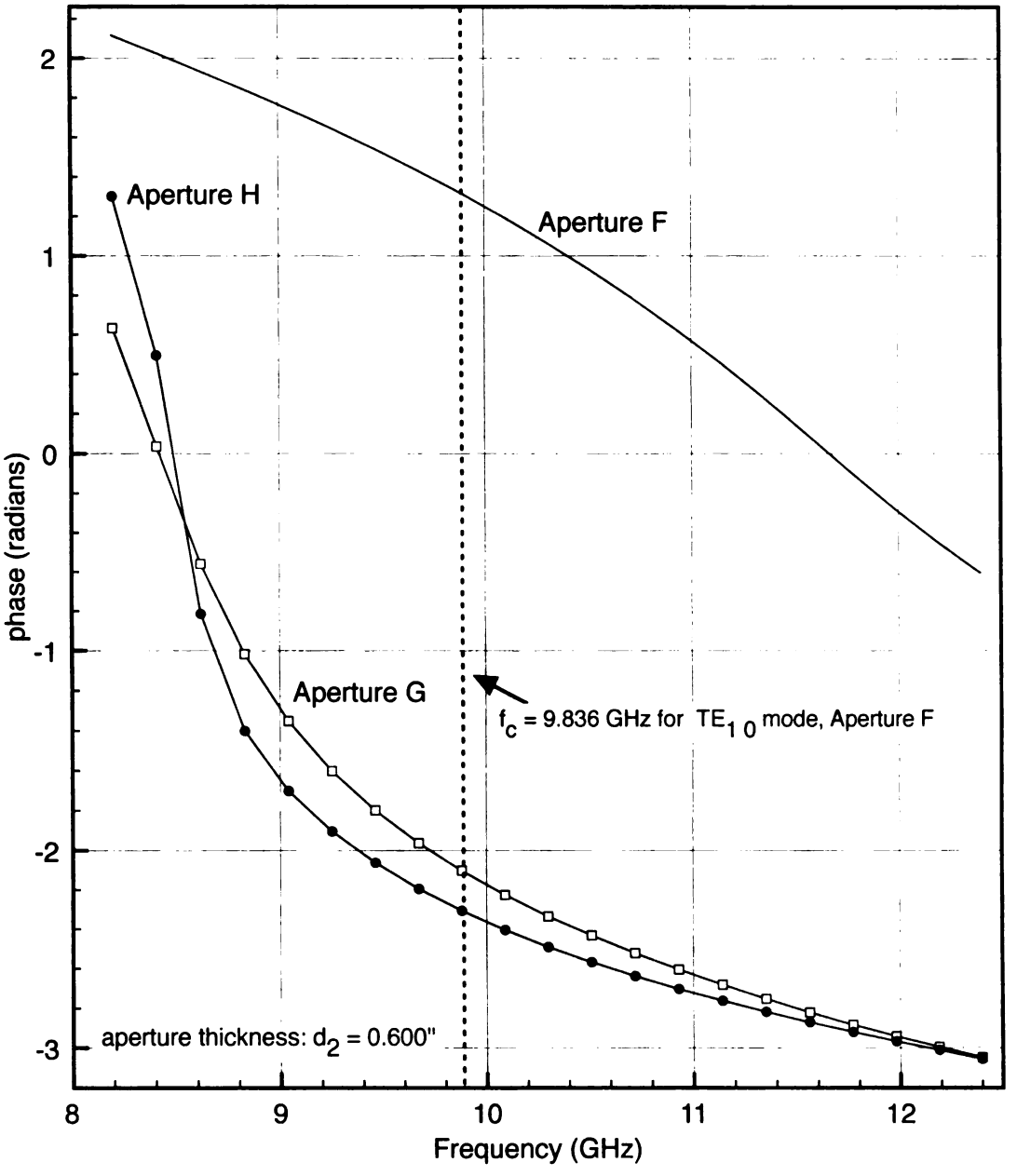


Figure 8.21. Phase of the reflection coefficient for 1 layer of Eccosorb FGM125, 0.125" thick, at 8.2-12.4 GHz for Apertures F, G, and H. The reflection coefficient, $S_{11}^{(2I)extr}$, is computed by extrapolating from the $TM_{1\,40}$ mode. Aperture thickness, d_2 =0.600".

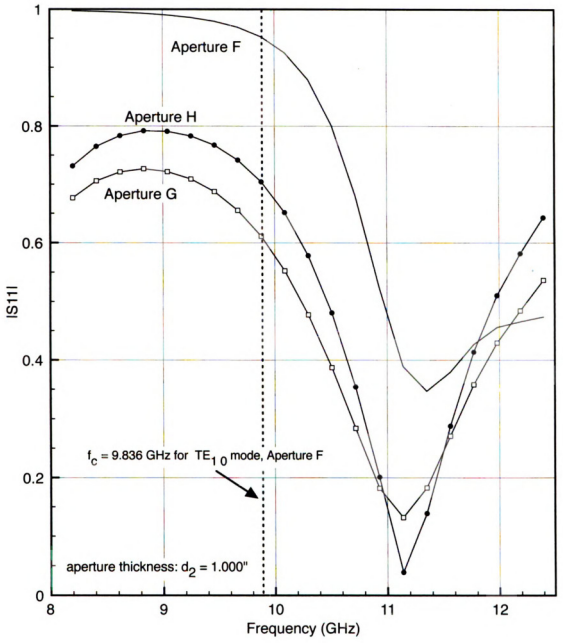


Figure 8.22. Magnitude of the reflection coefficient for 1 layer of Eccosorb FGM125, 0.125" thick, at 8.2-12.4 GHz for Apertures F, G, and H. The reflection coefficient, $S_{11}^{(2f)extr}$, is computed by extrapolating from the $TM_{1\,40}$ mode. Aperture thickness, d_2 =1.000".

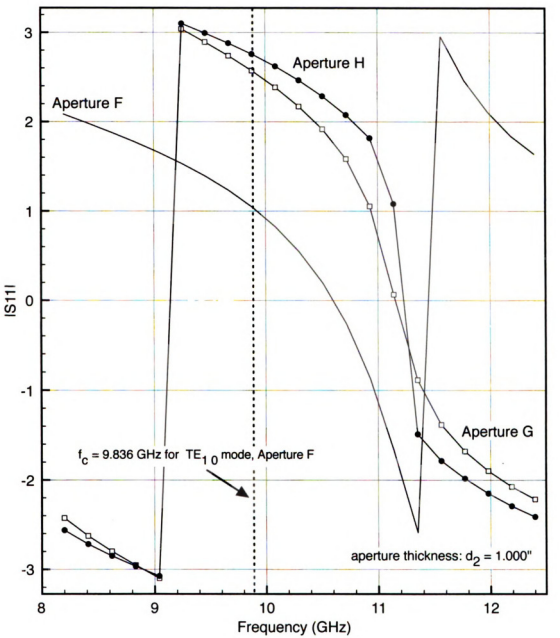


Figure 8.23. Phase of the reflection coefficient for 1 layer of Eccosorb FGM125, 0.125" thick, at 8.2-12.4 GHz for Apertures F, G, and H. The reflection coefficient, $S_{11}^{(2I)extr}$, is computed by extrapolating from the TM_{140} mode. Aperture thickness, d_2 =1.000".

Rewriting (6.8) - (6.11) for the two iris method produces

$$\sigma_{\epsilon_r'} = \left[\sigma^2_{|S_{11(1)}|}\left(\frac{\partial \epsilon_{r'}}{\partial |S_{11(1)}|}\right)^2 + \sigma^2_{\phi_1}\left(\frac{\partial \epsilon_{r'}}{\partial \phi_1}\right)^2 + \sigma^2_{|S_{11(2)}|}\left(\frac{\partial \epsilon_{r'}}{\partial |S_{11(2)}|}\right)^2 + \sigma^2_{\phi_2}\left(\frac{\partial \epsilon_{r'}}{\partial \phi_2}\right)^2\right]^{\frac{1}{2}} \tag{8.1}$$

$$\sigma_{\epsilon_r''} = \left[\sigma^2_{|S_{11(1)}|}\left(\frac{\partial \epsilon_{r''}}{\partial |S_{11(1)}|}\right)^2 + \sigma^2_{\phi_1}\left(\frac{\partial \epsilon_{r''}}{\partial \phi_1}\right)^2 + \sigma^2_{|S_{11(2)}|}\left(\frac{\partial \epsilon_{r''}}{\partial |S_{11(2)}|}\right)^2 + \sigma^2_{\phi_2}\left(\frac{\partial \epsilon_{r''}}{\partial \phi_2}\right)^2\right]^{\frac{1}{2}} \tag{8.2}$$

$$\sigma_{\mu_r'} = \left[\sigma^2_{|S_{11(1)}|}\left(\frac{\partial \mu_{r'}}{\partial |S_{11(1)}|}\right)^2 + \sigma^2_{\phi_1}\left(\frac{\partial \mu_{r'}}{\partial \phi_1}\right)^2 + \sigma^2_{|S_{11(2)}|}\left(\frac{\partial \mu_{r'}}{\partial |S_{11(2)}|}\right)^2 + \sigma^2_{\phi_2}\left(\frac{\partial \mu_{r'}}{\partial \phi_2}\right)^2\right]^{\frac{1}{2}} \tag{8.3}$$

$$\sigma_{\mu_r''} = \left[\sigma^2_{|S_{11(1)}|}\left(\frac{\partial \mu_{r''}}{\partial |S_{11(1)}|}\right)^2 + \sigma^2_{\phi_1}\left(\frac{\partial \mu_{r''}}{\partial \phi_1}\right)^2 + \sigma^2_{|S_{11(2)}|}\left(\frac{\partial \mu_{r''}}{\partial |S_{11(2)}|}\right)^2 + \sigma^2_{\phi_2}\left(\frac{\partial \mu_{r''}}{\partial \phi_2}\right)^2\right]^{\frac{1}{2}}. \tag{8.4}$$

In these equations, $S_{11(1)}$ and $S_{11(2)}$ correspond to the two different apertures used in the simulations. These formulas provide an estimate of the standard deviation on the extracted real and imaginary parts of the permeability and permittivity due to

random measurement error.

As the first step for this simulation, the values for $S_{11}^{thy(2I)}$ which are shown in Figure 8.18 and Figure 8.19 were used as the 'measured' S_{11} values for use in the extraction algorithm. The next step for estimating the standard deviations on the output parameters is to compute the derivatives found in (8.1) -(8.4). These derivatives were computed using the four term central difference formula described by (6.13). To compute the 16 derivatives found in (8.1) -(8.4), 16 different extractions were performed. The step size for the magnitude was chosen to be $\delta = 0.0005$. The step size for the phase was $\delta = 0.8 * \pi/180$. The extractions needed to evaluate the derivatives using (6.13) were simulated for the aperture placed against a piece of conductor-backed Eccosorb FGM125, 0.125" thick. Simulations were performed using the two iris method, and the material parameters were extracted using the extrapolation method. The extrapolations were performed using the $TM_{1\,20}$ mode.

An additional aperture, labeled Aperture I, was also simulated for its sensitivity to random measurement error. Initial sensitivity analysis demonstrated that Apertures G and H were less sensitive to noise, and require a relatively small number of modes for use in the solution. Aperture I, shown in Figure 8.24, was therefore designed with a similar geometry, but with a larger iris opening than either Aperture G or Aperture H.

The sensitivity analysis for Apertures F-I was performed for two frequencies in the band of interest, at 8.20 GHz and 10.09 GHz. The results are shown in Figure 8.25 and Figure 8.26. The standard deviations for Aperture F were an order of magnitude higher than the other three apertures and are not shown in the figure. The plots are normalized with respect to the standard deviation obtained from the sensitivity analysis for the two layer method.

Note that the standard deviations for the real and imaginary parts of the permittivity and permeability are quite close for Apertures G, H, and I in all four subplots.

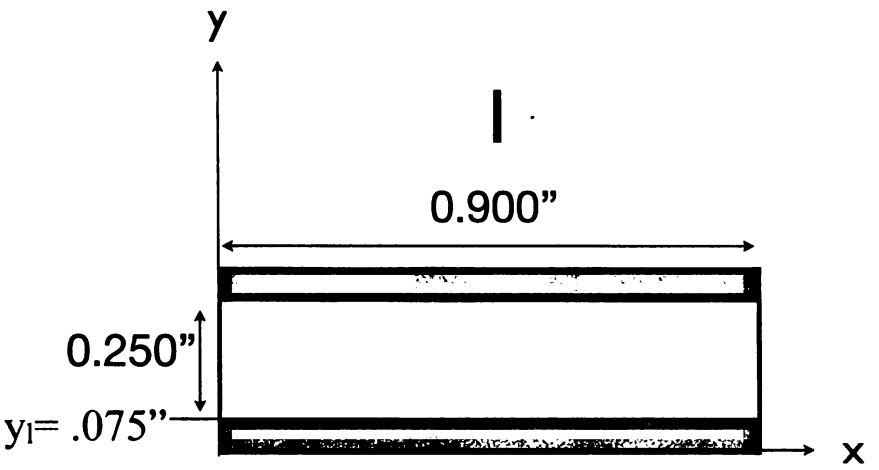


Figure 8.24. Geometry for Aperture I

These values are smaller than the standard deviations for the two layer method sensitivity analysis, using two layers of FGM125, shown in Figure 6.9. When the lower dielectric constant materials are used in the two layer method, the standard deviations shown in Figure 6.9 are roughly the same as those observed in Figure 8.25 and Figure 8.26. These standard deviations are only 3-5 times as large as the standard deviations observed for the two thickness method. Since the standard deviations for the two thickness method are small, as seen in Figure 6.8, it is reasonable to conclude that the two iris method and the two layer method, using a lower dielectric constant material for the top layer, are worth further simulation and experimental investigation. For both frequencies, the results of Aperture H show slightly less error sensitivity than the other apertures.

Recall that the goal of this sensitivity analysis is to develop an understanding

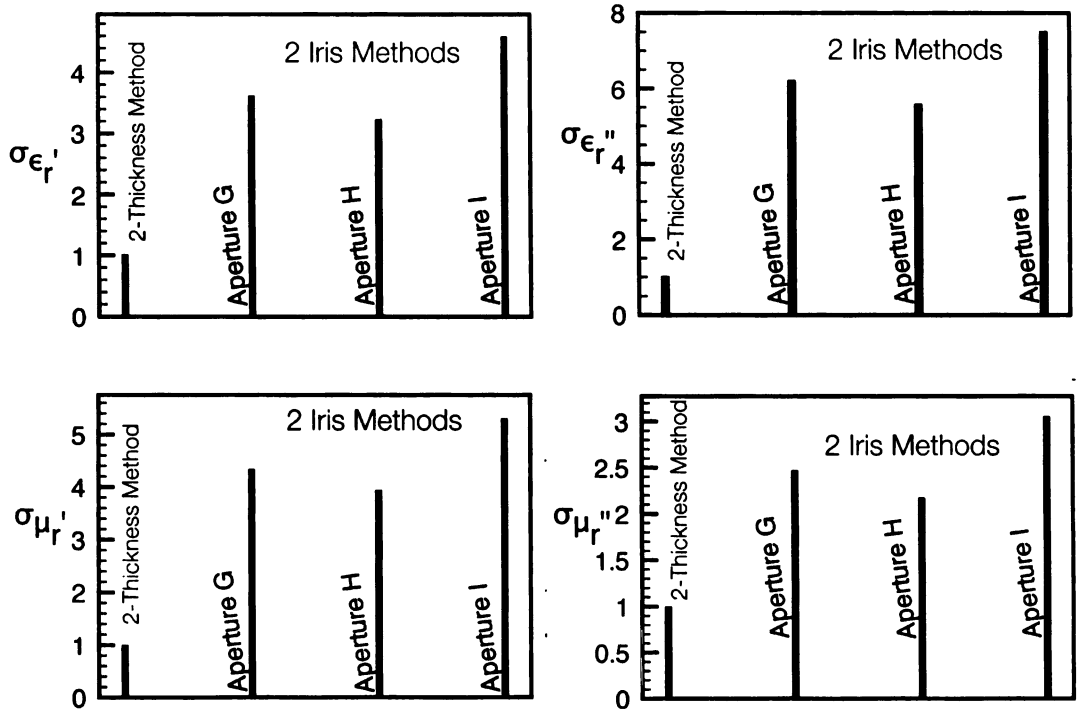


Figure 8.25. Standard deviations relative to the two thickness method of the material parameters due to random measurement error for the two aperture method at 8.20 GHz. Extractions were performed with the extrapolation method using the $TM_{1\,20}$ mode. Simulations are for 1 layer of Eccosorb FGM125, 0.125" thick. Aperture thicknesses for all apertures is 0.125".

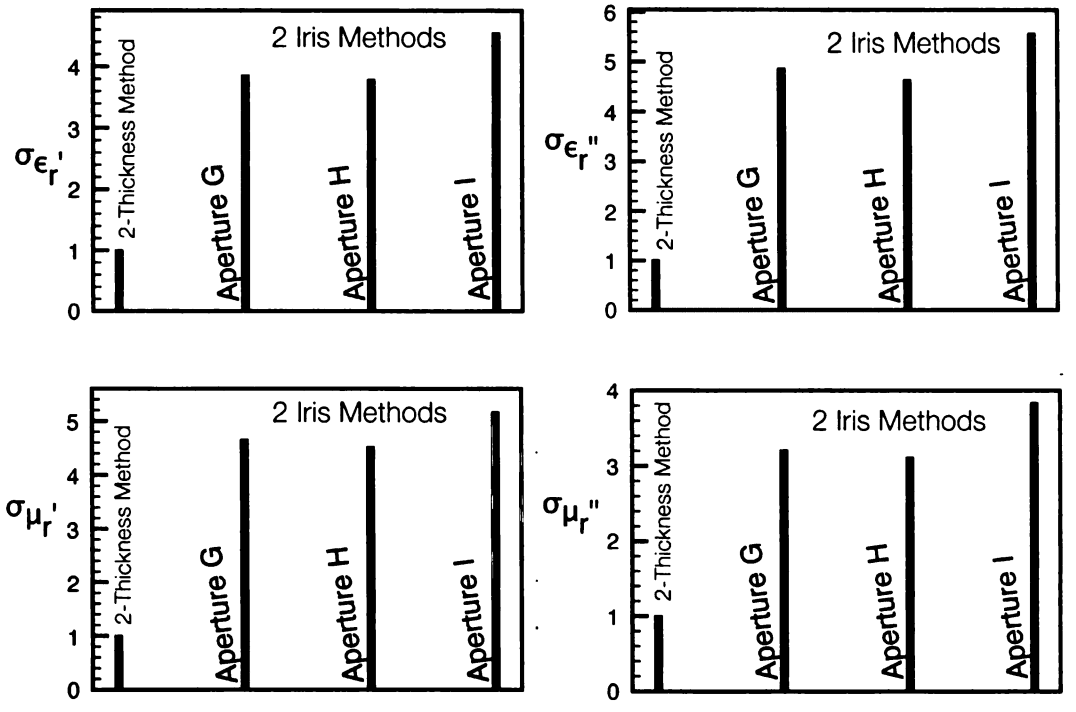


Figure 8.26. Standard deviations relative to the two thickness method of the material parameters due to random measurement error for the two aperture method at 10.09 GHz. Extractions were performed with the extrapolation method using the $TM_{1\,20}$ mode. Simulations are for 1 layer of Eccosorb FGM125, 0.125" thick. Aperture thicknesses for all apertures is 0.125".

the investigation to this point, Aperture H has proven to be desirable in the areas examined so far. It requires a small number of modes that need to be used in the solution. The extrapolation method is easily adapted to the two iris method using this aperture. When the sensitivity analysis for four different apertures is performed, Aperture H provides the best results of the apertures examined at the low end and midband of the X-band frequency range.

It is desirable to understand if Aperture H maintains the same level of noise sensitivity across the entire frequency range. Thus, the error sensitivity analysis was performed at 21 points across the X-band range, and the results are shown in Figure 8.27. For comparison purposes, the results for the sensitivity analysis for the two iris method are compared with the two thickness method.

The 95% confidence intervals in this figure show that the error sensitivity does vary across the frequency band. For ϵ_r', the error sensitivity decreases by about a factor of two from the low end of the frequency band to the high end. These intervals are about 3 times as large as the two thickness method at 8.2 GHz, and approximately twice as large at 12.4 GHz. An even larger decrease in the error bars is observed for the plot for ϵ_r''. Note that at the high end of the frequency band, the use of Aperture H for the two iris method produces error bars that are approximately the same as the two thickness method.

For the real part of the permeability, μ_r', the upper portion of the frequency band displays 95% confidence intervals that are approximately the same as those observed for the two thickness method. The confidence intervals are higher at the lower end of the frequency band. The 95% confidence intervals for μ_r'' are approximately the same across the entire frequency band, with values that are approximately twice those observed for the two thickness method. For all of the parameters observed, the results computed for Aperture H indicate that it is 1-3 times as sensitive to random measurement error as the two thickness method. Also, from the information

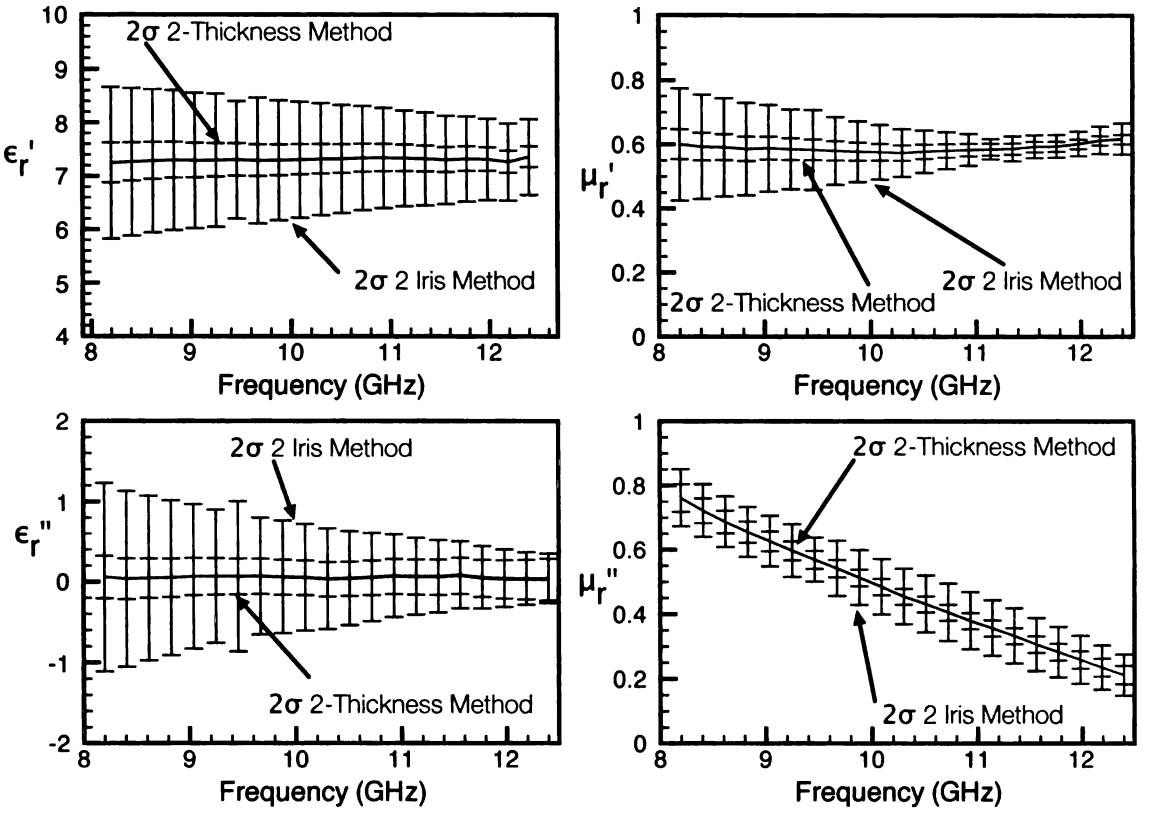


Figure 8.27. Sensitivity analysis for the two iris method due to random measurement error using Aperture H from 8.20 GHz to 12.40 GHz. Extractions were performed with the extrapolation method using the $TM_{1\,20}$ mode. Error bars show the 95% confidence level. Simulations are for 1 layer of Eccosorb FGM125, 0.125" thick. Aperture thickness, $d_2 = 0.125$".

found in Figure 6.9, Aperture H shows a comparable error sensitivity to the two layer method using a plastic material as the top layer. This sensitivity analysis suggests that Aperture H is a reasonable choice for experimental use in the two iris method.

8.5 Modal Analysis for Aperture H

The previous section examines the sensitivity of different apertures, and Aperture H in particular, to random measurement error. The other potential source of error that is analyzed in this dissertation is the error produced by using a finite number of modes in the material parameter extraction. This analysis is described in Chapter 6, and the modal analysis in this section follows the same procedure.

The values used as the 'measured' values in this simulation are the theoretical reflection coefficients for Aperture H, generated as the extrapolated values, $S_{11}^{extr(2I)}$. These are shown in Figure 8.18 and Figure 8.19. The two iris extraction method was carried out using different numbers of modes to calculate $S_{11}^{thy(2I)}$ in the solution. The results of this simulation are shown in Figure 8.28 - Figure 8.31.

Label	modes used	p	q
A	TE_{q0}		1, 3, 5, 7
B	TE_{q0}, TE_{12}, TM_{12}		1-11, odd
C	TE_{q0}, TE_{1p}, TM_{1p}	2, 4	1-11, odd
D	TE_{q0}, TE_{1p}, TM_{1p}	2, 4, 6	1-11, odd
E	TE_{q0}, TE_{1p}, TM_{1p} + extrapolation	2-20, even	1-11, odd

Table 8.1. Key for modes used in two aperture extraction method, Aperture H

Some similarities exist between these simulations and those which are shown for the two layer and two thickness methods in Chapter 6. In all four figures, as the number of modes in the solution are increased, the extracted values approach the

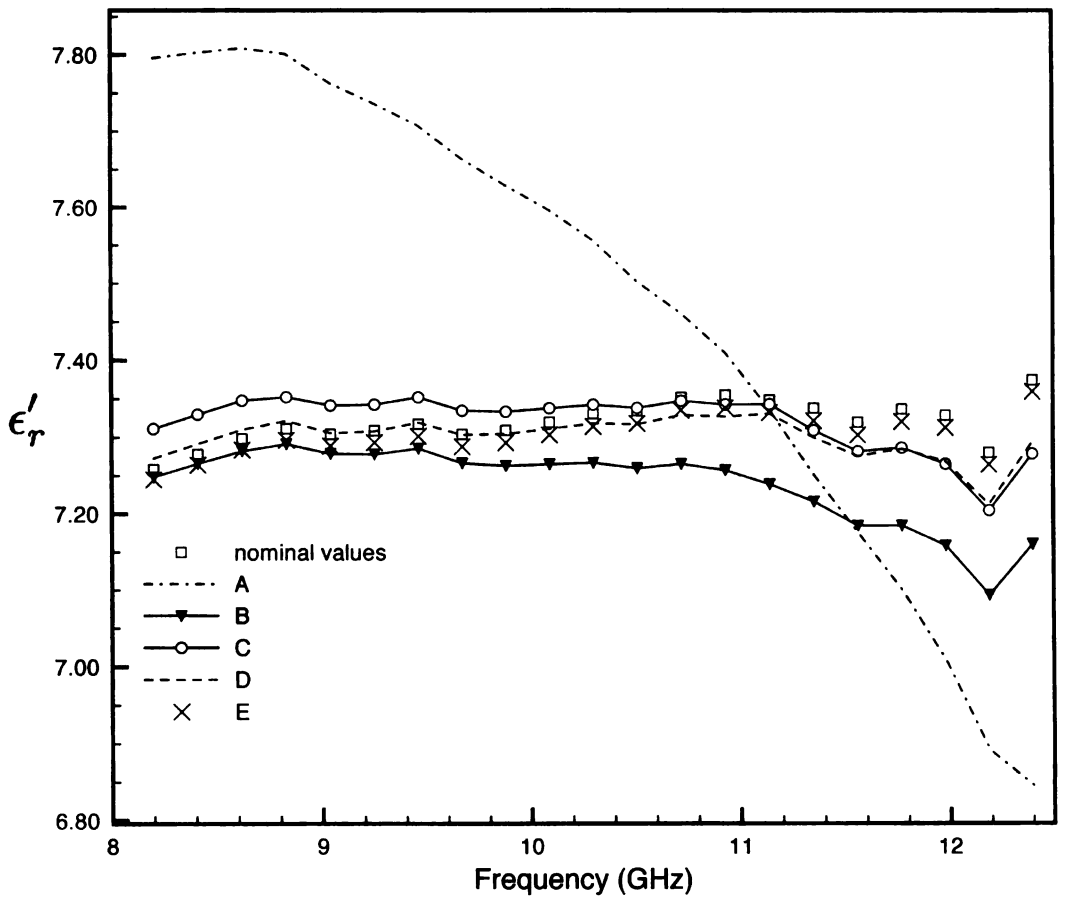


Figure 8.28. Extracted values of ϵ_r' for the two iris method with different numbers of modes used in the extraction. Simulations used Aperture H as the iris, from 8.20 GHz to 12.40 GHz. Simulations were for 1 layer of Eccosorb FGM125, 0.125" thick. The key for each line is found in Table 8.1 Aperture thickness = 0.125".

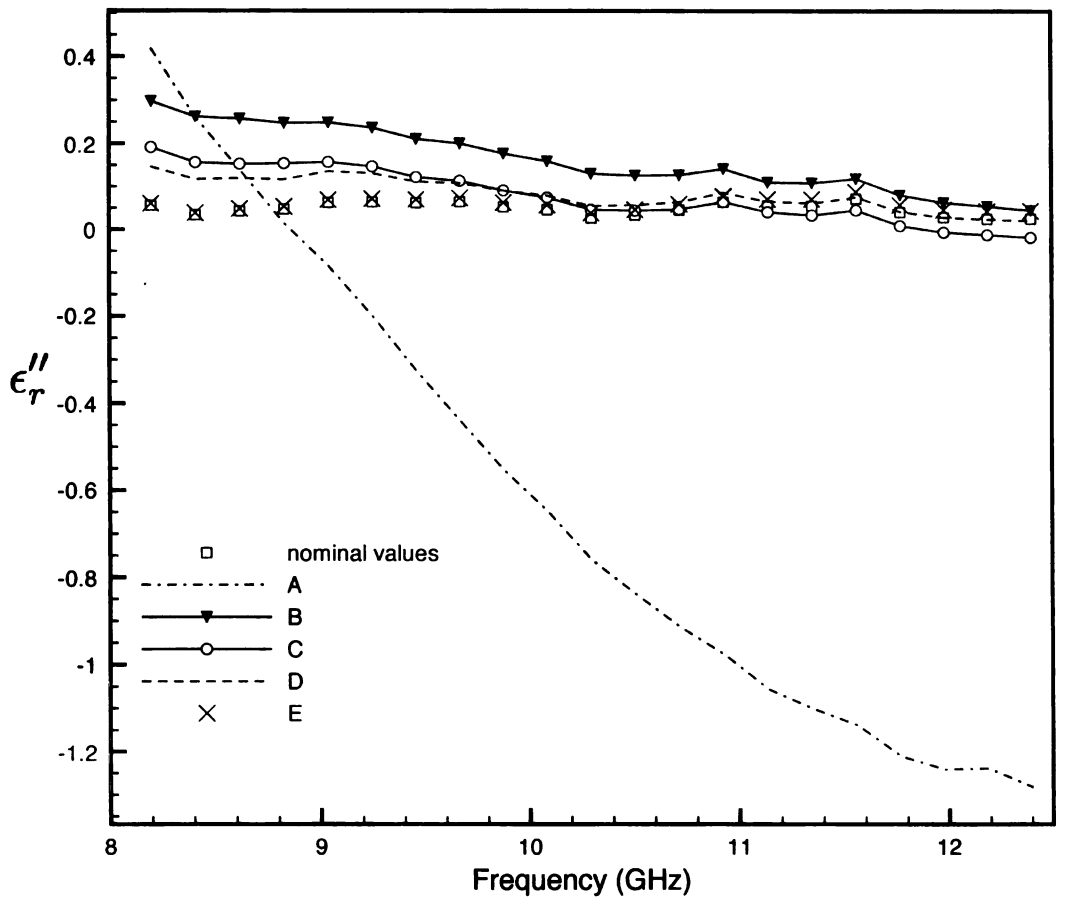


Figure 8.29. Extracted values of ϵ_r'' for the two iris method with different numbers of modes used in the extraction. Simulations used Aperture H as the iris, from 8.20 GHz to 12.40 GHz. Simulations were for 1 layer of Eccosorb FGM125, 0.125" thick. The key for each line is found in Table 8.1 Aperture thickness = 0.125".

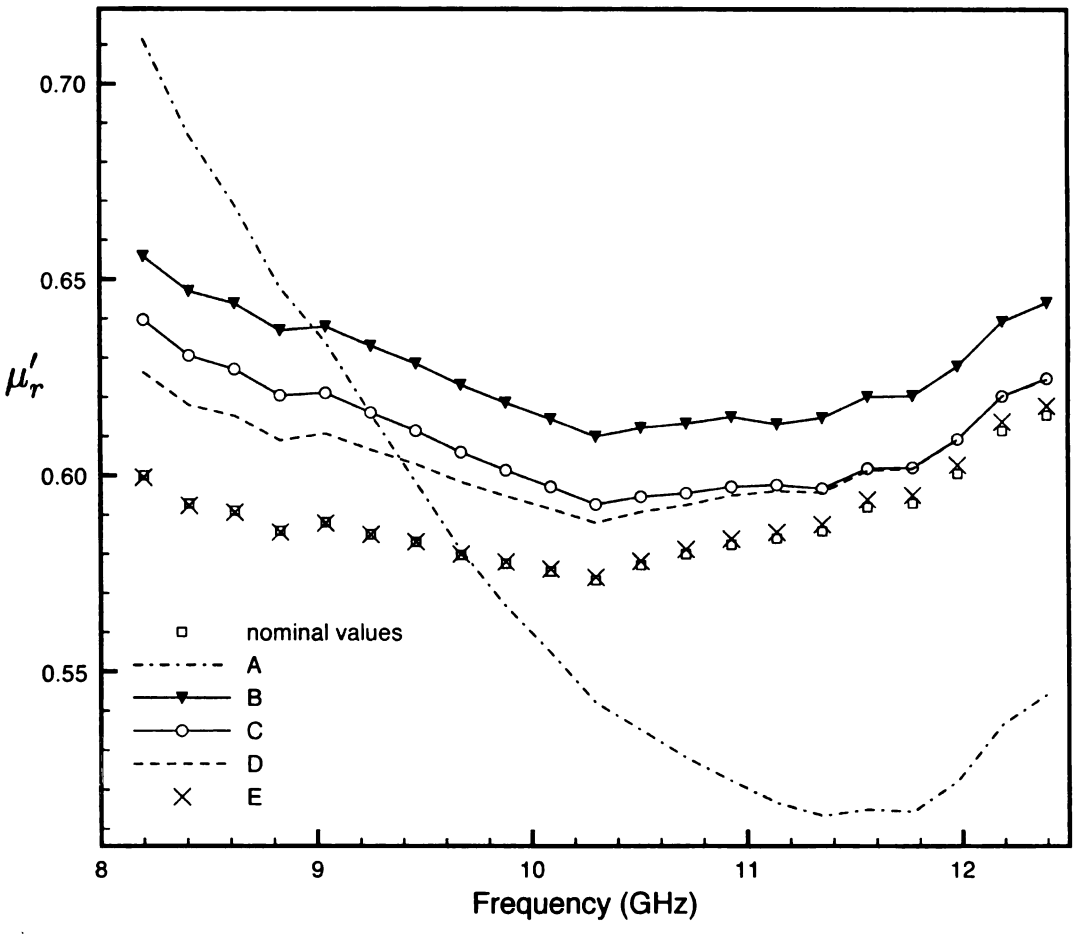


Figure 8.30. Extracted values of μ'_r for the two iris method with different numbers of modes used in the extraction. Simulations used Aperture H as the iris, from 8.20 GHz to 12.40 GHz. Simulations were for 1 layer of Eccosorb FGM125, 0.125" thick. The key for each line is found in Table 8.1 Aperture thickness = 0.125".

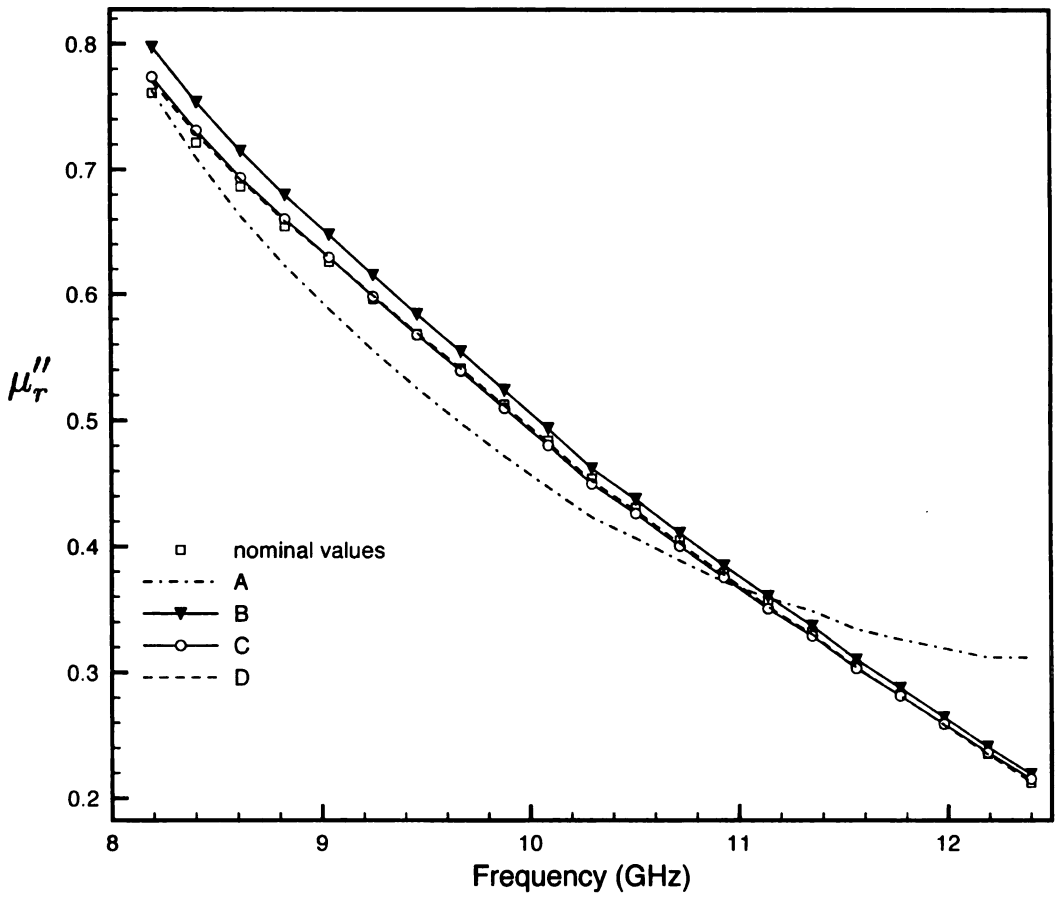


Figure 8.31. Extracted values of μ_r'' for the two iris method with different numbers of modes used in the extraction. Simulations used Aperture H as the iris, from 8.20 GHz to 12.40 GHz. Simulations were for 1 layer of Eccosorb FGM125, 0.125" thick. The key for each line is found in Table 8.1 Aperture thickness = 0.125".

nominal values. Consider Figure 8.28, which displays the extracted values for ϵ_r'. Note that once the $TM_{1\,2}$ mode is included, the shape of the plot across the frequency band resembles the nominal values. These values, shown in line B on the graph, have an error that varies less than 1% from the nominal values. At the high end of the frequency band, the errors are larger for line B, approximately 4% with respect to the nominal values. As the number of modes used in the solution is increased, the extracted values approach the nominal values.

Similar observations are seen for the plot of the extracted values for ϵ_r'' shown in Figure 8.29, and the extracted values for μ_r', shown in Figure 8.30. Note that in these figures, the largest errors are observed at the low end of the frequency bands when the extrapolation method is not employed. When the extrapolation method is employed, the extracted values are within 0.1% of the nominal values.

The plot of the extracted values for μ_r'' are shown in Figure 8.31. These also have similar characteristics to the other three figures. Notice that as more modes are included in the solution, the values also approach the nominal values. The values obtained by the extrapolation method are not plotted to avoid clutter on the figure, but they are within 0.5% of the extracted values.

8.6 Simulation Conclusions

This chapter contains two analyses of the effect of possible sources of error in the two iris method. An investigation regarding the computation of the theoretical reflection coefficient revealed the importance of the geometrical shape of the iris. It was shown that apertures which were similar in shape to the WR-90 waveguide and which were symmetric in the center of the waveguide cross section require the least amount of modes to make a significant contribution to the computation of the reflection coefficient. An extrapolation method similar to that developed for the two layer method has been employed to estimate the reflection coefficient due to a large number

of modes for different apertures. Apertures G and H require the lowest number of modes to compute the theoretical reflection coefficient when the matrix is being filled.

An error sensitivity analysis on potential choices of symmetrical apertures was undertaken, and it is shown that Aperture H exhibits the lowest sensitivity to random measurement error. Analysis showed that this error is 1-3 times as large as the error estimated for the two thickness method. It is also shown that by using the extrapolation method in a modal analysis, the extracted values are within 0.5% of the nominal values. As a result of these observations, it is concluded that Aperture H is a reasonable choice for a second aperture for use in the experimental two iris method.

The final step for the implementation of the two iris method, as well as the two thickness method and two layer method, is to build experimental devices to test the material extraction methods. Chapter 9 displays the experimental results of the two thickness method, two layer method, and two iris method.

CHAPTER 9

EXPERIMENTAL MATERIAL PARAMETER EXTRACTIONS USING THE TWO LAYER METHOD, TWO THICKNESS METHOD, AND THE TWO IRIS METHOD.

9.1 Introduction

In this chapter, the experimental procedure and setup for the three material characterization methods are described. The experimental apparatus and experimental prcedure are described in section 9.2. The results for the two thickness method are presented in section 9.3 and the two layer method results are presented in section 9.4. The results for the two iris method are discussed in section 9.5. Comparisons between the methods are made throughout this chapter.

9.2 Experimental Setup

For all three material extraction methods examined in this chapter, the experimental reflection coefficients are measured using flanged rectangular waveguide probes. These probes were created by machining a rectangular aperture in a $12'' \times 12'' \times 1/4''$ aluminum plate. One probe, labeled Aperture WR, is constructed with an aperture that is the same size as the opening in a WR 90 X-band waveguide ($0.400'' \times 0.900''$). This probe is used in the two layer and two thickness methods. A second probe was constructed that has the dimensions of Aperture H ($0.150'' \times 0.900''$), and both probes are used in the two aperture method. For both probes, a channel is cut in the center of the plate around the aperture so that the waveguide fits in the slot and may be centered around the aperture. The aperture opening is approximately 0.125" thick. The layout of the flange is shown in Figure 9.1. The actual measured dimensions of the apertures are shown in Table 9.1.

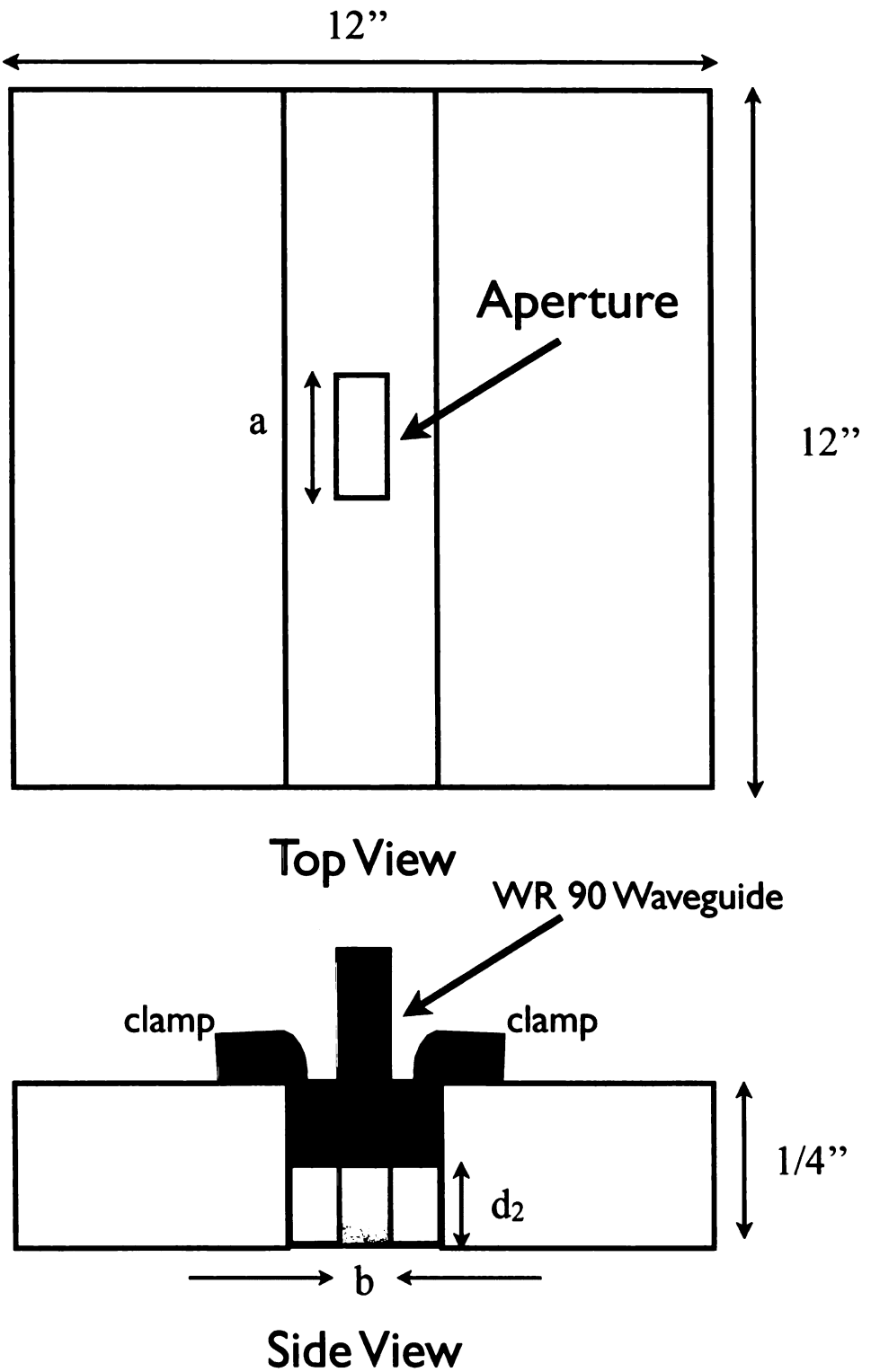


Figure 9.1. Top view of aluminum flange plate with aperture opening and side view of the aluminum plate with the waveguide attached. Dimensions a, b, and d_2 correspond to the aperture dimensions shown in Figure 7.1.

Dimension	Aperture WR	Aperture H
a	0.898"	0.898"
b	0.398"	0.148"
d_2	0.127"	0.122"

Table 9.1. Actual measured dimensions of Aperture WR and Aperture H.

The flanged plate is mounted to a section of WR 90 waveguide with clamps and is aligned using a piece of machined plastic. The plastic piece is inserted into the interior of the waveguide and the aperture to ensure a consistent alignment of the waveguide and the aperture. The plastic piece is removed after the waveguide is firmly clamped in place. The waveguide is connected to an HP 8510B Vector Network Analyzer (VNA) and the magnitude and phase of the reflection coefficient are measured in the frequency range of 8.2 - 12.4 GHz. A photo of the measurement setup is shown in Figure 9.2.

9.2.1 Calibration

The HP 8510C VNA is calibrated to the end of the waveguide using a Maury Microwave Model No: X7005M calibration kit. A short/short/load calibration procedure was used, where one offset short was of length 1.677 cm, the second short was offset by 0.559 cm, and the load was a fixed matched load. The two layer and two thickness methods were theoretically formulated with the reference plane at the flange/material boundary, so any measured reflection coefficients obtained in these experimental procedures must be properly phase shifted for each mode in the two layer and two thickness methods to account for the thickness of the flange, shown by d_2 in Figure 9.1. The two iris method is theoretically formulated with the reference plane at the end of the waveguide, so no phase shift of the measured S_{11} values is necessary.

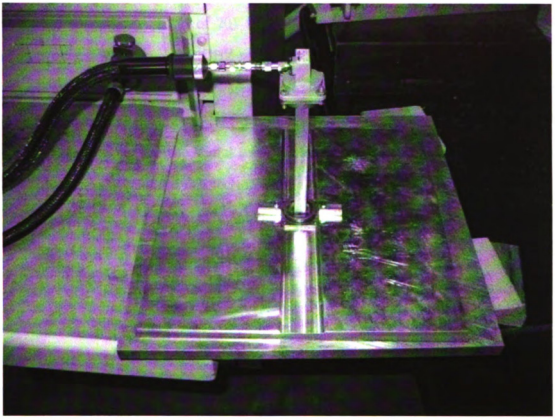


Figure 9.2. Photo of the measurement apparatus. The waveguide is attached to the top aluminum flange plate. The material sample is placed between the top plate and bottom aluminum conducting plate.

9.2.2 VNA settings

The source amplitude was set to 15 dBm, less than the stated receiver maximum of 17dBm for the S-parameter test set. Averaging was also used to reduce the random noise contribution and improve the signal to noise ratio. Experimentation with the possible settings determined that 512 averages was adequate to reduce the noise contribution, while keeping the time required to obtain a frequency sweep to approximately 30 seconds. A total of 201 frequency points were sampled in the X-band range, from a minimum of 8.2 GHZ to the maximum frequency of 12.4 GHz.

A stepped frequency setting was also employed, and the frequency sweep dwell time setting was 25 ms. This is the time duration that the network analyzer waits at a given frequency point for the signal to settle before taking the measurement. Longer dwell times increase the data collection time across the frequency band. It was found that 25 ms provided an acceptable balance of stability and acceptable collection time.

9.2.3 Measurement Procedure

Once the VNA settings are established and the measurement system is calibrated, reflection coefficient measurements may be taken using the waveguide probe. A material sample is placed on a metal plate, and the flanged waveguide probe is placed on top of the material sample. Although the material samples are theoretically machined or processed to a given thickness, the materials do have some variation in the sample thickness. Measurements made with a digital caliper on material samples revealed that the thickness at the edge could vary as much as 0.007" for a given 12" sample of nominal thickness 0.125". Recall that the problem formulation for all three extraction methods requires the knowledge of the thickness of the material. Thus, all samples were measured on all four sides and the mean of the measurements was used as the material thickness. It is recognized that this estimation of material thickness is a potential source of error in the extraction procedure.

Several of the materials measured are plastic or polymer material samples and may have variations in the sample thickness across the surface of the sample. It is desirable to have the best possible contact between the material and the flanged waveguide probe, and thus reduce the possibility of airgaps between the sample material and the flange. If an airgap is present, the theoretical problem in the waveguide region becomes a three layer medium between two parallel plates, which is not accounted for in the theory.

Two different types of measurements were recorded. In the first type, the flange was placed on the sample, two bricks were placed on the flange, and the reflection coefficient was recorded. Results from this method, especially when using the two layer method with a stiff top layer material, were mixed. The amount of pressure from the plate and bricks did not necessarily ensure a good contact with the material and airgaps might possibly exist. Due to the erratic extraction results, these results are not presented in this dissertation. A second, more effective method was employed to eliminate possible airgaps. A simple clamping system was designed and implemented using C-clamps to provide a good contact of the flange, the material under test, and the bottom conducting plate. Once the material is firmly clamped, the reflection coefficient is measured and recorded to a magnetic floppy disk by the VNA.

9.2.4 Sample materials

Several different material samples were obtained for use as the material under test in the material parameter extraction methods under investigation. A table of the $12'' \times 12''$ material samples and the measured thickness of the material sheet are shown in Table 9.2. The sample thickness was measured on all four sides of the material with a an electronic caliper and the mean of the four side measurements is shown in Table 9.2

Manufacturer	Material	Sample	thickness (inches)
Emerson & Cuming	Eccosorb FGM125	1	0.122
Emerson & Cuming	Eccosorb FGM125	2	0.122
Emerson & Cuming	Eccosorb FGM40	1	0.039
Emerson & Cuming	Eccosorb FGM40	2	0.039
Emerson & Cuming	Eccosorb MCS	1	0.039
Emerson & Cuming	Eccosorb MCS	2	0.039
Professional Plastics	Plexiglass	1	0.111
Professional Plastics	Plexiglass	2	0.109
Professional Plastics	Nylon	1	0.124
Professional Plastics	Nylon	2	0.124
Professional Plastics	PVC	1	0.119
Professional Plastics	PVC	2	0.119

Table 9.2. Material samples used in the material parameter extraction methods.

9.2.5 Measurement Position

It is possible that the material properties of the samples may be spatially dependent. To investigate this possibility, the material samples used in these experiments were measured at five different points on the sample. These measurements at different positions were obtained by lifting the top plate and moving it to the new measurement position. The sample and bottom conducting plate remained fixed in the same location. The two plates, with the sample in between, were then clamped together. The five measurement positions are shown in Figure 9.3, and will be referred to in the subsequent discussion of all three material parameter extraction methods.

9.3 Two Thickness Method Results

9.3.1 Introduction

This section reviews several material parameter extractions using the two thickness method. The data were collected on several different days over a period of weeks. This section examines the results obtained with different numbers of modes used in

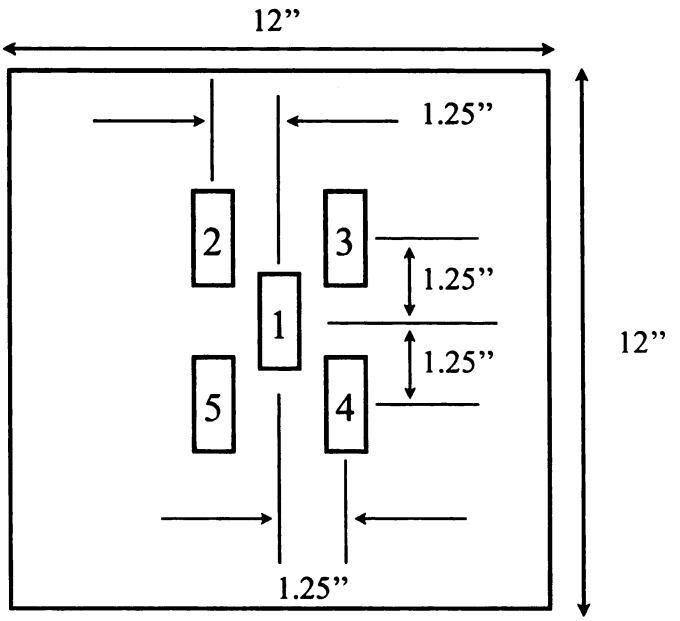


Figure 9.3. Measurement Positions for the material samples

the extraction.

9.3.2 Measured reflection coefficients

The measurements necessary for the two thickness method are the complex quantities $S_{11(1T)}^{meas}$ and $S_{11(2T)}^{meas}$, which are the reflection coefficient measurements for one and two thicknesses of a given material, respectively. A representative set of measurements taken at the five different measurement positions on Sample 2 and a stack of Sample 1 on top of Sample 2 of Eccosorb FGM125 is shown in Figure 9.4. In addition, the values which are computed for S_{11}^{extr} in Chapter 5 for two different thicknesses of Eccosorb FGM125 are shown for comparison. Note that there is a general agreement in the trend of the reflection coefficients for both thicknesses and for both phase and magnitude. However, the measured values were obtained from material samples that are 0.122" thick and 0.244" thick. S_{11}^{extr} was computed for samples that are 0.125"

thick and 0.250" thick. In addition, the material parameters used to compute S_{11}^{extr} are the nominal values shown in Table 5.1, which are not necessarily the true material parameters of the material sample.

9.3.3 Extraction results

It was noted in section 5.6.1 that the simulated extraction which used a different number of modes in the solution did affect the extracted values using the two thickness method. As more modes were used, the extracted material parameters moved in the direction of the nominal values, as shown in Figure 5.20 - Figure 5.23. A similar processing procedure was performed on a set of measured reflection coefficients for two different thicknesses of Eccosorb FGM125. In this configuration, $S_{11(1T)}^{meas}$ was obtained from sample 2, and $S_{11(2T)}^{meas}$ was recorded with sample 1 on top of sample 2. The results are shown in Figure 9.6 - Figure 9.9. Note that as the number of modes are increased, the extracted values move in a direction similar to that observed in Figure 5.20 - Figure 5.23. Also note that when the first 10 modes are used in the solution, the results are quite close to the values extracted using the extrapolation technique for ϵ_r'', μ_r', and μ_r''. The largest difference is seen in the plots for ϵ_r', where the values computed using the first 10 modes, line D, are separated by approximately 0.1 across the frequency band from those computed using the extrapolation method, line E.

The extrapolation technique requires approximately 500% more computational time to extract the material parameters shown in Figure 9.6 than the extraction performed using the first 10 modes. Thus, in the next several figures, the first 10 modes are used to compare measurements taken on several different days and from several different data sets. This choice aids in reducing the data processing time and provides the opportunity to observe a wide range of trends in the data for the two thickness method.

The two thickness method was used to extract the material parameters from mea-

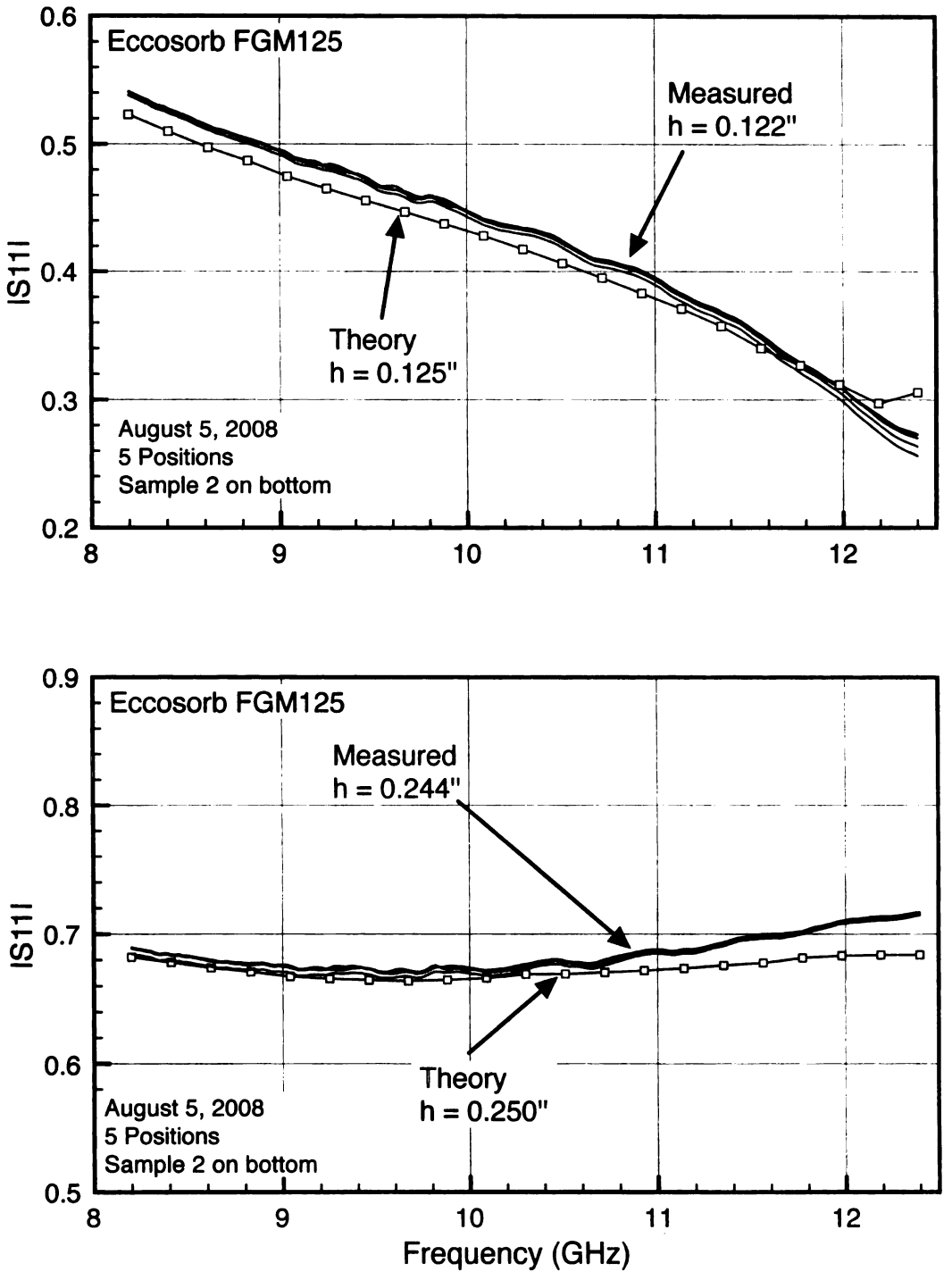


Figure 9.4. Comparison of $|S_{11}^{meas}|$ and $|S_{11}^{extr}|$ for two thicknesses of Eccosorb FGM125. Measurements were made for all 5 positions.

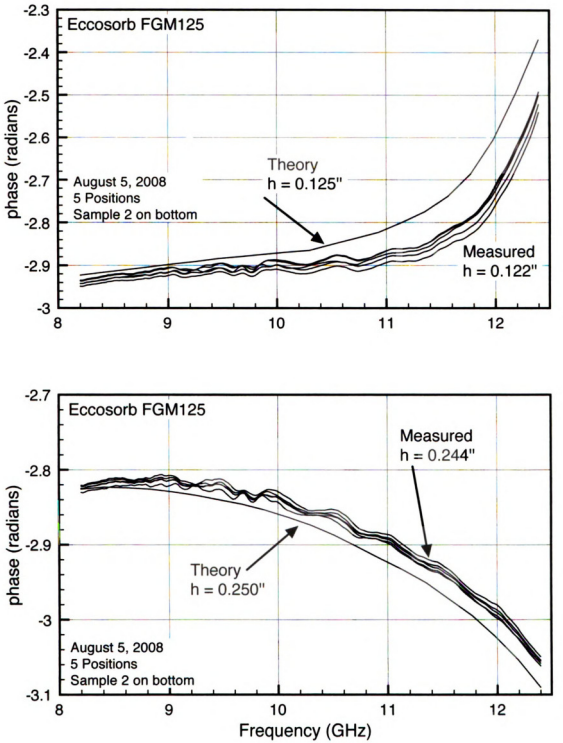


Figure 9.5. Comparison of $\phi_{(1T)}^{meas}$ and $\phi_{(2T)}^{meas}$ for Eccosorb FGM125. Measurements were made for all 5 positions.

surements taken on several different days. These data sets were processed identically using the first 10 significantly contributing modes, up to the TM_{18} mode, in the parameter extraction. The plot of the extracted values for sample 2 of Eccosorb FGM125, from five different data collection days, is shown in Figure 9.10 and Figure 9.11. Note the extracted values for both real and imaginary parts of the permittivity have a larger deviation in the figures. The permeability values, shown in Figure 9.11, show very little deviation among the extracted values. The mean and standard deviation of the extractions in Figure 9.10 and Figure 9.11 were computed, and the results are displayed in Figure 9.12 and Figure 9.13. The error bars on the plots show the 95% confidence interval for the data sets.

Label	modes used	p	q
A	$TE_{10}, TE_{30}, TE_{12}, TM_{12}$		
B	$TE_{10}, TE_{30}, TE_{12}, TM_{12}, TE_{14}, TM_{14}$		
C	$TE_{10}, TE_{30}, TE_{1p}, TM_{1p}$	2,4,6	
D	$TE_{10}, TE_{30}, TE_{1p}, TM_{1p}$	2,4,6,8	
E	$TE_{q0}, TE_{1p}, TM_{1p}$ + extrapolation	2-20, even	1, 3

Table 9.3. Key for modes used in the two thickness method extraction of experimental data.

Note that the general trend of these data are consistent with the confidence intervals simulated in section 6.7 and shown in Figure 6.8 for the two thickness method. Note that the 95% confidence intervals for the permittivity are roughly an order of magnitude larger than those for the permeability, which is consistent with Figure 6.8.

Measurements of the reflection coefficients for a different physical combination of Eccosrb FGM125 were also taken in the same data collection periods. In this case, $S^{meas}_{11(1T)}$ was obtained from sample 1, which is the bottom layer. The second measurement, $S^{meas}_{11(2T)}$, was obtained by placing sample 2 on top of sample 1. These

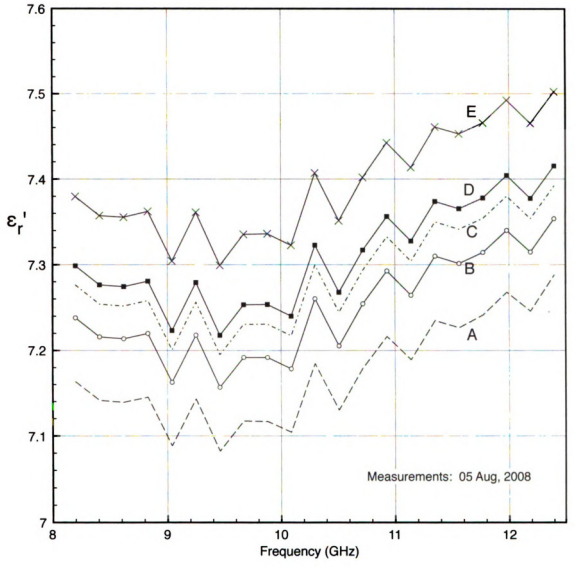


Figure 9.6. Extracted ϵ_r' values for Eccosorb FGM125 using the two thickness method. Bottom layer: sample 2. Top layer: sample 1. Different numbers of significantly contributing modes were included in the solution. The key for lines A-E is found in Table 9.3. Measurements taken at position 1.

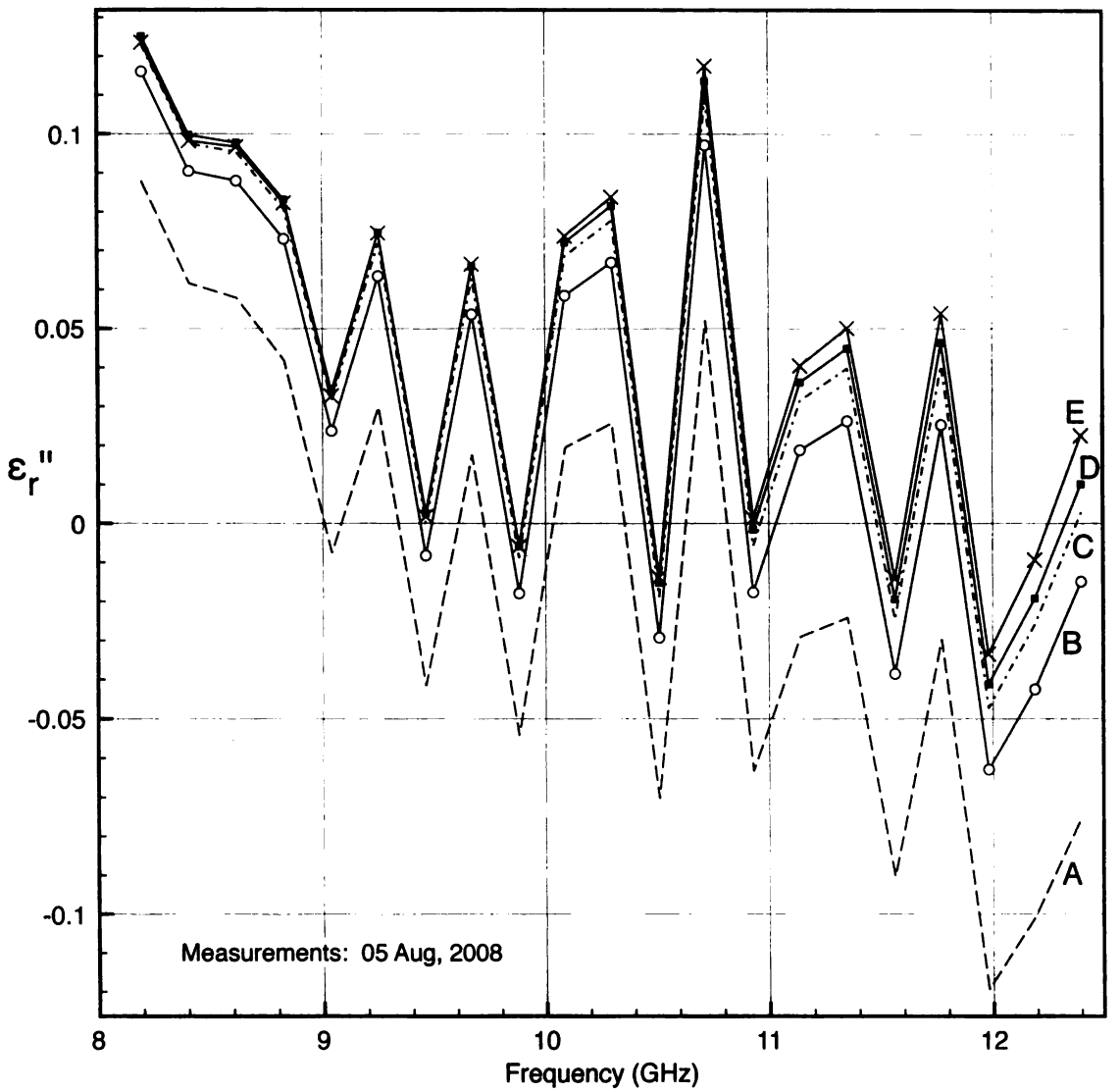


Figure 9.7. Extracted ϵ_r'' values for Eccosorb FGM125 using the two thickness method. Bottom layer: sample 2. Top layer: sample 1. Different numbers of significantly contributing modes were included in the solution. The key for lines A-E is found in Table 9.3. Measurements taken at position 1.

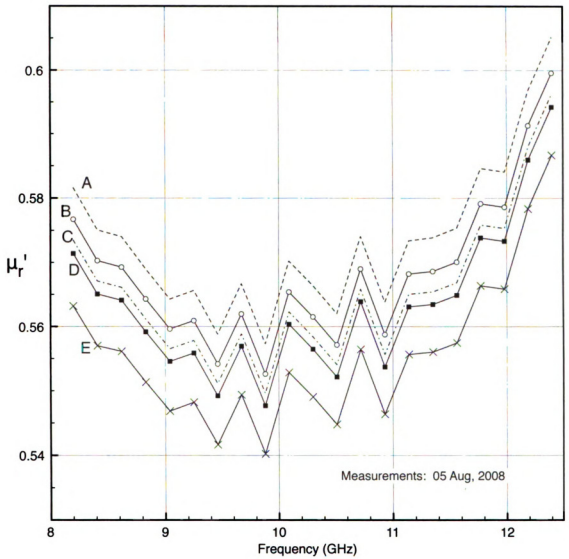


Figure 9.8. Extracted μ_r' values for Eccosorb FGM125 using the two thickness method. Bottom layer: sample 2. Top layer: sample 1. Different numbers of significantly contributing modes were included in the solution. The key for lines A-E is found in Table 9.3. Measurements taken at position 1.

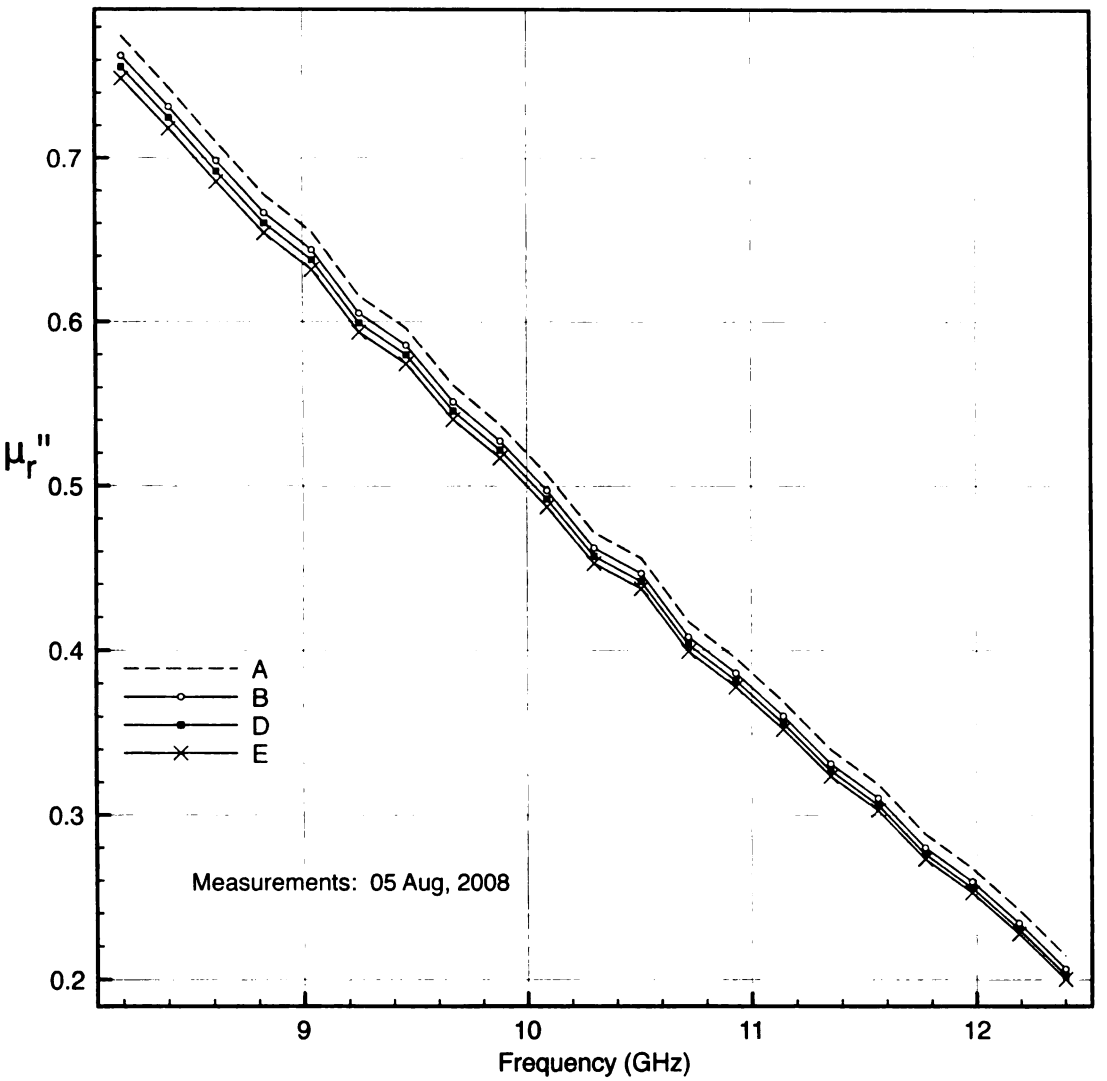


Figure 9.9. Extracted μ_r'' values for Eccosorb FGM125 using the two thickness method. Bottom layer: sample 2. Top layer: sample 1. Different numbers of significantly contributing modes were included in the solution. The key for lines A-E is found in Table 9.3. Measurements taken at position 1.

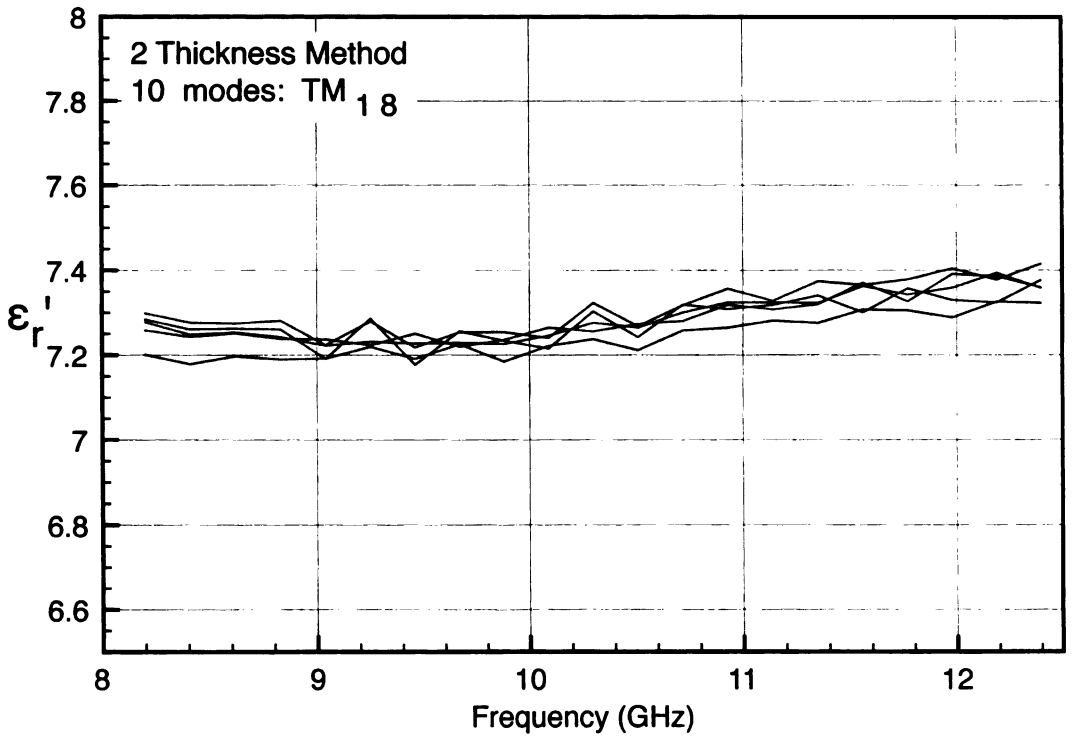


Figure 9.10. Extracted values for ϵ_r' for sample 2 of Eccosorb FGM125 using the two thickness method. Bottom layer: sample 2. Top layer: sample 1. These measurements were taken on 5 separate days. Measurement taken at position 1.

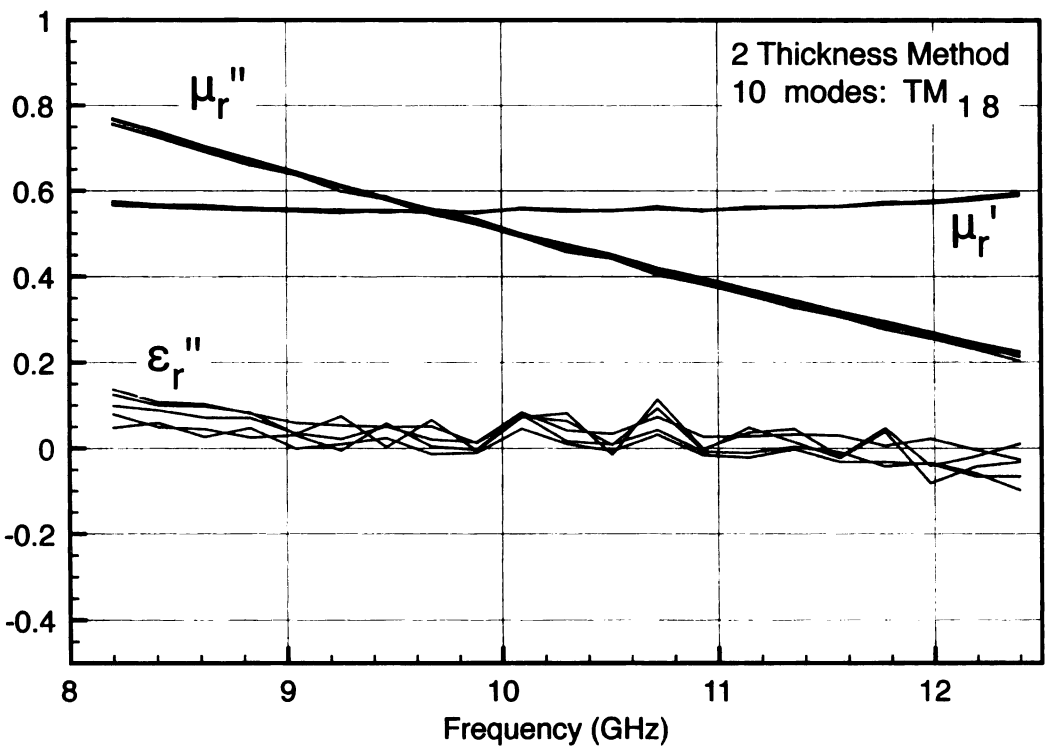


Figure 9.11. Extracted values for ϵ_r'', μ_r', and μ_r'', for sample 2 of Eccosorb FGM125 using the two thickness method. Bottom layer: sample 2. Top layer: sample 1. These measurements were taken on 5 separate days. Extractions were performed using the first 10 modes. Measurement taken at position 1.

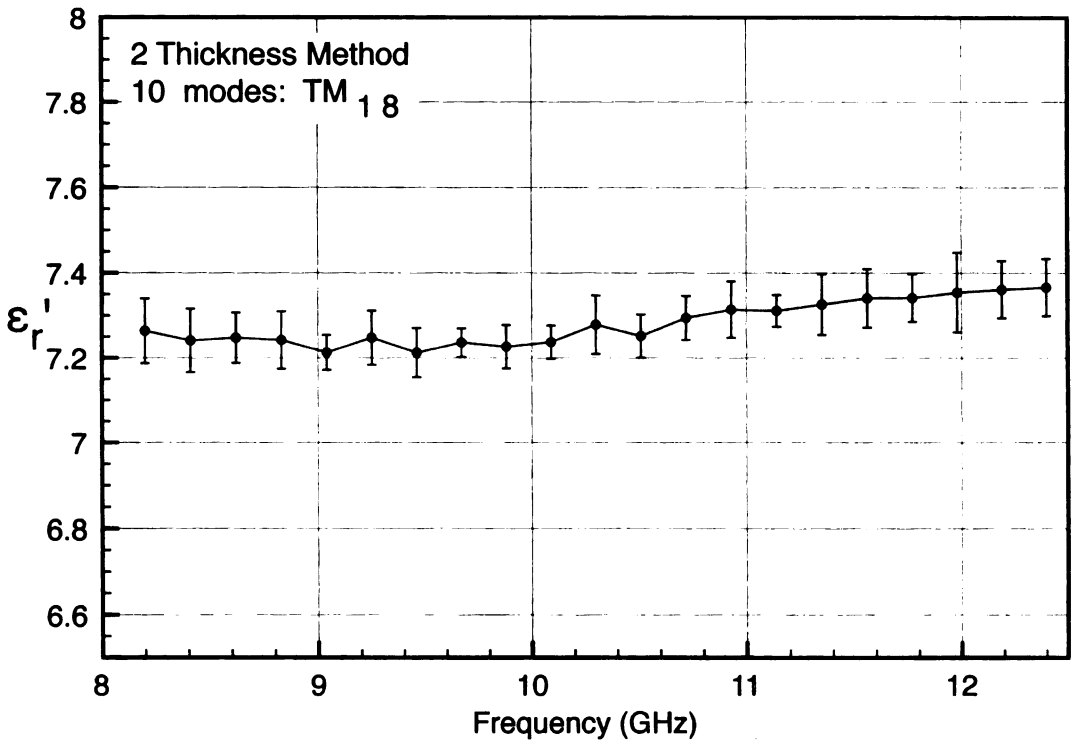


Figure 9.12. Mean extracted values for ϵ_r' for sample 2 of Eccosorb FGM125 using the first 10 modes in the two thickness method. Bottom layer: sample 2. Top layer: sample 1. The error bars represent the $\pm 2\sigma$, or 95% confindence intervals, for the extracted data shown in Figure 9.10. Measurement taken at position 1.

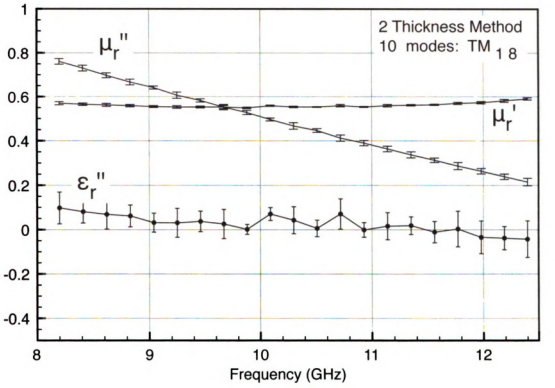


Figure 9.13. Mean extracted values for ϵ_r'', μ_r', and μ_r'', of Eccosorb FGM125 using the first 10 modes in the two thickness method. Bottom layer: sample 2. Top layer: sample 1. The error bars represent the $\pm 2\sigma$, or 95% confindence intervals, for the extracted data shown in Figure 9.11. Measurement taken at position 1.

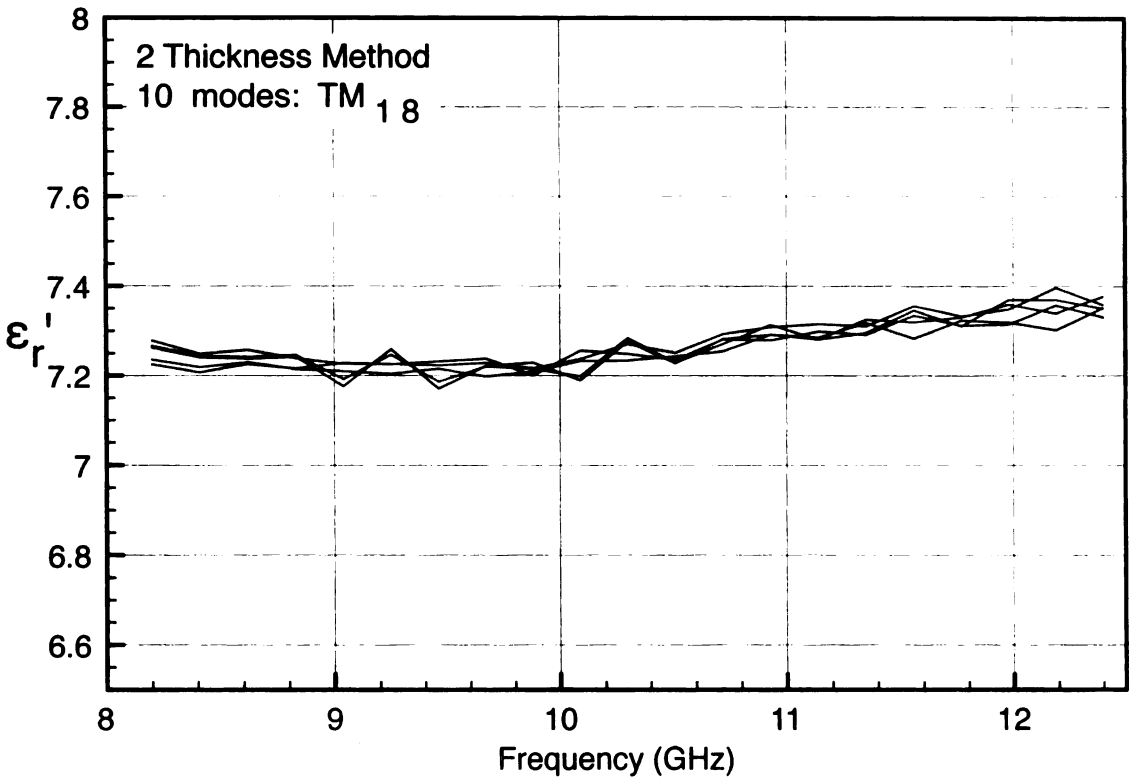


Figure 9.14. Extracted values for ϵ_r' for sample 1 of Eccosorb FGM125 using the two thickness method. Bottom layer: sample 1. Top layer: sample 2. These measurements were taken on 5 separate days. Measurement taken at position 1.

measurements were then used in the two thickness method to extract the material parameters for sample 1. Figure 9.14 - Figure 9.17 show the plots of the extracted data and the mean and standard deviation for all four parameters. These results are quite similar to those observed when the samples were placed in the opposite order.

The comparison of the two configurations of material is shown in Figure 9.18 and Figure 9.19. Note that the two figures show mean values that deviate from one another by less than 0.1% for the permittivity. The differences between the extracted permeability values in Figure 9.19 are indistinguishable.

Another example of the data extractions is shown in Figure 9.20 and Figure 9.21.

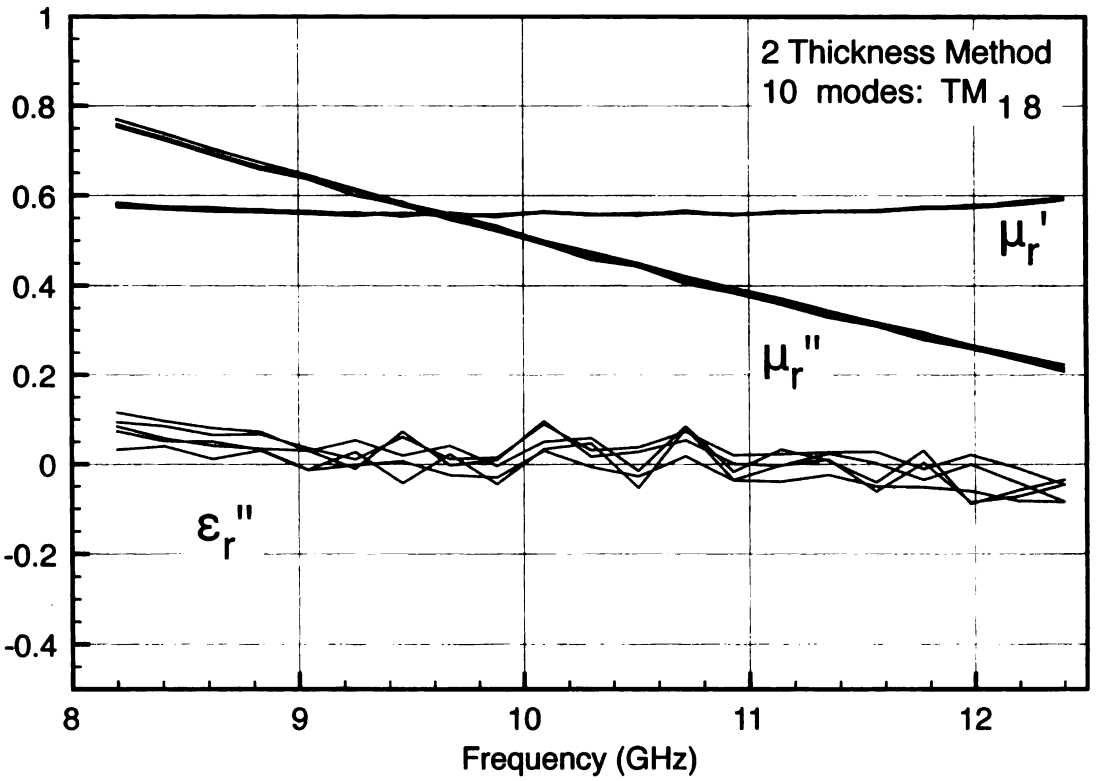


Figure 9.15. Extracted values for ϵ_r'', μ_r', and μ_r'', for sample 1 of Eccosorb FGM125 using the two thickness method. Bottom layer: sample 1. Top layer: sample 2. These measurements were taken on 5 separate days. Extractions were performed using the first 10 modes. Measurement taken at position 1.

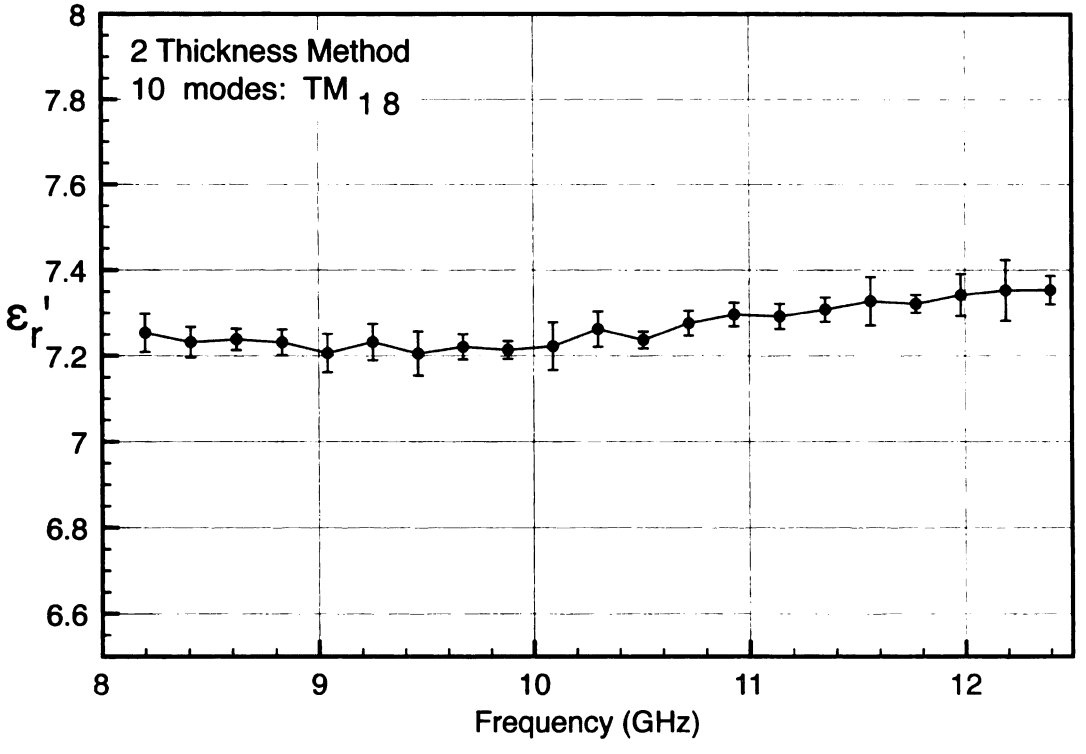


Figure 9.16. Mean extracted values for ϵ_r' of Eccosorb FGM125, using the first 10 modes in the two thickness method. Bottom layer: sample 1. Top layer: sample 2. The error bars represent the $\pm 2\sigma$, or 95% confindence intervals, for the extracted data shown in Figure 9.14. Measurement taken at position 1.

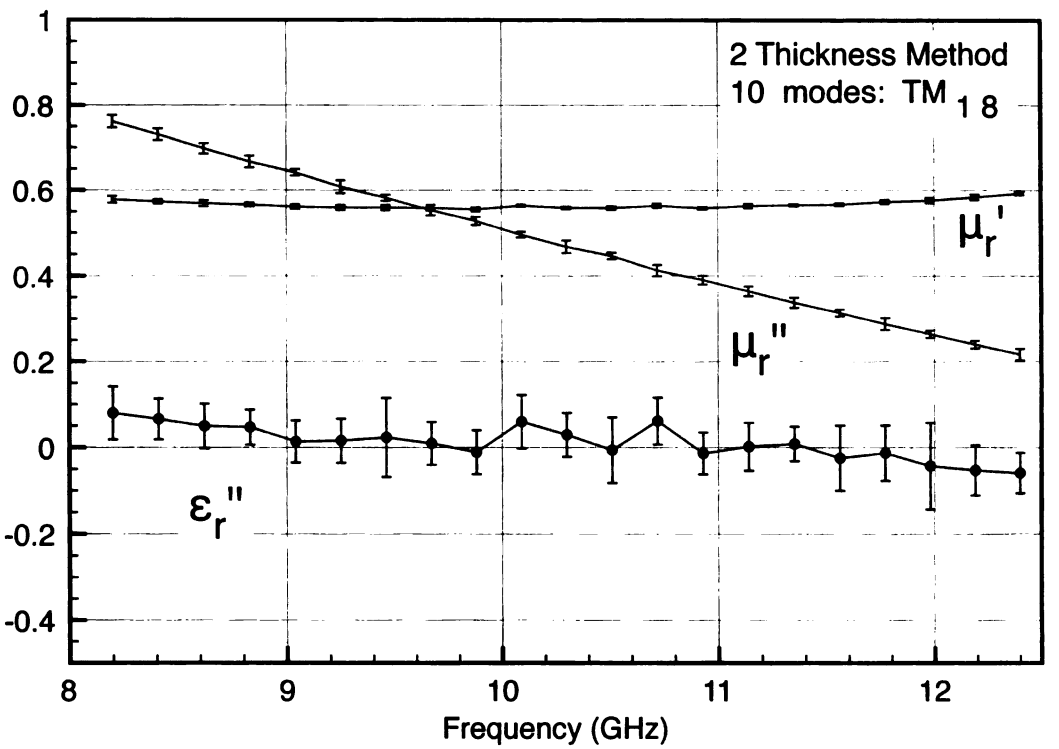


Figure 9.17. Mean extracted values for ϵ_r'', μ_r', and μ_r'', of Eccosorb FGM125, using the first 10 modes in the two thickness method. Bottom layer: sample 1. Top layer: sample 2. The error bars represent the $\pm 2\sigma$, or 95% confindence intervals, for the extracted data shown in Figure 9.15. Measurement taken at position 1.

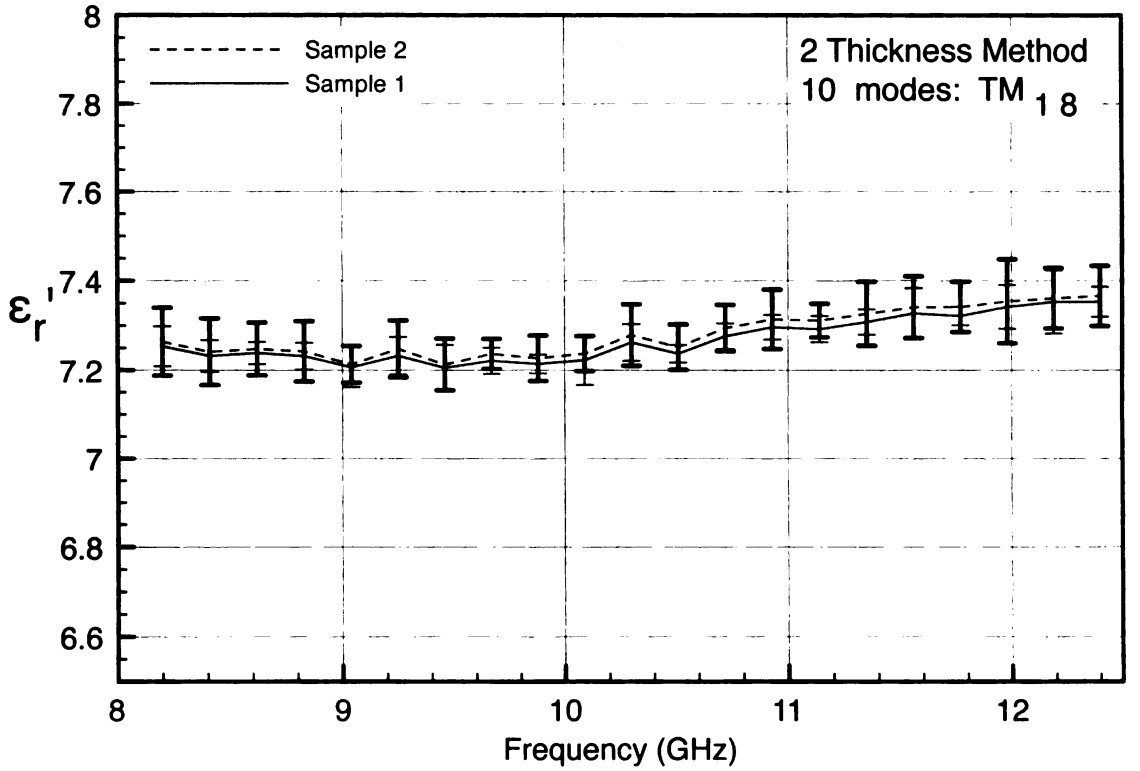


Figure 9.18. Comparison of the mean extracted values for ϵ_r' of Eccosorb FGM125 from Figure 9.12 and Figure 9.16. Legend describes the bottom layer. The error bars represent the $\pm 2\sigma$, or 95% confindence intervals. Measurement taken at position 1.

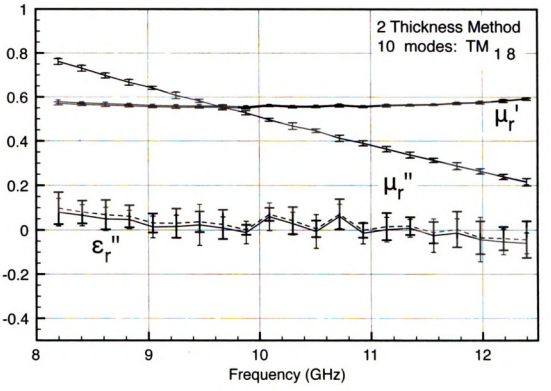


Figure 9.19. Comparison of the mean extracted values for ϵ_r'', μ_r', and μ_r'' of Eccosorb FGM125 from Figure 9.13 and Figure 9.17. Dotted line is for Sample 2 as the bottom layer, solid line is for Sample 1 as the bottom layer. The error bars represent the $\pm 2\sigma$, or 95% confindence intervals. Measurement taken at position 1.

For this extraction, the measured reflection coefficients shown in Figure 9.4 and Figure 9.5 were used in the two thickness method to extract the material parameters at all 5 positions, with sample 1 as the top layer and sample 2 as the bottom layer. Note that there is a slightly larger variation of the material parameters on one sample of material at the 5 different measurement positions than the variation observed by measuring one sample at the same measurement position 5 times. This indicates that there is a high degree of repeatability for the two thickness method when measuring the same sample at the same physical measurement position. The variability of the measurements made at different positions may indicate a spatial variance in the material parameters, spatial variance in the thickness of the material, or spatial variance in the experimental apparatus.

9.3.4 Two thickness extraction of Eccosorb FGM40

The two thickness method was also employed for another magnetic radar absorbing material with a higher permittivity, Eccosorb FGM40. The results of the material parameter extraction for Sample 1 are shown in Figure 9.22 and Figure 9.23. The first 10 significant modes were used in the extraction process. These modes are the same significantly contributing modes that were used for Eccsorb FGM125.

The solid lines are the extractions from measurements made at all 5 measurement positions, and the lines with the marker are the nominal values used in the simulations and found in Table F.4. The nominal values were for a different sample of FGM40 and were obtained using the waveguide T/R method by researchers at the Air Force Institute of Technology. Note that the values extracted using the two thickness method for ϵ_r'' and μ_r' have a high degree of agreement with the nominal values. However, the values for μ_r'' have a relative error of approximately 20-30% with respect to the nominal values. The two thickness values for ϵ_r' have a relative error of approximately 10% with respect to the nominal values.

The material properties stated by the manufacturer place the value of ϵ_r' near 30

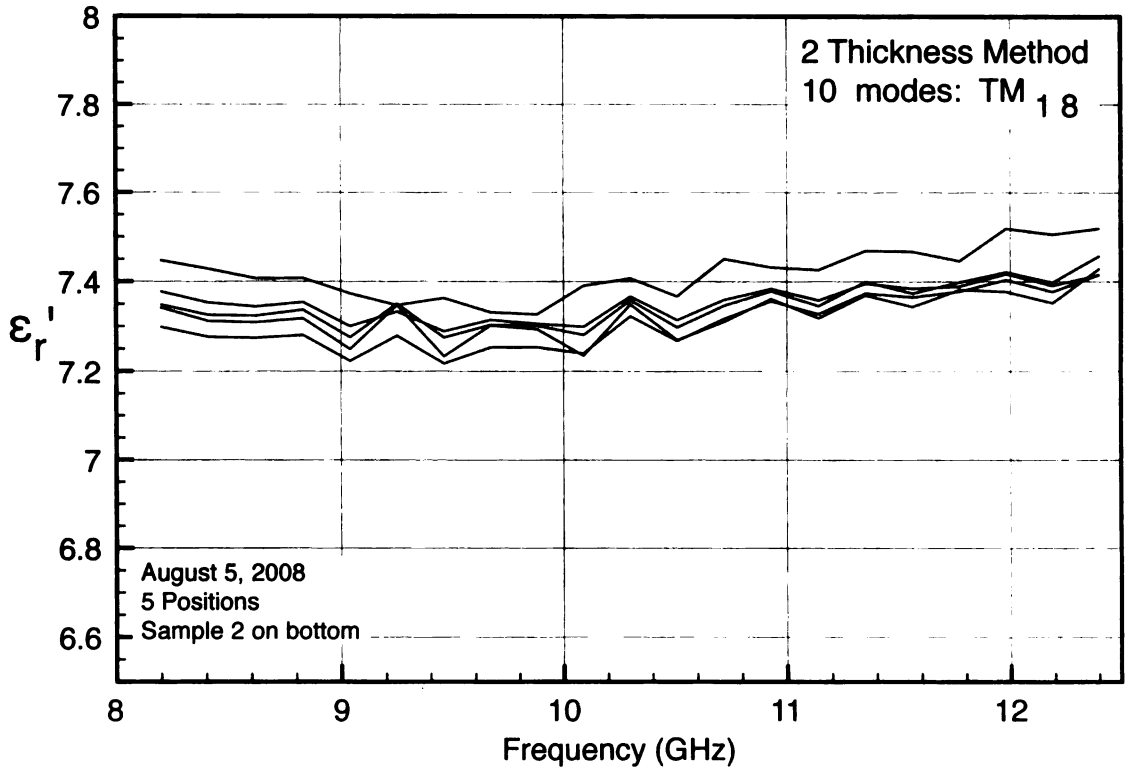


Figure 9.20. The extracted values for ϵ_r' from Eccosorb FGM125. Measurements taken at all 5 positions with Sample 2 as bottom layer

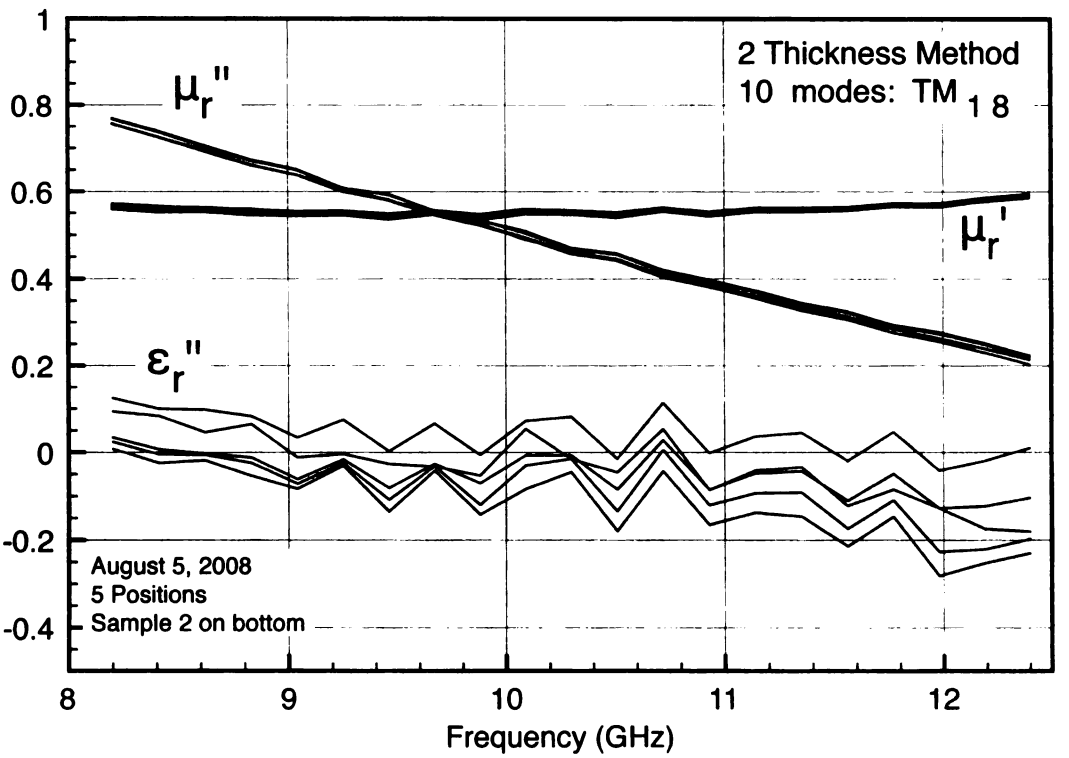


Figure 9.21. The extracted values for ϵ_r'', μ_r', and μ_r'' of Eccosorb FGM125. Measurements taken at all 5 positions with Sample 2 as bottom layer.

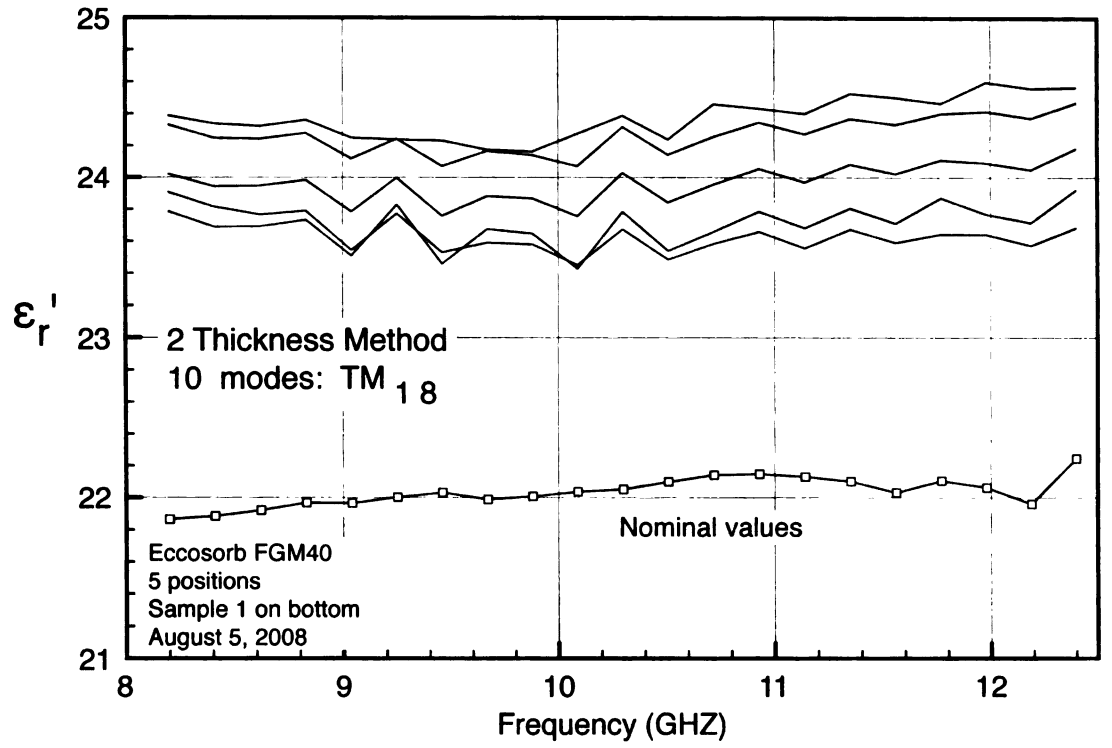


Figure 9.22. The extracted values for ϵ_r' from Eccosorb FGM40, with Sample 1 as the bottom layer. Measurement taken at all 5 positions. Nominal values are shown by $-\square-$.

for the X-band frequency range. Material parameter extractions by other researchers using different methods have resulted in published values for ϵ_r' of FGM40 in the range of $20 < \epsilon_r' < 27$ over the X-band frequency range [39], [63]. The other parameter values values obtained by the two thickness method also fall within the range of these published values. Thus these two thickness method results are reasonable extractions.

It is desirable to know if the extracted parameters demonstrate spatial variation when measured by the two thickness method. Measurements of FGM40 were taken on three different days. The two thickness method was used to extract the material parameters from these three data sets with Sample 2 as the top layer and Sample

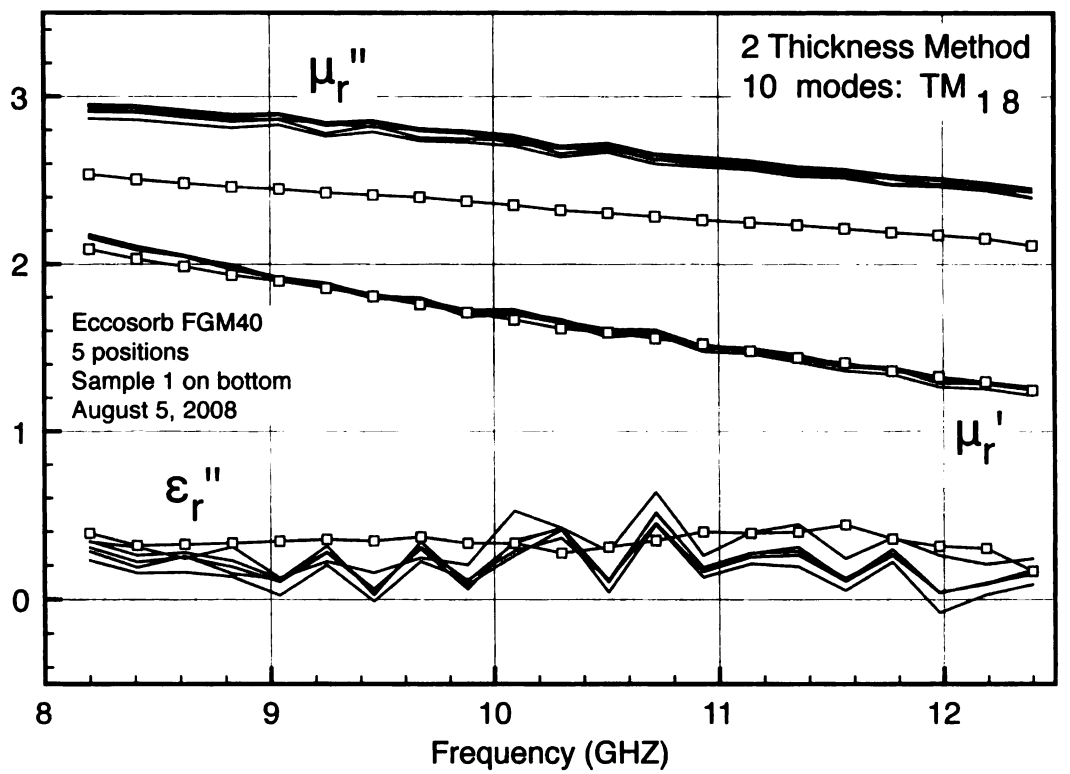


Figure 9.23. The extracted values for ϵ_r'', μ_r', and μ_r'' of Eccosorb FGM40, with Sample 1 as the bottom layer. Measurement taken at all 5 positions. Nominal values are shown by $-\square-$ markers.

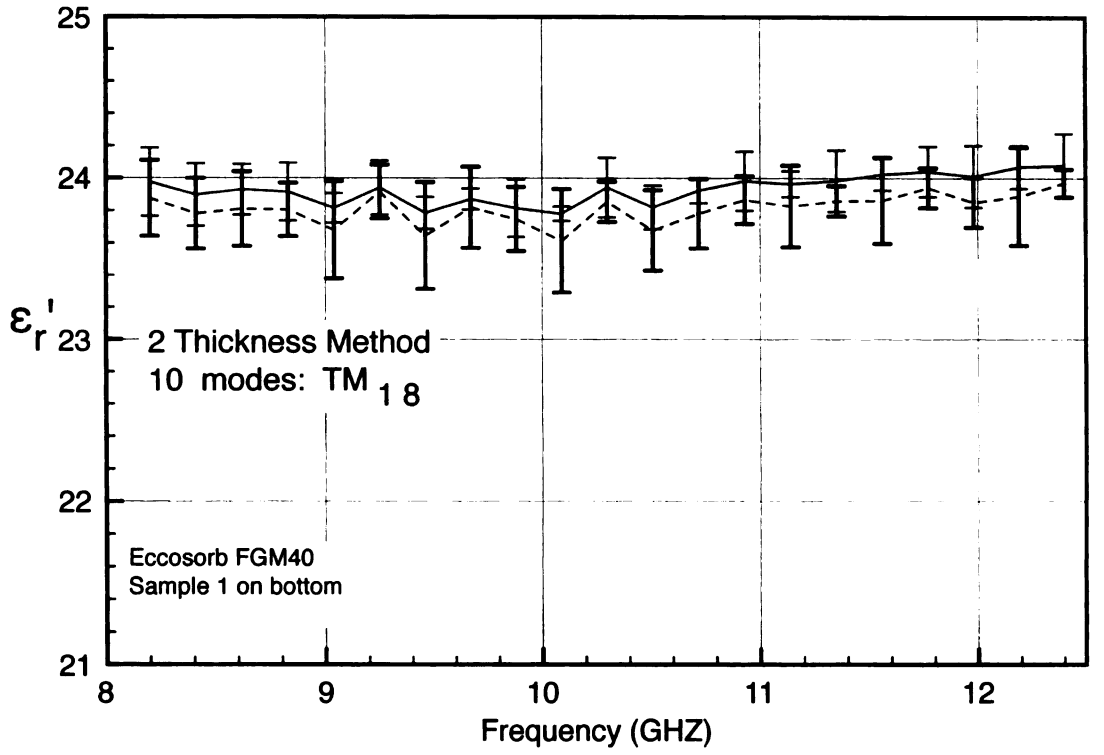


Figure 9.24. The mean extracted values for ϵ_r' from Eccosorb FGM40, with Sample 1 as the bottom layer. Solid line : position 1. Dotted line: position 2. Error bars are 95% confidence levels.

1 as the bottom layer. The mean and standard deviation of the three extracted material parameters were calculated for the extractions performed at position 1 and position 2. The results are displayed in Figure 9.24 and Figure 9.25. Note that the permeability values are very close to each other, and the confidence intervals overlap. For the permittivity, the mean values are not exactly the same, but the confidence intervals do overlap for this configuration as well. Note that the standard deviations were computed from only three extractions.

The same analysis was performed for FGM40 using the two thickness method, with Sample 1 as the top layer and Sample 2 as the bottom layer. The results,

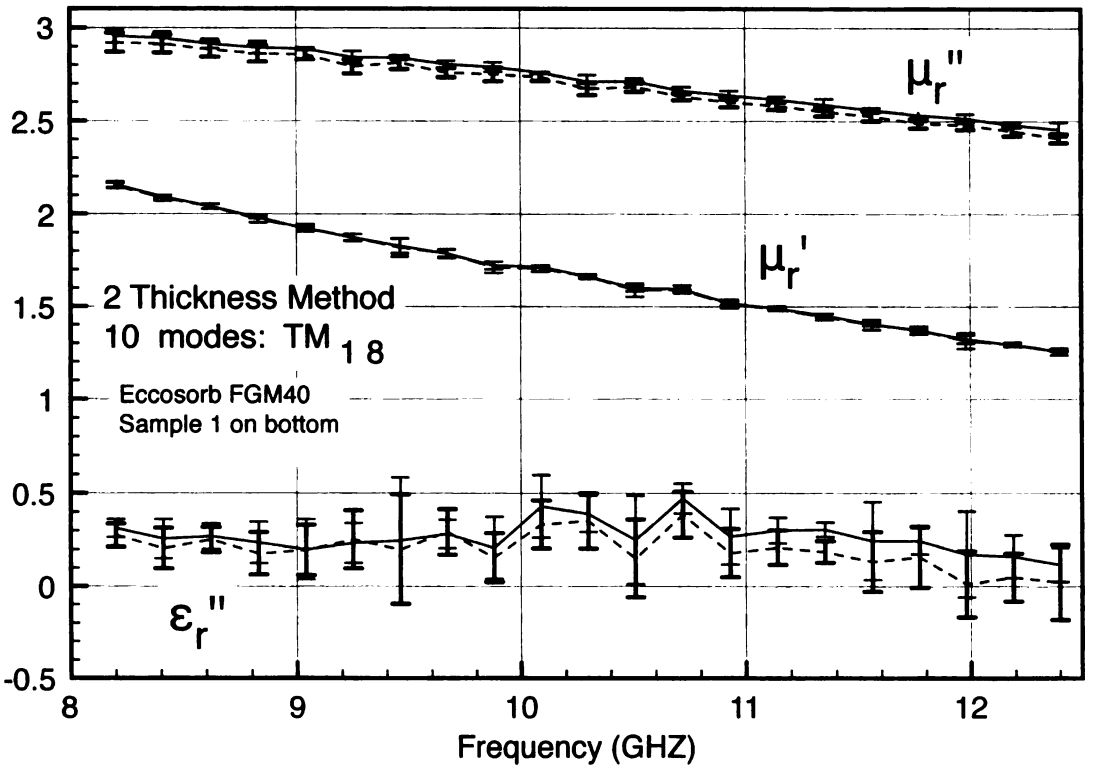


Figure 9.25. The mean extracted values for ϵ_r'', μ_r', and μ_r'' from Eccosorb FGM40, with Sample 1 as the bottom layer. Solid line : position 1. Dotted line: position 2. Error bars are 95% confidence levels.

which are displayed in Figure 9.26 and Figure 9.27, show a similar result for the permeability. The permittivity, however, shows a larger spatial deviation for ϵ_r', and the confidence intervals do not overlap for much of the band. The mean values for ϵ_r'' are also separated by approximately 0.3, and the confidence intervals overlap for part of the band. However, the mean values for ϵ_r'' are less than zero for most of the band, which is not a physically realizable material parameter. It should be noted that the mean and standard deviation were only calculated using data from 3 extractions, thus the results have limited significance. It does suggest, however, that there may be some spatial variation in the permittivity for Eccosorb FGM40 or in the measurement apparatus.

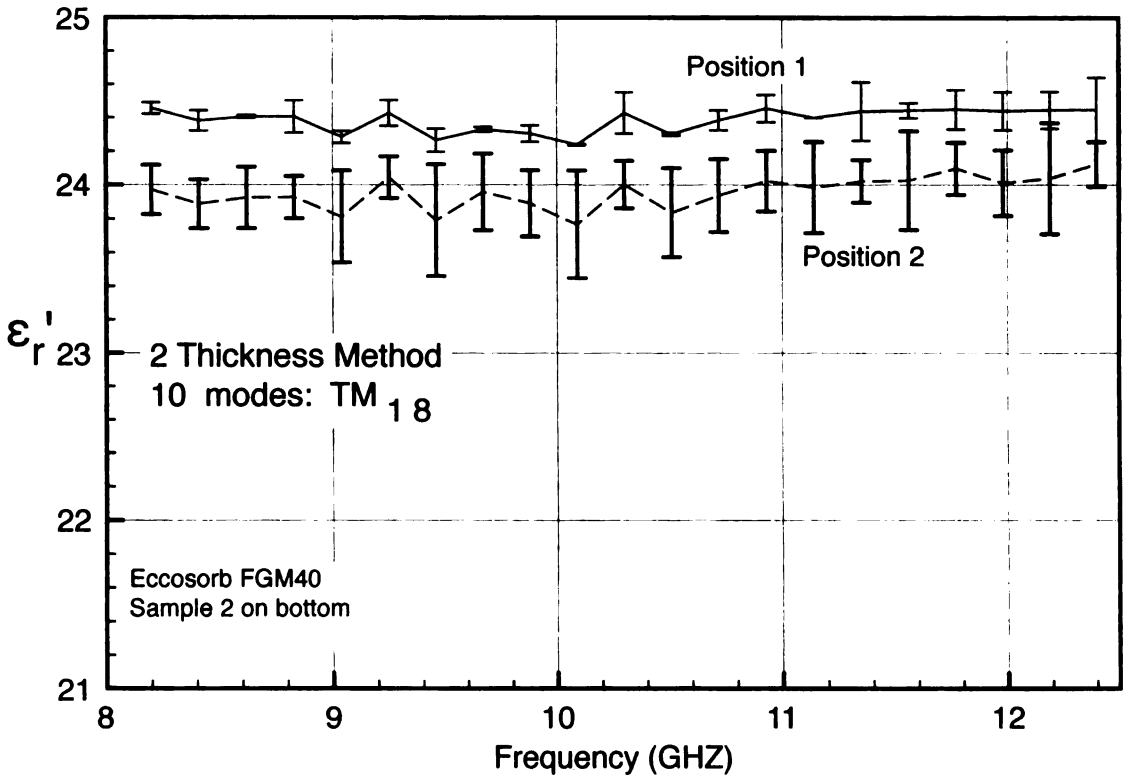


Figure 9.26. The mean extracted values for ϵ_r' from Eccosorb FGM40, with Sample 2 as the bottom layer. Solid line : position 1. Dotted line: position 2. Error bars are 95% confidence levels.

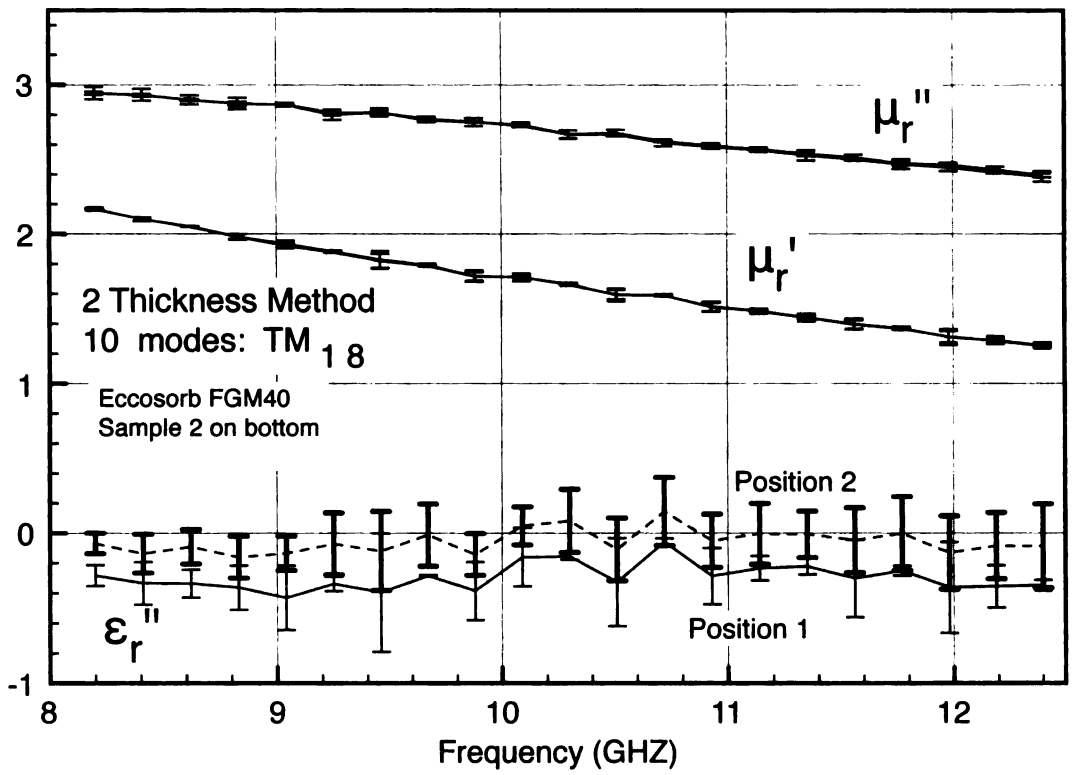


Figure 9.27. The mean extracted values for ϵ_r'', μ_r', and μ_r'' from Eccosorb FGM40, with Sample 2 as the bottom layer. Solid line : position 1. Dotted line: position 2. Error bars are 95% confidence levels.

9.4 Two Layer Method

Material parameters were also extracted from material samples using the two layer method. In section 9.4.1 and section 9.4.2, extraction results from two layers of Eccosorb FGM125 are examined. In addition, two layer method extractions using plastic materials for the top layer are examined in section 9.4.3.

9.4.1 Modal Analysis for 2 layers of Eccosorb FGM125

In section 9.3.3, a modal analysis is performed on the two thickness method to examine the effect of the number of modes on the extractions from actual measurements. A similar analysis is shown in Figure 9.28 - Figure 9.31 for the two layer method. The two layer method was used to extract data from two sets of reflection coefficients. The first measurement, $S^{meas}_{11(1L)}$, was obtained from sample 2. The second measurement, $S^{meas}_{11(2L)}$, was recorded with sample 1 on top of sample 2.

The same modes that were used in the two thickness method modal analysis in section 9.3.3 were used in this two layer modal analysis. The key for each line in the figures is shown in Table 9.3. Recall that a similar analysis was performed on synthesized data in Chapter 5. Note that the extracted values for μ'_r in Figure 9.28 show a similar trend to what is observed in Figure 5.26 at the upper end of the frequency band. As the number of modes is increased, the extracted values decrease. At the lower end of the frequency band, the trend is reversed, which is opposite of what was observed in the simulations. Also note that the extracted values from the measurements are approximately 20-30% lower with respect to the simulated extracted values. In addition, compare line E in Figure 9.28 with line E in Figure 9.8. Note that the two layer results are also 20-30% lower than those which resulted from the two thickness method.

The extracted values shown in Figure 9.29 do not show much similarity to the modal analysis that was performed on the simulated data in Figure 5.27. The values

for the two layer extraction do move downward in the upper end of the frequency band, but the values extracted using the extrapolation method are much larger than the values extracted using the two thickness method. When comparing the graph shown in Figure 9.29 to the modal analysis for the two thickness method in Figure 9.9, it is clear that when considering actual measurements, even using the extrapolation method does not produce values for μ_r' which agree with the two thickness method.

The extracted values for ϵ_r' shown in Figure 9.30 are also not similar to the simulated analysis found in Figure 5.24. The slope of the plots for the experimental data is in the downward direction. The slope of the plot of the simulated data extractions are in the opposite direction.

The plot for the data for ϵ_r'' shown in Figure 9.31 also shows a large difference compared to simulations. Increasing the number of modes in the solution does not improve the results or move them closer to the nominal values. Instead, these values for ϵ_r'' are less than zero, which is not physically possible.

From this modal analysis, it appears that when actual measurements have been made, increasing the number of modes in the solution does not necessarily provide results that agree with the two thickness method. This is consistent with the simulations that were performed in Chapters 5 and 6. The modal analysis of simulated data demonstrated that in the absence of measurement error, the extrapolation method would allow the extracted parameters to be retrieved from the nominal values. However, the measurement error sensitivity analysis in Chapter 6 suggested that the inclusion of random measurement error greatly increased the degree of uncertainty in the extracted parameters. In addition, other errors may be present in the measurement process which cause the extracted results to vary greatly. This modal analysis on measured data agrees with the simulations that using the two layer method with two layers of Eccosorb FGM125 is not a reliable material parameter extraction method.

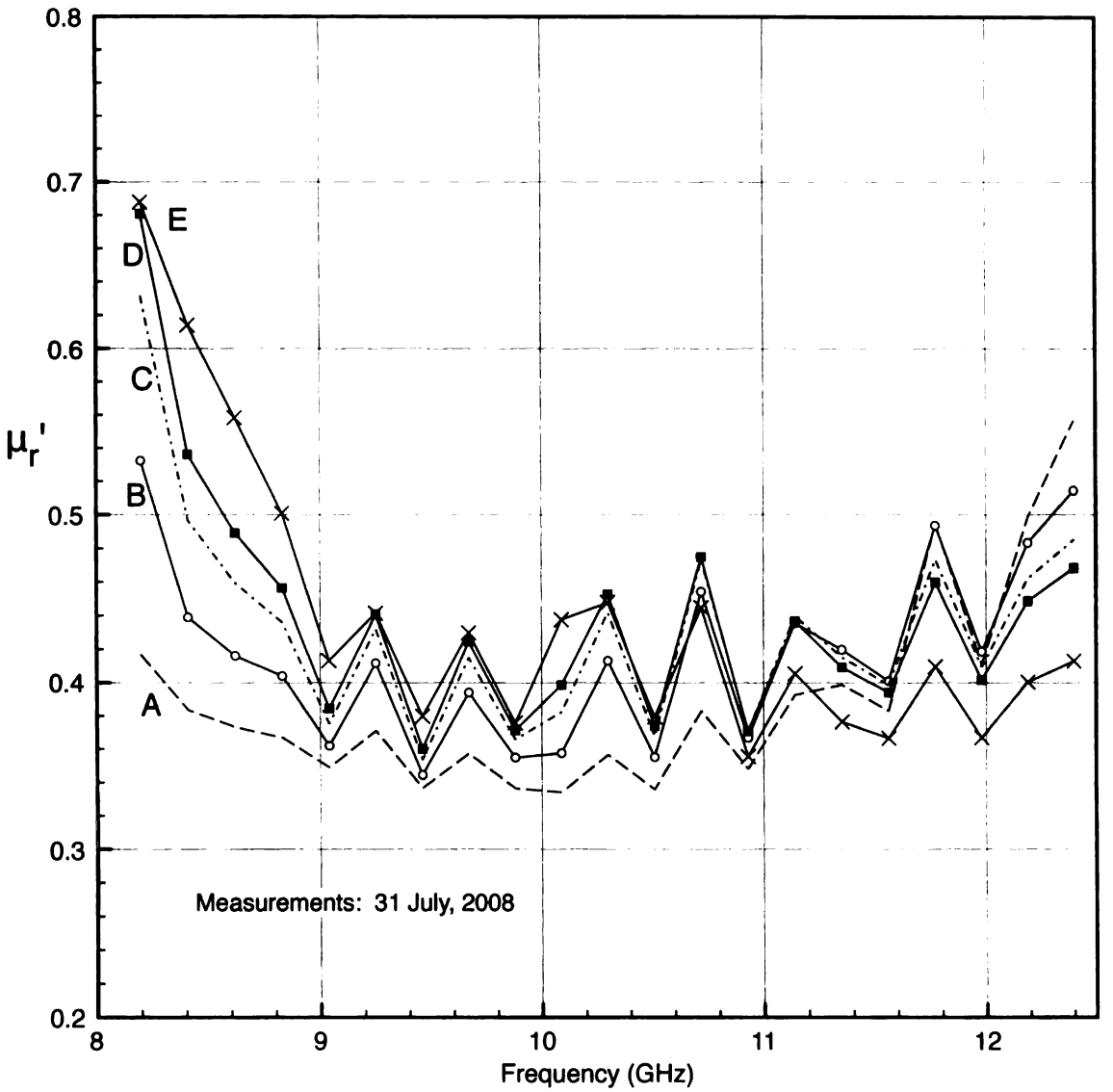


Figure 9.28. The extracted values for μ_r' from Eccosorb FGM125 using the two layer method, with Sample 1 as the top layer and Sample 2 as the bottom layer. Different numbers of modes used in the extraction. Measurements made at Position 1. Key for different numbers of modes found in Table 9.3.

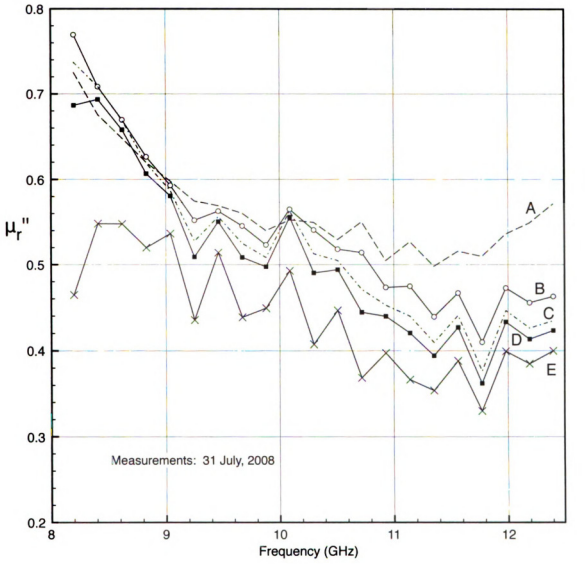


Figure 9.29. The extracted values for μ_r'' from Eccosorb FGM125 using the two layer method, with Sample 1 as the top layer and Sample 2 as the bottom layer. Different numbers of modes used in the extraction. Measurements made at Position 1. Key for different numbers of modes found in Table 9.3.

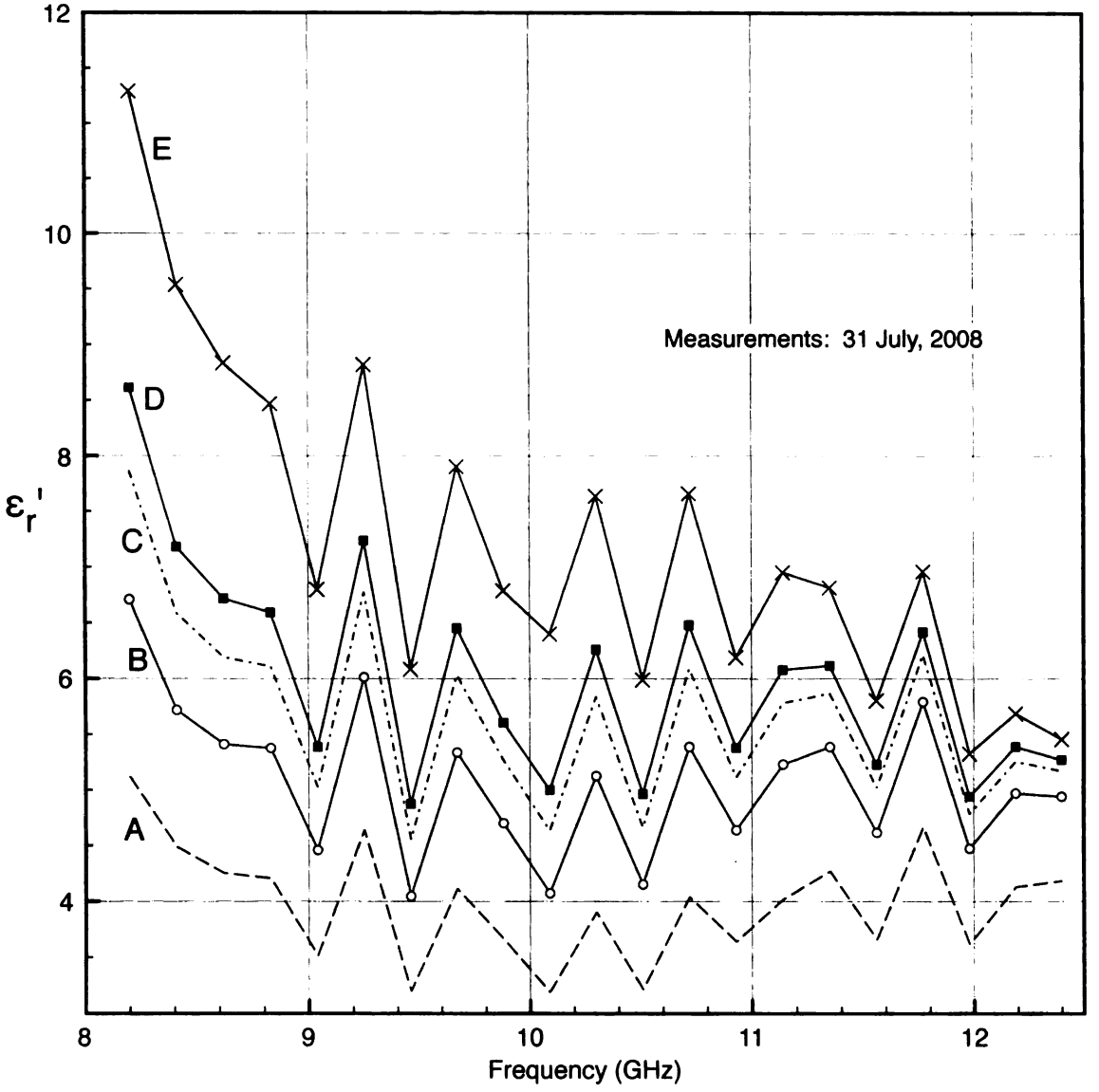


Figure 9.30. The extracted values for ϵ_r' from Eccosorb FGM125 using the two layer method, with Sample 1 as the top layer and Sample 2 as the bottom layer. Different numbers of modes used in the extraction. Measurements made at Position 1. Key for different numbers of modes found in Table 9.3.

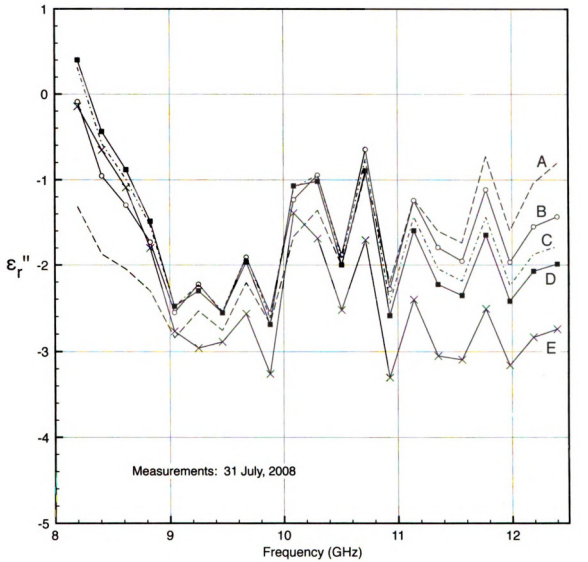


Figure 9.31. The extracted values for ϵ_r'' from Eccosorb FGM125 using the two layer method, with Sample 1 as the top layer and Sample 2 as the bottom layer. Different numbers of modes used in the extraction. Measurements made at Position 1. Key for different numbers of modes found in Table 9.3.

9.4.2 Additional Analysis for Two Layers of Eccosorb FGM125

It is possible that the data collected for Figure 9.28 - Figure 9.31 are corrupted with errors peculiar to that measurement set. To examine this possibility, data collections from other measurements of two layers of FGM125 were analyzed with the two layer method. Two thicknesses of Eccosorb FGM125 were measured at the 5 measurement positions, and the results from the material parameter extractions are shown in Figure 9.32 - Figure 9.35. The extracted data shown in these plots use the first 10 significant modes in the extraction.

Note that all four parameters show similar trends to those observed for the two layer method in Figure 9.28 - Figure 9.31. All of the extracted values for μ_r' in Figure 9.35 are approximately 20-30% lower with respect to the values derived using the two thickness method. The extracted values for μ_r'' in Figure 9.35 do not display a constant slope across the frequency band, a feature that was quite evident in the nominal values and the values extracted using the two thickness method. All of the extracted values for ϵ_r'' in Figure 9.35 are negative, which are non-physical values. In addition, the values for ϵ_r' are too high on the lower end of the frequency band, and too low on the upper end of the frequency band.

It was shown in Chapter 5, in Figure 5.22 - Figure 5.25, that simulated extractions that did not use the extrapolation method did not agree well with the permittivity values. When the extrapolation method was employed, the extracted values agreed with the nominal values in the simulation. Thus, to ensure that that the result is not simply due to not enough modes being used, the extrapolation was used on two sets of experimental data and compared with an extraction performed on the same set of measured data using the two thickness method. The result of this analysis is shown in Figure 9.36 - Figure 9.39.

Note that the two different sets of material parameters extrapolated using the two layer method agree well with each other, but do not agree with the parameters

extracted using the two thickness method for most of the figures. The two thickness method and two layer method extracted data used the exact same measurements for one layer and two layers of Eccosorb FGM125 in the August 05, 2008 data. The extracted values for ϵ_r' using the two layer method are the closest to the two thickness method in the middle of the frequency band, between 9 GHz and 11 GHz, as shown in Figure 9.36. However, the two layer method demonstrates values which deviate with respect to the two thickness method by $\pm 20\%$ or more in this region. As was shown in the error sensitivity analysis in Chapter 6, the confidence in the values derived by the two layer method in this region for ϵ_r' is not nearly as high as that for the two thickness method.

The other region where the extracted values from the two methods agree somewhat is from 10 GHz to 11.4 GHz in Figure 9.39, the plot of the values of μ_r''. One observation is that in the random measurement error sensitivity analysis for the two layer method, as shown in Figure 6.8, the region near 11GHz exhibited the lowest sensitivity to random measurement error.

The experimental results shown in these figures agree with the error sensitivity analysis from Chapter 6. The conclusion is that the two layer method, when using two different thicknesses of Eccosorb FGM125, has a much greater degree of uncertainty in the extracted parameters. One conclusion from the error sensitivity analysis is that the two layer method is much more sensitive to random measurement error than the two thickness method. An additional source of error not present in simulations is inaccurate knowledge of the material parameters of the top layer. The nominal values which were used in the simulations and are found in Table 5.1 were the material parameter values of the top layer in the two layer extractions. Since the nominal values are not derived exactly from the same sample, there are certainly errors associated with those valuse. The effect of these errors, as well as other possible errors in the two layer method, confirm the simulation observations that this method, when used

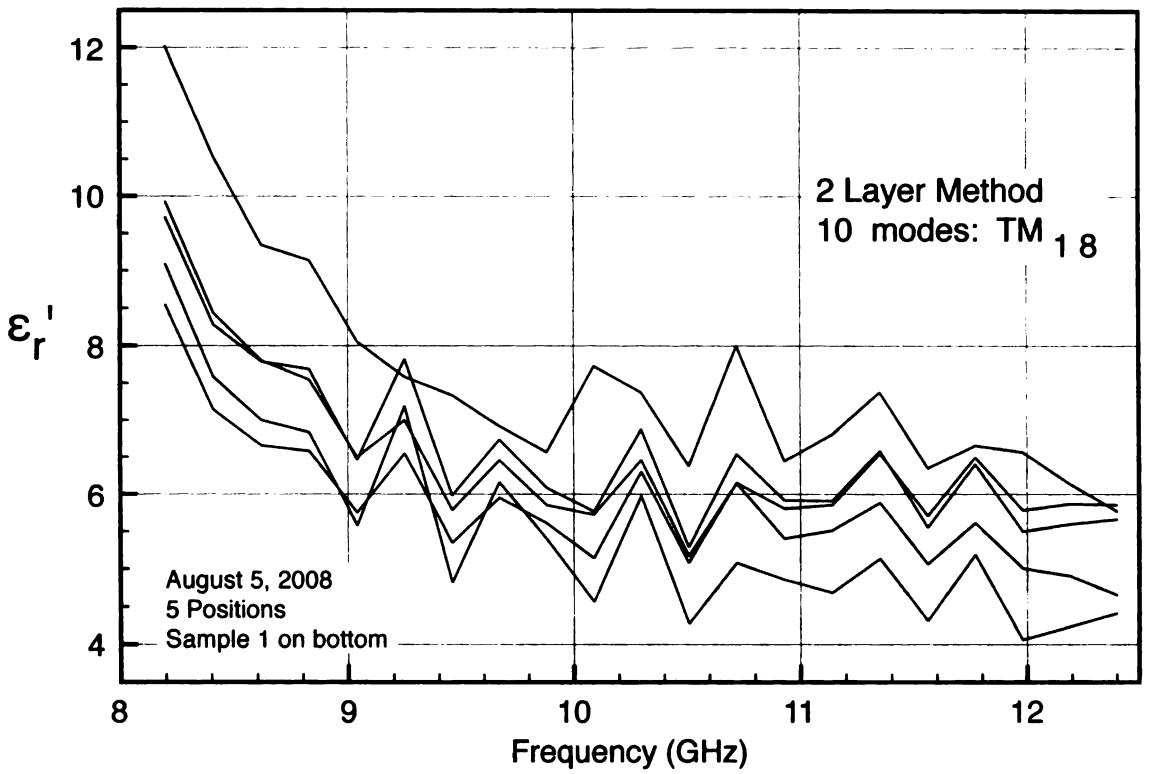


Figure 9.32. The extracted values for ϵ_r' from Eccosorb FGM125 using the two layer method, with Sample 2 as the top layer and Sample 1 as the bottom layer. Measurement taken at all 5 positions.

with two layers of Eccosorb FGM125, is much more sensitive to any sources of errors and the results are much less trustworthy.

9.4.3 Two Layer Method Extractions with Plastic Top Layer

The sensitivity analysis in Chapter 6 for the two layer method leads to some interesting conclusions regarding the choice of material for the top layer, when the bottom layer is Eccosrb FGM125. When a low dielectric constant material, such as PVC or Plexiglass is used as the top layer, simulations indicate that the two layer method, with these low dielectric constant materials as the top layer, is much less sensitive to those errors than using the two layer method with two layers of FGM125. Since

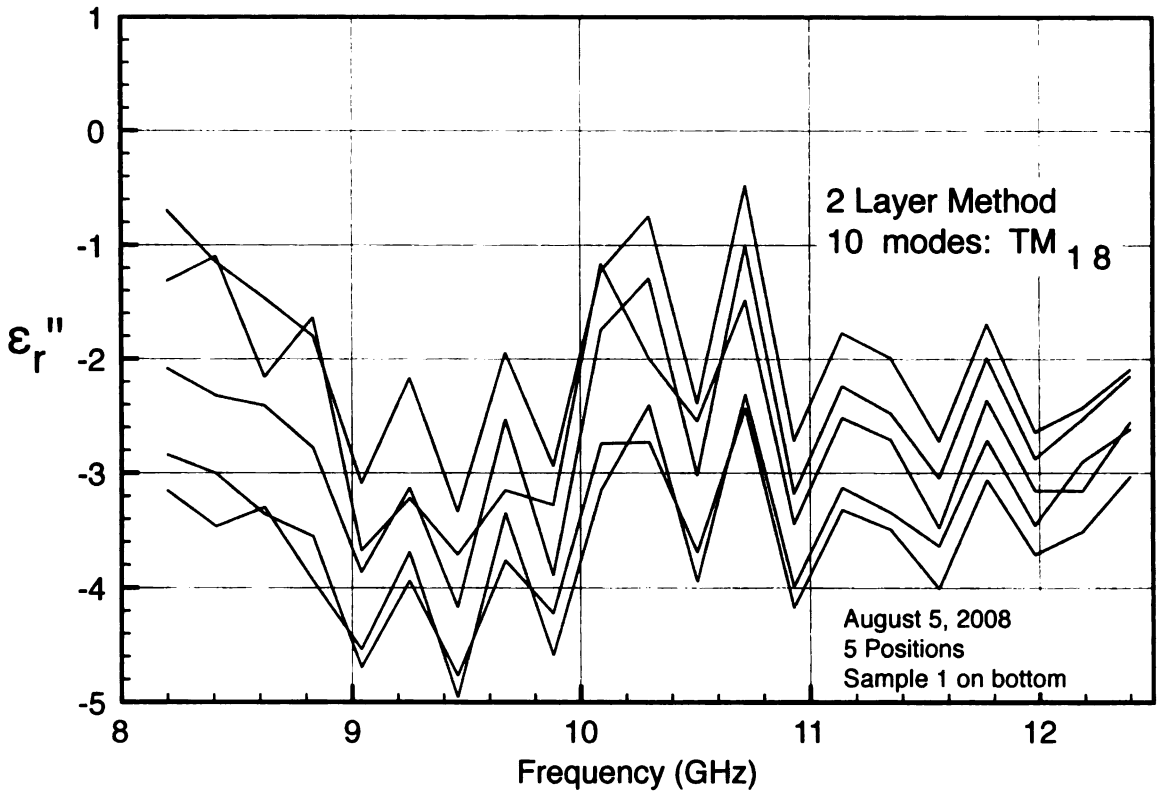


Figure 9.33. The extracted values for ϵ_r'' of Eccosorb FGM125 using the two layer method, with Sample 2 as the top layer, and Sample 1 as the bottom layer. Measurement taken at all 5 positions.

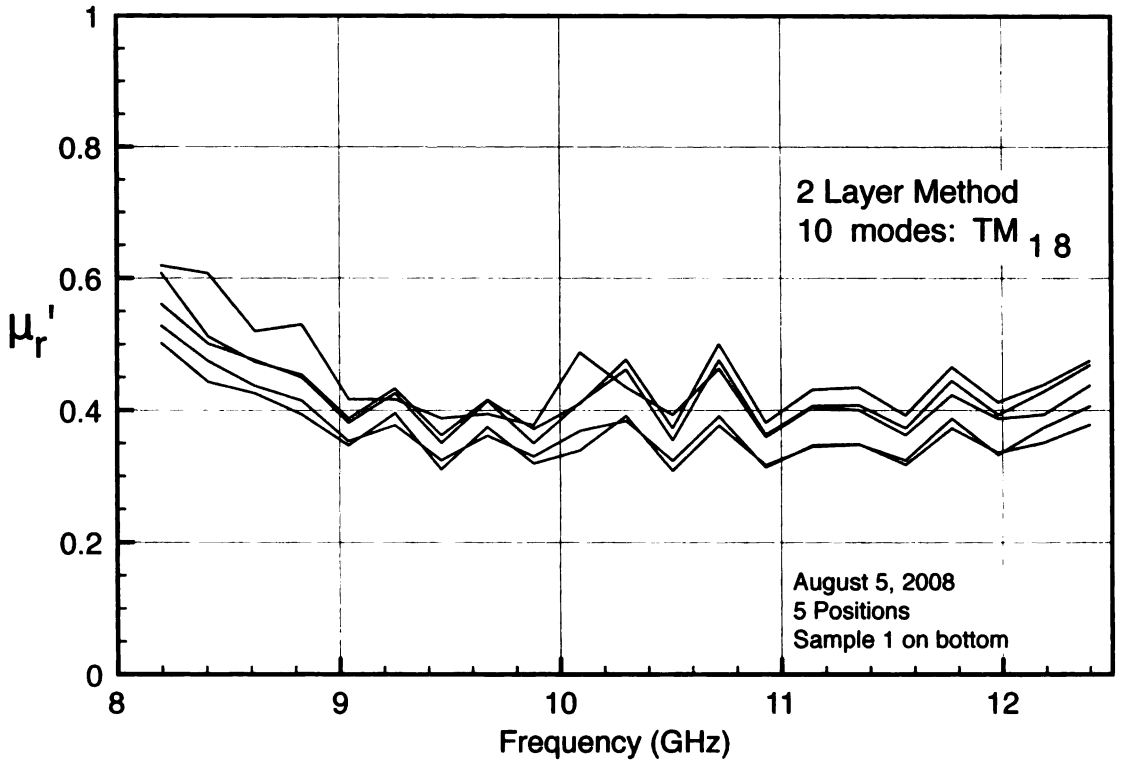


Figure 9.34. The extracted values for μ_r' of Eccosorb FGM125 using the two layer method, with Sample 2 as the top layer, and Sample 1 as the bottom layer. Measurements taken at all 5 positions.

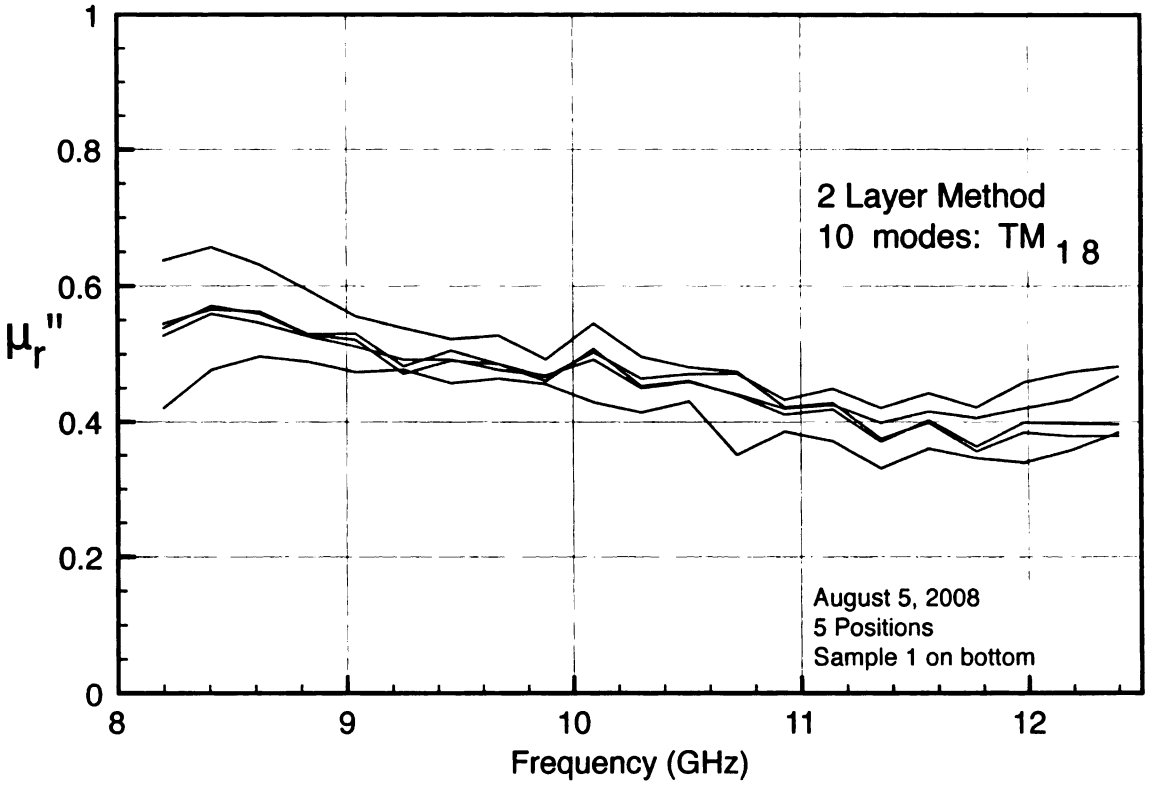


Figure 9.35. The extracted values for μ_r'' of Eccosorb FGM125 using the two layer method, with Sample 2 as the top layer, and Sample 1 as the bottom layer. Measurements taken at all 5 positions.

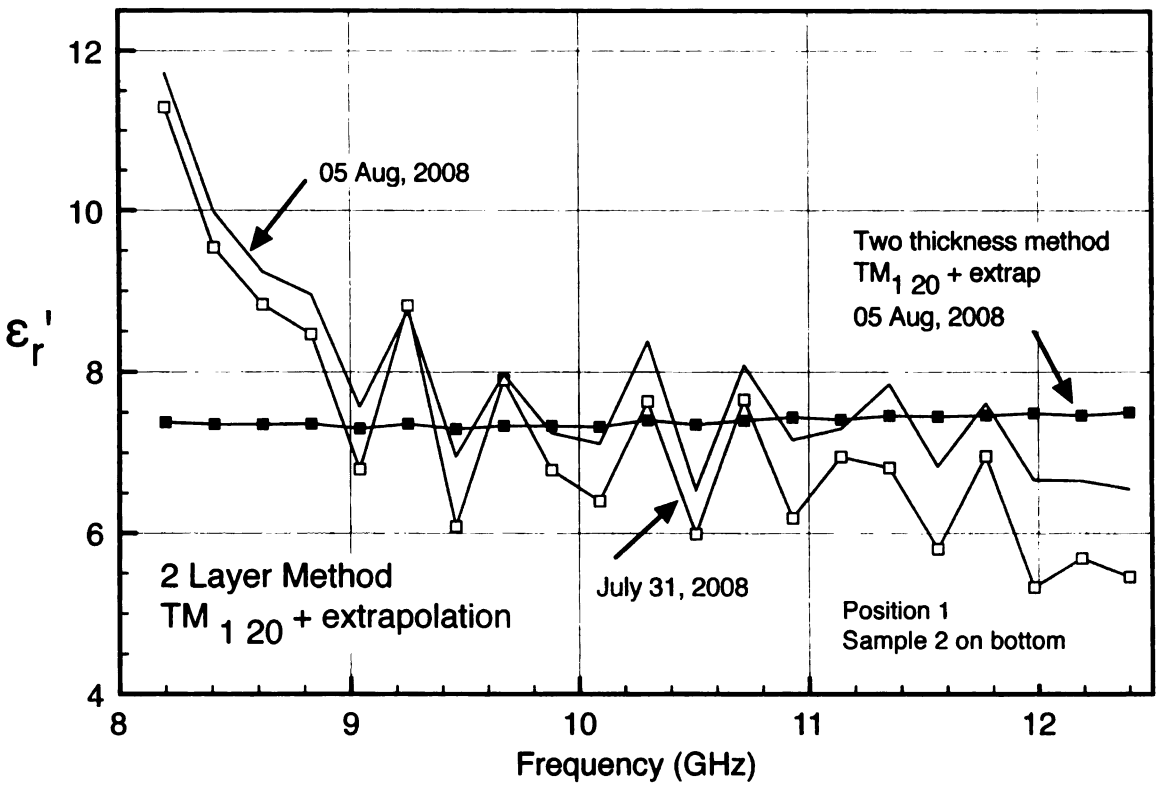


Figure 9.36. The extracted values for ϵ_r' of Eccosorb FGM125 using the two layer method, with Sample 1 as the top layer, and Sample 2 as the bottom layer. Measurements taken at position 1.

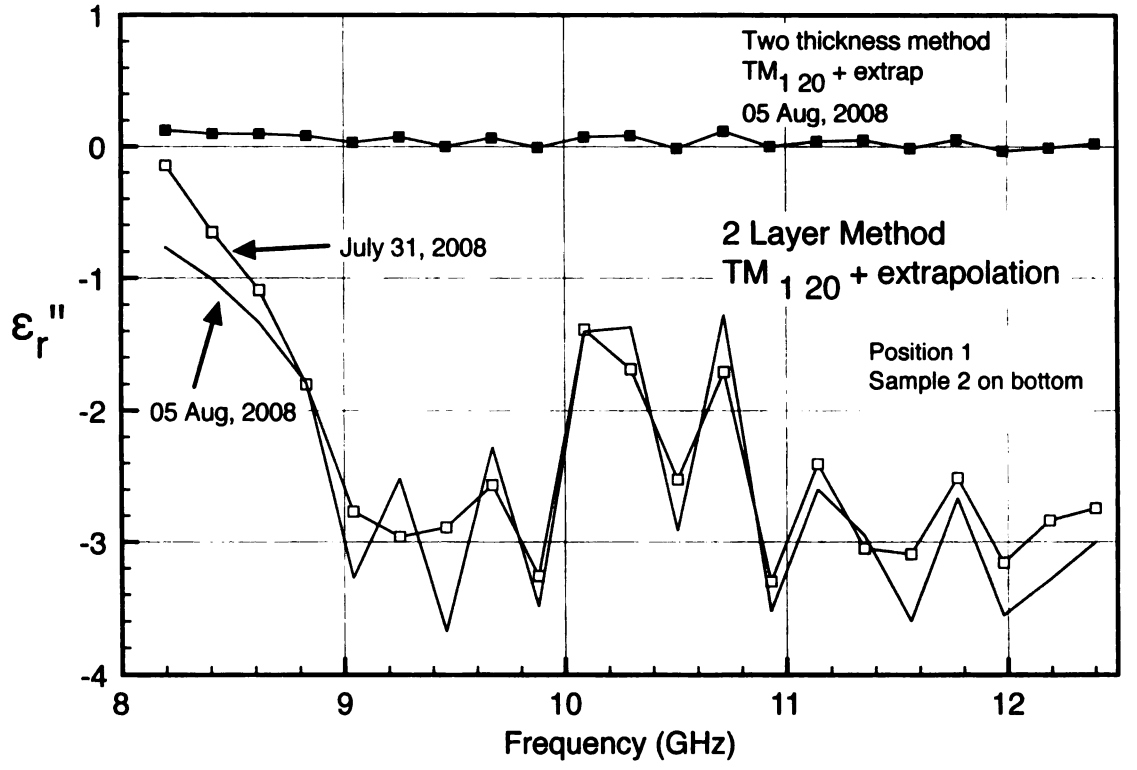


Figure 9.37. The extracted values for ϵ_r'' of Eccosorb FGM125 using the two layer method, with Sample 1 as the top layer, and Sample 2 as the bottom layer. Measurements taken at position 1.

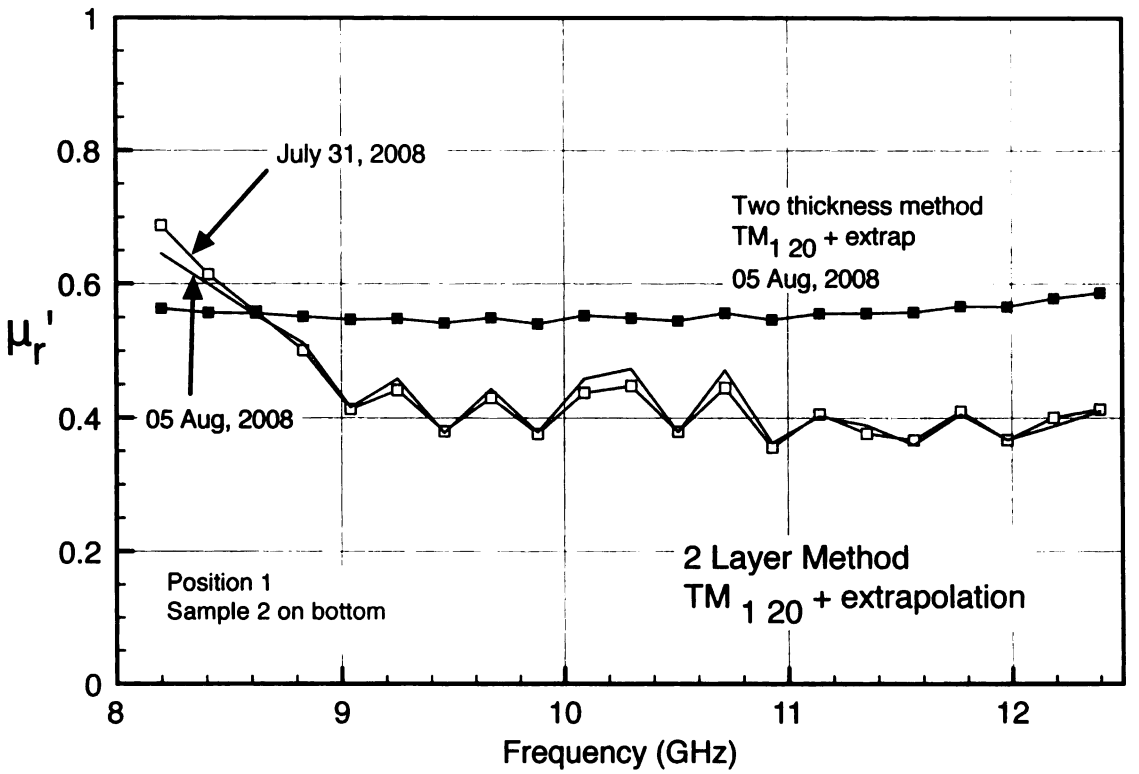


Figure 9.38. The extracted values for μ_r' of Eccosorb FGM125 using the two layer method, with Sample 1 as the top layer, and Sample 2 as the bottom layer. Measurements taken at position 1.

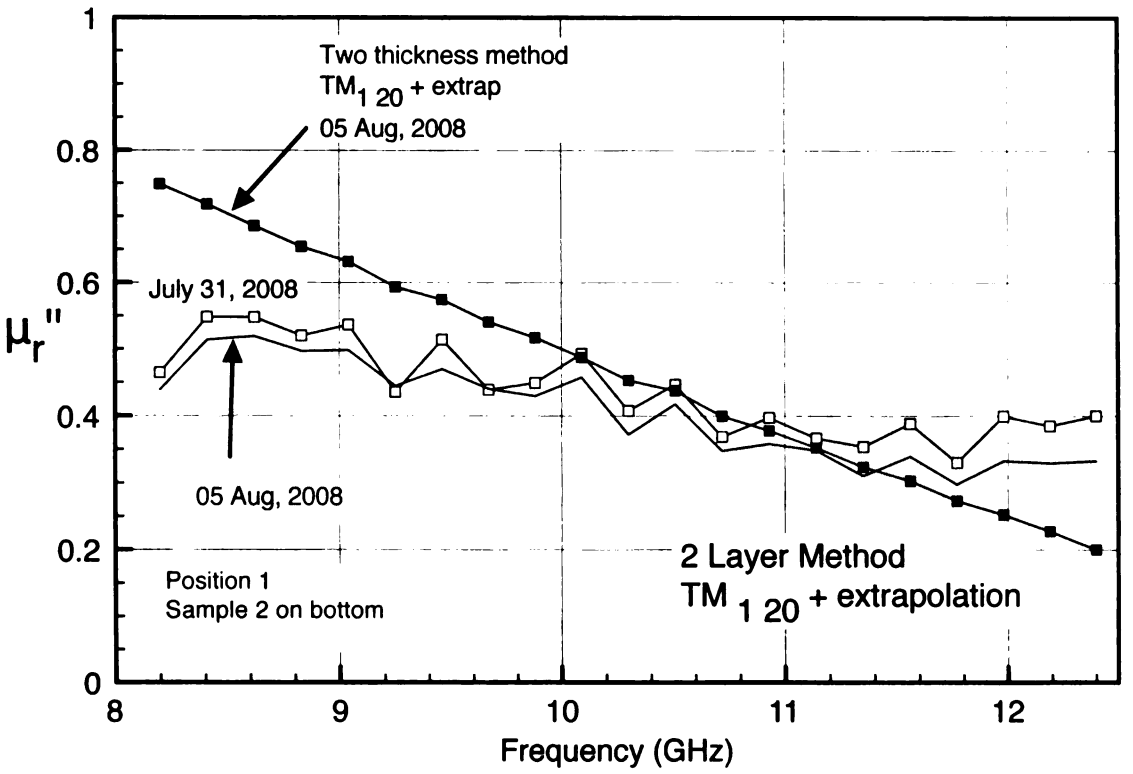


Figure 9.39. The extracted values for μ_r'' of Eccosorb FGM125 using the two layer method, with Sample 1 as the top layer, and Sample 2 as the bottom layer. Measurements taken at position 1.

the experiment confirmed the sensitivity analysis for two layers of Eccosorb FGM125, measurements were also taken for the two layer method using different materials for the top layer.

The primary measurements necessary for the two layer method are the complex quantities $S_{11(1L)}^{meas}$ and $S_{11(2L)}^{meas}$, which are the reflection coefficient measurements for one and two layers of material, respectively. An example of a set of measurements taken at measurement position 1 for two layers of material are shown in Figure 9.40 and Figure 9.41. In addition, the values which are computed for S_{11}^{extr} and shown in Figure 5.18 and Figure 5.19 are displayed for comparison.

Note that there is a general agreement in the trend of the reflection coefficients for both samples and for both phase and magnitude, but the patterns do have some variations between the measured and theoretical values. The measured values were obtained from material samples that have different thicknesses than those used in the theoretical computations. In addition, the material parameters used to compute $S_{11(2L)}^{extr}$ are the values shown in Table F.2 and Table F.3, which may not be the true material parameters of the material sample. These are possible explanations for the difference between theory and measurement.

The two layer method was used to extract the material parameters of Eccosorb FGM125 when Plexiglass, Nylon, and PVC were used as the top layer in the two layer method. All three methods used the extrapolation method, and the extrapolation was performed from the $TM_{1\,14}$ mode. Consider Figure 9.42, which shows the extracted values for ϵ_r' when all three materials were used as the top layer in the two layer method. For comparison purposes, the values extracted using the two thickness method are also plotted in the figure. Note that the values from the two layer method extractions are closer to the values extracted using the two thickness method than the values shown in Figure 9.36 - Figure 9.39. This is consistent with the error sensitivity analysis from Chapter 6. The same analysis predicted that plexiglass and PVC had

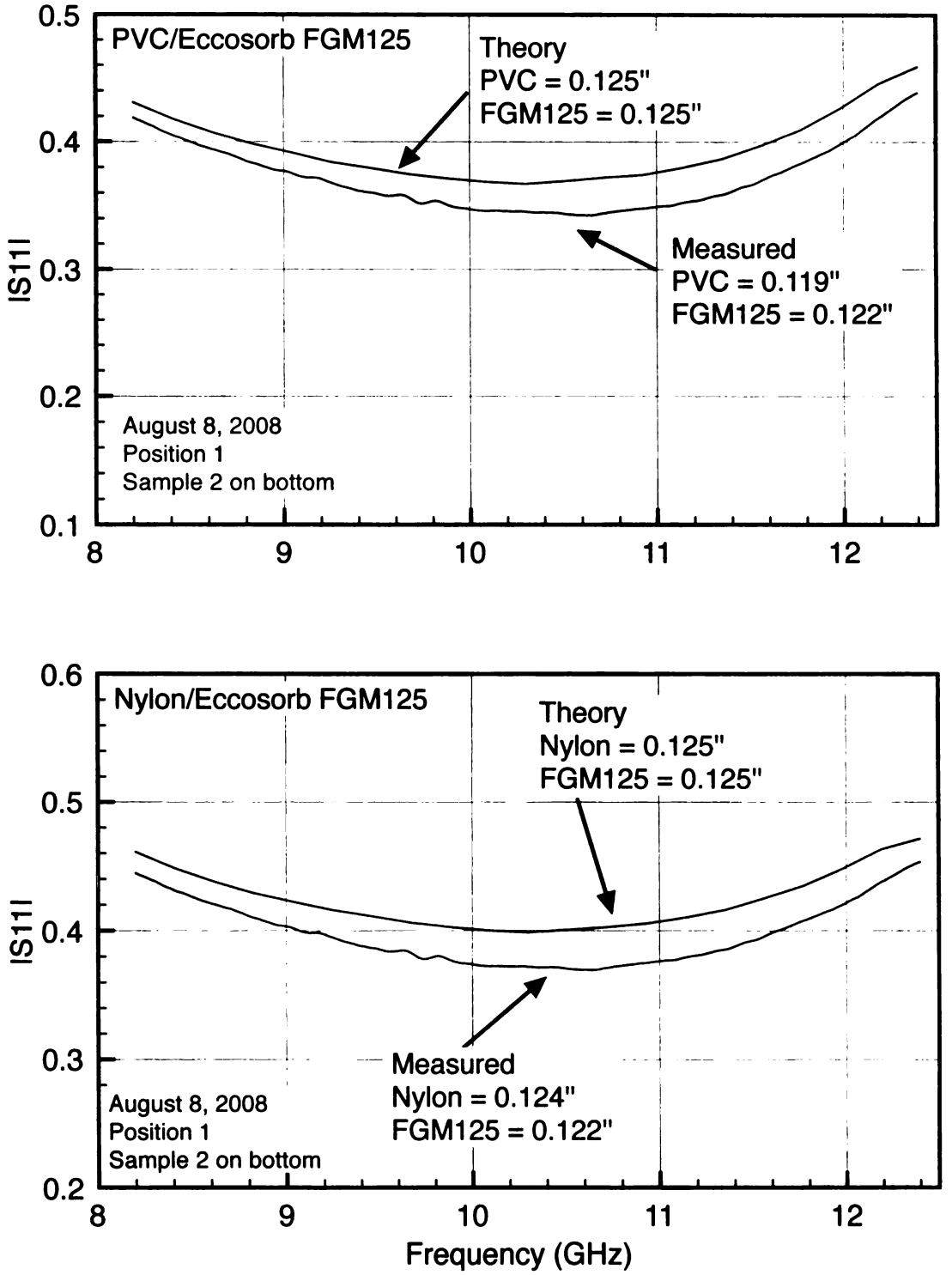


Figure 9.40. Comparison of $|S^{meas}_{11(2L)}|$ and $|S^{extr}_{11(2L)}|$ for one layer of Nylon on top of Eccosorb FGM125, and one layer of PVC on top of Eccosorb FGM125. Measurements made for position 1. PVC is Sample 1, Nylon is Sample 2.

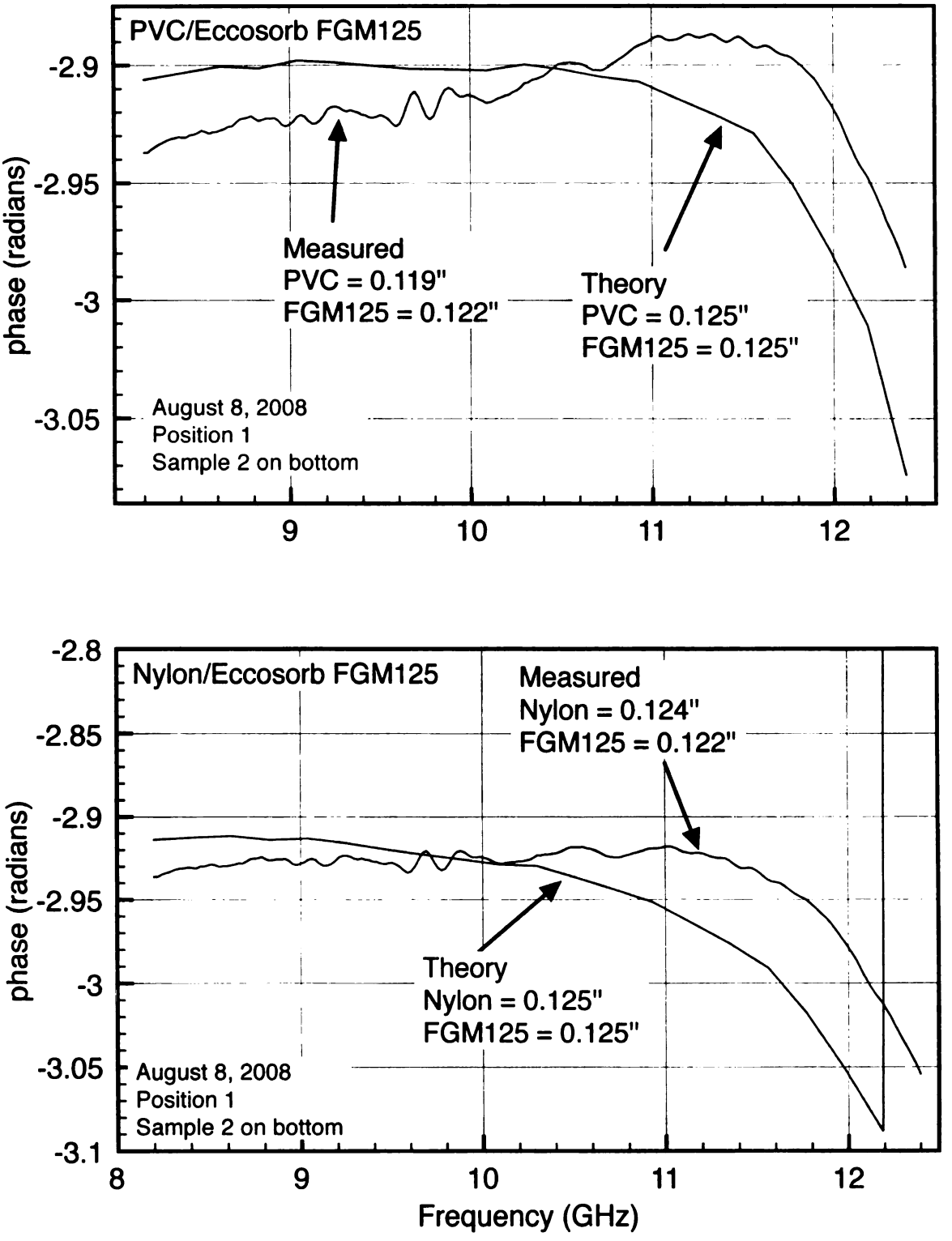


Figure 9.41. Comparison of $\phi_{(2L)}^{meas}$ and $\phi_{(2L)}^{thy}$ for one layer of Nylon on top of Eccosorb FGM125, and one layer of PVC on top of Eccosorb FGM125. Measurements made for position 1. PVC is Sample 1, Nylon is Sample 2.

slightly less sensitivity to measurement error than Nylon. From the data shown in Figure 9.42, it appears that using PVC as the top layer provides values that are the closest to those extracted using the two thickness method. Also note that the general trend of the extracted values appears to have less variance in the extracted values across the frequency band when compared to the results shown in Figure 9.37.

The imaginary part of the permittivity is shown in Figure 9.43 for the same four extractions. There is a high degree of variability in the extracted results. Values for ϵ_r'' are found in the range $|\epsilon_r''| \leq 0.7$ for Eccosorb FGM125. These are much better than those obtained using two layers of FGM125, but still include non-physical values, i.e. negative values of ϵ_r''.

Consider a similar plot for μ_r', found in Figure 9.44. Here, again note that using a top layer of PVC provides results that are closer to the two thickness method results. The two layer results tend to be lower than the two thickness results by less than 10% in the lower half of the frequency band, and higher at the upper end of the frequency band. All extracted results for PVC have errors of less than 10-15% with respect to the two thickness values. A similar pattern is observed in Figure 9.45, where the extracted values for μ_r'' using PVC as the top layer show the greatest agreement to the two thickness method.

From the measurements shown in Figure 9.42 - Figure 9.45, it appears that in this experimental situation, PVC may be the best choice of material for use in the two layer method. To further investigate the two layer method, five separate measurements were taken of a PVC-FGM125 material stack using the flanged waveguide probe. The material parameters were extracted using the extrapolation method, extrapolating from the $TM_{1\,14}$ mode. The mean and standard deviation of the parameters were calculated for the five extractions. The results are shown in Figure 9.46 - Figure 9.49.

For most of the frequency band, the values extracted using the two thickness method are within the 95% confidence intervals computed for the PVC two layer

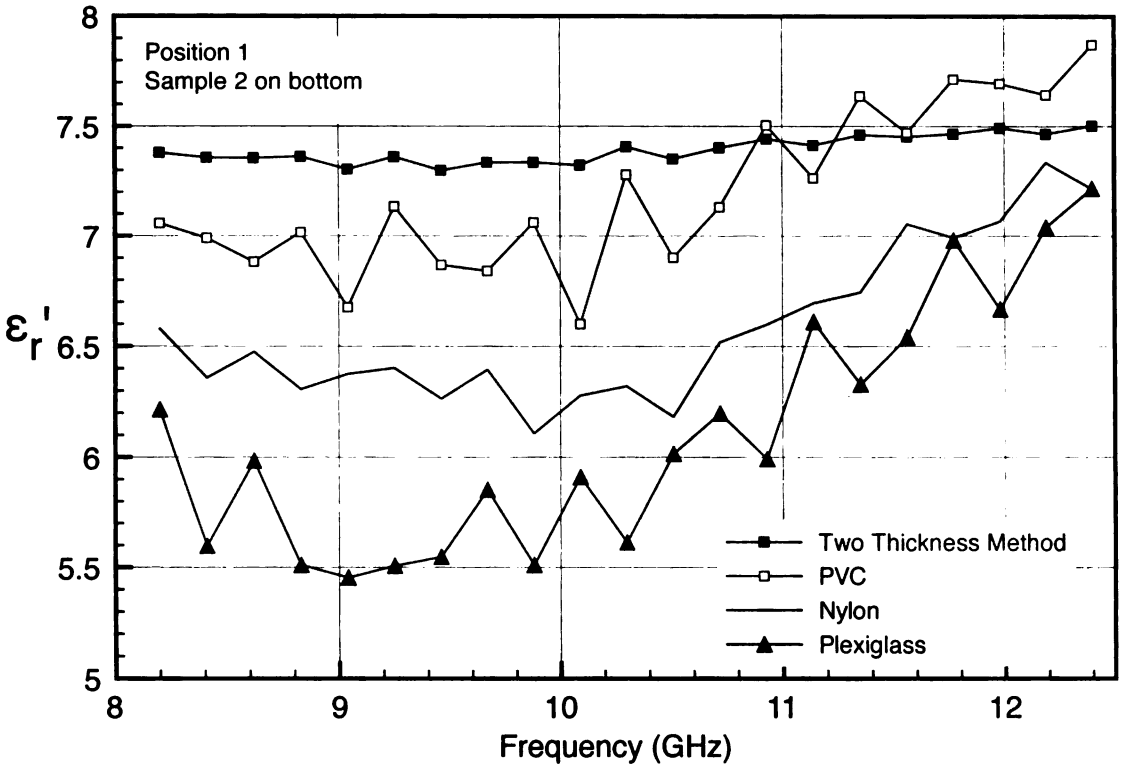


Figure 9.42. The extracted values for ϵ_r' of Eccosorb FGM125 using the two layer method, with Plexiglass, Nylon, and PVC as the top layer, and Sample 2 as the bottom layer. These results are compared with the extracted values obtained using the two thickness method. Measurements taken at position 1. PVC is Sample 1, Nylon is Sample 2, Plexiglass is Sample 2.

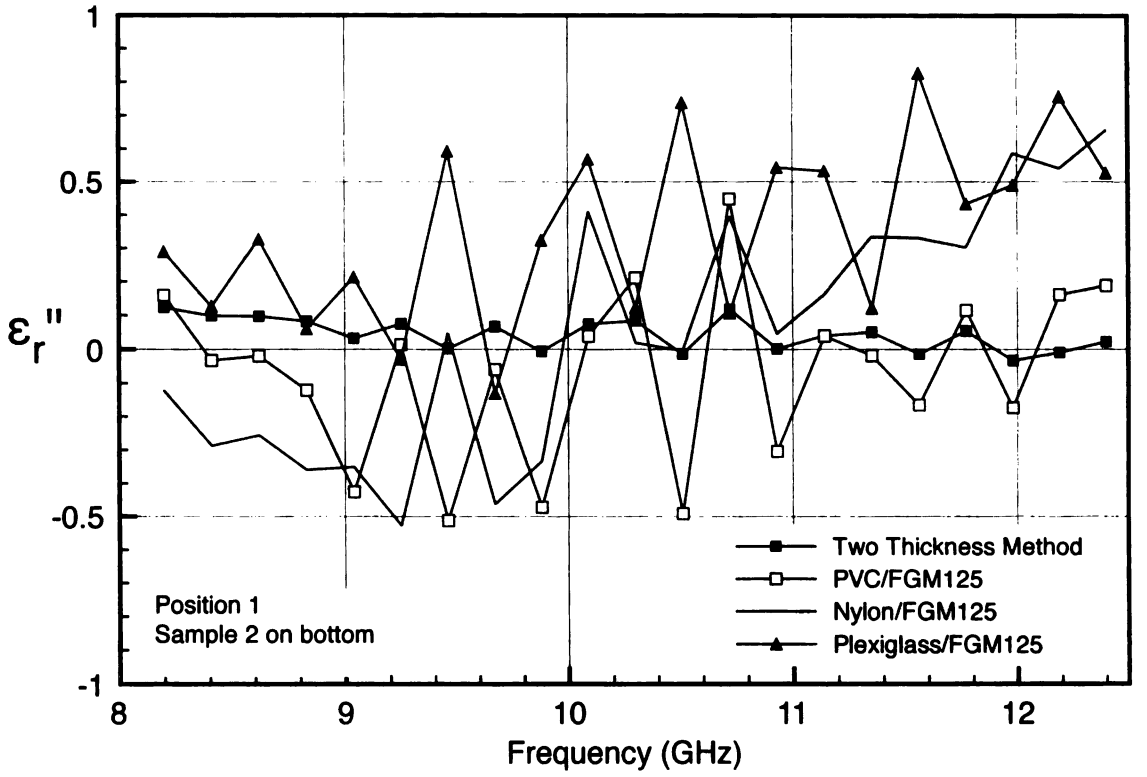


Figure 9.43. The extracted values for ϵ_r'' of Eccosorb FGM125 using the two layer method, with Plexiglass, Nylon, and PVC as the top layer, and Sample 2 as the bottom layer. Measurements taken at position 1. PVC is Sample 1, Nylon is Sample 2, Plexiglass is Sample 2.

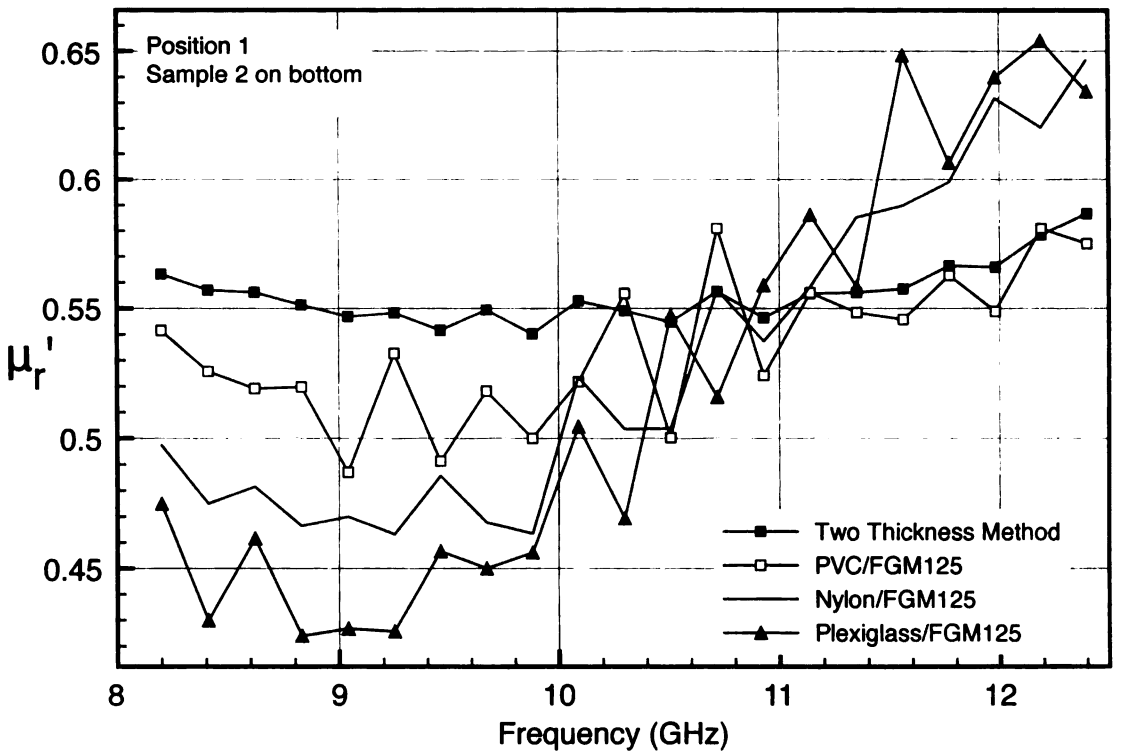


Figure 9.44. The extracted values for μ_r' of Eccosorb FGM125 using the two layer method, with Plexiglass, Nylon, and PVC as the top layer, and Sample 2 as the bottom layer. Measurements taken at position 1. PVC is Sample 1, Nylon is Sample 2, Plexiglass is Sample 2.

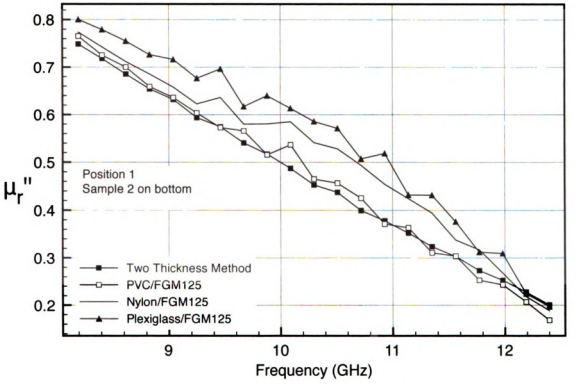


Figure 9.45. The extracted values for μ_r'' of Eccosorb FGM125 using the two layer method, with Plexiglass, Nylon, and PVC as the top layer, and Sample 2 as the bottom layer. Measurements taken at position 1. PVC is Sample 1, Nylon is Sample 2, Plexiglass is Sample 2.

method. Consider the extracted values for ϵ_r' shown in Figure 9.46. In the lower half of the frequency band, the two layer extracted values have a deviation of 10% with respect to the values extracted using the two thickness method. Near 11 GHz, the values for both methods are close to one another. At frequencies greater than 11 GHz, the two layer values are greater than the two thickness method values.

Figure 9.47 displays the extracted values of ϵ_r'' for both methods. Since Eccosorb FGM125 is not an extremely high loss dielectric material, the deviations observed by the two methods are difficult to characterize by any meaningful percentage representation. It is noted that the extracted values from the two thickness method are within the 95% confidence intervals of the two layer method. These two layer method values are much closer to the two thickness values than those derived from the two layer method using FGM125 as the top layer.

The two layer extracted values for μ_r' are even closer to the two thickness method extracted values. The largest deviation between the two layer and two thickness extracted values occurs at 9.04 GHz, where the two layer value is approximately 8% lower with respect to the values obtained using the two thickness method.

The extracted μ_r'' values for the two layer method are consistently higher than the two thickness values by approximately 0.05 at the lower two thirds of the frequency band, and they a re within 0.02 of each other at the high frequencies.

9.5 Two Iris Method

A second iris, as described in section 9.4, was constructed and fitted to the end of the WR-90 waveguide to obtain a second measurement of the material under test. The two iris method may then be used to extract the material parameters using reflection coefficient measurements with Aperture WR and the additional iris, Aperture H.

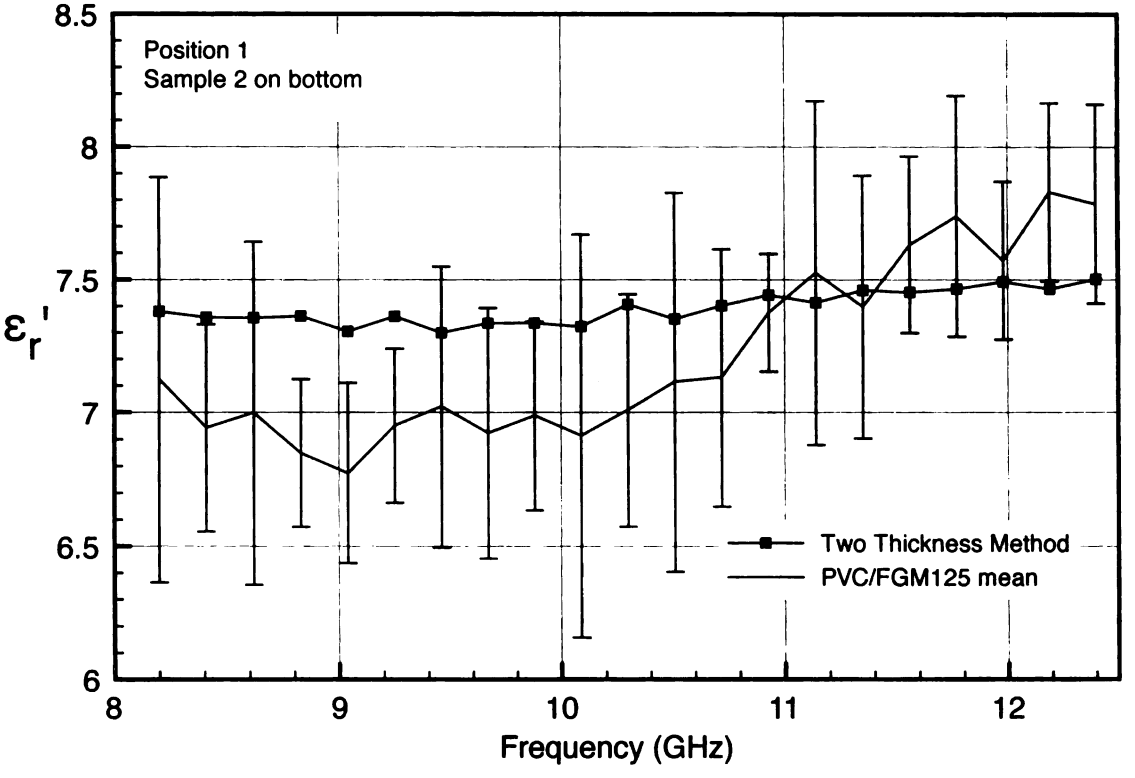


Figure 9.46. The extracted values for ϵ_r' of Eccosorb FGM125 using the two layer method, with PVC, Sample 1, as the top layer, and Sample 2 as the bottom layer. These results are compared with the extracted values obtained using the two thickness method. Measurements taken at position 1. Error bars denote the 95% confidence interval for the two layer method.

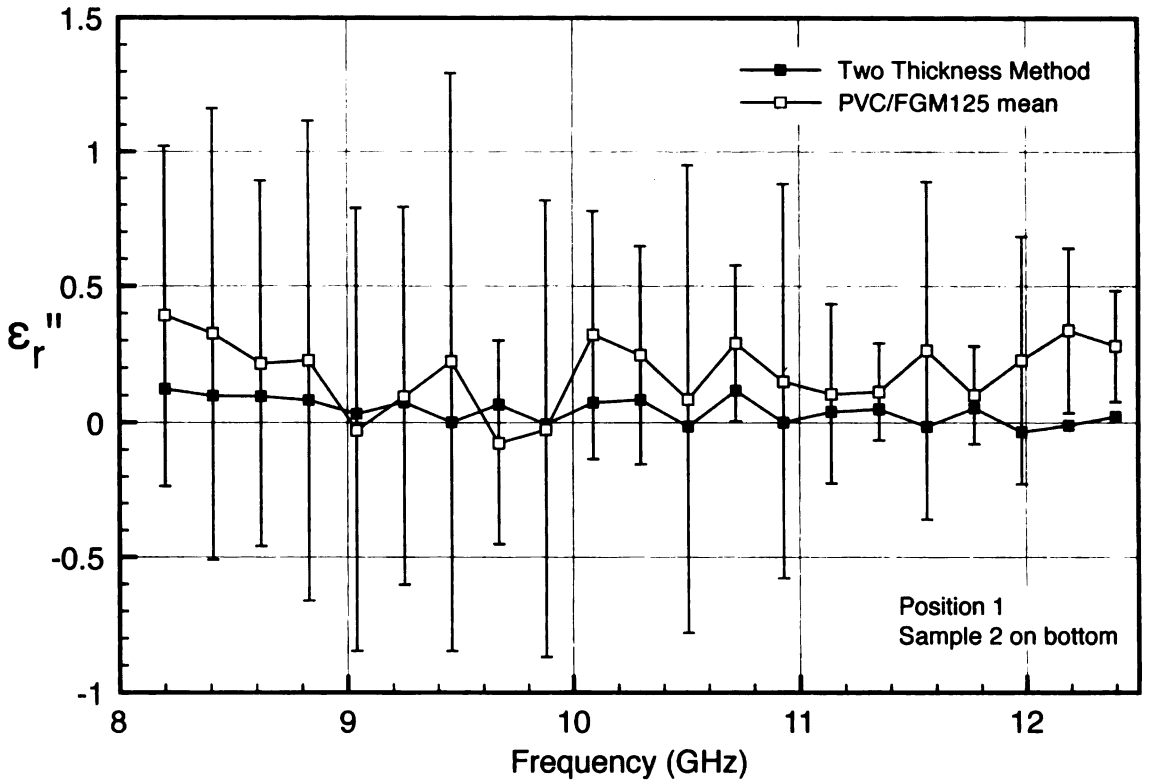


Figure 9.47. The extracted values for ϵ_r'' of Eccosorb FGM125 using the two layer method, with PVC, Sample 1, as the top layer, and Sample 2 as the bottom layer. These results are compared with the extracted values obtained using the two thickness method. Measurements taken at position 1. Error bars denote the 95% confidence interval for the two layer method.

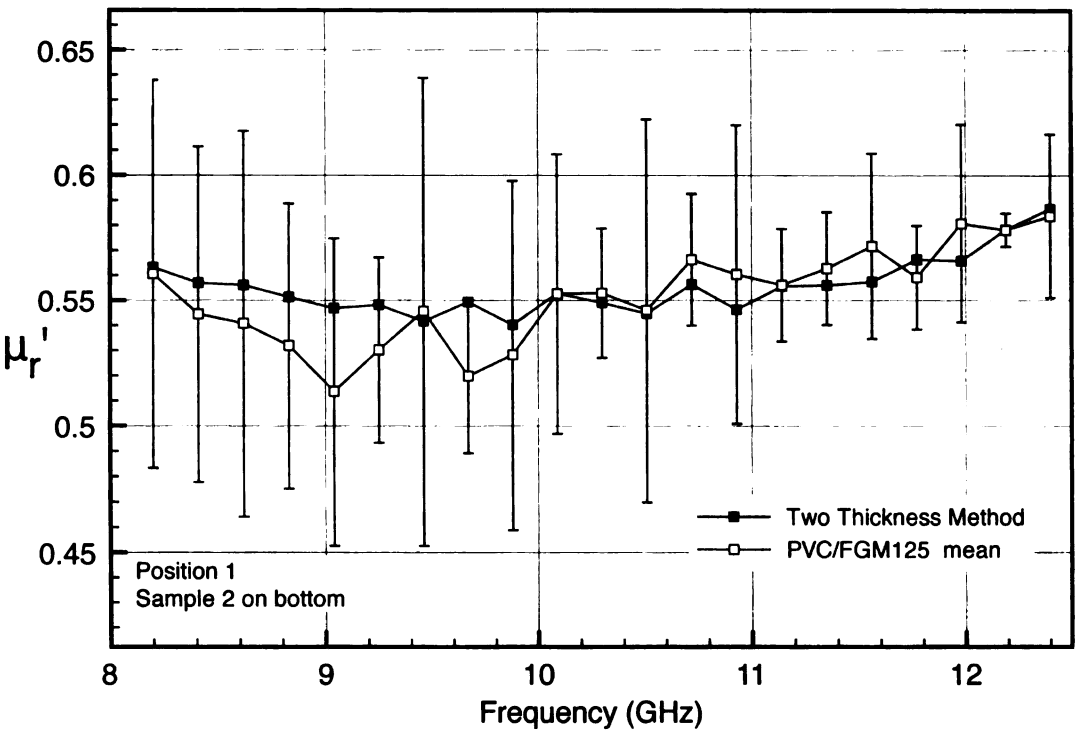


Figure 9.48. The extracted values for μ_r' of Eccosorb FGM125 using the two layer method, with PVC, Sample 1, as the top layer, and Sample 2 as the bottom layer. These results are compared with the extracted values obtained using the two thickness method. Measurements taken at position 1. Error bars denote the 95% confidence interval for the two layer method.

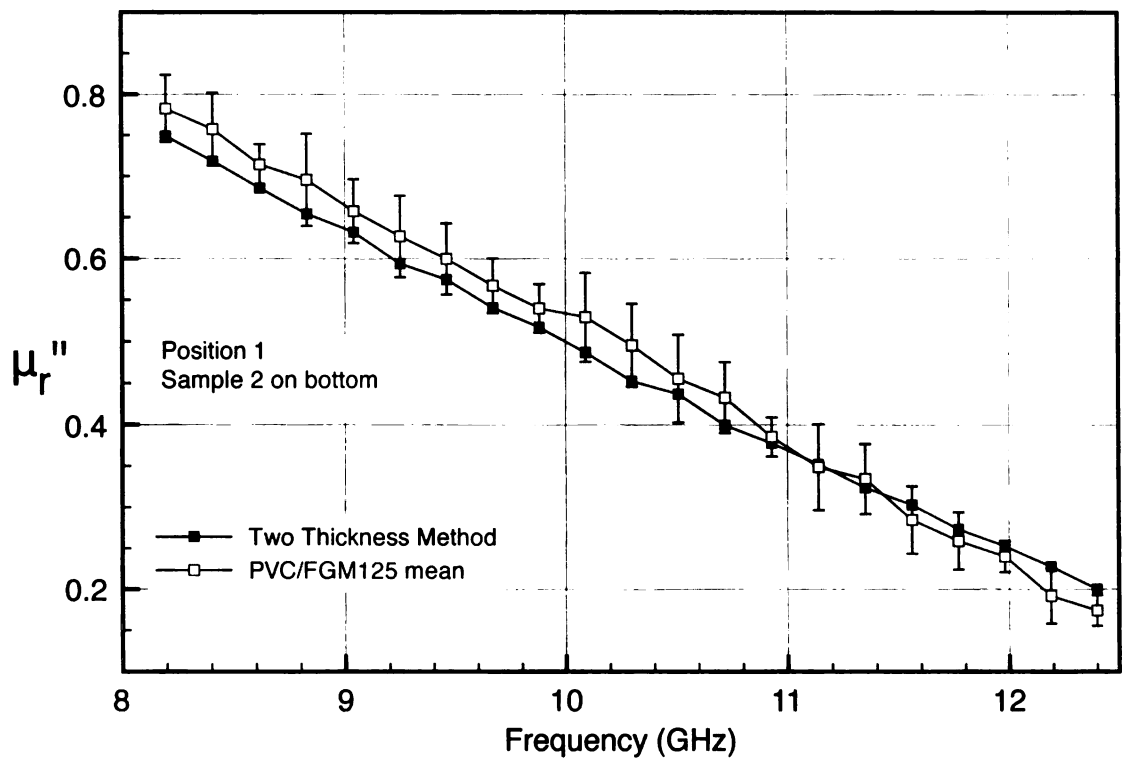


Figure 9.49. The extracted values for μ_r'' of Eccosorb FGM125 using the two layer method, with PVC, Sample 1, as the top layer, and Sample 2 as the bottom layer. These results are compared with the extracted values obtained using the two thickness method. Measurements taken at position 1. Error bars denote the 95% confidence interval for the two layer method.

9.5.1 Measurement vs. Theory

One set of measurements at all 5 positions is shown in Figure 9.50, and compared with the theoretical reflection coefficient values for Aperture H shown in Figure 8.18 and Figure 8.19. Note that there is good agreement between the measurements and theory for both magnitude and phase, even though the thickness of the actual measured sample is 0.003" inches thinner than that used in the simulation. The exception is the one outlier in the magnitude plot, which is the measurement taken at position 1.

9.5.2 Modal Analysis

A modal analysis on the measured data is helpful to understand how including more modes in the solution contributes to the extracted values. To aid in this understanding, two reflection coefficient measurements were obtained using two different apertures at the end of the waveguide. The first measurement, $S_{11(1)}^{meas(2I)}$ was taken using the full WR-90 aperture at the end of the waveguide. The second measurement, $S_{11(2)}^{meas(2I)}$, was obtained by placing Aperture H at the end of the X-band waveguide and measuring the material under test. Using these measured reflection coefficients, the two iris method was used to extract the material parameters of the material under test, one layer of Eccosorb FGM125, 0.122" thick. Different numbers of modes were used in calculating $S_{11}^{thy(2I)}$ for each aperture, and the modes used for each aperture are shown in Table 9.4. The resulting extracted parameters are shown in Figure 9.51 - Figure 9.54.

As more modes are included in the solution, the extracted values move toward the values obtained using the extrapolation method. Recall that a similar modal analysis is shown in Chapter 8 when synthesized values were used as the 'measured' reflection coefficient. It is helpful to compare the results of this experimental modal analysis with the modal analysis of synthesized data.

Compare Figure 9.51 with the extracted values for ϵ_r' in the synthesized modal

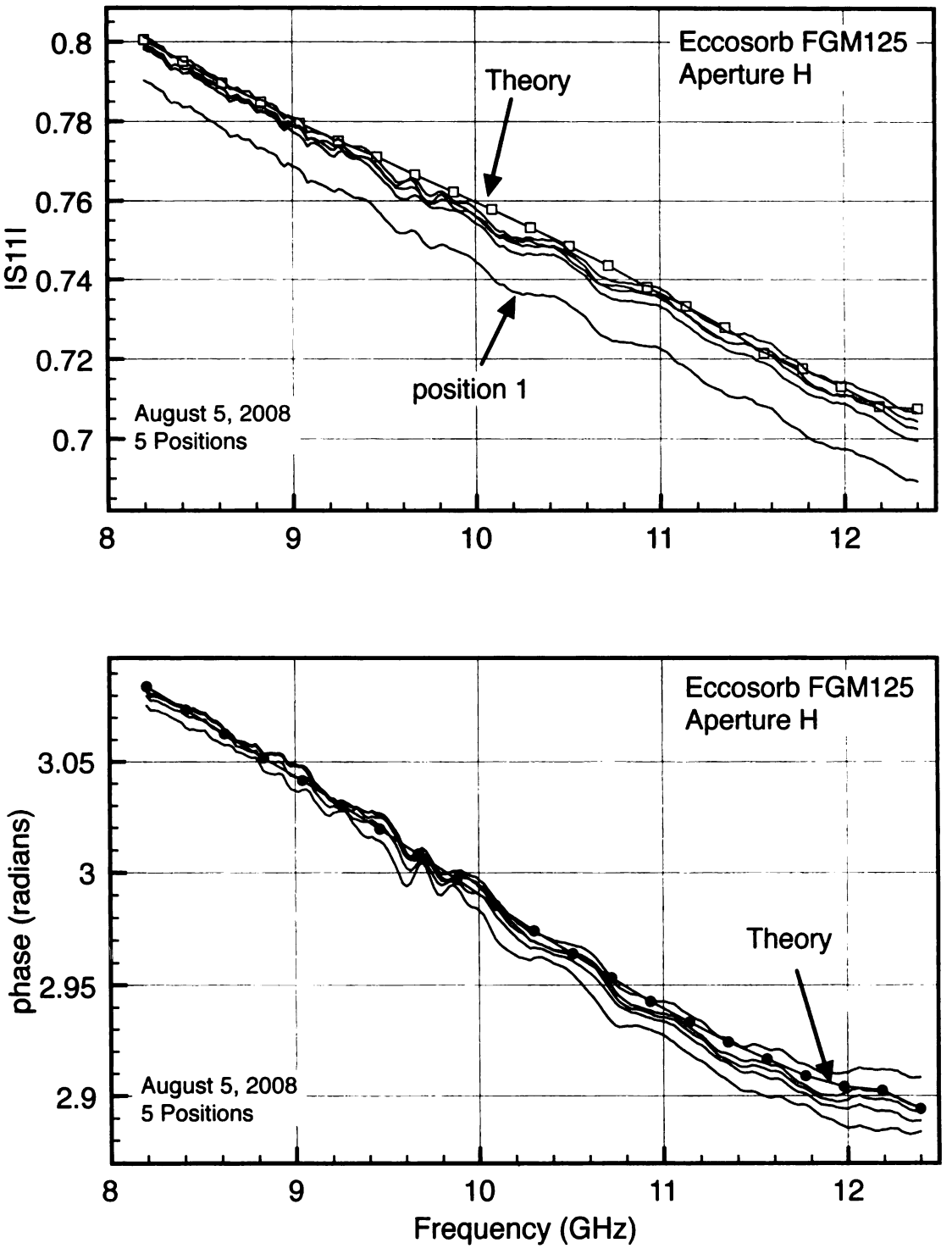


Figure 9.50. Comparison of the magnitude and phase of $S^{meas}_{11(2I)}$ and $S^{extr}_{11(2I)}$ for the two iris method. Simulated reflection coefficient is for Eccosorb FGM125, 0.125" thick. Measurements are at all 5 positions for Sample 2 of Eccosorb FGM125, 0.122" thick.

analysis, shown in Figure 8.28. The general trend of both figures agree, that as the number of modes is increased, the extracted values of ϵ_r' increase across the upper end of the frequency band. The simulated extractions, however, are larger at the lower end of the frequency band when the TM_{14} (line C) and TM_{16} (line D) are included in the solution. This is not the case in Figure 9.51, where the values increase with increasing numbers of modes in the lower end of the frequency band. Note that in both figures, when the TM_{18} mode is used, the values are within 1% of the values extracted using the extrapolation method.

Label	Aperture H: aperture modes used	p	q
A	TE_{q0}, TE_{12}, TM_{12}		1-7, odd
B	TE_{q0}, TE_{1p}, TM_{1p}	2, 4	1-7, odd
C	TE_{q0}, TE_{1p}, TM_{1p}	2, 4, 6	1-7, odd
D	TE_{q0}, TE_{1p}, TM_{1p}	2, 4, 6, 8	1-7, odd
E	TE_{q0}, TE_{1p}, TM_{1p} + extrapolation	2-20, even	1-7, odd
Label	Aperture WR: aperture modes used	r	s
A	TE_{s0}, TE_{12}, TM_{12}		1, 3
B	TE_{s0}, TE_{1r}, TM_{1r}	2, 4	1, 3
C	TE_{s0}, TE_{1r}, TM_{1r}	2, 4, 6	1, 3
D	TE_{s0}, TE_{1r}, TM_{1r}	2, 4, 6, 8	1, 3
E	TE_{s0}, TE_{1r}, TM_{1r} + extrapolation	2-20, even	1, 3

Table 9.4. Key for modes used in two iris extraction method, Aperture H and Aperture WR

The ϵ_r'' values extracted using the simulated reflection coefficients, shown in Figure 8.29, and measured reflection coefficients, shown in Figure 9.52, present a more contrasting picture. In both figures, when just the TM_{12} aperture modes are included in the computation of $S_{11}^{thy(2I)}$, the values for ϵ_r'' are higher on the lower end of the frequency band than they are on the higher end. However in the material parame-

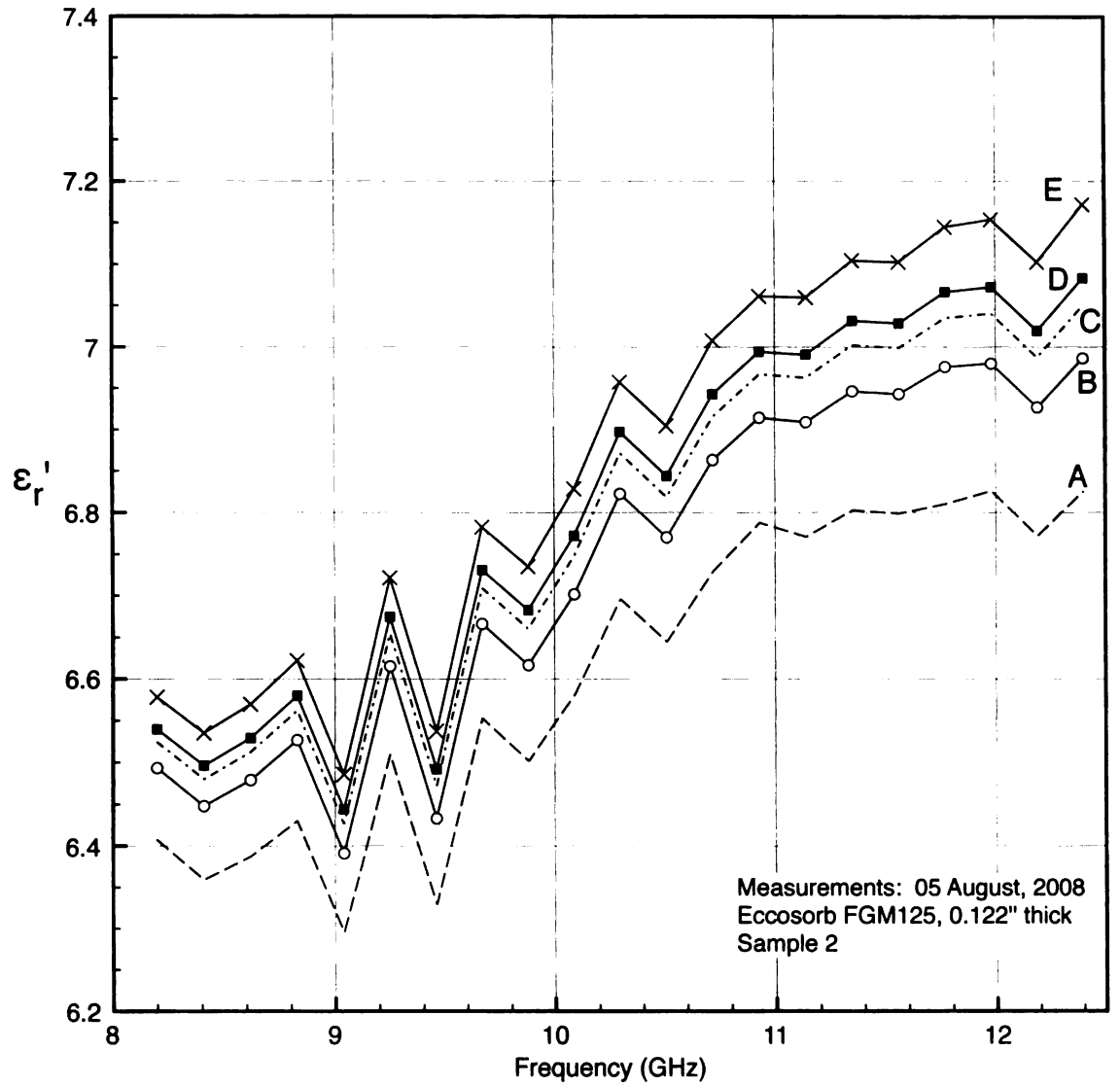


Figure 9.51. Extracted values of ϵ_r' using the two iris method. Different numbers of significant modes were used in the extraction. The key for each line is shown in Table Table 9.4. Measurements taken at position 1.

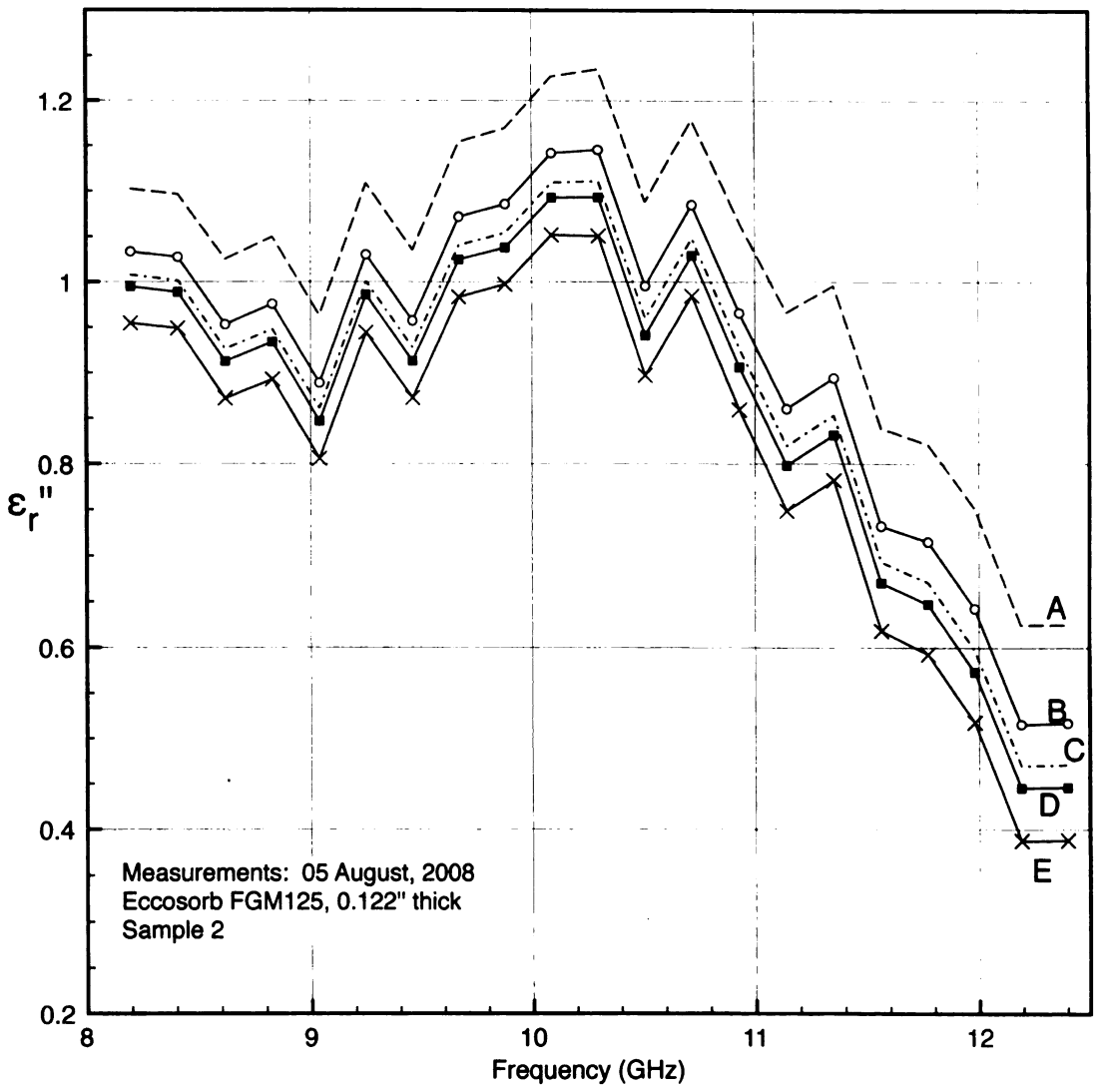


Figure 9.52. Extracted values of ϵ_r'' using the two iris method. Different numbers of significant modes were used in the extraction. The key for each line is shown in Table Table 9.4. Measurements taken at position 1.

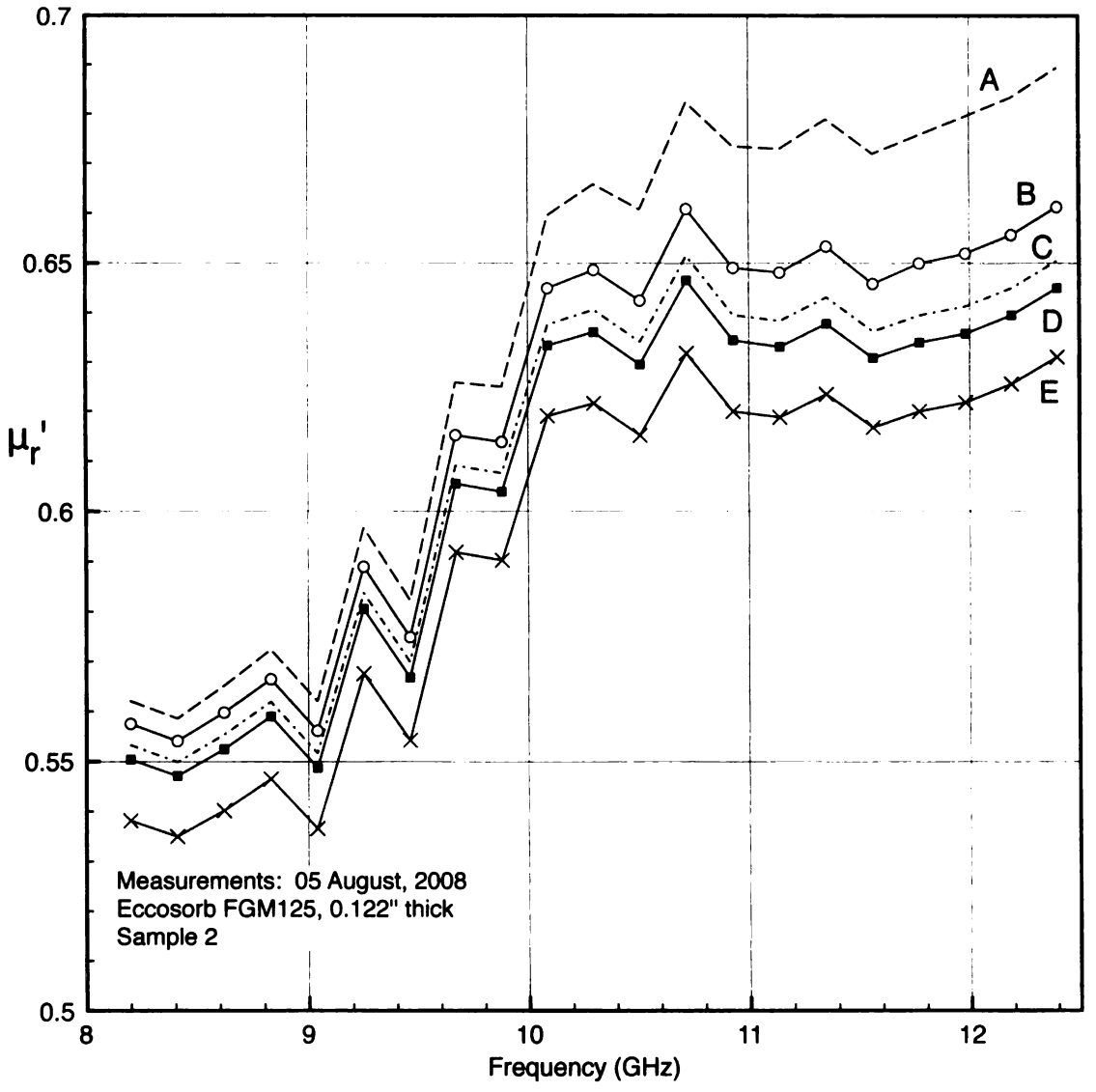


Figure 9.53. Extracted values of μ_r' using the two iris method. Different numbers of significant modes were used in the extraction. The key for each line is shown in Table Table 9.4. Measurements taken at position 1.

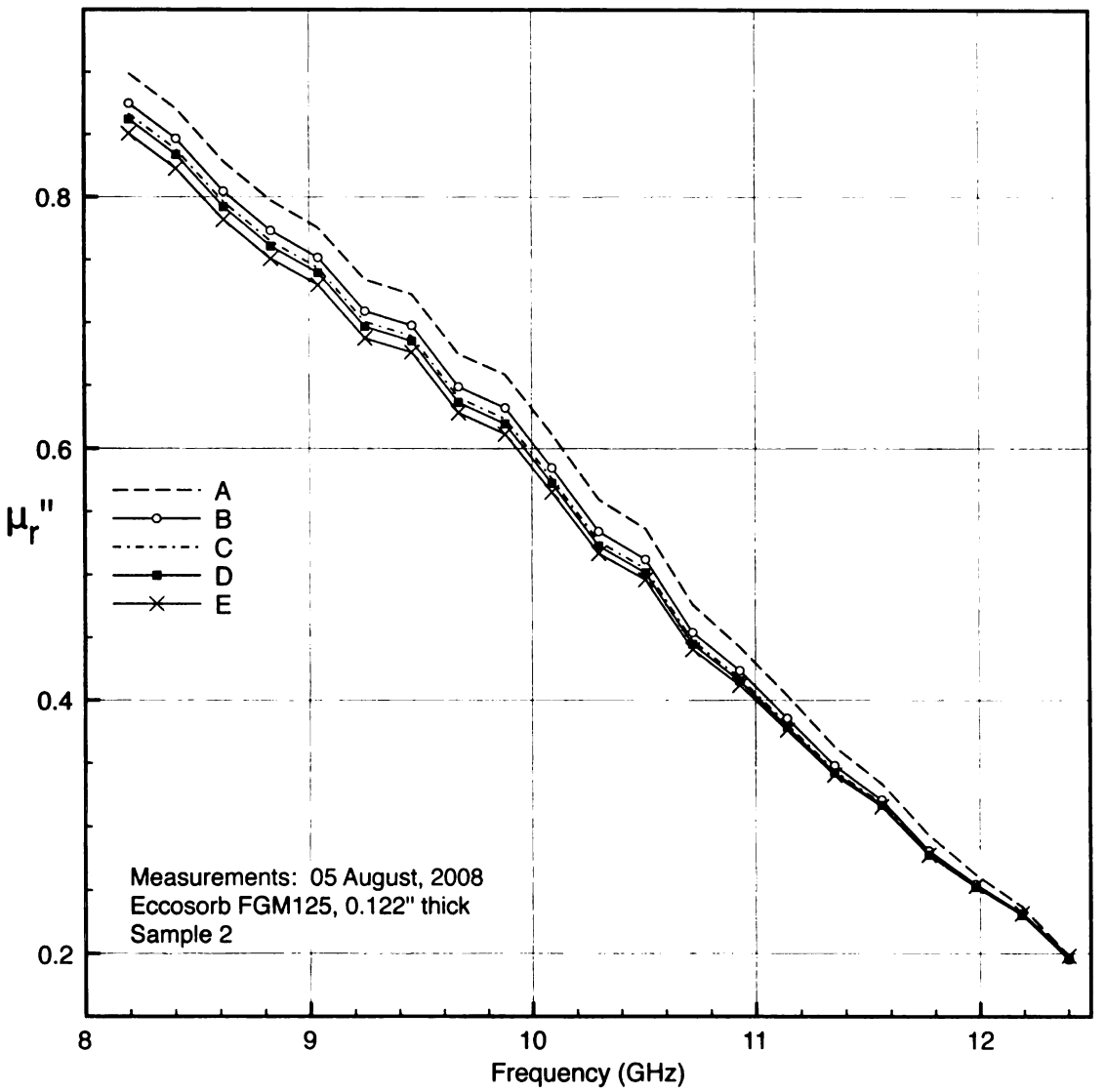


Figure 9.54. Extracted values of μ_r'' using the two iris method. Different numbers of significant modes were used in the extraction. The key for each line is shown in Table Table 9.4. Measurements taken at position 1.

ter extractions, these lower frequency extracted values are more than four times as large as the simulated extraction values. As the number of modes is increased in the simulated data extractions, the values for ϵ_r'' decrease. Using the extrapolation method, all of the values are below $\epsilon_r'' = 0.1$ in Figure 8.29. In the measured data in Figure 9.52, the values also decrease as more modes are included. However note that the extractions using the extrapolation method are considerably higher than the simulated results. Some possible reasons for this difference are discussed at the end of this section.

Consider Figure 8.30 and Figure 9.53 to examine the extracted values of μ_r'. The general trend in both figures as the number of modes is increased is that the values decrease across the frequency band. In the simulated modal extraction in Figure 8.30, the largest decrease in extracted values is seen at the lower frequencies, near 8.2 GHz. In the measured extractions, Figure 9.53, the largest decrease is observed at the upper frequencies greater than 11 GHz.

Figure 8.31 and Figure 9.54 have very similar trends in the plots. As the number of modes is increased, the values for μ_r'' decrease in value across the frequency band. The largest decrease is observed at the lower frequencies.

9.5.2.1 Discussion of Modal Analysis

Similar trends are observed in both the measured and simulated modal analyses. As more modes are included in the solution, each line in the graph progresses toward the values obtained by the extrapolation method. In the simulated analysis, Figure 8.29 - Figure 8.31, the extracted values using the extrapolation method are very close to the nominal values. In the experimental extractions which use actual measured reflection coefficients, it is noted that the values obtained by the extrapolation method differ from the simulated values by a significant amount in the permittivity extractions.

It is reasonable to conclude that other sources of error may contribute to the differences observed in the values obtained by extrapolation. These sources of error

may be the random measurement error, differences in the material height or structure, errors induced by an airgap error, or other issues with measurement equipment. It is possible to reduce some random measurement error by averaging several samples. It is noted that the outlier of the extracted data shown in Figure 9.50 was the measurement for $S_{11(2)}^{thy(2I)}$ used in these extractions, and could contribute to some of the differences observed.

In the next section, the differences in extracted values at different measurement positions and different samples are considered.

9.5.3 Two Iris Method Extractions

Recall that in Figure 9.50, $S_{11(2)}^{meas(2I)}$ are displayed for the 5 different measurement positions on Sample 2 of Eccosorb FGM125. The magnitude of the measured reflection coefficients clearly vary in Figure 9.50. Thus a comparison of the extracted values for this measurement set may provide some enlightening results.

These measurements and the corresponding measurements, $S_{11(1)}^{meas(2I)}$ for Aperture WR, were used in the two iris method to extract the material parameters of the sample. The modal analysis in section 9.5.2 showed that the values obtained by using the TM_{18} mode in the extraction resulted in values that were approaching the values obtained by the extrapolation method. Since the extrapolation method requires approximately 500% more computational time than using just the TM_{18} modes, an initial set of extractions were run using the significantly contributing modes up to the TM_{18} mode.

Figure 9.55 - Figure 9.58 display the extracted material parameters for the five different measurement positions on Sample 2. As might be expected from the reflection coefficient magnitude plot in Figure 9.50, the extracted parameters at position 1 in all three plots show the largest deviation from the extracted values obtained at the other positions, especially for the ϵ_r' values shown in Figure 9.55. It is possible that the measurement contained some amount of measurement error due to an airgap. It

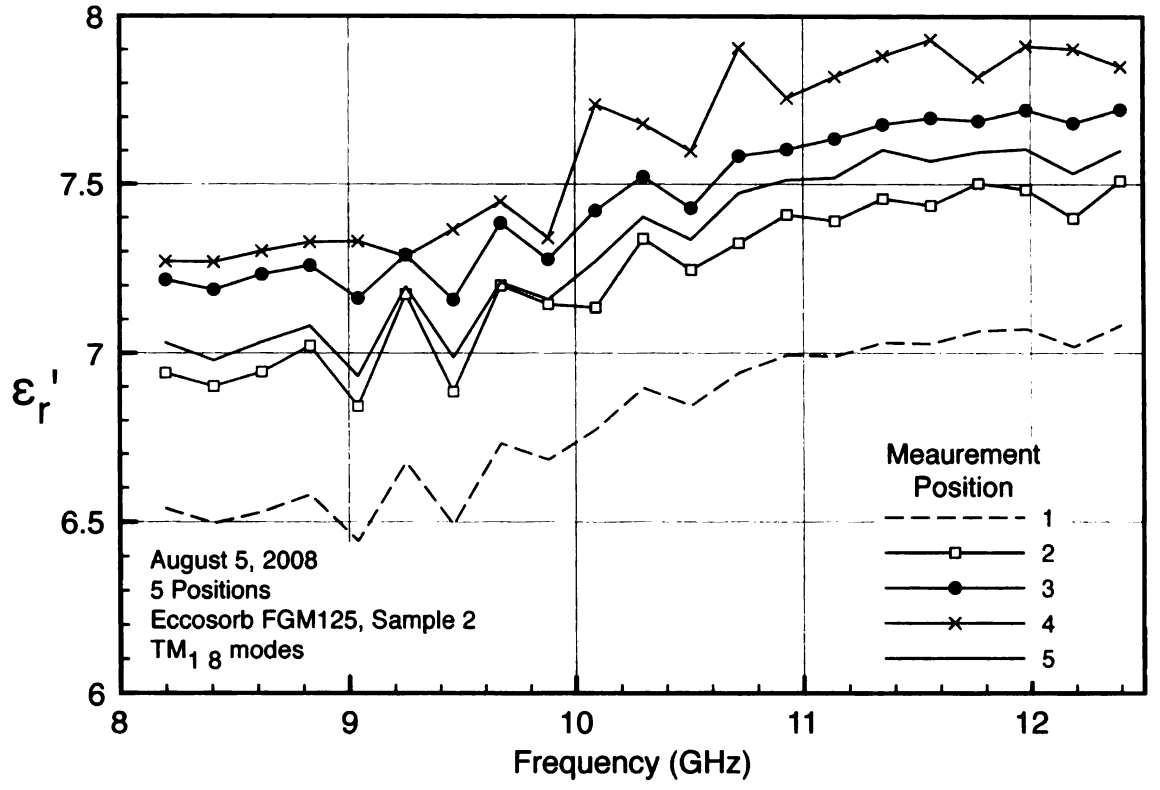


Figure 9.55. Extracted values of ϵ_r' using the two iris method at five different measurement positions. The significant modes up to the $TM_{1\,8}$ mode were used in the extraction.

is also possible that some variation in the material exists.

Consider the display for ϵ_r' in Figure 9.55. Note that although the magnitudes vary, the general shape of the plots across the frequency band is similar for the different measurement positions. It is interesting to note that the shape of these plots is also similar to the mean values extracted using the two layer method in Figure 9.46, with PVC as the top layer. In addition, note that the values extracted for ϵ_r'' are rather large in the lower part of the frequency band in Figure 9.56. As the frequency increases, the values approach the nominal values for ϵ_r'' of FGM125 and the values for ϵ_r'' extracted using the two thickness method.

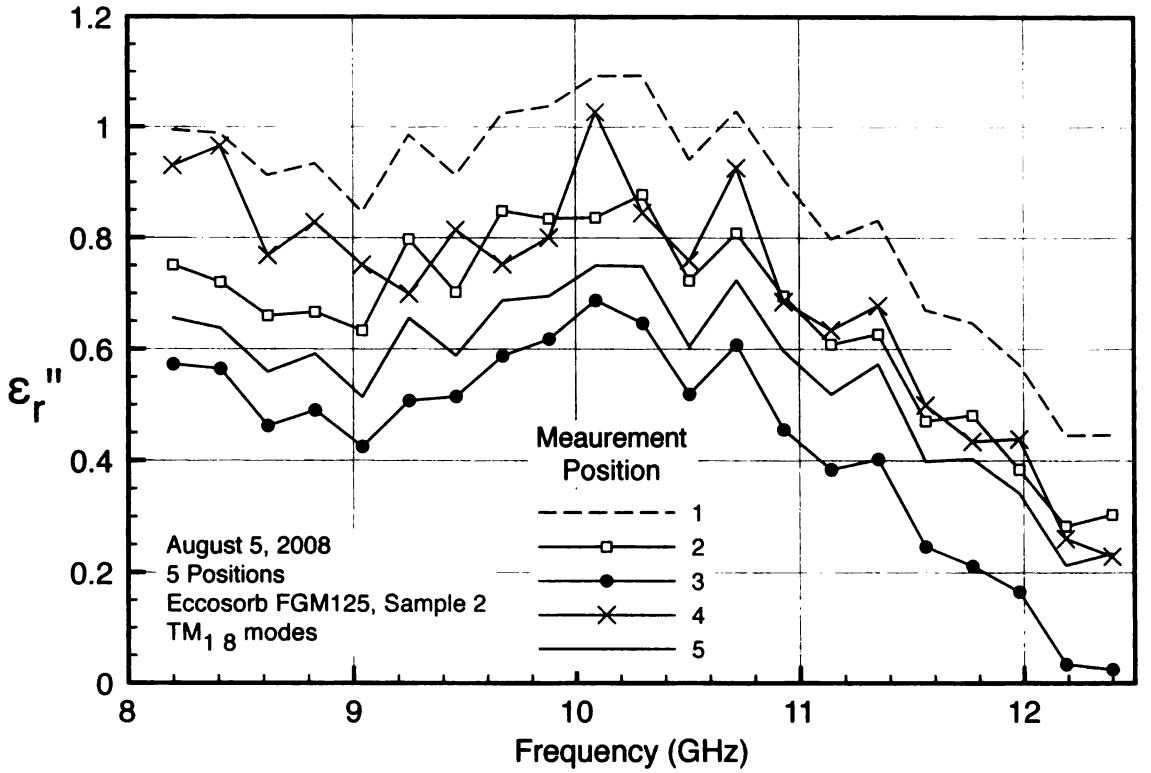


Figure 9.56. Extracted values of ϵ_r'' using the two iris method at five different measurement positions. The significant modes up to the $TM_{1\,8}$ mode were used in the extraction.

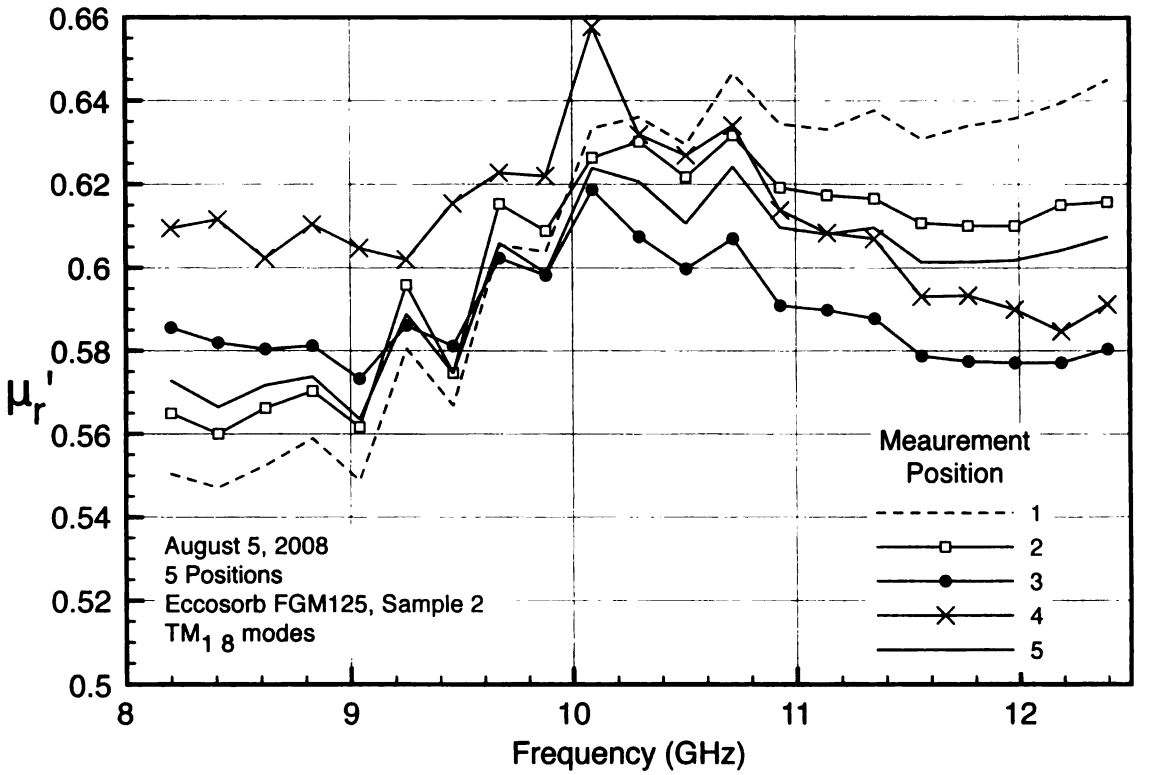


Figure 9.57. Extracted values of μ_r' using the two iris method at five different measurement positions. The significant modes up to the TM_{18} mode were used in the extraction.

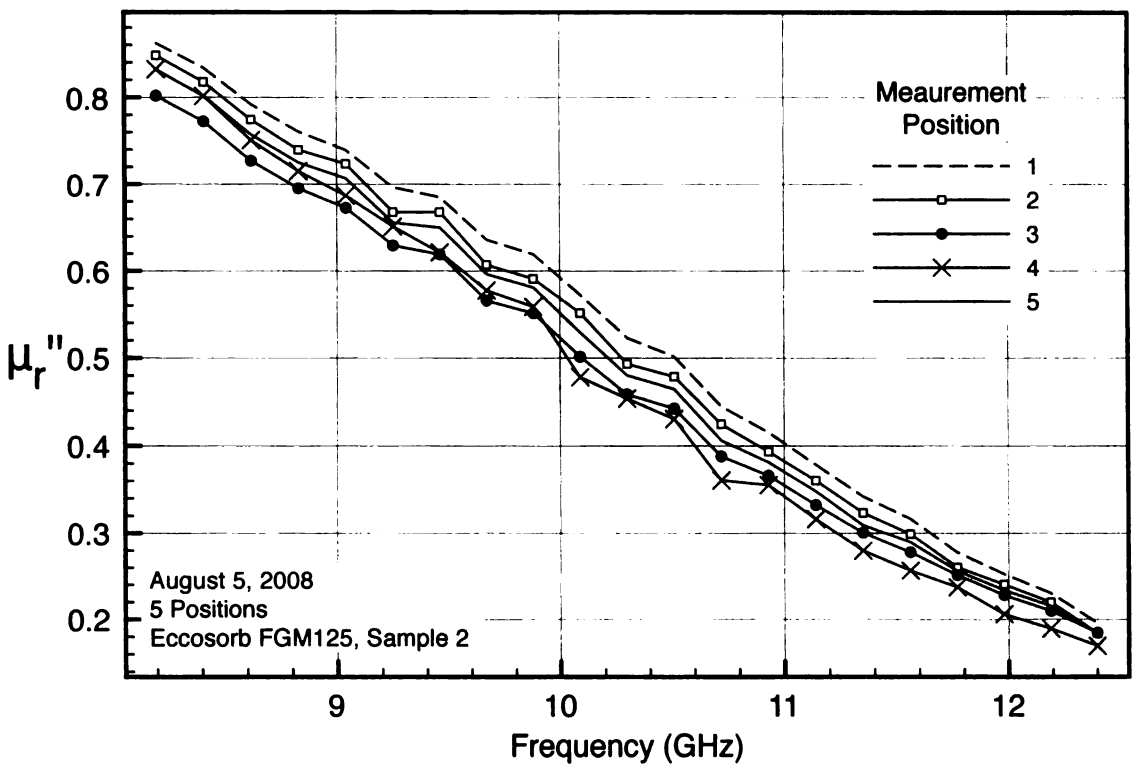


Figure 9.58. Extracted values of μ_r'' using the two iris method at five different measurement positions. The significant modes up to the TM_{18} mode were used in the extraction.

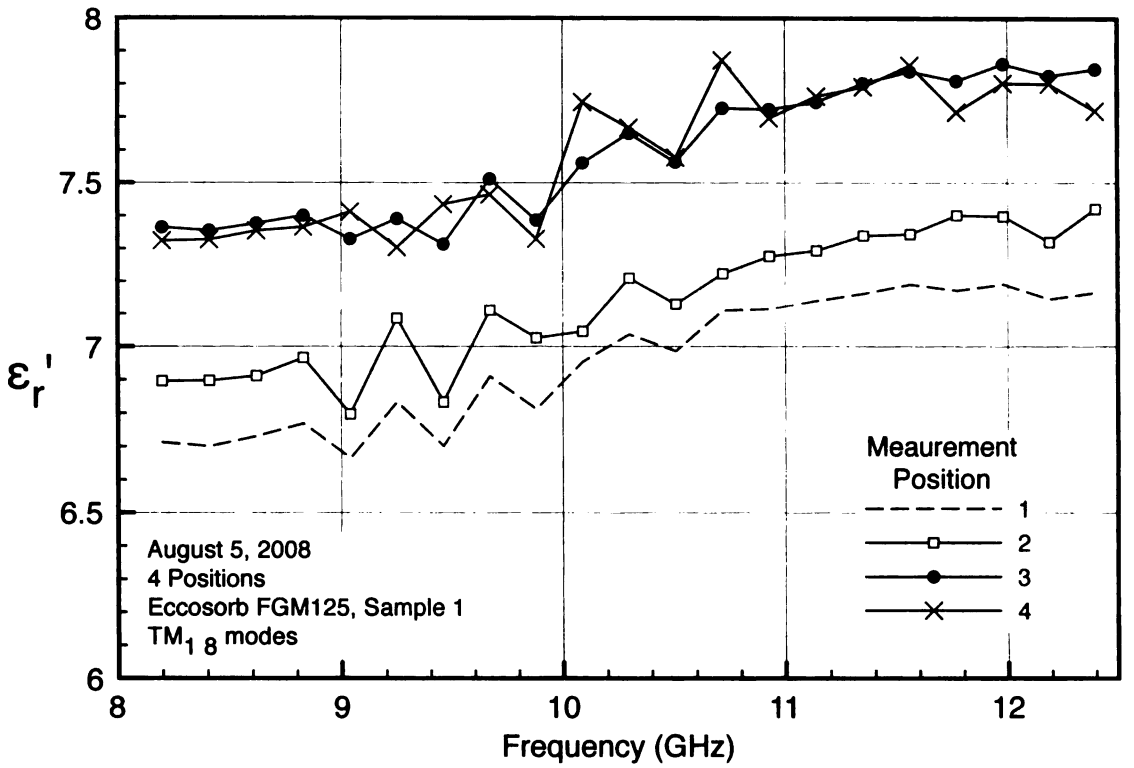


Figure 9.59. Extracted values of ϵ_r' using the two iris method at four different measurement positions. The significant modes up to the $TM_{1\,8}$ mode were used in the extraction.

A similar set of measurements was obtained during the same measurement set for Sample 1. Measurements of $S_{11(2)}^{meas(2I)}$ and $S_{11(1)}^{meas(2I)}$ were taken at four of the five measurement positions. The two iris method extraction procedure was performed on these data using the significantly contributing modes up to the $TM_{1\,8}$ mode. These extracted parameters are shown in Figure 9.59 - Figure 9.62.

In these plots for sample 1, there is no outstanding measurement position that appears to have results that are out of line with another measurement. The shape of the plots for ϵ_r' in Figure 9.59 also has similar features to those observed in Figure 9.55.

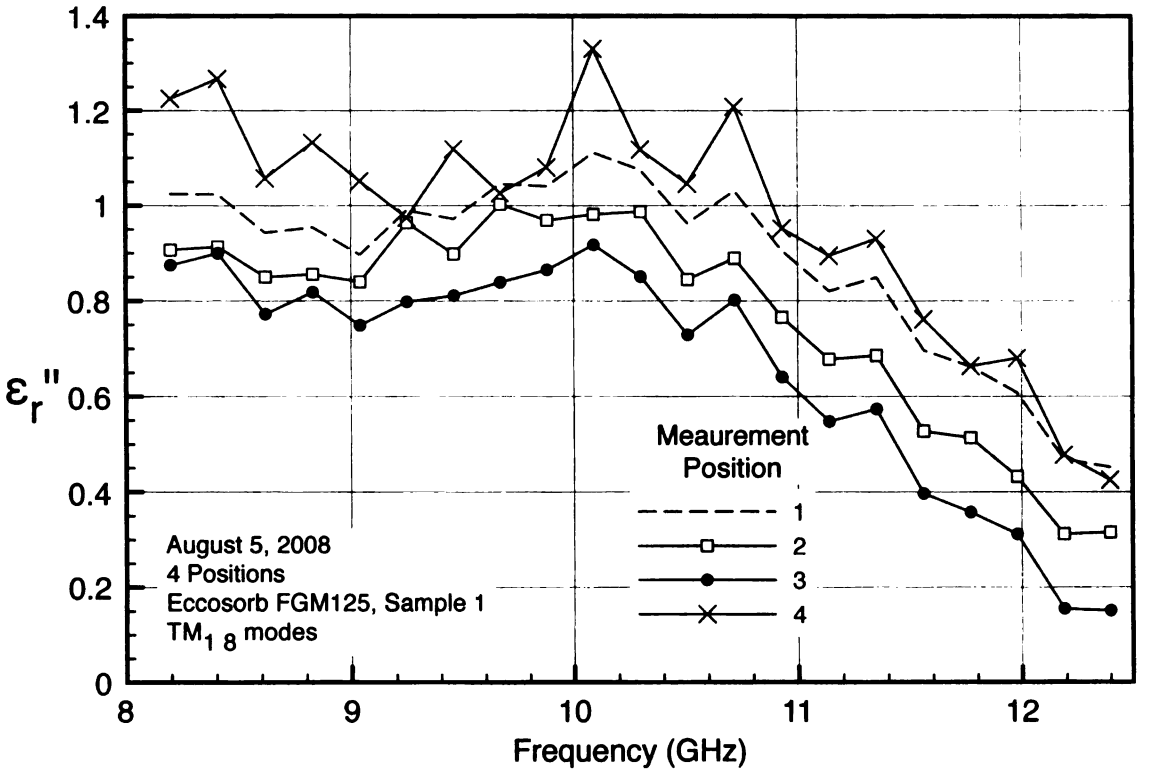


Figure 9.60. Extracted values of ϵ_r'' using the two iris method at four different measurement positions. The significant modes up to the $TM_{1\,8}$ mode were used in the extraction.

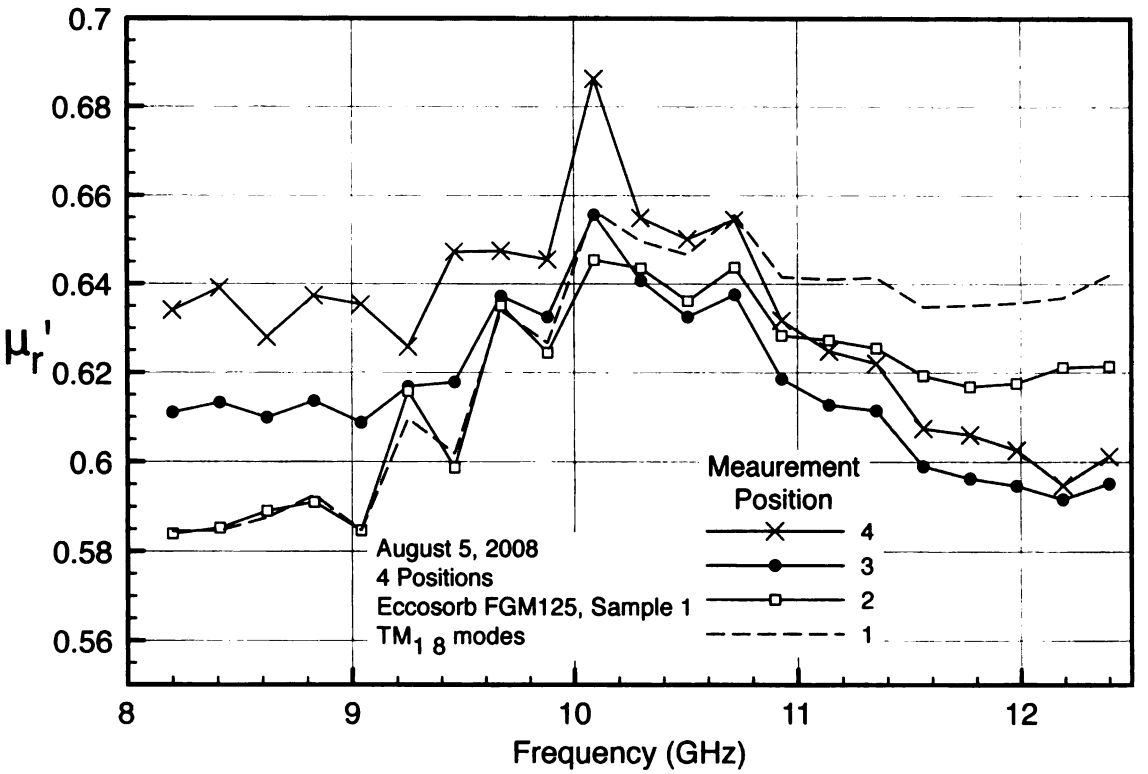


Figure 9.61. Extracted values of μ_r' using the two iris method at four different measurement positions. The significant modes up to the TM_{18} mode were used in the extraction.

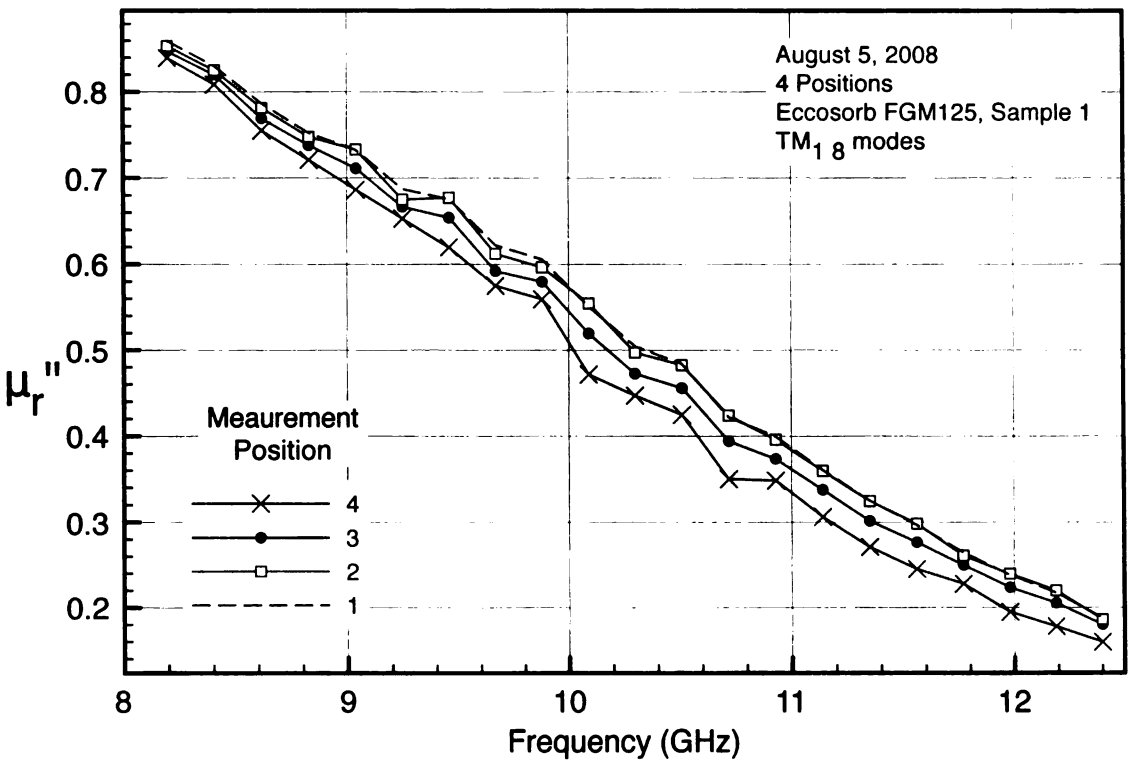


Figure 9.62. Extracted values of $\mu_r"'$ using the two iris method at four different measurement positions. The significant modes up to the TM_{18} mode were used in the extraction.

To examine if these variations are due to the specific measurement conditions or a given measurement set, or if the trends are consistent, the mean of four separate measurements was computed and plotted at Positions 1, 3, and 4. Although only four measurements are used, the mean of these extractions will reduce some of the contribution of the random errors in the measurements. These means were computed for both Sample 1 and Sample 2, and the results are shown in Figure 9.63 - Figure 9.66.

The results are very interesting, if not surprising. Note that in Figure 9.63 the values of ϵ_r' averaged for four different extractions for the two samples match up very well at position 1. At positions 3 and 4, the values extracted from each sample also are very close to one another across the frequency band. A similar observation is also found for the extracted values of μ_r' in Figure 9.65, and to a lesser degree for ϵ_r' in Figure 9.64 and μ_r'' in Figure 9.66.

It is possible that both Eccosorb FGM125 material samples have some variation or anisotropy in the composition of the material that is common to both samples. However, that would require that these 12"×12" samples happened to be oriented in the same direction when the measurements were made. This seems unlikely. A more likely explanation is one of the following arguments, which are similar. It is possible that at position 1, which is in the center of the sample, both samples may have a depression in the thickness of the material. This would allow for potential airgaps between the material and the aluminum flange at the aperture location. This would allow some energy to escape and thus reduce the magnitude of the reflection coefficient, as seen in Figure 9.50. Another similar explanation for these results is that a variation or warp in the aluminum plate in which Aperture H is cut, or a possible spatial variation in the bottom conducting plate, could lead to airgaps at specific measurement locations, but not at other locations. It is also possible that a combination of these could account for the observations made regarding Figure 9.63

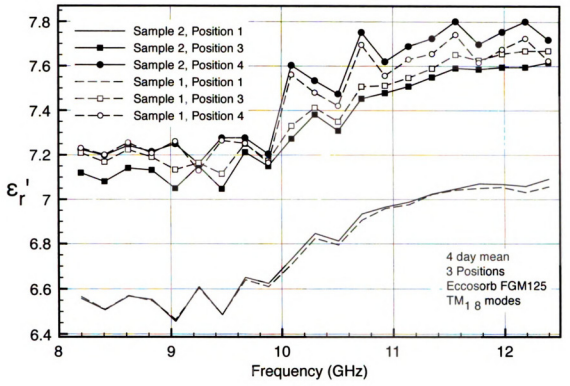


Figure 9.63. Mean extracted values of ϵ_r' using the two iris method at three different measurement positions. Four independent observations were averaged at each measurement position on each sample. The significant modes up to the $TM_{1\,8}$ mode were used in the extraction.

- Figure 9.66.

The extrapolation method was used to extract the material parameters from Sample 2 of Eccosorb FGM125 using the two iris method at positions 1 and 3. Extractions from three separate data collections were averaged, and the mean values at positions 1 and 3 are shown in Figure 9.67 - Figure 9.70. In addition, the mean values from the two layer method that used PVC as the top layer, which are shown in Figure 9.46 - Figure 9.49, are plotted in Figure 9.67 - Figure 9.70. The fourth line in these figures is the average of two extractions carried out using the two thickness method on Sample 2. All extractions used in creating these figures were carried out using the

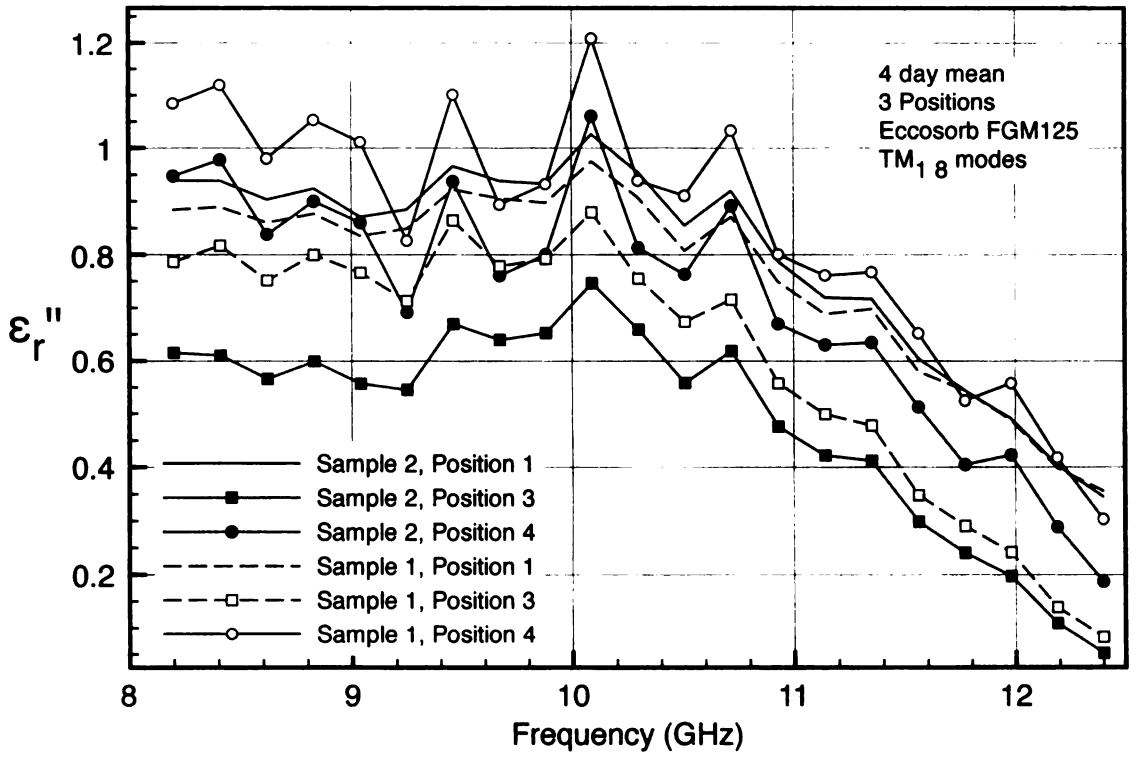


Figure 9.64. Mean extracted values of ϵ_r'' using the two iris method at three different measurement positions. Four independent observations were averaged at each measurement position on each sample. The significant modes up to the $TM_{1\,8}$ mode were used in the extraction.

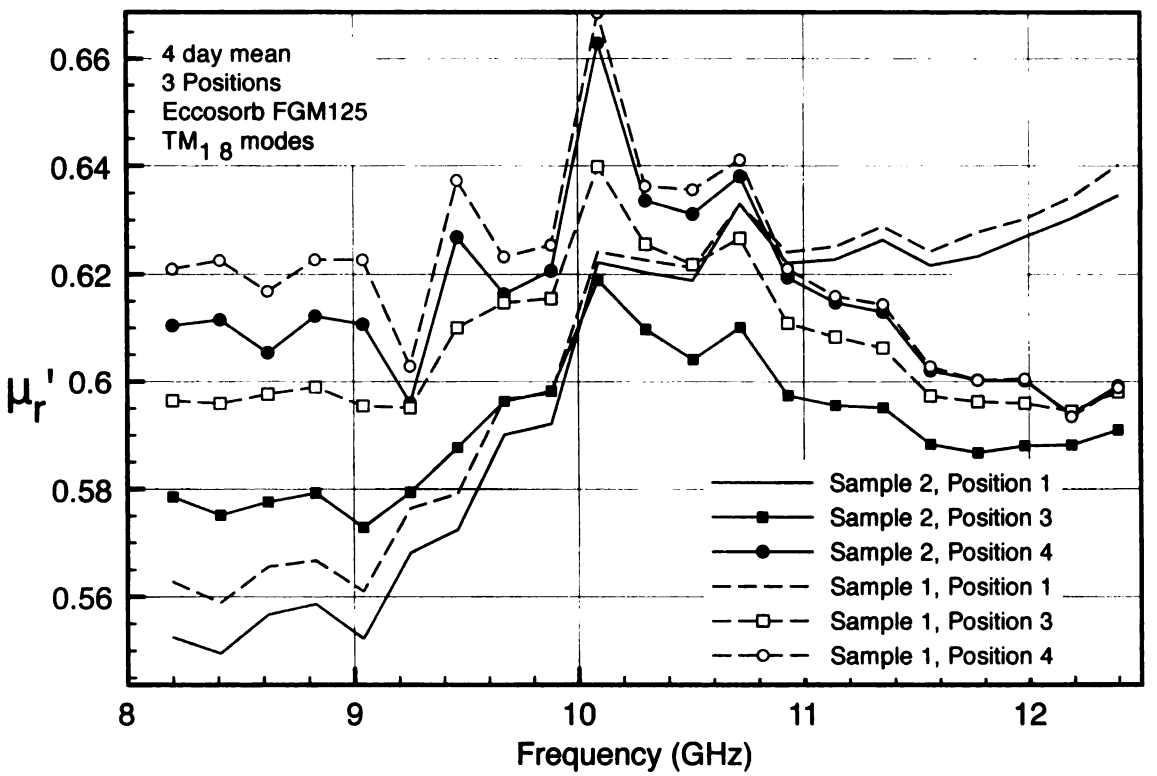


Figure 9.65. Mean extracted values of μ_r' using the two iris method at three different measurement positions. Four independent observations were averaged at each measurement position on each sample. The significant modes up to the TM_{18} mode were used in the extraction.

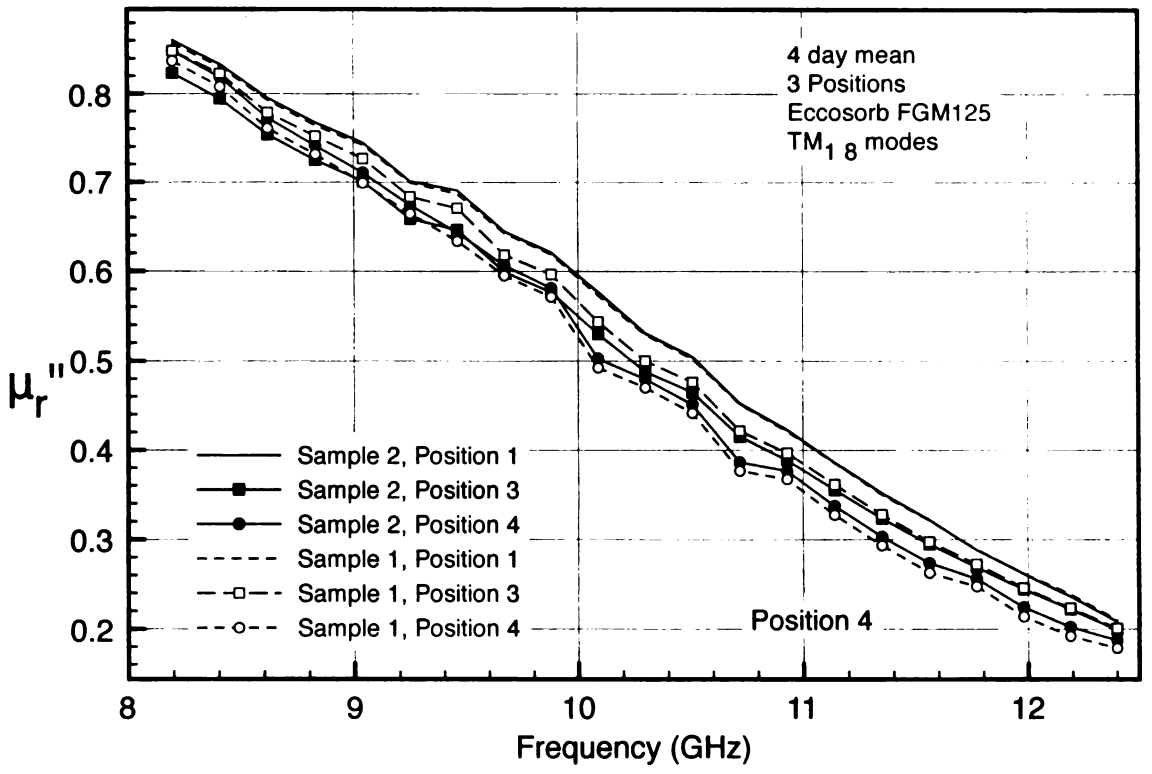


Figure 9.66. Mean extracted values of μ_r'' using the two iris method at three different measurement positions. Four independent observations were averaged at each measurement position on each sample. The significant modes up to the TM_{18} mode were used in the extraction.

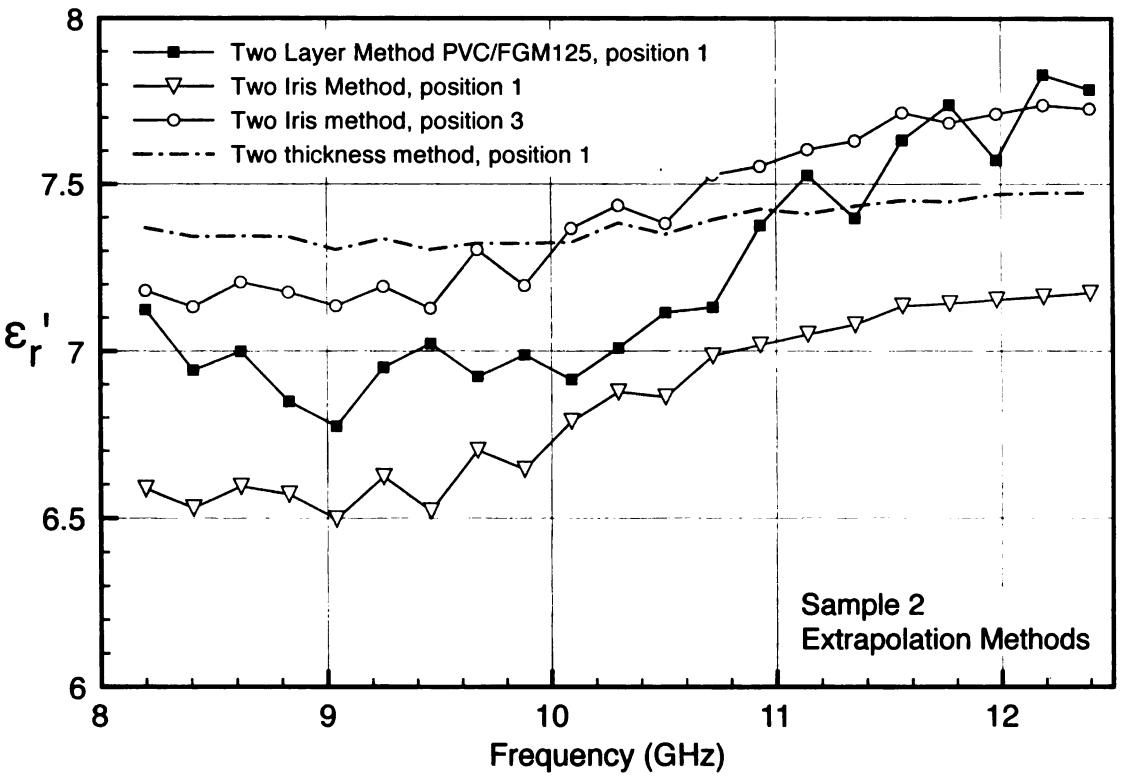


Figure 9.67. Mean extracted values of ϵ_r' using the two iris method, two thickness method, and the two layer method, where PVC was the top layer. Three extractions were averaged at each measurement position for the two iris method, 5 independent extractions were averaged for the two layer method, and two extractions were averaged for the two thickness method. All extractions performed using the extrapolation technique for that method.

extrapolation technique for that method.

9.6 Discussion of Results for Eccosorb FGM125

Figure 9.67 - Figure 9.70 represent the most clear comparison of the strengths and weaknesses of the three methods surveyed in this dissertation for the magnetic material Eccosorb FGM125. From the discussions earlier in this chapter and the conclusions of the sensitivity analysis, the two thickness method is the least sensitive to random measurement error and provides extracted values that are the closest to

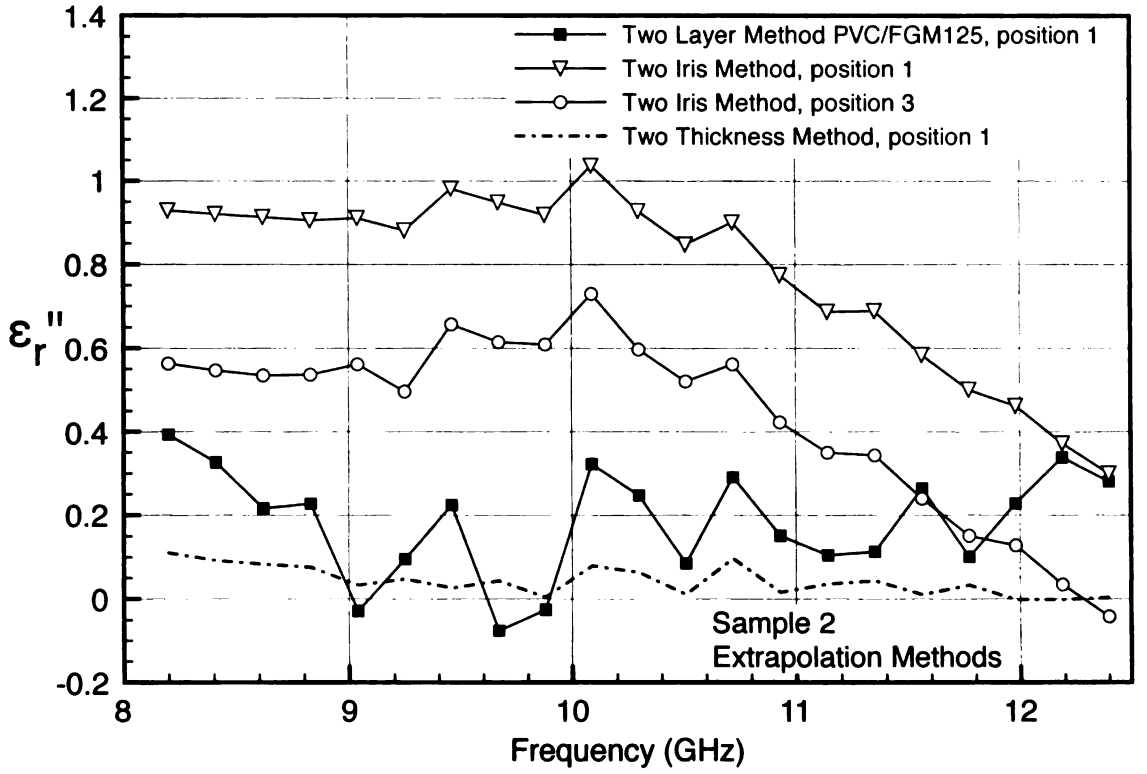


Figure 9.68. Mean extracted values of ϵ_r'' using the two iris method, two thickness method, and the two layer method, where PVC was the top layer. Three extractions were averaged at each measurement position for the two iris method, 5 independent extractions were averaged for the two layer method, and two extractions were averaged for the two thickness method. All extractions performed using the extrapolation technique for that method.

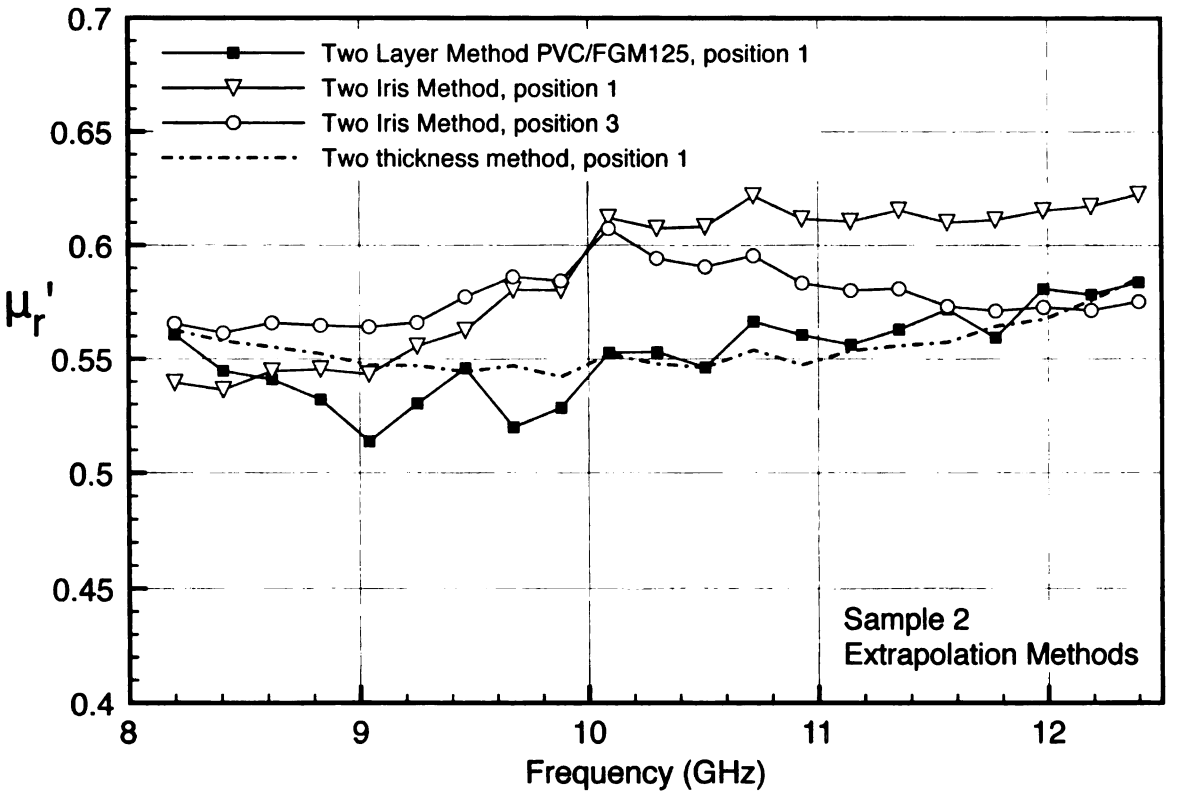


Figure 9.69. Mean extracted values of μ_r' using the two iris method, two thickness method, and the two layer method, where PVC was the top layer. Three extractions were averaged at each measurement position for the two iris method, 5 independent extractions were averaged for the two layer method, and two extractions were averaged for the two thickness method. All extractions performed using the extrapolation technique for that method.

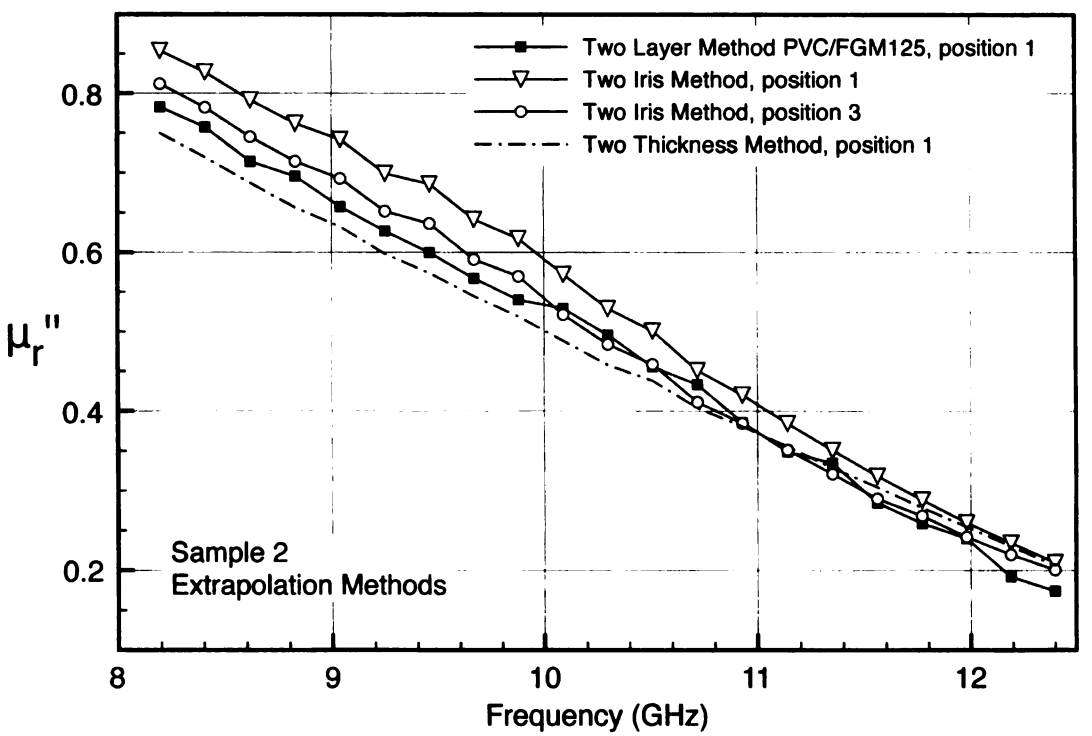


Figure 9.70. Mean extracted values of μ_r'' using the two iris method, two thickness method, and the two layer method, where PVC was the top layer. Three extractions were averaged at each measurement position for the two iris method, 5 independent extractions were averaged for the two layer method, and two extractions were averaged for the two thickness method. All extractions performed using the extrapolation technique for that method.

the nominal values that were obtained by researchers at the Air Force Institute of Technology using a T/R waveguide method for a sample of FGM125. Thus, the other two methods are compared to the two thickness method to understand the properties of those methods. Recall, however, that the two thickness method is only suited for a laboratory environment, and the interest in the other two methods is related to their ability to perform as *in situ* methods.

Consider the plot for ϵ_r' in Figure 9.67. The general shape of the two layer method and the two iris method values are similar across the X-band frequency range. The extracted values are lower at the low end of the frequency range and increase with increasing frequency. The two layer method values show the least variation across the frequency band, with a minimum value of approximately $\epsilon_r' = 7.3$ and a maximum value near $\epsilon_r' = 7.5$. The greatest agreement for this parameter is found between the two thickness method result and the two iris method result from position 3. The values extracted using the two iris method have a errors of less than 5% with respect to the two thickness method. The two layer and two iris method results are within 5% of each other for frequencies greater than 11 GHz.

The extracted values for ϵ_r'' are shown in Figure 9.68 for the three methods. The greatest agreement for this parameter is found between the two layer method and the two thickness method. The extracted values for the two layer method show a greater degree of variation than the two thickness method values, but this is not surprising considering the results of the error sensitivity analysis shown in Figure 6.9. That analysis predicted that the two layer values are four times more sensitive to random measurement error than the two thickness extractions.

In contrast, the values extracted from position 3 using the two iris method are larger for the majority of the frequencies investigated. Near 12 GHz, however, these values have decreased to be near those obtained from the two thickness method. This is also in agreement with the error sensitivity analysis results shown in Figure 8.27,

where the standard deviation to random noise near 12 GHz was approximately the same as that predicted for the two thickness method.

Figure 9.69 shows the extracted values for μ_r'. In this case, the two layer method result agrees most closely with the two thickness method across the entire frequency band. The two layer method values deviate at most by 10% with respect to the two thickness method. In the upper part of the frequency band, the extracted values are very close to one another. The two iris method also shows good agreement at position 3 in the lower and upper parts of the frequency band. In the middle of the frequency band, the two layer values have a maximum deviation of about 10% with respect to the two thickness method. The largest deviation is seen at position 1 for the two iris method.

The two layer method demonstrates the closest agreement with the two thickness method extracted values for μ_r' in Figure 9.70. The values are within 0.04 of the two thickness values for the entire frequency band. In the region from 10 GHz to 12.4 GHz, the two iris method values are almost identical to the two layer method values. However, the two iris values for μ_r' deviate from the two thickness method values by approximately 0.07 for the upper half of the frequency band.

It is noted that after the measurements used in this chapter were taken with Aperture H, the measurement apparatus was inspected. A large scratch, or gouge, was present on the bottom of the plate, emanating from the aperture itself outward for approximately 1 inch. It is possible that this gouge allowed some energy to escape at certain frequencies or configurations when the two iris method was being implemented. It is certainly possible that another measurement apparatus or the repair of the existing device may allow the results for the two iris method to more closely agree with the two thickness method extracted parameters.

CHAPTER 10

CONCLUSIONS

In this dissertation, three material characterization methods using a flanged rectangular waveguide probe are examined. Two methods are investigated for their viability for use as an *in situ* material characterization technique of a conductor-backed material. An iterative, two dimensional Newton's root search method was employed to estimate the material parameters of a conductor-backed lossy material. To carry out the root search, the theoretical reflection coefficient of the material using the waveguide probe must be calculated.

Previous authors have published limited investigations regarding the convergence of the reflection coefficient of a conductor-backed material slab when interrogated by a flanged open-ended waveguide probe. In this dissertation, research determined that certain modes play an important role in the estimation of the reflection coefficient. These modes are related to the symmetry of the waveguide and the properties of the material. An extrapolation method was developed for reducing the error in calculating the reflection coefficient. This extrapolation method is employed the material extraction methods for both a single layer of material and two layers of material interrogated by a single, flanged waveguide probe. It is also implemented for the reduced aperture configuration.

Using the extrapolation technique, an error sensitivity analysis due to random measurement error is also developed and is implemented. This technique estimates the standard deviation of the extracted parameters due to random measurement error. This sensitivity analysis is employed in each of the three methods to estimate the effect of random measurement error on the extracted material parameters from different conductor-backed materials. It is a useful tool in simulating material characterization

results.

The sensitivity analysis predicted that the two thickness method has the least sensitivity to random measurement error of the three methods. It also predicted that the two layer method with a plastic material for a top layer has approximately the same error sensitivity as the two iris method for some of the parameters. In addition, the sensitivity analysis was used to examine several different apertures in order to choose an aperture for implementation in the two iris method.

The two layer method and two iris method are two techniques suitable for *in situ* characterization of a conductor-backed material. They are developed and implemented in this dissertaion. The two layer method requires the derivation and implementation of a two layer Hertzian potential parallel plate dyadic Green's function. The two iris method is a new technique that requires the computation of the theoretical reflection coefficient from a rectangular iris placed in the end of a waveguide. The theoretical formulation necessary to compute the reflection coefficient is developed using a coupled mode matching and MFIE formulation.

Measurements of different materials were made and the permittivity and permeability of a lossy dielectric and magnetic material were extracted using all three characterization methods. The two thickness method shows a low variation in the extracted parameters, especially for the permeability. It also shows good agreement with nominal material parameters for a sample that were derived using a waveguide T/R method. The permittivity has a larger standard deviation. Unfortunately, the two thickness method is limited to a laboratory setting.

When a magnetic radar absorbing material, Eccosorb FGM125, is the material under test, the two layer method, with PVC as the top layer, and the two iris method produce similar results for the extracted parameters. These methods show more random variations in the extracted parameters than the two thickness method. The two layer method, with PVC as the top layer, agrees more closely with the two

thickness method than the two iris method in the characterization of ϵ_r'', μ_r', and μ_r''. The two iris method provides extracted values for the fourth parameter, ϵ_r', that are closer to the extracted values from the two thickness method. For both methods, the parameter that appears the most difficult to characterize is the imaginary part of the permittivity, ϵ_r'.

10.1 Suggestions for Future work

The two iris method and two layer method both show promise to characterize both ϵ and μ as an *in situ* method. However, additional work is needed to more fully understand the strengths and weaknesses of these methods. The following suggestions are given for future work to understand and develop these techniques.

Additional measurements for the two iris method, with repaired plate and additional materials

The gouge that was observed near the aperture on the bottom side of Aperture H may possibly have affected the measured data from Aperture H. Either a repair of the plate or the construction of another device will provide additional data to determine the viability of this technique for material characterization. Measurements of additional materials will give a greater understanding of the materials which may be most likely to respond to the two iris method.

Increase the Computational Speed of the Methods

The computer code used to implement these methods is research-grade code, designed to simply implement the theory developed in this dissertation. The speed could be increased significantly for all three methods by a complex plane analysis and implementation of the resultant pole series. Stewart [36] and Bogle [40] have implemented this technique for the single layer Green's function and achieved significant speed increases. Speed could also be increased by a more detailed modal analysis that could further reduce the size of the matrix used in obtaining the theoretical reflection

coefficient.

Examine other materials for the two layer method

Only a selected group of materials was examined for testing as the top layer in the two layer method. Additional simulations may uncover a common, easily used material for use as the top layer material in this method. Possible candidates for this top layer include styrofoam or another low loss dielectric with a dielectric constant near unity.

Test different thicknesses for two layer method

Only a select few thicknesses of different materials were used in simulations or experiments for the two layer method. Additional simulations may also allow for the discovery of an optimal thickness which may make the measurement technique more useful.

APPENDICES

APPENDIX A

WAVEGUIDE TRANSVERSE MODE FUNCTIONS AND ASSOCIATED INTEGRALS

This appendix provides the reader with the transverse waveguide mode functions and the associated integrals and functions that are used to solve the MFIE for the two thickness method and the two layer method. These mode functions are used in the two thickness method, the two layer method, and the two iris method.

A.1 Transverse Waveguide Mode Functions

The transverse waveguide mode expansion functions are well-known from the literature [41], [43]. In this dissertation, the notation for the qth mode is represented as a $TE_{u_q v_q}$ mode if it is TE_z, or as a $TM_{u_q v_q}$ mode if it is TM_z . The subscripts are chosen such that the first subscript, u_q, denotes the qth mode index in the x-direction. The second subscript, v_q, denotes the qth mode index in the y-direction. These mode functions satisfy the boundary conditions of the waveguide wall. For the X-band waveguide, the x-dimension, a, is larger than the y-dimension, b, as shown in Figure 2.1b.

For TE_z modes, the mode functions for the qth mode are

$$\vec{e}_q^{wg}(\vec{\rho}) = K_{uq\,vq}^{wg}\left[\hat{x}k_{yq}\cos\left(k_{xq}x\right)\sin\left(k_{yq}y\right) - \hat{y}\left(k_{xq}\right)\sin\left(k_{xq}x\right)\cos\left(k_{yq}y\right)\right] \quad \text{(A.1)}$$

$$\vec{h}_q^{wg}(\vec{\rho}) = \frac{K_{uq\,vq}^{wg}}{Z_q^{wg(TE)}}\left[\hat{x}k_{xq}\sin\left(k_{xq}x\right)\cos\left(k_{yq}y\right) + \hat{y}k_{yq}\cos\left(k_{xq}x\right)\sin\left(k_{yq}y\right)\right] \quad \text{(A.2)}$$

$$u_q = 0, 1, 2, ... \qquad v_q = 0, 1, 2, ..., \quad u_q + v_q > 0 \quad \text{(A.3)}$$

The directional impedance for the qth TE_z mode in a waveguide filled with free space

is

$$Z_q^{wg(TE)} = \frac{\omega\mu_0}{k_{zq}^{wg}}. \tag{A.4}$$

The additional terms are

$$k_{xq} = \frac{u_q\pi}{a}, \qquad k_{yq} = \frac{v_q\pi}{b}, \tag{A.5}$$

$$k_{cq}^2 = k_{xq}^2 + k_{yq}^2, \qquad k_{zq} = \sqrt{k_0^2 - k_{cq}^2}. \tag{A.6}$$

The term $K_{uq\,vq}^{wg}$ is the TE_z normalization constant, and it is defined in section A.2.

For TM_z modes, the mode functions are

$$\vec{e}_q^{\,wg}(\vec{\rho}) = N_{uq\,vq}^{wg}\left[-\hat{x}k_{xq}\cos\left(k_{xq}x\right)\sin\left(k_{yq}y\right) - \hat{y}k_{yq}\sin\left(k_{xq}x\right)\cos\left(k_{yq}y\right)\right] \tag{A.7}$$

$$\vec{h}_q^{\,wg}(\vec{\rho}) = \frac{N_{uq\,vq}^{wg}}{Z_q^{wg(TM)}}\left[\hat{x}k_{yq}\sin\left(k_{xq}x\right)\cos\left(k_{yq}y\right) - \hat{y}k_{xq}\cos\left(k_{xq}x\right)\sin\left(k_{yq}y\right)\right] \tag{A.8}$$

$$u_q = 1, 2, ... \qquad v_q = 1, 2, ... \tag{A.9}$$

The normalization constant $N_{uq\,vq}^{wg}$ is defined in section A.2. The waveguide impedance for the qth TM_z mode in a waveguide filled with free space is defined as

$$Z_q^{wg(TM)} = \frac{k_{zq}^{wg}}{\omega\epsilon_0}. \tag{A.10}$$

In the two layer method and the two thickness method, the material under test is interrogated using a flanged rectangular waveguide probe. When the incident field is the dominant TE_{10} mode,the physical symmetry of the waveguide and material requires that the reflected field components be symmetric about the center of the aperture [36]. It is shown by Bois [37] that only the modes for which u_n = odd and v_n = even are coupled with the incident TE_{10} mode. Thus, in the two layer and two thickness methods, these are the only modes considered.

A.2 Normalization constants

The transverse mode functions have the property of mode orthogonality, such that

$$\int_{CS} \vec{e}_n^{\,wg}(\vec{\rho}) \cdot \vec{e}_n^{\,wg}(\vec{\rho}) ds = 1 \tag{A.11}$$

For the TE case, this becomes

$$\int_{x=0}^{a}\int_{y=0}^{b} (K_{un\,vn}^{wg})^2 \left[k_{yn}^2 \cos^2(k_{xn}x)\sin^2(k_{yn}y)\right] + k_{xn}^2 \sin^2(k_{xn}x)\cos^2(k_{yn}y)\Big] dxdy = 1. \tag{A.12}$$

Equation (A.12) can be rewritten as

$$(K_{un\,vn}^{wg})^2 \left[k_{yn}^2 \int_{x=0}^{a} \cos^2(k_{xn}x)dx \int_{y=0}^{b} \sin^2(k_{yn}y)dy + k_{xn}^2 \int_{x=0}^{a} \sin^2(k_{xn}x)dx \int_{y=0}^{b} \cos^2(k_{yn}y)dy\right] = 1 \tag{A.13}$$

To evaluate (A.13), note the identities

$$\int \cos^2(ax)dx = \frac{x}{2} + \frac{1}{4a}\sin(2ax) \tag{A.14}$$

$$\int \sin^2(ax)dx = \frac{x}{2} - \frac{1}{4a}\sin(2ax). \tag{A.15}$$

Evaluating the integrals in (A.13) produces

$$1 = \begin{cases} (K_{un\,vn}^{wg})^2 \left[k_{yn}^2 \frac{ab}{4} + k_{xn}^2 \frac{ab}{4}\right] & u_n \neq 0, v_n \neq 0 \\ (K_{uq\,vq}^{wg})^2 \left[k_{yn}^2 \frac{ab}{2} + k_{xn}^2 \frac{ab}{2}\right] & u_n = 0 \, or \, v_n = 0 \end{cases} \tag{A.16}$$

Rearranging this equation leads to the TE normalization constant

$$K^{wg}_{un\ vn} = \begin{cases} \frac{2}{k_{cn}\sqrt{ab}} & u_n \neq 0,\ v_n \neq 0 \\ \\ \frac{\sqrt{2}}{k_{cn}\sqrt{ab}} & u_n = 0\ or\ v_n = 0 \end{cases} \tag{A.17}$$

By using a similar procedure, the normalization constant for the TM case is

$$N^{wg}_{un\ vn} = \frac{2}{k_{cn}\sqrt{ab}}. \tag{A.18}$$

A.3 Calculation of $f_{xn}(k_x, k_y)$, $f_{yn}(k_x, k_y)$, $g_{xm}(k_x, k_y)$, and $g_{ym}(k_x, k_y)$

In the calculation of the matrix elements for the MFIE in the two layer and two thickness methods, it is necessary to evaluate the integrals involving the transverse waveguide mode functions. These are defined as

$$f_{xn}(k_x, k_y) = \int_{CS} h^{wg}_{xn}(\vec{\rho}\,')e^{-j\vec{k}\cdot\vec{\rho}\,'}ds', \tag{A.19}$$

$$f_{yn}(k_x, k_y) = \int_{CS} h^{wg}_{yn}(\vec{\rho}\,')e^{-j\vec{k}\cdot\vec{\rho}\,'}ds', \tag{A.20}$$

$$g_{xm}(k_x, k_y) = \int_{CS} h^{wg}_{xm}(\vec{\rho})e^{j\vec{k}\cdot\vec{\rho}}ds, \tag{A.21}$$

$$g_{ym}(k_x, k_y) = \int_{CS} h^{wg}_{ym}(\vec{\rho})e^{j\vec{k}\cdot\vec{\rho}}ds. \tag{A.22}$$

First the integrals on the unprimed variables that are found in (A.21) - (A.22) are evaluated. These integrals involve sines and cosines and exponential functions. The first integral is

$$\int_0^a \sin(k_{xm}x)e^{jk_x x}dx = \frac{e^{jk_x a}e^{jk_{xm}a} - 1}{-2(k_x + k_{xm})} + \frac{e^{jk_x a}e^{-jk_{xm}a} - 1}{2(k_x - k_{xm})}. \tag{A.23}$$

As mentioned at the end of section A.1, the only modes which are supported by the

WR-90 waveguide in the two layer method and the two thickness method are those where the first index of the mth mode, u_m, is odd, and the second index, v_m, is even. Using this fact, the following formulas will be utilized in this appendix for the two layer method and the two thickness method:

$$e^{jk_{xm}a} = e^{ju_m\pi} = -1 \tag{A.24}$$

$$e^{-jk_{xm}a} = e^{-ju_m\pi} = -1 \tag{A.25}$$

$$e^{jk_{ym}b} = e^{jv_m\pi} = 1 \tag{A.26}$$

$$e^{-jk_{ym}b} = e^{-jv_m\pi} = 1 \tag{A.27}$$

This allows (A.23) to be rewritten as

$$\begin{aligned}\int_0^a \sin(k_{xm}x)e^{jk_x x}dx =& \frac{e^{jk_x a}+1}{2(k_x+k_{xm})} - \frac{e^{jk_x a}+1}{2(k_x-k_{xm})} \\ =& -\frac{k_{xm}\left(e^{jk_x a}+1\right)}{(k_x^2-k_{xm}^2)}\end{aligned} \tag{A.28}$$

The other integral to be evaluated with respect to the variable x is

$$\begin{aligned}\int_0^a \cos(k_{xm}x)e^{jk_x x}dx =& \frac{e^{jk_x a}e^{jk_{xm}a}-1}{2j(k_x+k_{xm})} + \frac{e^{jk_x a}e^{-jk_{xm}a}-1}{2j(k_x-k_{xm})} \\ =& -\frac{e^{jk_x a}+1}{2j(k_x+k_{xm})} - \frac{e^{jk_x a}+1}{2j(k_x-k_{xm})} \\ =& -\frac{k_x(e^{jk_x a}+1)}{j(k_x^2-k_{xm}^2)}\end{aligned} \tag{A.29}$$

The second integration variable in (A.21)-(A.22) is the y-dimension. Thus, the

following integrals are evaluated for use in (A.21)-(A.22):

$$\begin{aligned}\int_0^b \cos(k_{ym}y)e^{jk_y y}dy =& \frac{e^{jk_y b}e^{jk_{ym}b}-1}{2j(k_y+k_{ym})} + \frac{e^{jk_y b}e^{-jk_{ym}b}-1}{2j(k_y-k_{ym})} \\ =& \frac{e^{jk_y b}-1}{2j(k_y+k_{ym})} + \frac{e^{jk_y b}-1}{2j(k_y-k_{ym})} \\ =& \frac{k_y(e^{jk_y b}-1)}{j(k_y^2-k_{ym}^2)}\end{aligned} \tag{A.30}$$

$$\begin{aligned}\int_0^b \sin(k_{ym}y)e^{jk_y y}dy =& -\frac{e^{jk_y b}e^{jk_{ym}b}-1}{2(k_y+k_{ym})} + \frac{e^{jk_y b}e^{-jk_{ym}b}-1}{2(k_y-k_{ym})} \\ =& -\frac{e^{jk_y b}-1}{2(k_y+k_{ym})} + \frac{e^{jk_y b}-1}{2(k_y-k_{ym})} \\ =& \frac{k_{ym}(e^{jk_y b}-1)}{(k_y^2-k_{ym}^2)}\end{aligned} \tag{A.31}$$

Four additional integrals with respect to the primed variables are also used in the computation of (A.19) - (A.20). By applying similar techniques, the remaining integrals with respect to the primed variables are evaluated, producing

$$\int_0^a \sin(k_{xn}x')e^{-jk_x x'}dx' = -\frac{k_{xn}\left(e^{-jk_x a}+1\right)}{(k_x^2-k_{xn}^2)} \tag{A.32}$$

$$\int_0^a \cos(k_{xn}x')e^{-jk_x x'}dx' = \frac{k_x\left(e^{-jk_x a}+1\right)}{j(k_x^2-k_{xn}^2)} \tag{A.33}$$

$$\int_0^b \sin(k_{yn}y')e^{-jk_y y'}dy' = \frac{k_{yn}\left(e^{-jk_y b}-1\right)}{(k_y^2-k_{yn}^2)} \tag{A.34}$$

$$\int_0^b \cos(k_{yn}y')e^{-jk_y y'}dy' = -\frac{k_y\left(e^{-jk_y b}-1\right)}{j(k_y^2-k_{yn}^2)} \tag{A.35}$$

A.3.1 Function values for TE_z modes

The transverse waveguide mode functions are different for TE_z modes and TM_z modes, as shown in (A.1) - (A.2) and (A.7) - (A.8). As a result, the functions $f_{xn}(k_x,k_y)$ and $f_{yn}(k_x,k_y)$, which are the source mode functions, and $g_{xm}(k_x,k_y)$ and $g_{ym}(k_x,k_y)$, which are the observer mode functions, will be different for the two types of modes. First, the functions are evaluated for TE_z modes by using (A.1) - (A.2), where $\vec{h}_q^{wg}(\vec{\rho}) = \hat{x}h_{xq}^{wg}(\vec{\rho})+\hat{y}h_{yq}^{wg}(\vec{\rho})$. The first source mode function $f_{xn}(k_x,k_y)$ is evaluated, producing

$$\begin{aligned} f_{xn}(k_x,k_y) &= \int_{CS} h_{xn}^{wg}(\vec{\rho}')e^{-j\vec{k}\cdot\vec{\rho}'}ds' \\ &= \frac{K_{un\ vn}^{wg}}{Z_n^{wg(TE)}}\int_0^a\int_0^b k_{xn}\sin(k_{xn}x')\cos(k_{yn}y')e^{-jk_x x'}e^{-jk_y y'}dx'\,dy' \\ &= \frac{K_{un\ vn}^{wg}}{Z_n^{wg(TE)}}k_{xn}\int_0^a \sin(k_{xn}x')e^{-jk_x x'}dx'\int_0^b \cos(k_{yn}y')e^{-jk_y y'}dy'. \end{aligned} \tag{A.36}$$

Replacing the integrals in (A.36) with (A.32) and (A.35) produces

$$f_{xn}(k_x,k_y) = \frac{K_{un\ vn}^{wg}}{Z_n^{wg(TE)}}\frac{k_y k_{xn}^2\left(e^{-jk_y b}-1\right)\left(e^{-jk_x a}+1\right)}{j(k_y^2-k_{yn}^2)(k_x^2-k_{xn}^2)} \tag{A.37}$$

The function $f_{yn}(k_x,k_y)$ is evaluated using the integrals in (A.33) and (A.34),

yielding

$$
\begin{aligned}
f_{yn}(k_x,k_y) &= \int_{CS} h_{yn}^{wg}(\vec{\rho}\,')e^{-j\vec{k}\cdot\vec{\rho}\,'}ds' \\
&= \frac{K_{un\ vn}^{wg}}{Z_n^{wg(TE)}}\int_0^a\int_0^b k_{yn}\cos\left(k_{xn}x'\right)\sin\left(k_{yn}y'\right)e^{-jk_xx'}e^{-jk_yy'}dx'\,dy' \\
&= \frac{K_{un\ vn}^{wg}}{Z_n^{wg(TE)}}\frac{k_xk_{yn}^2\left(e^{-jk_yb}-1\right)\left(e^{-jk_xa}+1\right)}{j(k_x^2-k_{xn}^2)(k_y^2-k_{yn}^2)}
\end{aligned}
\tag{A.38}
$$

In a similar fashion, the integration of the functions over the unprimed variables, $g_{xm}(k_x,k_y)$, and $g_{ym}(k_x,k_y)$, yields

$$
\begin{aligned}
g_{xm}(k_x,k_y) &= \int_{CS} h_{xm}^{wg}(\vec{\rho})e^{j\vec{k}\cdot\vec{\rho}}ds \\
&= -\frac{K_{um\ vm}^{wg}}{Z_m^{wg(TE)}}\int_0^a\int_0^b k_{xm}\sin\left(k_{xm}x\right)\cos\left(k_{ym}y\right)e^{jk_xx}e^{jk_yy}dx\,dy \\
&= -\frac{K_{um\ vm}^{wg}}{Z_m^{wg(TE)}}\frac{k_yk_{xm}^2\left(e^{jk_yb}-1\right)\left(e^{jk_xa}+1\right)}{j(k_x^2-k_{xm}^2)(k_y^2-k_{ym}^2)}
\end{aligned}
\tag{A.39}
$$

$$
\begin{aligned}
g_{ym}(k_x,k_y) &= \int_{CS} h_{ym}^{wg}(\vec{\rho})e^{j\vec{k}\cdot\vec{\rho}}ds \\
&= \frac{K_{um\ vm}^{wg}}{Z_m^{wg(TE)}}\int_0^a\int_0^b k_{ym}\cos\left(k_{xm}x\right)\sin\left(k_{ym}y\right)e^{jk_xx}e^{jk_yy}dx\,dy \\
&= -\frac{K_{um\ vm}^{wg}}{Z_m^{wg(TE)}}\frac{k_xk_{ym}^2\left(e^{jk_yb}-1\right)\left(e^{jk_xa}+1\right)}{j(k_x^2-k_{xm}^2)(k_y^2-k_{ym}^2)}
\end{aligned}
\tag{A.40}
$$

A.3.2 Function values for TM_z modes

The functions $f_{xn}(k_x,k_y)$, $f_{yn}(k_x,k_y)$, $g_{xm}(k_x,k_y)$, and $g_{ym}(k_x,k_y)$ are evaluated for the TM_z modes in a manner similar to the steps taken in section A.3.1 for the TE_z modes. By utilizing the integrals in (A.28) - (A.35), the functions are evaluated,

producing

$$f_{xn}(k_x,k_y)=\frac{N^{wg}_{un\ vn}}{Z^{wg(TM)}_{n}}\frac{k_yk_{xn}k_{yn}\left(e^{-jk_yb}-1\right)\left(e^{-jk_xa}+1\right)}{j(k_y^2-k_{yn}^2)(k_x^2-k_{xn}^2)} \tag{A.41}$$

$$f_{yn}(k_x,k_y)=-\frac{N^{wg}_{un\ vn}}{Z^{wg(TM)}_{n}}\frac{k_xk_{yn}k_{xn}\left(e^{-jk_yb}-1\right)\left(e^{-jk_xa}+1\right)}{j(k_x^2-k_{xn}^2)(k_y^2-k_{yn}^2)} \tag{A.42}$$

$$g_{xm}(k_x,k_y)=-\frac{N^{wg}_{um\ vm}}{Z^{wg(TM)}_{m}}\frac{k_yk_{ym}k_{xm}\left(e^{jk_yb}-1\right)\left(e^{jk_xa}+1\right)}{j(k_x^2-k_{xm}^2)(k_y^2-k_{ym}^2)} \tag{A.43}$$

$$g_{ym}(k_x,k_y)=\frac{N^{wg}_{um\ vm}}{Z^{wg(TM)}_{m}}\frac{k_xk_{ym}k_{xm}\left(e^{jk_yb}-1\right)\left(e^{jk_xa}+1\right)}{j(k_x^2-k_{xm}^2)(k_y^2-k_{ym}^2)} \tag{A.44}$$

APPENDIX B

DERIVATIVE EQUALITY

From (3.19), the relationship of the normal potentials at the boundary $z = -d_1$ is

$$\mu_1 \frac{\partial}{\partial y}\Pi_{1z} = \mu_2 \frac{\partial}{\partial y}\Pi_{2z} \qquad at\ z = -d_1. \tag{B.1}$$

Note that in the two layer geometry, the spatial boundary between the materials is invariant with respect to the x-y plane. Using the inverse spatial Fourier transform approach from section 3.7 on (B.1) yields

$$\frac{\mu_1}{4\pi^2}\frac{\partial}{\partial y}\iint_{-\infty}^{\infty} \Pi_{1z}\left(k_x, k_y, z\right) e^{j\vec{k}\cdot\vec{\rho}} dk_x dk_y = \frac{\mu_2}{4\pi^2}\frac{\partial}{\partial y}\iint_{-\infty}^{\infty} \Pi_{2z}\left(k_x, k_y, z\right) e^{j\vec{k}\cdot\vec{\rho}} dk_x dk_y. \tag{B.2}$$

Moving the derivatives inside the integral and performing the derivatives yields

$$\frac{1}{4\pi^2}\iint_{-\infty}^{\infty} jk_y \left[\mu_1 \tilde{\Pi}_{1z}\left(k_x, k_y, z\right) - \mu_2 \tilde{\Pi}_{2z}\left(k_x, k_y, z\right)\right] e^{j\vec{k}\cdot\vec{\rho}} dk_x dk_y = 0. \tag{B.3}$$

Using the Fourier integral theorem, the terms in the brackets may be set to zero, yielding the relationship

$$\mu_1 \tilde{\Pi}_{1z}\left(k_x, k_y, z\right) - \mu_2 \tilde{\Pi}_{2z}\left(k_x, k_y, z\right) = 0. \tag{B.4}$$

Taking (B.4) and applying the forward transform yields

$$\iint_{-\infty}^{\infty} \left[\mu_1 \tilde{\Pi}_{1z}\left(k_x, k_y, z\right) - \mu_2 \tilde{\Pi}_{2z}\left(k_x, k_y, z\right)\right] e^{-j\vec{k}\cdot\vec{\rho}} dx dy = 0, \tag{B.5}$$

which produces

$$\mu_1 \Pi_{1z}(x, y, z) = \mu_2 \Pi_{2z}(x, y, z). \tag{B.6}$$

APPENDIX C

THE RELATIONSHIP OF THE SINGLE LAYER AND TWO LAYER PARALLEL PLATE GREEN'S FUNCTIONS

Recall from (3.225) that the two layer parallel plate dyadic Green's function for a tangentially directed source is represented in the spatial domain as

$$\bar{\bar{G}}^{pp}(x,y,z) = \begin{bmatrix} G_{xx} & 0 & \triangle \\ 0 & G_{yy} & \triangle \\ G_{zx} & G_{zy} & \triangle \end{bmatrix}, \tag{C.1}$$

where the $\triangle$ was not derived in this study, and each element of the matrix is a function of the spatial variables x, y, and z.

Each element can be described by its inverse transform,

$$G_{\alpha\beta}(\vec{r}|\vec{r}') = \frac{1}{4\pi^2}\iint_{-\infty}^{\infty} \tilde{G}_{\alpha\beta}(k_x,k_y,z)e^{j\vec{k}\cdot(\vec{\rho}-\vec{\rho}')}dk_x dk_y. \tag{C.2}$$

This appendix demonstrates that the two layer parallel plate Hertzian potential dyadic Green's function reduces to the single layer parallel plate Green's function when both layers are composed of the same material. This is only shown for the four elements which are needed in the two layer method and two thickness method in (C.1).

From Chapter 3, the elements of the parallel plate Green's functions which are of

interest from (3.213), (3.219), (3.222), and (3.224) are

$$\widetilde{G}_{xx}(k_x,k_y,z,z') = \frac{1}{j2\omega\mu_1 p_1}\cdot \left[e^{-p_1|z-z'|} + e^{p_1(z+z')} - 2\cosh p_1 z \cosh p_1 z' \frac{T_{ms}}{T_m} e^{-p_1 d_1}\right], \tag{C.3}$$

$$\widetilde{G}_{zx}(k_x,k_y,z,z') = \frac{-1}{j2\omega\mu_1 p_1}\cdot \left[jk_x\left(\frac{\mu_2\epsilon_2}{\mu_1\epsilon_1} - 1\right)\frac{\sinh\left(2p_2\left(d_1-h\right)\right)}{p_1 T_m T_e}\cosh p_1 z' \sinh p_1 z\right], \tag{C.4}$$

$$\widetilde{G}_{yy}(k_x,k_y,z,z') = \frac{1}{j2\omega\mu_1 p_1}\cdot \left[e^{-p_1|z-z'|} + e^{p_1(z+z')} - 2\cosh p_1 z \cosh p_1 z' \frac{T_{ms}}{T_m} e^{-p_1 d_1}\right], \tag{C.5}$$

$$\widetilde{G}_{zy}(k_x,k_y,z,z') = \frac{-1}{j2\omega\mu_1 p_1}\cdot \left[jk_y\left(\frac{\mu_2\epsilon_2}{\mu_1\epsilon_1} - 1\right)\frac{\sinh\left(2p_2\left(d_1-h\right)\right)}{p_1 T_m T_e}\cosh p_1 z' \sinh p_1 z\right]. \tag{C.6}$$

When the two layers of material are the same material, $\epsilon_1 = \epsilon_2$ and $\mu_1 = \mu_2$. Also note this makes $p_1 = p_2$. The first step is to evaluate the functions T_{ms}, T_m, and T_e. From (3.206) the expression for T_{ms} becomes

$$\begin{aligned} T_{ms} &= \left[\frac{p_2}{p_1}\sinh\left(p_2\left(d_1-h\right)\right) + \frac{\epsilon_2}{\epsilon_1}\cosh\left(p_2\left(d_1-h\right)\right)\right] \\ &= \sinh\left(p_2\left(d_1-h\right)\right) + \cosh\left(p_2\left(d_1-h\right)\right) \\ &= e^{p_2(d_1-h)}. \end{aligned} \tag{C.7}$$

From (3.184), the expression for T_m becomes

$$\begin{aligned} T_m &= \frac{p_2}{p_1}\cosh p_1 d_1 \sinh\left(p_2\left(d_1-h\right)\right) - \frac{\epsilon_2}{\epsilon_1}\sinh p_1 d_1 \cosh\left(p_2\left(d_1-h\right)\right) \\ &= \cosh p_1 d_1 \sinh\left(p_2\left(d_1-h\right)\right) - \sinh p_1 d_1 \cosh\left(p_2\left(d_1-h\right)\right) \\ &= \sinh\left(p_2\left(d_1-h\right) - p_1 d_1\right) \\ &= -\sinh(p_2 h). \end{aligned} \tag{C.8}$$

From (3.197), the expression for T_e becomes

$$\begin{aligned} T_e &= \frac{p_2}{p_1}\cosh\left(p_2\left(d_1-h\right)\right)\sinh p_1 d_1 - \frac{\mu_2}{\mu_1}\cosh p_1 d_1 \sinh\left(p_2\left(d_1-h\right)\right) \\ &= \cosh\left(p_2\left(d_1-h\right)\right)\sinh p_1 d_1 - \cosh p_1 d_1 \sinh\left(p_2\left(d_1-h\right)\right) \\ &= \sinh\left(p_1 d_1 - p_2\left(d_1-h\right)\right) \\ &= \sinh\left(p_2 h\right). \end{aligned} \tag{C.9}$$

Using (C.7), (C.8), and (C.9) in (C.3), and noting that $p_1 = p_2$, produces

$$\widetilde{G}_{xx}(k_x,k_y,z,z') = \frac{1}{j2\omega\mu_1 p_1}\cdot \left[e^{-p_1|z-z'|} + e^{p_1(z+z')} + 2\cosh\left(p_1 z\right)\cosh\left(p_1 z'\right)\frac{e^{-p_1 h}}{\sinh(p_1 h)}\right]. \tag{C.10}$$

This is also the expression for the other diagonal element, $\widetilde{G}_{yy}(k_x,k_y,z,z')$. When $\epsilon_1 = \epsilon_2$ and $\mu_1 = \mu_2$, the off-diagonal elements $\widetilde{G}_{zy}(k_x,k_y,z,z') = 0$ and $\widetilde{G}_{zy}(k_x,k_y,z,z') = 0$.

The diagonal elements of the single layer parallel plate Green's function are given

by Hanson [45] as

$$\widetilde{G}_{xx(H)}(k_x, k_y, z, z') = \frac{\cosh\left(p_1(t - |z_h - z_h'|)\right) + \cosh\left(p_1(t - (z_h + z_h'))\right)}{2p_1 \sinh\left(p_1 t\right)} \tag{C.11}$$

where t is the thickness of the material layer, and the coordinates z_h and z_h' are the observer and source coordinates, respectively, for the coordinate system used in Hanson's derivation. The two coordinate systems are shown in Figure C.1. The factor of $\frac{1}{j\omega\mu_1}$ is not present in the Green's function element in C.11, but is included in his derivation.

It remains to be shown that (C.11) is equivalent to (C.10) for the possible source and observer locations.

C.1 Case 1: $z' > z$

In evaluating the expression for the diagonal element, $\widetilde{G}_{xx}(k_x, k_y, z, z')$, when the source is greater than the observer, $|z - z'| = z' - z$, yields

$$\widetilde{G}_{xx}(k_x, k_y, z, z') = \frac{1}{j2\omega\mu_1 p_1} \cdot \left[e^{-p_1(z'-z)} + e^{p_1(z+z')} + 2(e^{-p_1 z} + e^{-p_1 z})(e^{-p_1 z'} + e^{-p_1 z'}) \frac{e^{-p_1 h}}{4\sinh(p_1 h)} \right] \tag{C.12}$$

This can be evaluated to produce

$$\widetilde{G}_{xx}(k_x, k_y, z, z') = \frac{1}{j\omega\mu_1} \cdot \left[\frac{e^{p_1(h-z'+z)} + e^{p_1(h+z+z')} + e^{-p_1(h+z-z')} + e^{-p_1(h+z+z')}}{4p_1 \sinh(p_1 h)} \right] \tag{C.13}$$

To evaluate the expression given by Hanson, observe from Figure C.1 that his

derivation uses a different set of coordinates to establish the same Green's function. A change of coordinates is made where $z' = -z'_h$ and $z = -z_h$. Thus, the equivalent case for $z' > z$ is where $z_h > z'_h$. Thus, when $z_h > z'_h$, then $|z_h - z'_h| = z_h - z'_h$. Using these values, (C.11) becomes

$$\widetilde{G}_{xx(H)}(k_x, k_y, z, z') = \frac{e^{p_1(t-(z_h-z'_h))} + e^{-p_1(t-(z_h-z'_h))} + e^{p_1(t-(z_h+z'_h))} + e^{-p_1(t-(z_h+z'_h))}}{4p_1 \sinh(p_1 t)} \tag{C.14}$$

Making the change of coordinates, z'_h can be replaced by $-z'$, z_h can be replaced by $-z$, and t is replaced by h. Thus, (C.14) becomes

$$\widetilde{G}_{xx(H)}(k_x, k_y, z, z') = \frac{e^{p_1(h+z-z')} + e^{-p_1(h+z-z')} + e^{p_1(h+z+z')} + e^{-p_1(h+z+z')}}{4p_1 \sinh(p_1 t)}, \tag{C.15}$$

which is equivalent to the term in brackets shown in (C.13).

C.2 Case 2: $z' < z$

In evaluating the expression for the diagonal element, $\widetilde{G}_{xx}(k_x, k_y, z, z')$, when the source is less than the observer, $|z - z'| = z - z'$, yields

$$\widetilde{G}_{xx}(k_x, k_y, z, z') = \frac{1}{j2\omega\mu_1 p_1} \cdot \left[e^{-p_1(z-z')} + e^{p_1(z+z')} + 2(e^{-p_1 z} + e^{-p_1 z})(e^{-p_1 z'} + e^{-p_1 z'}) \frac{e^{-p_1 h}}{4\sinh(p_1 h)} \right] \tag{C.16}$$

This can be rearranged to produce

$$\widetilde{G}_{xx}(k_x, k_y, z, z') = \frac{1}{j\omega\mu_1} \cdot \left[\frac{e^{p_1(h-z+z')} + e^{p_1(h+z+z')} + e^{-p_1(h-z+z')} + e^{-p_1(h+z+z')}}{4p_1 \sinh(p_1 h)} \right]. \tag{C.17}$$

To evaluate the expression given by Hanson, note from Figure C.2 that the equivalent case for $z' < z$ is where $z_h < z'_h$. Thus, when $z_h < z'_h$, then $|z_h - z'_h| = z'_h - z_h$. Using these values, (C.11) becomes

$$\widetilde{G}_{xx(H)}(k_x, k_y, z, z') = \frac{e^{p_1(t-(z'_h-z_h))} + e^{-p_1(t-(z'_h-z_h))} + e^{p_1(t-(z_h+z'_h))} + e^{-p_1(t-(z_h+z'_h))}}{4p_1 \sinh(p_1 t)}. \tag{C.18}$$

Making the change of coordinates, z'_h can be replaced by $-z'$, z_h can be replaced by $-z$, and t is replaced by h. Thus, (C.18) becomes

$$\widetilde{G}_{xx(H)}(k_x, k_y, z, z') = \frac{e^{p_1(h-z+z')} + e^{-p_1(h-z+z')} + e^{p_1(h+z+z')} + e^{-p_1(h+z+z')}}{4p_1 \sinh(p_1 h)}, \tag{C.19}$$

which is equivalent to the term in brackets shown in (C.17).

Thus, for the coordinate system used in the two layer method, when both layers are composed of the same material, the expression for the two layer parallel plate Green's function reduces to the single layer parallel plate Green's function for the first two diagonal elements. This derivation does not explore the elements for the third column of the Green's function, since the normal components of the current in

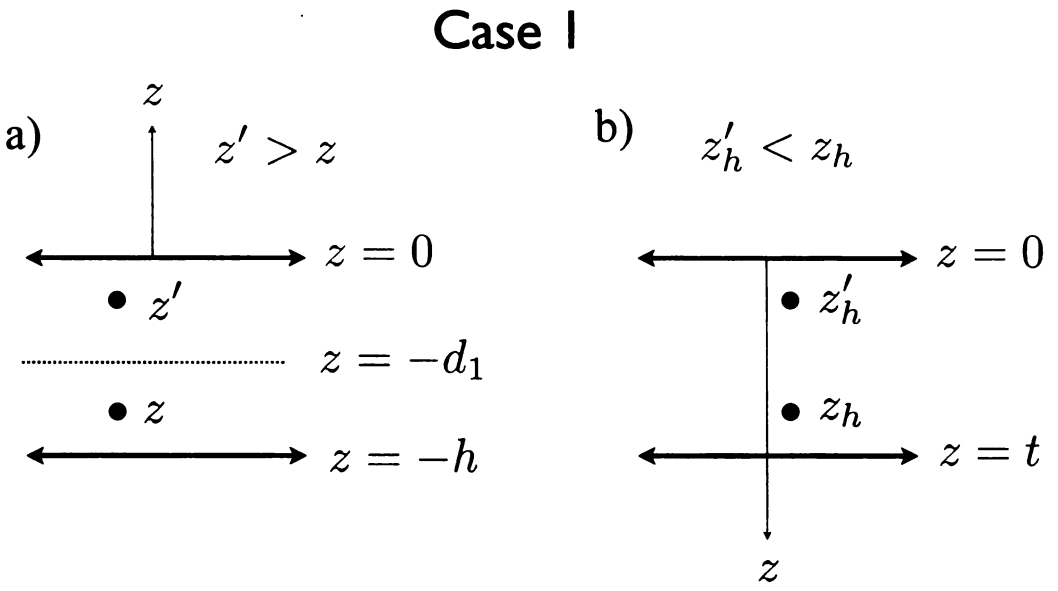


Figure C.1. Equivalent problem coordinate systems for a) this dissertation and b) Hanson's derivation. For case 1, where $z' > z$.

the aperture were not used in these methods.

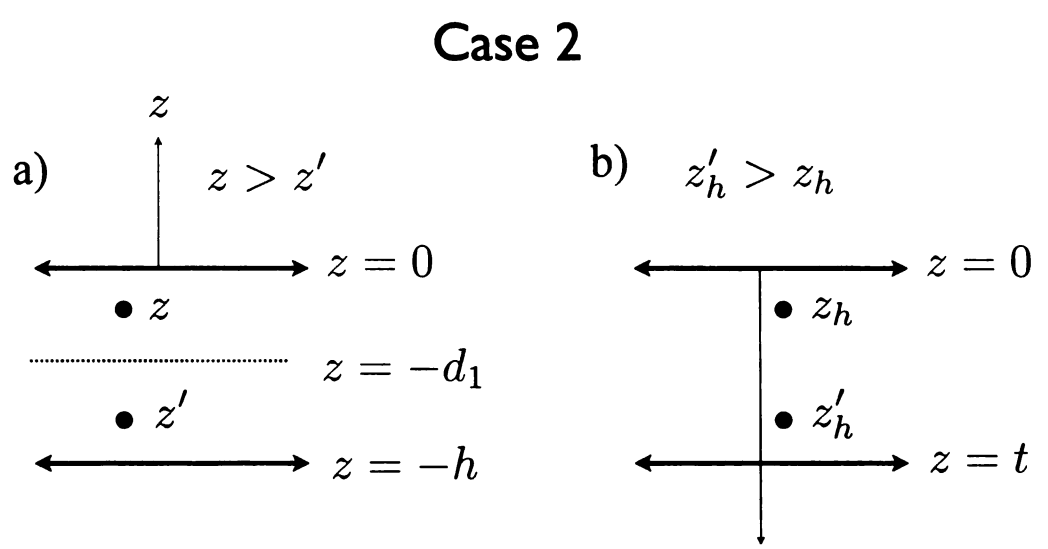


Figure C.2. Equivalent problem coordinate systems for a) this dissertation and b) Hanson's derivation. For case 2, where $z' < z$.

APPENDIX D

WAVEGUIDE CUTOFF FREQUENCIES FOR WR-90 WAVEGUIDE

Index (p)	Mode	f cutoff (GHz)
1	$TE_{1\,0}$	6.557
2	$TE_{3\,0}$	19.671
3	$TE_{1\,2}$	30.227
4	$TM_{1\,2}$	30.227
5	$TE_{5\,0}$	32.786
6	$TE_{3\,2}$	35.463
7	$TM_{3\,2}$	35.463
8	$TE_{5\,2}$	44.109
9	$TM_{5\,2}$	44.109
10	$TE_{7\,0}$	45.900
11	$TE_{7\,2}$	54.566
12	$TM_{7\,2}$	54.566
13	$TE_{9\,0}$	59.014
14	$TE_{1\,4}$	59.377
15	$TM_{1\,4}$	59.377
16	$TE_{3\,4}$	62.207
17	$TM_{3\,4}$	62.207
18	$TE_{9\,2}$	65.980
19	$TM_{9\,2}$	65.980
20	$TE_{5\,4}$	67.510
21	$TM_{5\,4}$	67.510
22	$TE_{11\,0}$	72.129
23	$TE_{7\,4}$	74.763
24	$TM_{7\,4}$	74.763
25	$TE_{11\,2}$	77.931
26	$TM_{11\,2}$	77.931
27	$TE_{9\,4}$	83.459
28	$TM_{9\,4}$	83.459
29	$TE_{13\,0}$	85.243
30	$TE_{1\,6}$	88.764
31	$TM_{1\,6}$	88.764

Table D.1. Index of waveguide modes and cutoff frequencies for WR-90 Waveguide

APPENDIX E

TRANSVERSE APERTURE MODE FUNCTIONS AND ASSOCIATED INTEGRALS

This appendix provides the reader with the description of the transverse aperture mode functions present in the aperture region. These mode functions are used in the two iris method. In addition, the calculation of the associated integrals and functions which are used in the two iris method are shown.

E.1 Transverse Aperture Mode Functions

The aperture region which exists in the two iris method may be thought of as a waveguide with different dimensions. The transverse aperture mode expansion functions are thus the well-known waveguide mode functions shown in Appendix A, with different dimensions for the waveguide walls.

For TE_z modes, the mode functions for the nth mode are

$$\begin{aligned}\vec{e}_n^{ap}(\vec{\rho}) =& K_{un\ vn}^{ap} \left[\hat{x} k_{Ayn} \cos\left(k_{Axn}(x-x_l)\right) \sin\left(k_{Ayn}(y-y_l)\right)\right. \\ & \left. -\hat{y}\left(k_{Axn}\right) \sin\left(k_{Axn}(x-x_l)\right) \cos\left(k_{Ayn}(y-y_l)\right)\right] \end{aligned} \tag{E.1}$$

$$\begin{aligned}\vec{h}_n^{ap}(\vec{\rho}) =& \frac{K_{un\ vn}^{ap}}{Z_n^{ap(TE)}} \left[\hat{x} k_{Axn} \sin\left(k_{Axn}(x-x_l)\right) \cos\left(k_{Ayn}(y-y_l)\right)\right. \\ & \left. +\hat{y} k_{Ayn} \cos\left(k_{Axn}(x-x_l)\right) \sin\left(k_{Ayn}(y-y_l)\right)\right] \end{aligned} \tag{E.2}$$

Since this is a TE_z mode, the directional impedance for the nth mode in the aperture filled with free space is

$$Z_n^{ap(TE)} = \frac{\omega\mu_0}{k_{zn}^{ap}}. \tag{E.3}$$

Additional terms used in this appendix are

$$k_{Axn} = \frac{u_n \pi}{Ax}, \qquad k_{Ayn} = \frac{v_n \pi}{Ay}, \tag{E.4}$$

$$k_{cAn}^2 = k_{Axn}^2 + k_{Ayn}^2, \qquad k_{zn} = \sqrt{k_0^2 - k_{cAn}^2}. \tag{E.5}$$

$$u_n = 0, 1, 2, ... \qquad v_n = 0, 1, 2, ..., \quad u_n + v_n > 0.$$

For TM_z modes, the mode functions are

$$\vec{e}_n^{ap}(\vec{\rho}) = N_{un\ vn}^{ap} \left[-\hat{x} k_{Axn} \cos\left(k_{Axn}(x - x_l)\right) \sin\left(k_{Ayn}(y - y_l)\right) \right.$$
$$\left. -\hat{y} k_{Ayn} \sin\left(k_{Axn}(x - x_l)\right) \cos\left(k_{Ayn}(y - y_l)\right) \right] \tag{E.6}$$

$$\vec{h}_n^{ap}(\vec{\rho}) = \frac{N_{un\ vn}^{ap}}{Z_n^{ap(TM)}} \left[\hat{x} k_{Ayn} \sin\left(k_{Axn}(x - x_l)\right) \cos\left(k_{Ayn}(y - y_l)\right) \right.$$
$$\left. -\hat{y} k_{Axn} \cos\left(k_{Axn}(x - x_l)\right) \sin\left(k_{Ayn}(y - y_l)\right) \right]$$
$$u_n = 1, 2, ... \qquad v_n = 1, 2, ... \tag{E.7}$$

The aperture impedance for the nth TM_z mode in the aperture filled with free space is defined as

$$Z_n^{ap(TM)} = \frac{k_{zn}^{ap}}{\omega \epsilon_0}. \tag{E.8}$$

The aperture normalization constants $N_{un\ vn}^{ap}$ and $K_{un\ vn}^{ap}$ are found in a similar manner to the waveguide constants found in Appendix A. They are given by

$$K_{un\ vn}^{ap} = \begin{cases} \dfrac{2}{k_{cAn}\sqrt{A_x A_y}} & u_n \neq 0,\ v_n \neq 0 \\ \\ \dfrac{\sqrt{2}}{k_{cn}\sqrt{A_x A_y}} & u_n = 0\ or\ v_n = 0 \end{cases} \tag{E.9}$$

By using a similar procedure, the normalization constant for the TM case is

$$N_{un\ vn}^{ap} = \frac{2}{k_{cAn}\sqrt{A_x A_y}}. \tag{E.10}$$

E.2 Calculation of $f_{xn}^{ap}(k_x, k_y)$, $f_{yn}^{ap}(k_x, k_y)$, $g_{xm}^{ap}(k_x, k_y)$, and $g_{ym}^{ap}(k_x, k_y)$

The calculation of the matrix elements of the matrix D in the two iris method requires the evaluation of the integrals involving the transverse aperture mode functions. These integrals are defined for the two iris method as

$$f_{xn}^{ap}(k_x, k_y) = \int_{\Omega_{ap}} h_{xn}^{ap}(\vec{\rho}\,')e^{-j\vec{k}\cdot\vec{\rho}\,'}ds', \tag{E.11}$$

$$f_{yn}^{ap}(k_x, k_y) = \int_{\Omega_{ap}} h_{yn}^{ap}(\vec{\rho}\,')e^{-j\vec{k}\cdot\vec{\rho}\,'}ds', \tag{E.12}$$

$$g_{xm}^{ap}(k_x, k_y) = \int_{\Omega_{ap}} h_{xm}^{ap}(\vec{\rho})e^{j\vec{k}\cdot\vec{\rho}}ds, \tag{E.13}$$

$$g_{ym}^{ap}(k_x, k_y) = \int_{\Omega_{ap}} h_{ym}^{ap}(\vec{\rho})e^{j\vec{k}\cdot\vec{\rho}}ds. \tag{E.14}$$

In order to evaluate (E.11) - (E.14), integrals involving sines and cosines must be evaluated. For the primed variables, the results of the following integrals are useful:

$$\int_{x_l}^{x_r} \sin\left(k_{Axn}(x' - x_l)\right)e^{-jk_x x'}dx' = k_{Axn}\frac{[cos(u_n\pi)e^{-jk_x x_r} - e^{-jk_x x_l}]}{k_x^2 - k_{Axn}^2} \tag{E.15}$$

$$\int_{y_l}^{y_t} \cos\left(k_{Ayn}(y' - y_l)\right)e^{-jk_y y'}dy' = -k_y\frac{[cos(v_n\pi)e^{-jk_y y_t} - e^{-jk_y y_l}]}{j(k_y^2 - k_{Ayn}^2)} \tag{E.16}$$

$$\int_{y_l}^{y_t} \sin\left(k_{Ayn}(y' - y_l)\right)e^{-jk_y y'}dy' = k_{Ayn}\frac{[cos(v_n\pi)e^{-jk_y y_t} - e^{-jk_y y_l}]}{(k_y^2 - k_{Ayn}^2)} \tag{E.17}$$

$$\int_{x_l}^{x_r} \cos\left(k_{Axn}(x' - x_l)\right) e^{-jk_x x'} dx' = -k_x \frac{[cos(u_n\pi)e^{-jk_x x_r} - e^{-jk_x x_l}]}{j(k_x^2 - k_{Axn}^2)} \quad \text{(E.18)}$$

The integrals over the unprimed coordinates are also needed. The evaluations for these integrals are

$$\int_{x_l}^{x_r} \sin\left(k_{Axm}(x - x_l)\right) e^{jk_x x} dx = k_{Axm} \frac{[cos(u_m\pi)e^{jk_x x_r} - e^{jk_x x_l}]}{(k_x^2 - k_{Axm}^2)} \quad \text{(E.19)}$$

$$\int_{y_l}^{y_t} \cos\left(k_{Aym}(y - y_l)\right) e^{jk_y y} dy = k_y \frac{[cos(v_m\pi)e^{jk_y y_t} - e^{jk_y y_l}]}{j(k_y^2 - k_{Aym}^2)} \quad \text{(E.20)}$$

$$\int_{y_l}^{y_t} \sin\left(k_{Aym}(y - y_l)\right) e^{jk_y y} dy = k_{Aym} \frac{[cos(v_m\pi)e^{jk_y y_t} - e^{jk_y y_l}]}{(k_y^2 - k_{Aym}^2)} \quad \text{(E.21)}$$

$$\int_{x_l}^{x_r} \cos\left(k_{Axm}(x - x_l)\right) e^{jk_x x} dx = k_x \frac{[cos(u_m\pi)e^{jk_x x_r} - e^{jk_x x_l}]}{j(k_x^2 - k_{Axm}^2)} \quad \text{(E.22)}$$

E.2.1 Function values for TE_z modes

The transverse aperture mode functions are different for TE_z modes and TM_z modes, as shown in (E.1), (E.2), (E.6), and (E.7). As a result, the functions $f_{xn}^{ap}(k_x, k_y)$ and $f_{yn}^{ap}(k_x, k_y)$, which are the source mode functions, and $g_{xm}^{ap}(k_x, k_y)$ and $g_{ym}^{ap}(k_x, k_y)$, which are the observer mode functions, will be different for the two types of modes. When the mode is a TE_z mode, (E.11) - (E.14) are evaluated using the TE_z mode function found in (E.2). The expression found in (E.2) can be decomposed into its scalar parts, $h_n^{ap}(\vec{\rho}) = \hat{x}h_x n^{ap}(\vec{\rho}) + \hat{y}h_x n^{ap}(\vec{\rho})$. The first source mode function,

$f_{xn}^{ap}(k_x, k_y)$ is then evaluated, producing

$$\begin{aligned} f_{xn}^{ap}(k_x, k_y) &= \int_{\Omega_{ap}} h_{xn}^{ap}(\vec{\rho}\,')e^{-j\vec{k}\cdot\vec{\rho}\,'}ds' \\ &= \frac{K_{un\ vn}^{ap}}{Z_n^{ap(TE)}} k_{Axn} \int_{x_l}^{x_r} \sin\left(k_{Axn}(x - x_l)\right)e^{-jk_x x'}dx'. \\ &\qquad \int_{y_l}^{y_t} \cos\left(k_{Ayn}(y - y_l)\right)e^{-jk_y y'}dy'. \end{aligned} \tag{E.23}$$

Replacing the integrals in (E.23) with (E.15) and (E.16) produces

$$\begin{aligned} f_{xn}^{ap}(k_x, k_y) = &- \frac{K_{un\ vn}^{ap}}{Z_n^{ap(TE)}} k_y k_{Axn}^2 \cdot \\ &\frac{[cos(u_n\pi)e^{-jk_x x_r} - e^{-jk_x x_l}][cos(v_n\pi)e^{-jk_y y_t} - e^{-jk_y y_l}]}{j(k_y^2 - k_{Ayn}^2)(k_x^2 - k_{Axn}^2)}. \end{aligned} \tag{E.24}$$

By following a similar procedure, the remaining functions are evaluated using the integrals in (E.15) - (E.22), producing

$$\begin{aligned} f_{yn}^{ap}(k_x, k_y) = &- \frac{K_{un\ vn}^{ap}}{Z_n^{ap(TE)}} k_x k_{Ayn}^2 \cdot \\ &\frac{[cos(u_n\pi)e^{-jk_x x_r} - e^{-jk_x x_l}][cos(v_n\pi)e^{-jk_y y_t} - e^{-jk_y y_l}]}{j(k_y^2 - k_{Ayn}^2)(k_x^2 - k_{Axn}^2)} \end{aligned} \tag{E.25}$$

$$\begin{aligned} g_{xm}^{ap}(k_x, k_y) = &\frac{K_{um\ vm}^{ap}}{Z_m^{ap(TE)}} k_y k_{Axm}^2 \cdot \\ &\frac{[cos(u_m\pi)e^{jk_x x_r} - e^{jk_x x_l}][cos(v_m\pi)e^{jk_y y_t} - e^{jk_y y_l}]}{j(k_y^2 - k_{Aym}^2)(k_x^2 - k_{Axm}^2)} \end{aligned} \tag{E.26}$$

$$g_{ym}^{ap}(k_x,k_y) = \frac{K_{um\ vm}^{ap}}{Z_m^{ap(TE)}} k_x k_{Aym}^2 \cdot \frac{[cos(u_m\pi)e^{jk_x x_r} - e^{jk_x x_l}][cos(v_m\pi)e^{jk_y y_t} - e^{jk_y y_l}]}{j(k_y^2 - k_{Aym}^2)(k_x^2 - k_{Axm}^2)}. \quad \text{(E.27)}$$

E.2.2 Function values for TM_z modes

The four functions $f_{xn}^{ap}(k_x,k_y)$, $f_{yn}^{ap}(k_x,k_y)$, $g_{xm}^{ap}(k_x,k_y)$, and $g_{ym}^{ap}(k_x,k_y)$, must also be evaluated for the case when the mode is a TM_z mode. By utilizing the integrals in (E.15) - (E.22), the functions are evaluated, producing

$$f_{xn}^{ap}(k_x,k_y) = -\frac{N_{un\ vn}^{ap}}{Z_n^{ap(TM)}} k_y k_{Axn} k_{Ayn} \cdot \frac{[cos(u_n\pi)e^{-jk_x x_r} - e^{-jk_x x_l}][cos(v_n\pi)e^{-jk_y y_t} - e^{-jk_y y_l}]}{j(k_y^2 - k_{Ayn}^2)(k_x^2 - k_{Axn}^2)} \quad \text{(E.28)}$$

$$f_{yn}^{ap}(k_x,k_y) = \frac{N_{un\ vn}^{ap}}{Z_n^{ap(TM)}} k_x k_{Axn} k_{Ayn} \cdot \frac{[cos(u_n\pi)e^{-jk_x x_r} - e^{-jk_x x_l}][cos(v_n\pi)e^{-jk_y y_t} - e^{-jk_y y_l}]}{j(k_y^2 - k_{Ayn}^2)(k_x^2 - k_{Axn}^2)} \quad \text{(E.29)}$$

$$g_{xm}^{ap}(k_x,k_y) = \frac{N_{um\ vm}^{ap}}{Z_m^{ap(TM)}} k_y k_{Axm} k_{Aym} \cdot \frac{[cos(u_m\pi)e^{jk_x x_r} - e^{jk_x x_l}][cos(v_m\pi)e^{jk_y y_t} - e^{jk_y y_l}]}{j(k_y^2 - k_{Aym}^2)(k_x^2 - k_{Axm}^2)} \quad \text{(E.30)}$$

$$g_{ym}^{ap}(k_x,k_y) = -\frac{N_{um\ vm}^{ap}}{Z_m^{ap(TM)}} k_x k_{Axm} k_{Aym} \cdot \frac{[cos(u_m\pi)e^{jk_x x_r} - e^{jk_x x_l}][cos(v_m\pi)e^{jk_y y_t} - e^{jk_y y_l}]}{j(k_y^2 - k_{Aym}^2)(k_x^2 - k_{Axm}^2)}. \quad \text{(E.31)}$$

E.3 Evaluation of Integrals Used in the Two Iris Method

The matrix equation that is described in section 7.6 requires the evaluation of two integrals that are combinations of the transverse mode functions from the aperture region, which are given in this appendix, and the waveguide region, which are given in Appendix A.

E.3.1 Integral used in D_2 and D_3

Calculating the matrix elements for the matrices D_2 and D_3 requires the evaluation of the integral found in (7.39), which is given by

$$\int_{\Omega_{ap}} \vec{e}_m^{wg}(\vec{\rho}) \cdot \vec{e}_n^{ap}(\vec{\rho}) ds. \tag{E.32}$$

Four possible cases exist for the evaluation of this integral, depending on whether the mode is TE_z or TM_z. The first case, which is the coupling between the $TE^{wg}_{u_m v_m}$ mode and the $TE^{ap}_{u_n v_n}$ mode, is evaluated here.

By using the mode functions in (A.1) and (E.1), the integral may be written as

$$\begin{aligned}
&\int_{\Omega_{ap}} \vec{e}_m^{wg(TE)}(\vec{\rho}) \cdot \vec{e}_n^{ap(TE)}(\vec{\rho}) ds = K^{wg}_{u_m v_m} K^{ap}_{u_n v_n} \cdot \\
&\int_{y_l}^{y_t} \int_{x_l}^{x_r} \left[\hat{x} k_{ym} \cos(k_{xm} x) \sin(k_{ym} y) - \hat{y}(k_{xm}) \sin(k_{xm} x) \cos(k_{ym} y)\right] \cdot \\
&\qquad \left[\hat{x} k_{Ayn} \cos(k_{Axn}(x - x_l)) \sin(k_{Ayn}(y - y_l)) \right. \\
&\qquad \left. -\hat{y} k_{Axn} \sin(k_{Axn}(x - x_l)) \cos(k_{Ayn}(y - y_l))\right] dx\, dy
\end{aligned} \tag{E.33}$$

By carrying out the dot product, (E.33) can be rearranged, yielding

$$\int_{\Omega_{ap}} \vec{e}_m^{wg(TE)}(\vec{\rho}) \cdot \vec{e}_n^{ap(TE)}(\vec{\rho}) ds = K_{u_m v_m}^{wg} K_{u_n v_n}^{ap} \cdot$$

$$\left\{ k_{ym} k_{Ayn} \int_{x_l}^{x_r} \cos\left(k_{xm} x\right) \cos\left(k_{Axn}(x - x_l)\right) dx \int_{y_l}^{y_t} \sin\left(k_{ym} y\right) \sin\left(k_{Ayn}(y - y_l)\right) dy \right.$$

$$\left. - k_{xm} k_{Axn} \int_{x_l}^{x_r} \sin\left(k_{xm} x\right) \sin\left(k_{Axn}(x - x_l)\right) dx \int_{y_l}^{y_t} \cos\left(k_{ym} y\right) \cos\left(k_{Ayn}(y - y_l)\right) d_y \right\}. \tag{E.34}$$

The integrals in (E.34) are standard integrals integrals that are needed to evaluate not only this case, but also other cases as well. To simplify the notation for the other cases, these integrals take a common form, where the expression for these definite integrals are [64]

$$\begin{aligned} \Phi_1(A, B, C, D, \alpha_1, \alpha_2) &= \int_{\alpha_1}^{\alpha_2} \cos\left(Ax + B\right) \cos\left(Cx + D\right) dx \\ &= \frac{\sin\left[(A - C)x + (B - D)\right]}{2(A - C)} + \frac{\sin\left[(A + C)x + (B + D)\right]}{2(A + C)} \Bigg|_{\alpha_1}^{\alpha_2} \end{aligned} \tag{E.35}$$

$$\begin{aligned} \Phi_2(A, B, C, D, \alpha_1, \alpha_2) &= \int_{\alpha_1}^{\alpha_2} \sin\left(Ax + B\right) \sin\left(Cx + D\right) dx \\ &= \frac{\sin\left[(A - C)x + (B - D)\right]}{2(A - C)} - \frac{\sin\left[(A + C)x + (B + D)\right]}{2(A + C)} \Bigg|_{\alpha_1}^{\alpha_2} \end{aligned} \tag{E.36}$$

Using the expressions found in (E.35) and (E.36), the integral for Case 1 is written

as

$$\int_{\Omega_{ap}} \vec{e}_m^{wg(TE)}(\vec{\rho}) \cdot \vec{e}_n^{ap(TE)}(\vec{\rho}) ds = K^{wg}_{u_m v_m} K^{ap}_{u_n v_n} \cdot$$

$$\Big\{ k_{ym} k_{Ayn} \Phi_1(k_{xm}, 0, k_{Axn}, -k_{Axn} x_l, x_l, x_r) \Phi_2(k_{ym}, 0, k_{Ayn}, -k_{Ayn} y_l, y_l, y_t)$$

$$- k_{xm} k_{Axn} \Phi_1(k_{ym}, 0, k_{Ayn}, -k_{Ayn} y_l, y_l, y_t) \Phi_2(k_{xm}, 0, k_{Axn}, -k_{Axn} x_l, x_l, x_r) \Big\} \tag{E.37}$$

The remaining three cases are evaluated using the correct mode functions found in (A.1), (A.7), (E.1) and (E.6). In addition, the expressions for the definite integrals found in (E.35) and (E.36) are used in each case. The results are shown in section 7.6.2.

E.3.2 Calculation of the Integral used in D_4 and b_2

Calculating the matrix elements for the matrices D_4 and b_2 requires the evaluation of the integral found in (7.40). This equation is

$$\int_{\Omega_{ap}} \vec{h}_m^{ap}(\vec{\rho}) \cdot \vec{h}_n^{wg}(\vec{\rho}) ds. \tag{E.38}$$

Similar to the integral described in section E.3.1 four possible cases exist for the evaluation of this integral, depending on whether the mode is TE_z or TM_z. The first case, which is the coupling between the $TE^{ap}_{u_m v_m}$ mode and the $TE^{wq}_{u_n v_n}$ mode, is evaluated here.

By using the mode functions in (E.2) and (A.2), the integral may be written as

$$\int_{\Omega_{ap}} \vec{h}_m^{ap}(\vec{\rho}) \cdot \vec{h}_n^{wg}(\vec{\rho}) ds = \frac{K_{u_m v_m}^{wg}}{Z_m^{wg(TE)}} \frac{K_{u_n v_n}^{ap}}{Z_n^{ap(TE)}} \cdot$$

$$\int_{y_l}^{y_t} \int_{x_l}^{x_r} \left[\hat{x} k_{Axm} \sin\left(k_{Axm}(x - x_l)\right) \cos\left(k_{Aym}(y - y_l)\right) \right. \tag{E.39}$$

$$\left. + \hat{y} k_{Aym} \cos\left(k_{Axm}(x - x_l)\right) \sin\left(k_{Aym}(y - y_l)\right) \right] \cdot \tag{E.40}$$

$$\left[\hat{x} k_{xn} \sin\left(k_{xn} x\right) \cos\left(k_{yn} y\right) + \hat{y} k_{yn} \cos\left(k_{xn} x\right) \sin\left(k_{yn} y\right) \right] dx\, dy. \tag{E.41}$$

This equation can be rewritten as

$$\int_{\Omega_{ap}} \vec{h}_m^{ap}(\vec{\rho}) \cdot \vec{h}_n^{wg}(\vec{\rho}) ds = \frac{K_{u_m v_m}^{wg}}{Z_m^{wg(TE)}} \frac{K_{u_n v_n}^{ap}}{Z_n^{ap(TE)}} \cdot$$

$$\left\{ k_{xn} k_{Axm} \int_{x_l}^{x_r} \sin\left(k_{xn} x\right) \sin\left(k_{Axm}(x - x_l)\right) dx \right.$$

$$\cdot \int_{y_l}^{y_t} \cos\left(k_{yn} y\right) \cos\left(k_{Aym}(y - y_l)\right) dy$$

$$+ k_{yn} k_{Aym} \int_{x_l}^{x_r} \cos\left(k_{xn} x\right) \cos\left(k_{Axm}(x - x_l)\right) dx$$

$$\left. \cdot \int_{y_l}^{y_t} \sin\left(k_{yn} y\right) \sin\left(k_{Aym}(y - y_l)\right) dy \right\}. \tag{E.42}$$

Note that the integrals are the definite integrals in (E.35) and (E.36). Using these,

the solution for the first case is

$$\int_{\Omega_{ap}} \vec{h}_m^{ap}(\vec{\rho}) \cdot \vec{h}_n^{wg}(\vec{\rho}) ds = \frac{K_{u_m v_m}^{wg}}{Z_m^{wg(TE)}} \frac{K_{u_n v_n}^{ap}}{Z_n^{ap(TE)}} \cdot$$

$$k_{xn} k_{Axm} \Phi_1(k_{Aym}, -k_{Aym} y_l, k_{yn}, 0, y_l, y_t) \Phi_2(k_{Axm}, -k_{Axm} x_l, k_{xn}, 0, x_l, x_r)$$

$$k_{yn} k_{Aym} \Phi_1(k_{Axm}, -k_{Axm} x_l, k_{xn}, 0, x_l, x_r) \Phi_2(k_{Aym}, -k_{Aym} y_l, k_{yn}, 0, y_l, y_t). \tag{E.43}$$

The remaining three cases may be evaluated using the correct mode functions found in (A.2), (A.8), (E.2) and (E.7). The expressions for the definite integrals found in (E.35) and (E.36) are used in each case. The results are shown in section 7.6.3.

APPENDIX F

NOMINAL MATERIAL PARAMETERS USED IN SIMULATIONS AND EXTRACTIONS

Frequency (GHz)	ϵ_r'	ϵ_r''	μ_r'	μ_r''
8..20	2.65092	0.007681	1	0
8.41	2.649761	0.007862	1	0
8.62	2.649316	0.007008	1	0
8.83	2.649935	0.008678	1	0
9.04	2.648905	0.008837	1	0
9.25	2.647959	0.01015	1	0
9.46	2.648739	0.010459	1	0
9.67	2.647993	0.012687	1	0
9.88	2.649164	0.009484	1	0
10.09	2.647778	0.010399	1	0
10.30	2.648175	0.008695	1	0
10.51	2.646818	0.009814	1	0
10.72	2.645332	0.012135	1	0
10.93	2.645869	0.012168	1	0
11.14	2.645337	0.01337	1	0
11.35	2.645205	0.012309	1	0
11.56	2.64418	0.012534	1	0
11.77	2.643859	0.011299	1	0
11.98	2.641871	0.011958	1	0
12.19	2.644393	0.016008	1	0
12.40	2.641839	0.013981	1	0

Table F.1. Nominal material parameters for Plexiglass, $\epsilon = \epsilon_0(\epsilon_r' - j\epsilon_r'')$ and $\mu = \mu_0(\mu_r' - j\mu_r'')$. These data were obtained using the waveguide T/R method. Data provided by Captain Milo Hyde IV from the Air Force Institute of Technology, Wright-Patterson AFB, Dayton, OH.

Frequency (GHz)	ϵ_r'	ϵ_r''	μ_r'	μ_r''
8.20	3.04000	0.04560	1	0
8.41	3.04000	0.04560	1	0
8.62	3.04000	0.04560	1	0
8.83	3.04000	0.04560	1	0
9.04	3.04000	0.04560	1	0
9.25	3.04000	0.04560	1	0
9.46	3.04000	0.04560	1	0
9.67	3.04000	0.04560	1	0
9.88	3.04000	0.04560	1	0
10.09	3.04000	0.04560	1	0
10.30	3.04000	0.04560	1	0
10.51	3.04000	0.04560	1	0
10.72	3.04000	0.04560	1	0
10.93	3.04000	0.04560	1	0
11.14	3.04000	0.04560	1	0
11.35	3.04000	0.04560	1	0
11.56	3.04000	0.04560	1	0
11.77	3.04000	0.04560	1	0
11.98	3.04000	0.04560	1	0
12.19	3.04000	0.04560	1	0
12.40	3.04000	0.04560	1	0

Table F.2. Nominal material parameters for Nylon, $\epsilon = \epsilon_0(\epsilon_r' - j\epsilon_r'')$ and $\mu = \mu_0(\mu_r' - j\mu_r'')$. These values were estimated from data found in [6], Figures 27 and 28, and were used in simulations and two layer method extractions.

Frequency (GHz)	ϵ_r'	ϵ_r''	μ_r'	μ_r''
8.20	2.74000	0.02055	1	0
8.41	2.74000	0.02055	1	0
8.62	2.74000	0.02055	1	0
8.83	2.74000	0.02055	1	0
9.04	2.74000	0.02055	1	0
9.25	2.73000	0.02075	1	0
9.46	2.73000	0.02075	1	0
9.67	2.73000	0.02075	1	0
9.88	2.73000	0.02075	1	0
10.09	2.73000	0.02102	1	0
10.30	2.73000	0.02102	1	0
10.51	2.73000	0.02075	1	0
10.72	2.73000	0.02048	1	0
10.93	2.72000	0.02013	1	0
11.14	2.72000	0.01986	1	0
11.35	2.72000	0.01958	1	0
11.56	2.72000	0.01986	1	0
11.77	2.72000	0.02013	1	0
11.98	2.72000	0.02040	1	0
12.19	2.72000	0.02067	1	0
12.40	2.72000	0.02040	1	0

Table F.3. Nominal material parameters for PVC, $\epsilon = \epsilon_0(\epsilon_r' - j\epsilon_r'')$ and $\mu = \mu_0(\mu_r' - j\mu_r'')$. These values were estimated from data found in [6], Figures 27 and 28, and were used in simulations and two layer method extractions.

Frequency (GHz)	ϵ_r'	ϵ_r''	μ_r'	μ_r''
8.20	21.863856	0.389687	2.08774	2.537062
8.41	21.883929	0.318737	2.029646	2.506912
8.62	21.920507	0.324559	1.985723	2.484385
8.83	21.967465	0.333066	1.933827	2.462539
9.04	21.964692	0.343633	1.898906	2.450044
9.25	22.001906	0.353791	1.855602	2.428029
9.46	22.031315	0.345285	1.806961	2.414185
9.67	21.988025	0.368626	1.760265	2.401059
9.88	22.007396	0.332044	1.711081	2.376234
10.09	22.036094	0.33191	1.667876	2.353727
10.30	22.050992	0.273677	1.615461	2.321913
10.51	22.097687	0.308843	1.59073	2.304856
10.72	22.140512	0.34663	1.556913	2.284405
10.93	22.147144	0.397863	1.522424	2.263506
11.14	22.129636	0.390059	1.481594	2.249675
11.35	22.100289	0.39625	1.440794	2.234218
11.56	22.030004	0.440157	1.41081	2.212991
11.77	22.103877	0.356636	1.361639	2.189474
11.98	22.061608	0.314166	1.325887	2.173054
12.19	21.958816	0.30133	1.296255	2.153083
12.40	22.24349	0.166144	1.245418	2.109965

Table F.4. Nominal material parameters for FGM40, $\epsilon = \epsilon_0(\epsilon_r' - j\epsilon_r'')$ and $\mu = \mu_0(\mu_r' - j\mu_r'')$. These data were obtained using the waveguide T/R method. Data provided by Captain Milo Hyde IV from the Air Force Institute of Technology, Wright-Patterson AFB, Dayton, OH.

Frequency (GHz)	ϵ_r'	ϵ_r''	μ_r'	μ_r''
8.20	1.50	0.000001	1	0
8.41	1.50	0.000001	1	0
8.62	1.50	0.000001	1	0
8.83	1.50	0.000001	1	0
9.04	1.50	0.000001	1	0
9.25	1.50	0.000001	1	0
9.46	1.50	0.000001	1	0
9.67	1.50	0.000001	1	0
9.88	1.50	0.000001	1	0
10.09	1.50	0.000001	1	0
10.30	1.50	0.000001	1	0
10.51	1.50	0.000001	1	0
10.72	1.50	0.000001	1	0
10.93	1.50	0.000001	1	0
11.14	1.50	0.000001	1	0
11.35	1.50	0.000001	1	0
11.56	1.50	0.000001	1	0
11.77	1.50	0.000001	1	0
11.98	1.50	0.000001	1	0
12.19	1.50	0.000001	1	0
12.40	1.50	0.000001	1	0

Table F.5. Material parameters for Material 1.5, $\epsilon = \epsilon_0(\epsilon_r' - j\epsilon_r'')$ and $\mu = \mu_0(\mu_r' - j\mu_r'')$. These values are for a fictitious material and are used in the sensitivity analysis to simulate a low loss, low-dielectric constant material

BIBLIOGRAPHY

BIBLIOGRAPHY

[1] A. von Hippel, ed., *Dielectric Materials and Applications,* MIT Press, Cambridge, Massachusetts, 1961.

[2] R. J. Cook, R. G. Jones, C. B. Rosenberg, "Comparison of Cavity and Open-Resonator Measurements of Permittivity and Loss Angle at 35 GHz," IEEE Trans. Instrum. Meas., vol. 23, no. 4, pp. 438-442, Dec. 1974.

[3] *Agilent Basics of Measuring the Dielectric Properties of Materials: Application Note,* Aigilent Technologies, 2006.

[4] J. Baker-Jarvis, M. D. Janezic, J. S. Grosvenor, and R. G. Geyer, *Transmission/Reflection and Short-Circuit Methods for Measuring Permitivity and Permeability,* NIST Technical Note 1355-R, Dec. 1993.

[5] A. Bogle, M. Havrilla, D. Nyquist, L. Kempel, and E. Rothwell, "Electromagnetic Material Characterization using a Partially-Filled Rectangular Waveguide," , J. of Electromagn. Waves and Appl., Vol. 19, No. 10, pp. 1291-1306, 2005.

[6] J. Baker-Jarvis, M. D. Janezic, B. F. Riddle, R. T. Johnk, P. Kabos, C. L. Holloway, R. G. Geyer, and C. A. Grosvenor, *Measuring the Permittivity and Permeability of Lossy Materials: Solids, liquids and Negative-Index Materials,* NIST Technical Note 1336, Feb. 2005.

[7] B. Kang, J. Cho, C. Cheon, and Y. Kwon, "Nondestructive Measurement of Complex Permittivity and Permeability Using Multilayered Coplanar Waveguide Structures," IEEE Microw. Wireless Compon. Lett., vol. 15, no. 5, May 2005.

[8] M. A. Stuchly, S. S. Stuchly, "Coaxial Line Reflection Methods for Measuring Dielectric Properties of Biological Substances at Radio and Microwave Frequencies-A Review," IEEE Trans. Instrum. Meas., vol. IM-29, no. 3, pp.176-183, Sept. 1980.

[9] L. Chen, C. Ong, C. Neo, V. V. Varadan, and V. K. Varadan, *Microwave Electronics: Measurement and Materials Characterisation,* John Wiley and Sons, West Sussex, England, 2004.

[10] B. Clarke, ed., *A Guide to the Characterization of Dielectric Materials at RF and Microwave Frequencies,* Institute of Measurement and Control, London, 2003.

[11] J. Baker-Jarvis, R. G. Geyer, "Dielectric Characterization of Low-loss Materials: A Comparison of Techniques.," IEEE Trans. Dielect. and Elect. Ins, vol. 5, no. 4, pp. 571-577, 1988.

[12] E. J. Vanzura, J. Baker-Jarvis, J. H. Grosvenor, M. D. Janezic, "Intercomparison of Permittivity Measurements Using the Transmission/Reflection Method in 7-mm Coaxial Transmission Lines," IEEE Trans. Microwave Theory Tech. vol. 42, no. 11, pp. 2063-2070, Nov. 1994.

[13] H. Bussey, "Measurement of RF properties of Materials-A Survey," Proc. IEEE, vol. 55, no. 6, pp. 1046-1053, June 1967.

[14] R. Zoughi, *Microwave Non-Destructive Testing and Evaluation*, Kluwer Academic Publishers, The Netherlands, 2000.

[15] A. M. Nicolson, G. F. Ross, "Measurement of the Intrinsic Properties of Materials by Time-Domain Techniques," IEEE Trans. on Instrum. Meas., vol. IM-19, pp. 377-82, Nov. 1970.

[16] W. B. Weir, "Automatic Measurement of Complex Dielectric Constant and Permeability at Microwave Frequencies," Proc. IEEE, vol. 62, no. 1, pp. 33-36, Jan. 1974.

[17] D. Lemaire, D. Cros, H. Jallageas, and P. Guillon, "Material characterisation from -160°C up to 800°C in centimeter and millimeter wavelength frequency band," 1996 Conference on Precision Electromagnetic Measurements Digest, pp. 72-73, 1996.

[18] V. V. Varadan, R. D. Hollinger, D. K. Ghodgaonkar, V. K. Varadan, "Free-Space, Broadband Measurements of High- Temperature, Complex Dielectric Properties at Microwave Frequencies," IEEE Trans. Instrum. Meas., vol. 40, no. 5, pp. 842 - 846, Oct. 1991.

[19] D. K. Ghodgaonkar, V. V. Varadan, and V. K. Varadan, "A Free Space Method for Measurement of Dielectric Constant and Loss Tangent at Microwave Frequencies, IEEE Trans. Instrum. Meas., vol. 37, pp. 789-793, June 1989.

[20] H. H. Ouslimani, R. Abdeddaim, and A. Priou, "Free-Space Electromagnetic Characterization of Materials for Microwave and Radar Applications," Progress In Electromagnetics Research Symposium 2005, Hangzhou, China, 2005.

[21] V. V. Varadan, K. A. Jose, V. K. Varadan, "In situ Microwave Characterization of Nonplanar Dielectric Objects," IEEE Trans. Microwave Theory Tech. vol. 48, no. 3, pp. 388-394, Mar. 2000.

[22] M.H. Umari, D. K. Ghodgaonkar, V. V. Varadan, V. K. Varadan, "A Free-Space Bistatic Calibration Technique for the Measurement of Parallel and Perpendicular Reflection Coefficients of Planar Samples," IEEE Trans. Instrum. Meas., vol. 40, no. 1, pp. 19 - 24, Feb. 1991.

[23] F. Smith, B. Chambers, and J. Bennett, "Methodology for accurate free-space chracterisation of radar absorbing materials," IEE Proc.-Sci. Meas. Technol., vol 141, no. 6, pp. 538 - 546, Nov. 1994.

[24] A. L. Cullen, "A new free-wave method for ferrite measurement at millimeter wavelengths," Radio Sci., vol. 22, no. 7, pp. 11681170, 1987.

[25] J. R. Mosig, J. E. Besson, M. G. Fabry, and F. E. Gardiol, "Reflection of an open-ended coaxial line and application to non-destructive measurement of materials," IEEE Trans. Instrum. Meas., vol. IM-30, , pp. 46-51, Oct. 1991.

[26] J. Baker-Jarvis, M. D. Janezic, P.D. Domich, R. G. Geyer, "Analysis of an open-ended coaxial probe with lift-off for nondestructive testing," IEEE Trans. Instrum. Meas., vol. 43, no. 5, pp.711-718, Oct 1994.

[27] S. I. Ganchev, N. Qaddoumi, S. Bakhtiari, R. Zoughi, "Calibration and measurement of dielectric properties of finite thickness composite sheets with open-ended coaxial sensors," IEEE Trans. Instrum. Meas., vol. 44, no. 6, pp.1023-1029, Dec 1995.

[28] S. Bringhurst, M. F. Iskander, and M. J. White,"Thin sample measurements and error analysis of high temperature coaxial dielectric probes," IEEE Microwave Theory Tech., vol. 45, pp. 20732083, Dec. 1997.

[29] S. I. Ganchev, "Nondestructive Microwave Measurements of Dielectric materials," 12th International Conference on Microwaves and Radar, 1998. MIKON '98, vol.3, pp.687-691, May 20-22, 1998.

[30] O. Tantot, M. Chatard-Moulin, and P. Guillon, "Measurement of Complex Permittivity and Permeability and Thickness of Multilayered Medium by an Open-Ended Waveguide Method," IEEE Trans. Instrum. Meas., vol. 46, no. 2, pp. 519 - 522, April 1997.

[31] C.W. Chang, K.M. Chen and J. Qian, "Nondestructive Measurements of Complex Tensor Permittivity of Anisotropic Materials Using a Waveguide Probe System," IEEE Trans. Microwave Theory Tech., vol. 44, no. 7, pp. 1081-1090, July 1996.

[32] V. Teodoridis, T. Sphicopoulos, F. E. Gardiol, "The Reflection from an Open-Ended Rectangular Waveguide Terminated by a Layered Dielectric Medium," IEEE Trans. Microwave Theory Tech., vol. 33, no. 5, pp. 359-366, May 1985.

[33] S. Bakhtiari, S. Ganchev, and R. Zoughi, "Open-Ended Rectangular Waveguide for Nondestructive Thickness Measurement and Variation Detection of Lossy Dielectric Slabs Backed by a Conducting Plate," IEEE Trans. Instrum. Meas., vol. 42, no. 1, pp. 19 - 23, February 1993.

[34] N. Maode, S. Yong, Y Jinkui, F. Chrnpung, and X. Deming, "An Improved Open-Ended Waveguide Measurement Technique on Parameters ϵ_r and μ_r of High-Loss Materials," IEEE Trans. Instrum. Meas., vol 47, no. 2, pp. 476 - 481, Apr. 1999.

[35] J. W. Stewart and M. J. Havrilla, "Electromagnetic Characterization of a Magnetic Material Using an Open-Ended Waveguide Probe and a Rigorous Full-Wave Multimode Model," J. of Electromagn. Waves and Appl., vol. 20, no. 14, pp. 2037-2052, 2006.

[36] J. Stewart, "Simultaneous Extraction of the Permittivity and Permeability of Conductor-Backed Lossy Materials Using Open-Ended Waveguide Probes," Ph.D. Dissertation, Air Force Institute of Technology, 2006.

[37] K. Bois, A. Benally, and R. Zoughi, "Multimode Solution for the Reflection Properties of an Open-Ended Rectangular Waveguide Radiating into a Dielectric Half-Space: The Forward and Inverse Problems," IEEE Trans. Instrum. Meas., vol. 48, no. 6, pp. 1131 - 1140, December 1999.

[38] C.W. Chang, K.M. Chen and J. Qian, "Nondestructive Determination of Electromagnetic Parameters of Dielectric Materials as X-Band Frequencies Using a Waveguide Probe System," IEEE Trans. Instrum. Meas., vol. 46, no. 5, pp. 1084 - 1092, October 1997.

[39] M.W. Hyde IV, and M.J. Havrilla "A Nondestructive Technique for Determining Complex Permittivity and Permeability of Magnetic Sheet Materials Using Two

Flanged Rectrangular Waveguides," Progress in Electromagn. Research., PIER 79, pp. 367-386, 2008.

[40] A. Bogle, "Electromagnetic Material Characterization of a PEC Backed Lossy Simple Media Using a Rectangular Waveguide Resonant Slot Technique," Ph.D. Dissertation, Michigan State Universisy, East Lansing, MI, 2007.

[41] R.E. Collin, *Field Theory of Guided Waves*, Second Edition, IEEE Press, Piscataway, NJ, 1991.

[42] R.F. Harrington, *Time-Harmonic Electromagnetic Fields*, IEEE Press, Pisctaway, NJ, 2001.

[43] E.J. Rothwell and M.J. Cloud, *Electromagnetics*, CRC Press, Boca Raton, Florida, 2001.

[44] R.F. Harrington, *Field Computation by Moment Methods*, MacMillan, New Yok, 1968.

[45] G. W. Hanson, and A. B. Yakolev, *Operator Theory for Electromagnetics: An Introduction*, Springer-Verlag, New York, 2001.

[46] M. Blischke, "Broadband Analysis of Radiating , Receiving and Scattering Characteristics of Microstrip Antennas and Arrays," Ph.D. Dissertation, Michigan State Universisy, East Lansing, MI, 1989.

[47] A. Papoulis, *The Fourier Integral and its Applications*, McGraw-Hill, New York, 1962.

[48] R.V. Churchill and J.W. Brown, *Complex Variables and Applications*, Fourth Edition, McGraw-Hill, New York, 1984.

[49] D. Marcuse, *Theory of Dielectric Optical Waveguides*, Academic Press, New York, 1974.

[50] W. Press, B. Flannery, S. Teukolsky, and W. Vetterling, *Numerical Recipes*, Cambridge University Press, Cambridge, 1986.

[51] R. Piessens, et. al., *Quadpack : a subroutine package for automatic integration*, Springer-Verlag, Berlin, 1983.

[52] S. G. Rabinovich, *Measurement Errors: Theory and Practice*, American Institute of Physics, New York, NY, 1993.

[53] C. Wilker, and D. Schreurs, "Guest Editorial on Measurement", IEEE Microwave Magazine., vol. 8, no. 4, pp. 6–13, Aug. 2007.

[54] N. Ridler,, B. Lee, J. Martens, K. Wong, "Measurement, Uncertainty, Traceability, and the GUM", IEEE Microwave Magazine., vol. 8, no. 4, pp. 44–53, Aug. 2007.

[55] H. D. Young, *Statistical Treatment of Experimental Data*, McGraw-Hill, New York, 1962.

[56] G. Dahlquist, and A. Bjorck, *Numerical Methods*, Prentice-Hall, Englewood Cliffs, NJ, 1974.

[57] J. Meeusen, "Error Analysis of Material Characterization Using a Wave Guide Applicator", M.S. Dissertation, Michigan State University, East Lansing, MI, 2004.

[58] C. Gerald, *Applied Numerical Analysis, Second Edition*, Addison-Wesley, Reading, MA, 1978.

[59] Random.org, http://www.random.org/, last accessed 10/28/2008.

[60] S.P. Dorey, M.J. Havrilla, L.L. Frasch, C. Choi, and E. J. Rothwell,"Stepped-Waveguide Material-Characterization Technique," IEEE Antennas Prop. Mag., vol. 46, no. 1, pp. 170-175, February 2004.

[61] Liu, K., Balanis, C.A., Birtcher, C.R., Barber, G.C., "Analysis of pyramidal horn antennas using moment methods," IEEE Trans. Antennas Propagat., vol 41, no. 10, pp. 1379 - 1389, 1993

[62] Stremler, I., *Communication Systems for Engineers*, Prentice Hall, New York, 1984.

[63] D. K. Ghodgaonkar, V. V. Varadan, and V. K. Varadan, "Free-Space Measurement of Complex Permittivity and Complex Permeability of Magnetic Materials at Microwave Frequencies, IEEE Trans. Instrum. Meas., vol. 39, pp. 387-394, April 1990.

[64] I Gradsteyn, and I. Resnick, *Table of Integrals, Series, and Products*, Academic Press, San Diego, 2000.

[65] M. Afsar, J.B. Birch, R.N. Clarke, Ed. G.W. Chantry, "Measurement of the Properties of Materials," Proc. IEEE, vol. 74, no. 1, pp. 183-199. Jan 1986.

[66] J. Encinar, and J. Rebollar, "Convergence of Numerical Solutions of Open-Ended Waveguide by Modal Analysis and Hybrid Modal-Spectral Techniques," IEEE Trans. Microwave Theory Tech., vol. MTT-34, no. 7, pp. 809-814, July 1986.

MICHIGAN STATE UNIVERSITY LIBRARIES
3 1293 03063 2941